Experimental Investigation of Drainage Effects Around Monopiles in Sand



Rory Fleminger

St. Edmund Hall

A thesis submitted for the degree of
Doctor of Philosophy

Department of Engineering Science
University of Oxford

Trinity 2025

Declaration

I declare that this report is entirely my own work and, except where stated, describes my own research.

Rory Fleminger
St. Edmund Hall

Acknowledgements

I would first like to thank my supervisors, Chris Martin and Orestis Adamidis. Without their expert guidance, unlimited patience, and constant enthusiasm, this would not have been possible. Orestis deserves special thanks for accompanying me on my research trip to Zurich, despite his second baby arriving imminently. Thank you both for giving me this opportunity.

I would like to express my gratitude to the team at Fugro for their support throughout numerous tests and special requests, particularly Tim, Ed, Nicole, Neil, and Niall. I am very grateful for the help you gave me, even though you had your own things to do.

Thank you to the whole team at ETH. The centrifuge experiments were highly successful and could not have been accomplished without your support. It was a privilege to work in your laboratory over the summer, and I felt exceptionally welcome. I extend my gratitude particularly to Thanassi, Liam, Ioannis, and Ralf.

Thank you to all my friends in Oxford and beyond, special mention to the Oxford group, who shared the DPhil journey with me.

Finally, thank you to Abi and my family for the emotional, financial, and nutritional support.

Abstract

The current trend in Offshore Wind Turbine (OWT) design is towards fewer, larger wind turbines in windfarms, with foundations regularly exceeding 10 m in diameter. Significant research has been conducted on monopiles with a low L/D ratio ($L/D \approx 3-6$). For monopiles in sandy soils, this research primarily relies on results from laboratory model tests or soil element tests conducted under fully drained conditions, which may not accurately reflect actual conditions. It is predicted that the drained assumption is likely to be inaccurate for large-diameter monopiles; a limited number of investigations in the literature predict a partially drained soil response. It has been suggested that the degree to which the diameter impacts drainage conditions is summarised through the non-dimensional factor $MkT/\gamma_w D^2$, where M is the soil stiffness, k is the permeability of the soil, T is the loading period, γ_w is the unit weight of water, and D is the pile diameter. However, further research is needed to verify this dimensionless drainage factor.

This thesis presents the results of an experimental campaign examining the impact and occurrence of partial drainage during cyclic loading of sands, and foundations in sand. The experimental campaign included a series of benchmark triaxial tests, advanced cyclic triaxial tests involving partial drainage, and centrifuge model tests examining the behaviour of large diameter monopiles. Results from the benchmark tests served as a baseline for subsequent testing and provided calibration data for the SANISAND-MS soil constitutive model. The findings aligned with much of the literature examining long-term cyclic triaxial loading of sands. Partially drained cyclic triaxial tests investigated the impact of partial drainage on clean and silty sand samples. The results indicated a clear increase in strain accumulation for partially drained tests compared with the fully drained benchmark results. This effect was more pronounced during tests on silty sand samples, which experienced a higher pore pressure response due to the collapsible fabric.

The centrifuge testing campaign examined the response of large-diameter monopiles in saturated sand under cyclic loading, focusing on the drainage regime. The test schedule facilitated a parametric investigation into the dimensionless drainage factor mentioned above, the results of which validated the hypothesis. Storm load testing revealed partially drained conditions in all cases. The loading history, however, altered the response. Where loads exceeded previously applied levels, pore pressure accumulation was observed. Conversely, where loads were equal to or lower than previous levels, no accumulation was observed; however, significant pore pressure oscillation remained present. Furthermore, an important observation regarding the impact of negative excess pore pressure on soil stiffness revealed potentially beneficial effects of partial drainage. This phenomenon was not observed during the element-level testing of sand samples, where partial drainage consistently induced greater strain accumulation. These findings highlight the limitations of element-level results for predicting foundation response under partially drained conditions.

List of publications

- **Fleminger, R.**, Adamidis, O., Martin, C. M., Ryan, G. V., Agalianos, A., Jones, L., Anastasopoulos, I., Peralta, P., Santos, N.C.. Experimental investigation of the drainage response around a large-diameter monopile. 5th International Symposium for Frontiers in Offshore Geotechnics (ISFOG), Nantes, 2025.

Table of contents

Table of contents xi

List of figures xv

List of tables xx

Abbreviations xxi

List of Symbols: Triaxial xxiii

List of Symbols: Centrifuge xxv

1 Introduction 1
- 1.1 Research motivation ... 1
  - 1.1.1 Trends in offshore wind turbines ... 1
  - 1.1.2 Cyclic loading of offshore wind turbines monopiles ... 3
  - 1.1.3 Large-diameter monopiles ... 5
  - 1.1.4 Research into cyclic loading of sands ... 6
- 1.2 Thesis structure ... 6
  - 1.2.1 Outline ... 6
  - 1.2.2 Chapter summary ... 7
- 1.3 Summary ... 8

2 Literature Review 9
- 2.1 Triaxial testing: sand behaviour under monotonic loads ... 9
  - 2.1.1 Stress paths and initial conditions ... 9
  - 2.1.2 Critical state ... 11
  - 2.1.3 Phase transformation ... 12
- 2.2 Triaxial testing: sand behaviour under cyclic loads ... 12
  - 2.2.1 Cycle definitions ... 12
  - 2.2.2 Undrained cyclic loading ... 13
  - 2.2.3 Drained cyclic loading ... 14
- 2.3 Triaxial testing: Silty sands ... 16
  - 2.3.1 Silty sand behaviour ... 16
  - 2.3.2 Effective void ratio ... 17
- 2.4 Triaxial testing: Partial drainage ... 18
- 2.5 Triaxial testing: Numerical modelling ... 21
  - 2.5.1 SANISAND ... 21
  - 2.5.2 HCA ... 22
  - 2.5.3 Contour diagrams - UDCAM/PDCAM ... 23
- 2.6 Triaxial testing procedure ... 25
  - 2.6.1 Triaxial test: Sample preparation methods ... 25
  - 2.6.2 Triaxial test: Advanced methodologies ... 29
- 2.7 Model testing: Monopile behaviour under monotonic loads ... 34
  - 2.7.1 Pile geometry ... 34
  - 2.7.2 Soil morphology effects ... 35
  - 2.7.3 Drainage effects ... 36

2.8 Model testing: Monopile behaviour under cyclic loads 37
2.8.1 Soil morphology effects 38
2.8.2 Typical loads 38
2.9 Model testing: Drainage around large diameter monopiles 40
2.10 Centrifuge testing principle 43
2.11 Summary 45

3 Cyclic Triaxial Testing of Congleton Sand: Methodology 46
3.1 Equipment 46
3.2 Material 49
3.2.1 Congleton HST-95 additional material data 51
3.3 Sample preparation investigation 52
3.4 Slurry deposition sample preparation procedure 54
3.4.1 Clean sand sample preparation 55
3.4.2 Sample density 57
3.4.3 Silty sand sample preparation 58
3.4.4 Final stages of sample preparation 58
Local strain instrumentation 59
Suction cap sample mounting 59
3.5 Test procedure 61
3.5.1 Test procedure by test type 62
3.5.2 End of test procedure 63
3.6 Bender elements 63
3.7 Silty sand samples 65
3.8 Partially drained samples 66
3.9 Test programme 68
3.9.1 Benchmark tests 69
3.9.2 Silty sand tests 71
3.9.3 Partial drainage tests 73
3.10 Data management and analysis 74
3.10.1 Data recording 74
3.10.2 Sample measurements 75
3.10.3 Measurement corrections 75
3.11 Summary 76

4 Triaxial Results I: Behaviour of Clean Sand 77
4.1 Monotonic benchmark results 79
4.1.1 Drained Monotonic Results 80
4.1.2 Undrained Monotonic Results 82
4.2 Monotonic constitutive model calibration 86
4.2.1 SANISAND-MS calibration: Bender element results 92
4.2.2 SANISAND-MS calibration: Simulation calibration results 93
4.2.3 Constitutive model performance - Monotonic results 96
4.3 Benchmark cyclic results 98
4.3.1 Cyclic benchmark results: Accumulated axial strain 102
4.3.2 Cyclic benchmark results: Accumulated volumetric strain 107
4.4 Cyclic constitutive model calibration 114
4.4.1 Constitutive model performance - Cyclic tests 118
4.5 Summary 120

5 Triaxial Results II: Fines and Partial Drainage 122

5.1 Cyclic undrained clean sand test 123
5.2 Fines content 125
5.3 Partial Drainage 131
5.3.1 Stiffness effects of partial drainage 139
5.4 Partially drained silty sand results 142
5.5 Summary 147

6 Centrifuge Testing of Monopiles: Methodology 150
6.1 Centrifuge test design 150
6.1.1 Objectives of the experimental campaign 150
6.1.2 Centrifuge test requirements 151
6.1.3 Centrifuge test constraints 152
6.2 Centrifuge 153
6.3 Equipment 155
6.3.1 Instrumentation 155
6.3.2 Actuator 156
6.4 Pile 159
6.5 Material 160
6.5.1 Gravel and Hostun sand 160
6.5.2 Calibration 161
6.5.3 Pluviation 162
6.6 Saturation 164
6.6.1 Viscous fluid 164
6.6.2 Saturation 165
6.7 Pre-test procedure and test management 166
6.8 Loads 167
6.8.1 Monotonic loading 167
6.8.2 Displacement controlled cyclic loading 167
6.8.3 Load controlled storm loading 168
6.9 Test programme 169
6.10 Data management and analysis 172
6.11 Summary 173

7 Centrifuge Testing of Monopiles: Results 175
7.1 Monotonic results 175
7.2 Reference displacement controlled cyclic tests 176
7.2.1 Reference first event 176
7.2.2 Reference repeat event 182
7.2.3 Reference first and repeat event comparison 182
7.3 Reference load controlled storm test 188
7.4 Dimensionless factor analysis 192
7.4.1 Dimensionless factor analysis: displacement controlled tests 192
First events equal drainage factor 193
Repeat events equal drainage factor 197
Varied drainage factor 200
Varied drainage factor with the same loading period 204
7.4.2 Load controlled storm tests: dimensionless factor analysis 206
Extreme storms equal drainage factor 207
Storms varied drainage factor 208
7.5 Load history analysis 211

Preloading before first event 212
First events with increasing amplitude 212
Repeat events with increasing amplitude 214
Repeat events with varied preloading 217
7.5.1 Load controlled storm tests: load history analysis 219
First storms with increasing amplitude 219
First storm and repeat 223
7.6 End of test pushover results 225
7.7 Discussion of partial drainage effects 227
7.8 Summary 229

8 Conclusions **232**
8.1 Introduction 232
8.2 Key contributions 232
8.2.1 Benchmark testing 232
8.2.2 Advanced cyclic triaxial tests 233
8.2.3 Centrifuge model testing 234
8.3 Key implications 236
8.4 Future work 237
8.4.1 Partially drained element testing 237
8.4.2 Centrifuge testing 237
8.4.3 Numerical modelling 238
8.5 Summary 238

Bibliography **240**

List of figures

1.1 LCOE trends of wind power 1
1.2 Predicted capacity of offshore wind 2
1.3 Share of offshore wind installation by foundation type 2
1.4 New wind farm installation water depth and distance to shore 3
1.5 Trend for larger wind turbine capacity 3
1.6 OWT load regime diagram 4
1.7 OWT load regime diagram 5

2.1 Monotonic stress paths 10
2.2 Monotonic stress paths 11
2.3 Idealised monotonic response: critical state and phase transformation 12
2.4 Cyclic loading definitions 13
2.5 Cyclic loading behaviour 14
2.6 Long-term drained cyclic triaxial results 15
2.7 Examples of bundling of load amplitudes during cyclic triaxial tests 16
2.8 Fines content: floating fabric, and plastic or non-plastic fines 17
2.9 Equivalent void ratio e^* effect on SSL 18
2.10 Partial drainage filter device 19
2.11 Monotonic partially drained triaxial results 20
2.12 Schematic of the bounding surfaces of SANISAND 21
2.13 HCA model 22
2.14 Contour diagram method 24
2.15 Sample preparation methods 26
2.16 Examples of methods of selection of arrival time 30
2.17 Barrel correction and bedding errors 31
2.18 Triaxial test image analysis strain measurement 33
2.19 PISA model and soil convection around monopiles 34
2.20 Monotonic centrifuge results with partial drainage 37
2.21 Monotonic centrifuge results with partial drainage 41
2.22 Monopile partial drainage 42

3.1 DYNTTS details 47
3.2 Instruments 48
3.3 particle size distribution test (PSD) of boreholes from the Hornsea wind farm (Fugro data archive) 49
3.4 PSD of boreholes from the Walney extension (Fugro data archive) 50
3.5 PSD results of Hornsea, Congleton and Leighton Buzzard: fraction E 51
3.6 Microscopy images of Hornsea and Congleton Sand 51
3.7 Sample preparation methods 52
3.8 Sample preparation monotonic compression results 53
3.9 Sample preparation gelatine results 54
3.10 Slurry deposition mould schematic 55
3.11 End of slurry deposition preparation 57
3.12 Local strain instrumentation 60
3.13 Suction cap mounting system 61
3.14 Bender element pedestal 64

3.15 Example bender element processing 64
3.16 Ball crusher for production of non-plastic fines and PD results of fines..... 65
3.17 Partially drained filter set-up..... 67
3.18 Partially drained filter schematic..... 68
3.19 End results of monotonic shearing 70
3.20 Benchmark cyclic test conditions..... 72

4.1 CIDc tests at $D_r = 50\%$ 79
4.2 CIDc tests at $D_r = 80\%$ 80
4.3 CIDe tests at $D_r = 50\%$ 81
4.4 CIDe tests at $D_r = 80\%$ 82
4.5 CIUc tests at $D_r = 50\%$ 83
4.6 CIUc tests at $D_r = 80\%$ 84
4.7 CIUc test results at $D_r = 80\%$ (zoomed view) 85
4.8 CIUe tests..... 85
4.9 Critical state line in $e - p'$ space..... 88
4.10 Calibration of M_c and M_e 89
4.11 Calibration of the phase transformation stress ratio M_b^c and M_b^e 90
4.12 Stress paths of CIUc tests identifying phase transformation 90
4.13 Calibration of parameters n^b and n^d..... 91
4.14 Calibration of SANISAND parameter A_0 92
4.15 Bender element results of $G_{\max}$ 94
4.16 Calibration of SANISAND parameter G_0 94
4.17 Simulated undrained monotonic results for selection of h_0..... 95
4.18 Calibration of hardening parameters h_0 and c_h 96
4.19 SANISAND-MS monotonic simulation results 97
4.20 SANISAND-MS monotonic simulation results updated h_0..... 98
4.21 Drained cyclic triaxial results 99
4.22 Schematic of damping ratio calculation..... 101
4.23 Bandpass filtered history of a drained cyclic test 102
4.24 Cycle-by-cycle damping ratio and stiffness 103
4.25 Cyclic axial strain accumulation results with varied e, p'_0..... 104
4.26 Results of ε_a^{acc} with variation ofη and ζ_b 106
4.27 Cyclic results at varied $\eta =$..... 107
4.28 Accumulated volumetric strain: varied e and p'_0 109
4.29 Accumulated volumetric strain: varied η and ζ_b 110
4.30 Cyclic flow rule benchmark tests..... 111
4.31 Instability line of undrained monotonic tests..... 112
4.32 G_{tan} stiffness response of drained cyclic extension test..... 112
4.33 G_{tan} stiffness response of drained cyclic compression test 113
4.34 μ_0 calibration 116
4.35 Calibration of G_0 using cyclic test data 116
4.36 Stress paths of tests affected by ζ 117
4.37 Calibration of SANISAND-MS parameter ζ..... 117
4.38 Test and simulation data for parametric variation of e and p'_0 119
4.39 Test and simulation data for parametric variation of η and ζ_b..... 120

5.1 Undrained cyclic triaxial results..... 124
5.2 Results of drained cyclic triaxial test on silty sand sample FC10_CIDC_-
80_200_150_60_c 126

5.3 Cyclic strain accumulation of silty sand samples $p'_0 = 200$ kPa 127
5.4 Cyclic strain accumulation of silty sand samples $p'_0 = 100$ and 300 kPa 129
5.5 Cyclic strain accumulation of silty sand samples $\eta = -0.5$ and $D_r = 50\%$ ... 130
5.6 Results of the partially drained cyclic triaxial test on clean sand PD1_-CIDC_80_200_150_60_a 132
5.7 Cyclic strain accumulation by filter, $p'_0 = 200$ kPa $e = 0.58$ $\eta = 0.75$ $\zeta_b = 0.3$ 134
5.8 Excess pore pressure accumulation for partially drained and undrained benchmark test 135
5.9 Partial drainage results ε_a^{acc} and $\Delta\bar{u}$, $p'_0 = 100$ kPa, $e = 0.58$, $\eta = 0.75$, $\zeta_b = 0.3$ 136
5.10 Partial drainage results ε_a^{acc} and $\Delta\bar{u}$, $p'_0 = 100$ kPa, $e = 0.58$, $\eta = 0.75$, $\zeta_b = 0.3$ 137
5.11 Partial drainage results ε_a^{acc} and p_e higher q_{ampl}, $p'_0 = 200$ kPa, $e = 0.58$, $\eta = 0.75$, $\zeta_b = 0.45$ 137
5.12 Excess pore pressure and volumetric strain response of partially drained test 138
5.13 All partially drained tests at $\eta = 0.75$ and $\zeta_b = 0.3$. 139
5.14 Secant stiffness G_{sec} of partially drained tests 140
5.15 G_{tan} response of characteristic partially drained test 141
5.16 Partial drainage fines content ε_a^{acc} and $\Delta\bar{u}$, $p'_0 = 200$ kPa $e^* = 0.58$ $\eta = 0.75$ $\zeta_b = 0.3$ 143
5.17 Excess pore pressure cycles FC10_PD1_80_200_150_60 143
5.18 Partial drainage fines content ε_a^{acc} and $\Delta\bar{u}$, $p'_0 = 100$ kPa $e^* = 0.58$ $\eta = 0.75$ $\zeta_b = 0.3$ 144
5.19 Excess pore pressure cycles FC10_PD1_80_100_75_30 144
5.20 Partial drainage fines content ε_a^{acc} and $\Delta\bar{u}$, $p'_0 = 300$ kPa $e^* = 0.58$ $\eta = 0.75$ $\zeta_b = 0.3$ 145
5.21 Excess pore pressure cycles FC10_PD1_80_100_75_30 146

6.1 Beam centrifuge 153
6.2 Strongbox details 154
6.3 Experimental layout 156
6.4 Instrumented pile 157
6.5 Instruments 158
6.6 Actuator details 159
6.7 Pluviation 162
6.8 pore pressure transducer (PPT) placement 163
6.9 Pile placement 163
6.10 Viscous fluid preparation 164
6.11 Applied head saturation plots 165
6.12 Saturation apparatus 166
6.13 Simulated load 169

7.1 Monotonic load-displacement plot 176
7.2 Reference displacement controlled test: loads and displacement 177
7.3 Extract load plot 178
7.4 Reference displacement controlled test: PPT measurement grid 179
7.5 Location of PPTs in the soil 180
7.6 Stiffness definition 181
7.7 Reference repeat displacement controlled test: loads and displacement 183
7.8 Reference first and repeat event: H_0 and y_0 184

7.9 Reference first and repeat event: u 184
7.10 Reference first and repeat event: u with key cycles..... 185
7.11 Reference first and repeat event: u distribution 186
7.12 Reference first event extract: y_0 and y_a 187
7.13 Reference first event extract: y_0 and H_0 187
7.14 Reference first event extract: H_0 and r_u 188
7.15 Reference load controlled storm test: loads and displacement 189
7.16 Stiffness definition storm..... 190
7.17 Reference load controlled storm test: PPT measurement grid..... 191
7.18 Dimensionless factor analysis, first events equal drainage factor: H_0 and y_0 . 194
7.19 Dimensionless factor analysis, first events equal drainage factor: y_a and u_{acc} 194
7.20 Dimensionless factor analysis, first events equal drainage factor: u 195
7.21 Dimensionless factor analysis, first events equal drainage factor: u with key cycles 195
7.22 Dimensionless factor analysis, first events equal drainage factor: u distribution, T3_1 and T4_1 196
7.23 Dimensionless factor analysis, first events equal drainage factor: u with key cycles 196
7.24 Dimensionless factor analysis, first events equal drainage factor: u distribution, T3_1 and T5_1 197
7.25 Dimensionless factor analysis, repeat events equal drainage factor: H_0 and y_0 198
7.26 Dimensionless factor analysis, repeat events equal drainage factor:u..... 199
7.27 Dimensionless factor analysis, repeat events equal drainage factor:u_{acc} 199
7.28 Dimensionless factor analysis, varied drainage factor: H_0 and y_0 200
7.29 Dimensionless factor analysis, varied drainage factor: u 201
7.30 Dimensionless factor analysis, varied drainage factor: u_{acc}..... 202
7.31 Dimensionless factor analysis, varied drainage factor: u with key cycles..... 202
7.32 Dimensionless factor analysis, varied drainage factor: u distribution 203
7.33 Dimensionless factor analysis, varied drainage factor: stiffness and dynamic analysis..... 203
7.34 Dimensionless factor analysis, varied drainage factor, same load frequency: H_0 and y_0 205
7.35 Dimensionless factor analysis, varied drainage factor, same load frequency: u 205
7.36 Dimensionless factor analysis, varied drainage factor, same load frequency: u_{acc} 206
7.37 Dimensionless factor analysis storm, extreme storms: H_0 and y_0 208
7.38 Dimensionless factor analysis storm, extreme storms: u 209
7.39 Dimensionless factor analysis storm, extreme storms:u_{acc}..... 209
7.40 Dimensionless factor analysis storm, varied drainage factor: H_0 and y_0 210
7.41 Dimensionless factor analysis storm, varied drainage factor: u 210
7.42 Load history analysis, preloading before first event: H_0 and y_0 213
7.43 Load history analysis, preloading before first event: u 213
7.44 Load history analysis, first events with increasing amplitude: H_0 and y_0 214
7.45 Load history analysis, first events with increasing amplitude: y_a and u_{acc} ... 215
7.46 Load history analysis, first events with increasing amplitude: u..... 215
7.47 Load history analysis, repeat events with increasing amplitude: H_0 and y_0.. 216
7.48 Load history analysis, repeat events with increasing amplitude: u 216
7.49 Load history analysis, repeat events with varied preloading: H_0 and y_0..... 217
7.50 Load history analysis, repeat events with varied preloading: u 218
7.51 Load history analysis, repeat events with varied preloading: u with key cycles 218

7.52 Load history analysis, repeat events with varied preloading: u distribution .. 219
7.53 Load history analysis, storm events with increasing amplitude: H_0 and y_0 .. 220
7.54 Load history analysis, storm events with increasing amplitude: u 220
7.55 Load history analysis, storm events with increasing amplitude:u_{acc} 221
7.56 Storm event T3_7 in depth 222
7.57 Load history analysis, repeat storm event: H_0 and y_0 223
7.58 Load history analysis, repeat storm event: u_{acc} 224
7.59 Load history analysis, repeat storm event: u with key cycles 224
7.60 Load history analysis, repeat storm event: u distribution 225
7.61 End of test pushover all tests 226

List of tables

2.1 Centrifuge scaling laws, where N is the applied centrifugal acceleration in units of g (Madabhushi, 2017) 44

3.1 Triaxial cell specifications 46
3.2 Volumetric control specifications 47
3.3 Additional instrument specifications 49
3.4 Material data 50
3.5 Shape characteristics of Congleton sand 52
3.6 Test parameters for different test types 62
3.7 Partial drainage filter permeability 67
3.8 Benchmark monotonic testing schedule 69
3.9 Benchmark cyclic testing schedule 71
3.10 Drained cyclic silty sand test schedule 73
3.11 Partially drained cyclic sand test schedule 74
3.12 Partially drained silty sand cyclic test schedule 74
3.13 Triaxial test recorded data channels 75
3.14 Measurements, Descriptions, and Units 76

4.1 Summary of drained monotonic results 83
4.2 Summary of undrained monotonic results 86
4.3 SANISAND-MS monotonic parameters and constitutive model formulations from Liu et al., 2019 87
4.4 SANISAND-MS parameters 96
4.5 SANISAND-MS cyclic parameters and constitutive model formulations from Liu et al., 2019 115
4.6 Updated SANISAND-MS parameters 118

6.1 Instrumentation 155
6.2 Monopile properties 160
6.3 Material properties 161
6.4 Load simulation inputs 168
6.5 Achieved void ratio and pore fluid viscosity 170
6.6 Test nomenclature 170
6.7 Test programme 171
6.8 Recorded measurements 173
6.9 Normalised factors 173

Abbreviations

CPT	Cone Penetration Test
CSL	Critical State Line
DFD	Dry Funnel Deposition
DYNTTS	Dynamic Triaxial Testing System
FLS	Fatigue Limit State
HCA	High-Cycle Accumulation model
LBS-E	Leighton Buzzard sand - size fraction E
LCOE	Levelised Cost of Electricity
LVDT	Linear Variable Differential Transformer
MM	Minimum and Maximum void ratio test
MT	Moist Tamping
OWT	Offshore Wind Turbine
P	Pile
PI	Plasticity Index test
PPT	Pore Pressure Transducer
PSD	Particle Size Distribution test
PTL	Phase transformation line
SANISAND	Simple Anisotropic Sand model
SCPTu	Seismic Cone Penetration Test, u denoting measurement of pore pressure u
SD	Slurry Deposition
SLS	Serviceability Limit State
T	Test
ULS	Ultimate Limit State

WP Water Pluviation

List of Symbols: Triaxial

e	Void ratio
ε_a^{acc}	Accumulated axial strain
ε_a	Axial strain
ε_v^{acc}	Accumulated volumetric strain
ε_v	Volumetric strain
η	Average cyclic stress ratio
$G_{\mathbf{max}}$	Small-strain shear modulus
G_0	Dimensionless small-strain shear modulus
λ	Compressibility
M_c	Critical state stress ratio in compression
M_e	Critical state stress ratio in extension
$\varphi_{\mathbf{cs}}$	Critical state friction angle
$\varphi_{\mathbf{p}}$	Peak friction angle
p'_0	Initial mean effective stress
p'	Mean effective triaxial stress
ψ	State parameter
q	Deviatoric stress
q_c	Cone penetration resistance
ρ	Density
$\sigma_{\mathbf{av}}$	Cyclic average load
$\sigma_{\mathbf{cyc}}$	Cyclic load amplitude
σ_e	Cyclic extreme load
σ_r	Cyclic return load

$\sigma_{\mathbf{ref}}$	Reference load, usually taken as the ultimate monotonic load at a given strain
u	Pore pressure
$\bar{u}$	Average cyclic pore pressure
Δu	Change in sample pore pressure, i.e. excess pore pressure
u_1	Pore pressure
v_s	Shear wave velocity
ζ_b	Cyclic load absolute amplitude ratio
ζ_c	Cyclic load amplitude direction ratio

List of Symbols: Centrifuge

D	Monopile Diameter
$D_{\mathbf{50}}$	Average particle size
Δy	Accumulated displacement
Δy_0	Accumulated mudline displacement
$D_{\mathbf{m}}$	Model monopile diameter
$D_{\mathbf{p}}$	Prototype monopile diameter
D_r	Relative density
$D_{\mathbf{ref}}$	Reference monopile diameter
E	Young's modulus
e	Load eccentricity
E_pI_p	Flexural rigidity of the pile
E_s	Young's modulus of the soil
η	Centrifugal acceleration and scaling factor
f	Loading frequency
f_c	Characteristic loading frequency (relative to reference monopile diameter)
γ'	Buoyant unit weight of soil
G_s	Specific gravity
H	Lateral load
H_0	Lateral mudline load
$H_{\mathbf{ULT}}$	Ultimate lateral load (at mudline displacement = $0.1D$)
I_p	Second moment of area of the pile
k	Permeability of soil
k_x	Stiffness with respect to displacement
L	Embedded depth of monopile

M	Bending moment in pile
M	Constrained stiffness at nominal depth in soil
μ	Pore fluid viscosity / Centrifugal scaling factor
ω	Rotational velocity
r_c	Radius of centrifugal rotation
r_p	Radius of the monopile
r_u	Excess pore fluid pressure ratio
$r_{\mathbf{u\ av}}$	Average excess pore fluid pressure ratio
T	Loading period
t	Time instant
θ	Monopile rotation
t	Monopile Wall Thickness
u	Excess pore fluid pressure
$u_{\mathbf{acc}}$	Accumulated excess pore fluid pressure
y	Displacement
y_0	Mudline displacement
$y_{\mathbf{0\ av}}$	Average mudline displacement
y_a	Actuator displacement
Z	Depth below the mudline

Chapter 1
Introduction

This thesis will provide experimental data and analysis of cyclic loading of sand. The work focuses on the typical cyclic loads experienced around offshore wind turbine (OWT) monopile foundations. The research was divided into two sections of experimental investigation: soil element testing using the cyclic triaxial test, and model testing of monopiles in a geotechnical centrifuge. The two experimental methods provide distinct investigation techniques to support the research aims, though are linked by the theme of drainage effects on soil response. The primary research aim of this thesis is the investigation of partial drainage effects during cyclic loading of sand, and foundations in sand. This chapter provides background information for the research aims and motivation, as well as an outline of the thesis structure.

1.1 Research motivation

1.1.1 Trends in offshore wind turbines

Offshore wind power is a rapidly growing constituent of global power supply, notably in northern European countries as well as China. The combined factors of increased effort to de-carbonise the power supply and reduce the levelised cost of electricity (LCOE) (Figure 1.1) are driving this trend. The predicted global capacity of offshore wind is 300 GW by 2031 (Figure 1.2), representing an annual capital expenditure of €180 billion. The economic benefit of cost savings in the design and construction of offshore wind turbines is clear.

Offshore wind turbines have been predominantly fixed-base on monopile foundations, over 80% of installations. Figure 1.3 shows the total installations of offshore wind turbines

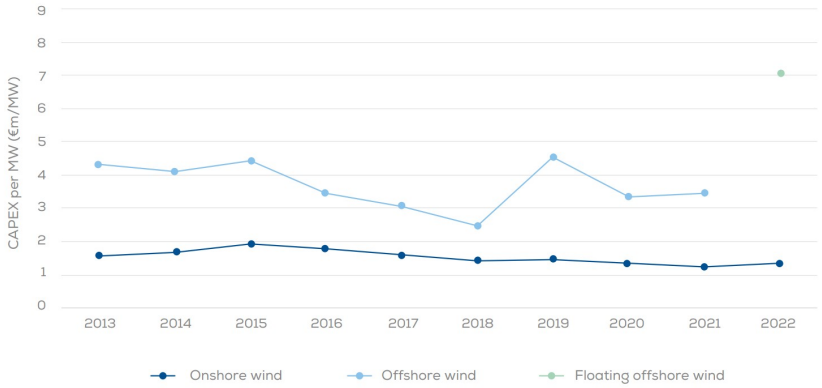

Figure 1.1: Trends of reduction in the CAPEX per MW of capacity (O'Sullivan et al., 2022)

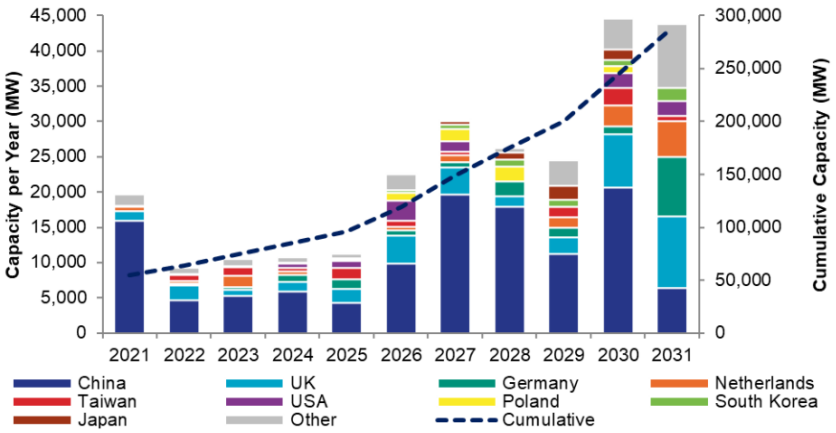

Figure 1.2: Predicted global capacity of offshore wind power (RenewableUK, 2025)

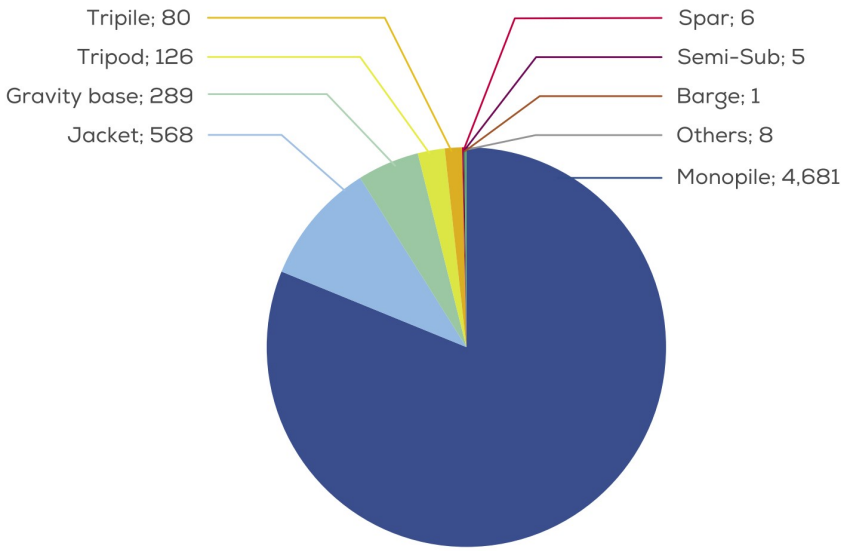

Figure 1.3: Share of offshore wind installation by foundation type. Monopiles make up over 80% of installations (O'Sullivan, 2020).

until 2020, with monopiles the most commonly used structure, 80%, and jacket structures making up 10%. The trend for new installations up to that year matched the distribution to date, with monopiles as 80% of new installations, and jackets 20%. The trend for new installations up to 2030 is predicted to move towards floating structures, however, this trend has not yet had a significant impact on the industry.

The selection of sites for new wind turbines has become increasingly limited as the best sites become occupied. Therefore, the new sites have tended to be in deeper water and located further from shore. Figure 1.4 shows the trend for larger wind farms at greater depths and distance to shore. Increases in depth and distance to shore shift the economics of site development to larger, higher capacity wind turbines. This is due to reduced overall construction cost in deeper waters for larger wind turbines. Additionally, the requirement for fewer maintenance trips over long distances reduces the operational cost. This trend

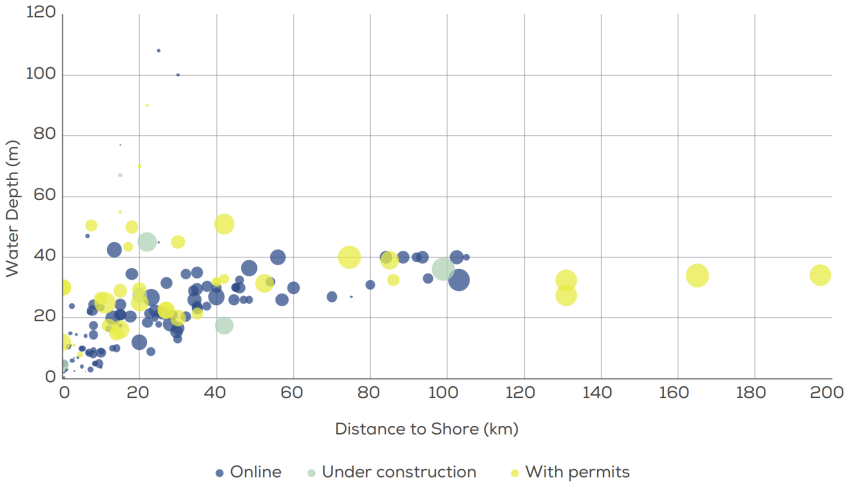

Figure 1.4: New wind farm installation water depth and distance to shore (O'Sullivan, 2020)

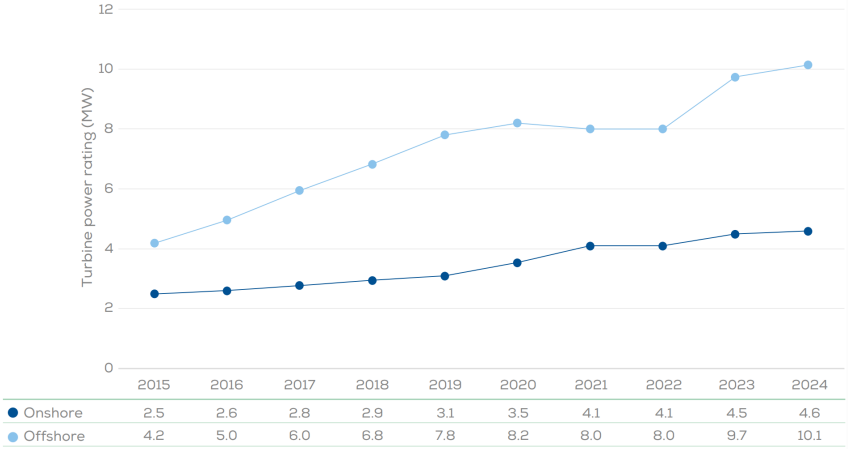

Figure 1.5: Trend for larger wind turbine capacity (Costanzo et al., 2025)

is shown in Figure 1.5 where the trend for turbine power rating has steadily increased year-by-year in offshore wind installations. The slower increase in onshore wind turbine size highlights the differences in economic factors, where maintenance and construction costs are not as important, and the selection of a turbine is more affected by the ratio of manufacturing cost to power output. The trend for larger offshore wind turbines has caused an increase in the monopile size, particularly diameter (D). Consequently, newly installed monopiles regularly exceed 10m in diameter (McCoy et al., 2024).

1.1.2 Cyclic loading of offshore wind turbines monopiles

The loading of OWT structures translated to the foundations consists primarily of lateral loads. These loads are induced by environmental conditions, such as wind and waves. The environmental conditions are cyclic in nature. Cyclic wind loading is induced by turbulence within the flow, as well as rotor rotation and blade shadowing of the turbine. Wave loading is cyclic by nature, with peaks in load corresponding to peaks in wave height. Figure 1.6 illustrates the mechanism for the cyclic loads experienced by an offshore wind turbine.

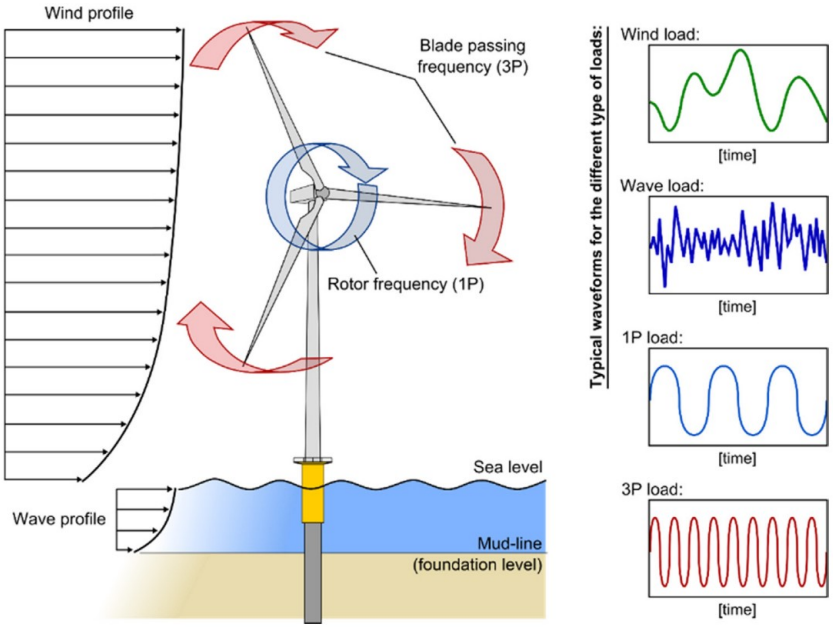

Figure 1.6: Schematic diagram of a typical load regime on an OWT showing loads and frequencies (Nikitas et al., 2016).

The environmental loads differ in magnitude and frequency, leading to a complicated multi-frequency load pattern experienced at the foundation. However, there are three major loading frequencies, corresponding to the wave loading frequency, rotor frequency, and blade passing frequency (Figure 1.7). In order to minimise the effect of resonance on the turbine structure, the designed natural frequency of the tower and foundation is targeted at the gap between the rotor and blade passing frequencies. This design technique is termed "soft-stiff".

The amplitudes of the wind and wave loads are generally concurrent. During low wind speed events, the general load on the turbine from wind and waves is low. In contrast, storm events induce increases in both wind and wave load. LeBlanc et al. (2010) show that the limited number of large loading cycles during extreme storms has a more significant impact on accumulated tilt than the millions of small cycles associated with normal operating conditions. The operational loads, during wind speeds $v < 12$ m/s, account for up 10^7 cycles during the lifetime (LeBlanc et al., 2010). Therefore, these load cycles are generally considered in fatigue limit state (FLS) design criteria. For serviceability limit state (SLS) and ultimate limit state (ULS) design criteria, with limitations of $0.1D$ permanent displacement (Byrne et al., 2017), the consideration of storm load events is more important. DNVGL-ST-0126 standard: *Support structures for wind turbines* (DNV AS, 2021), specifies that ULS and SLS loads from monotonic and cyclic loads should be considered, as well as pore pressure effects during cyclic loading. Furthermore, it is forecast that climate change will increase the intensity and regularity of storms (Wolf et al., 2020). Given this, it is essential to incorporate these storm loads in the design of future wind farm projects.

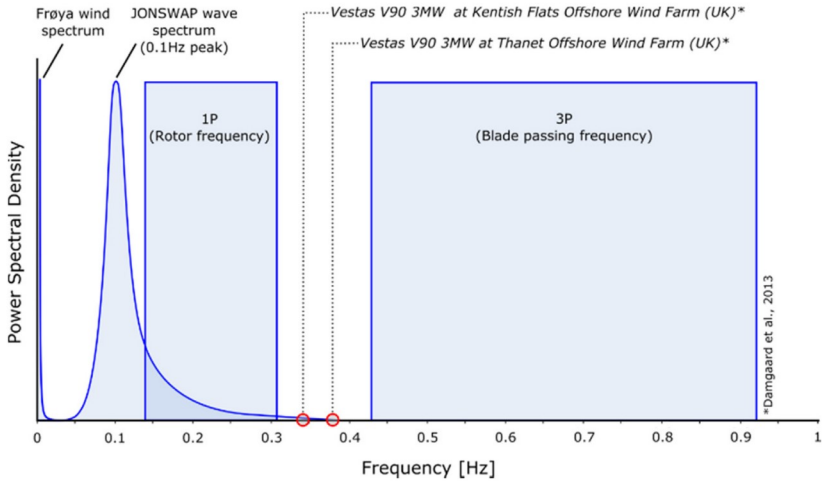

Figure 1.7: Frequency vs power spectral density plot of a typical load regime on an OWT (Nikitas et al., 2016).

1.1.3 Large-diameter monopiles

As OWT structures and foundations increase in size, the system behaviour is altered. One change is to the wind-induced loading frequency. The increase in rotor diameter reduces the rotational frequency for the same wind speed. However, the wave load frequency is unaffected. This leads to a greater crossover between the rotor rotation frequency and the wave loading frequency. This may lead to an increase in resonant loading.

Another important factor is the effect on the soil drainage regime. Modern monopiles have a large diameter and short embedment depth (L). Significant research has been conducted on monopiles with a low L/D ratio ($L/D \approx 3-6$) (Byrne et al., 2017), which has been incorporated into contemporary engineering practice. However, for monopiles in sandy soils this research primarily relies on results from fully drained tests, which may not accurately reflect actual conditions. The drainage pathway during horizontal loading is predominantly lateral, around the circumference of the monopile; thus, as the diameter increases, the drainage pathway lengthens. Therefore, during typical loading cycles on large-diameter monopiles it is likely that the soil will be partially drained (Zhu et al., 2020). There is a significant need to better understand and model cyclic loading on these structures, including the drainage conditions, especially as monopiles continue to increase in size.

The dominant drainage pathway during lateral cyclic loading is from the front of the pile to the back, around the circumference of the monopile. The increased length of the drainage pathway may lead to an increase in the accumulation of excess pore pressure. Klinkvort et al. (2018) predict that the degree to which the diameter impacts drainage conditions can be summarised through the non-dimensional factor $MkT/\gamma_w D^2$, where M is the soil stiffness, k is the permeability of the soil, T is the loading period, γ_w is the unit weight of water, and D is the pile diameter. Consequently, as the diameter increases, the drainage regime will change quadratically to being less drained. In current design

practice, cyclic loading of monopiles in sands, is generally considered to have a drained regime (DNV AS, 2021). The actual drainage regime may transition into partially drained with larger diameter monopiles, considering the scaling factor above. This effect will have a greater impact with greater amplitude of loading, owing to the increase in pore pressure dissipation required to approach a fully drained loading regime. However, further research is needed to verify the validity of this proposed dimensionless drainage factor.

1.1.4 Research into cyclic loading of sands

Modelling of OWT response to cyclic loading in new installations generally relies on data from site investigations, including cyclic triaxial tests, to calibrate various modelling techniques, such as the cyclic contour method (Andersen, 2015). Often the assumption is of drained cyclic loading, however, as discussed above, this assumption may be inaccurate. Investigations of partial drainage effects on foundation response are present in literature. These consist of element testing (Suzuki et al., 2020), centrifuge model testing (Takahashi et al., 2022; Zhu et al., 2021), and numerical modelling (Chaloulos et al., 2024; Jostad et al., 2019; Kementzetzidis et al., 2019). Simulations of monopile response invariably show a degree of pore pressure accumulation and oscillation. This excess pore pressure may result in a reduction in effective stress and increased pile rotation; however, the relationship is complex due to the stiffening effect of negative excess pore pressures behind the pile.

1.2 Thesis structure

1.2.1 Outline

The previous section outlined the ongoing trends in offshore wind production for increased turbine capacity and monopile diameter. The uncertainty in turbine installation cost driven by increasing foundation size is a major risk for developers. Therefore, there is a clear need for intensive research into large-diameter monopile foundation behaviour.

This thesis seeks to investigate a key area of uncertainty in monopile foundation design, namely the effect of partial drainage and fines content on the response of sands to cyclic loading. The thesis is divided into two areas of research methodology: soil element testing and model foundation testing. The use of element tests to calibrate numerical models is one of the main inputs to foundation design procedures used in industry. Therefore, this thesis presents element testing results specifically designed to investigate the cyclic loading response of sands. These results are used to calibrate a widely used constitutive model, SANISAND-MS (Liu et al., 2019). The calibrated parameters provided can be used for future numerical simulations of the model tests performed in the geotechnical centrifuge. The effect of fines content on the response to cyclic loading has been the focus of much research, however, the conclusions have been varied. This thesis provides data for direct comparison of clean and silty sand samples subjected to the same cyclic loading conditions. Furthermore, the effect of partially drained conditions has been investigated in

experimental testing and numerical modelling, however, this has not yet been verified with full scale or centrifuge model testing. The centrifuge model testing programme reported in this thesis aims to address this need.

1.2.2 Chapter summary

1. Introduction

This chapter provides background information to contextualise the research motivation, focusing on the increasing use and size of monopile foundations.

2. Literature Review

The literature review summarises the current state of research in cyclic loading of sands and highlights areas that require further investigation. Particular focus is given to partial drainage and fines content, which are investigated in Chapter 5.

3. Cyclic Triaxial Testing of Congleton Sand: Methodology

This chapter describes the methodology used for the cyclic triaxial tests reported in Chapters 4 and 5. The methodology includes the design of the testing method and the procedures involved in sample preparation, testing, and results analysis. Additionally, a summary of the findings from a sample preparation investigation is provided, as this investigation informed the methodology employed.

4. Triaxial Results I: Behaviour of Clean Sand Under Monotonic and Cyclic Loading

This chapter presents the results of a series of triaxial tests, both monotonic and cyclic. The test schedule aimed to examine the behaviour of sand subjected to drained and undrained cyclic loading, across a range of initial density conditions and stress states. These results provide the basis for constitutive model calibration and the benchmark for the subsequent examination of the effects of fines content and partial drainage on soil behaviour.

5. Triaxial Results II: Influence of Fines and Partial Drainage

This chapter builds on the previous chapter by examining fines content and partial drainage effects on soil behaviour. The tests were conducted under conditions consistent with those in the previous chapter. The investigation into fines content involved testing samples prepared to the same equivalent void ratio, e^*, at fines contents of 10 and 15%. The investigation into partially drained conditions imposed a filter to restrict sample drainage giving two distinct drainage levels.

6. Centrifuge Testing of Monopiles in Congleton Sand: Methodology

This chapter outlines the test design and procedures used for the centrifuge model tests. The test design procedure incorporates insights into the testing limitations of the equipment utilised, selection of the applied loads, and boundary effects. Subsequently, a comprehensive description of the developed methodology is presented.

7. Centrifuge Testing of Monopiles in Congleton Sand: Results

This chapter outlines the findings of the centrifuge investigation into drainage effects around monopile foundations in sand when subjected to cyclic loading. The campaign examined

the impact of monopile diameter and the cyclic loading regime (amplitude, frequency) on the drainage response during cyclic loading.

8. Conclusion

The conclusion summarises the findings of the thesis and highlights areas for future work.

1.3 Summary

This chapter provided an overview of the motivation and scope of research on large-diameter monopiles for offshore wind turbines (OWTs). Current industry trends indicate the routine installation of monopiles exceeding 10 m in diameter, driven by both economic and engineering considerations. The implications of this increase in monopile size, particularly the effect on the drainage regime within the soil, warrant systematic investigation. Following the discussion of research motivation, an outline of the subsequent thesis chapters was presented.

Chapter 2
Literature Review

This chapter outlines a review of the literature pertinent to the research outputs of this thesis. The review is divided into two sections, corresponding to the distinct research phases of this project. The first section focuses on triaxial testing of sand, with detailed discussions on the effects of fines content and partial drainage on the response of sand subjected to cyclic loading. The second section addresses the centrifuge testing campaign concerning the cyclic loading of large diameter monopiles. Both sections on triaxial and centrifuge research include a review of the literature regarding the behaviours of interest, along with studies that informed the methodologies employed.

2.1 Triaxial testing: sand behaviour under monotonic loads

This section outlines the behaviour of clean sand samples under monotonic triaxial loading. Triaxial monotonic loading can be performed under various conditions, including drained or undrained, and compression or extension. Monotonic stress paths are generally applied via the load ram, resulting in a stress path that is not entirely deviatoric. Below is a discussion of the major behaviours observed during monotonic loading.

2.1.1 Monotonic behaviour: Stress paths and initial conditions

The monotonic response is significantly dependent on the initial stress state and the stress path applied during loading. Additional influencing factors include drainage and soil morphology. Azeiteiro et al. (2017) examined the monotonic response of Hostun sand samples under a range of stress states and initial conditions. These results were intended to facilitate the calibration of monotonic constitutive models with critical state formulations. Figure 2.1 presents key figures from the study. Figure 2.1 (a) illustrates some of the stress paths that can be applied in triaxial tests. More complex stress paths may be applied using dynamic feedback; however, the paths shown are more straightforward to implement holding either the cell pressure or the ram load constant, whilst changing the other. The behaviour is dictated by the load applied and the initial conditions. The initial conditions may be isotropically consolidated, with no initial deviatoric stress, or anisotropically consolidated. However, anisotropic consolidation may also be considered part of the stress path. The stress paths displayed here represent tests with isotropically consolidated initial conditions. The greater the level of consolidation pressure, the further along the x-axis the stress path will commence. Therefore, the stress state begins further into the failure envelope, resulting in a greater distance to the critical state or phase transformation line (Figure 2.3). During loading, whether drained or undrained, the direction of the stress

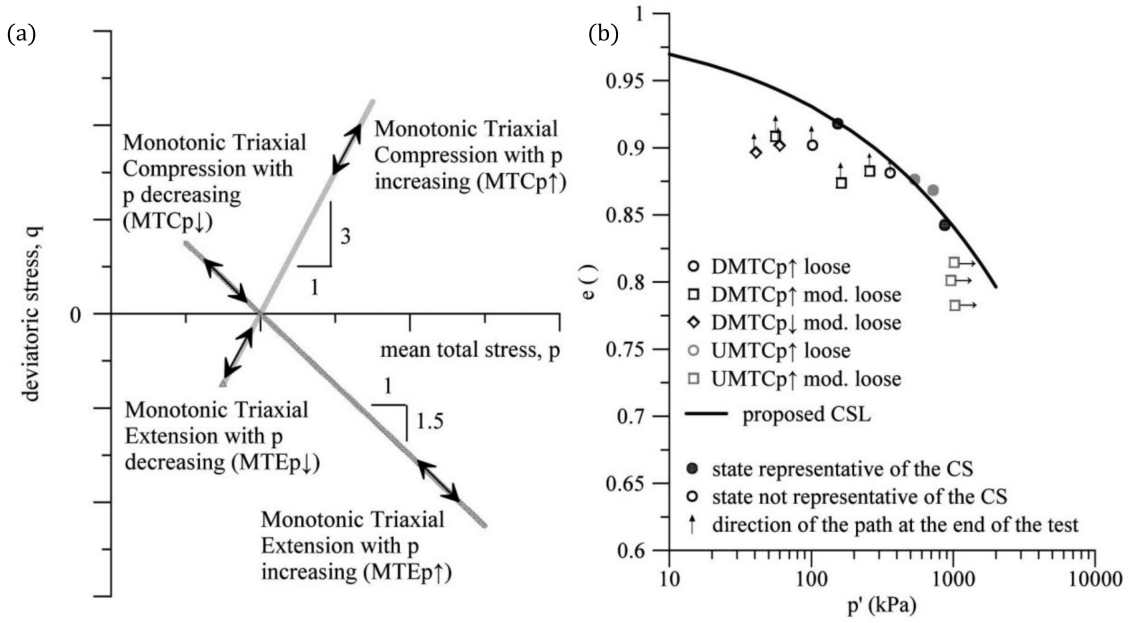

Figure 2.1: Figures from Azeiteiro et al. (2017), showing: (a) possible stress paths during triaxial monotonic loading in $q-p$ space, and (b) end results of triaxial tests, showing the formulation of the critical state line

path influences the behaviour. In the $\uparrow p$ paths, the lines sloping to the right indicate that the stress state approaches the failure envelope at an oblique angle, resulting in the sample experiencing significant loading before failure. For the $\downarrow p$ paths, the stress path heads directly toward the failure envelope and will reach critical state after a short duration of loading. This reflects the reducing mean effective stress, which reduces the soil strength. Moreover, the extension stress paths will fail under lower loading, as the failure envelope in extension exhibits a shallower gradient. In practice, triaxial extension tests rarely achieve critical state due to the occurrence of necking in the samples.

Figure 2.2 (a) shows drained monotonic test results, with deviator stress, q, against axial strain, ε_a. The results show an initial steep response, indicating higher initial stiffness, followed by a reduction in stiffness. The deviator stress increases towards the peak strength, followed by a softening phase with continued strain. Eventually, the response produces no further change in stress, for continued strain, indicating that the sample has reached ultimate strength. This does not necessarily indicate critical state, which also requires no further volumetric strain. The volumetric response in Figure 2.2 (b) shows that none of the tests have reached this point at the end of the test, indicating that they have not reached critical state. However, the endpoints, and the direction of strain at this point, can be used to formulate the CSL, as shown in Figure 2.1 (b), where the end points are close to the proposed line.

Figure 2.1 (b) illustrates the variation in response of drained and undrained tests within the $v-p$ space approaching the critical state line. Tests conducted under drained conditions demonstrate ongoing volumetric strain, with minimal changes in average stress during loading. This is depicted by a vertical line ascending towards the critical state line.

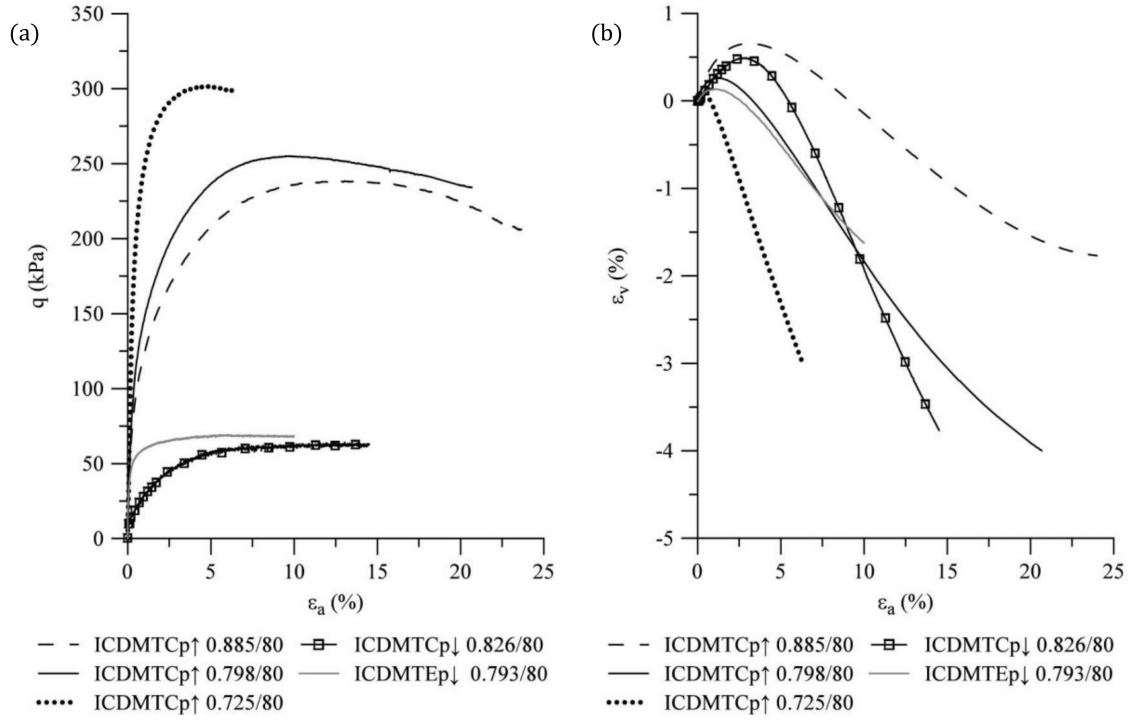

Figure 2.2: Figures from Azeiteiro et al. (2017), showing: (a) stress-strain response of triaxial compression tests in $q - \varepsilon_a$ space, and (b) volumetric strain response against axial strain

Conversely, tests carried out under undrained conditions show no volumetric strain while mean total stress continues to increase. This is represented by a horizontal line on the plot. The drained and undrained responses differ significantly; however, the endpoint on the critical state line remains consistent.

2.1.2 Monotonic behaviour: Critical state

Critical state soil mechanics was first proposed by Roscoe et al. (1958) and updated for application to sands by Wroth et al. (1965). The critical state, as previously discussed, is the point at which a soil exhibits continued shear strain, with no further increase in stress or volumetric strain. This concept underpins much of soil mechanics. The critical state is defined in the $q - p - v$ space as a single line onto which a soil falls from any initial condition after continued shearing. This provides a useful prediction for the ultimate failure conditions. In conservative design, the critical state friction angle, φ_{cs}, is adopted to determine the failure conditions. However, the peak friction angle, φ_{p}, is often employed in practice, as this offers additional strength in the design that would otherwise not be considered. An expansion of the critical state approach was developed by Been et al. (1985), introducing the state parameter, ψ. This approach exploited the known variation in soil behaviour depending on the distance from the critical state. The stress state and current void ratio define the state parameter. The critical state void ratio is determined by the mean effective stress. Therefore, for a given stress state, there is a defined critical state void ratio. The state parameter is defined as the difference between the current void

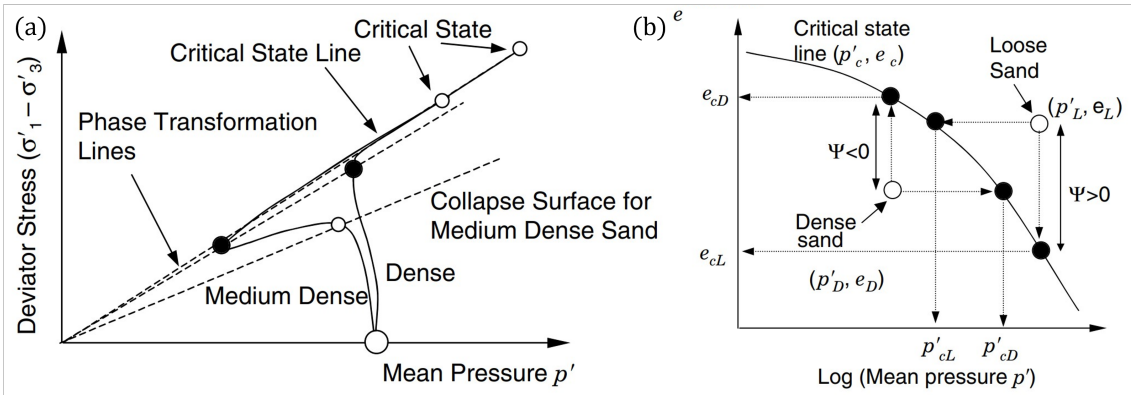

Figure 2.3: Diagrams of the idealised response of triaxial monotonic tests from Mitchell et al. (2005) showing: (a) the Critical State and Phase Transformation lines in stress space for undrained tests. Dense and medium-dense sands exhibit phase transformation during undrained loading. (b) The $e - ln(p)$ space response of soils on either side of the CSL

ratio and the critical state void ratio at a given stress level, $\psi = e_0 - e_c$. Thus, the sign and magnitude of the state parameter can be used to predict the behaviour of the sand under loading. Many constitutive models utilise this concept in their formulation.

2.1.3 Monotonic behaviour: Phase transformation

During undrained monotonic loading, a distinct change in the direction of load evolution in the $p' - q$ space, termed phase transformation, can occur. It is difficult to determine the point of phase transformation in drained tests, therefore, undrained results are used. This phenomenon is observed in dense or medium dense sands. Phase transformation follows an initial phase of contraction, which develops positive excess pore water pressures, and is succeeded by a phase of strain hardening until the critical state is attained. The point at which phase transformation occurs is defined along a line in the $p' - q$ space, known as the phase transformation line. This line originates at the point of zero stress and adheres to a gradient similar to that of the critical state line (CSL) (Figure 2.3), where the soil exhibits dilative, shear hardening behaviour. Provided the shear induced negative excess pore pressures do not cause cavitation, the soil will continue to shear until the critical state is achieved (Yoshimine et al., 1998).

2.2 Triaxial testing: sand behaviour under cyclic loads

The following section outlines the key behaviour of sand subjected to cyclic loading, specifically in the context of triaxial tests.

2.2.1 Cyclic behaviour: Cycle definitions

The additional complexity of cyclic loading necessitates further attention in defining the loading conditions. Balaam (2020) gives a comprehensive review of the best practice for presenting cyclic data, which provides the following definitions: $\sigma_{\text{av}} = \frac{\sigma_e + \sigma_r}{2}$; $\sigma_{\text{cyc}} = \frac{\sigma_e - \sigma_r}{2}$,

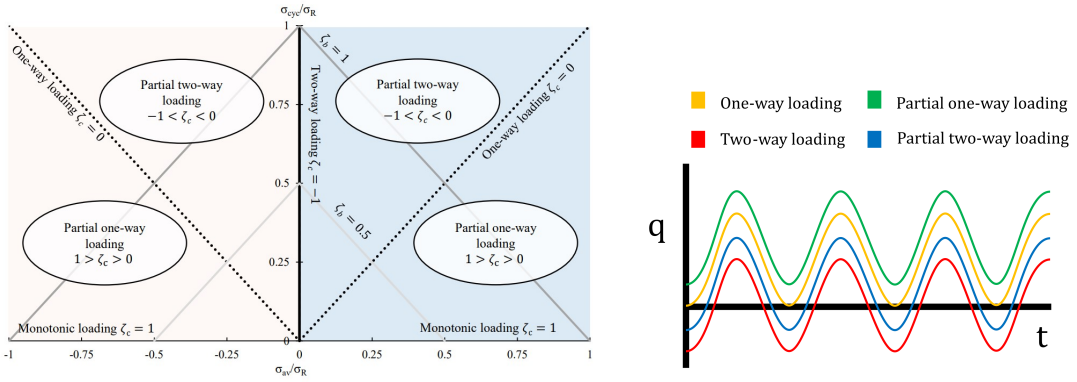

(a) (b)

Figure 2.4: Cyclic loading definition diagrams , showing: (a) contour diagram of cyclic loading parameters (from (Balaam, 2020)), and (b) time history of example cyclic loads.

where σ_e is the extreme load, σ_r is the reverse load, σ_{av} is the average stress, and σ_{cyc} is the cyclic amplitude. LeBlanc et al. (2010) introduced the terms ζ_b $(= \frac{\sigma_e}{\sigma_{ref}})$, and ζ_c $(= \frac{\sigma_r}{\sigma_e})$, for characterising cyclic loads. σ_{ref} is a reference load, often taken in relation to an ultimate load. These parameters can be used to populate cyclic stress contour diagrams (Figure 2.4(a)).

2.2.2 Cyclic behaviour: Undrained cyclic loading

Cyclic loading, particularly under undrained conditions, can lead to the failure of a foundation at loading levels significantly lower than those observed in monotonic serviceability and ultimate limit states. Loading of initially loose soil induces particle movement, resulting in compressive volumetric strain in drained conditions. However, under undrained conditions the compressive volumetric strain induces positive excess pore pressures, u. This process will eventually culminate in liquefaction and failure as the mean effective stress (p') approaches zero. Full liquefaction is characterised by the point at which pore water pressure equals the initial mean effective pressure. Conditions at failure depend on soil type, density, mean effective pressure, and fabric. Cyclic mobility, the development of shear strain with cyclic loading, can become substantial, leading to failure without total liquefaction of the soil. Thus, the definition of failure may vary based on the conditions. Cyclic failure definitions provided by Ishihara (1993) are traditionally applied in earthquake research. Failure is defined as the point at which the excess pore water pressure ratio, $r_u = 0.9\sigma'_0$, or when the double amplitude cyclic strain (defined as the strain difference between the forward and reverse load cycle), $\varepsilon_{\text{DA}} = 5\%$. For loose samples, the onset of liquefaction will induce large strains and flow failure. However, in medium and dense samples, immediately after liquefaction, there will be residual strength and strain will be limited, which may not be classified as failure despite r_u exceeding $0.9\sigma'$. Therefore, the failure criterion of $\varepsilon_{\text{DA}} = 5\%$ is more widely used. Undrained cyclic resistance is typically quantified using a cyclic resistance curve (Figure 2.5(a)). The cyclic resistance curve plots

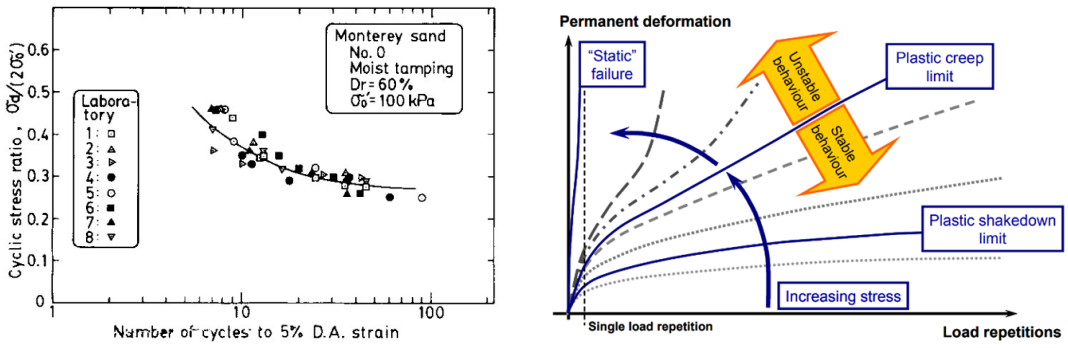

(a) (b)

Figure 2.5: Cyclic loading behaviour , showing: (a) cyclic resistance curve during undrained loading. The cyclic stress ratio is plotted against the number of cycles to liquefaction (Ishihara, 1993), and (b) typical responses of soil during long term drained cyclic loading (Theyse et al., 2007). The long term response depends on the loading level and the soil conditions.

cyclic stress ratio $\sigma_d/2\sigma'_0$, (where σ_d is the single amplitude cyclic stress and σ'_0 is the initial mean effective stress) against the number of cycles to $\varepsilon_{\text{DA}} = 5\%$. The plot can be used to determine the cyclic strength, usually defined as the cyclic stress ratio required to induce $\varepsilon_{\text{DA}} = 5\%$ failure in 20 cycles, which is given the notation CRR_{20}.

2.2.3 Cyclic behaviour: Drained cyclic loading

Drained cyclic loading, initially induces a contractive phase with significant strain. If load cycling persists, the soil response will reduce, and the response will settle into a densifying and ratcheting phase (Figure 2.5(b)). The cycles of loading and unloading provide energy to the soil particles, causing repacking of particles in a denser configuration. Theyse et al. (2007) show the variation of soil response with stress level and number of cycles in the context of pavement engineering. The predicted behaviour shows that at low amplitude, cyclic loading will eventually cause "shakedown", where the increment of permanent strain with each cycle will eventually reach zero at a high number of cycles. Above the plastic shakedown limit and below the plastic creep limit a "metastable" condition is reached where plastic strain increases linearly with each cycle. As the load levels exceed the plastic creep limit, increasing cycles will induce unstable rapid failure. This failure can occur at loads below the monotonic ULS level. However, an investigation by García-Rojo et al. (2005) showed that this is unlikely to be true. It was shown that, at a cyclic stress level sufficient to induce any strain in low cycle numbers, the substrate will never reach "shakedown".

Results of long-term drained cyclic triaxial tests contradict shakedown theory. Wichtmann et al. (2005) shows that the level of cyclic strain accumulation, in drained compressive cyclic tests, is dependent on the initial void ratio e_0 and the cyclic stress ratios, $\eta_{av} = q_{av}/p'_0$ and $\zeta_b = q_{ampl}/p'_0$. On a plot of ε_{acc} against $\log(N_{cyc})$ the rate of strain accumulation is linear for the first 10,000 cycles (Figure 2.6). After this the rate of strain accumulation, caused by ratcheting, begins to increase over-logarithmic. These results are not consistent

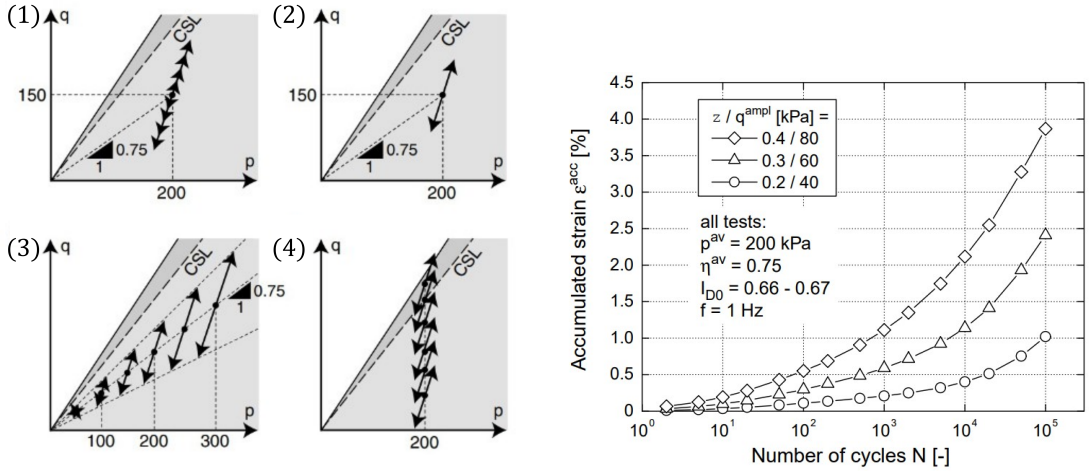

Figure 2.6: Long term drained cyclic triaxial loading response from (Wichtmann et al., 2005), showing: (a) the varied conditions of the cyclic tests performed. (1) a shows variations in the deviatoric cyclic amplitude, (2) shows the same test performed on samples of varied void ratio, (3) shows tests of varied p'_0, and (4) shows tests of varied stress ratios. (b) the variation in accumulated axial strain for tests with varied deviatoric cyclic amplitude.

with that of Theyse et al. (2007). The behaviour in extension is similar, albeit with a greater degree of accumulation for an equivalent negative stress ratio η_{av} (Wichtmann et al., 2007). This is consistent with the predictions from the distance of the current stress ratio from the bounding surface in extension. Additionally, the linear accumulation limit is exceeded at 1000 cycles, as opposed to 10,000 cycles in compression, indicating continuation of high levels of strain accumulation after many cycles. The continued strain accumulation after 10^5 cycles has implications for the long term behaviour of soils subjected to many cycles. Despite low cyclic stresses, given enough cycles, the accumulated strain may exceed SLS limits. Wichtmann et al. (2005) also found that the rate of cyclic loading had no effect on the strain accumulation, as long as drained conditions were maintained.

Low amplitude cyclic loading is sometimes termed cyclic pre-shearing and has been investigated by multiple studies. Blaker et al. (2019) found that an increase in the amplitude of drained pre-shearing increased the number of cycles required to induce cyclic failure but had no impact on the permanent shear strain at failure in subsequent undrained cyclic triaxial tests. Whereas, Ishihara et al. (1982) found that cyclic pre-shearing had no impact on resistance to liquefaction. Wichtmann et al. (2004) found that after the first few cycles of low amplitude drained cyclic loading, the number of cycles had no impact on small strain stiffness, despite an accumulation of strain through ratcheting. Mandolini et al. (2021) showed that the degree of strain accumulation during long-term low-amplitude cyclic loading, is greatly increased if the axes of the principal stress changes. Hollow-cylinder cyclic tests with continuous rotation of the principal stress, caused a 20% degradation in stiffness.

The behaviour during drained cyclic loading discussed above, refers to cyclic loading

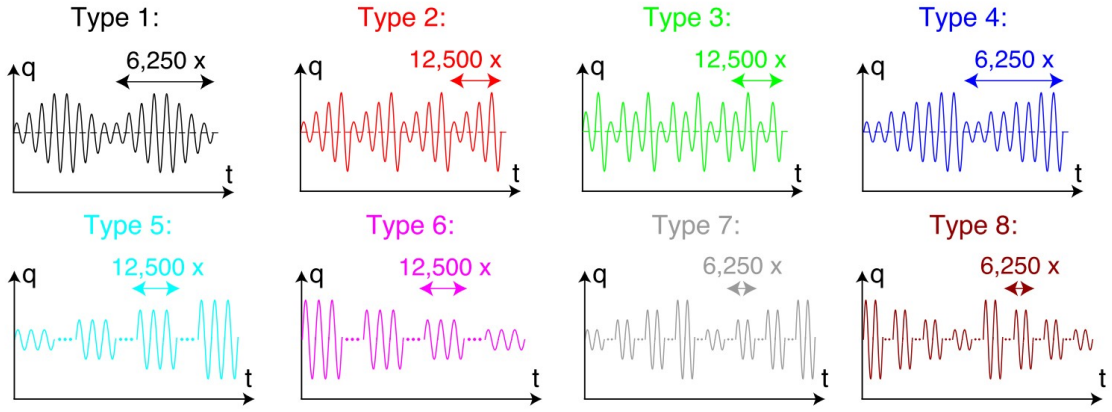

Figure 2.7: Bundling of loads for investigation of Miner's rule (Wichtmann et al., 2017)

conditions with uniform conditions throughout the test. The stress ratios imposed during the test have a significant impact on the strain accumulation. During cyclic tests with variations in stress level applied across the test, the behaviour is often predicted using Miner's rule (Miner, 1945). Stewart (1986) performed cyclic loading tests on ballast material, and showed that the ordering of loads had minimal impact on the overall strain accumulation. Wichtmann et al. (2010*b*) performed a series of drained cyclic tests with bundles of cycles of uniform stress, with variations in the order of stress magnitude. The results show minimal dependence in the accumulated strain on the load ordering. Furthermore, the cyclic flow rule, $\dot{\varepsilon}_q^{\mathrm{acc}}/\dot{\varepsilon}_v^{\mathrm{acc}}$, is unaffected by the load ordering. However, applying the loads in uniform bundles may have oversimplified the results. Cyclic load histories with a complex load pattern are often separated into bundles of uniform stressed using "rain flow" counting methods to simplify modelling and analysis. Wichtmann et al. (2017) performed a series of tests with varied load bundling, as shown in Figure 2.7. Here, the loads are applied in a varied manner, with full separation of load amplitudes, and mixed load histories. The results of the cyclic tests showed a greater degree of strain accumulation with uniform bundles. Therefore, the bundling procedure can be seen as conservative, if inaccurate. However, the cyclic flow rule was very similar in all cases.

2.3 Triaxial testing: Silty sands

2.3.1 Silty sand behaviour

Natural deposits of sand commonly contain silt, it is rare to find a truly clean sand deposit (Section 3.2). Therefore, despite complications, it is important to include silt in research and attempts to model cyclic loading. Lade et al. (1997) found that undrained monotonic behaviour of silty sand at low densities differed to typical soils, showing increased dilatancy and resistance to static liquefaction at higher mean effective pressures. However, Yamamuro et al. (1997) found that at low density and low mean effective pressure the resistance to static liquefaction of undrained tests was increased with increased fines content. They also showed a trend towards a greater range of void ratios from e_{min} to e_{max}. The concept of

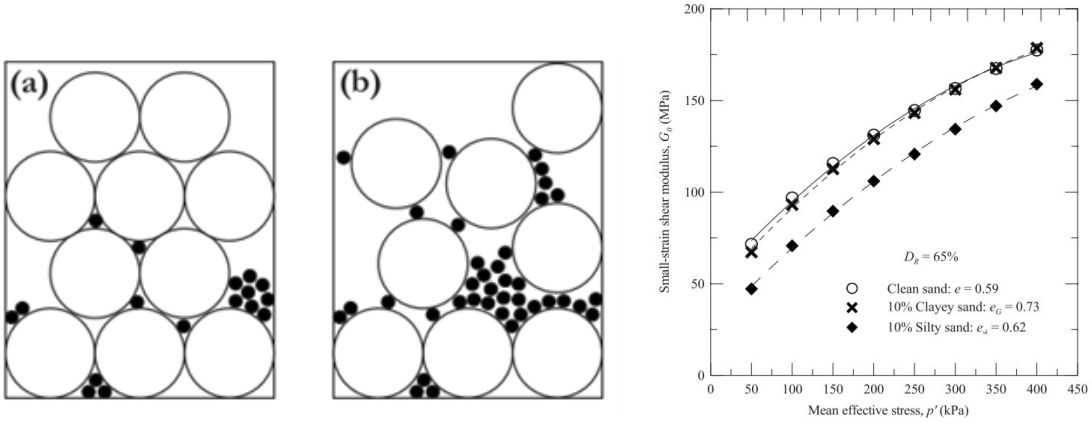

(a) (b)

Figure 2.8: Fines behaviour within sand from Carraro et al. (2009): (a) floating fabric diagram, the percentage of fines within the soil affects how it sits within the contact matrix, and (b) effect of plasticity on small strain stiffness of silty sand samples.

a sand skeleton void ratio was developed by Kuerbis et al. (1988*a*) which shows that as the fines content approaches a certain threshold value the response is dominated by the behaviour of silt-sand interactions, as the sand-sand contacts are replaced. This effect is termed floating fabric as shown in Figure 2.8(a) (Carraro et al., 2009), where the larger sand particles are said to be floating in a matrix of fines. The threshold for this behaviour is between 25-30% fines (Salgado et al., 2000). Lafayette et al. (2000) observed that the small strain stiffness of soil decreases with increased silt but that the peak stiffness and critical state friction angle are increased with small amounts of additional silt. J. Yang et al. (2018) performed a series of bender element and resonant column tests on samples with non-plastic fines. The results also showed that increases in fines, cause a reduction in small strain stiffness. However, the method of testing, BE or RC, affected the magnitude of the change. The impact of silt content on cyclic behaviour has been shown to be highly influenced by the plasticity of the fines. Ishihara et al. (1980) found that non-plastic fines generally had a detrimental effect on the cyclic strength, but that plastic fines could significantly increase cyclic strength. Erten et al. (1995) observed that in low amplitude, strain controlled, cyclic triaxial tests, silt content had minimal effect on the development of excess pore pressures. They observed that for large strain cyclic tests the addition of both plastic and non-plastic fines caused an increase in accumulated pore water pressure.

2.3.2 Silty sand: Effective void ratio of silty sands

The complicated relationship between fines content and soil response is partially due to the variability of the packing configuration of the silt particles within the soil matrix. At higher fines content, the void ratio will decrease, without an increase in the density of the stress network. Rahman et al. (2011) showed that the location of the steady state line varies with changes in fines content at the same global void ratio. Considering this, multiple studies have sought to create a unifying parameter which accounts for the apparent stress

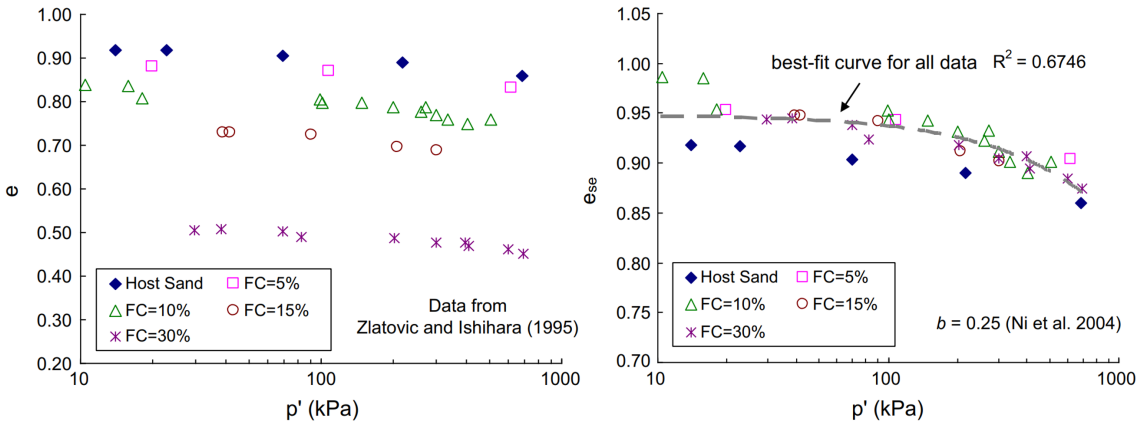

Figure 2.9: Results from J. Yang et al. (2015) showing the use of the equivalent void ratio e^* to create a unified steady state line in $e^* - \ln p'$ space.

skeleton which takes on loading, as an alternative to the global void ratio e. Examples of this include the sand skeleton void ratio e_{sk} (Kuerbis et al., 1988*a*), the intergranular void ratio (Georgiannou et al., 1990), and the equivalent intergranular void ratio e_{eq} or e^* (Rahman et al., 2014; Thevanayagam et al., 2000). Thevanayagam et al. (2000) found that at an equivalent global void ratio , increase in fines content decreases cyclic strength up to the fines content threshold which induces floating fabric, after which the cyclic strength is increased. However, they also found that, comparing samples based on intergranular void ratio, an increase in fines at low fines content increased the cyclic strength. Thevanayagam (2007) showed that the ratio between sand particle and fines particle size was important when predicting the impact of e^*. The use of the equivalent void ratio has been shown to be effective in unifying the response of silty sand samples. J. Yang et al. (2015) show that increases in fines content, cause the SSL to move downwards in $e - ln(p')$ space, but, when plotted in $e^* - ln(p')$ space, the steady state lines fall into one, indicating the effectiveness of the equivalent void ratio (Figure 2.9). Carraro et al. (2009) states that these methods are unable to distinguish between different types of fines, particularly plastic and non-plastic. Results show that shear strength increases with fines content in concordance with previous studies but show that non-plastic fines have a more significant effect than plastic fines (Figure 2.8(b)).

2.4 Triaxial testing: Partial drainage

Experimental investigations into the effects of partial drainage using the triaxial test are somewhat limited. The imposition of a partially drained condition is more complicated than fully drained or undrained. Two methods for this aim, imposition of a controlled volumetric strain rate using the volume control cylinder, or a “filter” to restrict flow placed between the sample and the back volume control cylinder. Additionally, the rate of loading either monotonic or cyclic can impose a partially drained condition within the sample. This method is less rigorous than the imposition of a volumetric control, as the rate effects of rapid loading cannot be entirely assigned to the drainage regime. Matešić et al.

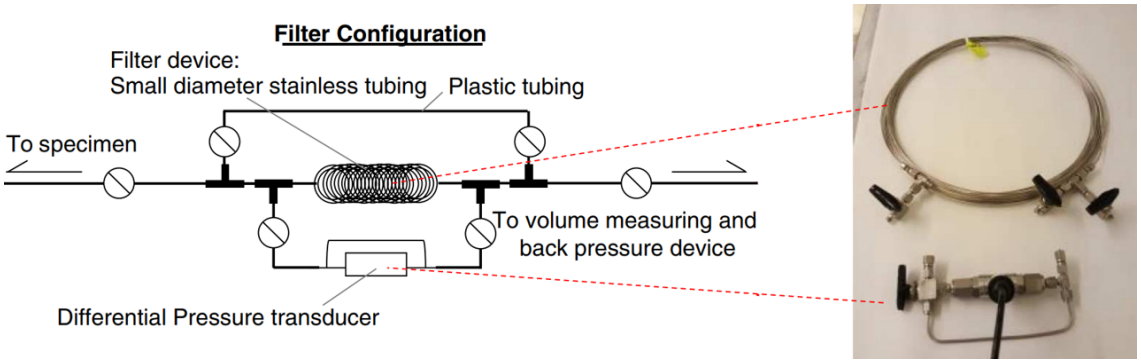

Figure 2.10: Partial drainage filter device used for monotonic testing in Suzuki et al. (2020)

(2003) found that increases in the strain rate during cyclic loading on dry sands induces a moderate increase in the shear modulus.

Monotonic investigations into the effect of partial drainage show an increase in the strength and stiffness of soils during triaxial testing. Watanabe et al. (2013) induced partially drained conditions using changes in the rate of strain, and showed that reduction in drainage increased the peak deviator stress achieved under the same initial conditions. Tests were completed at an axial strain rate of $\dot{\varepsilon}_a = 0.005 - 250\%/s$. The greatest increase in strength was found at a strain rate of $\dot{\varepsilon}_a = 50\%/s$. Under these conditions, the negative excess pore pressure peaked at $\varepsilon_a = 7.5\%$, before plateuaing with continued strain. The volumetric strain was minimal, but not zero, during this test. At strain rates above this, $\dot{\varepsilon}_a = 150$ and $250\%/s$, the drainage regime was effectively undrained, with almost zero volumetric strain, and continued accumulation of negative excess pore pressure until the end of the test. The results show a higher peak deviator stress in the $\dot{\varepsilon}_a = 50\%$, indicating that a partially drained response may have more benefit than fully undrained. Watanabe et al. (2013) provided a synthesis of existing data on model and triaxial tests, and subsequently conducted a series of triaxial tests.

However, these results are contradicted by the study of Suzuki et al. (2020). This investigation studied partially drained effects on monotonic loading in sands. The imposition of partial drainage was completed using a "filter" device (Figure 2.10). Samples were loaded with the same initial conditions, but drained through filters of differing resistance to flow. Flow resistance was classified using a constant head, and measurement of the flow over time. The results were compared to monotonic drained and undrained tests, with the undrained test achieving the greatest deviatoric stress, terminating at the point of cavitation (Figure 2.11). In comparison of the partially drained results, the greater resistance to flow induced increased peak strength, with a closer response to the undrained test. However, none of the tests reached the deviatoric stress induced during undrained testing. The volumetric strain reached similar levels at the end of the test, however, the rate of volumetric strain was affected by the filter resistance. The greater the resistance, the later the point of peak dilation, caused by an overall reduction in the rate of volumetric strain. Consequently, the point of peak strength was at higher axial strain as the filter

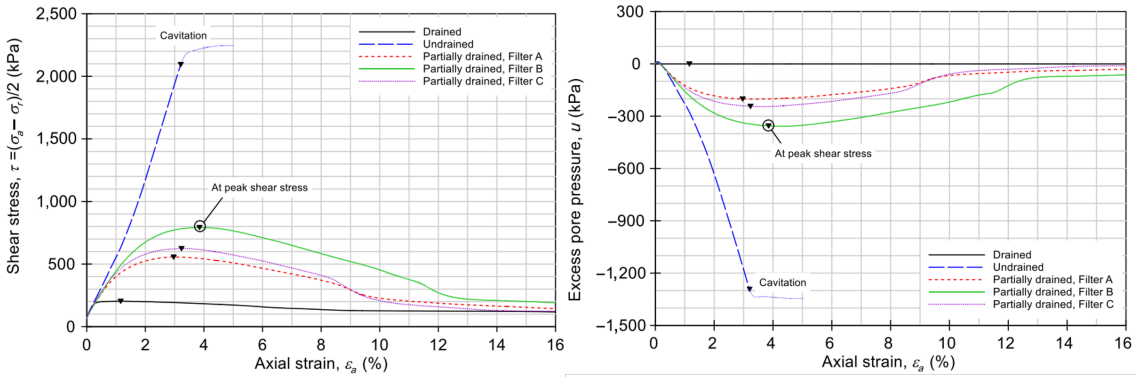

Figure 2.11: Monotonic partially drained triaxial results from Suzuki et al. (2020) showing increased deviatoric stress with increased resistance to sample drainage.

resistance increased.

Results of cyclic loading under partially drained conditions were produced using the same apparatus. Jostad et al. (2021) performed a series of four partially drained cyclic triaxial tests on two sands prepared to a relative density of 80%. The samples were anisotropically consolidated to $p'_0 = 127$ kPa, $q = 110$ kPa, and loaded with cycles of $q_{ampl} = 200$ kPa, representing stress ratios of $\eta_{av} = 0.87$ and $\zeta_b = 1.58$. These stress ratios are high for cyclic tests, in order to magnify the effect of partial drainage. The sample drainage was restricted using a filter with flow capacity 1.9×10^{-3} mm^3/s/kPa, then variations in drainage regime were achieved by altering the loading rate. The flow restriction was high, therefore, the loading rate was low, $T = 60 - 500s$. This minimised issues with the loading rate effects discussed above. The samples were loaded with 140 cycles. Three tests showed continued accumulation of excess pore pressure over the full 140 cycles. One test, performed with a loading period of $T = 500s$, exhibited dissipation of excess pore pressure after 13 cycles. The results showed a relationship between accumulated volumetric strain, and the pore pressure and bulk modulus. This relationship is consistent with undrained cyclic tests, where the rate of volumetric strain is zero, and the accumulated pore pressure is $\Delta u = f(\Delta p' \cdot K)$.

Chen et al. (2020) examined the impact of partial drainage on strain accumulation in granular fill material. The authors highlight that strictly the tests should not be considered element tests, as the pressure conditions varied through the height of the sample. Samples of gravel sand mix were prepared in 100 mm diameter cylinders, and loaded with packets of 10,000 cycles of increasing cyclic amplitude. The results showed an initial accumulation of excess pore pressure after each packet caused by contraction, followed by a dissipation phase. The accumulation of axial strain was attributed to an initial contractive behaviour, with continued high rates of axial strain in the pore pressure dissipation phase.

Partial drainage is an important consideration in earthquake engineering. Adamidis et al. (2022) conducted a series of cyclic triaxial tests with a controlled rate of back volume inflow. The rate of inflow was representative of pore fluid upflow from a liquefiable zone, into a permeable inflow layer, during a seismic event. The results demonstrated an

increase in the susceptibility to liquefaction of inflow zones subjected to constant pore fluid inflow. This methodology can also be applied with a constant rate of outflow, simulating a restriction to drainage during cyclic loading.

2.5 Triaxial testing: Numerical modelling

Soil constitutive models are the system of equations that aim to describe and predict the behaviour of the ground subjected to loading. At the most fundamental level, the constitutive model represents a stress-strain relationship. The complex nature of soil necessitates a sophisticated model for comprehensive description. Moreover, the varied loading and ground conditions require models that are tailored for specific applications. The data from triaxial testing can be employed to calibrate and develop constitutive models. These models are often employed in finite element analysis and aim to directly represent fundamental soil behaviour, contrasting with secondary modelling methods like p-y curves or cyclic contours. The following section outlines the design and application of particular important constitutive models for modelling cyclic loading of sand.

2.5.1 SANISAND

Cyclic loading constitutive models typically fall into two categories, commonly referred to as extrinsic and intrinsic. Intrinsic approaches model the response of each cycle, individually tracking the response of every element within the mesh and updating the load history accordingly. The intrinsic approach employs various model types. One significant subdivision of intrinsic modelling is bounding surface plasticity, of which the simple anisotropic sand model (SANISAND) family is the most prominent (Dafalias et al., 2004; 2016; Liu et al., 2019; Manzari et al., 1997; Taiebat et al., 2008). The sand response is characterised by "surfaces" that alter the model response based on the distance of the stress state to the surface (Figure 2.12). The model adopts the state parameter approach, Rowe's dilatancy theory, critical state theory, and a bounding surface to populate a multi-surface map in the deviatoric plane. Load reversal, a critical feature of cyclic loading, is

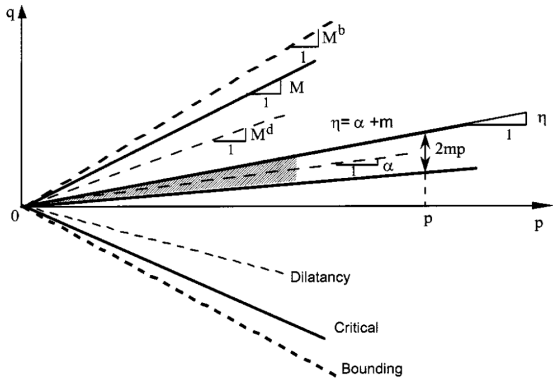

Figure 2.12: Schematic of the bounding surfaces of SANISAND (Dafalias et al., 2004)

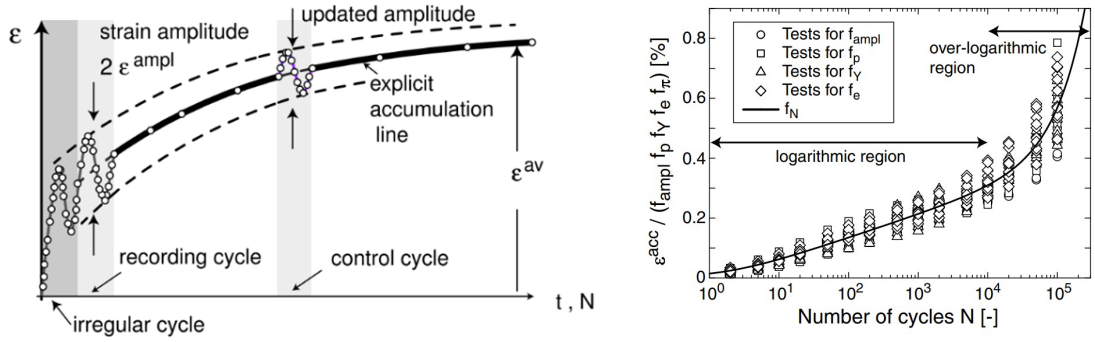

(a) (b)

Figure 2.13: Key figures from the High-Cycle Accumulation (HCA) model (Niemunis et al., 2005), showing: (a) a schematic of the extrinsic approach, the trend of strain accumulation is extrapolated, and (b) triaxial test results showing the strain accumulation trend against the number of cycles.

facilitated through a differential of the evolving stress ratio, η. Two bounding surfaces are defined: one for compression and another for extension. While in compression, the plastic modulus is defined as $H = h(M^b - \eta)$, whereas in extension, the equation alters to $H = h(M^b + \eta)$, indicating that the stress state now relates to the extension bounding surface. Modelling the cyclic ratcheting of sands through memory-enhanced bounding surface plasticity (Liu et al., 2019) is a contemporary update of the SANISAND model focussed on predicting high-cycle drained response of sand. The model has 16 calibrated parameters. Some parameters are calculated directly from monotonic triaxial data e.g. G_0 from the small strain response of a stress-strain plot, M from large strain monotonic tests. Other parameters are arbitrarily set based on previous SANISAND formulations or trial and error e.g. ν (Poisson's ratio) or m (elastic yield surface). Others are calibrated based on curve fitting to cyclic data to match the response e.g.μ_0 which is set to match the computed data with the experimental for ε_{acc} per cycle number. Within the paper, the model is tested against validating data, not used in the calibration process, and shows reasonable agreement with the experimental data. However, inaccuracy is introduced as the model approaches cyclic loads closer to failure, over-predicting strain. A total of 16 calibrated parameters is in the mid-range of typical advanced constitutive models for sand, and all come from element testing or FE trial and error procedures, which is preferable. Azeiteiro et al. (2017) provide a methodology for calibrating monotonic, critical state, bounding surface plasticity models with a series of triaxial and bender element tests. In total they completed 34 tests with a variety of stress paths and initial conditions. This high number of tests would be impractical for use in industry, though the calibration allows use for varied stress states. The calibration procedure could be conducted with fewer tests, although this would reduce confidence in the performance.

2.5.2 HCA

The extrinsic approach models a limited number of cycles intrinsically to plot a stress strain curve which is then extrapolated to give an evolving stiffness as a function of cycle

number (Figure 2.13). This reduces the overall computational cost which is therefore useful for modelling a high number of cycles. In contrast, intrinsic models which compute multiple stages of every cycle have a feasible upper limit of $\approx$ 100 cycles, and suffer from accumulated numerical errors which impact accuracy. A prominent example of an extrinsic cyclic model is the High-Cycle Accumulation model (HCA) (Niemunis et al., 2005). This model is formulated to allow an extrapolation of the trend of stiffness and strain accumulation after the first few cycles. Using the extrapolation, the FE model will predict strain at the element level for a given number of cycles. The model includes stiffness calibration for varied initial conditions and load paths, allowing varied response across the model. The calibration tests are varied parametrically with respect to $\varepsilon_{\text{ampl}}$, cycle number N, cyclic p'_0, ζ_{b}, e, and the change of the polarization of the strain loop. The results presented in Figure 2.13(b) show the normalised strain accumulation is approximately logarithmic, with strain accumulation increasing over-logarithmic at very high numbers of cycles. This relationship is key to the model, as it allows the prediction of strain with respect to any of the parameters above.

Wichtmann et al. (2010*a*) present a series of cyclic triaxial tests designed specifically to calibrate the HCA model. The model required the production of a large number of cyclic triaxial tests, under varied conditions for calibration. However, the author's intention was that further use of the HCA model would require a limited set of these tests, to fit the relationships previously determined to the new results. The plots shown in Figure 2.6(a) show the variation in triaxial tests performed. The design of these series of tests enabled the calculation of constants required for the calibration of the HCA model. The constants were computed using a curve fitting algorithm from the results of each series, an example of which is shown in Figure 2.6(b). Alongside these triaxial tests, a test to obtain φ_{cs} was required, this study used the angle of repose, and an isotropic consolidation test to obtain the bulk modulus, K, and the Poisson's ratio, ν.

2.5.3 Contour diagrams - UDCAM/PDCAM

The contour diagram method for monopile design has been widely adopted in industry (Andersen, 2015; Jostad et al., 2015). It is an empirical framework for interpreting the results of cyclic triaxial and simple shear tests on soils subjected to repeated loading. The method provides a practical means of assessing soil degradation, pore pressure generation, and strain accumulation under cyclic stresses representative of offshore and foundation loading conditions. In this approach, cyclic test data are summarised in the form of a contour diagram that relates the cyclic shear stress ratio (τ_c/σ'_{vc}), the average static shear stress ratio, and the number of load cycles applied. For modelling of drained cyclic loading, the strain accumulation after a set number of cycles is measured and input into the contour diagram. Lines of equal number of cycles to a given accumulated strain value are plotted in contours in stress space. In order to model partially drained conditions, undrained element tests are used to calibrate the accumulation of pore pressure for a given number of cycles

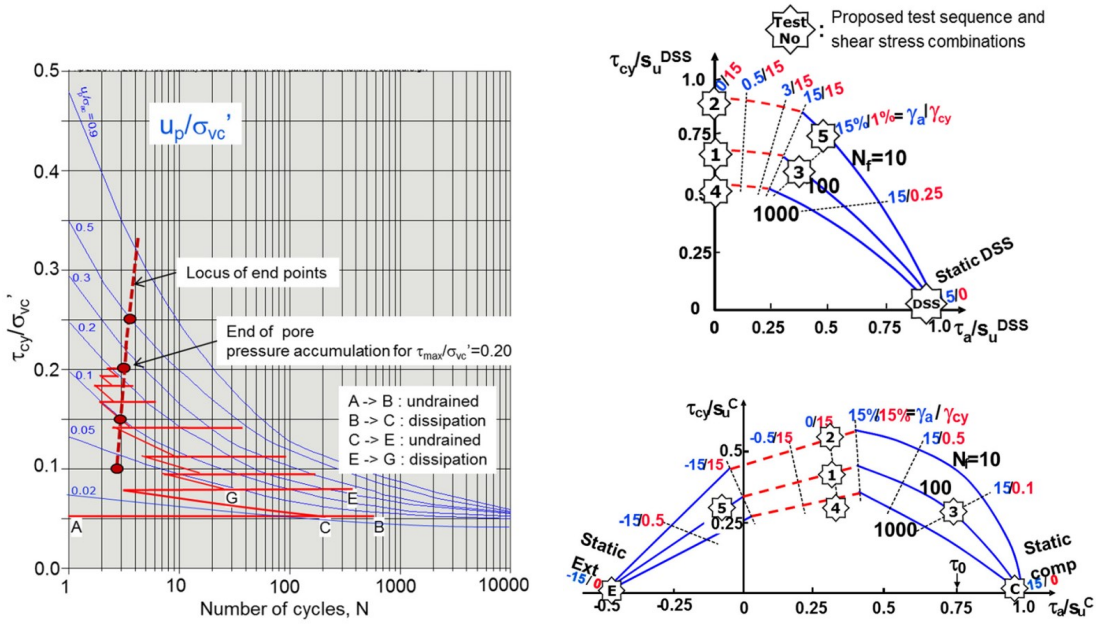

(a) (b)

Figure 2.14: Contour diagram method (Andersen, 2015), showing: (a) predicting excess pore pressure accumulation with an equivalent path of loads, and (b) required element tests for calibrating a contour diagram. The contour diagrams presented here are derived from element tests on clay samples. The same procedure is employed with sand samples, however the results are normalised with values of σ'_{ref} instead of σ'_{vc} and s_u.

at a given cyclic stress ratio. The dissipation rate is then determined numerically with a given soil permeability.

Contour diagrams can be used to model the effective cycle number of a combination of loads of different cyclic stress ratio both in terms of strain and excess pore pressure accumulation (Figure 2.14(a)). After determining the equivalent number of cycles at the maximum cyclic stress ratio, the overall predicted strain and pore pressure accumulation at the set number of cycles is calculated.

Calibration of a new contour diagram can be completed with a reduced number of tests, which are then used to calibrate existing contour diagrams. The method proposed by Andersen (2015) recommends a minimum of six DSS or seven cyclic triaxial tests to complete this procedure (Figure 2.14(b)).

While the contour diagram method is empirical and relies on laboratory calibration for each soil type and density, it remains widely used for offshore foundation design and for interpreting cyclic triaxial and DSS test results. Its strength lies in condensing complex cyclic soil behaviour into a simple, practical graphical format suitable for design charts and long-term cyclic loading assessments.

2.6 Triaxial testing procedure

2.6.1 Triaxial test: Sample preparation methods

Sample preparation considerations

The triaxial test aims to examine the behaviour of soils under real-world conditions, including their state and stress levels. For sand samples, where the use of undisturbed specimens is often impractical, sample reconstitution is necessary prior to testing. An effective reconstitution method is essential for accurate representation, considering various influencing factors. The following section outlines these considerations.

Sample density is arguably the most important consideration in sample preparation, especially at large strains. The soil response is significantly influenced by the void ratio. Critical state soil mechanics (Roscoe et al., 1958), and the state parameter formulation (Been et al., 1985), use the void ratio as a key predictor for soil response. Thus, it is essential to produce samples with a known and reliable density for effective testing. Moreover, a homogeneous density profile across the sample is vital. Some methods are prone to forming low-density zones within the samples, particularly at the surface. This can lead to the onset of bedding errors that affect the calculations of strain (Baldi et al., 1988) and reduce liquefaction resistance (Vaid et al., 1988).

Fabric is the term that describes the particle arrangement within a sample. The asymmetric morphology of most sand particles allows for a variable microstructure within the sample. The choice of sample preparation method significantly influences the achieved fabric. Many sample preparation methods aim to reproduce the naturally occurring fluvial deposits of sands (Kuerbis et al., 1988*b*). This deposition style creates a cross-anisotropic structure, resulting in a heterogeneous response across loading directions. Conversely, reconstitution methods that do not rely on pluviation create a more isotropic structure. This can lead to a response that does not accurately replicate reality. Considerations of fabric are critical when examining small strain loading, where the initial particle arrangement significantly impacts response (Wichtmann et al., 2020). This finding is supported by numerical micromechanical simulations of small strain stiffness response (Zeghal et al., 2015).

The size of the sample significantly influences the measured response. During loading, the idealised theoretical response should induce deformation in a right-cylinder shape. However, end plate friction results in an inconsistent deformation profile, characterised by restricted lateral strain at the ends and barrelling towards the centre. To mitigate this effect, most samples are prepared with a 2:1 ratio of length to diameter (Sarsby et al., 1980). This approach improves the deformation profile towards the centre of the sample. Moreover, an increase in the overall size of the sample diminishes the impact of this effect, thereby providing a more accurate representation of the soil response. Nonetheless, this consideration affects the practicality of preparation concerning the materials used and manual handling.

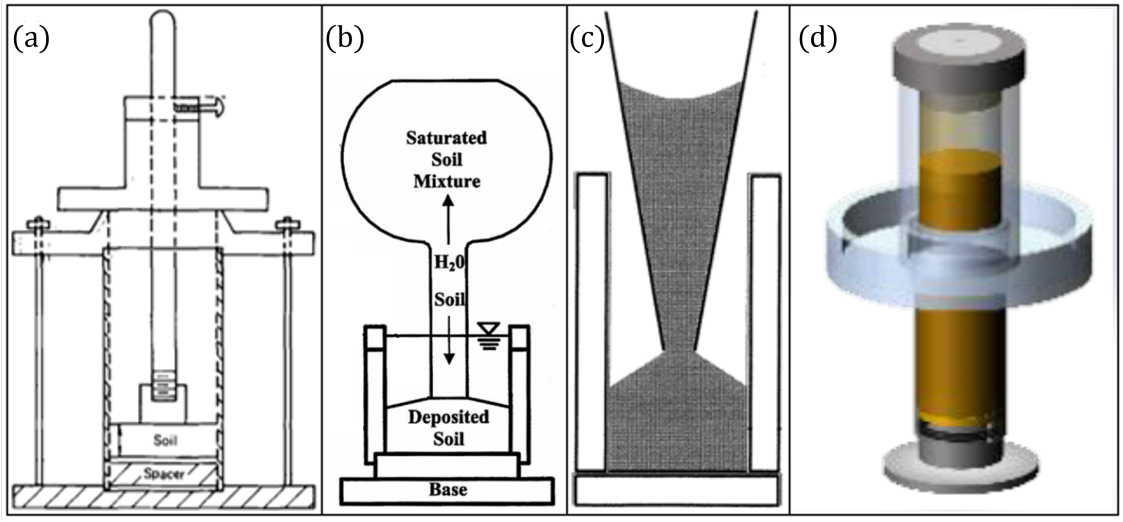

Figure 2.15: Sample preparation methods for sands, showing: (a) moist tamping (MT) (Ladd, 1978), (b) water pluviation (WP) (Wood et al., 2008), (c) dry funnel deposition (DFD) (Zlatovic et al., 1997), (d) slurry deposition (SD) (Dominguez-Quintans et al., 2019).

A final consideration is the inclusion of fines within the sample. For research purposes, clean sand with narrow grading is often used. However, silty sands represent a significant aspect of study. Firstly, the majority of sands encountered during site investigations contain at least some fines. Secondly, the presence of fines significantly impacts the response. Therefore, the ability to incorporate fines in the prepared sample is a crucial consideration. The standard methods of pluviation, both wet and dry, prohibit the inclusion of fines. The disparity in particle size between sand and silt induces different fall velocities, leading to a sample with distinct layers of sand and silt. The most commonly used methods for the reconstitution of silty sand samples are moist tamping, dry funnel deposition, and slurry deposition.

Considering these factors, a discussion of sample preparation methods is provided below.

Moist tamping, Ladd undercompaction

Moist tamping (Figure 2.15 (a)) is a commonly employed reconstitution method in research and site investigation. The advantages include a broad range of achievable void ratios for samples, straightforward preparation, and the capacity to incorporate silt in the process. The methodology most widely adopted is that of Ladd (1978). This method adds layers of uniform weight, but varying compaction depth throughout the height of the sample. This ensures the sample density is homogeneous with depth. The lower layers are undercompacted, allowing for further compaction to achieve a uniform density as additional layers are added. The method accommodates the inclusion of fines, as the silty-sand sample is thoroughly mixed with a small quantity of water, $w_c \approx 5 - 15\%$, prior to compaction. This ensures that the silt and sand are combined, and held together before compaction. However, this also introduces a level of cohesion that alters the fabric

during preparation. The isotropic fabric is often described as a honeycomb structure. This honeycomb structure is collapsible and more susceptible to liquefaction (Vaid et al., 1999; Yao et al., 2023). Studies have demonstrated notable differences in soil response, particularly at low relative density, where moist tamping samples can display contractive behaviour compared to the dilative response of pluviated samples (Dominguez-Quintans et al., 2019; Ghionna et al., 2006). However, the results in literature do not consistently corroborate this finding. Wichtmann et al. (2020) examined the response of sands prepared by moist tamping compared with pluviation methods. This study showed that samples prepared using moist tamping were less contractive during undrained monotonic tests than air-pluviated samples. During drained low amplitude cyclic tests, the level of deviatoric strain accumulation was greater in moist tamping (MT) samples of low density. Within the testing, the study examined the effect of the number of tamped layers; samples of 8 and 50 layers were tested. The trend of greater accumulation was amplified in samples prepared with a lower number of layers. This may be explained by a greater level of heterogeneity in the reduced number of layers. At the boundary between layers samples do not have a uniform density profile. At higher densities, the trend was reversed, with greater accumulation observed in the pluviated samples. This observation, as well as the lack of agreement between studies, highlights the inconsistency of the moist tamping method.

Water pluviation

Water pluviation (WP) (Figure 2.15 (b)) is a widely used method in research. The technique is robust and repeatable, yielding uniform samples with fabric that aligns with the natural fluvial deposition process. The sample is prepared by saturating the required mass of sand in a vacuum flask prior to deposition. This results in a well-saturated sample without the need for CO_2 flushing. Following the de-airing procedure, the sample is pluviated into a mould filled with water. The sand falls into the mould, and the displaced water is drawn into the flask. For optimal results, deposition is conducted at nearly zero drop height. Particles reach terminal velocity in the water at 0.2 cm (Vaid et al., 1984), thus precluding variations in density related to drop height. This practice enhances homogeneity and streamlines the process, as drop height becomes less critical during preparation. To achieve the desired density, vibration or tapping is employed. Wichtmann et al. (2020) compared tapping and vibration, revealing identical responses during drained cyclic loading. To mitigate the effect of a low-density zone at the surface, a surcharge is frequently placed on the sample during vibration. Yao et al. (2023) investigated the impact of varied sample preparation methods on carbonate sands. Their study demonstrated that the most anisotropic samples were produced using air pluviation, though water pluviation yielded similar results. Samples prepared via moist tamping were observed to be significantly isotropic. The anisotropic pluviated samples exhibited the lowest φ_{cs} and the highest λ (compressibility). Vaid et al. (1999) compared the response of reconstituted samples to frozen “undisturbed” samples. The findings indicated that, during undrained monotonic tests, water-pluviated samples exhibited the closest agreement with undisturbed alluvial

samples. This method is widely regarded as the most effective for closely graded clean sand samples. However, it is unsuitable for reconstituting well-graded particulate materials. As discussed, this limitation arises from the formation of layers of particles with differing sizes.

Dry funnel deposition

Dry funnel deposition (DFD) (Figure 2.15 (c)) is a method employed to prepare well-graded samples, including fines. This technique involves the use of a funnel that is raised, allowing the sample to pour into the mould. To prevent the build-up of static electricity, which could alter the fabric, a paper or card funnel is used (Cubrinovski et al., 2002; Zlatovic et al., 1997). The funnel is raised with zero drop height. The sample is subsequently densified through vibration or tapping to achieve the desired density. The methodology mitigates the formation of a layered sample. However, during deposition, the sand particles roll over the surface. Consequently, the fabric achieved does not correspond to the fluvial method. In fact, this method induces a response akin to the shearing response, resulting in a sample that is somewhat isotropic. Due to the complex particle interactions during deposition, small variations in the method can lead to significantly different fabrics. The results from the sample preparation investigation produced in chapter 3 support this observation. Moreover, the pattern of anisotropy is arranged concentrically towards the centre of the mould, reflecting the flow pattern emanating from the funnel (Wood et al., 2008). Additionally, the response is inconsistent across studies. Z. X. Yang et al. (2008) indicates that DFD samples exhibit a greater strength than pluviated samples during monotonic loading, while Sze et al. (2014) show the opposite. Y. Li et al. (2018) reveal that the liquefaction resistance is enhanced for DFD samples. The variation in response between DFD and WP samples is most pronounced at low density. This discrepancy is likely due to the need for densifying vibrations in higher density samples, which yield similar fabrics during particle rearrangement.

Slurry deposition

Slurry deposition (Figure 2.15 (d)) is a variation of the water pluviation method developed to incorporate fines. The sand-silt mixture is contained in a sealed mould with an extension collar to facilitate sample mixing. The extension collar is typically the same length as the sample mould, creating a space double the required amount to aid mixing while suspended in water. The entire apparatus is prepared with sufficient sand and silt to achieve the desired density and fines content, with the remaining space filled with water. The procedure for introducing the sand, silt, and water may vary, with the objective of enhancing the initial saturation ratio; however, the final preparation is generally consistent. Once the mixture is prepared, the entire apparatus is rotated and inverted for a specified period to generate a well-mixed slurry. After mixing, the slurry is allowed to settle, and the mould is vibrated to achieve the desired density. Studies advocating for the use of slurry deposition (SD) (Carraro et al., 2008; 2009; Dominguez-Quintans et al., 2023; Kuerbis

et al., 1988*b*) suggest that the method is suitable for site investigation. However, the fines content achieved is reduced from the initial preparation. During the settlement phase, due to the lower speed of settlement, a significant proportion of fines remains suspended in the excess water. The method depends on an excess fines content in the initial preparation to accommodate some losses. Therefore, the method is unsuitable for site investigation, where testing of the full sample is essential, and the addition of excess fines is not practical. Furthermore, for preparing samples with high degrees of fines content, $f_c > 20\%$, at high relative densities, $D_r > 80\%$, the level of material within the apparatus limits efficient mixing of the sample. Additionally, the method has a lower range of achievable void ratios, presenting both a lower maximum and higher minimum than alternative methods, particularly MT (Kuerbis et al., 1988*b*).

However, in the process of researching sands with some fines content, the SD method offers significant advantages. It is the only method that allows for the creation of a silty sand sample using the pluviation deposition method for an alluvial fabric. This results in uniform samples with anisotropic fabric. Assuming that the WP method reconstitutes the most representative sand samples, the similarity of response between SD and WP samples is a notable benefit. The results of multiple studies (Dominguez-Quintans et al., 2023; Kuerbis et al., 1988*b*; Wood et al., 2008) demonstrate that the method achieves uniform density and fines content throughout the sample. The behaviour is shown to be less contractive and, therefore, less prone to liquefaction than samples produced using MT (Carraro et al., 2008). The monotonic response of SD and WP samples is very similar at both loose and dense initial states (Kuerbis et al., 1988*b*). Dominguez-Quintans et al. (2023) indicates that the response of SD samples is less stiff and less contractive than that of MT samples.

2.6.2 Triaxial test: Advanced methodologies

The following section presents additional considerations for the preparation of a triaxial test sample. The methods detailed are employed in advanced triaxial testing to minimise potential errors and provide further classifying results.

Bender elements

The use of bender elements in triaxial testing is a non-destructive method for assessing small strain stiffness, $G_{\max}$ of triaxial samples. The method was first presented by Shirley et al. (1978). The developed apparatus involved piezoelectric crystals that oscillate with very small strain cycles at an applied frequency. The oscillation results in a low-amplitude shear wave, which can be used to calculate the shear modulus, $G_{\max}$, using Equation (2.1).

$$G_0 = \rho \cdot v_s \tag{2.1}$$

The strain applied is $\approx 0.001\%$ (Dyvik et al., 1987). The method has since been updated to create a rigorous, consistent methodology frequently employed in research and

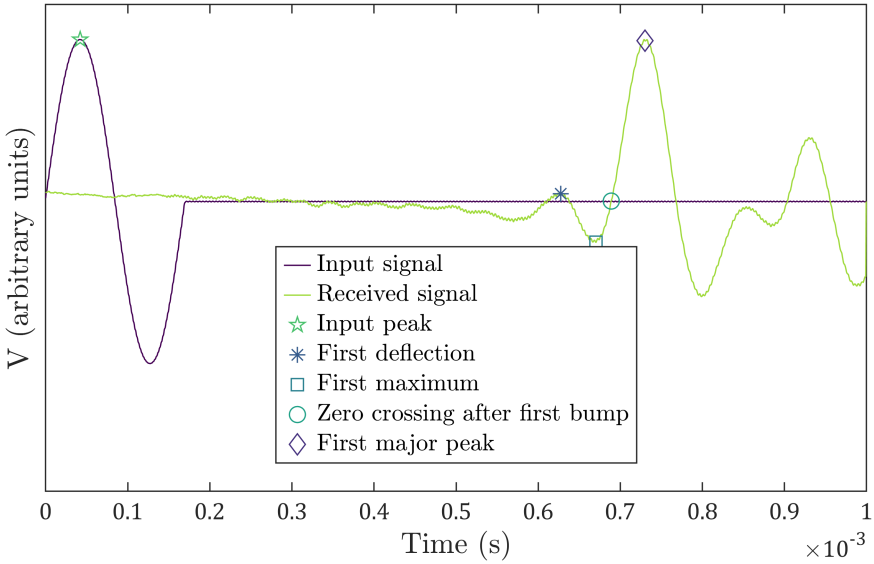

Figure 2.16: Examples of methods of selection of arrival time in bender element tests in the time domain

industry. The density, ρ, is assumed to be uniform and calculated based on the measured sample volume and mass. However, the assessment of arrival time, and hence shear wave velocity, v_s, is more complicated. Issues such as near field effects can complicate the interpretation of the received signal (Arulnathan et al., 1998). Certain factors can mitigate the impact of near field effects, including reducing the height-to-diameter ratio, using sine waveforms instead of square waves, increasing the frequency of excitation, and raising the voltage of the transmitting element (Clayton, 2011). However, issues with selection of the arrival time for recording still arise (Figure 2.16). Multiple methods exist for this procedure. The most commonly used method, due to its simplicity, is the peak-to-peak method. However, due to pulse broadening, the results for travel time are consistently higher than those from other methods (Clayton, 2011; Da Fonseca et al., 2009). A more accurate method, in the time domain, employs the first arrival, which mitigates the effect of wavelength elongation in the assessment of v_s (Arulnathan et al., 1998). Nevertheless, determining the point of first arrival presents challenges. A subset of this method is the first crossing method, which identifies the arrival point as when the trace first crosses zero following an initial disturbance in the received signal. The time difference is taken between the start of the input signal and this point. It has been shown that this provides a more accurate and consistent measure of $G_{\max}$ than the peak-to-peak method (Arulnathan et al., 1998). To mitigate the issues of subjective assessment of v_s, and near field effects, a field of research has emerged into the use of frequency domain analysis. Frequency domain analysis methods, such as π-point phase comparison (Arulnathan et al., 1998; Greening et al., 2004), yield repeatable results for v_s, but are consistently lower than those obtained from time domain analysis. A further method is wavelet analysis (Bonal et al., 2012). This approach mitigates the impact of near field effects, as the wavelets are identifiable by a singularity in the signal. These methods also produce consistent results; however,

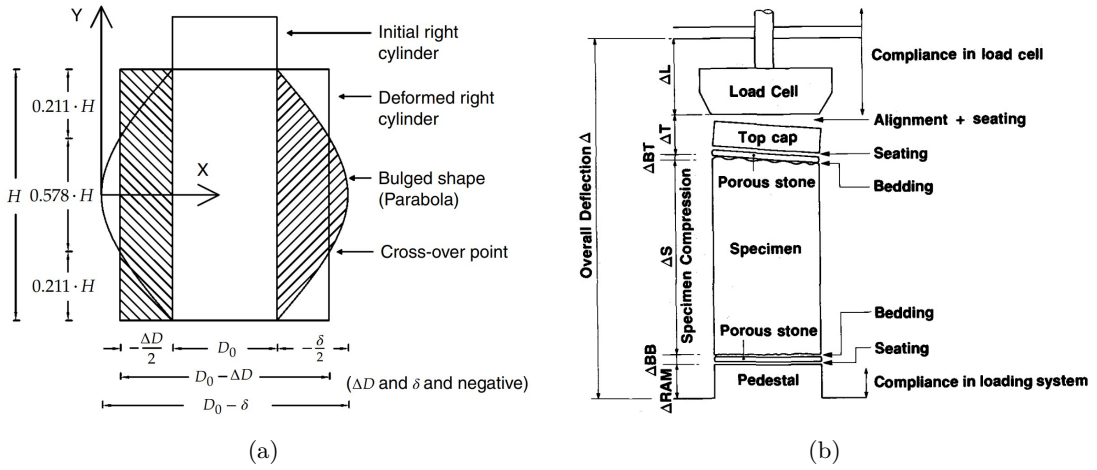

Figure 2.17: Triaxial test considerations , showing: (a) barrel correction calculation (Lade, 2016) (b) bedding and system compliance errors (Baldi et al., 1988)

the calculated value of $G_{\max}$ is consistently different from the time domain methods, with approximately 20% faster v_s. Therefore, the chosen method between first arrival and frequency domain is somewhat arbitrary as long as a consistent methodology is employed across all analyses.

Sample bedding

The issue of sample bedding can lead to inaccurate measurements of strain, particularly at low density and low strain. Certain sample preparation methods are prone to creating low density zones at the surface. Furthermore, the sample setup can result in gaps between the ram, top cap, porous stones, and the sample as shown in Figure 2.17(b) (Baldi et al., 1988; Sarsby et al., 1980). If not addressed, this can lead to the overestimation of initial strain during consolidation or early loading. This can be mitigated during the sample preparation phase. Firstly, the methodology can incorporate sacrificial material at the surface, which is removed prior to the addition of the top cap, eliminating the low density zone at the top surface. Secondly, the height of the sample can be measured after a small vacuum (≈ -5 kPa) is applied. This process removes the effects of irregularities in sample setup and ensures adequate contact at all points prior to measurement. This is most easily accomplished with samples that are pre-saturated during the preparation phase, i.e. WP and SD.

Lubricated end plates

Triaxial test theory assumes a uniformly deforming right cylinder. This continuum assumption fails when the sample barrels or forms a shear plane. Porous stone end plates introduce friction at the sample ends, constraining deformation and contributing to barrelling. Barrelling induces a non-uniform stress state throughout the sample and partially invalidates assumptions employed to calculate the sample cross-sectional area, which is

crucial for accurate stress and strain results. The application of lubricated end plates mitigates the effects of end plate friction. A double layer of membrane, separated by a thin layer of grease, is affixed to the ends, incorporating a small hole for drainage and, if necessary, bender elements. Lubricated ends have been shown to significantly reduce sample barrelling (Rowe et al., 1964). This has been shown to greatly improve the measurement of stiffness and strength (Kuwano et al., 2002). However, the results are imperfect, and the complication of the methodology allows for inconsistency in results. Furthermore, the vacuum grease and membrane deformation can contribute to further bedding errors (Lo et al., 1989; Molenkamp et al., 1983). Furthermore, the use of lubricated end plates is prohibited in the slurry deposition method, where the free moving membrane may dislodge and protrude into the the sample during the mixing process.

Measurement corrections

Membrane resistance to sample deformation arises from the inherent elastic stiffness of the membrane. This effect is most pronounced at low stress levels, where the stress exerted by the membrane is comparable in magnitude to the overall applied stress. ASTM D7181-20 (2020) provides the following correction for deviator stress: $\Delta(\sigma_1 - \sigma_3) = (4E_m \cdot t_m \cdot \varepsilon_1)/D_c$ where: D_c is the diameter of the sample after consolidation; E_m is the Young's modulus of the membrane; t_m is the membrane thickness; ε_1 is the axial strain. This correction should be applied if the error exceeds 5%.

The use of a flexible membrane is essential for a triaxial test. However, this may lead to membrane penetration into the sample, resulting in inaccurate measurements of sample volume and volumetric strain (Baldi et al., 1984). This effect is most pronounced with larger particle sizes, or low relative density, as the gaps for the membrane to bridge become larger. The sand tested in this project was fine-grained $D_{50} = 0.15$ mm, hence this was not a significant concern.

Another important aspect is the impact of barrelling. As discussed, the idealised shape of sample deformation is that of a right cylinder; however, this assumption is seldom accurate. This aspect is particularly relevant at large strains. The sample typically deforms into a barrel shape, with increased radial strain towards the centre of the sample. Furthermore, continued straining towards the critical state often produces a shear plane diagonally across the sample. These conditions have been studied extensively, and a somewhat unified solution for analysis has been formulated to correct the results. This method is summarised by Lade (2016) which is shown in Equation (2.2). This correction assumes a parabolic shape of deformation (Figure 2.17(a)). However, the correction does not apply to samples where a shear plane has formed. A standard approach to this is to record up to the point at which the shear plane becomes apparent (Azeiteiro et al., 2017).

$$A_{\text{barrel}} = A_{\text{cylinder}} \cdot \left(2 - \sqrt{\frac{1-\varepsilon_a}{1-\varepsilon_v}}\right) \tag{2.2}$$

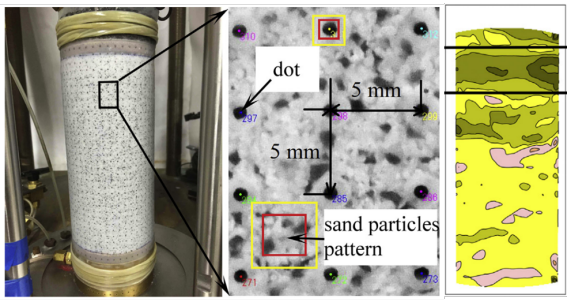

Figure 2.18: Image analysis for strain measurement, (a) Sample mounted with transparent membrane and dots;(b) Zoom view of (a); (c) Heat map of axial strain (Zhao et al., 2018)

Local strain measurements

When measuring small strains, factors such as bedding errors and instrument sensitivity become increasingly significant. At larger strains, phenomena such as barrelling become more pronounced. Local strain instrumentation can mitigate these issues, in addition to the mitigation measures mentioned above. Local strain encompasses any measurement of sample deformation directly from the specimen. This approach provides an accurate measure of the actual sample deformation, thereby reducing potential measurement errors. An additional benefit is the capacity to deliver higher resolution measurements for recording small strain responses. Multiple methods exist for measuring local strain, including Hall effect transducers (Drnevich et al., 1989; Garga et al., 1997), electrolytic level sensors (Jardine et al., 1984), image-based analysis (Zhao et al., 2018), and the most widely employed system of sample-mounted LVDTs developed by Brown (Brown et al., 1980; 1974).

Image-based analysis (Figure 2.18) offers the advantage of not disturbing the specimen and can yield highly detailed results; however, it is the most time-consuming method and does not provide live results essential for calculating values such as Poisson's ratio.

Locally mounted LVDTs provide an effective and precise method for measuring local strain. The method was first proposed by Clayton et al. (1986), and has since been developed into a rigorous and widely used setup (Escribano et al., 2019; Tatsuoka et al., 1994). It operates by mounting high-resolution linear variable differential transformers (LVDTs) to the exterior of the sample. The mounting points span the mid-range of the sample, with the sensor secured at the upper mount, and a freely moving pin resting on the lower mount. The mounting can be reinforced with staples inserted through the outer membrane and into the inner sample. This is more readily accomplished with clay samples, which do not require a vacuum for setup. In contrast, sands typically necessitate a combination of CA glue and silicone for attachment of the mounts. Challenges arise when conducting experiments that require the measurement of both small and large strains on the same sample. The appropriate range of detection and resolution can be chosen for the specific test. Measurement sensitivity is improved with reductions in the measurement

range, which may become inadequate during tests that encompass the full range of strain. For cyclic tests, a low-range, high-resolution sensor is most suitable. The combination of low-range high-resolution local strain measurements and high-range lower-resolution global measurements enable measurement across the full range of the test, with sufficient resolution in small strain. However, the methodology has certain drawbacks. The mounting of the LVDTs introduces disturbances to the sample; consequently, applying a partial vacuum on the sample is essential. When examining behaviour at low stress levels, these disturbances may influence the results. Moreover, as the sample undergoes significant deformation, the gauges are susceptible to misalignment, leading to inaccuracies.

2.7 Model testing: Monopile behaviour under monotonic loads

2.7.1 Monotonic behaviour: Pile geometry

Monopile geometries have evolved in design as their primary function has changed. Early research into piles focused on the long, slender piles of oil rigs, with large L/D ratios often exceeding 100. The design approach developed for these piles was termed the p-y method. This method predicted the soil pressure response with depth along the pile. However, the behaviour of these piles differs from that of modern monopiles used for OWTs. Modern monopiles feature a large diameter, D, and a short embedment depth, L. The PISA project (Burd et al., 2020) analysed contemporary geometries of monopiles

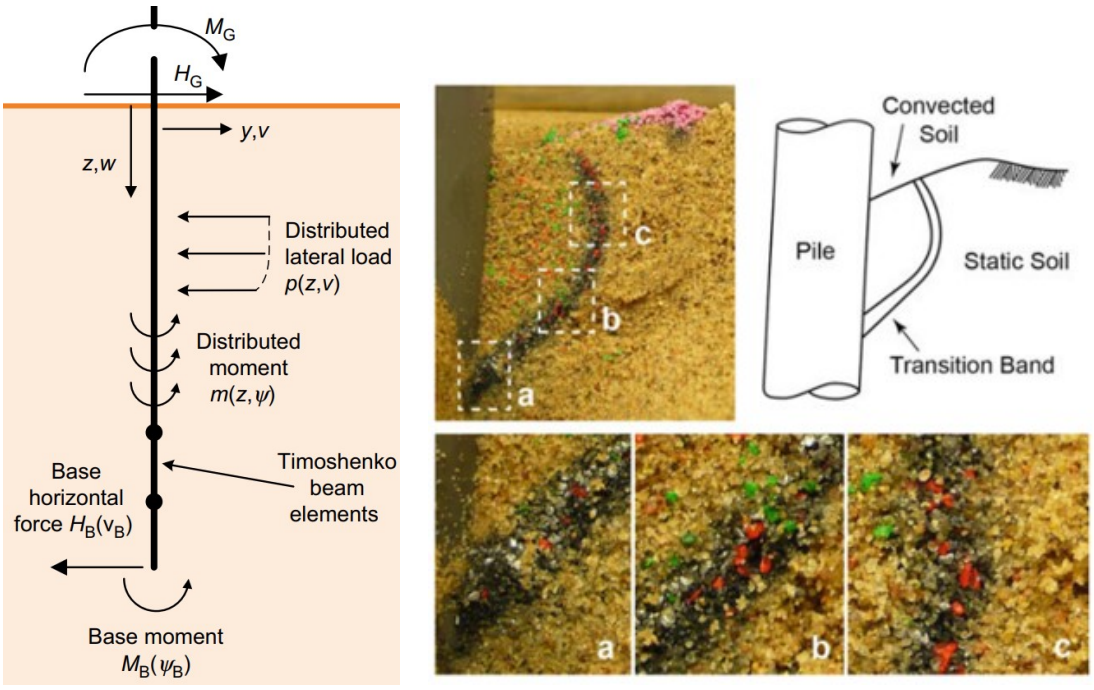

(a) (b)

Figure 2.19: (a) PISA 1D model of monopile lateral loading response (Byrne et al., 2020*b*). (b) Soil convection around a monopile during centrifuge modelling (Cuéllar et al., 2012).

in clay and sand to update the p-y approach for the low L/D, rigid monopiles employed for OWTs. The primary focus was on the monotonic response of these piles. Field-scale test results were integrated into advanced finite element models, resulting in a simplified 1D model capable of predicting the response of these modern monopiles. The 1D model incorporated several assumptions, such as linear independent soil springs and Timoshenko beam elements (Figure 2.19(a)). These results have been widely adopted in industry. The cyclic response of piles was not extensively considered in this project and is the focus of a follow-up initiative, the PICASO project (Byrne et al., 2020*a*). The findings of the PISA project indicate that large diameter monopiles used for OWTs exhibit a distinctly different response compared to the long, slender piles from oil rigs. During monotonic loading up to a specified ultimate displacement, usually defined as $0.1D$, the pile displays largely rigid rotation around a point along its length. The resulting soil displacement forms a cone of heave in front of the pile at the surface. Below the point of rotation, there is a reversal of loading, with compression behind the pile and extension in front. During monotonic loading, the type of soil has a significant effect. Loaded sands demonstrate a fully drained response, with soil strength dependent on Z. Loading into clay soils results in an undrained response, often leading to the onset of gapping in the tensile zones. This phenomenon can cause a substantial reduction in load capacity.

The impact of monopile geometry significantly affects the response. The major geometrical parameters which impact the response are, D, L, e (load eccentricity), and t (pile thickness). These factors affect the stiffness, drainage regime, strength, and fatigue limit. Typically in the assessment of the FLS criteria, the most important consideration is t, alongside system stiffness. ULS and SLS factors have a more complex relationship. The results of the PISA project (Burd et al., 2020) show that increases in L increase stiffness and strength for a given D. The model produced in Burd et al. (2020) shows that increases in D increases the degree of internal bending moment for a given lateral load. In relation to this effect, the system stiffness is also increased with D. Load eccentricity, e, is an independent variable in OWT design dictated by the turbine size and sea depth at the location of installation. The degree of moment applied to the monopile is increased with e and must be taken into account in the design process. Typically, increases in e lead to a corresponding increase in L.

2.7.2 Monotonic behaviour: Soil morphology

The response of the monopile to monotonic loading is heavily dictated by soil morphology. Key factors influencing this response include permeability, friction angle, and shear modulus. The drainage of the soil system significantly affects the response, discussed in Section 2.7.3. Another important soil characteristic is the shear modulus, G. This characteristic has gained significance in wind turbines, where the system stiffness design is constrained within the range of characteristic loading frequencies. To mitigate the impact of resonant frequencies on foundation response, the structural stiffness is designed to align with the 1p and 3p frequencies of the turbine, as illustrated in Figure 1.7. An accurate prediction

of the system stiffness necessitates knowledge of the soil's shear modulus. This can be determined using seismic cone penetration test (SCPTu), derived from values of v_s (shear wave velocity) and q_c (cone tip resistance). This approach is referred to as soft-stiff design. However, it has been demonstrated that the stiffness of the system evolves over time due to densification during cyclic loading. Cuéllar et al. (2012) shows that cyclic loading induces a convective rearrangement of sand particles around the monopile, particularly at the surface (Figure 2.19(b)). This rearrangement results in densification and a stiffening soil response. Thus, to accurately predict the foundation response at inception and throughout its lifetime, a measure of the $G_{\max}$ and the evolution of stiffness after cyclic loading is required. Additionally, the soil stiffness is crucial for predicting the SLS. The extent to which the anticipated loads experienced during the lifespan of the monopile induce rotation and displacement is governed by both the initial and evolved soil stiffness.

Monopile foundation design across the wind farm is performed with limited site investigation in order to reduce the cost of the early design phase. Typical site investigation campaigns will carry out a range of borehole tests and cone penetration tests (CPTs), with only a limited number of points chosen for in depth analysis through lab tests such as triaxial tests. Therefore, the use of CPT for classification and calibration is important for efficient design across a project. One key use of CPT results is the determination of shear strength, and the inferred D_r. Jamiolkowski et al. (2003) provided a framework for the processing of CPT data. This study used a calibrated chamber of known density and pre-determined soil behaviour to calibrate a CPT test. CPT test results provide the value q_c, which is used to compute an estimate of soil strength characteristics and D_r. Further examination was provided by Robertson (2009). The study produced contour diagrams for interpretation of standard CPT results, and more advanced methods such as SCPTu. From interpreting these results, an estimate of the soil conditions, such as D_r, $G_{\max}$, and soil type can be obtained. Alongside this, boreholes are taken at multiple locations for basic soil morphology classification tests. These results are then calibrated in reference to the sites chosen for in-depth analysis. Typical classification tests include PSD, SD, Minimum and maximum void ratio test (MM), andplasticity index test (PI). These tests provide basic morphological characteristics for input into empirical relationships, such as the Bolton empirical relationship for peak strength (Bolton, 1986), the state parameter (Been et al., 1985), or the Hardin and Black relation for shear modulus (Hardin et al., 1968).

2.7.3 Monotonic behaviour: Drainage effects

The accumulation of excess pore water pressure, u, leads to a reduction in effective stress, consequently affecting strength and stiffness. Conversely, reduced drainage can lead to increased excess negative pore pressure, which has a stiffening and strengthening effect. During monotonic loading, the drainage regime is typically divided into two distinct categories: drained and undrained, applicable to sand and clay soils, respectively. The impact of loading rate during monotonic loading has been shown to significantly affect the

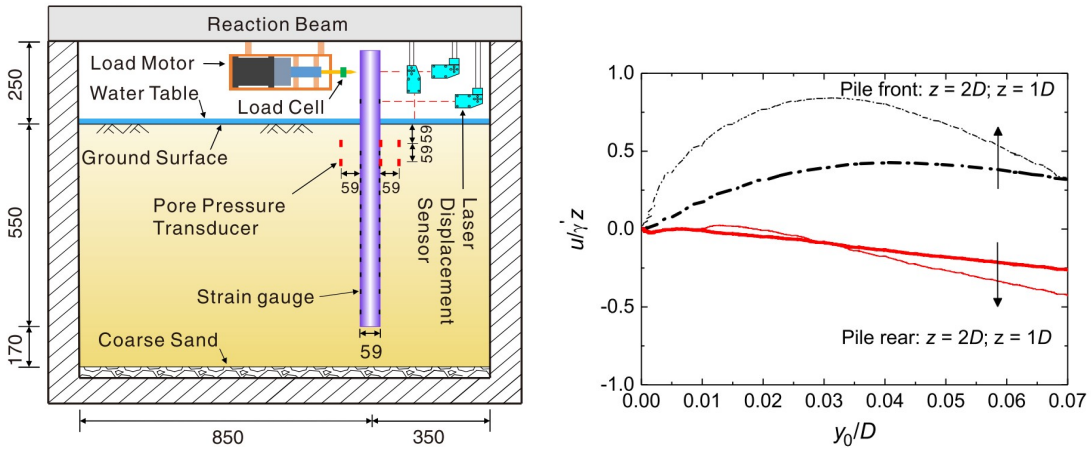

(a) (b)

Figure 2.20: Monotonic centrifuge results with partial drainage from Zhu et al. (2021), showing: (a) cross section of the experimental set up with pore pressure sensors in the soil, and (b) results of a monotonic push inducing excess pore pressure accumulation in the soil.

response. Byrne et al. (2020*d*) and Byrne et al. (2020*c*) indicate that the pile response is considerably stiffer during rapid loading in both clay and sand soils. If pore pressures are permitted to dissipate, stiffness recovers to lower levels characteristic of slower load speeds. This indicates the presence of significant negative excess pore pressures resulting from soil shearing, which increases effective stress. The increased stiffness is more pronounced in clay soil, exhibiting a 33% increase in strength per log_{10}-cycle of loading rate, compared to 7.5% for sand. This corresponds to the higher permeability of sand soil, facilitating a greater degree of u dissipation and reduced negative excess u. Instances where loading rate affects drainage conditions and, consequently, the foundation response, can be classified as partially drained. The degree of partial drainage in monotonic testing has been examined in multiple studies. Zhu et al. (2021) presents results with findings similar to those of the PISA tests (Figure 2.20). Increased stiffness is observed in cases where the loading rate is elevated and full drainage does not occur. Although the sign of u accumulation is positive in front of the pile, reducing effective stress, there is a significant degree of negative u behind the pile that accounts for the increased stiffness. Additionally, results indicate that partially drained cases demonstrate higher levels of bending deformation at equivalent horizontal displacements. Numerous other studies support the finding of a directly proportional relationship between loading rate and stiffness for monotonically loaded monopiles. Zhu et al. (2020) shows a positive correlation between shear modulus and loading rate, also noting an inverse relationship with bearing capacity. This agrees with the findings of Matešić et al. (2003) in simple shear tests.

2.8 Model testing: Monopile behaviour under cyclic loads

In reality, the loading regime of OWTs is rarely monotonic, and the design criteria serve as a benchmark. Loading on OWT foundations is cyclic, influenced by environmental

conditions such as wind and wave loading, as well as structural variations, as illustrated in Figure 1.7. Thus, an important consideration in design is the cyclic response of the foundation. Moreover, the cyclic loading regime and its effects can be more onerous than a nominal ultimate failure load (LeBlanc et al., 2010). The following section outlines the behaviour of OWT foundations under cyclic loads and the critical parameters that affect this.

2.8.1 Cyclic behaviour: Soil morphology

As with monotonic response, soil morphology is critical in the response of a foundation, particularly its effect on permeability, friction angles, and dilation. Permeability is significantly influenced by morphology. Particle size and shape alter the range of minimum and maximum void ratios, which is essential for predicting permeability (Shahabi et al., 1985), as well as state parameter related strength predictions. Additionally, particle shape affects the degree of adsorption, another factor that controls permeability. Degrees of sphericity and angularity significantly influence friction and dilation angles, which are important for predicting strength, stiffness, and pore pressure response (Mitchell et al., 2005).

Another important consideration is the global distribution of morphology. As previously discussed, most natural deposits of sand exhibit an anisotropic distribution. This anisotropy induces differential behaviour under various stress angles. The angle of anisotropy is predominantly horizontal; however, geological processes may cause alterations in the plane. Moreover, the presence of layers with distinct deposits results in differential behaviour. This is key for all aspects of analysis, however most important in the consideration of drainage. Where a layer of high permeability is enclosed by layers of low permeability this can lead to liquefaction (Adamidis et al., 2022).

2.8.2 Cyclic behaviour: Typical loads

Figure 1.7 shows the major factors responsible for loading on the turbine structure. Low-frequency variations in wind and wave strength form the lowest frequency cycles. Wave loading is usually in the order of 0.1 - 0.13 Hz (Gaertner et al., 2020), and forms the most significant proportion of the horizontal load, H. However, the eccentricity of this load is lower than the wave, so forms a less significant proportion of the moment. The cycling of the rotor and blades form the 1p and 3p load frequencies. This multi-excitation frequency is formed of varying amplitude, and load height. However, in analysis it is often simplified to a singular signal at a specified height to represent the combination of loads and moments. OWT moments are predominantly lateral, owing to the high load eccentricity, however, the ratio of lateral to vertical load is usually $\approx 1:1$ (Villalobos Jara, 2006).

The impact of cyclic loading on the foundation distinct from monotonic loading is the imposition of varied loads, load relaxation, ratcheting, pore pressure build up, and multi-directional loads. These effects combined can lead to a more onerous load condition, even in amplitudes of far lesser magnitude than the monotonic case. Furthermore, the consideration

of time factors in cyclic loading is of greater importance. Over the lifetime of the wind turbine, the foundation will experience 10^9 cycles of varying amplitude. The importance of these low amplitude, "operational" loads is debated, however, these may cause strain accumulation through ratcheting, and changes in system stiffness via densification.

In modelling cyclic loads, a standard approach is the rain counting method (Rychlik, 1987), as discussed in Section 2.2.3. This approach sorts a multi-amplitude load history into a sequence of loads of matched amplitude. The load packets are often applied in ascending order, although this is not requisite. The ability to apply loads in varied order is based on the assumption of Miner's rule (Miner, 1945). When loads have been sorted using the rain-counting method, Miner's rule has validated with triaxial testing (Wichtmann et al., 2017), and numerical modelling (Liu et al., 2022) for drained conditions. The response is most different for these studies when the largest amplitude loads are applied first or last. The validity of a rain-counted idealised load history is less clear when performed under partially-drained conditions. The rate of u accumulation is greater the higher the load amplitude, therefore, grouping all of the high amplitude loads together will lead to greater accumulation of u. Consequently, the effective stress will be reduced leading to increased strain accumulation.

For the testing of storm loading conditions, either physical or numerical modelling, a load time history is required. Given the sensitive nature of the data, load measurements from instrumented piles in reality are not readily available in academia. Therefore, modelling methods are usually performed to simulate a storm load history (Bachynski et al., 2019; Ryan et al., 2024*b*). The resulting time history is a complex multi-frequency, multi-amplitude load.

Simulations of storm load time histories reveal the importance of dynamics in the maximum mudline bending moment. Ryan et al. (2024*b*) simulated storm load conditions using varied wave load models. It was shown that the presence of irregular sea states can induce higher loading frequencies that approach the first tower modal frequency. The resonance associated with this loading condition increased the foundation load by up 15%. Furthermore, the wave tower interaction produces a non-linear wave loading profile which increases the peak load applied, often not considered in wave loading simulations.

Page et al. (2019) compared recommendations for wave loading simulations in design standards with simulated hindcast storm data. The results showed asymmetric storm load profile across the 35 hr storm period. This implies a potential increase in the wave load, owing to varied loading period, which increase the assumed load profile during a storm.

Design of OWTs must assess the predicted loads that will be applied throughout its lifetime. Loading will vary based on environmental conditions and will encompass a range of amplitudes. The typical considerations are of storm events "operational" loads - low level cycling from typical environmental conditions. The operational loads, as discussed, will make up the majority of load cycles experienced, and will be idealised into an average load and number. Storm loads must be simulated based on expected environmental conditions. The storm load will be based on the predicted largest storm for a given time period.

Depending on the stipulations of the contractor, the design storm can be for a varied lifespan, typically it is for a 50 year storm. However, the magnitude of storms is predicted to increase with climate change, and therefore, the prediction may become inaccurate (Wolf et al., 2020).

There is debate as to whether the lower number of high-amplitude storm loading cycles, or high number of low-amplitude cycles is most important in the design. 1g model tests performed by Leblanc et al. (2010) show that the degree of rotation is greatest in the low number of high-amplitude cycles. This result showed greater rotation than for the ULS monotonic load. The implication is that the SLS load criteria should be dictated by the predicted cyclic loading response, and is more critical than ULS. These results were corroborated by (Zhu et al., 2021), showing greater accumulation of strain for lower load than the monotonic case.

Multi-directional loads

Cyclic loading on OWT foundations is formed of a multi-frequency excitation from the wind, wave and structural rotation. Owing to the relationship between wind direction and wave formation, the cyclic loads tend to be unidirectional. However, the temporal lag between changes in wind and wave direction, coupled with the effects of tidal streams and storm surges, results in multi-directional cyclic loads. Investigations into the response to multi-directional loading are inconclusive. Richards (2019) showed that the multi-directional case was most onerous, owing to rotations in the principal stress direction. However, LeBlanc et al. (2010) predicted that partially one-way, unidirectional loading caused the greatest degree of pile rotation. This load case was shown to exceed the rotation caused by the ULS load case. This was also demonstrated in the results of Albiker et al. (2017), however, they did not consider multi-directional loading, only comparing one way and two way load cases.

2.9 Model testing: Drainage around large diameter monopiles

Increases in monopile diameter, required to support larger OWTs, have multiple implications on the system response. Page et al. (2021) summarised the impact of increases in monopile and tower diameter: decreased first tower modal frequency, increased rigidity of the pile leading to higher soil mobilisation, increased importance of wave loads, and changes in the wave load profile due to wave diffraction. The combination of the lower tower modal frequency and higher wave load frequency, may lead to resonance issues.

The centrifuge experimental campaign was focussed on the drainage regime around large diameter monopiles subjected to cyclic loading. The following section outlines the relevant literature focussed on this issue. Studies into this issue include experimental and numerical investigations. As discussed in Chapter 1, the issue of drainage around monopiles is increasing in significance with the installation of large diameter monopiles.

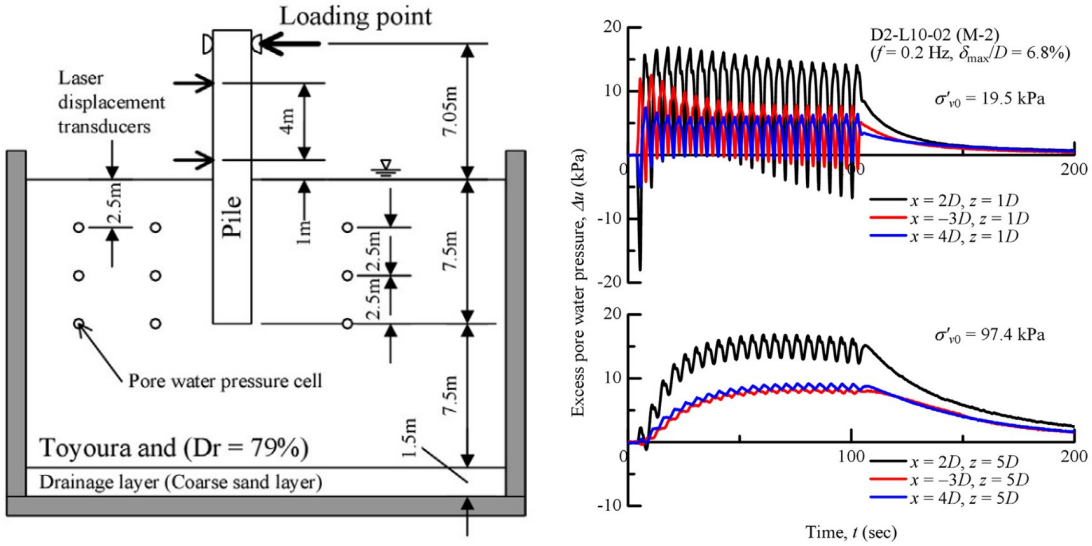

(a) (b)

Figure 2.21: Cyclic results of a centrifuge test examining partial drainage from Takahashi et al. (2022), showing: (a) cross section of the experimental set up with pore pressure sensors in the soil, and (b) results of cyclic loading inducing excess pore pressure accumulation within the soil.

The experimental campaign was focussed on the response of sandy soils, as such this review will not discuss the behaviour of clay soils. The drainage response around clay soils are effectively undrained at the loading rate relevant to the problem, therefore the increase in diameter will have no novel effect.

Monopiles experience predominantly lateral loading, hence the drainage pathways driven by differential loading are predominantly lateral. The loading regime imposes a zone of compression in front of the pile, with a tensile zone behind. In the initial compressive response, where no dilative shearing occurs, the pore pressure response is positive. Behind the pile there is a corresponding negative suction zone. This pore pressure gradient induces a pore fluid flow from high to low pressure. The drainage pathway is lateral around the circumference of the pile.

Klinkvort et al. (2018) suggest a non-dimensional scaling factor for the drainage regime, $MkT/\gamma' D^2$, where M is the soil stiffness at a nominal confining pressure, k is the soil permeability, T is the loading period, γ' is the buoyant unit weight of the soil, and D is the monopile diameter. This shows that the degree of drainage is inversely proportional to D^2. Therefore, as monopile diameters increase, the degree of drainage will reduce. Coupled analysis of soils shows that increased positive excess pore pressure induces a reduction in effective stress and stiffness, and therefore increased displacement. This is potentially an issue in the installation of new generation monopiles.

The numerical modelling of S. Li et al. (2019) corroborated the hypothesis of the non-dimensional drainage factor. The study showed that the drainage rate is dependent on loading period, T, with increased accumulation of u with lower T (Figure 2.22(a)). However, this investigation also showed that the stiffness was increased with reduced

drainage Figure 2.22(b).

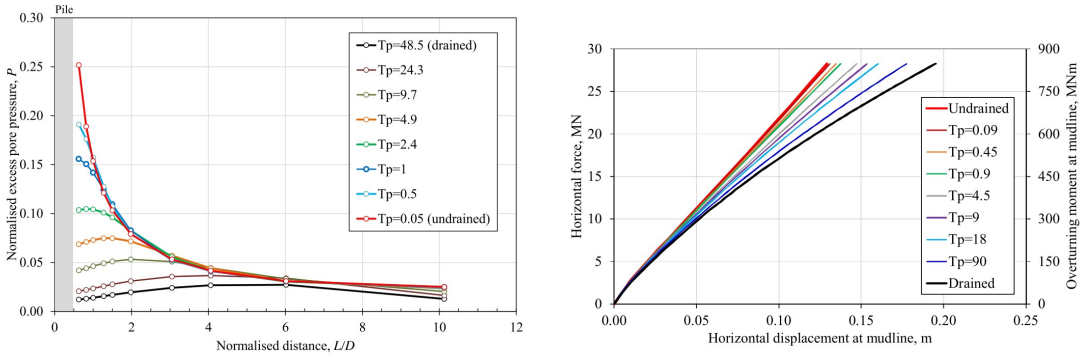

(a) (b)

Figure 2.22: Results of numerical model of drainage around monopiles from S. Li et al. (2019) , showing: (a) accumulation of p_e increased with reduced loading period, and (b) reduced displacement with reduced loading period.

Experimental investigations of cyclic loading of monopiles have demonstrated the importance of drainage considerations. Zhu et al. (2021) performed centrifuge tests of monotonic and cyclic loading on large diameter monopiles in sand, with additional focus on the wave-induced pore pressure oscillation. The results showed an increase in soil degradation during cyclic loading at depth with increases in pile diameter. This is consistent with the findings of Page et al. (2019) regarding increased pile rigidity. Increased loading rates induced pore pressure accumulation, causing a reduction in system stiffness. Takahashi et al. (2022) also observed pore pressure accumulation during cyclic loading of monopile foundations in centrifuge tests on sand (Figure 2.21). The impact of the slenderness ratio was analysed, demonstrating improved contribution of base resistance to the foundation response for larger diameter monopiles. Pore pressure response consisted of a rapid accumulation phase for the first 10 cycles, followed by a steady state in accumulated excess pore pressure where dissipation is equal to or exceeds accumulation. The rate of dissipation is greater near the surface, where the distance to the boundary is reduced.

In addition, there exists multiple numerical investigations into the drainage regime around monopiles in sand. Liao et al. (2019) modelled a rocking monopile in sandy soil, and showed the combined effects of wave pressure on the seabed and monopile rocking induced significant u accumulation. The rate of pore pressure accumulation was greatest near the surface, induced by increased displacement, and closest to the monopile where the impermeable surface inhibited drainage. Tasiopoulou et al. (2021) modelled the effect of soil permeability on the system response to cyclic loading. It was found that the initial stage of cyclic loading induced similar response to the drained case, however, pore pressure accumulation reached a critical level, at which point rapid accumulation would occur, causing significant reduction in stiffness. The results of these simulations have not been shown in experimental results. Chaloulos et al. (2024) used existing centrifuge data to validate 3D FE simulations of cyclic loading. Loading of low permeability soils, such as silty sands, induced high levels of pore pressure accumulation. This was contrasted with

high permeabilty soils, where pore pressure dissipation prevented accumulation outside of the immediate vicinity of the monopile. Good agreement between the experimental and numerical results showed a lack of detail in the simplified design procedures, and design errors associated with the drainage regime. Kementzetzidis et al. (2019) showed that partially drained conditions can have a significant impact on the dynamic response of the foundation, with increased damping especially during weak vibrations.

2.10 Model testing procedure: Centrifuge testing principle

Physical modelling of foundations in centrifuges can address some of the drawbacks of FEM and constitutive models. Centrifuge testing allows for a realistic distribution of ground stresses at a model scale by artificially increasing gravity. The scaling laws are an important consideration when designing the experiment. For tests which model cyclic loading the scaling of time is important, but the differing scales of drainage and dynamic forces means that a simple scale conversion will not suffice. To deal with this issue, fluids with different known viscosities can be used to change the drainage time in line with dynamic time scaling. The sand particles themselves are not scaled as changing them would alter the particle morphology and affect the modelled stress-strain response. This assumes that the defining feature of the soil response is the stress-strain curve, which does not alter when scaled geometrically. This assumption holds if the particles are sufficiently small compared to the feature of interest. If the ratio of B/D_{50} is greater than 50 the scaling holds (Garnier et al., 2007). When modelling a pile in sand the design and implementation of the recording instruments is important. A regularly tested model is the p-y curve which requires an estimation of the bending moments within the pile (Choo et al., 2016). Bending moments can be calculated from measurements of strain along the length of the pile. This requires the application of strain gauges to the surface of the pile, which must be sufficiently small to not influence the soil response. A popular method is foil gauges. Geotechnical centrifuge testing is a process used to allow small scale model testing, at increased g levels in order to replicate the correct stress distribution in the soil. 1g model testing has uses in the research into fundamental soil response. However, the scaling issues associated with this style of testing, inhibit its use in direct investigation of foundations. A particular issue is the increased dilative response of the soil. The reduced effective stress, relative to depth along the pile, allows for a greater degree of dilation during shearing. Therefore, the fundamental soil response is not representative of the soil in reality. Centrifuge testing increases the applied g field, with associated increases in effective stress distribution with depth. Therefore, theoretically the response is the same as for the full scale. Scaling is measured as 1:η, where η is the applied gravitational acceleration.

Centripetal acceleration is applied to the soil in a rotating device. There are two main types of geotechnical centrifuges, drum and beam. Drum type centrifuges are compact, and allow for a very high rotational speed, and hence applied gravitational field, for a long period of time. The major drawback is the difficulty in model preparation, the model must

be prepared, then rotated under zero applied acceleration. This necessitates a degree of soil cohesion to hold the model and soil in place during the installation phase. Furthermore, the low radius of rotation induces a high degree of gravitational field differential across the depth of the model.

Beam centrifuge experiments are prepared in a strongbox, which is mounted to a cradle, then spun on the cradle to apply the centripetal acceleration. The attributes of this system are converse to the drum centrifuge. The system is large and requires a lot of space and power. Therefore, the applied rotation limit is lower than the drum centrifuge, and can be applied for a shorter time to limit damage to the drive system. However, the arm can be long, allowing for a greater radius of rotation. This creates a more uniform g-field across the depth of the model. Furthermore, the simple installation on a horizontal cradle allows for more complex models.

Acceleration is calculated from Equation (2.3), showing the proportional relationship with the square of rotation. Despite a more uniform g field across the depth, there is a small degree of variation in applied g. The target depth is in relation to the zone of interest, for the experiments, 1/3rd depth of the pile was targeted.

$$a_c = \omega \cdot r^2 \tag{2.3}$$

The scaling of key parameters within the model follow set scaling laws, summarised in Table 2.1. Using these scaling laws, the centrifuge test can provide a more realistic representation of reality.

Table 2.1: Centrifuge scaling laws, where N is the applied centrifugal acceleration in units of g (Madabhushi, 2017)

	Scaling law	
Parameter	**model/prototype**	**Units**
Length	1/N	m
Area	$1/N^2$	m^2
Volume	$1/N^3$	m^3
Mass	$1/N^3$	$Nm^{-1}s^2$
Stress	1	Nm^{-2}
Strain	1	-
Force	$1/N^2$	N
Bending moment	$1/N^3$	Nm
Seepage velocity	N	ms^{-1}
Time (consolidation)	$1/N^2$	s
Time (dynamic)	1/N	s
Frequency	N	s^{-1}
Displacement	1/N	m
Acceleration/Acceleration due to gravity (g)	N	ms^{-2}

2.11 Summary

This chapter provided a summary of the literature review in the areas of soil mechanics, constitutive modelling, element testing, and centrifuge model testing of monopiles. The research objectives, which focus on investigating drainage effects in element testing, required a review of the literature pertaining to partial drainage and silt–sand element behaviour. Advanced element testing procedures were critically examined and summarised. Constitutive modelling under cyclic loading was reviewed, with emphasis on state-of-the-art models such as SANISAND-MS. Furthermore, the behaviour of large-diameter monopiles in sand was analysed. A notable gap in the literature was identified regarding the drainage regime around large-diameter monopiles in sand subjected to cyclic loading.

Chapter 3
Cyclic Triaxial Testing of Congleton Sand: Methodology

The following chapter outlines the methodology employed for the triaxial testing in this thesis. This chapter includes findings from an investigation into three sample preparation techniques suitable for reconstituting silty sand samples. The triaxial testing schedule comprised three related test schedules. These test phases included benchmark testing on clean sand, tests on silty sand samples, and tests involving partial drainage. The three sections required distinct set-up methodologies.

3.1 Equipment

The following section outlines the equipment used, and the set-up and calibration required for the instruments.

The triaxial tests were conducted using a GDS Instruments 40 kN 5 Hz Dynamic Triaxial Testing System (DYNTTS) (Figure 3.1) at the Fugro GB Ltd laboratories in Wallingford. The technical specifications of the system are summarised in Table 3.1. The triaxial system is dynamically controlled with a direct closed loop of load-displacement, allowing for cycles with load or displacement control. Load and displacement are controlled by a screw-driven ram through the base of the cell. The ram is balanced to maintain constant cell pressure during cyclic loading.

Cell and sample volume and pressure are controlled through pressure/volume controllers (Figure 3.2). The specifications are summarised in Table 3.2. The back pressure is monitored through the internal PPT of the volume controller. The cell pressure is monitored by an external PPT at the cell tap, connected to a remote feedback module on the cell volume controller. The pressure/volume controllers are capable of maintaining a given pressure or volume, defined in the control software of the triaxial testing system.

Table 3.1: Triaxial cell specifications

Specification	**Value**	**Accuracy/Resolution**
Max load (kN)	40	<0.1%
Max loading frequency (Hz)	5	-
Max cell pressure (MPa)	2	-
Displacement range (mm)	100	0.2×10^{-3}
Max sampling frequency (kHz)	5	-

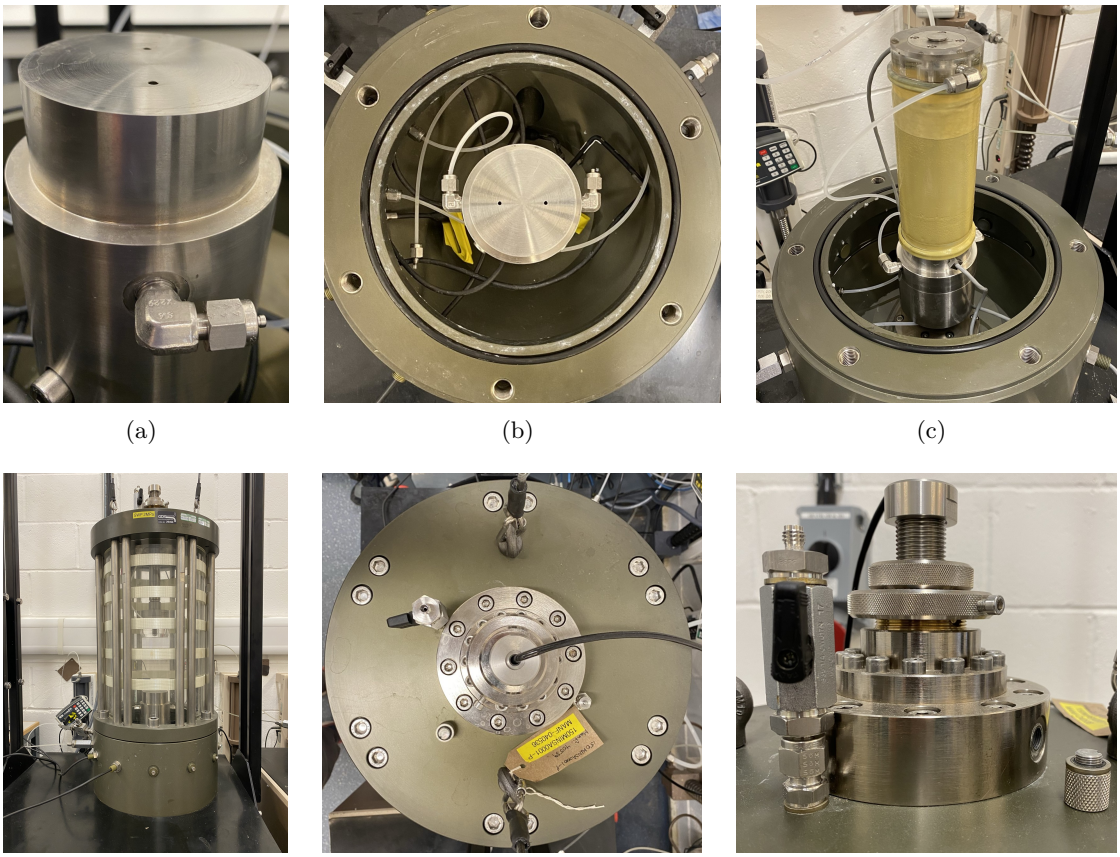

(a) (b) (c)

(d) (e) (f)

Figure 3.1: Triaxial setup, showing: (a) base pedestal, (b) base pedestal in place on axial ram, (c) sample in place held with negative pore pressure induced effective stress, (d) whole set-up with sample and cell installed, (e) load cell mounting system, (f) top cell drain and suction cap tap.

Table 3.2: Volumetric control specifications

Specification	Value	Accuracy	Resolution
Pressure range (MPa)	2	0.15% FRO	1 kPa
Volumetric range (ml)	200	0.25%	1×10^{-3}
Min flow rate (ml/min)	1×10^{-5}	0.50%	-
Max flow rate (ml/min)	22.5	0.50%	-

Alongside the standard equipment of the DYNTTS, additional equipment was used for certain tests. The sensors employed and the measurements taken are summarised in Table 3.3. Bender elements were used to obtain the shear wave velocity through the sample, for measurements of $G_{\max}$. Sample-mounted axial and radial LVDTs were employed to take local strain measurements during cyclic tests, which provide a higher level of accuracy for small-strain measurement and mitigate issues such as bedding errors. Standalone PPTs were used to obtain readings of the sample pore pressure and cell pressure; these provide more accurate measures of fluid pressure than the internal PPTs within the volume control cylinders.

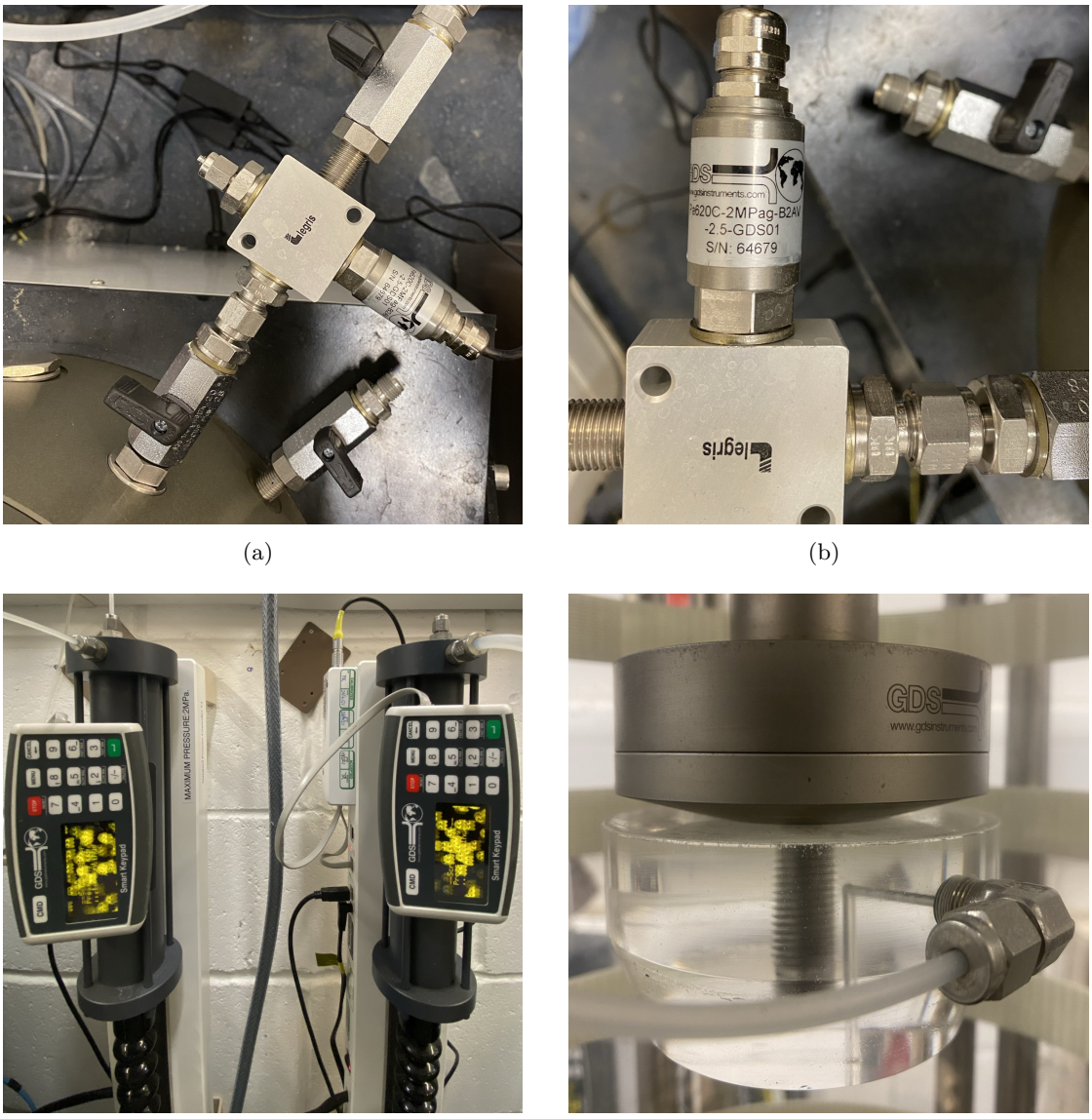

(a) (b)

(c) (d)

Figure 3.2: Instruments of triaxial setup, showing: (a) cell pressure PPT, (b) base drain pore pressure PPT, (c) cell and back volume controller, (d) internal cell load cell.

Table 3.3: Additional instrument specifications

Instrument	Measurement	Unit	Range	Accuracy
Bender element	Shear wave velocity	m/s	-	-
Axial LVDT	Local axial deformation	mm	± 5	0.1% FRO
Radial LVDT	Local radial deformation	mm	± 5	0.1% FRO
External PPT	Sample pore pressure, Cell pressure	kPa	2000	0.15% FRO

3.2 Material

The following section provides the classification of the sand used for experimental work in this project. Classification of three sands is provided: batched boreholes from Hornsea wind farm, Congleton HST-95, and Leighton Buzzard Sand - fraction E (Leighton Buzzard sand - size fraction E (LBS-E)). Prior to the experimental phase of the project, analysis was completed of typical sands found in North Sea offshore wind farms. The data used for this phase was from the archive of Fugro GB Marine Ltd. Figure 3.3 and Figure 3.4 present particle size distribution (PSD) results from Fugro archive data of the Hornsea wind farm, and Walney extension. The plots show data from PSD tests of sand extracted from boreholes across each site. The results show that the sands from both sites were fine and at least partially silty, which agrees with findings from literature (Jones et al., 2020). The sands selected for the testing phase of the DPhil were chosen to closely match the PSD of the sands found in the offshore wind sites mentioned above. The readily available sands that matched this morphology were Congleton HST-95 and LBS-E. Figure 3.5 shows the PSD results obtained by the author from batched Hornsea sand boreholes obtained from the Fugro sample archive, Congleton, and LBS-E. The results reveal a close match

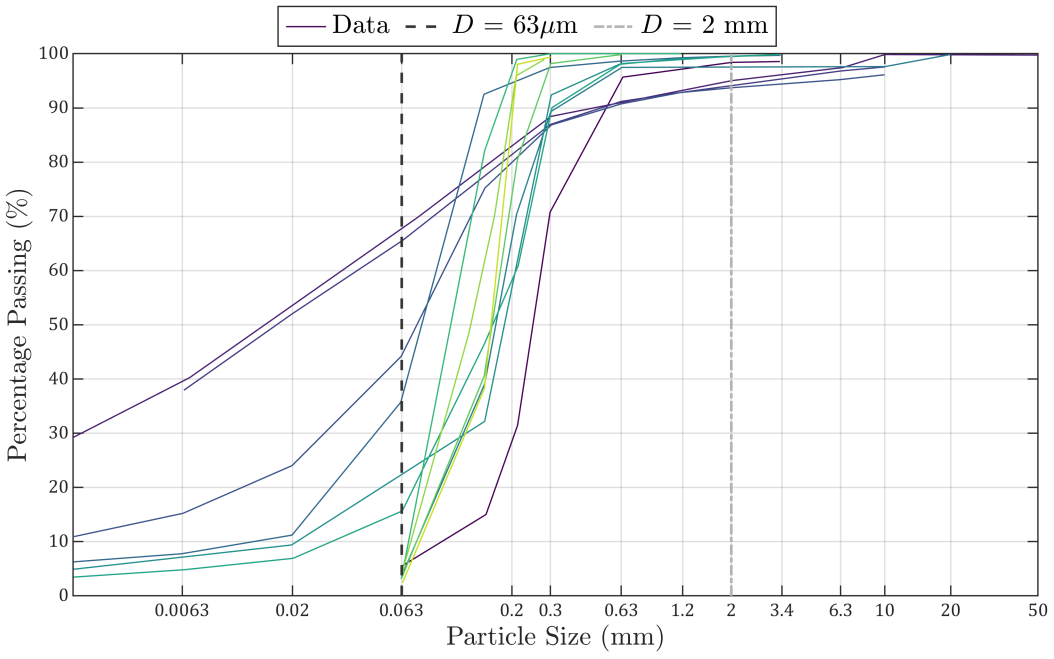

Figure 3.3: PSD of boreholes from the Hornsea wind farm (Fugro data archive)

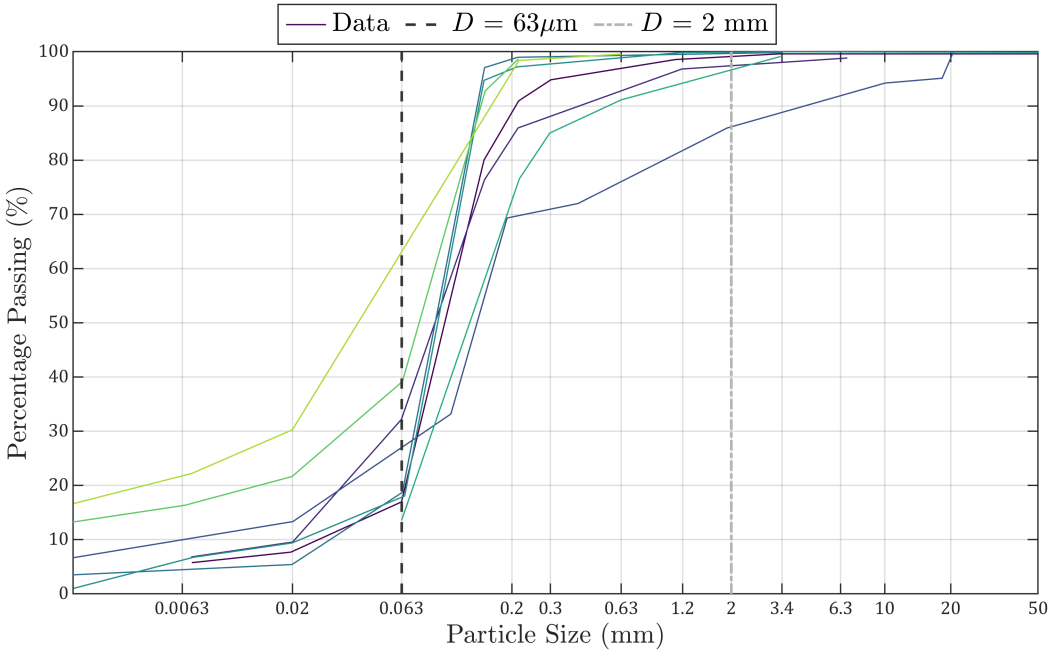

Figure 3.4: PSD of boreholes from the Walney extension (Fugro data archive)

in the particle size distribution of all three sands, with Congleton the closest matched. Additionally, Congleton sand was available at a low cost in large quantities, which was advantageous considering the requirement for a large quantity of sand for the centrifuge testing phase. Therefore, Congleton HST-95 sand was chosen as the material for testing. Furthermore, the finding that sand from both sites was partially silty across all boreholes informed the decision to examine the impact of fines content during cyclic loading.

The sand morphology table, Table 3.4, confirms the similarity of the sands analysed. The classification data presented here is based on tests conducted by the author. Values of e_{min} and e_{max} were taken using two separate methodologies which provided concurrent results (DGI, 1996; Knudsen, S. et al., 2021). Specific gravity was measured using the methodology of Wallace (2021). The values of particle size were taken from the results of PSD tests using the methodology of the British Standards Institution (1990).

Table 3.4: Material data of Congleton HST-95, LBS-E, Hornsea

Parameter	**Congleton HST-95**	**LBS-E**	**Hornsea**
Specific gravity, G_s	2.63	2.65	2.65
Minimum void ratio, e_{min}	0.538	0.634	-
Maximum void ratio, e_{max}	0.782	0.999	-
Median grain size, D_{50} (mm)	0.150	0.102	0.154
10% passing, D_{10} (mm)	0.075	0.069	0.070
Coefficient of uniformity, D_{60}/D_{10}	2.15	1.62	2.37

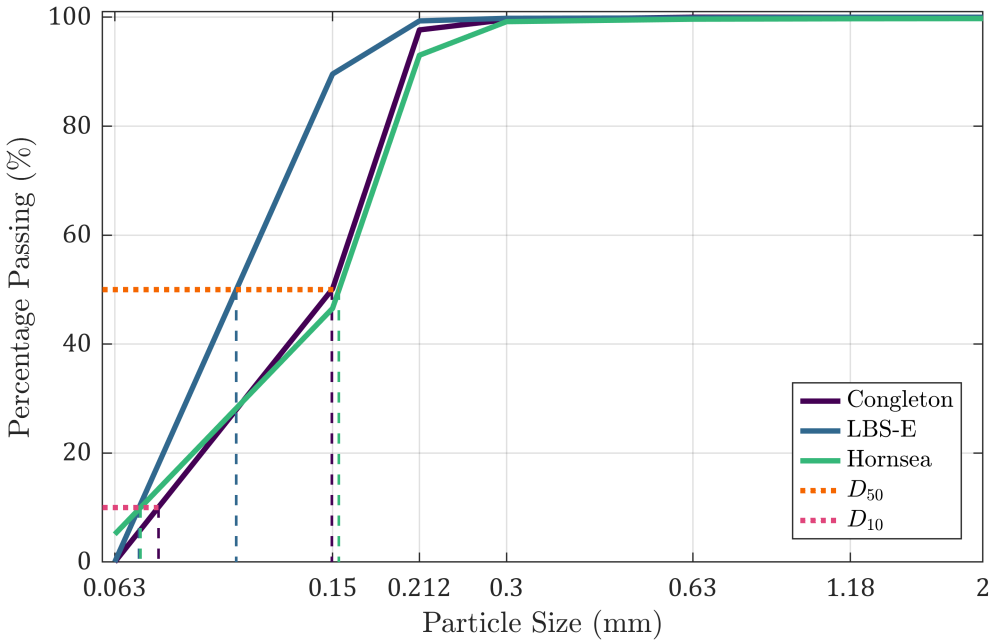

Figure 3.5: PSD of combined Hornsea sand samples, with Congleton and LBS-E

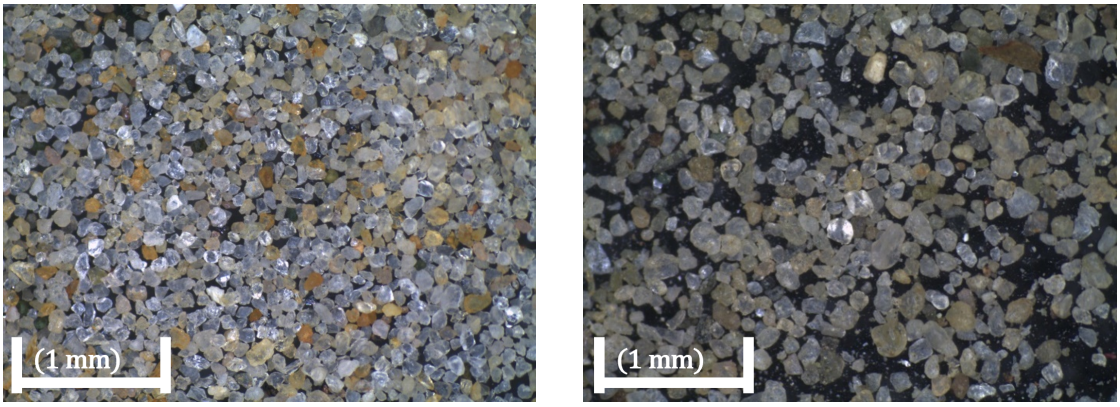

(a) (b)

Figure 3.6: Microscopy images of: (a) Congleton sand, (b) Hornsea batched sand.

3.2.1 Congleton HST-95 additional material data

The initial material classification tests informed the choice of Congleton sand for the testing phase. The following section shows additional classification tests performed on Congleton sand. Figure 3.6 shows comparisons of optical microscopy images of Congleton and Hornsea sands. The images show similar morphology in terms of angularity, sphericity, and mineralogy. The image of Congleton sand shows a composition of at least 95% quartz, which matches well with the Hornsea sand. A series of scans using the Retsch GmbH CAMSIZER P4 were used for classification of Congleton sand's shape characteristics, the results of which are summarised in Table 3.5. Details of the calculations of these values can be found in the manual (Retsch GmbH, 2018). These values show Congleton sand to consist primarily of round particles.

Table 3.5: Shape characteristics of Congleton sand. Values are taken from scan results using Retsch GmbH Camsizer P4.

Parameter	Value
Sphericity, $\frac{4\pi A}{P^2}$	0.905
Symmetry, $\frac{1}{2}[1 + min(\frac{r_1}{r_2})]$	0.899
Convexity, $\sqrt{\frac{A}{A_{conv}}}$	0.998

3.3 Sample preparation investigation

Before the main body of experimental work, a sample preparation investigation was conducted to inform the selection of the sample preparation method. Three sample preparation methods were examined for further use, with the primary requirement being the ability to prepare homogeneous silty sand samples. The methods included MT (Ladd undercompaction method) (Ladd, 1978), DFD, and SD. A series of monotonic triaxial compression tests were completed to assess the suitability of each method for producing samples with repeatable results. Further samples were produced in gelatine to evaluate the production of samples with uniform density and fines content. These tests were conducted using Leighton Buzzard sand, as the Congleton sand required for the main experimental phase of the DPhil had not yet been acquired.

The results of the triaxial tests are summarised in Figure 3.8. A total of four tests were completed for each sample preparation method. The tests were performed drained at $D_r = 80\%$, with two tests conducted at each density. The deviatoric stress and volumetric strain are plotted against axial strain in Figure 3.8. The findings exhibit consistent outcomes

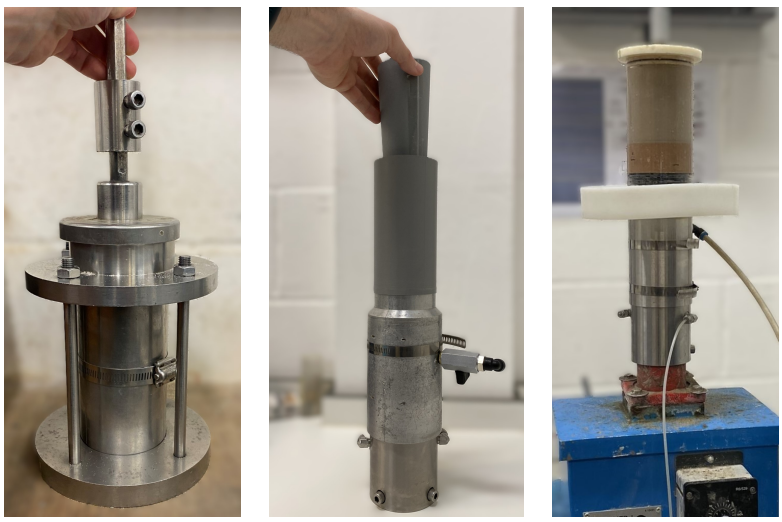

(a) (b) (c)

Figure 3.7: Sample preparation methods used during sample preparation investigation, showing: (a) moist tamping (Ladd undercompaction), (b) dry funnel deposition, (c) slurry deposition.

for each preparation method across the different densities; however, the most repeatable results are observed in the SD samples.

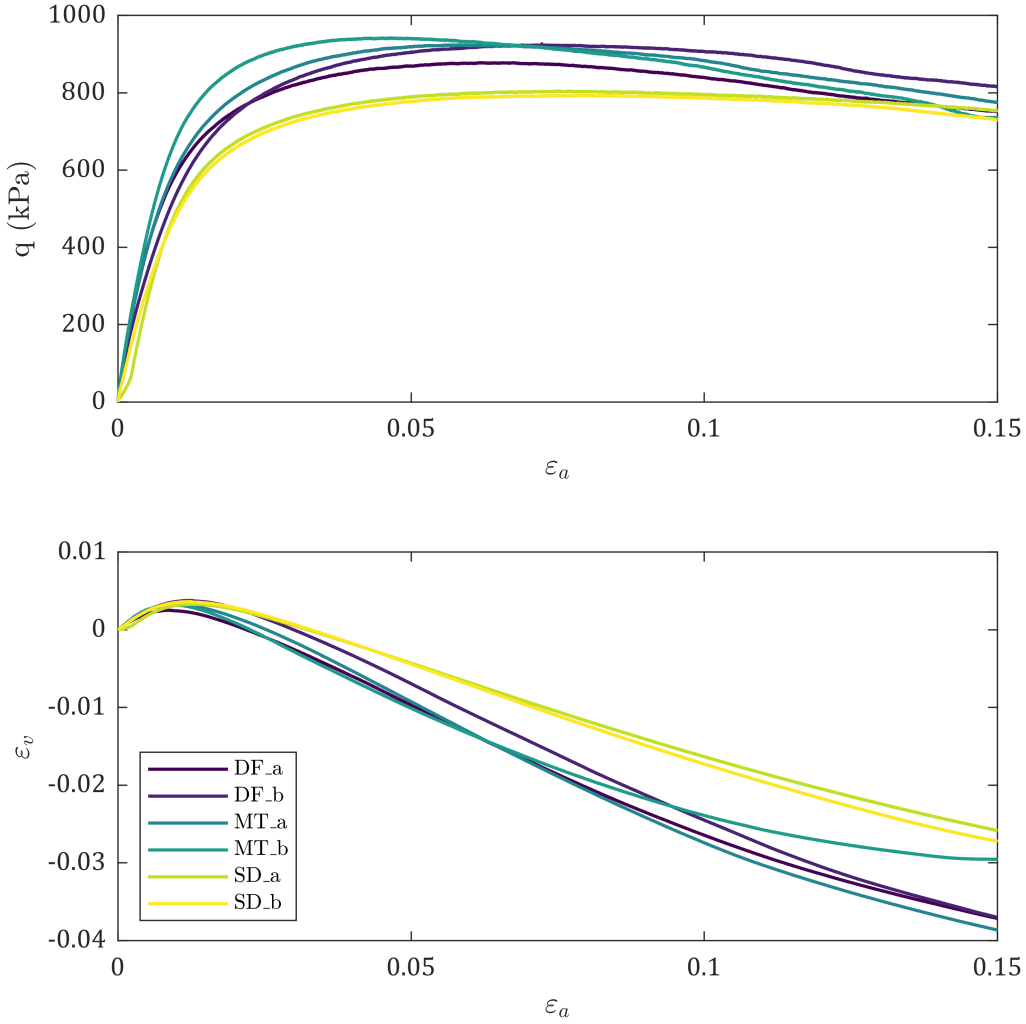

Figure 3.8: Results of the triaxial tests in the sample preparation investigation. The results from the slurry deposition tests showed greater consistency in the stress-strain response and the volumetric response.

In order to verify that the proposed SD method was capable of producing samples with uniform density and fines distribution, a gelatine-saturated sample was produced. The sample was prepared to 10% fines content and an 80% global void ratio, and saturated with gelatine according to the methodology of Emery et al. (1973). The sample was then divided into 10 sections of approximately equal size, each of which was analysed for density and fines content. The results of Figure 3.9 indicate that the SD preparation method produced uniform density and fines content across the full height of the sample.

Given the higher repeatability observed between the samples prepared using SD, increased confidence for the method documented in the literature, and the successful verification of the sample homogeneity, the slurry deposition method was selected for sample preparation.

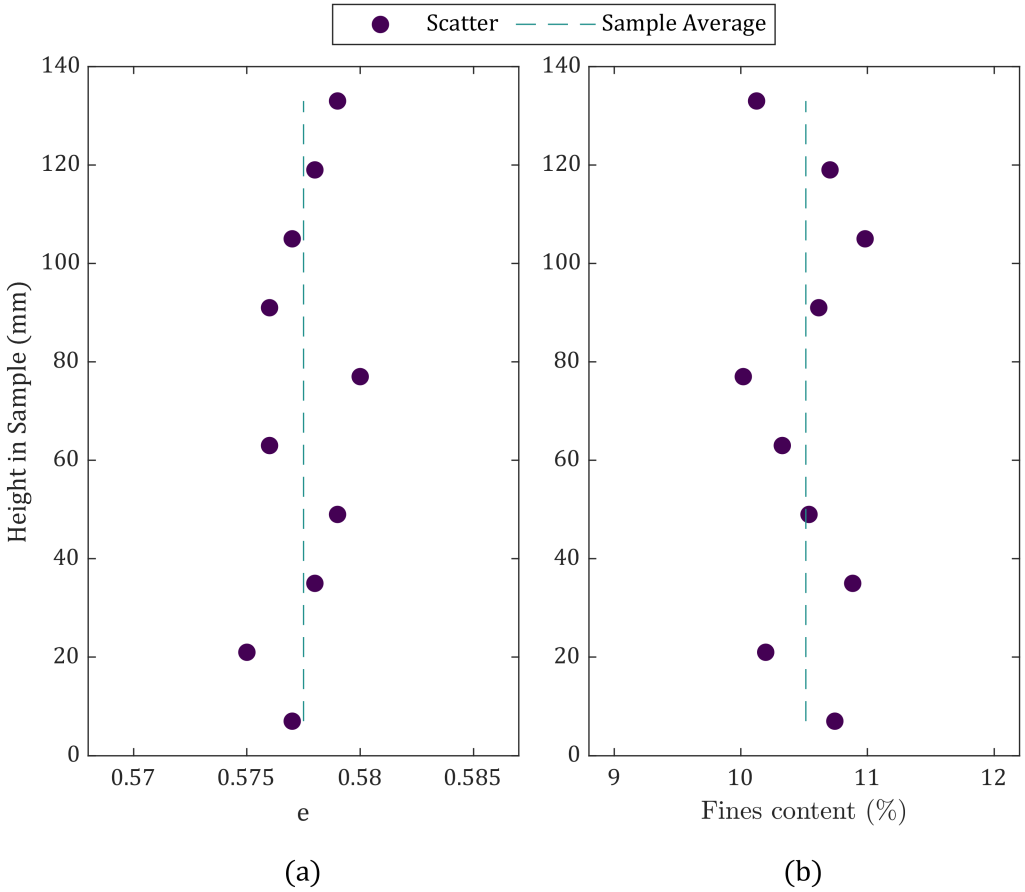

Figure 3.9: Sample density and fines content results for slurry deposition sample prepared using gelatine, showing: (a) void ratio distribution along the sample, and (b) fines content distribution

3.4 Slurry deposition sample preparation procedure

The following section outlines the methodology employed for the selected method of slurry deposition sample preparation. The methodology was developed in accordance with the recommended practices established in the literature (Carraro et al., 2008; Dominguez-Quintans et al., 2023; 2019; Vaid et al., 1999).

A diagram of the full setup for sample preparation using the slurry deposition method is shown in Figure 3.10. The setup creates a sealed cylindrical void with a diameter of 70 mm and a height of 280 mm. The height is double that of the final prepared sample. The additional space provided by the clear extension collar allows for the suspension of solid material in water, forming the slurry required for mixing. Vacuum is applied to the split mould to hold the membrane to the side, and applied to the top cap to draw out any air bubbles entrained in the slurry. The internal diameter of the split mould is 0.6 mm larger than that of the extension collar to accommodate the rubber membrane of 0.3 mm thickness, ensuring a uniform diameter throughout the entire length of the internal void. This configuration promotes purely vertical settlement of the slurry to form the desired fabric. A summary of the sample preparation procedure is provided below.

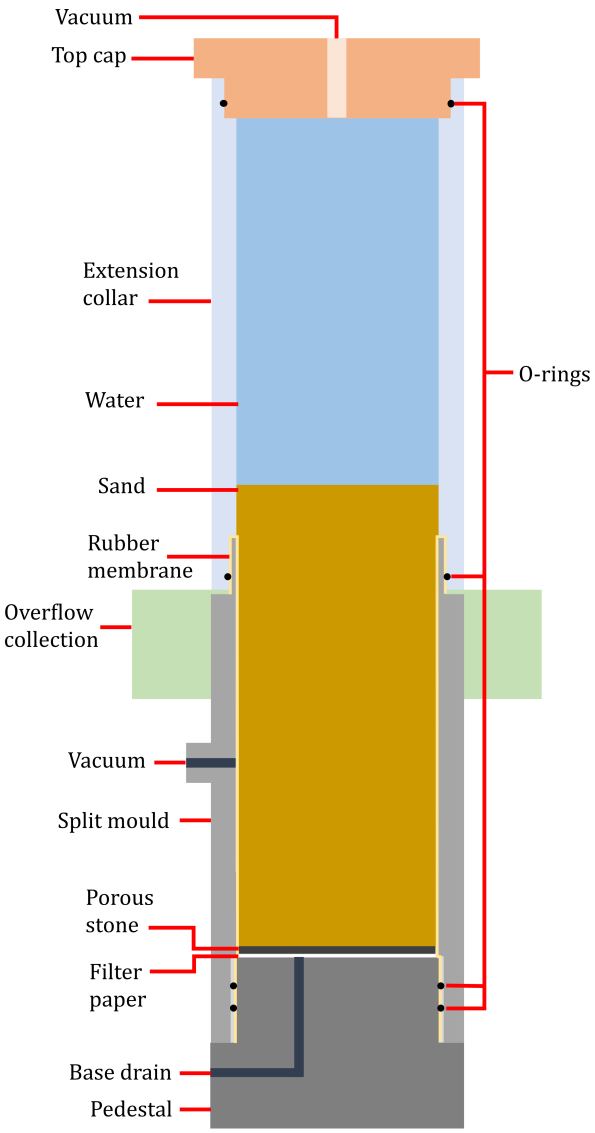

Figure 3.10: Slurry deposition mould schematic

3.4.1 Clean sand sample preparation

1. Remove the pedestal from the load ram of the DYNTTS, and place a filter paper and porous stone on the pedestal, with the thickness of each being measured. The filter paper is placed beneath the porous stone to prevent movement during the mixing process.

2. The thickness of the membrane is recorded at three positions: top, middle, and bottom. The membrane is carefully slid over the pedestal and porous stone, then sealed to the pedestal with o-rings.

3. The split mould is attached and secured with jubilee clips, then the membrane is pulled down over the top. The membrane is sealed to the split mould using o-rings, then vacuum is applied to hold the membrane to the sides.

4. The overflow collection and extension collar are attached. The extension collar fits tightly to the o-rings on the split mould to create a seal.

5. De-aired water is added to 60% of the height of the split mould. The required sand is then added (details of the quantity required are provided in Section 3.4.2), slowly through a funnel and sieve which minimises the incorporation of air.

6. The slurry deposition mould top cap is added to the extension collar, which is sealed with an o-ring around the lip of the top cap.

7. De-aired water is introduced through the base drain, whilst a vacuum is simultaneously applied through the slurry deposition mould top cap. Water is drawn through from the base, and displaced air bubbles are removed by the vacuum; this process continues until the water reaches the level of the top cap.

8. The entire setup, containing the sand and water, is inverted by hand to create a slurry, performing this inversion at least 20 times.

9. The setup is placed on a vibration table and, before vibration is applied, allowed to settle for 5 minutes.

10. Vibration is applied using the vibration table until the uppermost level of the sand reaches the relevant mark on the side of the extension collar, indicating the required density (Section 3.4.2).

11. The pedestal is carefully reattached to the ram of the DYNTTS, and the base drain is attached to the back volume control outlet (Figure 3.11(a)).

12. The excess water left in the extension collar is removed using a suction bottle, before removing the extension collar. This will leave a layer of sand above the top surface of the split mould (Figure 3.11(b)).

13. The surplus sand is removed using a clean straight knife and directed into the overflow collection. The removal process is completed slowly and carefully to create a clean straight top surface of sand.

14. The overflow is then removed from the set-up, and the exposed membrane over the edge of the split mould is thoroughly cleaned. Two o-rings are slid over the split mould at this point in order to seal the membrane to the sample top cap in step 16.

15. A saturated filter paper, porous stone, and then top cap are installed.

16. The membrane is transferred from the split mould onto the top cap, which is sealed with the o-rings on the split mould. The vacuum on the split mould is now removed (Figure 3.1(c)).

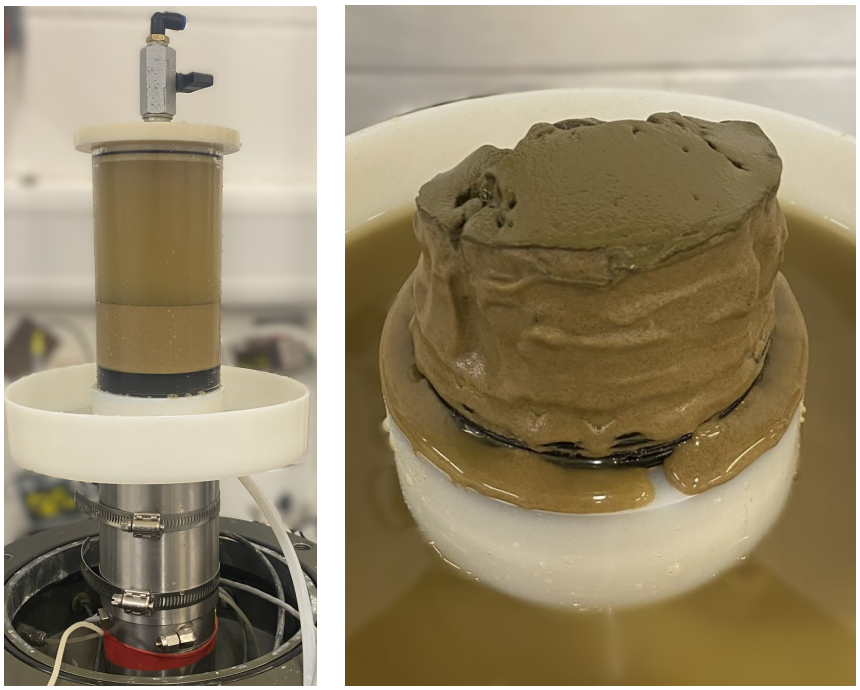

(a) (b)

Figure 3.11: Final stages of sample preparation: (a) slurry deposition apparatus mounted to the triaxial ram (vacuum is still applied to the membrane), and (b) excess sand left after the extension collar is removed.

17. A back pressure of -10 kPa is applied to the sample using the back pressure controller. This provides the necessary strength for removing the split mould. The volume of the sample recorded with the back pressure controller should stabilise after 1 min, which indicates there are no leaks.

18. The split mould is now removed, and the taps to the sample are closed, ensuring constant sample volume until the test procedure begins.

3.4.2 Sample density

The slurry deposition procedure requires the removal of the uppermost portion of sand, in order to maintain a consistent density throughout the final sample (no surcharge is added, therefore the top of the sand is low density). This removed portion is of varied density, and therefore of variable mass. Therefore, to achieve the required density a degree of trial and error is required, producing multiple dummy samples where the final density is measured. The procedure outlined by Carraro et al. (2008) recommends producing a plot of sample density versus vibration time to calibrate the level of densification needed to reach the target density. This method was attempted by the author; however, it was found that the density achieved through vibration was variable, even under identical conditions (i.e. the same sand mass and vibration settings). Consequently, the method was adapted to obtain more consistent results.

A horizontal reference line was marked on the clear slurry deposition mould extension collar. The sand was then vibrated until the top surface of the sand in the mould aligned with this line. The position of the line was determined through trial and error, initially assuming a uniform sand density throughout the mould. In practice, the sand near the top of the sample—above the level of the split mould—was found to be less dense due to the reduced surcharge. Therefore, the reference line was positioned slightly higher than the uniform density assumption would predict. For each series with varying density or fines content, a new set of trial-and-error checks was required to recalibrate the procedure for the target density.

3.4.3 Silty sand sample preparation

When preparing a silty sand sample the procedure is consistent, apart from the preparation of the required silt. The additional method used for preparing silty sand samples is detailed below:

1. Determine the necessary amount of silt for the desired silt content, calculated based on the premise of a uniform distribution of silt throughout the total volume of water in the split mould and extension collar.

2. Add de-aired water and silt into a conical flask, then apply a vacuum while agitating the silt to form a saturated silt slurry.

3. The required amount of sand is added to the split mould. Subsequently, the silt slurry is added, using de-aired water to rinse the conical flask thoroughly.

4. During the mixing process, additional inversion is required ensure the silt is fully integrated into the slurry. The complete mixing of the slurry was checked visually during the inversion process.

3.4.4 Final stages of sample preparation

Once the sample has been prepared and mounted in the triaxial rig, further steps are required before the test begins. Firstly, the sample volume is measured. This is completed with nine measurements of the diameter, three points each from the top, middle, and bottom of the sample. Additionally, three measurements are taken of the height, taken at three points 120° apart around the circumference. If local strain instrumentation is required - used in all cyclic loading tests - it can be installed now. Following this, the suction cap, a flexible plastic cap used to connect the top ram to the sample, is mounted. Next, the cell is installed, and filled with water. Finally, the sample is raised using the triaxial ram in order to dock the sample to the top ram, ensuring a sealed fit. After this the test procedure can begin.

Local strain instrumentation

The application of local strain instrumentation to capture the small-strain response during cyclic loading required additional setup following the completion of the sample preparation phase. Three LVDTs were employed: two axial and one radial. Details of the sensors used are provided in Table 3.3. In order to capture the response effectively, the LVDTs were mounted to the sample in a careful repeatable manner, shown in Figure 3.12. The two axial LVDTs were mounted diametrically on the sample, with the two supports equally spaced from the midheight of the sample. The distances between the supports were measured for calculating axial strain, with a target distance of 40 mm. The LVDT sensor was secured within the top mount to locate the pin at the centre of the measurement range at the commencement of the test. The bottom mount supported a flat plate on which the pin rested. The bottom of the pin was weighted with a small bolt to mitigate any friction within the sensor. The radial LVDT was mounted on a radial belt, with fixtures securing it to opposite sides of the sample. The LVDT pin was attached with bolts on one side, while the sensor was held in place by a mount on the opposite end of the belt. All samples were 70 mm in diameter; therefore, the sensor and pin placement needed to be established only once, with the pin positioned at the midpoint of the range at the start of the test. Initial placement was completed using CA glue to hold the mounts in place while a layer of silicone sealant was applied to the mounts. This was allowed to cure for 1 hour prior to flooding the cell. The LVDT wiring was managed using metal elbows to orient the sensors correctly. The axial LVDTs were mounted as close to vertical as possible, and the radial belt was mounted as close to horizontal as possible.

Suction cap sample mounting

The suction cap mounting system permitted attachment of the sample to the upper ram and load cell with minimal disturbance. This system was employed in all tests, including compression tests where no tension was applied to maintain centralisation of the sample on the ram. Details of the suction cap system are shown in Figure 3.13. A viscoelastic suction cap was placed on the top cap of the sample, which docked with an acrylic plate attached to the load cell. A thin layer of grease was applied to the suction cap to aid sealing. The suction cap was placed onto the top cap after sample preparation including sample measurement and the addition of local strain instrumentation (if applicable). Although the sample had been placed under negative back pressure, providing a low level of strength, the suction cap was positioned as carefully as possible to minimise disturbance. After installation of the suction cap, the cell was lowered onto the triaxial rig, with the ram lowered to prevent contact with the sample and the load cell. The cell was flooded, with the suction cap tap and the top cell drain open (Figure 3.1(f)), allowing the suction cap line to fill with water. Subsequently, only the top drain was closed. The sample was then slowly raised using load control until the load cell registered 0.01 kN. The suction cap would then be mounted lightly to the acrylic plate (Figure 3.13(b)). While maintaining

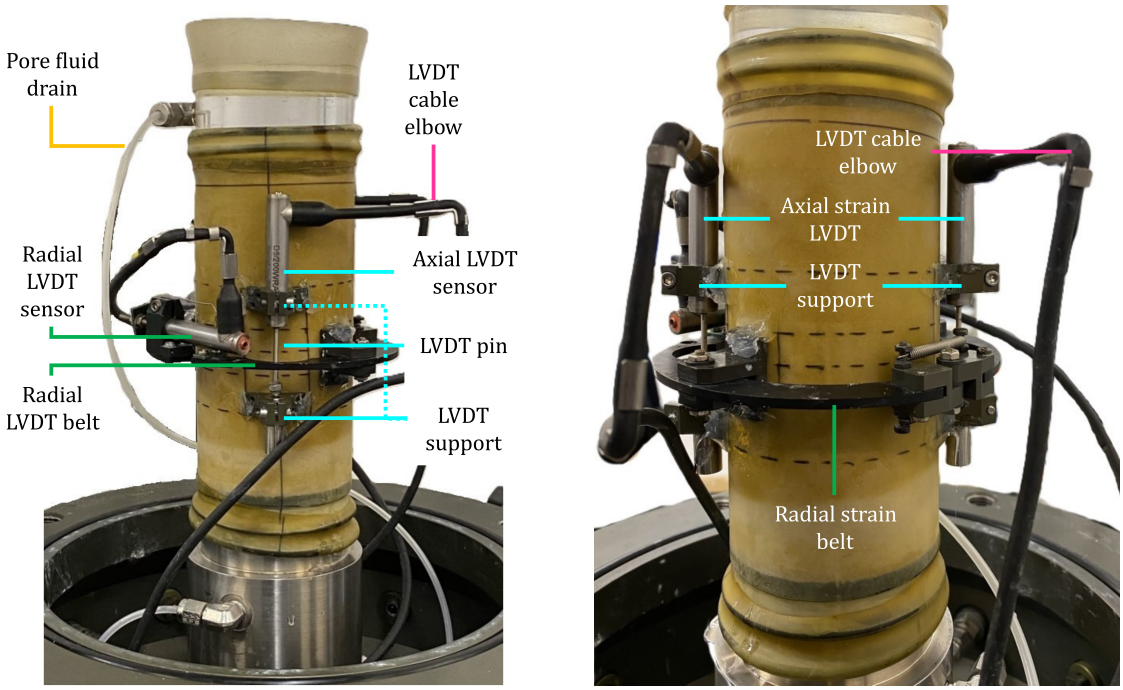

Figure 3.12: Local strain instrumentation installed on a sample showing perpendicular views. The local strain instrumentation was a complete GDS triaxial system.

a 0.01 kN load, a cell pressure of 30 kPa was applied. The pressure difference between the cell water and the water contained within the suction cap led to a reduction in load, inducing the load control to slowly raise the sample. Once all water had been expelled from this void, and the top cap was fully in contact with the acrylic plate, the load stabilised. The suction cap tap was then closed, and the load was reduced to 0 kN. If the sample was properly mounted, the suction would hold the sample in place at 0 kN load.

The system described above allowed for effective engagement of the sample with the load cell with minimal disturbance. Additionally, the water held within the suction cap line minimised any compliance within the system during reverse loading owing to the incompressibility of water, as opposed to air.

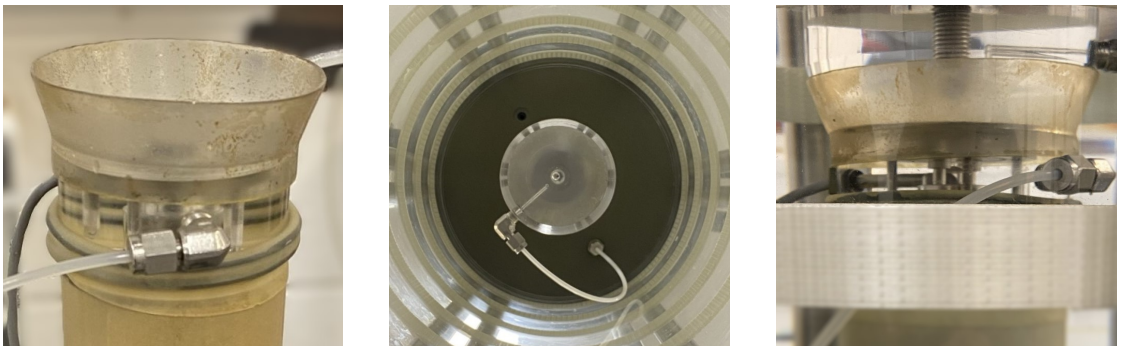

(a) (b) (c)

Figure 3.13: Suction cap mounting system used for connecting sample to top ram, showing: (a) viscoelastic suction top cap, (b) suction cap mount in centre of cell, and (c) sample connected to the top ram.

3.5 Test procedure

The initial stages of the test procedure are identical for all test types. The methodology employed is based on the standards provided by ASTM (ASTM D7181-20, 2020) and Fugro in-house procedures (Fugro, 2020). The test stages are as follows:

Stage 1: Set-up stage. The current pore pressure and cell pressure are read, and the back pressure and cell pressure controllers are set to maintain this. The sample taps are now opened to allow control of pore pressure.

Stage 2: Saturation ramp. The back pressure and cell pressure are both ramped simultaneously, $\Delta u, \Delta\sigma_r = 200$ kPa, maintaining the effective mean effective stress at the level created by the sample preparation procedure. The resulting cell pressure is 230 kPa.

Stage 3: Skempton B value check. The sample taps are closed, and the cell pressure is increased by 100 kPa. The change in pore pressure is also recorded. The B value is taken as $B = \Delta u/\Delta\sigma_r$. The sample is deemed to be saturated if the B value exceeds 0.98.

Stage 4: Isotropic consolidation. The final pore pressure at the end of the B check is recorded, and the back pressure is set to maintain this value. The cell pressure is then ramped to the final required consolidation pressure, at a rate of 10 kPa/min. This ensures the rate of consolidation is slow enough not to cause damage to the sample fabric. After the cell pressure has reached the stipulated pressure, the sample is then left for 1 hour to allow for full consolidation. The sample should be checked for leaks at this point; the sample is considered to be satisfactorily sealed if the rate of volume change settles to under 400 mm^3/hour.

Stage 5: Anisotropic consolidation (if required). The deviatoric load is applied via the ram to the required pressure, at a rate of 10 kPa/min. The sample is left for 1 hour after consolidation.

Following these initial stages the test procedure will vary based on the test completed. The loading applied in all cases is controlled by the software. The conditions are summarised in Table 3.6.

Table 3.6: Test parameters for different test types

Test type	**Control**	**Load cell (kN)**	**Local strain**	**Load rate**	**Sampling freq. (Hz)**
Drained monotonic	Disp.	5	N	3 mm/hr	0.1
Undrained monotonic	Disp.	25	N	3 mm/hr	0.1
Drained cyclic	Load	5	Y	0.1 Hz	5
Undrained cyclic	Load	5	Y	0.1 Hz	5

3.5.1 Test procedure by test type

Drained monotonic loading

- Drained monotonic tests are completed using a 5 kN load cell. The monotonic load is applied using displacement control, at an axial strain rate of 3 mm/hr, up to a limit of 15% axial strain.
- Pore pressure is read using an external PPT attached to the base drain. The base tap is closed after the PPT in order to isolate the PPT from the back pressure controller.

Undrained monotonic loading

- A load cell with a range of 25 kN is required. The load application parameters are consistent with the drained monotonic tests.
- Both the base and top taps of the sample are sealed, with pore pressure read from the base drain.

Cyclic loading

- A load cell with a 5 kN range is used.
- Cyclic conditions are applied load controlled.
- Loading for both drained and undrained tests are applied at a frequency of 0.1 Hz.
- For tests with 2000 cycles or fewer, data is sampled at 50 points per cycle.
- For tests exceeding 2000 cycles, 50 data points per cycle are recorded for the initial 2000 cycles, while 20 points per cycle are recorded for the remaining cycles.
- For drained cyclic tests, after completion of the cycles, a monotonic axial load is applied until 15% axial strain is attained.

3.5.2 End of test procedure

- The cell and back pressure are ramped down, then a vacuum is applied to the sample at a pressure of -15 kPa, to preserve the final state of the sample.
- The cell is removed, then the final condition of the sample is documented with a photograph.
- The sample is transferred to to a pre-weighed tin, the membrane is rinsed with water to ensure all sand is added to the tin. The sample is then dried in an oven to record the final dry mass.

For silty sand samples:

- Follow the identical procedure.
- After recording the total dry mass, the sample is washed using water over a sieve with a 63 µm aperture.
- The sample is dried before recording the final weight of the clean sand.

3.6 Bender elements

In order to determine small-strain shear modulus values, $G_{\max}$, bender elements were used. Figure 3.14 shows the pedestal used for the bender element tests. The travel distance of the shear wave is taken as the distance from the tip of the output element to the tip of the receiver element. The porous stones used had holes matching the size of the bender housing and matched the thickness of the bender housing protrusion.

Figure 3.15 depicts an example of the selection of the travel time. The results depicted are of a sample prepared to $D_r = 80\%$, consolidated to $p' = 50$ kPa. Each bender element test stage was subjected to a range of input frequencies, from 4 - 20 kHz. The input and output signals were plotted on the same axes in order to select the most appropriate arrival time, given the variance evident in the plot. The method of time selection was the "first crossing" method, as this provides consistent results in the time domain (Adamidis et al., 2017). The time value is used to calculate $G_{\max}$ using Equation (3.1), with measured values of sample height and density required.

$$G_0 = \rho V_s^2 \tag{3.1}$$



Figure 3.14: Pedestal with inbuilt output bender element for shear wave testing. A matched and calibrated receiver bender element is mounted to the top cap. To allow for mounting the slurry deposition mould, the pedestal was modified for the wiring to be introduced below the lip.

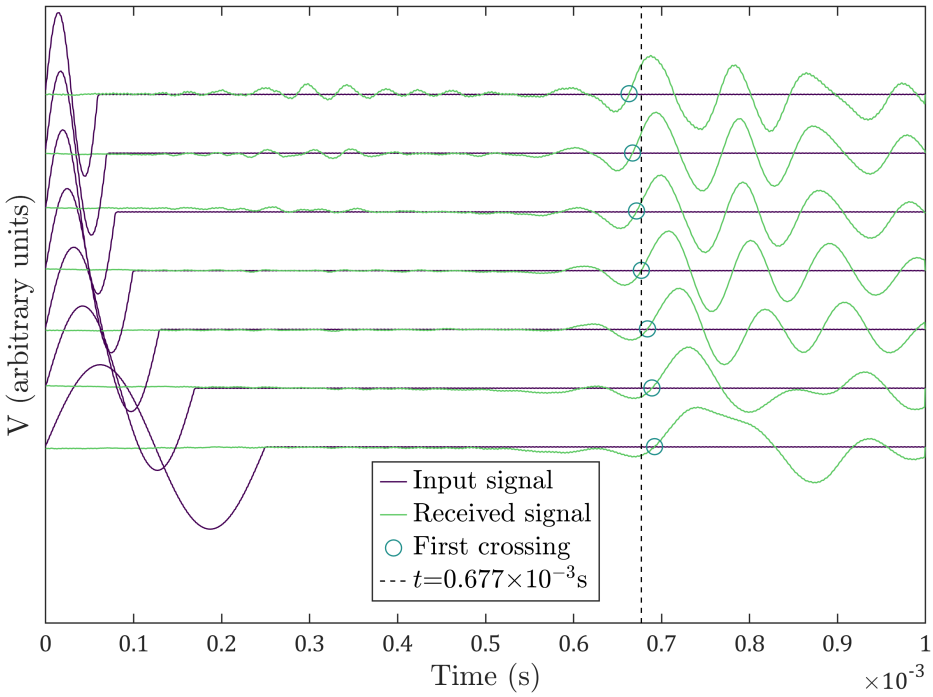

Figure 3.15: Example of bender element processing to determine the point of first arrival. Multiple signals of increasing frequency were applied at each consolidation phase to give the best estimate of the arrival time. The selected time is overlaid with a dashed line.

3.7 Silty sand samples

The additional aspects of the methodology required for the testing of silty sand samples are presented here. The fines content and density of these samples were designed to match the equivalent void ratio, e^*, of the benchmark samples. The e^* is defined using Equation (3.2) (Thevanayagam et al., 2002), where f_c is the fines content, and b quantifies the contribution of the fines. The value b can be calibrated in varying ways. The determination of b used in this thesis is taken from Rahman et al. (2011). The formulation is shown in Equation (3.3), where f_{thre} is the threshold fines content, $r = D_{10}^{sand}/d_{50}^{fines}$, and $k = 1 - r^{0.25}$. The factor f_{thre} is defined by trends in the CSL in $e - ln(p')$ space. At low fines content, increases in fines lead to a reduction in the critical state void ratio at a given mean effective stress. At high fines content, the opposite is true. Therefore, f_{thre} is the fines content at which the CSL reaches a minimum void ratio. Using a range of data, Rahman et al. (2011) produced an empirical relationship for defining f_{thre}. This is shown in Equation (3.4), where $\chi = d_{50}^{fines}/D_{10}^{sand}$.

$$e^* = \frac{e + (1-b)f_c}{1 - (1-b)f_c}; \quad 0 < b < 1 \tag{3.2}$$

$$b = \left[1 - \exp\left(-0.3\frac{(f_c/f_{\text{thre}})}{k}\right)\right] \times \left(r\frac{f_c}{f_{\text{thre}}}\right)^r \tag{3.3}$$

$$f_{\text{thre}} = 0.40\left(\frac{1}{1 + e^{0.5-0.13\chi}} + \frac{1}{\chi}\right) \tag{3.4}$$



(a)

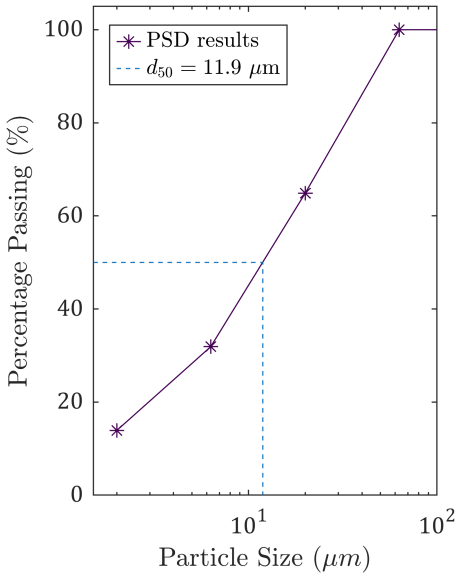

(b)

Figure 3.16: Non-plastic fines for silty sand tests, showing: (a) production of non-plastic fines using a ball mill on Congleton sand, and (b) particle size distribution results from silt sedimentation test on crushed Congleton silt.

In this project the fines used for the silty sand testing were produced artificially from Congleton sand. Congleton sand was ground using a Retsch Planetary Ball Mill PM 100 (Retsch GmbH, Germany) (Figure 3.16(a)). The ball mill was only able to grind small quantities of sand in a single batch, well below the amount required for the total testing phase. Congleton sand was weighed out into 100 g batches, then introduced to the ball mill. The ball mill was set at 400 rpm, for 3 minutes, to produce the fines. These steps were repeated multiple times, until the required amount of fines was produced. The complete batch was then classified in order to maintain consistent fines throughout all tests.

The classification of the fines produced is presented here. The particle size distribution of the fines produced was measured using a silt sedimentation test following the methodology of ISO (2022), the results of which are presented in Figure 3.16(b). From these results the value of d_{50} 11.9 µm can be taken for use in the calculation of b in Equation (3.3).

3.8 Partially drained samples

The methodology for the partially drained cyclic triaxial tests is discussed here. The general approach was based on the concept presented in Suzuki et al. (2020). Partial drainage conditions were induced using a "filter" between the sample and the back volume controller to reduce the permeability of the drainage flow. A photograph of the set-up is shown in Figure 3.17, and a schematic is shown in Figure 3.18. During testing the applied cyclic loading was identical in condition to the benchmark tests, at the same load frequency and amplitude, differing only in the filter permeability.

The filter housed a tube with compacted silt in order to control the permeability of the filter. Geo-textile, secured with silicone sealant, was employed at both ends of the tube to maintain the silt's position within the filter. Silt was compacted into the tube dry, then saturated using pressurised de-aired water flowing between the back volume controller and the cell volume controller. The filter was isolated with two-way valves to allow sealing of the filter after saturation until the cyclic loading phase. In order to ensure a complete seal of the filter, the bolt threads were sealed with Loctite pipe sealant.

Two series of partially drained tests were completed, with varying density of the compacted silt and therefore varying permeability. The filter was left undisturbed between tests of the same series, to allow for consistent permeability. However, a new test-specific measurement of the filter permeability was recorded immediately prior to each test. Permeability was determined by applying a pressure differential between the back volume controller and cell volume controller. The change in volume over a 10 minute period with a 10 kPa pressure differential gave the flow rate per unit pressure difference for the filter using Equation (3.5). The permeability measurement was recorded with a baseline back pressure of 350 kPa to minimise pressure differences between the sample and the filter once connected. The pressure differential was set to 0 kPa after the measurement was taken, then allowed to settle for 10 minutes. Typical values of filter permeability are given in Table 3.7

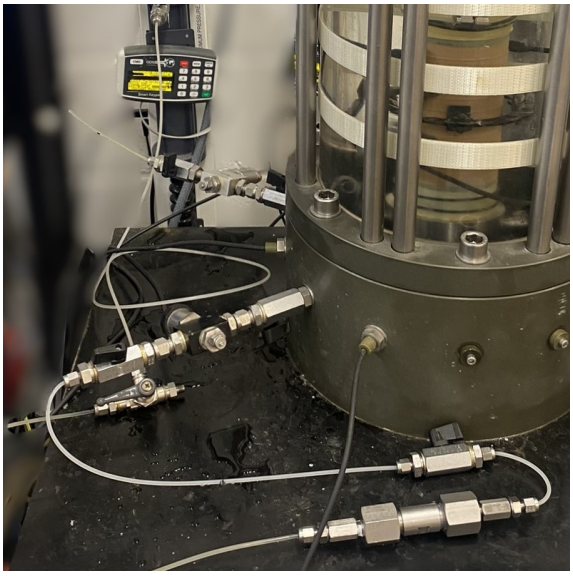

Figure 3.17: Arrangement of partially drained filter, with pore pressure transducers on both top drain linked to the filter, and base drain with a closed tap.

$$\text{Filter permeability} = \frac{\Delta V}{\Delta T p} = \frac{Q}{p} \tag{3.5}$$

Table 3.7: Typical values for partial drainage filter permeability

Series	Q/p **(mm³/s/kPa)**
Partial drainage filter 1	5×10^{-3}
Partial drainage filter 2	1×10^{-2}

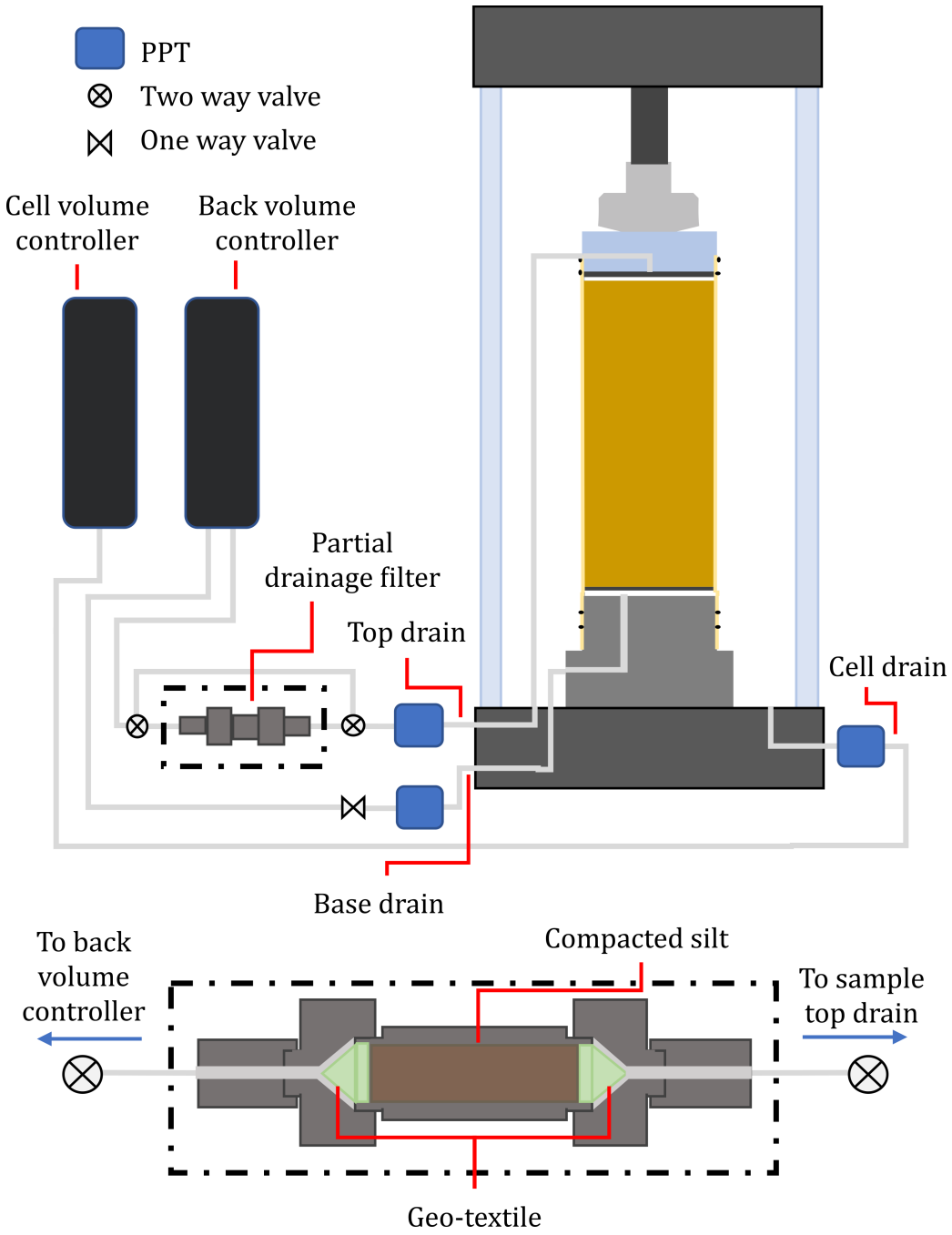

Figure 3.18: Schematic of partial drainage filter used in partial drainage cyclic tests. The filter is isolated by two two-way valves, allowing consolidation without use of the filter. The permeability is controlled by the density of the compacted silt held within the filter.

3.9 Test programme

The following section outlines the test schedule, with the motivation for the tests performed. The aim of the triaxial testing phase of the DPhil was to examine the effects of drainage on the response of clean and silty sand to cyclic loading. In order to provide data for comparison, the first phase of testing involved testing of clean sand under drained and undrained conditions with monotonic and cyclic loading. These tests are termed the

Table 3.8: Benchmark monotonic testing schedule

Testname	Test type	e_0	D_r	p'_0
BM_CIDc_50_100_a	CIDc	0.628	63	100
BM_CIDc_50_100_b	CIDc	0.642	57	100
BM_CIDc_50_300	CIDc	0.646	56	300
BM_CIDc_50_50	CIDc	0.640	58	50
BM_CIDc_80_50	CIDc	0.604	73	50
BM_CIDc_80_100_a	CIDc	0.575	85	100
BM_CIDc_80_100_b	CIDc	0.570	87	100
BM_CIDc_80_300_a	CIDc	0.564	89	300
BM_CIDc_80_300_b	CIDc	0.579	83	300
BM_CIDe_50_50	CIDe	0.662	49	50
BM_CIDe_50_100_a	CIDe	0.642	58	100
BM_CIDe_50_100_b	CIDe	0.665	48	100
BM_CIDe_50_300	CIDe	0.628	63	300
BM_CIDe_80_50	CIDe	0.597	76	50
BM_CIDe_80_100_a	CIDe	0.588	80	100
BM_CIDe_80_100_b	CIDe	0.570	87	100
BM_CIDe_80_300	CIDe	0.579	83	300
BM_CIUc_50_100_a	CIUc	0.645	56	100
BM_CIUc_50_100_b	CIUc	0.658	51	100
BM_CIUc_50_300	CIUc	0.636	60	300
BM_CIUc_80_100_a	CIUc	0.598	75	100
BM_CIUc_80_100_b	CIUc	0.599	75	100
BM_CIUc_80_100_c	CIUc	0.561	91	100
BM_CIUc_80_100_d	CIUc	0.604	73	100
BM_CIUc_80_100_e	CIUc	0.586	80	100
BM_CIUc_80_1200	CIUc	0.570	87	1200
BM_CIUc_80_800	CIUc	0.570	87	800
BM_CIUe_50_100_a	CIUe	0.658	51	100
BM_CIUe_50_100_b	CIUe	0.659	50	100
BM_CIUe_50_300	CIUe	0.647	56	300
BM_CIUe_80_100	CIUe	0.584	81	100
BM_CIUe_80_300	CIUe	0.580	83	300

benchmark tests. The second phase of testing examined the impact of fines content and partial drainage on soil response.

3.9.1 Benchmark tests

The testing schedule of the benchmark tests aimed to provide an extensive database of the response of Congleton sand under a range of loading conditions. The choice of tests was designed to provide adequate data for calibration of constitutive models, particularly

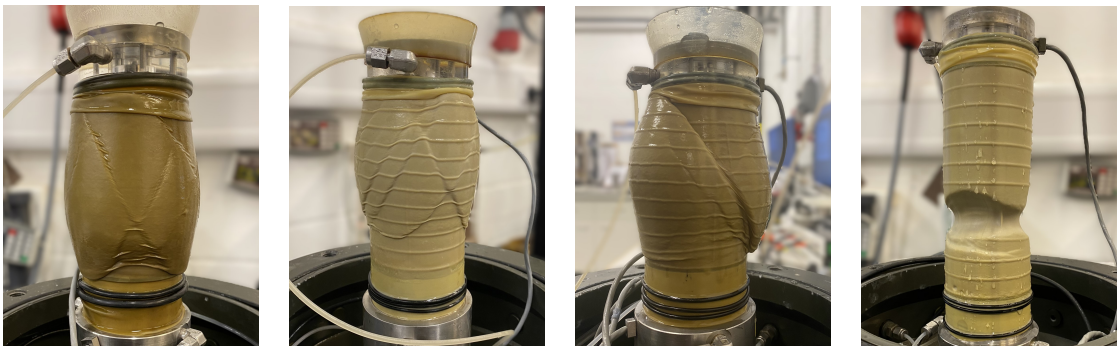

(a) (b) (c) (d)

Figure 3.19: End results of monotonic shearing, showing during compression tests, (a) x-shaped shear plane, (b) multiple shear planes, (c) single shear plane, and during extension tests, (d) necking formed during shearing.

SANISAND-MS (Liu et al., 2019) and HCA (Wichtmann et al., 2015). For this aim, a range of tests were completed with variations in void ratio, mean effective stress, drainage, compression and extension, monotonic and cyclic.

Benchmark monotonic tests

For the monotonic testing phase, the test schedule design was completed following the practice shown in Azeiteiro et al. (2017). This gave tests completed at a range of relative densities, of medium and high density (50% and 80% D_r), under drained and undrained conditions, with a range of stress paths. The benchmark monotonic test schedules is outlined in Table 3.8. The table presents the achieved void ratio post consolidation e_0, relative density D_r, and the mean effective stress p'_0. All tests were performed starting from isotropically consolidated conditions. Test types CID_c and CIU_c had compressive stress paths with strain control, leading to a stress path of $+q$ and $p' = q/3$. Test types CID_e and CIU_e had extensive stress paths, with stress paths of $-q$ and $p' = q/3$. CID_c and CID_e were performed drained. CIU_c and CIU_e were performed undrained. All tests were performed at an axial displacement rate of 3 mm/hr, which was sufficiently slow for fully drained conditions in the drained tests (excess pore pressures were monitored during testing). The tests were sheared until at least $\varepsilon_a = 0.15$, however, presented results have been truncated at the onset of a non-uniform stress state i.e. shear planes or necking in compression and extension tests respectively. Examples of the types of shear planes and necking during testing are shown in Figure 3.19. Furthermore, the results of undrained compression tests have been truncated at back pressure $u = 30$ kPa, where entrained air bubbles begin to precipitate.

Benchmark cyclic tests

The benchmark clean sand cyclic test schedule is detailed in Table 3.9. The test schedule followed a similar design to the drained cyclic tests performed in Wichtmann et al. (2005).

This schedule allowed investigation into the effect of four major parameters, (e_0, p'_0, q_{av}, q_{cyc}), as demonstrated in Figure 3.20. Some of the tests featured in multiple parametric series, including BM_CIDC_80_200_150_60, which was included in most series.

For the investigation of e_0, three tests were completed at nominal initial void ratios of $e_0 = 0.674, 0.623, 0.577$ (corresponding to $D_r = 30, 50, 80\%$), with initial conditions of $p'_0 = 200$ kPa, $q_{av} = 150$ kPa, $q_{cyc} = 60$ kPa, representing stress ratios of $\eta = 0.75$ and $\zeta_b = 0.3$. The investigation of p'_0 was carried out with $p'_0 = 50, 100, 200, 300$ kPa, at $e = 0.58$ ($D_r = 80\%$), at stress ratios of $\eta = 0.75, 0.35, -0.5$ and $\zeta_b = 0.3$. The q_{av} series was carried out with variations in $\eta = -0.5, 0, 0.25, 0.75, 1$ at $p'_0 = 100, 200, 300$ kPa, and $e = 0.58$, $\zeta_b = 0.3$. Variations in q_{cyc} were completed with $q_{cyc} = 30, 60, 90$ kPa ($\zeta_b = 0.15, 0.3, 0.45$) only on samples of $e = 0.58$, $p'_0 = 200$ kPa, $q_{av} = 150$ kPa representing $\eta = 0.75$. These investigations allowed investigation into the relationships between the selected parameters and accumulated strain at varied levels. All tests were cycled to at least 2000 cycles, with most up to 10,000 cycles. The loading was applied at 0.1 Hz, which was sufficiently slow for fully drained conditions, resulting in a small oscillation in pore pressure of $\Delta u = \pm 2$ kPa.

Table 3.9: Benchmark cyclic testing schedule

Test	e_0	p'_0 **(kPa)**	$q_{\mathbf{av}}$ **(kPa)**	$q_{\mathbf{cyc}}$ **(kPa)**	η	ζ
BM_CIDC_80_50_37.5_15	0.582	50	37.5	15	0.75	0.3
BM_CIDC_80_100_25_30	0.584	100	25	30	0.25	0.3
BM_CIDC_80_100_75_30	0.598	100	75	30	0.75	0.3
BM_CIDC_80_100_-50_30	0.579	100	-50	30	-0.5	0.3
BM_CIDC_30_200_150_60	0.674	200	150	60	0.75	0.3
BM_CIDC_50_200_150_60	0.623	200	150	60	0.75	0.3
BM_CIDC_80_200_150_30	0.585	200	150	30	0.75	0.15
BM_CIDC_80_200_150_60	0.577	200	150	30	0.75	0.3
BM_CIDC_80_200_150_90	0.581	200	150	60	0.75	0.45
BM_CIDC_80_200_0_60	0.557	200	0	60	0	0.3
BM_CIDC_80_200_200_60	0.573	200	200	60	1	0.3
BM_CIDC_80_200_50_60	0.554	200	50	60	0.25	0.3
BM_CIDC_80_200_-100_60	0.573	200	-100	60	-0.5	0.3
BM_CIDC_80_300_225_90	0.571	300	225	90	0.75	0.3
BM_CIDC_80_300_75_90	0.577	300	75	90	0.25	0.3
BM_CIDC_80_300_-150_90	0.572	300	-150	90	-0.50	0.3

3.9.2 Silty sand tests

The details of the silty sand testing schedule are provided here. As discussed in Section 3.7, the void ratio definition of the silty sand samples followed the methodology of Rahman et al. (2011) for the equivalent void ratio e^*. Table 3.10 presents the initial conditions and

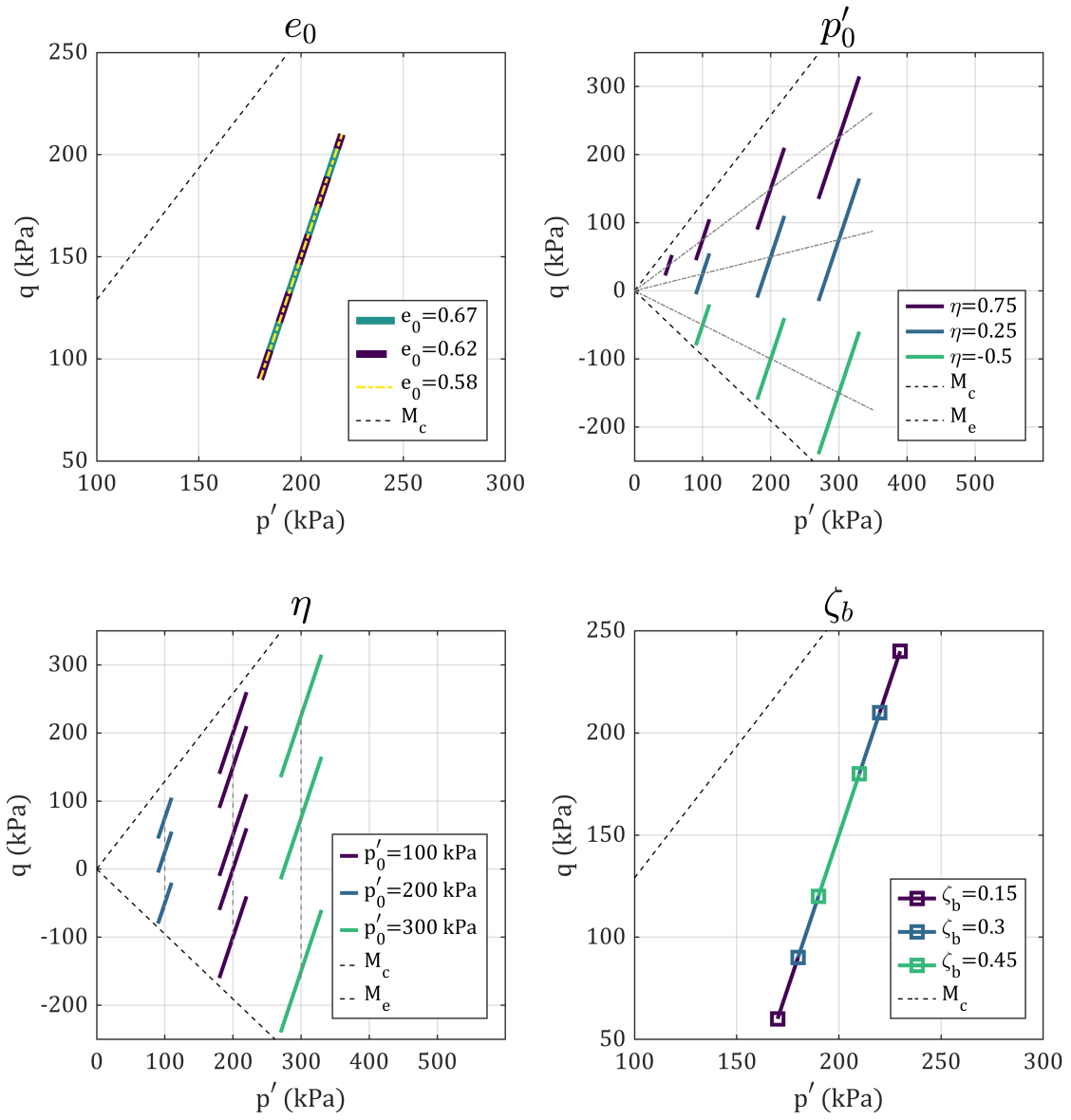

Figure 3.20: Stress paths of the drained cyclic triaxial test series with variation of key parameters. One series of varied $e_0 = 0.58, 0.62, 0.67$ tests performed with the same stress path $p'_0 = 200$ kPa, $\eta = 0.75$, $\zeta_b = 0.3$. Three series of varied p'_0 at $\eta = 0.75, 0.25, -0.5$, with $e_0 = 0.58$, $\zeta_b = 0.3$. Three series of varied η, at $p'_0 = 100, 200, 300$ kPa, and $e_0 = 0.58$, $\zeta_b = 0.3$. One series of varied $\zeta_b = 0.15, 0.3, 0.45$, at $p'_0 = 200$ kPa, $e_0 = 0.58$, $\zeta_b = 0.3$.

loads applied to the silty sand samples. The schedule contains two series of samples, at 10 and 15% fines content. The equivalent global void ratio was targeted at $e^* = 0.58$, 80% D_r for a clean sand sample. As can be seen in the values of global void ratio, e_{glob}, the overall sample density is much higher than the clean sand samples: $e_{glob} \approx 0.45$ for fc=10%, and $e_{glob} \approx 0.34$ for fc=15%. However, the hypothesis of the equivalent void ratio predicts the fines particles to fill voids without contributing significantly to the stress matrix, therefore having minimal impact on strength.

Tests were completed at the same stress levels as some of the benchmark cyclic tests, facilitating comparison for investigation of the impact of fines content. The lower stress

Table 3.10: Testing schedule of the drained silty sand cyclic test series

Test name	e_{glob}	**fc**	e^*	p'_0 **(kPa)**	η	ζ_b
FC10_CIDC_80_100_75_30	0.451	0.10	0.590	100	0.75	0.3
FC10_CIDC_80_200_150_60_a	0.443	0.10	0.577	200	0.75	0.3
FC10_CIDC_80_200_150_60_b	0.481	0.09	0.600	200	0.75	0.3
FC10_CIDC_80_200_150_60_c	0.407	0.13	0.580	200	0.75	0.3
FC10_CIDC_80_200_150_60_d	0.440	0.10	0.579	200	0.75	0.3
FC10_CIDC_80_200_150_60_e	0.427	0.11	0.572	200	0.75	0.3
FC10_CIDC_80_200_-100_60	0.439	0.10	0.571	200	-0.5	0.3
FC10_CIDC_80_300_225_90	0.442	0.10	0.573	300	0.75	0.3
FC15_CIDC_50_200_150_60	0.438	0.14	0.636	200	0.75	0.3
FC15_CIDC_80_200_150_60_a	0.336	0.17	0.559	200	0.75	0.3
FC15_CIDC_80_200_150_60_b	0.335	0.16	0.541	200	0.75	0.3
FC15_CIDC_80_200_150_60_c	0.326	0.17	0.546	200	0.75	0.3
FC15_CIDC_80_200_-100_60	0.378	0.15	0.582	200	-0.5	0.3
FC15_CIDC_80_300_225_90	0.359	0.16	0.578	300	0.75	0.3

ratios, $\eta_{av} = 0, 0.25$, were not tested in order to reduce the total number of tests required, and because these stress ratios had lower overall strain accumulation.

These tests were performed at the same loading frequency as the benchmark cyclic tests. The permeability is reduced by the presence of fines, so a series of initial load frequency tests were performed to validate the drained condition. These tests showed no pore pressure accumulation, and similar low values of pore pressure accumulation to the benchmark tests, $\Delta u = \pm 2 - 3$ kPa.

3.9.3 Partial drainage tests

The testing schedule for the partially drained cyclic tests on clean sand is presented in Table 3.11. The tests were performed with variations in e_0, p'_0, and q_{ampl}, maintaining an average cyclic stress ratio $\eta_{av} = 0.75$. The tests included two levels of filter permeability; however, as indicated by the filter permeability values, the flow resistance varied throughout the test series due to the characteristics of the silt-based filter. During the testing phase, the drainage induced by loading caused flow through the filter. It is likely that preferential drainage pathways formed within the filter, leading to small variations in drainage between each test.

The tests were performed at the same cyclic frequency, 0.1 Hz, in order to investigate the impact of partial drainage conditions.

A second series of partially drained cyclic tests on silty sand samples was performed with a limited number of tests. This test schedule is presented in Table 3.12.

Table 3.11: Testing schedule of the partially drained clean sand cyclic test series

Test name	e_0	**Filter perm. ($mm^3/s/kPa$)**	p'_0 **(kPa)**	η	ζ_b
PD1_CIDC_80_100_75_30	0.575	2.95×10^{-3}	100	0.75	0.3
PD1_CIDC_80_200_150_60_a	0.567	4.84×10^{-3}	200	0.75	0.3
PD1_CIDC_80_200_150_60_b	0.584	5.06×10^{-3}	200	0.75	0.3
PD1_CIDC_80_200_150_60_c	0.582	5.27×10^{-3}	200	0.75	0.3
PD1_CIDC_80_200_150_90	0.582	7.55×10^{-3}	200	0.75	0.45
PD1_CIDC_80_300_225_90	0.578	7.55×10^{-3}	300	0.75	0.3
PD2_CIDC_80_100_75_30	0.591	1.05×10^{-2}	100	0.75	0.3
PD2_CIDC_80_200_150_60	0.559	5.91×10^{-2}	200	0.75	0.3
PD2_CIDC_80_300_225_90	0.565	5.78×10^{-3}	300	0.75	0.3

Table 3.12: Testing schedule of the partially drained silty sand cyclic test series

Test name	$e*$	**fc**	**Filter perm. ($mm^3/s/kPa$)**	η	ζ_b
FC10_PD1_CIDC_80_100_75_30	0.575	0.1	5.15×10^{-3}	0.75	0.3
FC10_PD1_CIDC_80_200_150_60	0.581	0.11	5.13×10^{-3}	0.75	0.15
FC10_PD1_CIDC_80_300_225_90	0.577	0.1	4.94×10^{-3}	0.75	0.3

3.10 Data management and analysis

The following section details the recorded data and analysis methods used for the triaxial testing programme. This includes details of the data recording of the DYNTTS system, initial sample measurements during the sample preparation phase, and the measurement correction procedures used during the data analysis.

3.10.1 Data recording

All tests were performed using the GDS DYNTTS system. The test control software includes the ability to vary the data recorded. Monotonic tests were recorded with a sampling frequency of 0.1 Hz, equivalent to a data point for $\varepsilon_a = 0.006\%$ when sheared at 3 mm/hr. Cyclic tests were recorded at 50 points per cycle for the first 2000 cycles, then 20 points per cycle thereafter. Some tests, including all cyclic tests, employed local strain measurements, which therefore included further recorded values. The saved data was provided in engineering units, with calibration factors already applied. Calibration was performed by the author to the standards of Fugro, a United Kingdom Accreditation Service (UKAS) accredited professional laboratory, with annual updates. A summary of the data recorded is provided in Table 3.13. Additional channels are also recorded consisting of calculated values from the GDS software, which are unused in analysis. Data is saved in .gds files which are comma separated, and provide values for all channels at each sampling point. Additional values such as sample height and diameter, test name, date, are also recorded in the preamble to the test data.

The sample height and diameter are used by the control software to provide estimates of the current cross-sectional area. This cross-sectional area was calculated based on the right cylinder assumption, using values of axial strain and initial diameter. During anisotropic consolidation, the value of q was input into the control software, which used the value of the current area to calculate the load applied. Additionally, the value of cyclic stress, which was input as a load, rather than a stress, required the use of the estimated current cross-sectional area. The use of load, rather than cyclic stress amplitude was chosen following the Fugro cyclic test standards. The implication of this, is that if large strains occur, inducing changes in area, the deviator stress will change across the length of the test. However, the method is more rigorous, as it does not rely on the internal control software to continually update its estimate of sample area. Using local strain instrumentation, and measurement corrections, can provide a better outcome.

Table 3.13: Triaxial test recorded data channels

Channel	Value	Sensor	Unit
1	Stage Number	Control software	-
4	Radial Pressure	External PPT	kPa
5	Radial Volume	Cell volume/pressure controller	mm^3
6	Back Pressure	Back volume/pressure controller	kPa
7	Back Volume	Back volume/pressure controller	mm^3
8	Load Cell	Submersible load cell	kN
9	Pore Pressure	External PPT	kPa
10	Axial Displacement	Screw driven load ram	mm
13	Local Axial 1	Axial LVDT	mm
14	Local Axial 2	Axial LVDT	mm
15	Local Radial	Radial LVDT	mm

3.10.2 Sample measurements

Details of the measurements taken of the initial sample conditions were provided in the sample preparation procedure (Section 3.4), and a summary is provided here (Table 3.14).

3.10.3 Measurement corrections

The measurement corrections applied in processing are summarised here, details of which are given in Section 2.6.2. During monotonic testing, corrections of membrane stress, and barrel deformation were applied. Cyclic loading results have no corrections applied, as the use of local strain instrumentation mitigated potential issues. The membrane stress correction used followed the recommendations of ASTM D7181-20 (2020), which is summarised in Equation (3.6). The results of this were only applied if the radial stress error exceeded 5%, as recommended in the standard. Barrel corrections were applied using the methodology of Lade (2016). This correction is summarised in Equation (3.7).

Table 3.14: Measurements, Descriptions, and Units

Measurement	Description	Unit
Sample height	3× 120° apart, top cap to pedestal lip	mm
Diameter	3 × 3 120° apart, top middle bottom	mm
Membrane thickness	3× top middle bottom membrane	mm
Mass added	Mass added to slurry deposition mould	g
Final mass	Sample and cutting dry mass	g
Fines added	Fines added to slurry	g
Fines content	Sample dry mass pre-post clean	g
Local strain distance	Distance between LVDT supports	mm
Partial drainage filter	Filter flow resistance	$mm^3/s/kPa$

$$\Delta(\sigma_1 - \sigma_3) = (4E_m \cdot t_m \cdot \varepsilon_1)/D_c \tag{3.6}$$

$$A_{\text{barrel}} = A_{\text{cylinder}} \cdot \left(2 - \sqrt{\frac{1-\varepsilon_a}{1-\varepsilon_v}}\right) \tag{3.7}$$

3.11 Summary

This chapter described the testing methodology employed for the triaxial element testing conducted in this thesis. The selected methodology was informed by the literature review and a comparative investigation of three sample preparation techniques: Moist Tamping, Dry Funnel Deposition, and Slurry Deposition. Samples prepared using the slurry deposition method exhibited the greatest consistency and were therefore adopted. The slurry deposition procedure was summarised, including additional steps required for advanced testing methods. The test programme was then presented, with a rationale for the chosen test schedule and a description of the test conditions. Finally, the data management and processing approach was outlined.

Chapter 4
Triaxial Results I: Behaviour of Clean Sand Under Monotonic and Cyclic Loading

The following chapter presents the results from a series of monotonic and cyclic triaxial tests on clean Congleton sand. The purpose of these tests was to provide benchmark results for comparison with tests on silty and partially drained sand. The suite of tests was designed to yield results encompassing a range of key parameters, including relative density D_r, mean effective stress p'_0, drainage conditions, and stress paths. The test schedule is provided in Chapter 3. This chapter is divided into the results of monotonic and cyclic tests. Within each of these sections, the results presented are further subdivided into the complete test response and a synthesis of results to provide values suitable for calibrating SANISAND style constitutive models.

These tests generate a novel dataset reflecting the response of Congleton sand to various triaxial tests. The testing methodology integrated a variety of advanced triaxial techniques to achieve the experimental aims. The use of slurry deposition for sample preparation, applicable to clean and silty samples, combined with drainage-restricted conditions that induce a partially drained response, yields novel experimental findings on significant behaviour. Additional novelty is introduced through long-term drained cyclic triaxial tests, accompanied by comprehensive local sensor data. Other examples of this testing type in the literature (Wichtmann et al., 2005) employ global strain measurements; however, the implementation of local strain instrumentation reduces issues related to compliance, bedding, and lower resolution measurements. Wichtmann et al. (2005) also does not provide data on the sample pore pressure, which is a key measurement in the assessment of partially drained conditions.

The experimental dataset presented in this chapter is for Congleton sand. This sand is gaining popularity in geotechnical model testing in the UK (K. Cheng et al., 2020; Qi et al., 2022), as previous alternatives – particularly Leighton Buzzard Sand – have recently become too expensive. The experimental results provide a novel dataset of Congleton sand behaviour, suitable for the calibration of advanced soil constitutive models. Combined with model testing efforts, this data will facilitate the effective evaluation of new constitutive models. In this chapter, the results of the testing schedule are employed to calibrate the SANISAND-MS constitutive model.

The test results below present typical data from triaxial testing. All results include data on deviator stress q and axial strain ε_a, along with relevant details of the triaxial

stress path in $p' - q$ space (typically for undrained tests) and pore pressure response. For drained tests, separate plots of the volumetric response are also included. The results are presented with axial and volumetric strain, rather than pure deviatoric strain, to enhance clarity. Additionally, the axial strain response is the most accurate, as the local strain instrumentation provides high-resolution data of vertical displacement. The inferred volumetric response may be affected by minor issues with membrane leakage, particularly in tests conducted over an extended duration (high cyclic drained tests).

The calibration of SANISAND-MS parameters was successfully completed for the drained cyclic tests. However, the calibration procedure highlighted certain issues with the model. The recommended calibration procedure employs a combination of drained and undrained monotonic tests for the majority of parameters. Nevertheless, the simulated results indicate that certain parameters, e.g. h_0, are better calibrated when the condition of interest is emphasised, specifically if the soil is drained or undrained. This raises concerns about applicability across all conditions. Furthermore, the calibration of cyclic tests was targeted at the maximum number of cycles; however, if a different number of cycles is selected, the calibrated value may differ as well. Therefore, the predicted response is less certain if there is a different number of cycles than that tested. This presents challenges for predictive modelling of full-scale problems. In this case, explicit cyclic models, such as HCA (Niemunis et al., 2005) or the cyclic contour method (Andersen, 2015) may be better suited. Finally, the relationship between compression and extension stress ratios in both monotonic and cyclic results is summarised through a single parameter, c, in the SANISAND-MS model. Whilst this is helpful in significantly reducing the required number of tests and calibrated parameters, it may lead to oversimplification. The value of c is calibrated by the ratio of M_e/M_c, which therefore only requires sufficient additional extension tests for the selection of M_e. However, the results show significant variation in the accumulation of axial strain in cyclic tests with a negative stress ratio. This variation is not well accounted for in the cyclic simulations that are calibrated using compressive tests. This is possibly explained by the onset of instability at the instability state line in extension tests, which is not observed in the compression tests. Furthermore, the ratio of the phase transformation line (PTL) and critical state line (CSL) in stress space is not consistent between the compression and extension tests. This difference is not accounted for in the SANISAND-MS model.

Certain key soil behaviours are highlighted in the results below. The results of the monotonic tests demonstrate typical responses dependent on mean effective stress and density. Congleton sand exhibits an early, strong peak, accompanied by significant post-peak softening. The undrained monotonic tests indicate that the initial fabric resulting from the slurry deposition sample preparation procedure is predominantly contractive, a finding also observed in the drained monotonic tests. This contractive fabric is further evidenced in the drained cyclic results, which show significant volumetric strain, even at low axial strain, as observed in the two-way cyclic tests. The drained cyclic tests reveal that the cyclic stress ratios, including the average cyclic stress ratio η and the cyclic amplitude stress

ratio ζ_b, along with the initial void ratio, are key predictors of soil response. In contrast, mean effective stress has a relatively minor impact on response when other parameters are maintained.

4.1 Monotonic benchmark results

Presented in this section are the results of the benchmark monotonic tests. The test schedule was designed to provide sufficient data to calibrate the parameters of soil constitutive models for monotonic loading, including SANISAND style models following the recommendations of Azeiteiro et al., 2017. These tests were conducted under both drained and undrained conditions, with compression and extension loading across a range of mean effective stresses and relative densities. The tests were performed on samples prepared using slurry deposition (Section 3.4). Measurements were recorded using global sensors for load and displacement, as the significant strain during monotonic testing exceeded the capacity of the local strain instrumentation. Drained monotonic tests employed a 5 kN load cell, while undrained tests utilised a 25 kN load cell, selected to optimise the load cell range for improved accuracy and resolution. The samples were sheared to a minimum of 15% axial strain, with a displacement controlled load at 3 mm/hr (ε_a= 2.14%/hr). During extension tests, the samples were sheared to 15% axial strain; however, the onset of necking, typical of extension tests, limits the range of results presented. The results for the monotonic extension tests have been truncated at the point of necking.

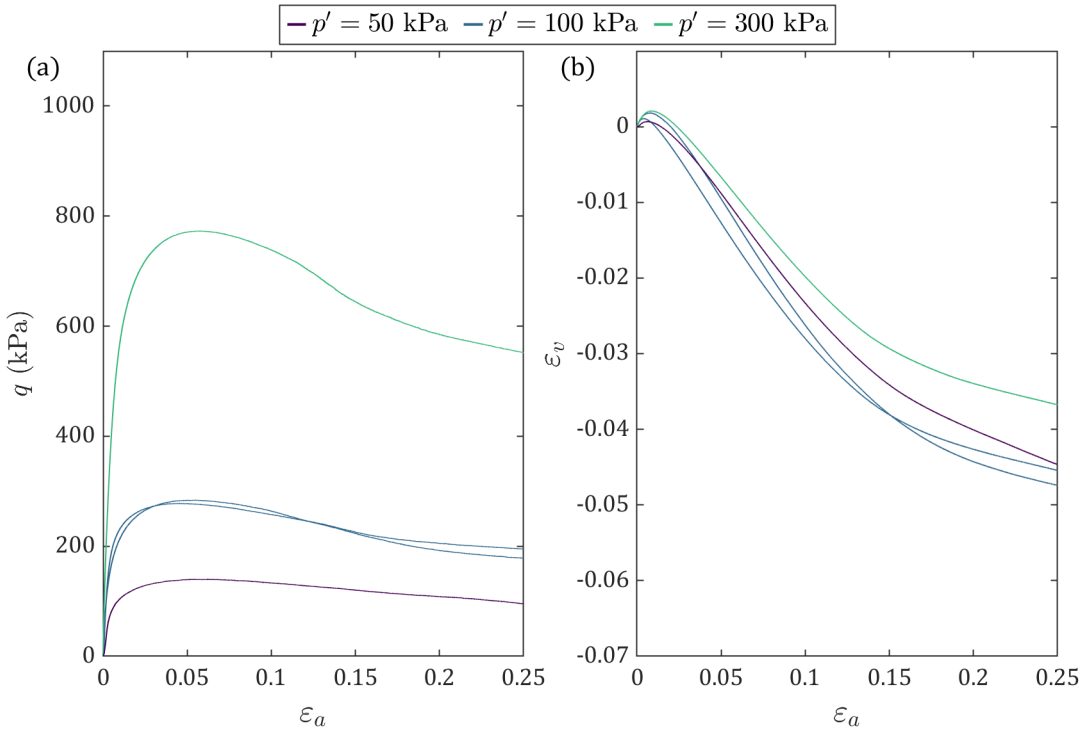

Figure 4.1: Drained monotonic compression results at $D_r = 50\%$

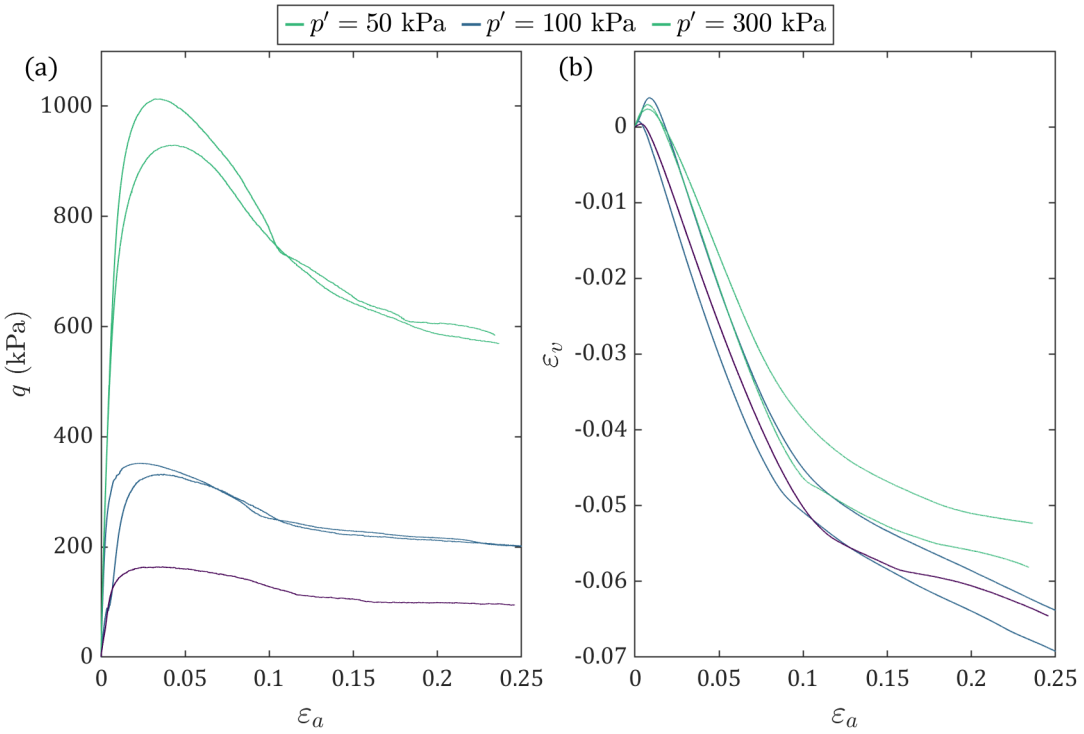

Figure 4.2: Drained monotonic compression results at $D_r = 80\%$

4.1.1 Drained Monotonic Results

The drained monotonic compression tests are presented here. The results depicted in Figure 4.1 illustrate the stress-strain response of drained monotonic compression tests, with samples prepared to $D_r = 50\%$, $e = 0.64$. The deviatoric stress versus axial strain response demonstrates an increase in peak and residual stress with rising initial mean effective stress, p'_0.

Figure 4.2 shows the drained monotonic response of samples prepared to $D_r = 80\%$, $e = 0.57 - 0.58$. The expected trend of greater deviatoric stress response with increasing mean effective stress is evident here. The residual stress for repeated tests under identical conditions remains consistent. However, the peak response exhibits variability, with a difference of ≈ 100 kPa. The volumetric response demonstrates a greater degree of initial compression for the test with $p'_0 = 300$ kPa.

The general trend across all monotonic drained compression tests aligns with typical results reported in the literature. The degree of contractiveness in the volumetric response increases with reduced density. This observation is consistent with results from tests on Hostun sand from Azeiteiro et al. (2017), where tests with increased void ratio demonstrate greater contraction. Furthermore, the overall trend for volumetric strain against axial strain presents similar magnitudes across tests. At $\varepsilon_a = 15\%$, the volumetric strain attains $\varepsilon_v \approx 4\%$ for medium density tests, and $\varepsilon_v \approx 6\%$ for high density tests. The results of Azeiteiro et al. (2017) indicate $\varepsilon_v \approx 2\%$ for medium density tests, and $\varepsilon_v \approx 4\%$ for high density tests. Consequently, the findings reveal a greater degree of dilation for the Congleton sand results in comparison to those of the Hostun sand.

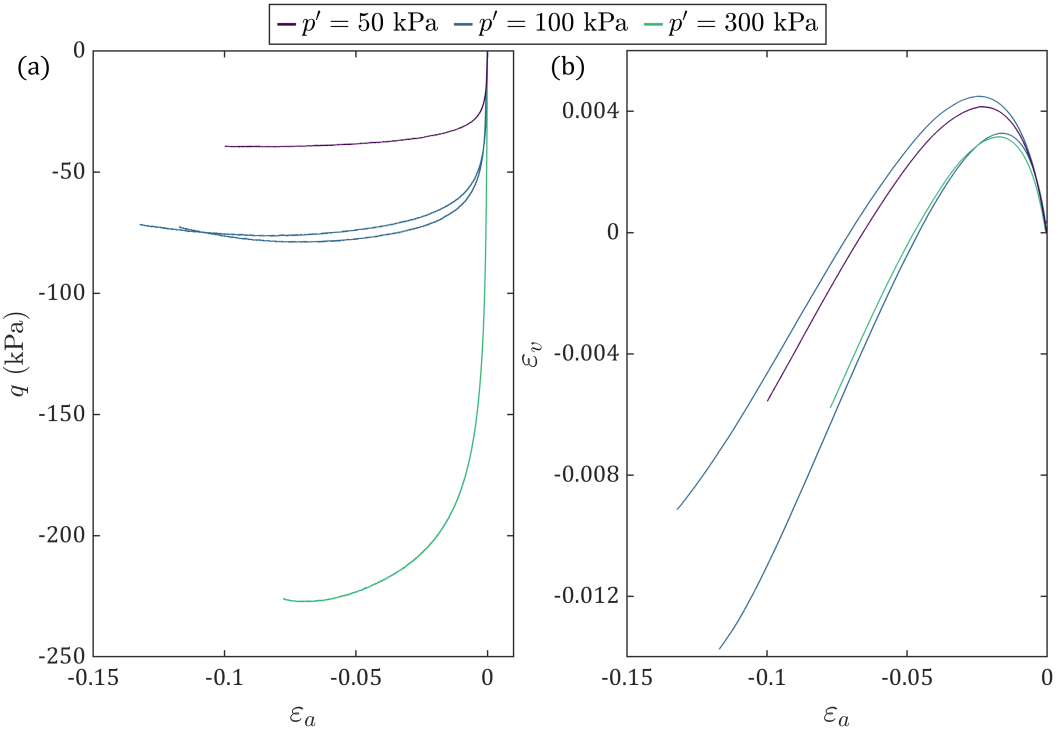

Figure 4.3: Drained monotonic extension results at $D_r = 50\%$

The point of peak stress response occurs earlier and is more pronounced in the high density results. However, the mean effective stress has less effect on the point of peak response. In general the effect of increased mean effective stress is associated with a later peak. Results of Azeiteiro et al. (2017) are presented at only one mean effective stress; however, the variation in void ratio demonstrates a later, less pronounced peak in the loose samples, which is consistent with the present results for Congleton sand. Monotonic testing results from Wichtmann et al. (2015) support these findings, indicating a later peak with higher mean effective stress. The point of peak strength is similar for both samples, at $\varepsilon_a \approx 4\%$. However, the degree of post-peak softening is substantially less for the Hostun tests, with approximately a 10% post-peak reduction compared to $\approx 30\%$ for the Congleton tests.

The test results have been presented to completion of the test, at $\varepsilon_a = 25\%$. However, the onset of shear planes within the sample is likely to have occurred much earlier. In the test results, sudden drops in deviator stress and reductions in volumetric strain rate are likely caused by the emergence of shear planes. This effect is more evident in the high-density samples. The formation of a shear plane can create the illusion of achieving a critical state. However, shear planes localise the development of volumetric strain before the residual stress ratio is reached. The final state of the samples was documented in each test, and clear shear planes were visible for all samples. Therefore, it was concluded that none of the samples had reached a critical state.

Figure 4.3 shows the results of drained monotonic extension tests on samples prepared to $D_r = 50\%$, $e = 0.64 - 0.66$. The results have been truncated at the point of necking.

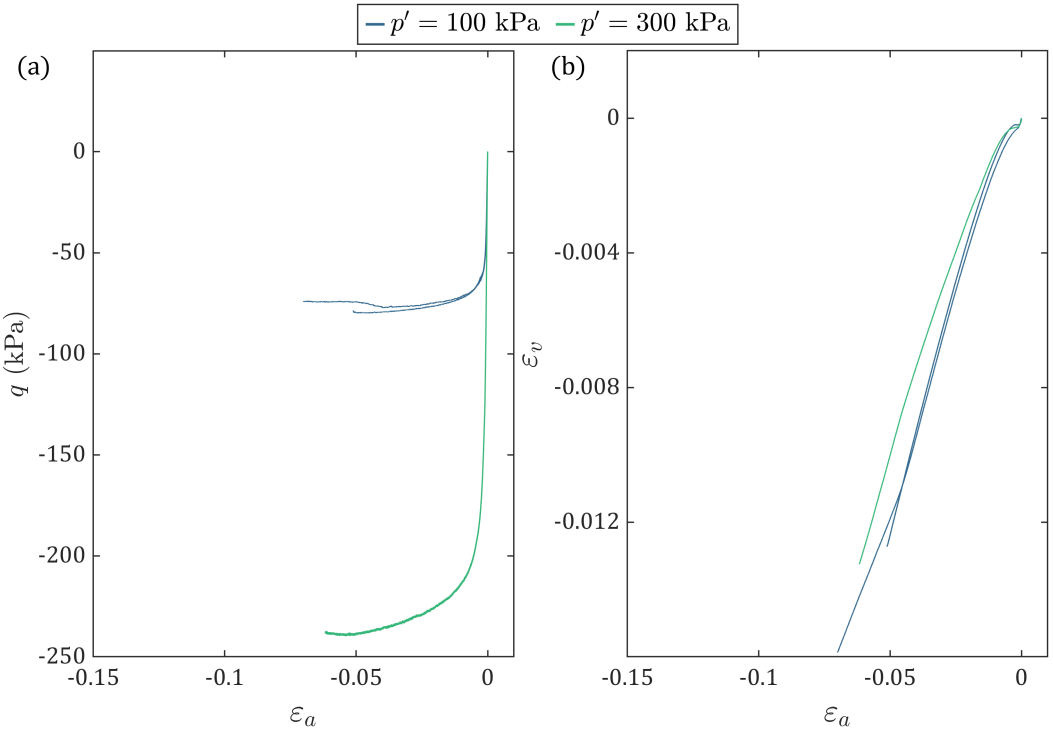

Figure 4.4: Drained monotonic extension results at $D_r = 80\%$

The deviatoric stress response increases in line with increases in mean effective stress, p'_0. The repeat tests at $p'_0 = 100$ kPa show similar stress response with axial strain, albeit with variation in the volumetric response.

Figure 4.4 shows the results of drained monotonic extension tests on samples prepared to $D_r = 80\%$, $e = 0.58 - 0.59$. The volumetric response is consistent across all tests.

As discussed, the results of the extension tests have all been truncated at the point of necking. This is evident in the results, marked by a sudden drop in deviator stress. The point of necking occurs shortly after the attainment of peak shear stress. Consequently, the results of the high-density tests are terminated earlier than those of the medium-density tests. In line with the compression tests, the peak stress in the high-density samples occurs earlier. Overall, the magnitude of volumetric strain is low for all tests. This aligns with the low level of axial strain achieved prior to termination. The results of the medium-density tests demonstrate a significantly more contractive phase initially, followed by dilation commencing at $\varepsilon_a = 2.5\%$. The high-density tests exhibit minimal contraction, if any. The value of the peak stress ratio η_{pk} is consistently lower in the triaxial extension tests than in the compression tests (Table 4.1) reflecting the decreasing p' stress path and the typical reduction in friction angle observed in triaxial extension tests (Mitchell et al., 2005).

4.1.2 Undrained Monotonic Results

Presented here are the results of the undrained monotonic tests in both compression and extension, for samples prepared to $D_r = 50\%$ and 80%. The CIUc tests conducted at $D_r = 50\%$ were carried out by Yide Wang on Congleton sand prepared using the water

Table 4.1: Summary of drained monotonic results

Test name	e_0	D_r	p'_0	p'_{res}	e_{res}	q_{pk}	η_{pk}	η_{res}	ψ_{pk}
BM_CIDc_50_100_a	0.628	63	100	156	0.712	284	1.46	1.03	-0.12
BM_CIDc_50_100_b	0.642	57	90	160	0.728	278	1.44	1.07	-0.11
BM_CIDc_50_300	0.646	56	300	468	0.714	773	1.39	1.08	-0.11
BM_CIDc_50_50	0.640	58	50	80	0.723	140	1.45	1.00	-0.11
BM_CIDc_80_50	0.604	73	50	84	0.707	164	1.58	1.13	-0.13
BM_CIDc_80_100_a	0.575	85	100	169	0.675	333	1.57	1.19	-0.17
BM_CIDc_80_100_b	0.570	87	100	162	0.690	352	1.62	1.07	-0.18
BM_CIDc_80_300_a	0.564	89	300	496	0.655	1014	1.59	1.18	-0.19
BM_CIDc_80_300_b	0.579	83	300	492	0.662	930	1.53	1.16	-0.17
BM_CIDe_50_50	0.662	49	50	36	0.671	-40	-1.11	-1.09	-0.11
BM_CIDe_50_100_a	0.642	58	100	74	0.665	-79	-1.10	-0.98	-0.13
BM_CIDe_50_100_b	0.665	48	100	75	0.680	-77	-1.04	-0.95	-0.10
BM_CIDe_50_300	0.628	63	300	224	0.637	-228	-1.02	-1.01	-0.14
BM_CIDe_80_50	0.597	76	50	38	0.595	-37	-1.03	-0.98	-0.17
BM_CIDe_80_100_a	0.588	80	100	82	0.628	-77	-1.10	-0.61	-0.18
BM_CIDe_80_100_b	0.570	87	100	73	0.590	-80	-1.09	-1.08	-0.20
BM_CIDe_80_300	0.579	83	300	221	0.600	-240	-1.10	-1.08	-0.19

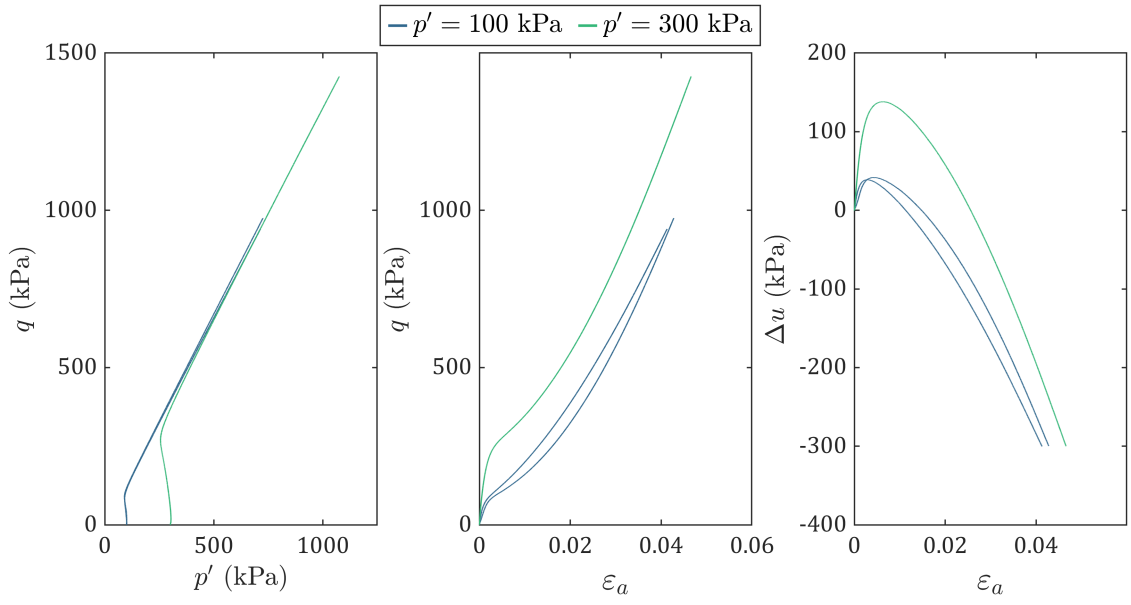

Figure 4.5: Undrained monotonic compression results at $D_r = 50\%$

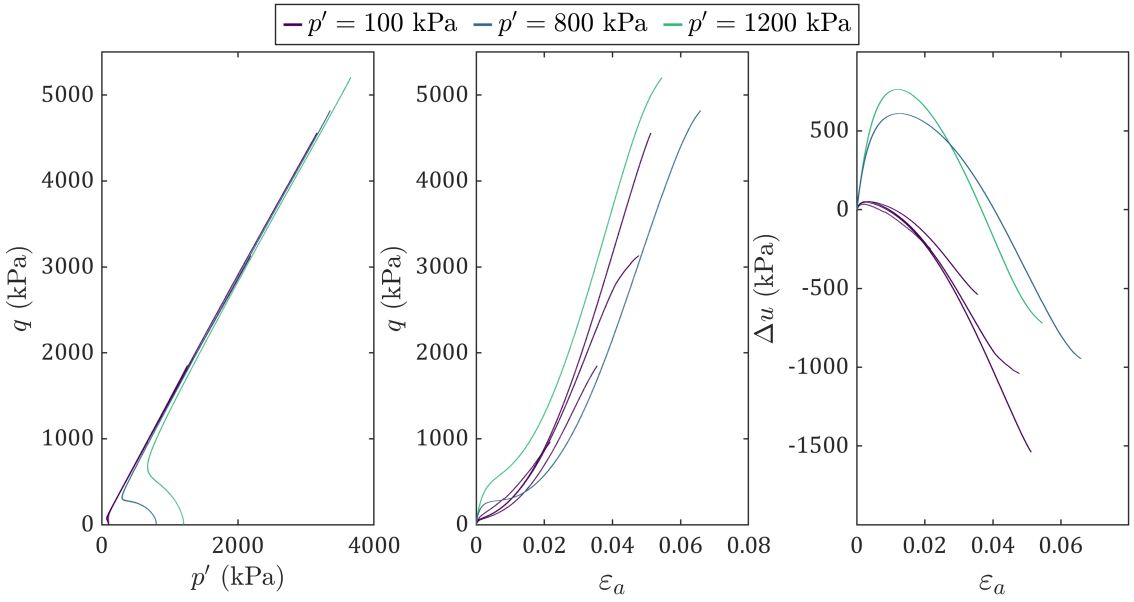

Figure 4.6: Undrained monotonic compression results at $D_r = 80\%$

pluviation method. Figure 4.5 shows the results of undrained monotonic tests on samples prepared to $D_r = 50\%$. Tests were sheared to $\varepsilon_a = 0.15$; however, the results have been truncated at $u = 30$ kPa. The negative excess pore pressure caused by shear-induced dilation resulted in low pore pressures. This induced air bubbles, previously dissolved in the high-pressure pore water, to come out of solution, resulting in a tapering off of the pore pressure response towards a minimum of $u = -60$ kPa. To mitigate this effect, $u = 30$ kPa was selected as the cutoff point at which air bubbles begin to come out of solution. The $p'-q$ plot shows a similar stress path after the phase transformation. The response at both mean effective stresses exhibits minimal contraction, with a greater level of contraction observed in the $p'_0 = 300$ kPa test. This is confirmed in the pore pressure plot, which indicates a higher degree of positive excess pore pressure in the early phase of the test.

Figure 4.6 and Figure 4.7 present the results of undrained monotonic tests on samples prepared at $D_r = 80\%$, $e = 0.57 - 0.60$. In line with the results of Figure 4.5, the results are truncated at $u = 30$ kPa. The pore pressure response of repeat tests conducted at $p'_0 = 100$ kPa shows varied levels of pore pressure response at elevated strains. This variation arises from the tests being performed at different levels of initial back pressure, permitting increased dilation before the $u = 30$ kPa cut-off. Nonetheless, the initial pore pressure response exhibits similar contractive behaviour, as evident in Figure 4.7. The relative contractive response of the sample tested with $p'_0 = 800$ kPa is more pronounced.

Figure 4.8 presents the results of undrained monotonic extension tests on samples prepared to $D_r = 50\%$ and 80%. Samples prepared at lower D_r exhibit a more pronounced contractive response, as evidenced by the plots of $p' - q$ and $\varepsilon_a - \Delta u$.

The results of the monotonic undrained compression tests demonstrate typical outcomes, as documented in the literature (Azeiteiro et al., 2017; Wichtmann et al., 2015). Samples prepared at a lower density exhibit a more contractive behaviour when sheared at

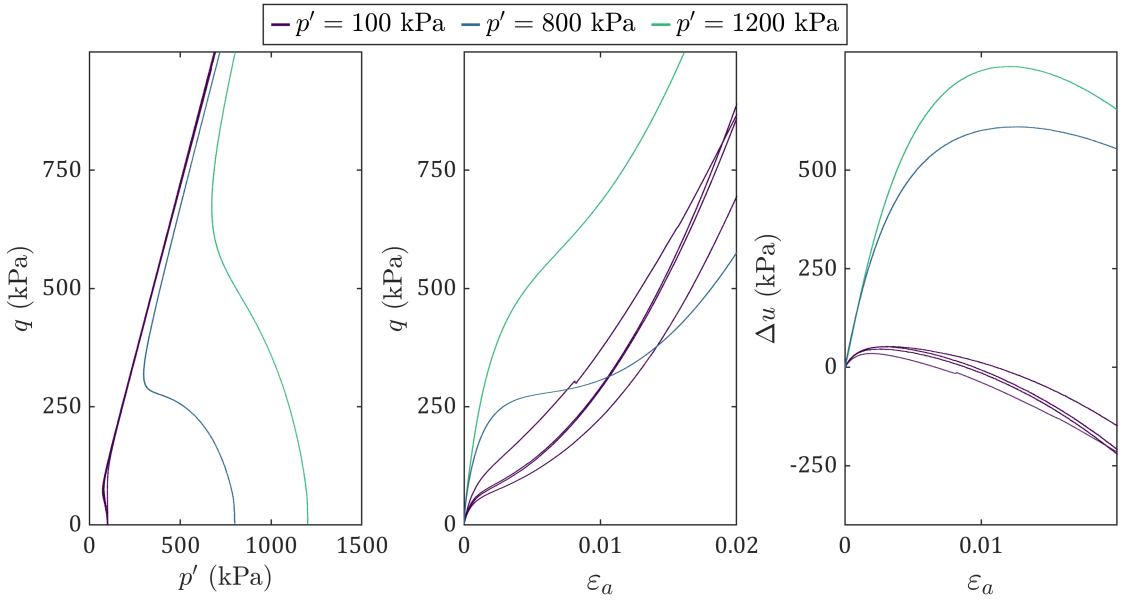

Figure 4.7: Undrained monotonic compression results at $D_r = 80\%$ (zoomed view)

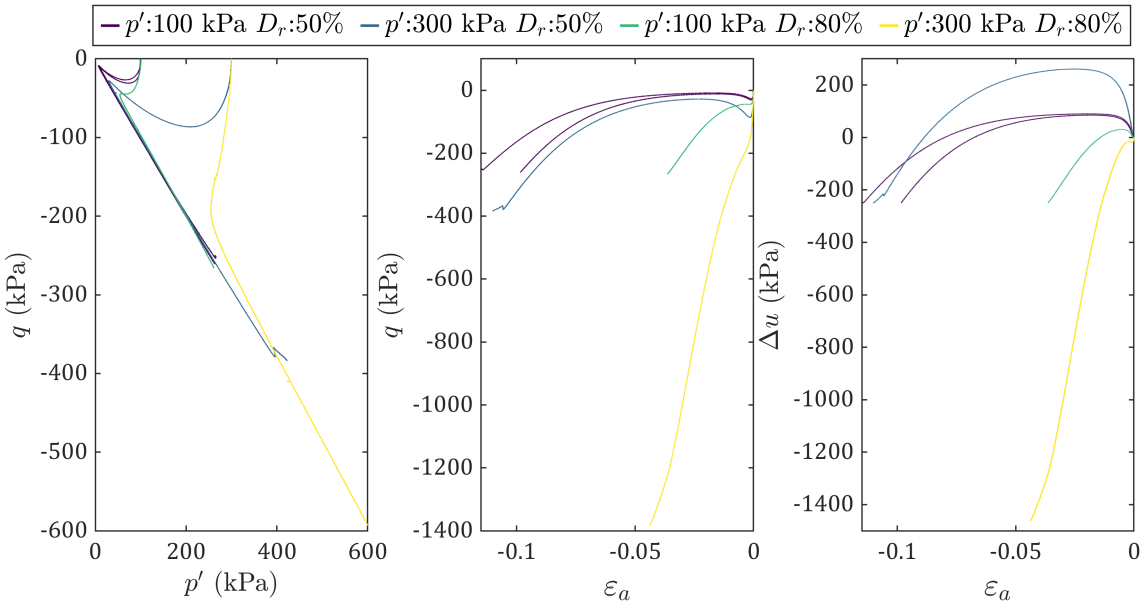

Figure 4.8: Undrained monotonic extension results at $D_r = 50, 80\%$

the same mean effective stress. Direct comparison of the results with existing literature is complicated due to the influence of relative densities and the state parameter. Qualitatively, the degree of contraction observed in the results of Azeiteiro et al. (2017) on Hostun sand is significantly greater, indicating a point of instability in lower density samples. This phenomenon is also evident in the results for Karlsruhe sand (Wichtmann et al., 2015) which show considerable contraction prior to reaching the phase transformation line. This observation may be attributed to the limited range of densities used in the present tests on Congleton sand. At a lower density, the presence of an unstable stress state may have occurred.

Results of the CIUe tests are presented in Figure 4.8. The results indicate a markedly

more contractive response, with a distinct point of instability observed in three out of the five tests. The degree of contraction increases for the lower density samples, as evidenced in the CIUc tests. Results have been truncated at the point of $u = 30$ kPa. The test conducted at $D_r = 80\%$ and $p'_0 = 300$ kPa shows minimal contraction, resulting in negligible positive excess pore pressure accumulation before dilation-induced suction occurs. In the lower density tests, a clear depiction of the quasi steady state is observable, which is only identified in one of the compression tests. The tendency for more contractive behaviour, and occurrence of the ISL and QSL, is also seen in the results of CIUe tests performed by Wichtmann et al. (2015). As such, in both the results on Karlsruhe and Congleton sand, the PTL occurs at a lower stress ratio. The relative ratio between the SSL and PTL in stress space is approximately maintained.

Table 4.2: Summary of undrained monotonic results

Test name	e_0	D_r	p'_0	p'_{res}	η_{pts}	η_{pk}	η_{res}	ψ_{res}	ψ_{pk}
BM_CIUc_50_100_a	0.645	56	100	780	1.35	1.35	0.98	-0.12	-0.12
BM_CIUc_50_100_b	0.658	51	100	767	1.32	1.32	0.87	-0.11	-0.11
BM_CIUc_50_300	0.659	50	300	1130	1.33	1.33	1.05	-0.13	-0.13
BM_CIUc_80_100_a	0.598	75	100	1413	1.49	1.49	1.02	-0.17	-0.17
BM_CIUc_80_100_b	0.599	75	100	2323	1.45	1.43	1.04	-0.17	-0.17
BM_CIUc_80_100_c	0.561	91	100	3275	1.46	1.45	0.95	-0.21	-0.21
BM_CIUc_80_100_d	0.604	73	100	3542	1.45	1.36	0.94	-0.16	-0.16
BM_CIUc_80_100_e	0.586	80	100	831	1.45	1.45	0.65	-0.18	-0.18
BM_CIUc_80_1200	0.570	87	1200	3813	1.43	1.43	0.98	-0.20	-0.20
BM_CIUc_80_800	0.570	87	800	3521	1.45	1.45	1.07	-0.20	-0.20
BM_CIUe_50_100_a	0.658	51	100	370	-1.02	-1.04	-1.03	-0.11	-0.11
BM_CIUe_50_100_b	0.659	50	100	316	-1.03	-1.07	-1.04	-0.11	-0.11
BM_CIUe_50_300	0.647	55	300	521	-1.02	-1.05	-0.97	-0.12	-0.12
BM_CIUe_80_100	0.584	81	100	364	-1.04	-1.07	-1.03	-0.18	-0.18
BM_CIUe_80_300	0.580	83	300	1299	-1.04	-1.07	-1.05	-0.19	-0.19

4.2 Monotonic constitutive model calibration

This section presents the calibration of the SANISAND-MS constitutive model (Liu et al., 2019), using the results of the monotonic tests described above. The parameters calibrated using these monotonic results are summarised in Table 4.3. The formulation of the SANISAND-MS model differs slightly from other SANISAND models, particularly in the terms involving A_0 and n^d; consequently, the calibration procedure is also distinct. The calibration procedure employed adheres to the recommendations found in the literature (Azeiteiro et al., 2017; Liu et al., 2019; Taiebat et al., 2008).

The calibration of the CSL usually requires tests that have reached the critical state. Due to factors occurring during testing, such as the formation of shear planes, dilation-induced cavitation, and necking, achieving a fully developed critical state during triaxial

Table 4.3: SANISAND-MS monotonic parameters and constitutive model formulations from Liu et al., 2019

Term	Constitutive equation	Function
G_0	$G = G_0 p_{atm}[(2.97-e)^2/(1+e)](p/p_{atm})^{1/2}$	Dimensionless shear modulus
ν	$K = 2(1+\nu)G/[3(1-2\nu)]$	Poisson's ratio
e_0	$e_c = e_0 - \lambda_c(p_c/p_{atm})^{\xi}$	Reference critical void ratio
λ_c, ξ		CSL shape terms
m	$f = \sqrt{(\mathbf{s}-p\mathbf{a}):(\mathbf{s}-p\mathbf{a})} - \sqrt{2/3}pm$	Yield locus opening
M	$\mathbf{r}^b_\theta = \sqrt{2/3}g(\theta)M\exp(-n^b\Psi)\mathbf{n}$	Critical stress ratio (comp.)
n^b		Void ratio dependence
c		Compression:extension strength ratio
h_0, c_h	$b_0 = G_0 h_0(1-c_h e)/\sqrt{p/p_{\text{atm}}}$	Hardening terms
A_0	$D = \left[A_0 \exp\left(\beta\langle\tilde{b}^M_d\rangle/b_{\text{ref}}\right)\right](\mathbf{r}^d_\theta - \mathbf{r}):\mathbf{n}$	Intrinsic dilatancy term
n^d	$\mathbf{r}^d_\theta = \sqrt{2/3}g(\theta)M\exp(n^d\Psi)\mathbf{n}$	Void ratio dependence

testing can be challenging. As previously discussed, none of the monotonic tests performed in this study were deemed to have reached the critical state. In the drained tests, the formation of shear planes prevented this. In undrained tests, the highly dilative response induced cavitation before the critical state was attained. Furthermore, identifying the critical state line (CSL) using undrained tests is complicated by local drainage issues within samples caused by strain non-uniformity (Klotz et al., 2002). Thus, the proposed critical state line presented in Figure 4.9 is derived from the results of Dilip et al., 2025, based on partially drained monotonic tests conducted on Congleton sand. Triaxial monotonic compression tests were performed with coupled shear-volumetric strain paths to identify the locus of the phase transformation and post-peak stress instability points, indirectly ascertaining the critical state line. The resulting CSL for Congleton sand is employed here. The results of the monotonic tests from the present study are presented alongside the proposed CSL from Dilip et al. (2025). The results demonstrate that the critical state was not reached in any of the tests under either drained or undrained conditions. The formulation of the CSL in SANISAND-MS follows the form $e_c = e_0 - \lambda_c(p_c/p_{atm})^{\xi}$. This differs from the form used in Dilip et al. (2025), necessitating the selection of shape factors, λ and ξ, to match this as closely as possible, focusing on the range at lower stress levels. The reference critical state void ratio e_0 was maintained. The values of the calibrated model parameters for the CSL were $\lambda = 0.015$, $\xi = 0.5$, and $e_0 = 0.767$.

Monotonic results of undrained and drained, compression and extension, in the $q - p'$ space are employed to calibrate the model parameters M, critical stress ratio in compression,

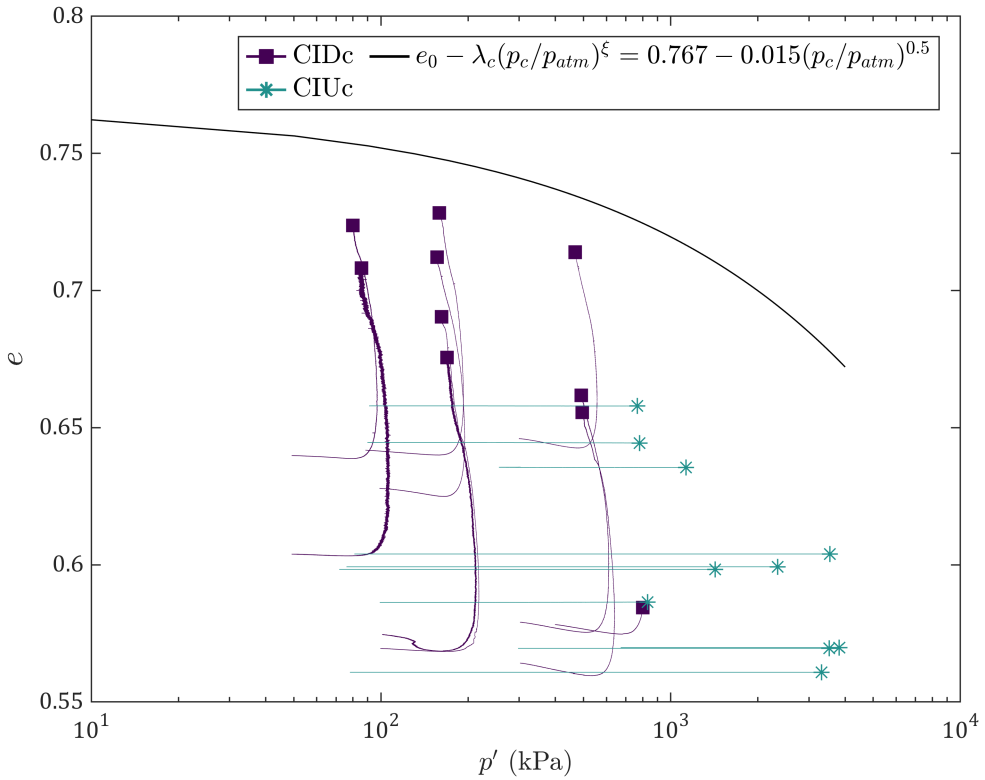

Figure 4.9: Critical state line in $e - p'$ space with monotonic drained and undrained compression results from the present study. The CSL shown is adapted from Dilip et al., 2025 to fit the form used in SANISAND-MS.

and c, compression to extension strength ratio. Despite the tests not reaching critical state, the stress ratio is consistent towards the end of the tests; therefore, these values can be obtained from the monotonic results. The plots in Figure 4.10 display the results of all monotonic tests in $q - p'$ space, Figure 4.10(a) provides the complete results, and Figure 4.10(b) presents an extract. The end points of the tests are indicated with markers. In compression, the endpoints of the drained tests are consistently lower than those of the undrained tests. This discrepancy arises because the undrained tests have been truncated at $u = 30$ kPa, preventing the expected drop in η as the tests approach critical state. This behaviour is characteristic of undrained monotonic compression tests, where, post-phase transformation, the stress path maintains a stress ratio that exceeds M_c before marginally decreasing to M_c (Tamang et al., 2022). Consequently, the chosen value of $M_c = 1.29$ serves as the best approximation considering all of the displayed endpoints. In extension, the endpoints of the drained tests are near peak strength, as the results have been truncated at the onset of necking. Thus, the value for $M_e = 0.95$ is weighted in favour of the undrained tests. This leads to the model parameter $c = M_e/M_c = 0.74$. The calibrated parameters fall within the expected range; for instance, the calibrated parameters of Karlsruhe Sand from Liu et al. (2019) yield $M_c = 1.27$ and $c = 0.712$.

Figure 4.11 presents the results for calibration of the phase transformation stress ratio M_{pts}. This provides values of $\eta^c_{pts} = 1$ and $\eta^e_{pts} = -0.8$. The point of phase transformation has been labelled on the plot. This is defined as the point of inflection in the stress path,

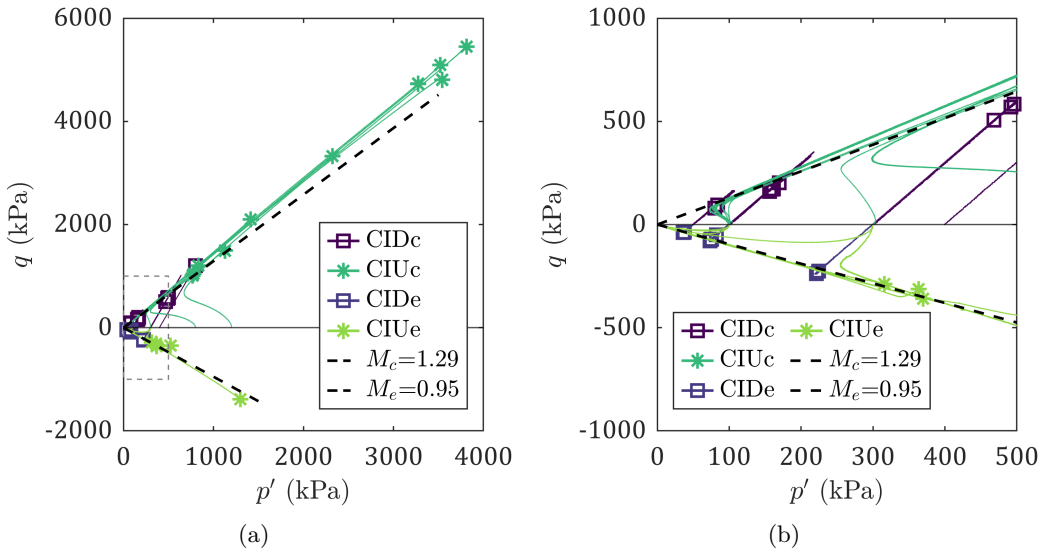

Figure 4.10: Monotonic compression and extension stress paths for the calibration of M_c and M_e, showing (a) full range of stress path results, and (b) results extract for greater clarity at low p'

specifically, the point of minimum p'. Taiebat et al. (2008) recommend taking the point of minimum u for phase transformation. However, this differs from recommendations in most literature on the subject (Ishihara, 1993), where the point of minimum p' is typically utilised. The results of the tests indicated minimal contraction, and no onset of instability or quasi-steady state, which complicated the identification of the point of phase transformation. The results shown in Figure 4.12 illustrate this. The stress path is nearly vertical, indicating a prolonged stage of the test at similar mean effective stress. Thus, identification of the stress ratio for phase transformation using the point of minimal p' is challenging due to noise in the results. The calibration of SANISAND does not require direct input of the PTL stress ratio; however, this highlights an issue with the calibration of n^d.

Figure 4.13(a) presents the calibration of the void ratio dependence factor at peak strength, n^b. The relevant SANISAND-MS formulation, $\mathbf{r}^b_\theta = \sqrt{2/3}g(\theta)M\exp(-n^b\Psi)\mathbf{n}$, yields the value n^b, derived from the negative gradient of the line of best fit through the origin of Figure 4.13(a). The points presented are derived from undrained and drained monotonic compression tests, specifically at the point of peak stress ratio. At these points, values of $\ln(\eta^b/M_c)$ are plotted against ψ_B (state parameter at peak stress ratio). The line of best fit should pass through the origin (Taiebat et al., 2008), with the gradient of this line providing the calibrated parameter $-n^b = -1.19$. There is significantly less scatter in this plot compared to the plot for n^d, providing greater confidence in the selected value. A clear distinction is also evident between the values from the drained tests and those from the undrained tests. Given the desired simulations of drained cyclic tests, the selected parameter was weighted in favour of the drained monotonic tests.

Figure 4.13(b) presents the void ratio dependence factor at phase transformation. The identification of the phase transformation point is most readily derived from the results of

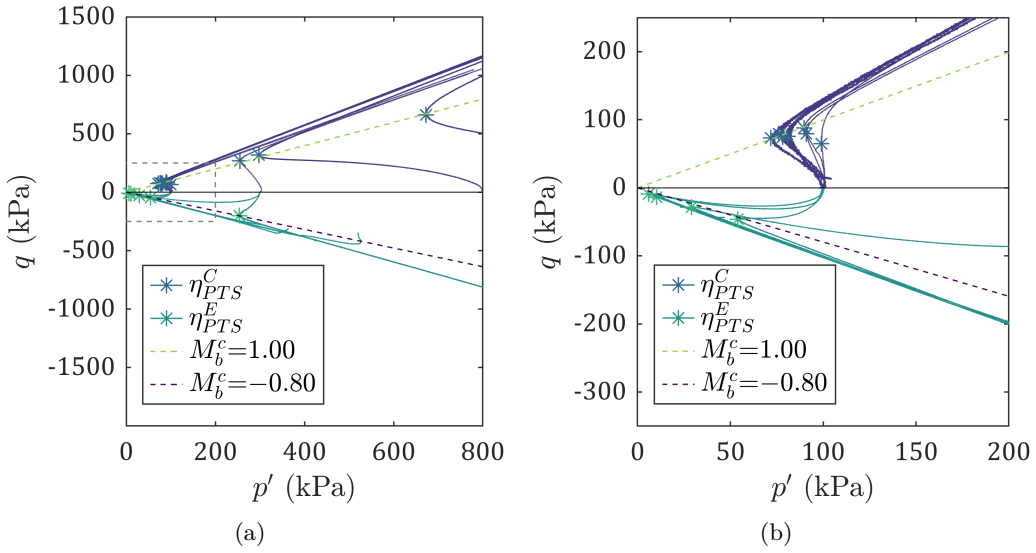

Figure 4.11: Monotonic compression and extension stress paths for the calibration of the phase transformation stress ratio M_b^c and M_b^e (a) full range of stress path results, and, (b) results extract for greater clarity at low mean effective stress.

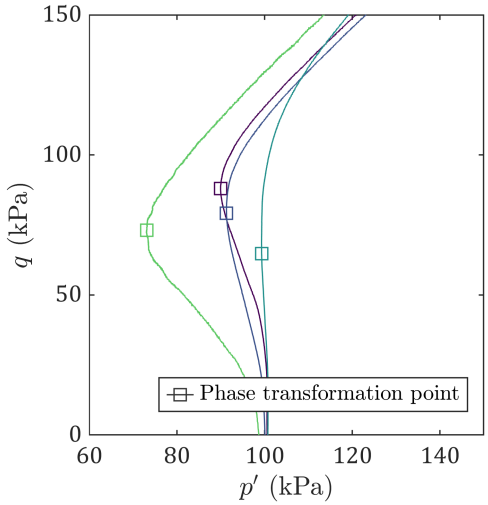

Figure 4.12: Stress paths of CIUc tests, showing the difficulty of identifying the point of phase transformation.

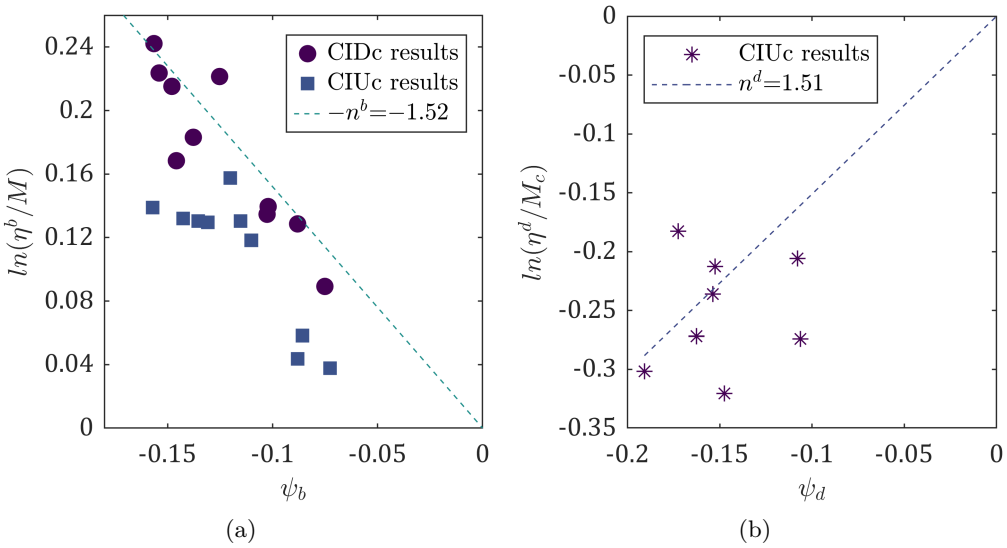

Figure 4.13: Calibration of SANISAND parameters, showing (a) drained and undrained monotonic points of peak stress ratio for the calibration of n^b. The line of best fit is forced through the origin and the points of the drained monotonic compression tests are given additional weight to better calibrate for drained conditions. The negative of the gradient of the line of best fit gives the calibrated value of n^b. (b) Points of phase transformation in undrained compression results for the calibration of n^d. The line of best fit is forced through the origin, the gradient of which gives the value of n^d.

undrained monotonic tests. Consequently, the results presented here are solely from CIUc tests. Given the large range of possible points for certain tests, as discussed in relation to Figure 4.12, results have been excluded where the phase transformation stress ratio η_{PTS} is outside the range of normal values. The gradient of the line of best fit forced through the origin and through the points plotted on $\ln(\eta^d/M_c)$ vs ψ_d yields the value of $n^d = 1.51$. However, as can be seen in the presented results, there is significant scatter. Therefore, the selection of a plausible value of n^d could be within a large range, significantly affecting simulated results.

Calibration of the dilatancy parameter A_0 is completed using the results of CIDc tests. The calibration of this parameter is presented in Figure 4.14, where the graph displays D against $\eta - (q/p')$. The term D is calculated using Equation (4.1) (Been et al., 2004), with $G_{\max}$ derived from bender element results, and $K_{\max}$ obtained from G and ν using the expression in Table 4.3.

$$D = \frac{d\varepsilon_q^p}{d\varepsilon_q^e} \approx \frac{\delta\varepsilon_j - \delta\varepsilon_j^e}{\delta\varepsilon_q - \delta\varepsilon_q^e} \approx \frac{(\varepsilon_{j+1} - \varepsilon_j) - (p'_{j+1} - p'_j)/K_{\max}}{(\varepsilon_{q,j+1} - \varepsilon_{q,j}) - (q_{j+1} - q_j)/(3G_{\max})} \tag{4.1}$$

The implementation of this in Matlab required forward loop numerical differentiation to calculate a value of D for each data point in the test results. The plotted results span from $\varepsilon_a = 0.2$ until the termination of the test, as illustrated in Azeiteiro et al., 2017. The value of A_0 corresponds to the gradient of the line of best fit, $A_0 = 1.0$. The line of best fit must pass through the origin, which restricts the selection of the gradient. There are evident trends in the results, with steeper gradients indicating a higher value of A_0;

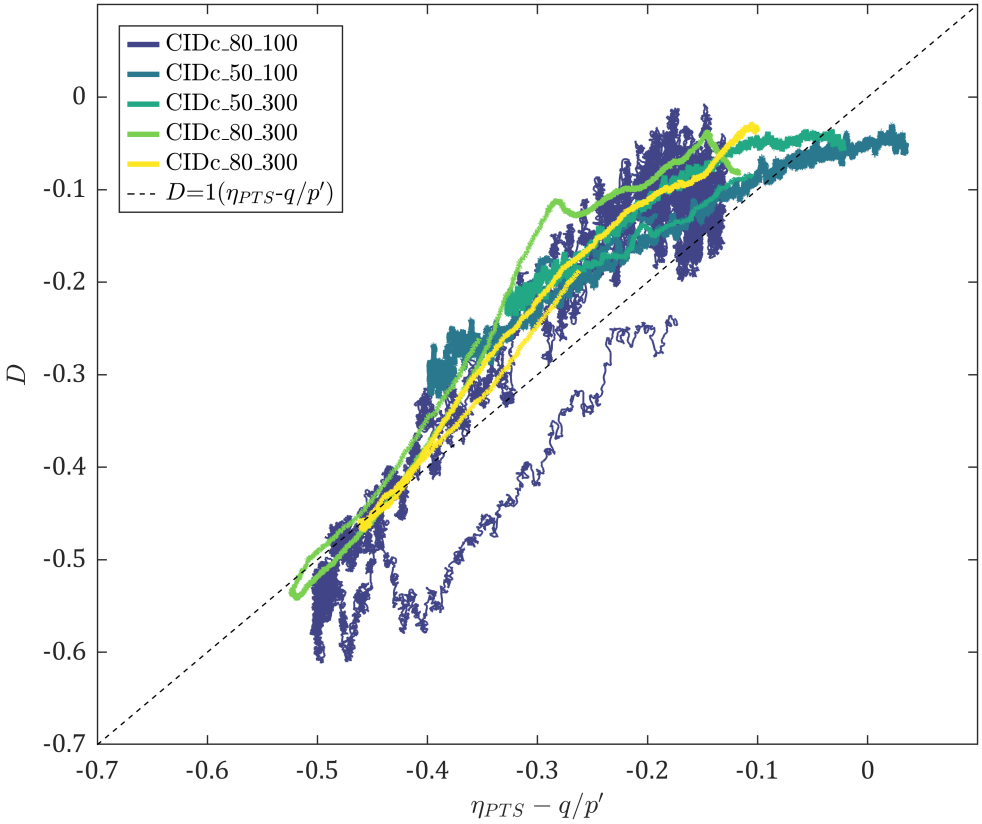

Figure 4.14: Dilatancy from Equation (4.1) plotted against $\eta_{PTS} - q/p'$ for the calibration of SANISAND parameter A_0.

however, these lines do not pass through the origin. Nonetheless, a range of values could still be selected for A_0 that would fit the plot appropriately. The selected value of $A_0 = 1$ is in the mid-range of observed values and is in agreement with literature (Azeiteiro et al., 2017; Liu et al., 2022). The results for Congleton sand are more dilative than those for Hostun sand; thus, a higher value may be more suitable. However, in the simulations of both monotonic and cyclic tests presented below, the value of $A_0 = 1$ yields the best results.

4.2.1 SANISAND-MS calibration: Bender element results

The following section presents the results of bender element tests used to derive the dimensionless shear modulus, G_0. Bender element results were obtained from one sample prepared by the author to the target density of most tests in the schedule at $D_r = 80\%$, $e_0 = 0.585$, using the slurry deposition method. Additionally, three bender element tests were conducted by Yide Wang, employing the water pluviation sample preparation method at varied densities. The initial fabric was assumed to be consistent, considering the similar deposition method. The bender element results, of $G_{\max}$ against mean effective stress, p', are presented in Figure 4.15. The samples were prepared to the target density and then isotropically consolidated to the targeted mean effective stress. No unloading steps were incorporated into the test stages. At each consolidation stage, a range of input frequencies

was applied to provide the most accurate measure of shear wave velocity. The values of $G_{\max}$ are derived using the same method of V_s selection for both series, as detailed in Section 3.6. There is a clear distinction between the two methods of sample preparation, with significantly higher values of $G_{\max}$ in the slurry deposition sample. However, the variation in void ratio must be accounted for. For greater confidence in the results of the slurry deposition samples, further tests at varying densities could be conducted.

Figure 4.16 shows the derivation of the dimensionless shear modulus, G_0, used for the SANISAND-MS formulation. Values of $G_{\max}$ from the bender element tests are normalised by $p_{atm}f(e)$, where $f(e)$ is provided in Equation (4.2) from Hardin et al., 1963.

$$f(e) = \frac{(2.97 - e)^2}{1 + e} \tag{4.2}$$

In the formulation of SANISAND-MS, the power of p'/p_{atm} is fixed at 0.5. With this formulation, the fitted line aligns with all normalised results of $G_{\max}$ from the bender tests. Here, the normalised values demonstrate a clear distinction between the slurry deposition and water pluviation results. The expression for G_0 yields values of $G_0 = 305$ and $G_0 = 260$ for the slurry deposition and water pluviation samples, respectively. This confirms a measurable difference in the generated fabric between the two depositional methods, as once normalised by the void ratio function, the slurry deposition samples exhibit a stiffer initial fabric. The value selected for model calibration is $G_0 = 305$, given that the sample preparation method and void ratio is similar to most tests conducted. The chosen value of $G_0 = 305$ falls within the expected range, although it is higher than some other results reported in literature. The calibrated value for Karlsruhe sand in Liu et al. (2019) is $G_0 = 110$, and for Hostun sand in Azeiteiro et al. (2017) it is $G_0 = 293$.

Considering the variation in bender element results between the two sample preparation methods, this raises the issue of the applicability of some of the monotonic tests performed by Yide Wang on Congleton sand. These tests were prepared using water pluviation, which has been shown to exhibit a varied initial fabric. However, the monotonic calibration values are derived from data points at higher strain ranges, $\varepsilon_a > 2.5\%$. At this stage, the initial fabric has a diminished impact on behaviour, with sand morphology likely to be of increased importance. Therefore, for calibration these results can be used with caution, particularly regarding peak strength and phase transformation. Additionally, all tests conducted at high density, $D_r = 80\%$ were completed by the author. As most tests were performed at this density, the calibration results should remain valid.

4.2.2 SANISAND-MS calibration: Simulation calibration results

The hardening parameters h_0 and c_h require trial and error triaxial test simulations to select the relevant values. The simulations used for this process, as well as subsequent simulations of single element results using SANISAND-MS, were produced using a soil test driver available at the University of Oxford, developed by Orestis Adamidis. Figure 4.17 illustrates the effect of variations in h_0 on the simulated results of q vs p' and q vs ε_a. In

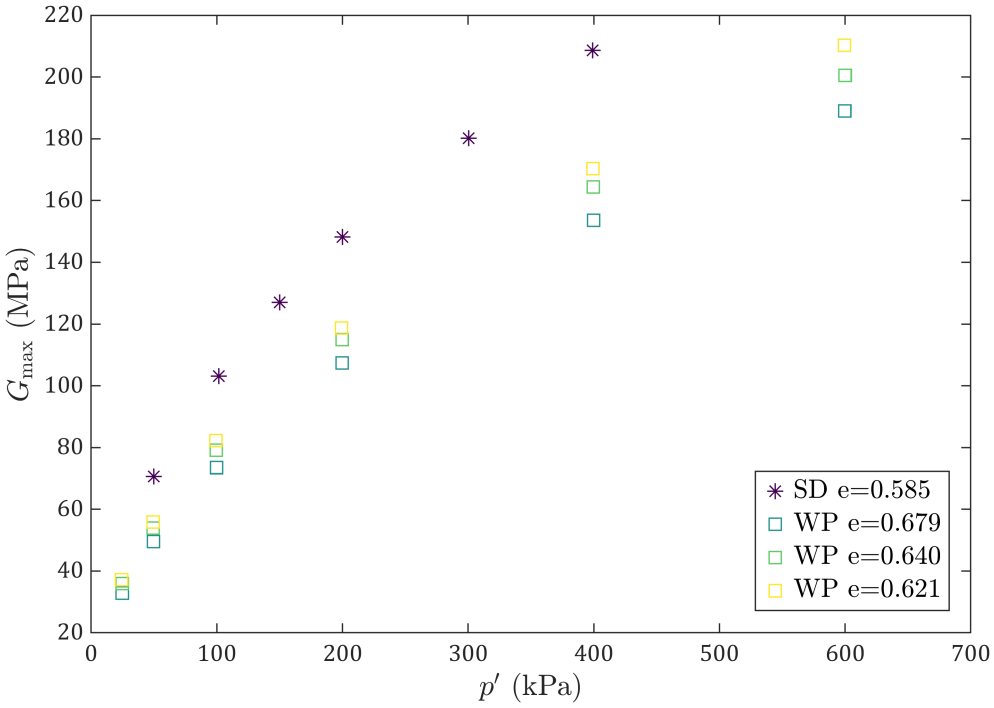

Figure 4.15: Bender element results at varied density and mean effective stress p'. Results with a $*$ marker from slurry deposition prepared sample, and a $\square$ marker from water pluviation samples. Values of $G_{\max}$ from interpretation of bender element results with same method

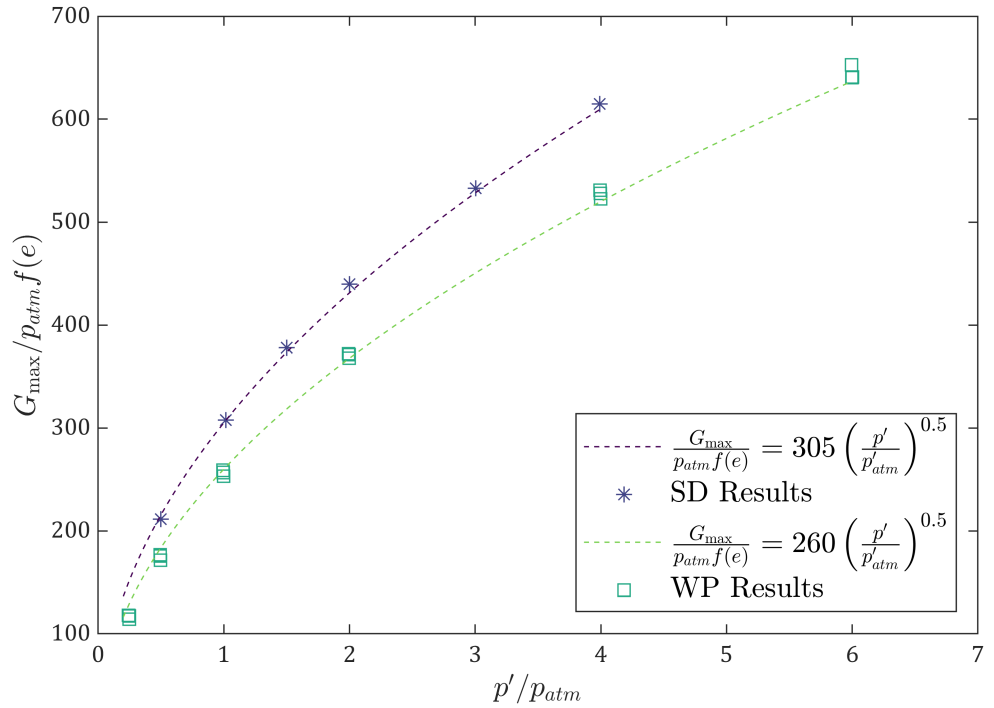

Figure 4.16: Results of $G_{\max}/p_{atm}f(e)$ against p'/p_{atm} for calibration of G_0 SANISAND parameter. The different preparation methods produced samples with a variation in G_0, therefore the chosen parameter was $G_0 = 305$, as the cyclic test samples were prepared in this way.

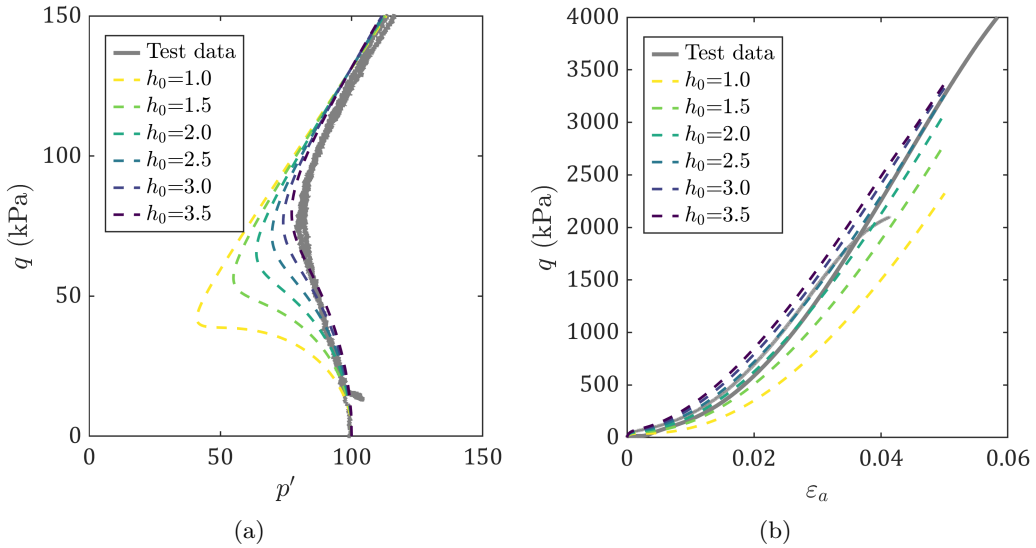

Figure 4.17: Simulated undrained monotonic results for selection of h_0. The process was repeated for all test results for calibration of h_0 and c_h. Results shown of (a) q against p', (b) q against ε_a. The chosen value from these results was $h_0 = 3$.

the stress-strain response, q vs ε_a, increases in the value of h_0 correspond to heightened deviatoric stress for a given strain. For the stress path response, q vs p', an increase in h_0 leads to a decrease in the contractive response, with the phase transformation occurring at higher mean effective stress. From the simulations, a value of h_0 is selected to provide the best fit to the results, with greater emphasis on the results of q vs ε_a. The overall strain of the tests was terminated at $\varepsilon_a \approx 5\%$, due to cavitation, which limited the strain range available for calibration. As shown in the plot of q vs ε_a, the selected value varies depending on the chosen strain range. A medium value of $\varepsilon_a = 3\%$ was selected, and the simulation closest to the results at that point was identified. A lower strain range may have been preferable for calibration with respect to simulations of cyclic tests, as this aligns more closely with the strain range of cyclic tests. However, at this smaller strain range, variations in h_0 have minimal effect.

Given the effect of dilation on the degree of contractiveness in the stress path response, altering the value of A_0 can provide a better response, as demonstrated in Dilip et al. (2025). However, this option was not pursued for several reasons. Firstly, the calibrated value from the drained monotonic tests has a physical meaning therefore should not be ignored. Secondly, considering this calibration (Figure 4.14), if any change were to be made, the value of A_0 should be increased. The fit of the simulated results performed better with a significantly lower value of A_0. Finally, the calibrated values were selected with priority given to the drained results to enhance the simulation of the drained cyclic tests; hence, the undrained fitting was considered less critical.

The value of c_h was set at a constant value across all simulations. Using the selected values of h_0, a plot of $h_0(1 - c_h \cdot e)$ against e was generated, as illustrated in Figure 4.18. A fitted line of $h_0(1 - c_h \cdot e)$ was superimposed to intersect the results, yielding values of

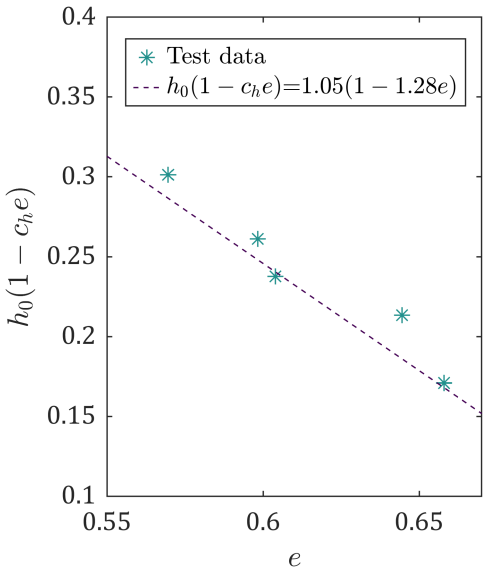

Figure 4.18: Values of $h_0(1-c_he)$ from selected values of hardening modulus in undrained simulations, against e, for calibration of the hardening parameter h_0.

$h_0 = 1.05$ and $c_h = 1.277$. Comparison of the value of c_h with existing literature depends on the range of e of the sand tested. In Liu et al. (2019), the value of $c_h = 1.01$ for Karlsruhe sand is applied across a range of void ratios of $e = 0.577 - 0.874$, which is larger than the range for Congleton of $e = 0.538 - 0.782$; therefore, across the range of densities, the variation in the hardening parameter is similar. However, the calibrated value of $h_0 = 1.05$ for Congleton sand is significantly lower than $h_0 = 5.95$ for Karlsruhe sand. Examining the simulations presented below suggests that this may be an erroneous value for Congleton, which would be expected to be closer to the value from Liu et al. (2019).

A summary of the calibrated values is presented in Table 4.4. The values of Poisson's ratio, ν, and the yield locus opening, m, remain at their default values (Liu et al., 2019), as these configurations yield satisfactory results in the simulations discussed below.

Table 4.4: SANISAND-MS parameters

Elasticity		Critical state					Yield surface	Plastic modulus			Dilatancy	
G_0	ν	M	c	λ_c	e_0	ξ	m	h_0	c_h	n^b	A_0	n^d
305	0.05	1.29	0.74	0.015	0.767	0.5	0.01	1.05	1.28	1.52	1.0	1.51

4.2.3 Constitutive model performance - Monotonic results

Following the calibration of the monotonic parameters of the SANISAND-MS model, the performance was evaluated through retrospective simulations. These simulations were performed on tests that were utilised during the calibration procedure; therefore, the results do not serve as full validation. Figure 4.19 shows the results of a series of simulations for varied conditions. The results demonstrate reasonable agreement in the peak stress ratio. However, the peak occurs at much later strain in all cases, highlighting an issue with

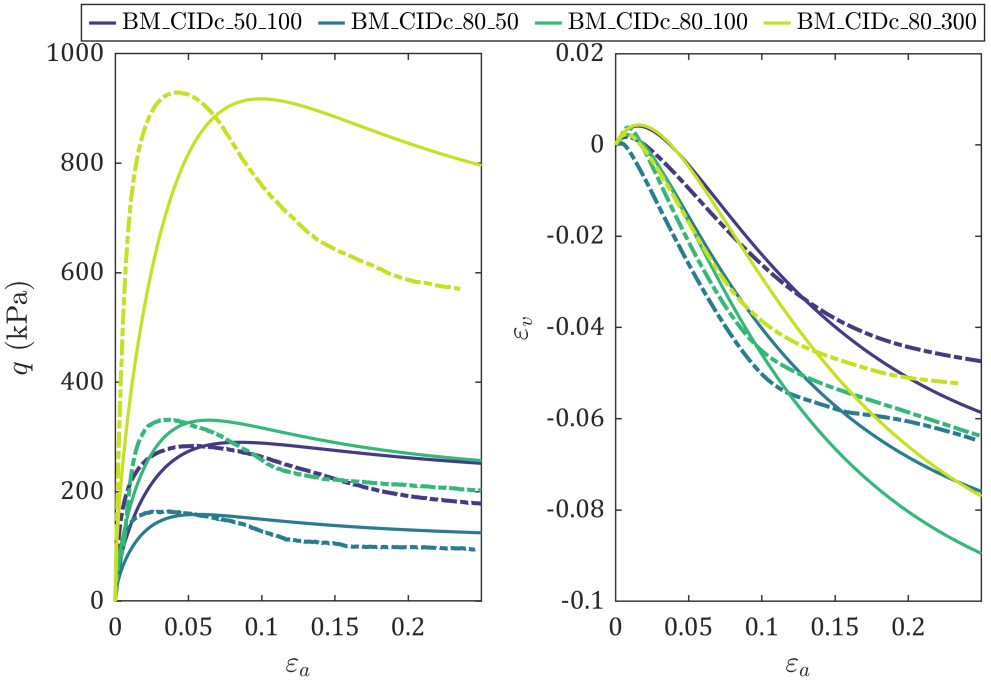

Figure 4.19: SANISAND-MS monotonic simulation results, test data presented as a dashed line in the same colour as the simulation results.

the parameters affecting the hardening modulus (h_0 and c_h). It is likely that the use of undrained monotonic results for the calibration procedure provided unsuitable values of h_0 and c_h. Additionally, the degree of post-peak softening is significantly less than the test data; in all instances, the residual stress is at least 20% greater in the simulation. This is influenced by A_0, the dilatancy parameter; with a higher value, the degree of post-peak softening would increase, thus yielding results that would match more closely. However, this adjustment would also alter the volumetric response, which displays reasonably good agreement. Furthermore, the effect of each parameter on the simulation is interlinked, complicating the calibration procedure. The post-peak softening response is not considered to be critical for modelling the drained cyclic tests. Therefore, considering the physical meaning of A_0 as previously discussed, the value of A_0 was maintained. Considering the volumetric response, at low strain, the test data is less contractive than the simulation. At higher strain, the test data shows a tapering off in dilation not observed in the simulation; this is likely due to the onset of strain localisations, i.e., shear planes.

Considering the issues discussed above, a recalibration of the parameters with a focus on the drained monotonic test results was performed. The value of h_0 was reselected based on drained monotonic tests, rather than undrained tests as recommended in the prescribed methodology. Simulations with varied h_0 were plotted against the test results; the closest match based on the point of peak stress was selected for the value of h_0 in each test. The calibration of c_h was repeated with the same procedure, using plots of $h_0(1 - c_h \cdot e)$ vs e to obtain the final values of h_0 and c_h. The updated calibrated values were $h_0 = 4.67$ and $c_h = 1.44$. The updated value of h_0 is closer to the value for Karlsruhe sand (Liu

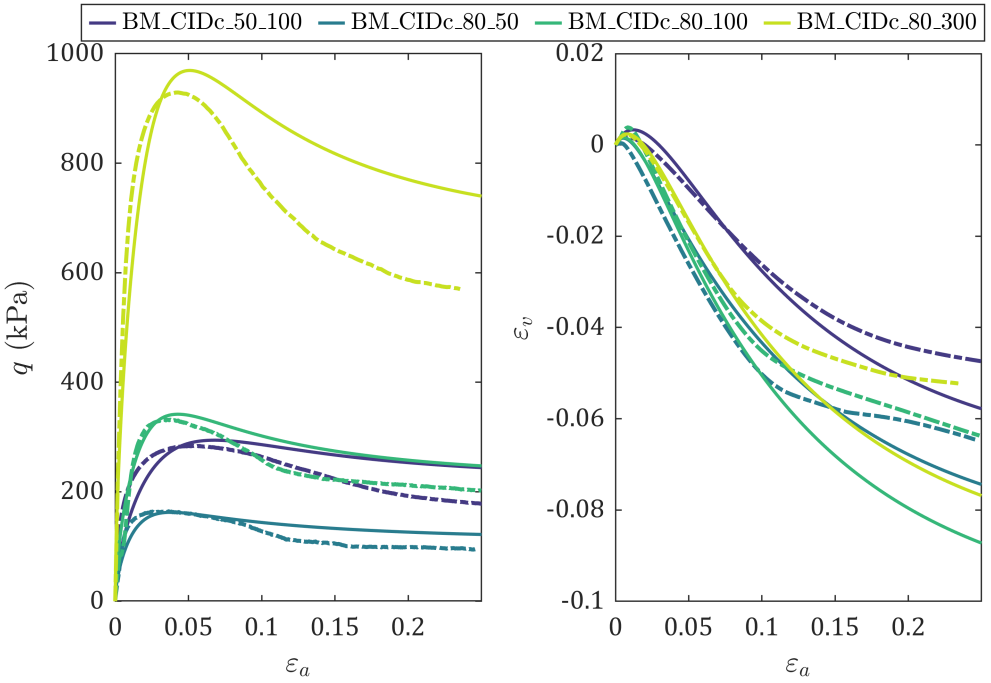

Figure 4.20: SANISAND-MS monotonic simulation results with updated h_0, test data presented as a dashed line in the same colour as the simulation results.

et al., 2019). Simulations of monotonic response with the updated values for h_0 and c_h are presented in Figure 4.20. Here it can be seen that the occurrence of the peak stress response is more closely matched between the simulations and the results. Additionally, the volumetric response is more consistent, particularly in regard to the contractive response at small strain.

4.3 Benchmark cyclic results

The following section presents the results of the drained cyclic benchmark tests, alongside the calibration and validation of SANISAND-MS. The testing schedule aimed to vary key parameters of drained cyclic loading, including void ratio e, average cyclic deviatoric stress η, cyclic deviatoric stress amplitude ratio ζ_b, and initial mean effective stress p'. The range of tests was appropriate for calibrating SANISAND-MS (Liu et al., 2019), and the HCA model (Wichtmann et al., 2010*a*). The stress paths of the cyclic tests are detailed in Figure 3.20.

The central baseline cyclic test, which is present in all parametric variations, is BM_-CIDC_80_200_150_60 (benchmark, drained cyclic, $D_r = 80\%$, $p'_0 = 200$ kPa, $\eta = 0.75$ ($q_{av} = 150$ kPa), $\zeta_b = 0.3$ ($q_{ampl} = 60$ kPa)). The results of this test are presented in Figure 4.21. The response across all tests is fundamentally similar; therefore, this figure represents a typical response.

The stress path of this test exhibited extreme stress in the forward compressive half of the cycle below the PTL and M_c; therefore, the expected volumetric strain response was entirely contractive. The deviator stress applied, illustrated in the plot of q vs Cycle,

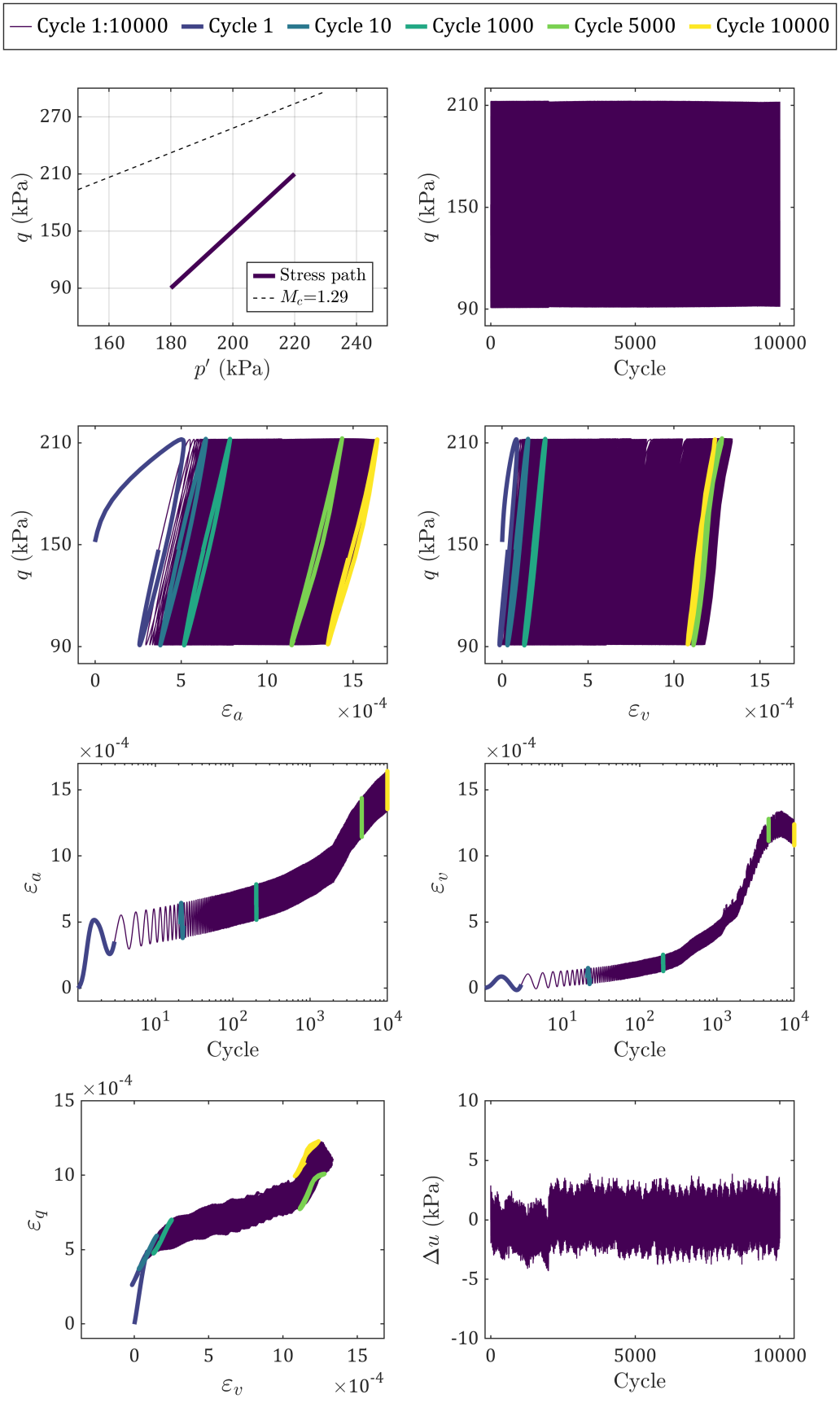

Figure 4.21: Drained cyclic triaxial results of BM_CIDC_80_200_150_60

remained consistent throughout the test. This occurred despite the fact that the loading was applied as a constant force variation rather than a stress variation. Consequently, the consistent deviator stress suggests minimal change in cross-sectional area, indicative of minimal strain accumulation.

The plot of q vs ε_a indicates the highest strain—albeit still of relatively small amplitude—during the first cycle, with decreasing strain amplitude and accumulation in subsequent cycles. This initial cycle is referred to as the "first irregular cycle" by Wichtmann in his work on drained cyclic triaxial tests (Wichtmann et al., 2005; 2010*a*). The first cycle exhibits the greatest degree of strain amplitude, along with a variable degree of strain accumulation, as observed in the data presented here. Consequently, due to the irregular effect of the first cycle, it is excluded from the analysis of strain accumulation versus cycle number. This procedure has been applied in all further analysis within this thesis.

The plot of deviator stress against volumetric strain shows a similar response to the axial strain. However, the degree of strain accumulation is limited during the initial cycles compared to the axial response. Consequently, excluding the first cycle from the strain accumulation analysis has a diminished effect, resulting in a relatively larger overall volumetric response than anticipated. The initial slow phase of volumetric response may arise from minimal changes in external pore pressure experienced by the volume control cylinder, which adjusts to maintain a constant back pressure. Given that the volumetric strain and resultant pore pressure are low, the back pressure controller may take time to respond to this change. The typical cyclic flow rule (gradient of $\varepsilon_q - \varepsilon_v$) for drained cyclic tests within this range of stress ratios exhibits a gradient of 1:1 (Wichtmann et al., 2017). However, as illustrated in the plot of ε_q vs ε_v, the gradient observed here is shallower, indicating a volumetric response that is higher than expected. Moreover, following the slower initial volumetric response, the overall volumetric strain accelerates in the mid-range of cycles, before experiencing a deceleration as the sample densifies. This acceleration in volumetric response leads to a variable gradient of the cyclic flow rule, which is atypical. Nonetheless, it is anticipated that the degree of volumetric strain should diminish as the sample densifies.

The plot of ε_a vs Cycle shows an approximately linear accumulation of strain in semilog space, which begins to occur above the logarithmic rate after approximately 2000 cycles. A similar relationship is evident in the volumetric response, ε_v vs Cycle, although the linear relationship in semilog space is exceeded earlier, around 700 cycles. This linear accumulation of strain, followed by an over-logarithmic accumulation, is typical of drained cyclic triaxial tests, as observed in numerous studies, e.g. Wichtmann et al. (2005). However, comparison of the overall magnitude of strain accumulation indicates that the results here demonstrate low strain accumulation, with ε_a^{acc}= 0.1% after 10,000 cycles, in contrast to $\varepsilon_a^{acc} = 1\%$ for Karlsruhe sand in a comparable test (Wichtmann et al., 2005).

The pore pressure response, Δu vs Cycle, indicates an essentially drained response.

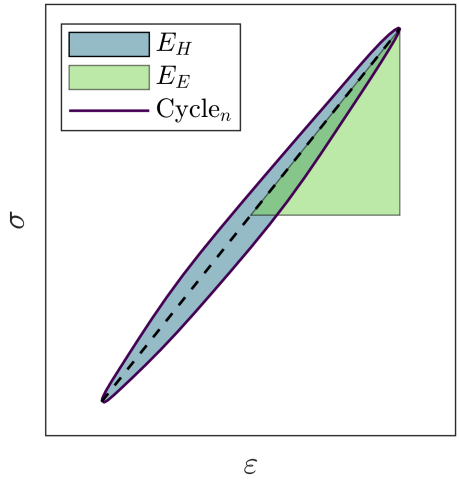

Figure 4.22: Schematic of damping ratio calculation performed on a bandpass filtered loop of stress-strain response to remove ratcheting.

The loading rate of 0.1 Hz was selected as a compromise between the feasibility of completing the testing schedule and ensuring a drained response. Some pore pressure response is evident, with a lag occurring between the loading and the response from the volume control cylinder. However, the cycles of $\Delta u = \pm 2$ kPa are equivalent to 1% p'.

To determine the damping ratio, values of the area enclosed in a closed cyclic loop, E_H, and the area of the triangle enclosed between $(\varepsilon_{av}, \sigma_{av})$, $(\varepsilon_{max}, \sigma_{max})$, and $(\varepsilon_{max}, \sigma_{av})$, E_E, as depicted in Figure 4.22. The value of the damping ratio is taken as $\eta = E_E/E_H$. Due to the effect of ratcheting, the loops of cycling are not closed. Various methods have been proposed to mitigate this issue, as detailed in Richards, 2019. The method employed here passes the values of ε_a through a Butterworth bandpass filter using Matlab. This removes the low-frequency values of axial strain accumulation that represent the ratcheting effect, along with the high-frequency noise of the strain, producing smooth closed loops. An indication of the result of the filtering process is provided in Figure 4.23. The highlighted cyclic loops demonstrate how the filtering process yields closed loops suitable for damping ratio and stiffness calculations. The trend for each cyclic loop as the test progresses is an increase in cyclic axial strain amplitude with increasing cycle number. This is illustrated by cycles of a shallower gradient, with an increased range of ε_a. Furthermore, the area enclosed by the loops decreases as the cycle number increases.

The results presented in Figure 4.24 are derived from Figure 4.23. The plot of damping ratio, ξ vs Cycle, demonstrates a trend of reduced damping ratio with each cycle. A damping ratio value is calculated for each cycle using a for-loop in Matlab. There is an initial steep drop in the value, which stabilises and subsequently recovers after 2000 cycles. This phenomenon can be attributed to the densifying effect of cyclic loading. The values of damping ratio are comparatively high relative to other findings in the literature. Typical values for this strain range are around $\xi = 0.1$ (Mog et al., 2022). This elevated damping ratio may elucidate the relatively low degree of accumulated strain. Furthermore, there are distinct cycles of increased damping ratio at regular intervals. This could be a result of

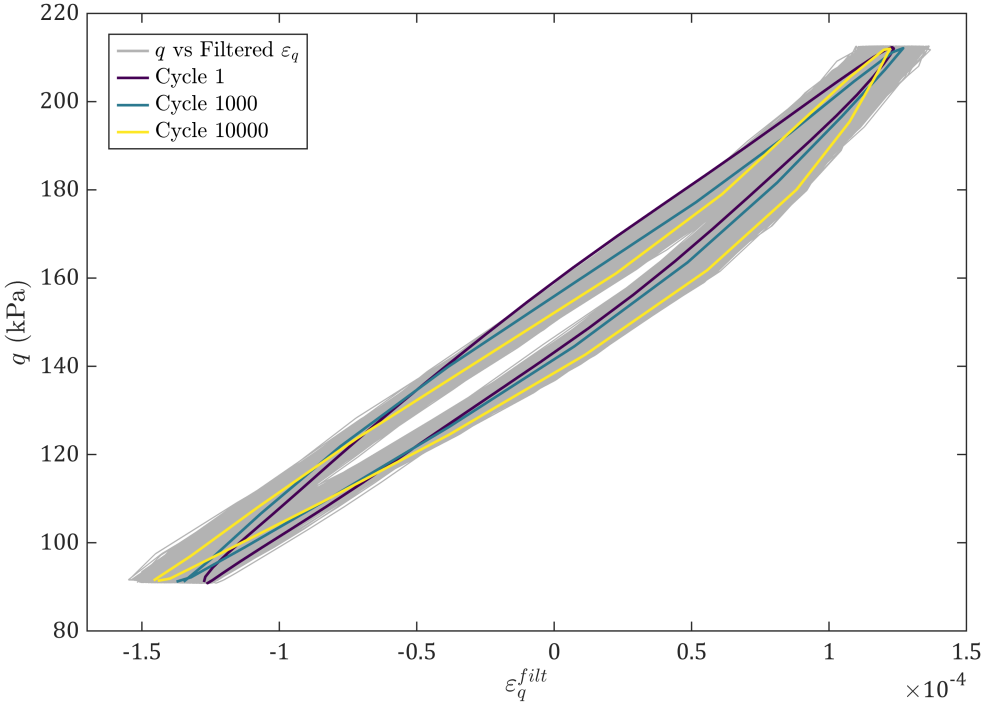

Figure 4.23: Bandpass filtered history of a drained cyclic test showing a decrease in enclosed area and stiffness gradient as the test progresses.

heat cycles within the laboratory, which has been recorded to undergo temperature cycles across 4 hours, equivalent to 1,440 cycles at 0.1 Hz.

The trend for G_{sec} in Figure 4.24(b) demonstrates a reduction in stiffness with increasing cycle number. The value of secant stiffness is derived using the points of maximum axial strain and minimum axial strain within each cycle of the bandpass-filtered signal. The initial response indicates a stiffness close to, or slightly exceeding, the expected value of $G_{\max} = 160$ kPa from the bender element results at $p' = 200$ kPa. However, this sample was anisotropically consolidated, which may affect the anticipated value for stiffness. Moreover, the noise present in the results suggests that the actual value may be lower. As the test advances, with higher axial strain, the secant stiffness decreases as expected, consistent with the typical S-shaped plots of shear modulus against strain.

4.3.1 Cyclic benchmark results: Accumulated axial strain

During long-term drained cyclic loading, the result of greatest interest is usually the accumulated strain. The following section presents results of accumulated strain against cycle number across a range of initial conditions. The data presentation adheres to the recommendations of Wichtmann et al. (2005) for analysis of long-term drained cyclic triaxial tests. However, the advised value for analysis is $\varepsilon_{acc} = \sqrt{(\varepsilon_a^{acc})^2 + 2(\varepsilon_r^{acc})^2}$, which is not included here. Instead, axial strain accumulation ε_a^{acc} is primarily focussed on, with volumetric strain accumulation presented separately. The local strain instrumentation used gave good results for axial strain, however, radial strain results were not registered by the radial strain belt at such small values. This is due to the design of the set-up,

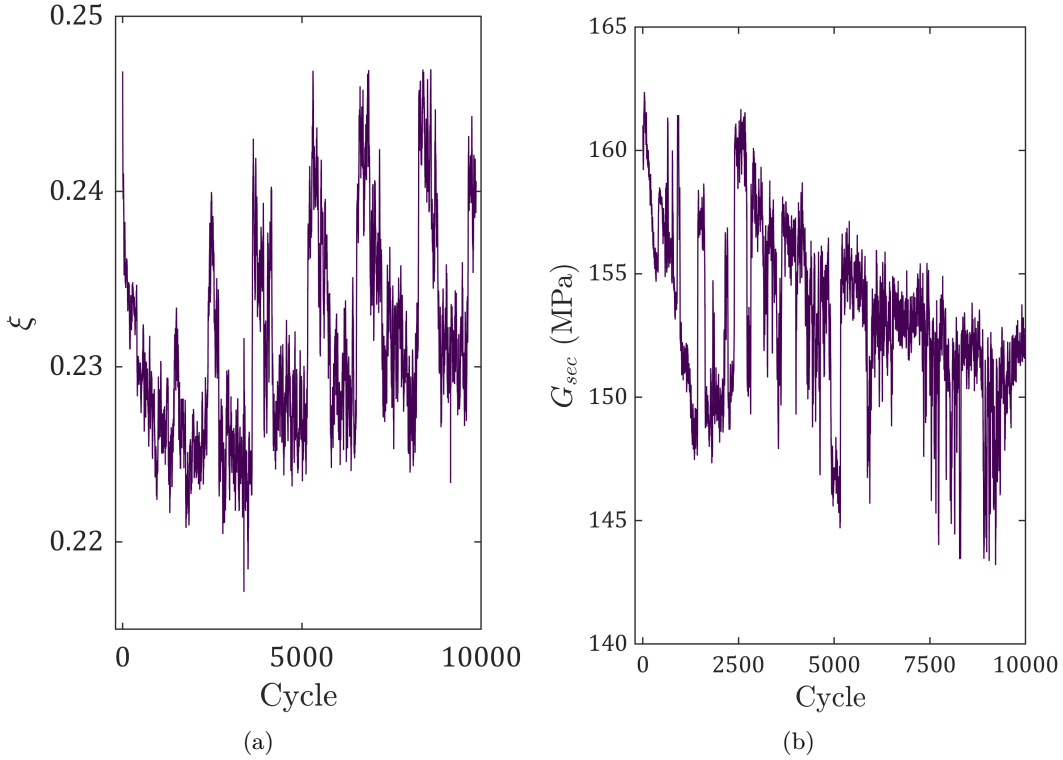

Figure 4.24: Cycle-by-cycle results of (a) damping ratio, (b) secant stiffness

with a spring to hold the belt to the sample, which restricted the movement of the belt at small strains. Measurements of volumetric strain taken by the back volume controller were of lower resolution, and are affected by small issues with membrane permeability. Therefore, as the results of axial strain are most reliable, axial strain results are preferred. The volumetric strain results are presented separately, and provide good results across the full length of the test. This is then used for analysis of the cyclic flow rule (Wichtmann et al., 2017) at varied cyclic stress ratios.

The plots of accumulated strain against cycle number are presented after cycle 1, the 'irregular cycle', following the recommendations of Wichtmann et al. (2005). The plots are displayed in semi-logarithmic space to emphasise the linear relationship between cyclic strain accumulation and cycle number. Values of strain accumulation are marked at cycles 10, 100, 1000, 2000, 5000, and 10,000. These points serve as references for comparison with the numerically simulated results shown later.

Void ratio - e

Figure 4.25(a) presents the results of three drained cyclic tests performed under the same conditions, with variations in the initial void ratio. Each test was subjected to 10,000 cycles at $p'_0 = 200$ kPa, and $\eta = 0.75$, $\zeta_b = 0.3$. As expected, the rate of strain accumulation increases with a reduction in density. The lower-density sample permits greater contraction and exhibits reduced stiffness. However, even at low density, $D_r = 30\%$, $e = 0.674$, the

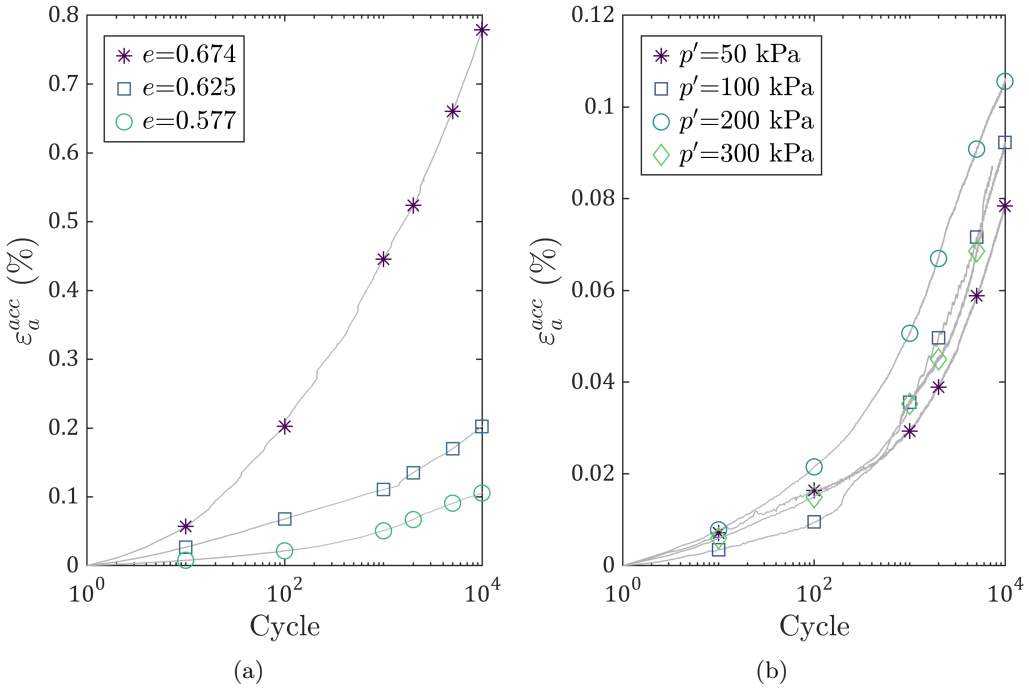

Figure 4.25: Cyclic axial strain accumulation results with parametric variations in (a) void ratio e, (b) average mean effective stress p'_0.

final accumulated strain after 10,000 cycles of $\varepsilon_a = 0.7\%$ is moderate. By comparison, the results of Wichtmann et al. (2010*a*) for a sample of 80% relative density attained 1% axial strain after 10,000 cycles. For calibration of the HCA model (Niemunis et al., 2005), the results of these tests should be normalised by the void ratio by dividing the strain accumulation results by the function $f(e) = \frac{(C_e - e)^2}{1+e} \cdot \frac{1+e_{\text{ref}}}{(C_e - e_{\text{ref}})^2}$, where C_e is a parameter to be calibrated to account for the variation in strain caused by void ratio differences. This function, with the calibrated value of $C_e = 0.54$ for Karlsruhe sand (Wichtmann et al., 2010*a*), implies that higher void ratios will accumulate greater strain, as evidenced by the results here.

The variation observed in the low density sample is unexpectedly large. When C_e is calibrated for the high and medium density samples for normalisation to the same strain accumulation, it yields a value of $C_e = 0.1$. The resulting strain accumulation of the low density sample is double that of the high and medium density samples. This underscores the unexpectedly large strain accumulation observed here. A repeat test of the low density sample should be conducted to enhance confidence in the results.

Despite this, each test exhibits a similar trend in strain accumulation. There is an initial linear response in semi-logarithmic space, succeeded by an over-logarithmic strain accumulation after approximately 2000 cycles. The low-density sample demonstrates over-logarithmic behaviour earlier in the test.

Mean effective stress - p'_0

The following section presents results of tests conducted under identical conditions, with variations in mean effective stress. The absolute magnitudes of q_{ampl} and q_{av} varied; however, the ratios of cyclic stress to mean effective stress, ζ_b, η_{av}, remained constant within each series. The first series, comprising the greatest number of tests, was performed at $n_{av} = 0.75$ and $\zeta_b = 0.3$, $D_r = 80\%$, the results of which are detailed in Figure 4.25(b). Across the range of p'_0, the accumulated strain is similar at all cycle numbers, with an overall accumulated strain after 10,000 cycles of $\varepsilon_a \approx 0.1\%$. There is no discernible trend regarding the variation of accumulated strain with mean effective stress. The results of this series align with expectations, suggesting that accumulated strain is influenced by stress ratios rather than the absolute stress amplitude. These findings concur with the conclusions of Wichtmann et al. (2010*a*), which indicate minimal variation in strain response with differing levels of mean effective stress. It should be noted that the variation in strain accumulation resulting from changing p'_0 leads to small increases in strain accumulation with decreased levels of p'_0 in the results of Wichtmann et al. (2010*a*). This observation contradicts the results presented here, which show the lowest strain accumulation at the conclusion of the test, under the lowest mean effective stress of $p'_0 = 50$ kPa.

Average cyclic stress ratio - η

Figure 4.26(a) shows the results of tests with varied cyclic stress ratios η. Tests in this series were loaded under identical conditions, $D_r = 80\%$ ($e = 0.57 - 0.59$), $p'_0 = 200$ kPa $\zeta_b = 0.3$, with variations in the average cyclic stress ratio $\eta = -0.5, 0, 0.25, 0.75, 1$. The rate of strain accumulation at $\eta = 0$ is low, but exhibits a negative trend. The stress path of this test is equally distributed between the negative and positive stress spaces. The stress path of the $\eta = 0.25$ test also briefly crosses into the negative deviatoric stress region. The axial strain response is minimal for this test. Given the difference in soil strength within the compression and extension regimes, this behaviour may be anticipated. However, the results of Wichtmann et al. (2007) indicate a slightly positive strain direction for the $\eta = 0$ case and a more pronounced positive (contractive axial) response for the $\eta = 0.25$ case. In all instances, the results for Congleton and Karlsruhe sands show minimal strain accumulation at these low stress ratios. The differences in the trends of positive and negative strain accumulation at this low strain level may arise from localised issues within the sample, rather than representing a generalisable case. It can be observed in the results of Figure 4.27, at certain points in the axial strain response of the $\eta = 0.25$, the rate of axial strain accumulation may be either positive or negative.

As the stress ratio increases in magnitude, whether positive or negative, the trends in strain accumulation become clearer. There is a steady increase in strain accumulation with an increase in η in the positive range. The highest stress ratio, $\eta = 1$, has a stress path that crosses the PTL ($\eta = 1$ Figure 4.11) in stress space. Therefore, the high rate of axial strain accumulation observed is anticipated. The results of Wichtmann et al.

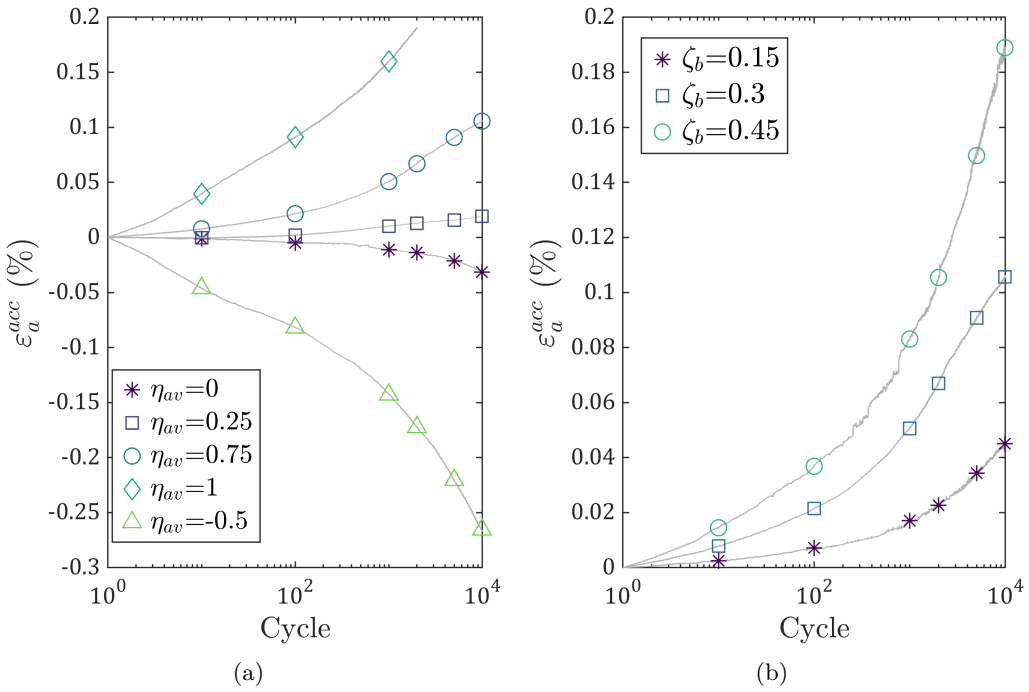

Figure 4.26: Results of ε_a^{acc} with variation of (a) η and (b) ζ_b. All tests were completed with other controlled parameters held constant. Tests of η variation were completed with conditions $e = 0.58$, $p'_0 = 200$ kPa, $\zeta_b = 0.3$. Tests of ζ_b variation were completed with conditions $e = 0.58$, $p'_0 = 200$ kPa, $\eta = 0.75$.

(2007) indicate almost entirely deviatoric strain accumulation at this high stress ratio. When comparing the results of $\eta = +1$ and $\eta = -0.5$, despite the cyclic stress ratio being double in magnitude, the rate of strain accumulation remains similar. This underscores the differences in behaviour in extension, as previously discussed. Further explanation of this behaviour is provided below in relation to Figure 4.32.

Figure 4.27 shows the comparison of strain accumulation at each level of η, loaded with the same ζ_b and prepared to the same D_r. The rate of strain accumulation at all levels of p'_0 is evidently dependent on the average cyclic stress ratio, η. This further corroborates the results of Figure 4.25(b). The rate of strain accumulation remains essentially independent of p'_0 across all stress ratios.

Cyclic amplitude - ζ_b

Figure 4.26(b) presents the results of the test series with variations in the cyclic amplitude, as quantified by the parameter ζ_b. All tests were conducted under identical conditions, $D_r = 80\%$ ($e = 0.58$), $p_{init} = 200$ kPa, $\eta = 0.75$, with variations in cyclic amplitude $\zeta_b = 0.15, 0.3, 0.45$. As anticipated, the rate of strain accumulation increases with greater ζ_b. The relationship between accumulated strain and stress ratio ζ_b is approximately proportional, with double the strain achieved for each doubling of stress ratio.

The results of the benchmark drained cyclic tests presented above show that the strain accumulation rate is a function of e, ζ_b, and η. Strain accumulation increases with

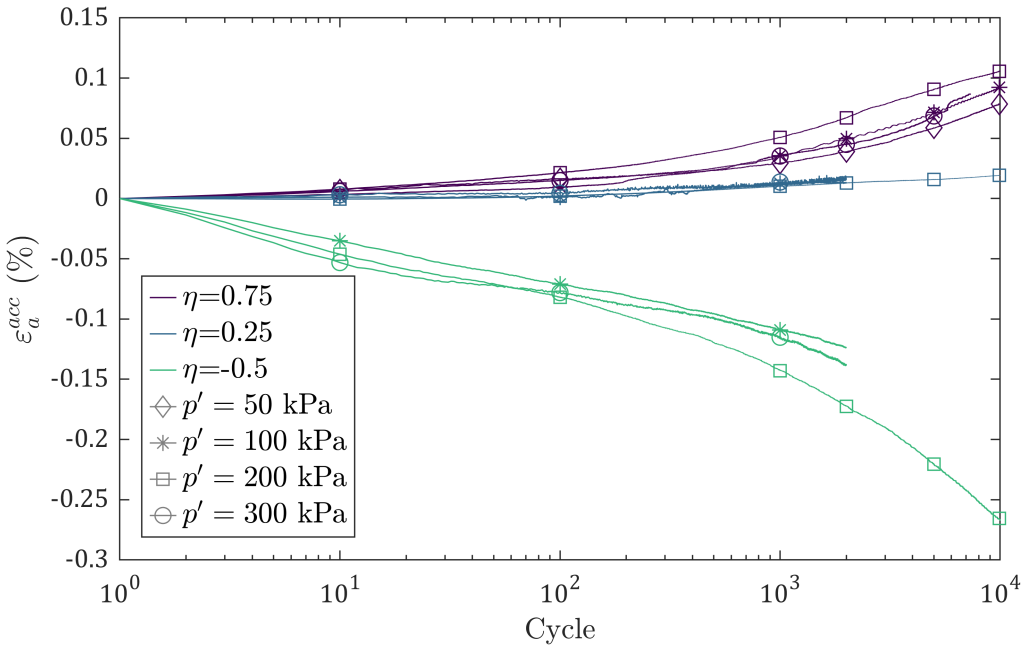

Figure 4.27: Cyclic results at varied η with varied mean effective stress p'_0 and maintained relative density. Results show similar results at all mean effective stresses at the same cyclic stress ratio η.

rising stress ratios, whether considering the average or cyclic amplitude ratio. Additionally, a reduction in sample density increases the rate of strain accumulation. This aligns with expectations, as lower density samples are more capable of contraction. However, cyclic strain accumulation was shown to be independent of p'_0 when other conditions are maintained. These observations are consistent with the effective stress principle, wherein shear strength depends on the effective normal stress. Consequently, despite the magnitude of load increasing for tests with higher mean effective stress, stiffness and strength increase proportionally while the strain accumulation rate is maintained. The rate of strain accumulation across all tests was relatively low compared with relevant results found in the literature, $\varepsilon_a^{acc} = 0.1\%$ in comparison to $\varepsilon_a^{acc} = 1\%$ after 10,000 cycles for Karlsruhe sand subjected to the same conditions (Wichtmann et al., 2005). This suggests that the sand forms a very stiff fabric. However, despite low strain accumulation, the trends of accumulation broadly correspond with findings in the literature.

4.3.2 Cyclic benchmark results: Accumulated volumetric strain

The following section presents the results of accumulated volumetric strain ε_v^{acc} from the drained benchmark cyclic triaxial tests. The results are organised according to variations in the same key test parameters from the axial strain plots above, e, p'_0, η, and ζ_b. The data presented below adheres to the same methodology employed for axial strain measurements. The first 'irregular' cycle is excluded, and trends of strain accumulation commence at the beginning of the second cycle. As discussed, the measurements of volumetric strain recorded with the back volume controller possess lower resolution as a percentage of the measured change. Additionally, the measurements are affected by issues with membrane

permeability. Small holes may be present in the membrane, or an imperfect seal may be created between the membrane and the fixtures. The permissible limit of 400 mm^3/hr detected during the sample preparation phase (Section 3.4) represents a low, but non-zero, volumetric strain rate. Additionally, these small leaks may be exacerbated by loading during the testing phase. Consequently, the results are less reliable than those for axial strain. However, as will be observed, the trends for volumetric strain remain discernible.

Throughout the duration of a test, distinct fluctuations are observed in the trace. This is likely attributable to variations in lab temperature, as discussed in reference to Figure 4.24(a). This effect could not be mitigated in the methodology; however, it has not significantly impacted the overall trend.

The trends of volumetric strain accumulation are more complex than those of axial strain. In certain instances, the degree of accumulated compressive volumetric strain is constrained by the onset of shearing-induced dilation. Furthermore, results from extension tests demonstrate compressive volumetric strain, despite extension in the axial direction. Tests in which the stress path intersects the PTL ($\eta = 1$ Figure 4.11) exhibit dilative negative volumetric strain. The extent of strain and the transition point to the negative strain regime depend on the proportion of the stress path above the PTL. Tests with a low average stress ratio, $\eta = 0, 0.25$ show significant volumetric strain despite minimal axial strain. This indicates that two-way and partially one-way cyclic loading have a densifying effect with minimal deviatoric strain component.

The first plot, Figure 4.28(a), shows the trends of accumulated volumetric strain with variations in void ratio e. These tests were performed at a range of relative densities, under identical loading conditions with $p'_0 = 200$ kPa, $\eta = 0.75$, and $\zeta_b = 0.3$. The initial trend for compressive strain is approximately related to density, with the highest rate of contraction observed in the lowest density sample. The trends for volumetric strain are consistent with the axial strain for these tests, with greater strain accumulation of both axial and volumetric strains occurring with reduced density. However, the early phases of cycling show similar results for the high and medium density samples. In the later stages of cycling, the high density sample exhibits a reduced rate of contraction, which eventually begins to dilate. The dilative shearing observed in the denser sample, but not in the medium sample, with continued axial strain is expected. The medium density sample is further from critical state, and therefore phase transformation, thus exhibiting greater contraction. The results of the $e = 0.577$ test are consistent with the characteristic results presented in Figure 4.21. As previously discussed, the volumetric strain is unexpectedly large. Consequently, the deviation from the expected trend related to density is likely due to minor erroneous results.

The results of the tests with varied mean effective stress p'_0, shown in Figure 4.28(b), demonstrate consistent outcomes across all levels of mean effective stress. These results illustrate the volumetric strain accumulation of the same samples shown in Figure 4.25(b). The trends observed correlate with the axial strain results, exhibiting minimal behavioural differences among the samples. The initial stages of cycling reveal slight volumetric

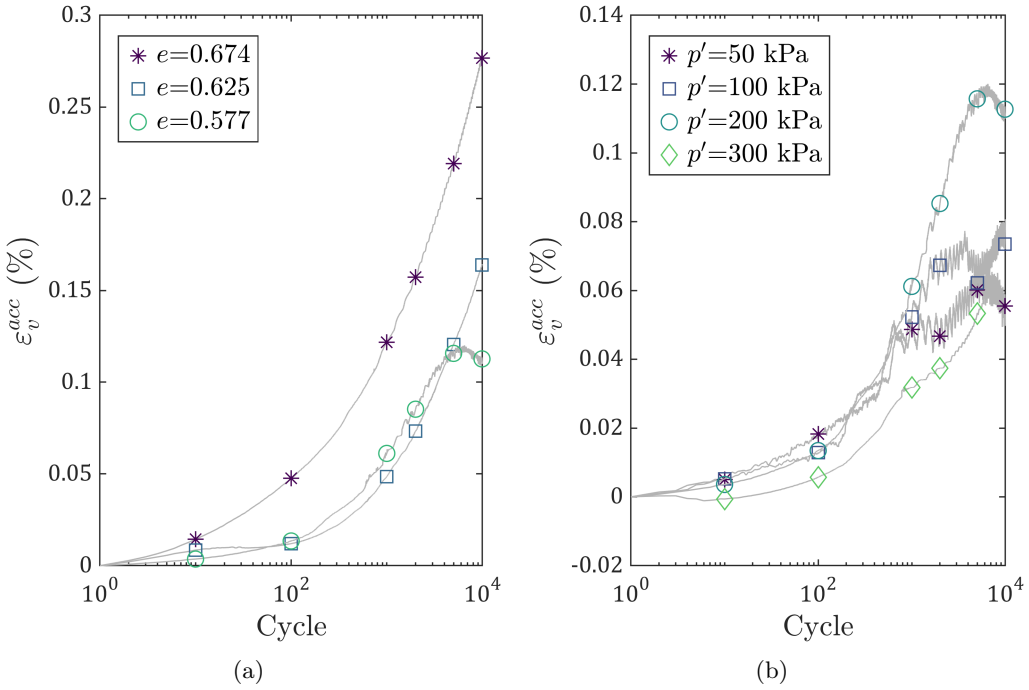

Figure 4.28: Accumulated volumetric strain showing, (a) variations in void ratio e with maintained conditions $p_0' = 200$ kPa, $\eta = 0.75$, $\zeta_b = 0.3$, and (b) variations in mean effective stress p_0' with maintained conditions $e = 0.58$, $\eta = 0.75$, $\zeta_b = 0.3$.

contraction, which accelerates after approximately 100 cycles. This trend is apparent in all instances. After approximately 5000 cycles, the rate of volumetric strain accumulation levels off to a consistent rate. The densifying effect of volumetric contraction brings the samples closer to the PTL, subsequently reducing the rate of volumetric strain. With an increased number of cycles, these tests may begin to exhibit dilative shearing alongside continued axial strain.

Here, the erroneous volumetric strain response of the characteristic cyclic plot (Figure 4.21) is visible. The results of $p_0' = 200$ kPa is significantly higher than the remaining tests, which all exhibit a very similar response. This should be noted in the comparison of other test series, that the central baseline test of $D_r = 80\%$, $p_0' = 200$ kPa, $\eta = 0.75$, and $\zeta_b = 0.3$ has a higher than expected volumetric strain.

The graphs presented in Figure 4.29 provide the volumetric strain accumulation results of the varied stress ratio series. The first series of varied η, Figure 4.29(a), illustrates the volumetric strain response corresponding to the test series of Figure 4.26(a). These results underscore the diverse volumetric response of tests subjected to loads that cross into the extension regime. During the cycles of tests $\eta = -0.5, 0, 0.25$, the deviatoric stress is partially or wholly negative. Consequently, the axial strain experienced is minimally contractive or negative. However, as is evident in the results, the volumetric strain remains contractive in all cases. Moreover, the magnitude of volumetric strain accumulation exceeded that of the axial strain for $\eta = 0, 0.25$. The stress path induced a constant contractive volumetric strain, contrasting with the axial strain which experienced reversal.

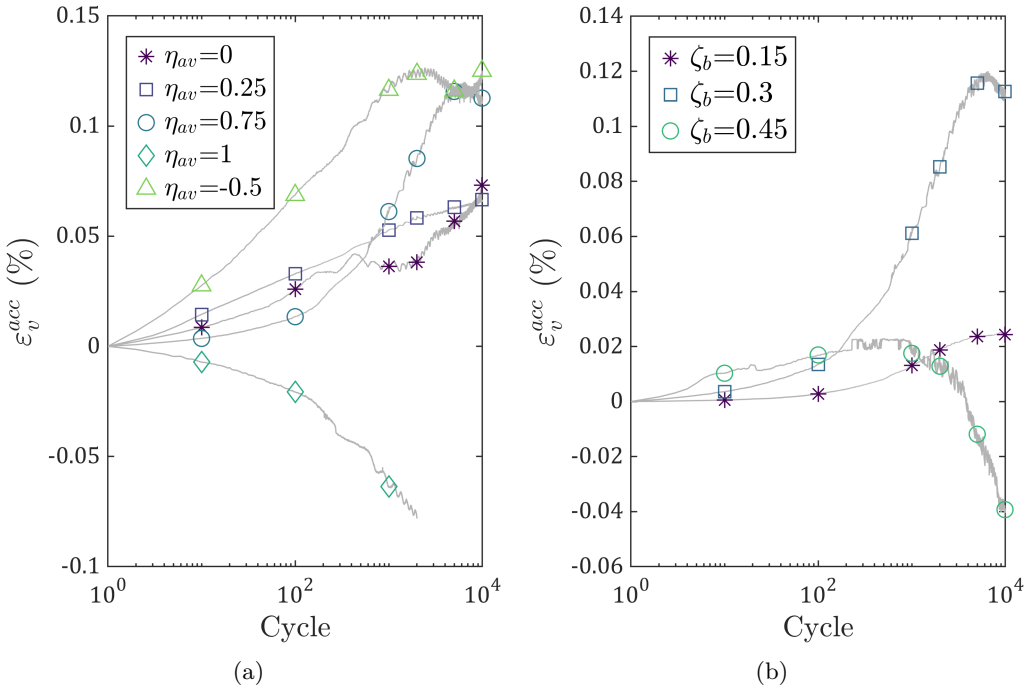

Figure 4.29: Accumulated volumetric strain showing, (a) variations in average stress ratio η with maintained conditions $e = 0.58$, $p'_0 = 200$ kPa, $\zeta_b = 0.3$, and (b) cyclic amplitude ratio ζ_b with maintained conditions $e = 0.58$, $p'_0 = 200$ kPa, $\eta = 0.75$.

Conversely, the results for $\eta = 1$ indicate dilative volumetric accumulation. The stress path crossed the PTL ($\eta = 1$ Figure 4.11) for over half of the time, and the shearing-induced dilation resulted in consistently negative volumetric strain accumulation.

The plots shown in Figure 4.29(b) provide the volumetric response of the ζ_b series, corresponding to the axial strain response depicted in Figure 4.26(b). For the tests $\zeta_b = 0.15, 0.3$, where the stress path did not intersect the PTL, the volumetric strain accumulation aligned with the axial strain response, demonstrating increased contraction with higher cyclic stress amplitude. Conversely, the results of $\zeta_b = 0.45$ display an initially contractive response followed by dilation induced by shearing. The stress path crossed the PTL during every cycle; therefore, the shearing trend observed later in the test is somewhat unexpected. This phenomenon may be attributed to a contractive collapsible fabric in the early phase of the test. Subsequently, following densification, continued shearing resulted in dilation and negative volumetric strain.

Figure 4.30 shows the accumulated ε_q vs ε_v response of all tests with a maintained void ratio e and cyclic stress amplitude ζ_b. All tests presented were conducted on samples prepared to $D_r = 80\%$ and subjected to cyclic amplitude $\zeta_b = 0.3$. Each trace of the same colour represents a test with varied mean effective stress but consistent cyclic stress ratios η and ζ_b. It can be observed that the cyclic flow rule is maintained when a sample is subjected to the same stress ratio η. The trend within each test is not always consistent, with changes in gradient indicating a transition in the strain regime. However, across the range of tests, the gradient remains consistent for each stress ratio η. This finding

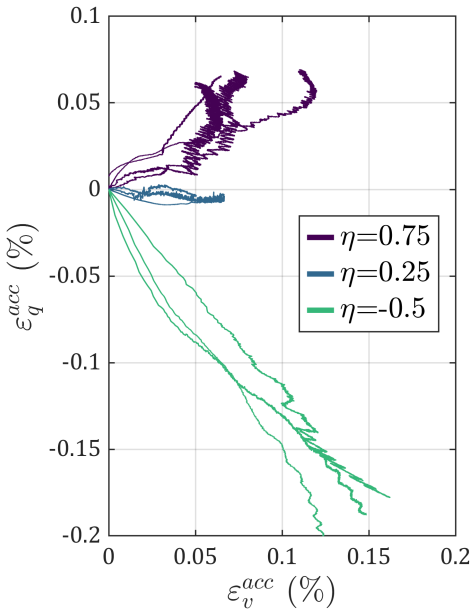

Figure 4.30: Cyclic flow rule, ε_q vs ε_v, at varied average cyclic stress ratio η

is corroborated by existing literature. Wichtmann et al. (2017) indicated that despite variations in the magnitude of loading, if the average stress ratio is maintained, the cyclic flow rule remains consistent.

The tests at $\eta = 0.25$ in Figure 4.30 exhibited minimal axial shearing, with greater volumetric shearing; therefore, the flow rule indicates a predominance of volumetric strain accumulation. This phenomenon can be attributed to the two-way cyclic loading, which induces minimal axial strain in either direction. This purely volumetric strain regime signifies general densification, with minimal shearing. This finding is significant for the design of offshore foundations. Typical loading regimes in the operational state tend to be either partially one-way or two-way. This is partly due to the impact of rocking waves (Liao et al., 2019). Consequently, the expected loading regime will induce densification of the surrounding soil, mitigating the effects of collapsible fabric during higher magnitude load events.

The results of the tests with $\eta = 0.75$ in Figure 4.30 demonstrate a consistent positive gradient, indicating positive contractive deviatoric strain. In the results, the increased volumetric response of the $p'_0 = 200$ kPa test (Figure 4.21) is observed with a lower gradient. The variability in the response of these tests is the least consistent among all cases. The gradient of the negative stress ratio, $\eta = -0.5$, exhibits the steepest response, despite having a lower average cyclic stress ratio than the $\eta = 0.75$ case. This observation is partly attributed to the lower strength in extension. However, this may be further explained by the existence of an instability stress point in the negative stress space. Examining the plot of Figure 4.31 reveals a distinct point of instability in the results of the CIUe monotonic tests, at a stress ratio of $\eta = -0.43$. Further analysis of an extension drained cyclic test (see next paragraph) highlights the impact of this instability stress level (ISL).

The plots shown in Figure 4.32 demonstrate the tangent shear modulus response

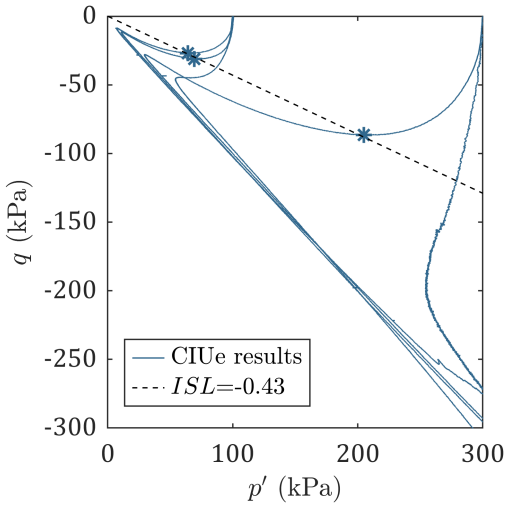

Figure 4.31: Instability line of undrained monotonic tests

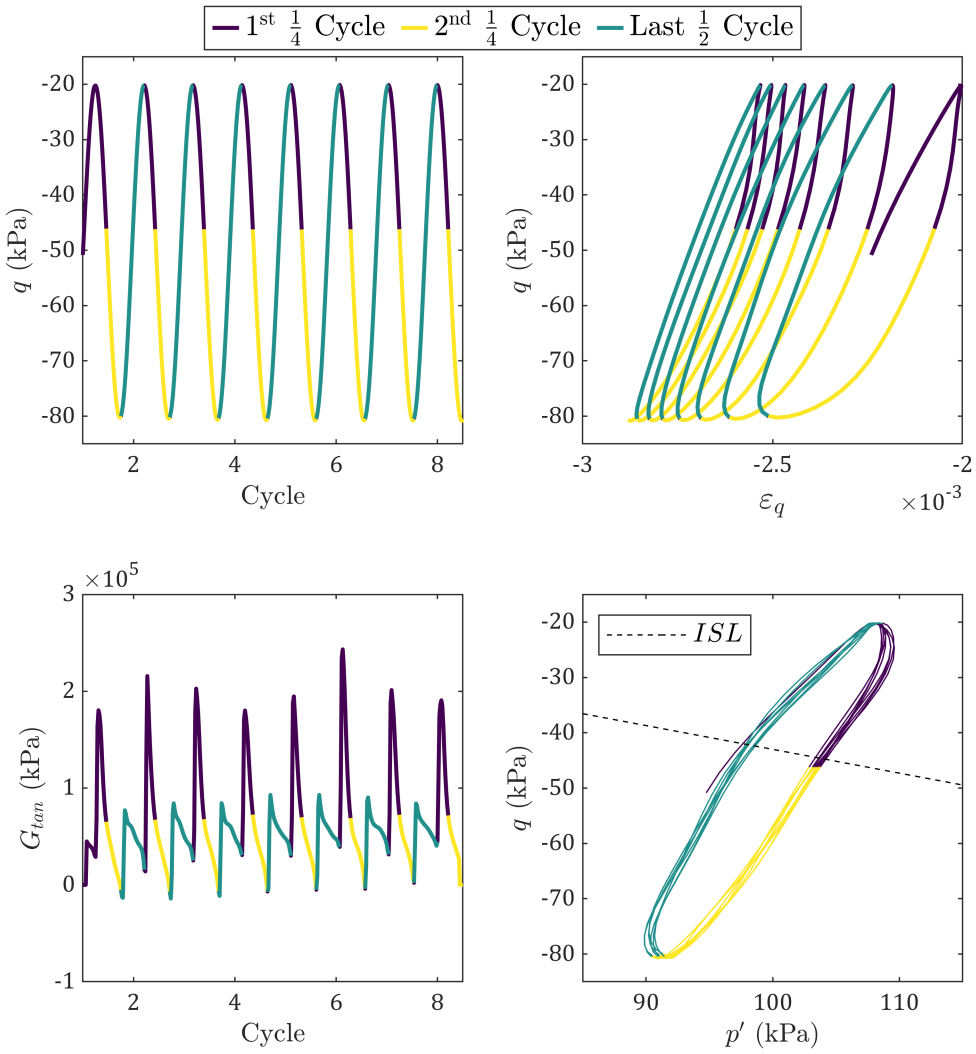

Figure 4.32: G_{tan} stiffness response of drained cyclic extension test BM_CIDC_80_100_-50_60

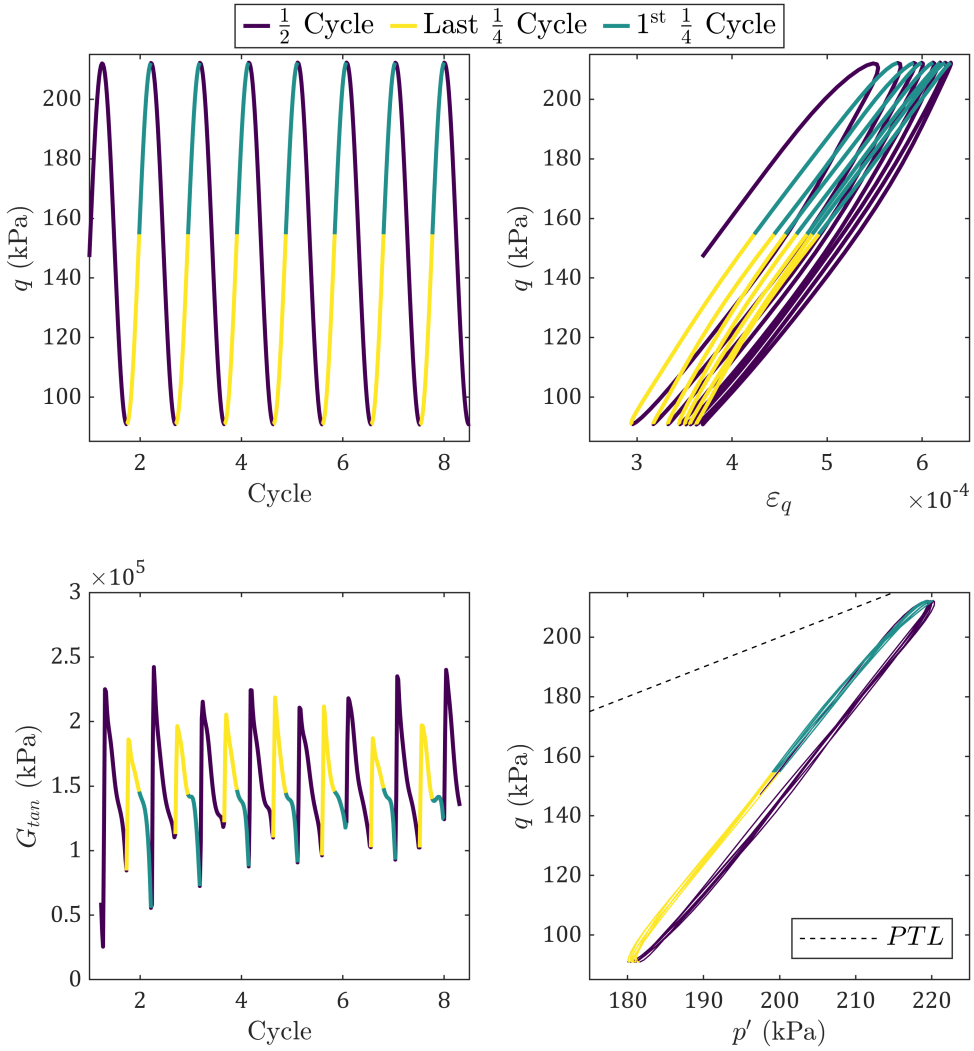

Figure 4.33: G_{tan} stiffness response of drained cyclic compression test BM_CIDC_80_200_150_60

throughout the loading cycles. Where the stress path exceeds the instability line in $p' - q$ space in the negative forward loop of the cycle, the trace is highlighted in yellow. These points within the time history are matched on the remaining plots, representing the 2nd 1/4 cycle. The plot of G_{tan} against cycle number reveals a significant drop in stiffness during this phase of cycling. This is also evident in the plot of q against ε_q, where the strain accumulation accelerates. The secant stiffness approaches zero at the extreme, indicating constant strain accumulation with no stress increase, i.e. a horizontal line on the $q - \varepsilon_a$ plot. This underscores the effect of exceeding the instability stress state, even under drained conditions. In the 1st 1/4 cycle, the stiffness is higher but drops rapidly as the stress state approaches the instability stress point. The stiffness recovers quickly in the backward half of the cycle, accounting for the purely negative strain accumulation.

Examination of the CIUc monotonic tests shows no ISL (Figures 4.5 and 4.6). The low range of densities tested accounts for this, as an instability point would likely be found at a lower density. Results of undrained monotonic tests performed by Wichtmann et al. (2015)

demonstrate instability in both positive and negative stress space. However, instability occurs at higher densities in extension tests.

The stiffness response of the compressive drained cyclic test shown in Figure 4.33 does not exhibit this trend. Considering the absence of an ISL stress ratio in compression, this is not marked on the stress path. Instead, the cycles are divided into quarters in the forward cycle loop and the return half of the cycle. The largest drop in stiffness occurs during the forward load, as the stress state approaches the PTL. This is anticipated, as this represents the most extreme load during the cycling. However, the tangent stiffness remains significantly higher, and consequently, the strain response is reduced in comparison. There is no clear ISL; therefore, as the stress path never crosses the PTL, the displacement accumulation remains limited.

4.4 Cyclic constitutive model calibration

The following section presents the calibration of SANISAND-MS concerning the cyclic parameters. These parameters are summarised in Table 4.5. The model parameters outlined in Table 4.3 are also applied during cyclic loading; however, the following parameters exclusively influence cyclic loading.

The calibration procedure for the cyclic tests highlighted certain issues with the SANISAND calibration process. The low levels of strain observed in the drained cyclic tests created discrepancies with the calibrated values of h_0 and G_0. The stiffness observed during the cyclic tests exceeded the predictions based on the calibrated monotonic values. The value of G_0 possesses a clear physical significance and should be retained. Conversely, the value of h_0 acts primarily as a fitting parameter and should be adjusted for improved results. The overestimation of strain accumulation in the simulated data indicated that the value of μ_0 selected could not rectify the predicted response, even at very large values. Given that the calibrated parameters exhibit limited applicability across diverse testing scenarios, the confidence in extrapolated predictions beyond the tested range is low.

Cyclic calibration - μ_0

The first parameter calibrated was μ_0, the cyclic ratcheting parameter. This parameter serves as a curve fitting coefficient, necessitating trial and error simulations to determine the optimal value. The results presented in Figure 4.34(a) display the test data results from BM_CIDC_80_200_150_60 alongside simulated SANISAND-MS outcomes. The variation in cyclic axial strain accumulation attributable to μ_0 is illustrated, with an increase in the selected value resulting in decreased cyclic strain accumulation. The selected value from this calibration was $\mu_0 = 220$. It is evident that the trend for strain accumulation does not align between the test data and the simulations, exhibiting significantly more strain in the early phase of the simulation. The calibrated value was determined to achieve a satisfactory match with the long-term results. The simulated outcome provides a reasonably good correspondence to the test data. However, as the simulation is optimised

for the endpoint of the test results, the calibrated parameter is best suited for the 10,000 cycle range. Consequently, if the cycle range were to differ, a different value would need to be selected.

Figure 4.34(b) shows the effect of varied hardening modulus on the simulated cyclic strain amplitude. The simulations with the parameters that were calibrated from the monotonic calibration, $h_0 = 4.67$ $c_h = 1.44$, show significantly larger cyclic strain amplitude than the test results. This results in a considerable accumulation of strain during the early cycles. Calibration of the cyclic strain accumulation parameter μ_0 had limited impact on the accumulated strain at reasonable values. The calibrated value for Karlsruhe sand was $\mu_0 = 260$ (Liu et al., 2019), during simulations of Congleton sand for the current study values exceeding $\mu_0 = 2000$ were required to achieve similar cyclic strain amplitudes. Additionally, at high values of μ_0, the rate of strain accumulation after 5000 cycles reduced below the logarithmic rate, contrary to the experimental results. Modifying the hardening modulus, h_0, to simulate lower strain amplitudes achieves a more accurate representation of the strain accumulation rate with cycle number. The traces presented have been filtered with a low-pass Butterworth filter to eliminate ratcheting, thereby clarifying the cyclic strain amplitude.

Figure 4.35 shows the simulations of cyclic data with variations in the shear modulus parameter G_0. The second cycle is highlighted, as it provides a more consistent comparison compared to the first irregular cycle. The rate of strain accumulation in the early cycles with calibrated parameters $G_0 = 305$, $h_0 = 4.67$, $c_h = 1.27$ exceeds the total accumulated strain after 10,000 cycles in the test data. Thus, this clearly does not represent the test data adequately. The unloading stiffness of the simulated data is significantly less than that of the test data, indicating that the elastic simulation of the cyclic test is inaccurate. Altering the parameter to $G_0 = 460$ yields a better result. However, the calibration of G_0 is conducted using bender test values, which have physical significance, and the value $G_0 = 460$ is considerably greater than other calibrated values of this SANISAND-MS parameter found in the literature. Consequently, it is not considered a valid calibration procedure to alter G_0 in this manner.

Considering the above, the selected parameters for cyclic simulation (see Table 4.6) were $\mu_0 = 220$, $h_0 = 10$, $c_h = 1.27$, and the shear modulus remained at $G_0 = 305$.

Table 4.5: SANISAND-MS cyclic parameters and constitutive model formulations from Liu et al., 2019

Term	Constitutive equation	Function
μ_0	$h = \frac{b_0}{(\mathbf{r}-\mathbf{r}_{\text{in}}):\mathbf{n}} \exp\left[\mu_0 \left(\frac{p}{p_{\text{atm}}}\right)^{0.5} \left(\frac{b^M}{b_{\text{ref}}}\right)^2\right]$	Ratcheting parameter
β	$D = \left[A_0 \exp\left(\beta \langle \tilde{b}_d^M \rangle / b_{\text{ref}}\right)\right] (\mathbf{r}_\theta^d - \mathbf{r}) : \mathbf{n}$	Dilatancy memory parameter
ζ	$\mathrm{d}m^{\mathrm{M}} = \sqrt{3/2}\mathrm{d}\alpha^{\mathrm{M}} : \mathbf{n} - (m^{\mathrm{M}}/\zeta)\, f_{\text{shr}} \langle -\mathrm{d}\varepsilon_{\text{vol}}^{\mathrm{p}} \rangle$	Memory surface shrinkage parameter

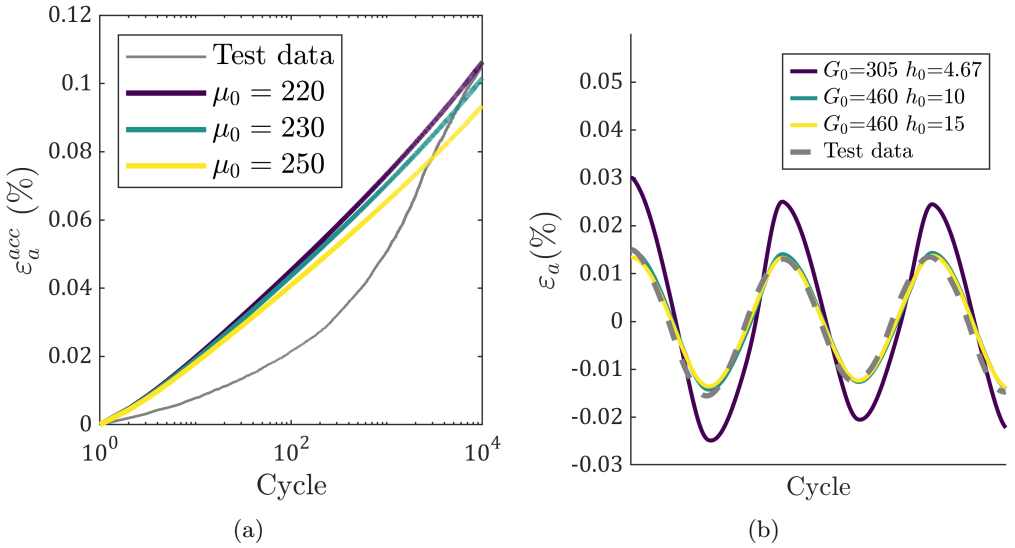

Figure 4.34: Plots showing, (a) calibration of μ_0 for test BM_CIDC_80_200_150_60, and (b) strain amplitude plot showing the effect of varied SANISAND-MS parameters G_0 and h_0.

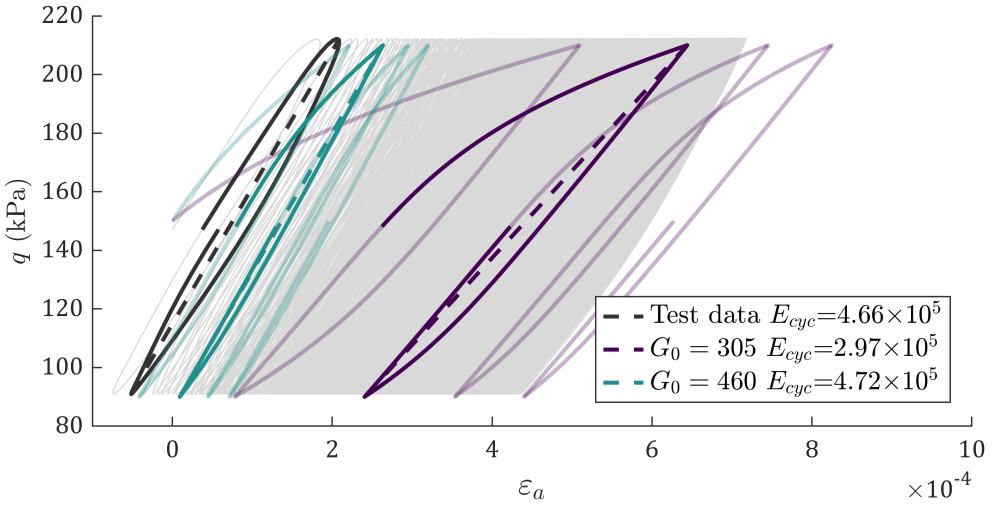

Figure 4.35: Calibration of SANISAND-MS parameter G_0 for better fitting to test data.

Cyclic calibration - ζ

The memory surface shrinkage parameter, ζ, only affects simulated results where the stress path crosses the phase transformation line $\eta_{pts} = 1.0$ (Liu et al., 2019). The test BM_CIDC_80_200_200_60 ($\eta = 1$) crossed the PTL during the compressive load cycle (Figure 4.36(a)). Additionally, test BM_CIDC_80_200_150_90 exceeded the PTL at the extreme of the compressive load (Figure 4.36(b)). Therefore, these tests were relevant for the calibration of ζ. Examining the results of the calibration shown in Figure 4.37, it is evident that variation in ζ has minimal impact on the simulated results. This is potentially attributable to the value of n^d calibrated from the monotonic results. It has been shown that the stress ratio of phase transformation can be significantly lower in cyclic loading cases (Möller et al., 2024). It is likely that with a better fitting of the early stages of

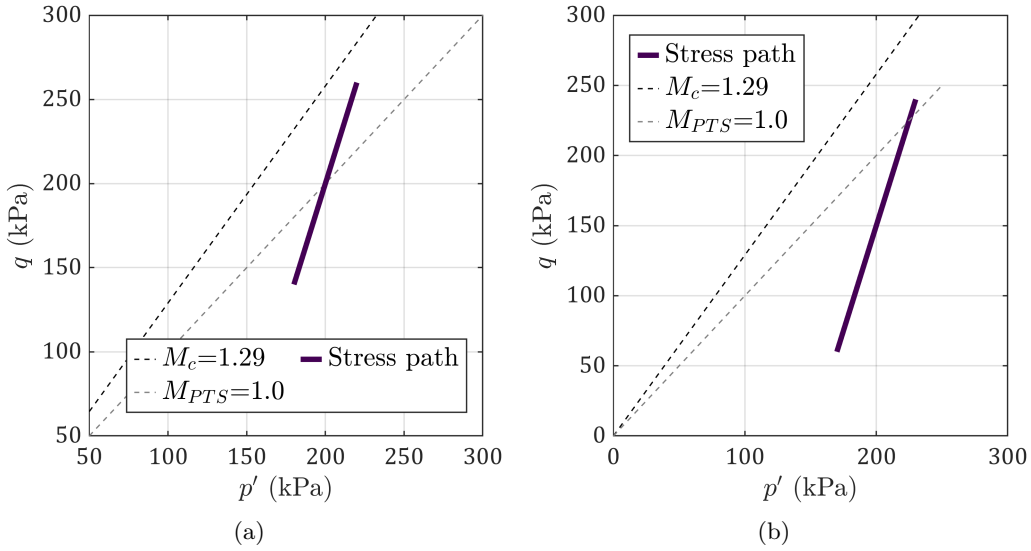

Figure 4.36: Stress paths of tests where the SANISAND-MS parameter ζ will affect the simulated results. ζ has been shown to only affect results where the stress path crosses the PTL. The stress paths shown are, (a) BM_CIDC_80_200_200_60, (b) BM_CIDC_80_200_150_90.

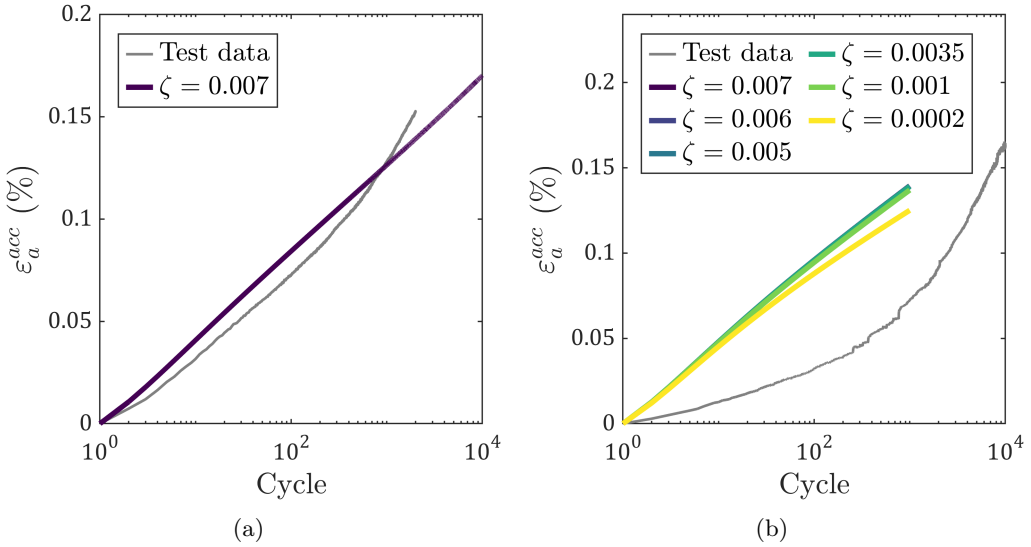

Figure 4.37: Calibration of SANISAND-MS parameter ζ with simulations and test data from, (a) BM_CIDC_80_200_200_60, (b) BM_CIDC_80_200_150_90. The chosen value was $\zeta = 0.007$.

cycling, i.e. with higher values of h_0 and G_0, the effect of ζ would be more pronounced. The selected value with the best fit for both tests was $\zeta = 0.007$, which is close to the calibrated value $\zeta = 0.0005$ in Liu et al. (2019).

The final values employed in the cyclic simulations below are presented in Table 4.6. The selected value of h_0 was modified to better align with the cyclic strain accumulation and amplitude. The value of G_0 was maintained at its original setting, given its connection to actual data. Although adjusting the value of h_0 relative to the monotonic calibration value is not optimal, this approach enables testing of the cyclic model's performance under varied conditions.

Table 4.6: Updated SANISAND-MS parameters

G_0	ν	M	c	λ_c	e_0	ξ	m	h_0	c_h	n^b	A_0	n^d	μ_0	ζ	β
305	0.05	1.29	0.74	0.015	0.767	0.5	0.01	10	1.45	1.52	1.0	1.51	220	0.007	1

4.4.1 Constitutive model performance - Cyclic tests

The following section presents the results of cyclic loading simulations using the calibrated parameters. Figures in this section display the simulated results as solid lines, with the corresponding test data indicated by markers of the same colour. The marker points are consistent with those highlighted in the test result plots. In all cases presented, the issue identified in the calibration of μ_0 persists (Figure 4.34(a)), characterized by greater strain accumulation in the initial cycling phase in order to satisfactorily match results across the full length of the test. The simulations match the test results in general trends with strain accumulation affected by sample density e, and the stress ratio parameters η, and ζ_b.

The void ratio, strength, and dilatancy dependent factors were calibrated using monotonic data. Figure 4.38(a) shows the simulations and test data of the parametric void ratio series. The tests and simulations were performed with varied void ratios and other parameters maintained, $p'_0 = 200$ kPa, $\eta = 0.75$, and $\zeta_b = 0.3$. The data for $e = 0.577$ ($D_r = 80\%$) provides the best match between simulated and test data. This is expected as the calibration of μ_0 was completed using this data. Given that the majority of tests were conducted at this void ratio, this is the most significant case for consistency between test and simulation. The data for $e = 0.625$ ($D_r = 50\%$) demonstrates good agreement, particularly at high cycle numbers. However, the effect of low void ratio, $e = 0.674$ ($D_r = 30\%$) is less significant in the simulated data than in the test data. This aligns with the discussion of void ratio effects for Figure 4.25(a), where the expected strain accumulation for the low-density test was half of what was actually realised. At low cycle numbers in the simulations, the rate of strain accumulation is very similar across all densities, after which the data begins to diverge beyond 100 cycles. This contrasts with the test data, which shows a substantial divergence in strain accumulation even at low cycle numbers. Given that only a single test for each of the varied void ratios was performed in the cyclic test series, the discrepancy between test and simulation results could be attributed to anomalous test results. However, to enhance simulation outcomes, increasing the value of the c_h parameter would facilitate better agreement.

Figure 4.38(b) shows tests and simulations with varied p'_0 and other parameters maintained, $e = 0.58$, $\eta = 0.75$, and $\zeta_b = 0.3$. The results show similar trends between the simulation and experimental results. Specifically, the mean effective stress does not significantly affect the response; only stress ratios do. However, the trend of the simulated results indicates slightly greater strain accumulation at lower mean effective stress, which contrasts with the test data. The marginal increase in the simulated strain accumulation at lower mean effective stress aligns with the findings of Wichtmann et al. (2005). These results informed the formulation and calibration of the SANISAND-MS model, thus

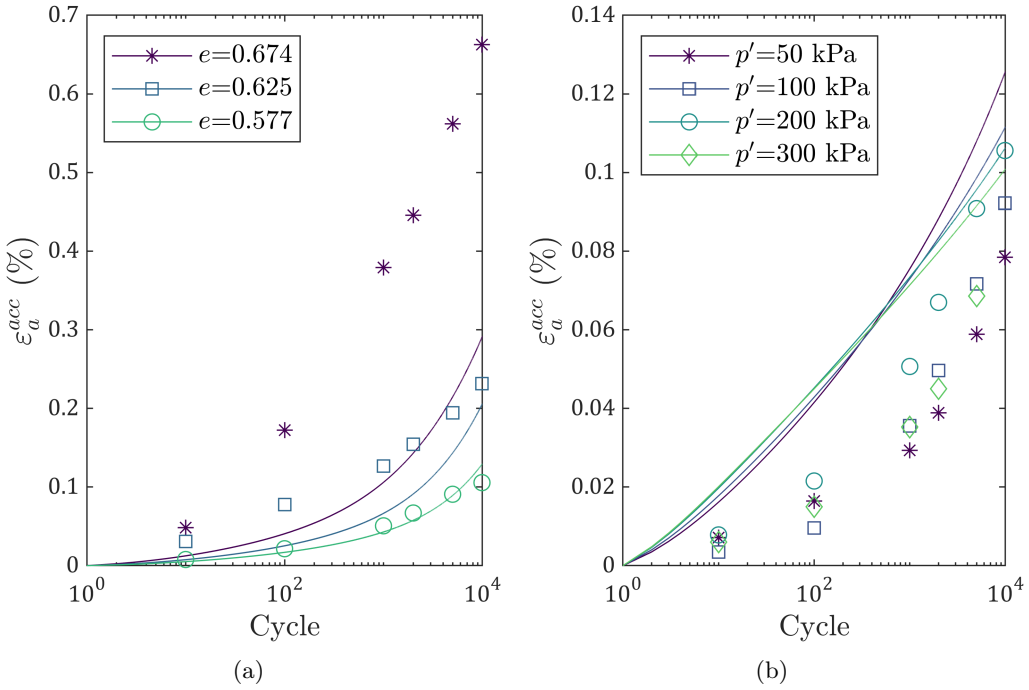

Figure 4.38: Test and simulation data for parametric variation of (a) void ratio e, with other parameters maintained $p'_0 = 200$ kPa, $\eta = 0.75$, and $\zeta_b = 0.3$. (b) Average mean effective stress p'_0, with other parameters maintained $e = 0.58$, $\eta = 0.75$, and $\zeta_b = 0.3$..

agreement with this behaviour is anticipated. Within SANISAND-MS, the formulation of the hardening modulus in Equation (4.3) below (Liu et al., 2019) and the power factor $(p'/p_{atm})^{0.5}$ account for this behaviour, allowing for minimal dependence on the mean effective stress. The relatively low spread of results among all tests in the series does not permit a conclusive determination of the behaviour; a greater number of tests might enhance confidence in the results.

$$h = \frac{b_0}{(r - r_{\text{in}}) : \mathbf{n}} \exp\left[\mu_0 \left(\frac{p'}{p_{\text{atm}}}\right)^{n=0.5} \left(\frac{b^M}{b_{\text{ref}}}\right)^{w=2}\right] \tag{4.3}$$

Figure 4.39 shows the test and simulation data related to parametric variations of the stress ratio. The results of Figure 4.39(a) present the test data and simulations for variations in η while maintaining conditions of $e = 0.58$ ($D_r = 80\%$), $\zeta_b = 0.3$, and $p'_0 = 200$ kPa. The data and simulation show good agreement, indicating well calibrated parameters of SANISAND-MS for η, for positive (compression) stress ratios. The simulated results for $\eta = -0.5$ show significantly greater strain accumulation than the test data. SANISAND-MS only allows for calibration of extension tests through the value of c. Increased flexibility in calibration for negative (extension) stress ratios would yield better simulated outcomes. However, this would greatly increase the number of calibrated parameters and tests required. Figure 4.39(b) shows the results of test and simulation data with variations in ζ_b whilst maintaining all other conditions, $e = 0.58$ ($D_r = 80\%$), $\eta = 0.75$, and $p'_0 = 200$ kPa. This also shows good agreement between test data and simulation. The test $\zeta_b = 0.45$

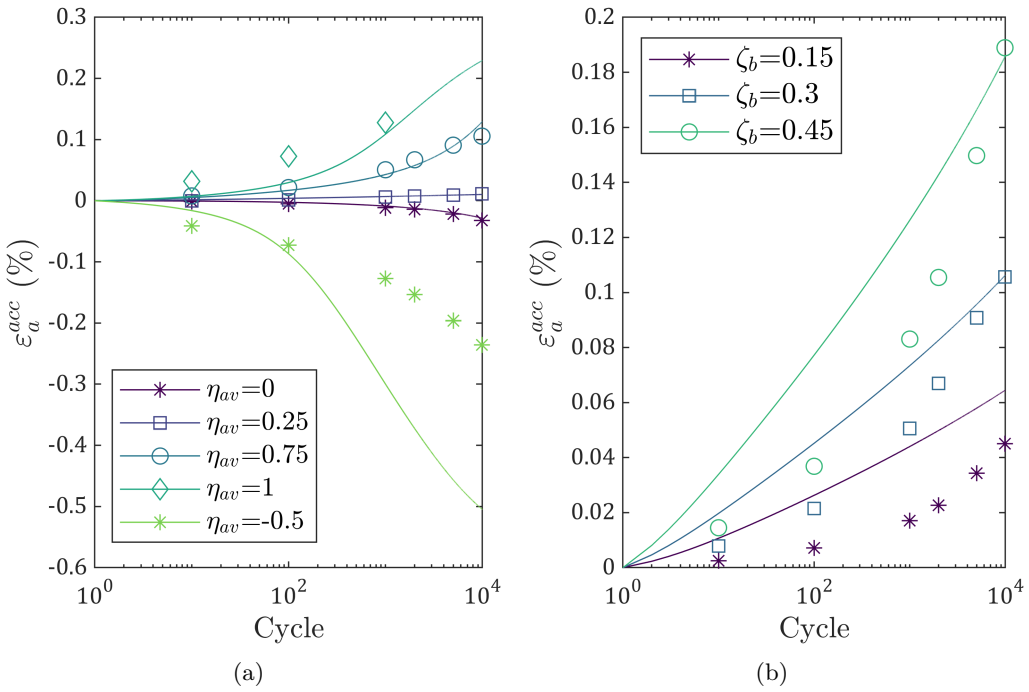

Figure 4.39: Test and simulation data for parametric variation of (a) average cyclic stress ratio η , with other parameters maintained $e = 0.58$, $p'_0 = 200$ kPa, and $\zeta_b = 0.3$. (b) Cyclic amplitude ratio ζ_b , with other parameters maintained $e = 0.58$, $p'_0 = 200$ kPa, and $\eta = 0.75$.

had a stress path that exceeded the PTL; consequently, the agreement with the results confirms good calibration of parameter ζ. However, since this test was used for calibration, this result is anticipated. A test with a more extreme stress ratio would provide better validation of this. These results demonstrate that within the typical range of void ratio of $e = 0.58$ ($D_r = 80\%$), the model performs well in reproducing test results. The calibration of stress ratio related factors is shown to be effective, and within a low range of void ratio variation, the model performs adequately.

4.5 Summary

The results of the monotonic and cyclic triaxial tests conformed to the expected general trends of stress and strain, according to the effective stress principle. During monotonic testing, the peak and residual strength correlated with the mean effective stress in both compression and extension. The undrained monotonic tests exhibited variability in contractive behaviour; however, the onset of phase transformation remained consistent in terms of stress ratio, η_{pts}. The variability in contractiveness was likely due to deviations from the target void ratio, as evidenced in the plot of Figure 4.13(b), which displayed a consistent relationship between the onset of phase transformation and the actual void ratio represented with the state parameter. Albeit, anomalous results were excluded from the plot to achieve a clear value for n^d. The variation in results is most likely attributable to a vertical gradient in $q - p'$ space during phase transformation (Figure 4.12), which resulted

in a wide range of stress ratios over a similar value of p'. Observations of trends in the results of extension tests were limited due to the onset of necking. Nonetheless, the strain range of the undrained tests was greater than that of the drained tests.

The results of the drained cyclic tests demonstrated trends in axial strain accumulation, ε_a^{acc}, depending on void ratio, e, and stress ratio parameters: cyclic amplitude stress ratio ζ_b and average cyclic stress ratio η. When stress ratios and void ratio were maintained, the rate of strain accumulation was essentially independent of mean effective stress, p'_0. These observations align with findings in the literature regarding long-term drained cyclic strain accumulation (Wichtmann et al., 2010*a*). However, the magnitude of strain accumulation with cycle number was minimal for the majority of tests, with $\varepsilon_a^{acc} \approx 0.1\%$ after 10,000 cycles. The design of test series in the literature (Wichtmann et al., 2010*a*) identified the rate of strain accumulation across a range of initial conditions, particularly η, and subsequently selected a suitable central point within the range of parametric variation, aiming for a target $\varepsilon_a^{acc} = 1\%$ after 10,000 cycles. The test schedule for this project focused instead on conditions that reflect those encountered in practice, to provide a relevant comparison with the model testing phase (Chapters 6 and 7). Consequently, the range of strain accumulation was low. This minimised the overall impact of parametric variations of the test conditions. In some cases, where overall strain accumulation was low $\varepsilon_a^{acc} \approx 0.05\%$ (e.g. $\eta = 0.25$), trends were difficult to ascertain.

Model calibration was predominantly performed using the results of monotonic tests. This procedure adhered to the recommendations in the literature for SANISAND-MS calibration (Azeiteiro et al., 2017; Dilip et al., 2025; Liu et al., 2019). The calibration prioritised drained results to better capture the behaviour evident in drained cyclic tests. Consequently, the calibration procedure deviated from certain recommendations (e.g. the A_0 procedure from Dilip et al. (2025)); this was necessary to accurately model the drained behaviour. During calibration, it was observed that certain parameters, particularly A_0 and h_0, required significantly different values to adequately represent drained and undrained behaviour. The results of the extension tests were constrained due to necking, as previously discussed, which hindered effective calibration in negative deviatoric stress space. Nevertheless, the formulation of SANISAND-MS requires only an ultimate strength ratio between compression and extension, while all other factors are calibrated solely using the results of compression tests. The model provided a good representation of the response to two-way cyclic loading, encompassing both compression and extension stress states. However, for one way tests involving pure extension, $\eta = -0.5$, the model overpredicted the rate of strain accumulation. A greater level of calibration focused on extension stress states would be beneficial. Furthermore, simulations using the SANISAND-MS model aligned well with the test data at high cycle numbers, facilitated by the calibration of the ratcheting parameter, μ_0. However, the rate of strain accumulation at lower cycle numbers was inconsistent in capturing the response. Calibrating the model parameters, particularly the hardening parameters of h_0 and c_h, with respect to the cyclic data would likely have yielded improved results.

Chapter 5
Triaxial Results II: Influence of Fines and Partial Drainage on Long Term Cyclic Loading

The presence of fines in soils, as discussed in Section 3.2, is prevalent in offshore soils, particularly in the North Sea. Limited data is available in the literature regarding the response of silty sands to long-term cyclic loading. The testing schedule of this chapter assesses the equivalent void ratio framework (Rahman et al., 2008) for predicting the response of soil subjected to cyclic loading. A bespoke sample preparation procedure was developed for the preparation of silty sand samples on the GDS DYNTTS cyclic triaxial system, based on the methodology of Carraro et al. (2008). The samples were prepared to the same equivalent void ratio e^* and loaded under the same conditions as the benchmark cyclic triaxial tests for parametric verification of the equivalent void ratio concept. The testing schedule included a range of fines contents, sample densities, and cyclic stress ratios for verification under diverse conditions.

Further to the silty sand investigation, a series of partially drained triaxial tests were conducted to examine the effect of partially drained conditions on soil response. The test schedule incorporated a novel method to create a partially drained regime by restricting drainage from the sample with a low permeability filter. The filter concept was based on the work of Suzuki et al. (2020); however, a simpler design with a silt-based filter was employed. The testing schedule mirrored the design of the silty sand tests, incorporating a range of stress ratios and sample densities in two series with different degrees of restricted drainage. Drainage was controlled by the packing density of the silt within the filter.

Having completed a range of benchmark tests on clean, fully drained samples in Chapter 4, this permitted a direct assessment of the effects of fines content and partial drainage on soil response. The key point of comparison was the rate of axial strain accumulation with cycle number. Results in the literature for silty sand samples subjected to drained cyclic loading suggest that the equivalent void ratio concept is unable to accurately predict the axial strain response during such loading. Tafili et al. (2024) suggest that strain accumulation is reduced with increasing fines content in tests on samples with the same e^*. These tests were conducted on sands with added plastic fines. The assumed cause of this discrepancy in strain, despite the same response during monotonic loading, is the settling of fines into the contact zone during cyclic loading, which would otherwise have been displaced during continuous shearing. However, the results of the tests performed for this thesis do not align with this finding. The tests conducted on sands mixed with

non-plastic fines exhibited a similar strain response for samples with the same e^*. The difference in plasticity of the fines may account for the observed variation. It is well established that the type of fines significantly influences soil response (Carraro et al., 2009). The mechanism enabling fines to settle into contact zones may depend on the adhesion properties of the fines, which increase with higher plasticity.

Results of partially drained cyclic tests in the literature demonstrate an increase in axial strain accumulation with reduced drainage (e.g. Jostad et al. (2021)). The excess pore pressures developed during cycling are dependent on volumetric strain, bulk modulus, and resistance to drainage. Consequently, elevated pore pressures result in a reduction in effective stress and an increase in accumulated shear strain. The results presented in this thesis align with these findings, with the highest degree of additional strain accumulation, compared to the benchmark results, occurring with the maximum pore pressure accumulation. This phenomenon is influenced by the applied stresses and the degree of drainage restriction.

Finally, a series of partially drained tests on silty sand were conducted. These results offer novel testing, absent from existing literature. The results indicated a higher degree of collapsibility in the silty sand samples, which consequently led to increased pore pressure and axial strain accumulation.

5.1 Cyclic undrained clean sand test

The following section presents the results from a benchmark undrained cyclic triaxial test. A single undrained test was performed with conditions $e = 0.58$, $p'_0 = 200$ kPa, $q_{cyc} = 150$ kPa ($\eta = 0.75$), $q_{ampl} = 60$ kPa ($\zeta_b = 0.3$). This test mirrors the baseline drained cyclic triaxial test (BM_CIDC_80_200_150_60 Table 3.9), albeit under undrained conditions. The results are presented in Figure 5.1. The uppermost plots show the load path, in total stress, applied to the sample. The initial stress path fell below the PTL and CSL. The amplitude of the applied cyclic load (kN) remained uniform throughout the test; however, a slight reduction in deviator stress was observed as the test progressed. This is indicative of an increase in cross-sectional area as the sample deformed. This effect was not evident in the drained tests, where sample deformation was significantly lower. The plot of q against ε_a displays high cyclic strain amplitude in the early cycles, which becomes more uniform throughout the test. The cycle loop gradient becomes slightly shallower as the test progresses. The degree of axial strain accumulation per cycle decreases throughout the test, despite an increase in excess pore pressure.

The plot of ε_a against cycle number is presented on a logarithmic x-axis. The rate of strain accumulation is approximately linear for the initial 100 cycles, followed by a rapid acceleration after 500 cycles. Examination of the plot of r_u against cycle number shows that this acceleration begins after the excess pore pressure ratio exceeds 0.2. The rate of pore pressure accumulation increases logarithmically until this point, at approximately 500 cycles. This induces a significant reduction in stiffness, leading to increased strain

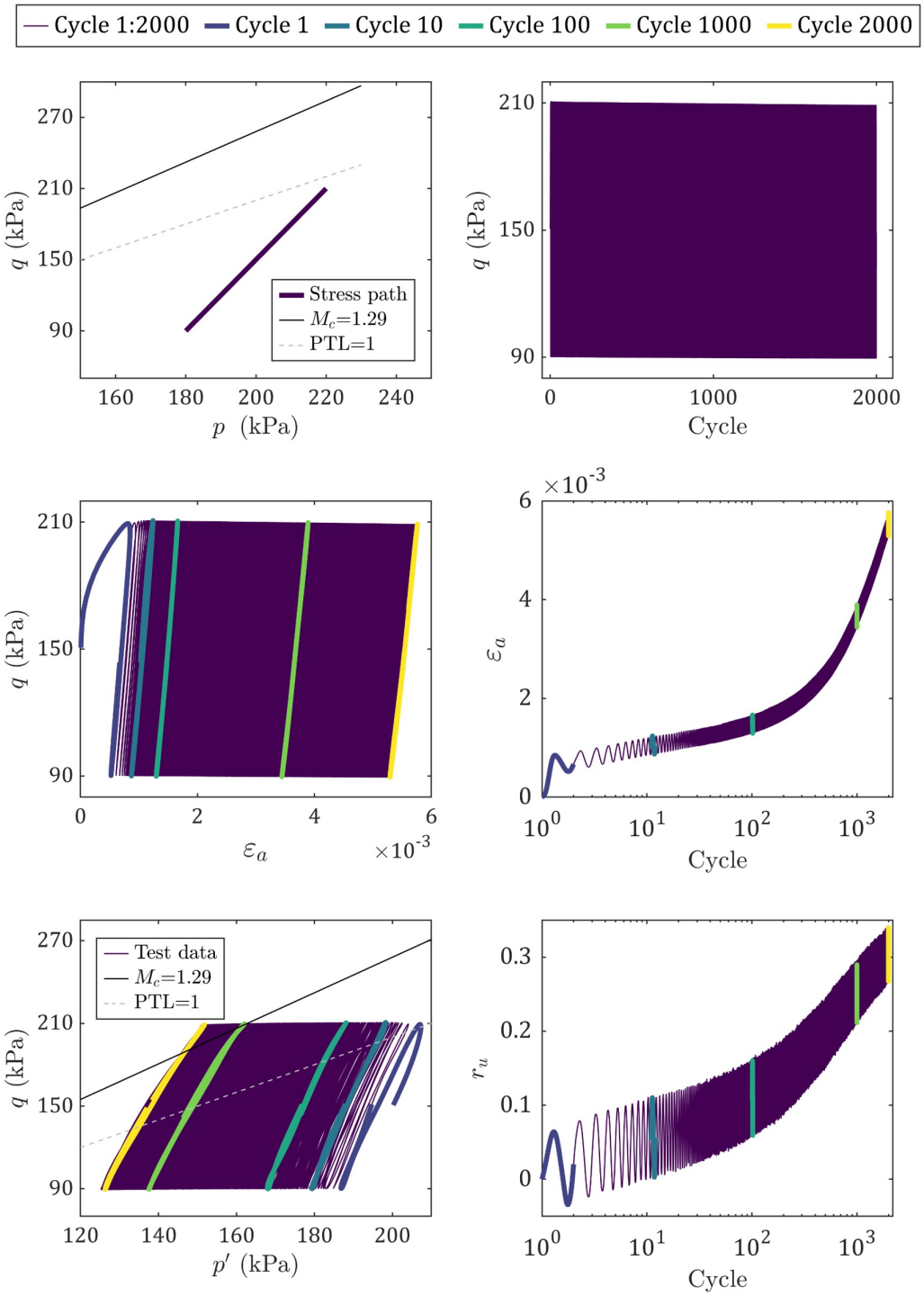

Figure 5.1: Results of undrained cyclic triaxial test BM_CIUC_80_200_150_60

accumulation. As the rate of strain increases, the rate of pore pressure accumulation also rises. The relationship between increased compressive strain and excess pore pressure is demonstrated here. The plot of q against p' illustrates the reduction in stiffness. As excess pore pressure accumulates, the trace migrates to the left, indicating a reduction in mean effective stress p'. As the trace migrates, the stress path begins to cross the PTL and CSL. This accounts for the increased rate of axial strain accumulation induced by continuous migration across the PTL.

The sample does not exhibit failure, experiencing moderate cyclic strain amplitude and a maximum excess pore pressure ratio of $r_u \approx 0.3$. Anisotropic consolidation of this sample likely restricted liquefaction and failure. The results of Wichtmann et al. (2015) demonstrate that for a similar test conducted at $D_r = 66\%$, $p'_0 = 200$ kPa, $\eta = 0.75$ $\zeta_b = 0.25$, the stress path in $p' - q$ space is constrained by the CSL. Stress relaxation behaviour ceases at this threshold, resulting in minimal further increases in excess pore pressure. This observation is generalisable to all instances of anisotropically consolidated undrained tests. The behaviour shown in these results aligns with the findings of Wichtmann. However, strain accumulation persists after the stress path reaches this limiting state. The rate of strain accumulation for the undrained case is significantly greater than that observed in drained tests under the same initial conditions (Figure 4.21).

5.2 Fines content

An initial series of drained cyclic triaxial tests, conducted under the same conditions as the benchmark drained cyclic tests, investigated the effect of fines content. The tests aimed to maintain approximately the same effective void ratio, e^*, for each sample, focusing on $e^* = 0.58$. The test schedule is presented in Section 3.9.2. Several tests were conducted under identical conditions to assess the repeatability of results. Since the tests used the same loading conditions as the benchmark test (BM_CIDC_80_200_150_60 Table 3.9), the results were compared to evaluate the validity of the equivalent void ratio e^* concept.

Figure 5.2 provides comprehensive results of a silty sand drained cyclic triaxial test, FC10_CIDC_80_200_150_60_c. The stress path was identical to the benchmark test BM_CIDC_80_200_150_60, prepared to $e^* = 0.58$ with a fines content FC= 10%. The sample was subjected to 10,000 cycles, at $p'_0 = 200$ kPa, $q_{av} = 150$ kPa ($\eta = 0.75$), $q_{ampl} = 60$ kPa ($\zeta_b = 0.3$). The plot of q against ε_a exhibits a typical response, with the initial loading producing a significant proportion of the overall strain, followed by a densifying phase where subsequent cycles induce less permanent strain. The enclosed area of the cyclic loop decreases with cycle number, and the loop gradient remains approximately constant. Axial strain ε_a against cycle number also demonstrates a response similar to the benchmark testing, with a linear accumulation in semi-logarithmic space of strain during the first 1000 cycles, followed by accumulation over the logarithmic rate in the subsequent cycles. The cyclic strain amplitude diminishes as the test progresses. Volumetric strain shows a comparable trend, but with lower overall accumulated strain at all stages. The

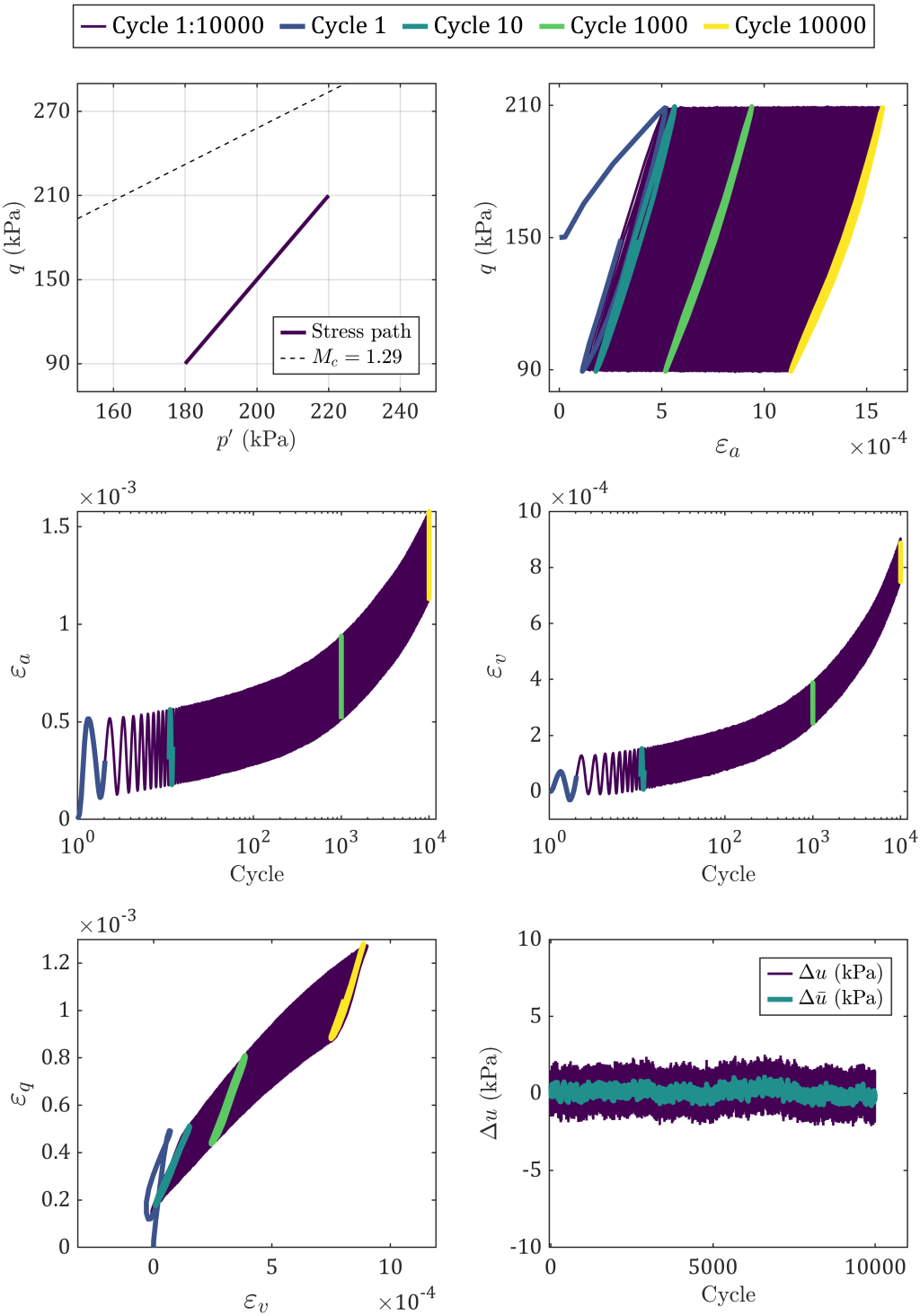

Figure 5.2: Results of drained cyclic triaxial test on silty sand sample FC10_CIDC_80_200_150_60_c

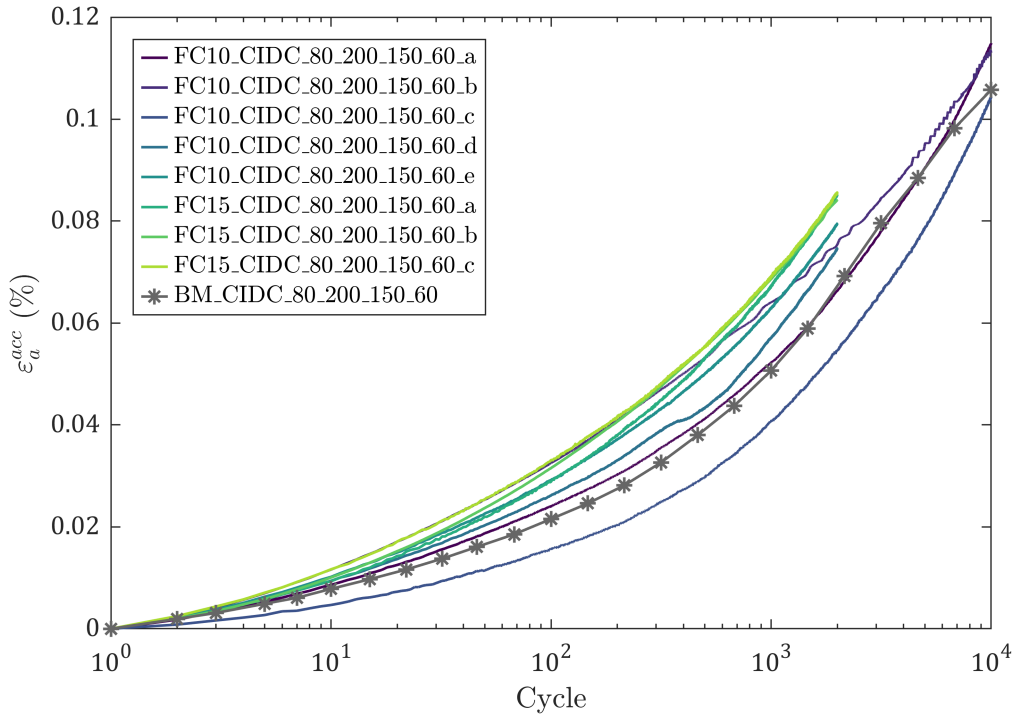

Figure 5.3: Cyclic axial strain accumulation, ε_a^{acc}, assessing repeatability of fines content tests and comparing with benchmark test BM_CIDC_80_200_150_60, $p'_0 = 200$ kPa, $\eta = 0.75$, $\zeta_b = 0.3$, $e^* = 0.58$

volumetric strain remains compressive throughout the test, showing no deceleration in the strain rate. The rate of volumetric strain accumulation increases relative to axial strain as the test continues. This is evident in the plot of ε_q against ε_v, where the gradient decreases with increasing strain, indicating a higher proportion of volumetric strain. This finding is consistent with the trends observed in the benchmark tests (Figure 4.21). Finally, despite a lower global void ratio resulting in reduced sample permeability, and testing conducted at the same rate as the clean benchmark tests, the test is fully drained, as shown by the pore pressure plot.

The overall trends of axial and volumetric strain accumulation observed in this test align with the clean drained cyclic triaxial tests of the benchmark series. The accumulation rate of pore pressure is minimal, consistent with the benchmark tests, with any excess pore pressure resulting from the lag between the applied load and the response of the back pressure controller. This test was conducted with the same equivalent void ratio as the $D_r = 80\%$ series of clean sand tests, providing initial validation of the equivalent void ratio concept.

Figure 5.3 presents the results of a series of silty sand tests performed under the same initial conditions $e^* \approx 0.58$, $p'_0 = 200$ kPa, $\eta = 0.75$, $\zeta_b = 0.3$, with 10% and 15% fines content. These tests were conducted to assess the repeatability of the sample preparation method for producing samples at the target equivalent void ratio. Consequently, these tests also validate the repeatability of the cyclic strain accumulation results. The results are compared with the clean sand benchmark test (BM_CIDC_80_200_150_60), which

has the same equivalent void ratio and loading conditions. There is a degree of scatter within the results, although the overall trend is consistent. Within the scatter of the $FC = 10\%$ samples, certain tests exhibit a higher degree of initial axial strain accumulation, while others demonstrate lower initial accumulation. However, after the full duration of the test, the degree of strain accumulation levels out. The tests with high initial strain tend to converge to the same level as the benchmark test, while the opposite occurs for those with low initial strain. Although all samples were prepared to the same e^*, the FC= 15% samples exhibit a slightly higher degree of strain accumulation across all cases. The FC= 10% samples are more aligned with the benchmark. This may indicate that the b value in the equivalent void ratio equation is miscalibrated. Selection of an alternative b value may improve the prediction of strain accumulation for these samples in future work.

The results illustrate the efficacy of the equivalent void ratio concept in predicting the strain response of drained cyclic tests. However, the findings are contradictory to those of Tafili et al. (2024). These authors demonstrated that for samples prepared to the same equivalent void ratio with varying percentages of plastic fines content, the equivalent void ratio method failed to yield a unified response. Furthermore, the results indicated that as fines content increased, the degree of strain accumulation decreased. This contradicts the results presented here, where increased fines content induces greater strain accumulation. Tafili et al. (2024) posited that fines were retained at the contact points of the soil skeleton, thereby providing additional resistance to plastic strain. The results presented here contradict this assumption. With higher fines content, the degree of axial strain accumulation increases, for the same equivalent void ratio. This suggests that the fines within the soil skeleton provide a lower degree of the overall strength of the soil matrix, compared with the results of Tafili et al. (2024). Tafili et al. (2024) tested samples prepared with plastic fines, as opposed to the non-plastic fines used for the present study. The increase in plasticity allows for greater particle adhesion, facilitating the mechanism suggested by these authors. Conversely, the non-plastic fines employed in the present study exhibit lower particle adhesion and are more readily displaced from inter-particle contact points to occupy voids in the soil skeleton, rather than enhancing soil skeleton density. Consequently,in samples with higher fines content, where sand density is reduced, the stress skeleton is less tightly packed, resulting in lower strength.

Despite some variations in the response of samples with differing fines content, the degree of disparity is low. This indicates that, in the case of non-plastic fines, the equivalent void ratio provides a reliable prediction of the strain response.

Figure 5.4 presents the results of an additional series of tests on silty sand samples. The stress ratios applied are consistent with those in the previous tests, though these tests have varying initial mean effective stress p'_0. The results of the benchmark tests indicate that the mean effective stress has a minimal impact on cyclic strain accumulation, with variations in the stress ratio exerting a greater influence (Figure 4.25(b)). Consequently, the predicted results should be similar to the tests with $p'_0 = 200$ kPa presented above (Figure 5.3). In both instances, $p'_0 = 100$ kPa and $p'_0 = 300$ kPa, the same trend is apparent.

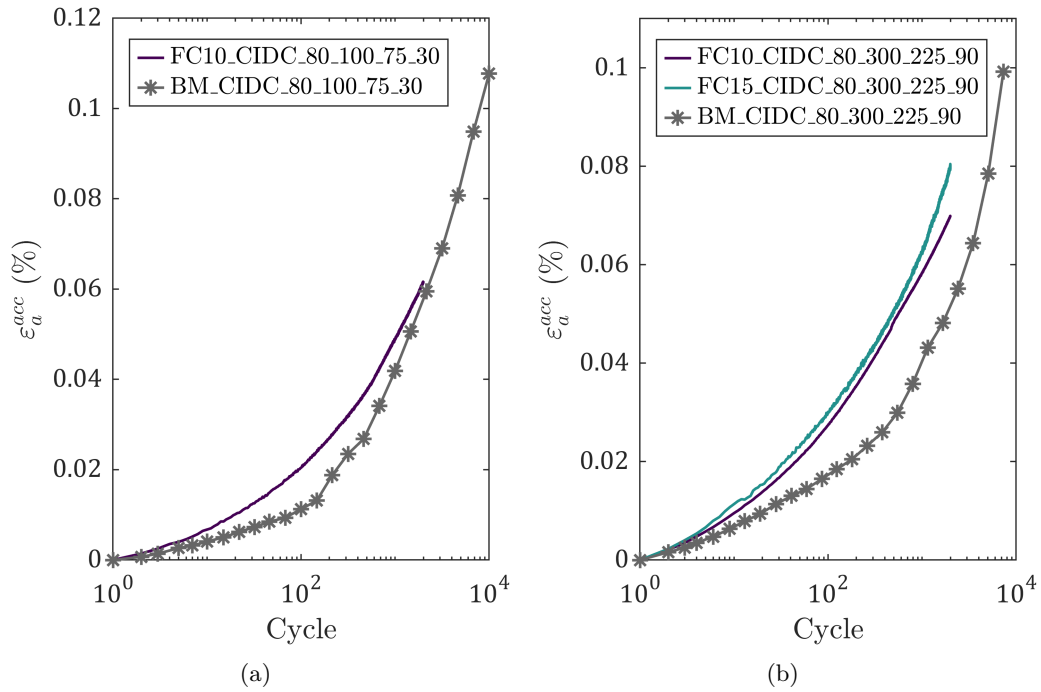

Figure 5.4: Cyclic axial strain accumulation comparison of silty sand samples with benchmark, for $\eta = 0.75$, $\zeta_b = 0.3$, $e^* = 0.58$ at (a) $p'_0 = 100$ kPa, (b) $p'_0 = 300$ kPa

The axial strain accumulation response is comparable between the clean sand benchmark and the fines content tests. Furthermore, in the test with $p'_0 = 300$ kPa (Figure 5.4(b)) the FC= 15% sample exhibits slightly greater strain accumulation than the FC= 10% or clean sample. These results further confirm the efficacy of the equivalent void ratio concept.

The results presented in Figure 5.5 demonstrate further tested conditions. Figure 5.5(a) illustrates the axial strain accumulation response of silty sand samples at FC= 10% and FC= 15% tested in extension ($\eta = -0.5$). Once again, the response of the silty sand samples is shown to be comparable to the relevant clean benchmark test (BM_CIDC_-80_200_-100_60), albeit with a closer agreement for the FC= 10% sample. Figure 5.5(b) shows a silty sample prepared to a lower density, i.e. a higher equivalent void ratio at $e^* = 0.64$. The response is again similar to the relevant benchmark clean sand test. This indicates that the equivalent void ratio is an effective predictor of response across a range of void ratios. This finding is significant as it demonstrates that, despite the potential for a more collapsible fabric with lower density and the presence of fines, the equivalent void ratio accounts for this variability and provides reliable predictions of response.

The results presented in this section provide strong validation of the equivalent void ratio concept for predicting soil response. Across a range of stress ratios, mean effective stresses, and void ratios, the response aligns closely with the clean sand benchmark response for the same value of e^*. However, at elevated fines content, the correlation is less precise. This trend is evident in all tests, with a closer response observed in the $FC = 10\%$ samples and greater strain accumulation in the $FC = 15\%$ samples.

The method employed for predicting the proportion of fines contribution to strength

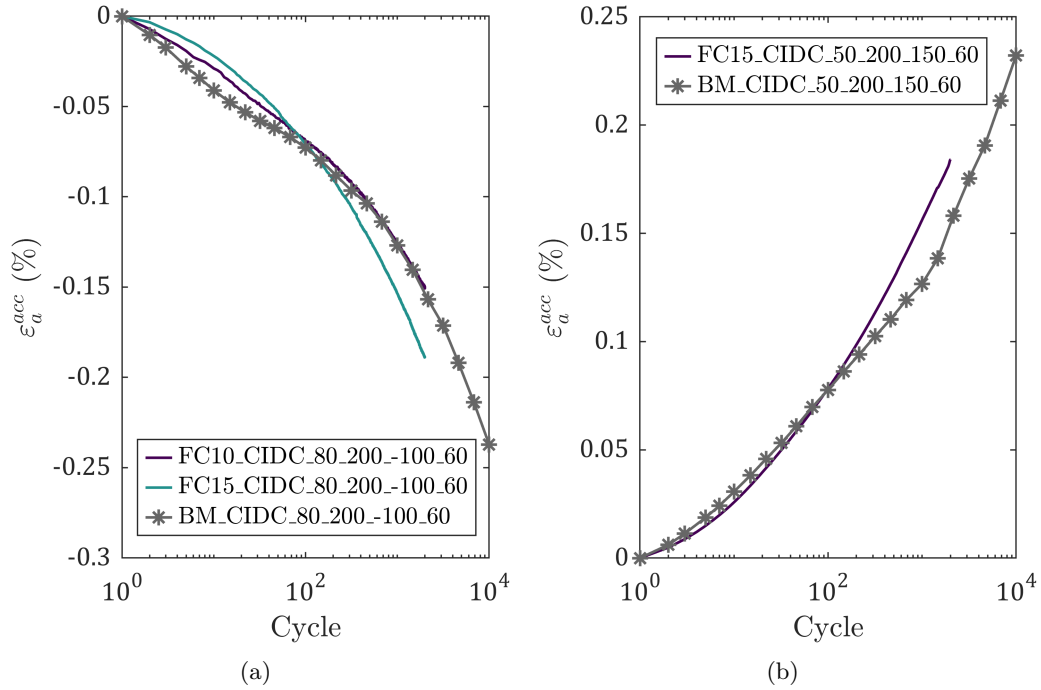

Figure 5.5: Cyclic axial strain accumulation comparison of silty sand samples and benchmark, (a) $p'_0 = 200$ kPa, $\eta = -0.5$, $\zeta_b = 0.3$, $e^* = 0.58$. (b) $p'_0 = 200$ kPa, $\eta = 0.75$, $\zeta_b = 0.3$, $e^* = 0.64$.

was taken from Tamang et al. (2022), as discussed in Chapter 3. The key parameter defining the relative importance of the fines within the sample is the parameter b (Equation (3.2)). Tamang provides an empirical relationship for calibrating b, using the ratio of particle sizes between the sand and the fines. This method was applied directly in the present study for calculating the appropriate proportion of fines to produce samples with the same e^*. Considering no further calibration was performed to refine the value of b, the agreement in results is good.

Global void ratio measurements generally indicate that for low to medium fines contents, increases in fines lead to a decrease in the intercept of the CSL in $e - \ln(p')$ space (J. Yang et al., 2015). The equivalent void ratio is intended to standardise the CSL for test series with varying fines content. Thus, if the equivalent void ratio achieves a unified CSL, it follows that maintaining the stress ratio of cyclic tests should yield a similar response.

The results presented here are applicable for practical purposes. The presence of fines within natural sand deposits is common. Furthermore, the percentage of fines within distinct soil layers can vary considerably. Therefore, the equivalent void ratio parameter can significantly reduce the number of tests required to predict the response throughout the full depth of the soil profile under examination.

Finally, the results demonstrate that the slurry deposition method produced silty sand samples with reliable outcomes. The series of repeat tests presented in Figure 5.3 displayed consistent results with those performed under identical conditions. However, the methodology necessitated the addition of excess fines to compensate for fines lost in the slurry. This limitation may preclude its application in the assessment of deposits for

actual foundation design, as the inclusion of excess fines would entail a significant degree of sample wastage.

5.3 Partial Drainage

This section presents the results of a series of cyclic triaxial tests on clean sand under imposed partially drained conditions. The drainage regime was created by placing a granular filter between the sample drain and the back volume controller, as described in Chapter 3. The tests completed were prepared to the same conditions as the relevant benchmark drained cyclic test on clean sand, therefore results are presented in comparison to this benchmark. Two series of tests were completed with varied resistance to flow within the partial drainage filter. The tests labelled PD_1 have a higher resistance to flow $\approx 5 \times 10^{-3}$ mm^3/s/kPa, and PD_2 have lower resistance $\approx 5 \times 10^{-2}$ mm^3/s/kPa. The results presented focus on the accumulated axial strain ε_a^{acc} and excess pore pressure Δu. Volumetric strain results are presented in Figure 5.6; these results are typical of the remaining tests, and directly linked to the pore pressure response, therefore they are not presented for subsequent tests.

Figure 5.6 presents the sample response of PD1_CIDC_80_200_150_60_a. The initial applied stress path, along with deviator stress against cycle number, is presented in the uppermost plots. These conditions align with the benchmark test BM_CIDC_-80_200_150_60 (Figure 4.21), albeit involving a lower total cycle count. The reduced cycle number was implemented to accelerate the testing throughput. The load history plot displays consistent deviator stress throughout the test, indicative of a minimal change in cross-sectional area. The axial and volumetric strain accumulation is low, consistent with the fully drained benchmark test. Furthermore, the degree of volumetric strain is somewhat limited by the partial drainage filter; therefore, the minimal area change implied by the consistent load is anticipated.

The plot of q vs ε_a depicts a characteristic response to cyclic loading, with high initial strain during the early cycles. During these initial cycles, there is a pronounced degree of ratcheting, evident through open cyclic loops. As the test progresses, the area enclosed within a cyclic loop reduces, and the permanent strain per cycle is significantly reduced. This trend is also observable in the plot of ε_a against cycle number. In this context, the rate of strain accumulation is linear in the semi-logarithmic representation. There are early indications of acceleration in the rate of axial strain accumulation over the logarithmic rate; however, due to the limited number of cycles conducted, this trend is not fully established. The benchmark test began to demonstrate over-logarithmic strain accumulation around 2000 cycles; thus, with additional cycles, this trend is likely to have become more pronounced.

The plot volumetric strain ε_v against cycle number exhibits a response similar to that of the axial strain, although it displays a lower overall accumulated strain by the conclusion of the test. Nevertheless, the cyclic amplitude is markedly lower than the axial

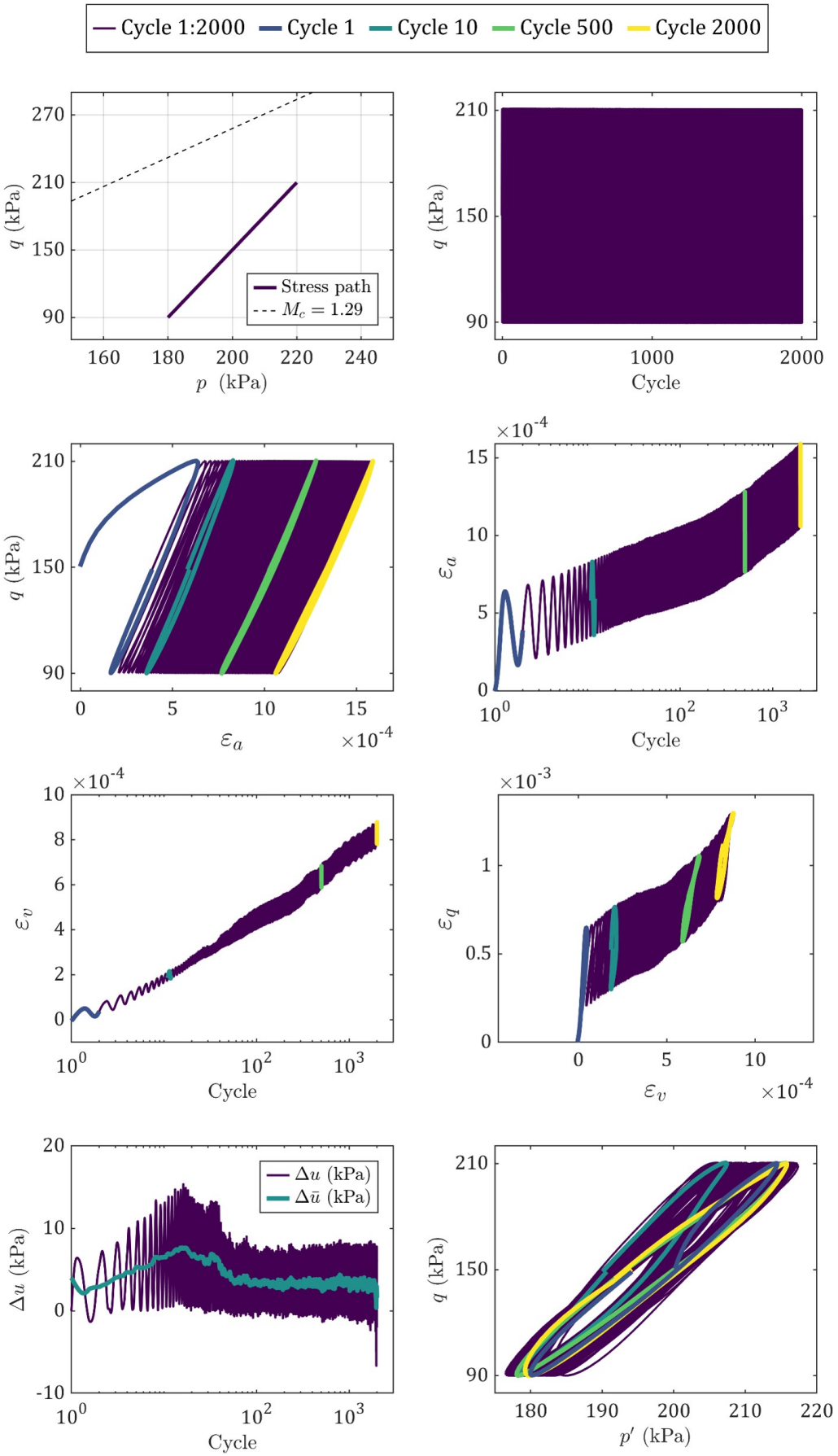

Figure 5.6: Results of the partially drained cyclic triaxial test on clean sand PD1_CIDC_80_200_150_60_a

strain response, especially during the initial cycles. This observation aligns with the test conditions; specifically, the degree of cyclic volumetric strain amplitude was significantly diminished by the presence of the partial drainage filter. The filter reduces the rate of drainage, thereby dampening the high-frequency in-cycle oscillation of volumetric strain. After approximately 50 cycles, the volumetric cyclic strain amplitude rises, although the pattern of volumetric strain accumulation remains linear.

The plot of ε_q against ε_v shows an approximately linear response throughout the test. The gradient of the highlighted cycles of $\varepsilon_q - \varepsilon_v$ increases with cycle number, which corresponds to the higher cyclic volumetric response seen in the plot of ε_v against cycle number.

The pore pressure response is shown in Δu against cycle number. The value of Δu is taken as the $u - u_1$ (the pore pressure at the start of the test), and $\Delta\bar{u}$ (the average cyclic pore pressure) is $\bar{u} - u_1$. The pore pressure response demonstrates initial accumulation in the early cycles, followed by dissipation, which tails off to a constant level of $\Delta\bar{u} \approx 5$ kPa ($r_u = 0.025$). This is a moderate pore pressure response, close to fully drained. The point of constant dissipation, i.e. the point where pore pressure cycles enter a stready state, correlates with the point of increased cyclic volumetric strain response. The point of maximum accumulated excess pore pressure corresponds to a higher accumulated volumetric strain rate, as expected, where the increased differential pressure between the applied back pressure and mean sample pore pressure induces a higher flow rate. During the later cycles, in which the average pore pressure remains constant, this aligns with a consistent rate of flow in the volumetric response in logarithmic space. The steady-state excess pore pressure response is counterintuitive, as the actual rate of volumetric response reveals a reduction in accumulation if plotted linearly. This would imply that the pore pressure should continue to dissipate. However, the actual magnitude of pore pressure response is low; therefore, the pressure differential across the filter is also low. Furthermore, the minimum of the cycles of excess pore pressure is approximately 0 kPa, which may suggest that the stress path inhibits the formation of negative pore pressure and thus maintains the average excess pore pressure above 0 kPa. Additionally, the accumulated axial strain response corresponds to the pore pressure response. As excess pore pressure reduces, the accumulated axial strain rate reduces. The plot of q against p' shows changing stress ratio throughout the test. During cycle 10, when the excess pore pressure is highest, the mean effective stress is reduced. However, during cycle 1 and cycles 500 and 2000, the stress path is similar.

The response presented here aligns with findings reported in the literature. Jostad et al. (2021) conducted a limited number of partially drained cyclic triaxial tests on various sands. The partial drainage condition was established using a filter, adhering to the methodology of Suzuki et al. (2020). The results indicated that the applied cyclic loads induced a pore pressure accumulation response dependent on volumetric strain, filter resistance, and bulk modulus. There was no data provided on shear strain. Nevertheless, across the 100 cycles applied to the samples, the trends for accumulated pore pressure were analogous to the

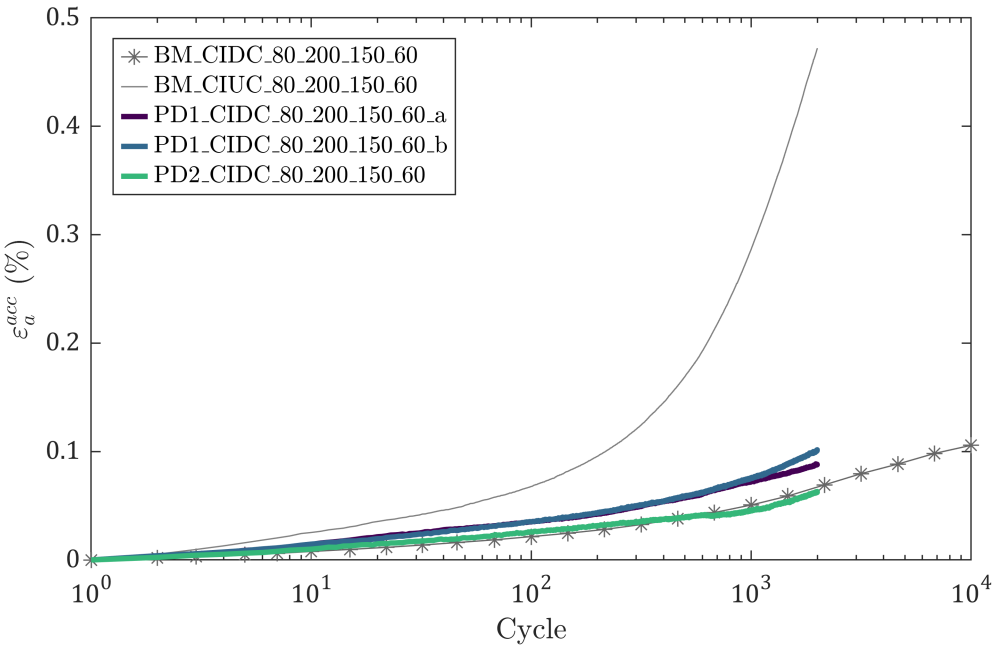

Figure 5.7: Cyclic strain accumulation comparison between partially drained tests and benchmark drained and undrained tests. All tests performed at with same initial conditions and loads, $p'_0 = 200$, kPa $e = 0.58$, $\eta = 0.75$, $\zeta_b = 0.3$.

results presented here.

Figure 5.7 shows the accumulated axial strain response of three partially drained tests conducted under identical loading conditions: two with higher resistance filters - PD1, and one with lower resistance to flow - PD2. These results are compared with the axial strain responses from the drained and undrained benchmark tests, which were also performed under the same loading conditions. The rate of strain accumulation is greater in the partially drained tests with higher resistance to flow; both PD1 tests clearly exhibit greater strain accumulation than the drained benchmark. The PD2 test reveals a response very similar to that of the fully drained benchmark, indicating minimal change for the lower level of flow resistance and induced partial drainage. The highest rate of strain accumulation is observed in the undrained test, while the partially drained results fall between the drained and undrained responses. These findings align with expectations, as reduced drainage leads to increased pore pressure accumulation, decreased mean effective stress and consequently lower stiffness and strength.

The trend of increased strain accumulation in the undrained and partially drained tests exhibits minimal change relative to the drained test in the early stages. The undrained test, characterised by increased accumulated excess pore pressure, demonstrates higher strain accumulation, which begins to increase rapidly during the later stages of the test. The partially drained tests show a moderate increase in strain accumulation throughout the test, resulting in a cumulatively greater degree of strain accumulation at termination.

Figure 5.8 shows the corresponding pore pressure response of the same tests; the drained benchmark test is not presented here as there is no average pore pressure response. The average excess pore pressure $\Delta\bar{u}$ is plotted against the cycle number (with linear x-axis

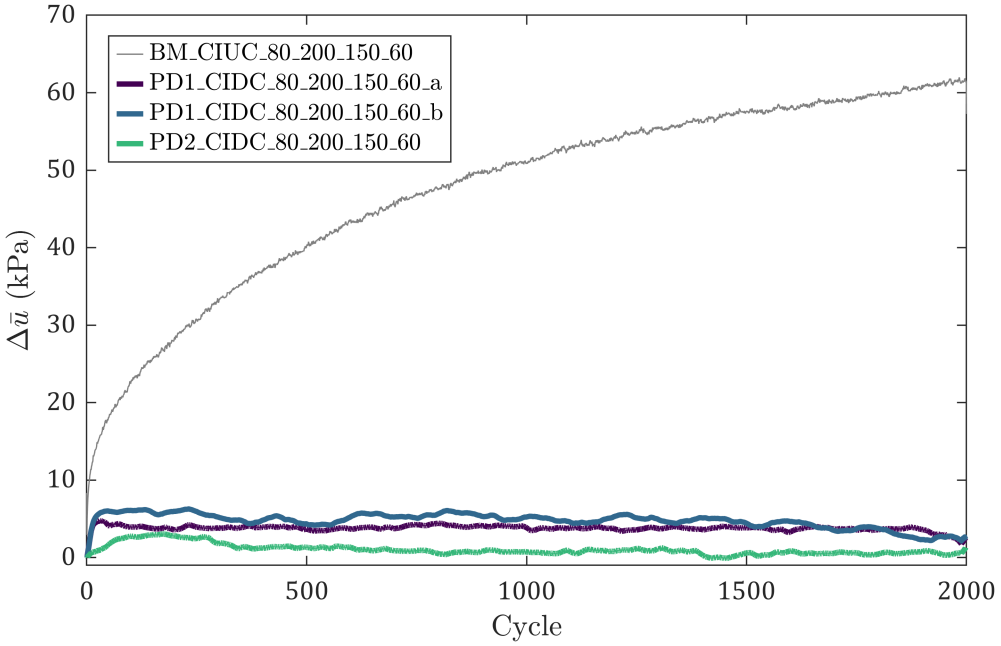

Figure 5.8: Excess pore pressure accumulation for partially drained tests and the relevant undrained benchmark test, $p'_0 = 200$ kPa, $e = 0.58$, $\eta = 0.75$, $\zeta_b = 0.3$.

in this case). For the PD1 tests there is a rapid rise in excess pore pressure, which initially follows a similar gradient of the undrained test, before stopping at $\Delta\bar{u} \approx 5$ kPa. Following the rise there is a slow dissipation phase, however it does not reach $\Delta\bar{u} = 0$ kPa. This aligns with the continuous accumulation of compressive volumetric strain during cycling. During the PD2 test the rate of pore pressure accumulation is slower, reaching a lower maximum, followed by dissipation to $\Delta\bar{u} = 0$ kPa. The initial increase in pore pressure, followed by dissipation or steady response, is due to the volumetric response of the sample. During the early cycles, the sample is far more contractive and collapsible. This is seen in all tests, where the first cycle induces the greatest degree of axial strain. The restricted drainage induces an increase in pore pressure. Following this initial collapsible phase, the rate of strain accumulation, volumetric and axial, decreases rapidly. Therefore, the combination of pore pressure dissipation, and reduced pore pressure accumulation leads to the diversion from the undrained response.

The results of the accumulated axial strain (Figure 5.7), and the excess pore pressure response (Figure 5.8) are linked. The elevated rate of strain accumulation in the undrained condition is attributed to the accumulated excess pore pressure. In contrast, when some flow of pore fluid is permitted in the partially drained tests, the rate of axial strain accumulation is only slightly increased relative to the drained benchmark, where there is no inhibition of pore fluid flow.

Figure 5.9 and Figure 5.10 show the results of further tests within the partially drained test series, at $p'_0 = 100, 300$ kPa, compared with their relevant benchmark. Here, the trends are consistent with those presented above. Lower permeability filters result in higher degrees of excess pore pressure and axial strain accumulation. Additionally, there is a

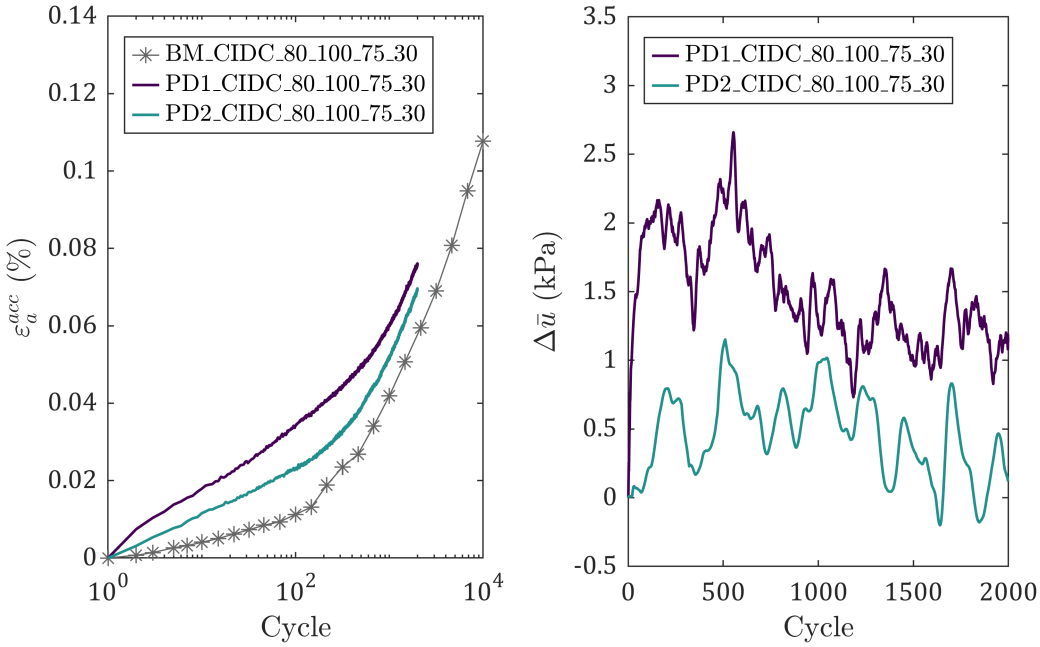

Figure 5.9: Partially drained test results for $p'_0 = 100$ kPa, $e = 0.58$, $\eta = 0.75$, $\zeta_b = 0.3$, showing, (a) axial strain accumulation ε_a^{acc}, and (b) moving mean excess pore pressure $\Delta\bar{u}$.

clearer depiction of varied strain accumulation rates during the PD1 tests. During the contractive phase of the early cycles, the excess pore pressure is highest, which induces lower stiffness and higher axial strain accumulation. As the pore pressure begins to dissipate, the samples densify, and the rate of strain accumulation drops below that of the relevant benchmark test. The low stiffness facilitates faster densification than the benchmark, resulting in a denser, stiffer sample at the same number of cycles. This is combined with lower volumetric strain and excess pore pressure, leading to a reduced rate of strain accumulation compared to the benchmark. This trend is observable in all tests.

Figure 5.11 shows the strain accumulation and pore pressure response of test PD1_-CIDC_80_200_150_90. This test has a higher cyclic amplitude ratio ζ_b than the previous tests; therefore, the rate of strain accumulation, axial and volumetric, is greater. The elevated initial volumetric strain induces a high $\Delta\bar{u}$, which accumulates rapidly. Consequently, the rate of axial strain accumulation is significantly higher than in the benchmark test. Unlike the other tests, there is minimal dissipation, despite the higher accumulated pore pressure. Nevertheless, the rate of axial strain accumulation slows in comparison to the relevant benchmark test.

The pore pressure response of this test is somewhat unexpected. The volumetric strain response of the equivalent drained benchmark test exhibits dilative volumetric strain after approximately 500 cycles. This is due to the stress path crossing the PTL stress ratio. However, there is no dilation evident in the pore pressure response of the partially drained test, as would be anticipated with the onset of dilation. The correspondence between volumetric strain and accumulated excess pore pressure during the test is shown in

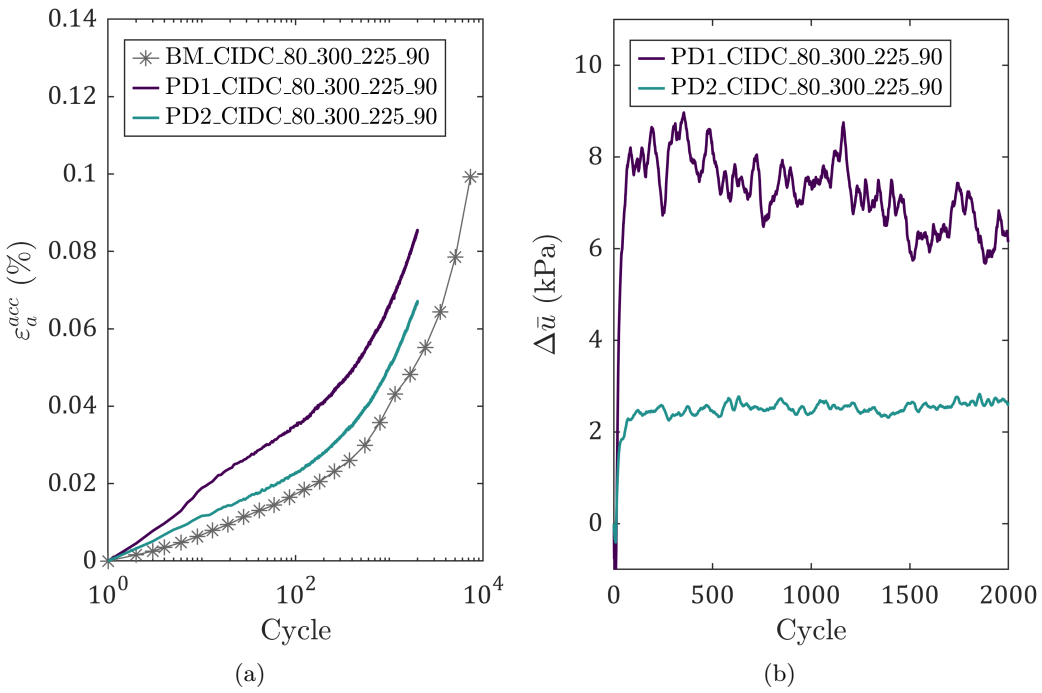

Figure 5.10: Partially drained test results for $p'_0 = 300$ kPa, $e = 0.58$, $\eta = 0.75$, $\zeta_b = 0.3$, showing, (a) axial strain accumulation ε_a^{acc}, and (b) moving mean excess excess pore pressure $\Delta\bar{u}$.

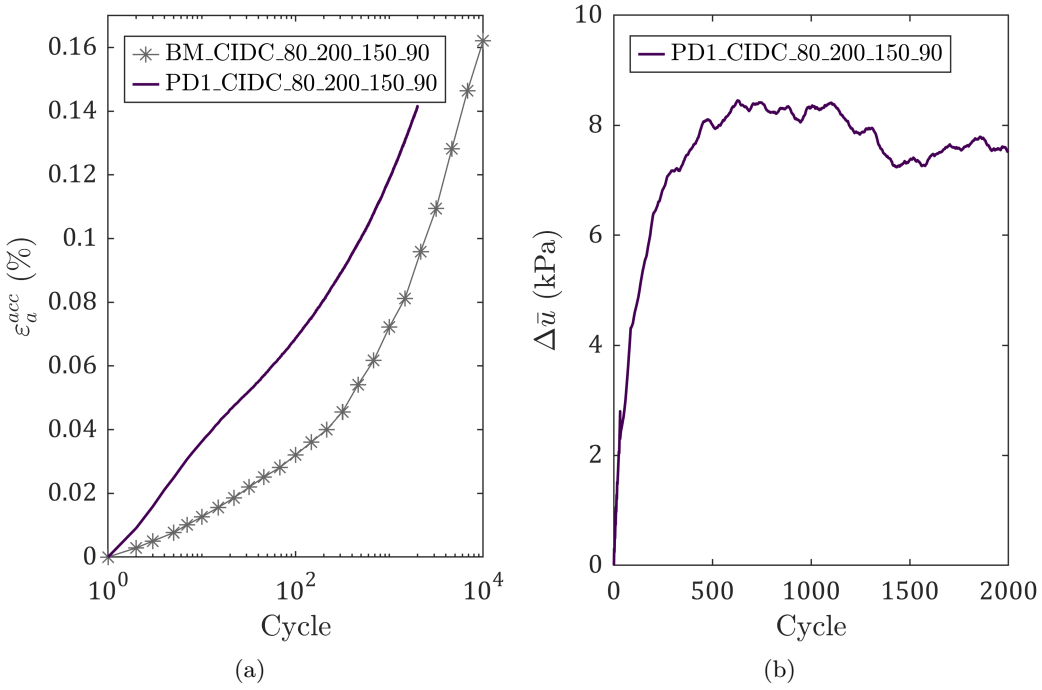

Figure 5.11: Partially drained test results for $p'_0 = 200$ kPa, $e = 0.58$, $\eta = 0.75$, $\zeta_b = 0.45$, showing, (a) axial strain accumulation ε_a^{acc}, and (b) moving mean excess pore pressure $\Delta\bar{u}$.

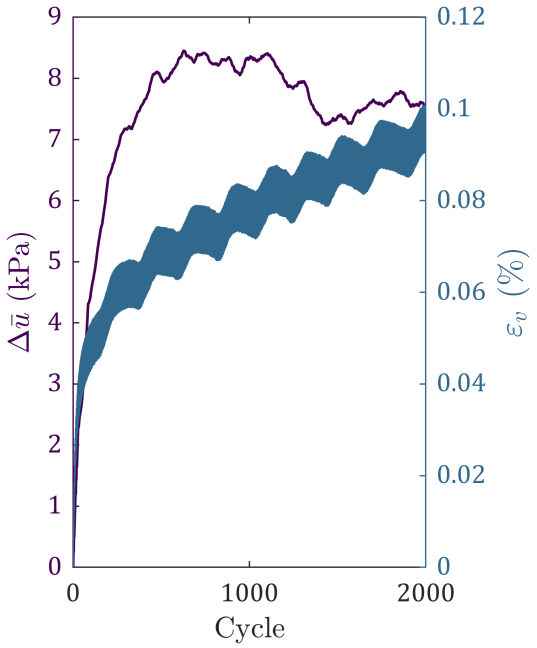

Figure 5.12: Excess pore pressure and volumetric strain response of test PD1_CIDC_80_200_150_90 $p'_0 = 200$ kPa, $e = 0.58$, $\eta = 0.75$, $\zeta_b = 0.45$

Figure 5.12; there is no evidence of dilative behaviour. The rate of contractive volumetric strain remains consistent after the early cycles, explaining the observed lack of dissipation. The absence of dilative behaviour is attributable to the imposition of a partially drained flow regime. In an undrained test with equivalent stress ratios, a continued contractive response of the sample would be expected (Wichtmann et al., 2015).

Figure 5.12 further shows that the rate of excess pore pressure accumulation is proportional to the degree of volumetric strain. Pore pressure dissipation occurred continuously throughout the test, as demonstrated by the accumulated volumetric strain. Consequently, sustaining excess pore pressures necessitates ongoing sample contraction over and above the rate of sample drainage. The volumetric strain measured is external to the sample; thus, the pore pressure developed reflects a degree of volumetric strain that is not accounted for in the volumetric strain measurements. As the drainage from the sample is constricted, when the sample contracts a certain portion of the pore fluid displaced by sample contraction is prohibited from draining from the sample. The effect of this phenomenon is increased pore pressure, as the fluid in the sample becomes additionally compressed by sample contraction. Jostad et al. (2021) illustrates the interplay between pore pressure and volumetric response with Equation (5.1), where $\Delta\varepsilon_{vol,av}$ denotes the total volumetric strain of the sample, both measured and unmeasured. Therefore, the degree of pore pressure accumulation is contingent upon the bulk modulus of the sample and the volumetric strain.

$$\Delta\varepsilon_{vol,av} = \Delta p'/K + \Delta\varepsilon_{vol,acc} \tag{5.1}$$

Figure 5.13 shows the summary of all partially drained tests at $\eta = 0.75$ and $\zeta_b = 0.3$. The mean effective stress varies across the tests; however, the results of the benchmark

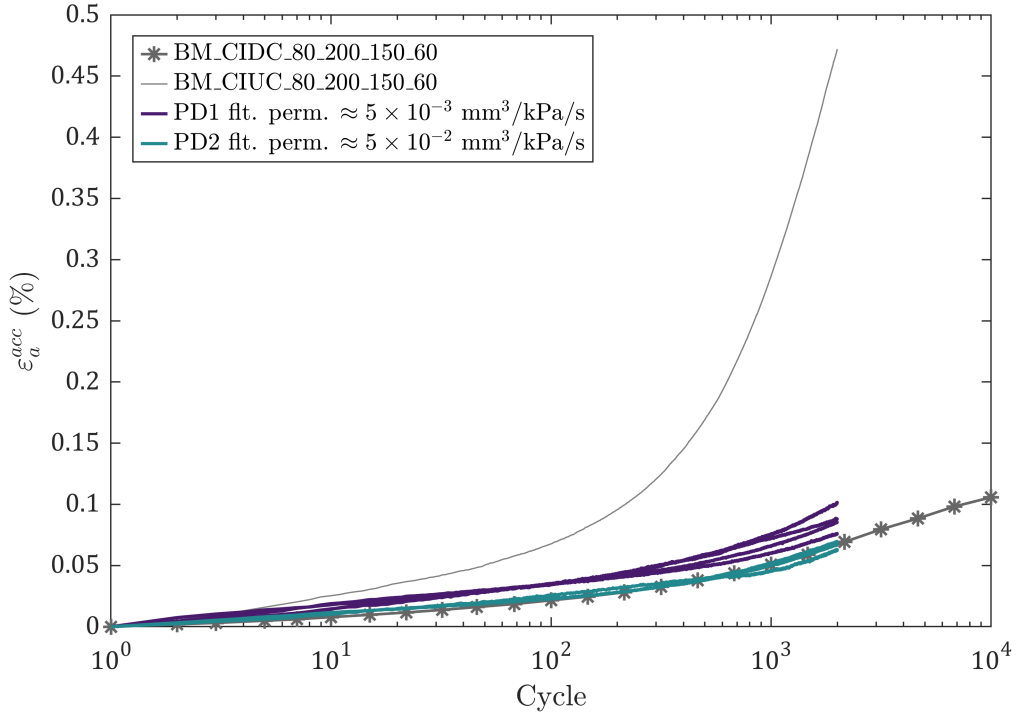

Figure 5.13: All partial drainage tests at $\eta = 0.75$ and $\zeta_b = 0.3$, with drained (BM_CIDC_80_200_150_60) and undrained (BM_CIUC_80_200_150_60) benchmark test comparisons. Although the mean effective stress is varied, results from benchmark tests show this has minimal effect on strain accumulation. When the filter has lower permeability (PD1) the rate of strain accumulation is higher.

testing indicate this has minimal effect on the accumulated axial strain. A clear trend is observed, with increased accumulated strain corresponding to a reduction in filter permeability. The results from this section demonstrate that during partially drained cyclic loading, the positive excess pore pressure is developed across a range of stress ratios. The reduction in effective stress caused by this phenomenon leads to a slight decrease in stiffness. Despite the low permeability of the filter, the minimal volumetric strain during the cyclic triaxial tests performed at this density results in low accumulation of excess pore pressure, with an excess pore pressure ratio of $r_u < 0.01$.

5.3.1 Stiffness effects of partial drainage

This section examines the impact of pore pressure accumulation on the secant stiffness G_{sec} during partially drained cyclic loading. The reduced effective stress caused by pore pressure accumulation results in a decrease in stiffness, which partly explains the increase in strain accumulation.

The results presented in Figure 5.14 illustrate the effect of increased pore pressure on the secant stiffness. The calculation of secant stiffness follows the method demonstrated in Figure 4.23. The findings indicate that in all cases, the initial stiffness is close to G_{max}, followed by a clear drop in secant stiffness at around 10 cycles. This effect coincides with the increase in excess pore pressure. The decline in secant stiffness is anticipated with

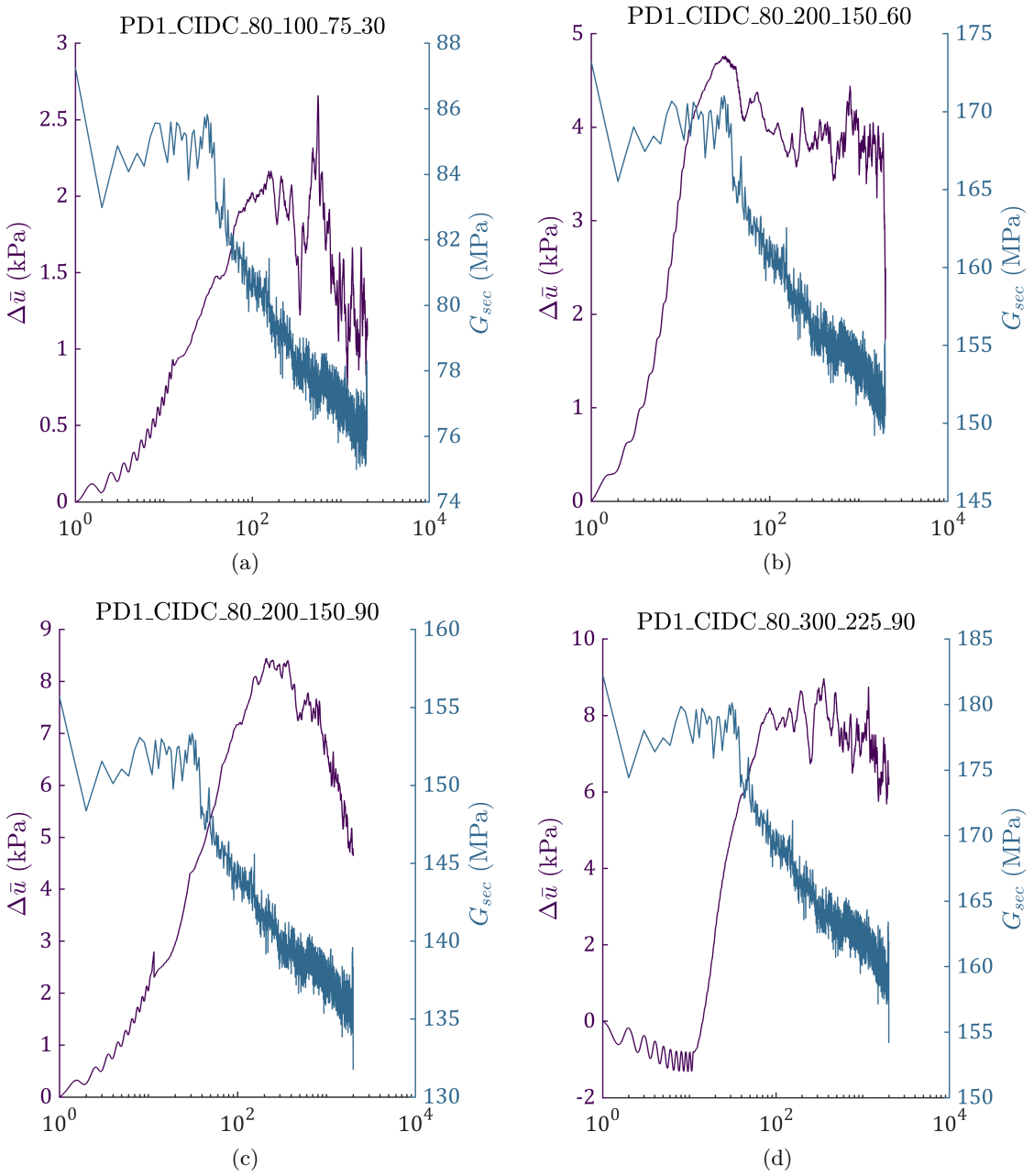

Figure 5.14: Secant stiffness G_{sec} and pore pressure response $\Delta\bar{u}$ in partially drained tests , showing tests: (a) PD1_CIDC_80_100_75_30, (b) PD1_CIDC_80_200_150_60_a, (c) PD1_CIDC_80_200_150_90, (d) PD1_CIDC_80_300_225_90.

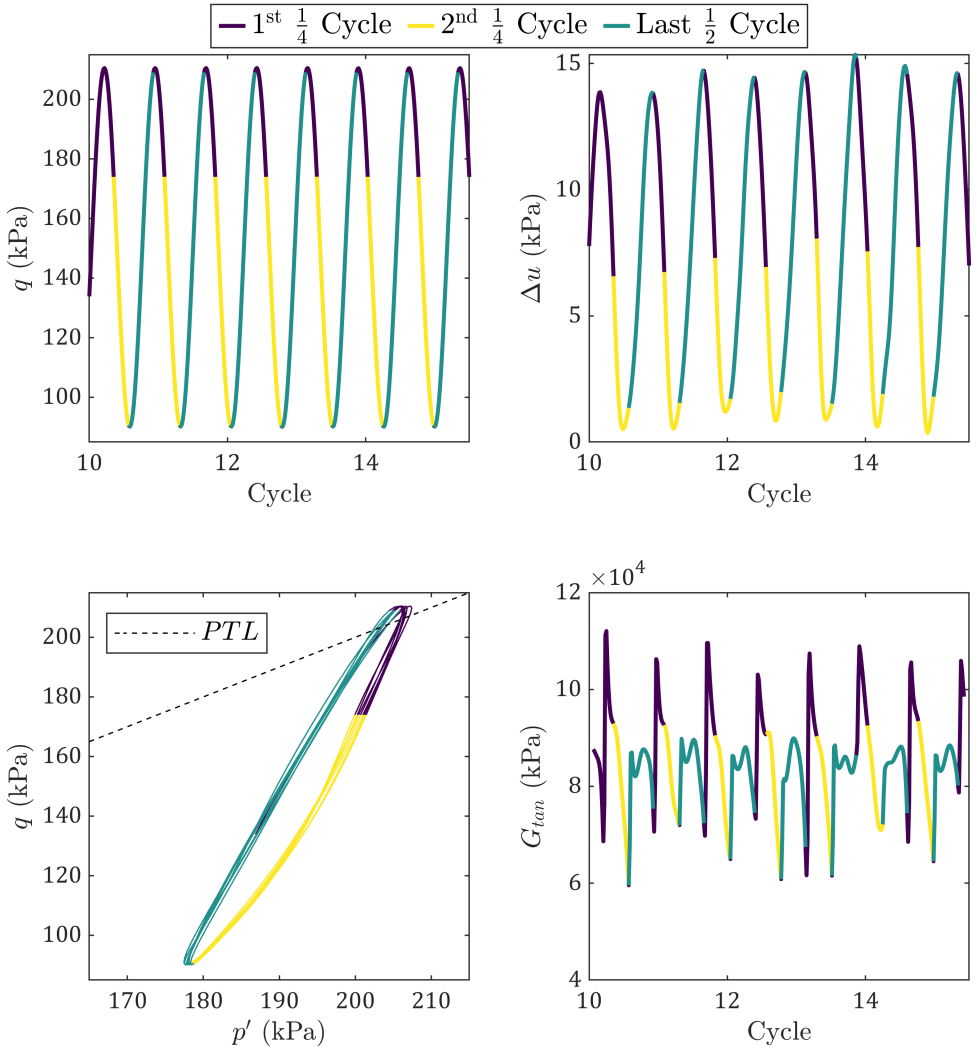

Figure 5.15: Tangent shear stiffness G_{tan} and pore pressure response of characteristic partially drained test PD1_CIDC_80_200_150_60_a

increasing cycle number, as evidenced in the literature with the characteristic S-shaped curves of G_{sec} versus γ. However, the significant drop observed at cycle 10 suggests a causal link between pore pressure and stiffness.

Figure 5.15 shows the tangent shear stiffness response of the partially drained test PD1_CIDC_80_200_150_60_a. The stress path response, q vs p', indicates that during cycles 10-15, where the peak pore pressure response was observed (Figure 5.6), the mean effective stress was significantly reduced. The stress path is centred around an average of $\approx$ 190 kPa, compared with the 200 kPa target. The graph of G_{tan} against cycle number demonstrates that during the forward load cycle, where the excess pore pressure peaks, the tangent shear stiffness exhibits reduced peaks. The equivalent results from the clean drained test (Figure 4.33) reveal a considerably larger peak in the stiffness response in the mid-range of the forward load cycle. The reduction in stiffness in this midrange coincides with the left-hand side of the stress path cycles, representing lower mean effective pressure. The stress path of the drained test did not show this variation in mean effective stress

between the forward and reverse load. This accounts for the loss of the peak stiffness response in the mid-range of the cycles in Figure 5.15. Furthermore, the cycles of tangent stiffness are centred around a lower midpoint. Therefore, overall, the stiffness of the partially drained test is lower, correlating with the increase in accumulated axial strain.

5.4 Partially drained silty sand results

This section presents the results of a series of tests on partially drained silty sand. The test methodology incorporated the same fines content and partial drainage techniques, with samples having matched e^* to drained and partially drained tests. The samples were all prepared to FC= 10% and $e^* = 0.58$, and subjected to cyclic stress ratios of $\eta = 0.75$ and $\zeta_b = 0.3$ with varied mean effective stress. The results are presented against the relevant benchmark drained and undrained tests, as well as partially drained tests on clean sand.

Figure 5.16 presents the results of the partially drained silty test FC10_PD1_80_-200_150_60 against the results of the corresponding drained, partially drained, and undrained tests on clean sand. Figure 5.16(a) depicts the accumulated axial strain against cycle number, and Figure 5.16(b) shows the average excess pore pressure. The drained silty sand test, which exhibited very similar results to the clean drained test, is not presented for clarity. The total accumulated axial strain is significantly higher than both the benchmark drained test and the clean partially drained test. Additionally, the early cycles exhibit greater accumulation than the clean undrained test. Examining the pore pressure response, the initial cycles rapidly accumulate excess pore pressure, exceeding that observed in the undrained clean test. Following the accumulation phase, there is an initial rapid dissipation, followed by slower dissipation down to $\Delta\bar{u} \approx 5$ kPa. The rate of axial strain accumulation is linked to the pore pressure response, with the highest rate of accumulation occurring at the peak of excess pore pressure. However, despite dissipation, the strain accumulation rate remains above the clean sand partially drained response.

Figure 5.17 shows the complete pore pressure response, along with the average overlay, for the clean partially drained and undrained tests, as well as the partially drained silty test. In the initial stages, the silty sample displayed the highest magnitude of cyclic pore pressure oscillation. The degree of oscillation diminished throughout the test for the silty sand sample. In contrast, the undrained test on clean sand maintained a similar magnitude of oscillation throughout the duration of the test.

The results of the remaining partially drained silty sand tests, FC10_PD1_80_-100_75_30 and FC10_PD1_80_300_225_90 depict similar outcomes. Figure 5.18 and Figure 5.19 illustrate the response of the comparable test conducted at $p'_0 = 100$ kPa. The results demonstrate a more moderate excess pore pressure accumulation, accompanied by a corresponding increase in axial strain. The pore pressure oscillation response of the silty sand sample in Figure 5.19 is lower than that of the clean sand test under equivalent loading conditions, despite a higher average response. This trend mirrors the earlier test, characterised by rapid pore pressure accumulation in the initial phase, followed by gradual

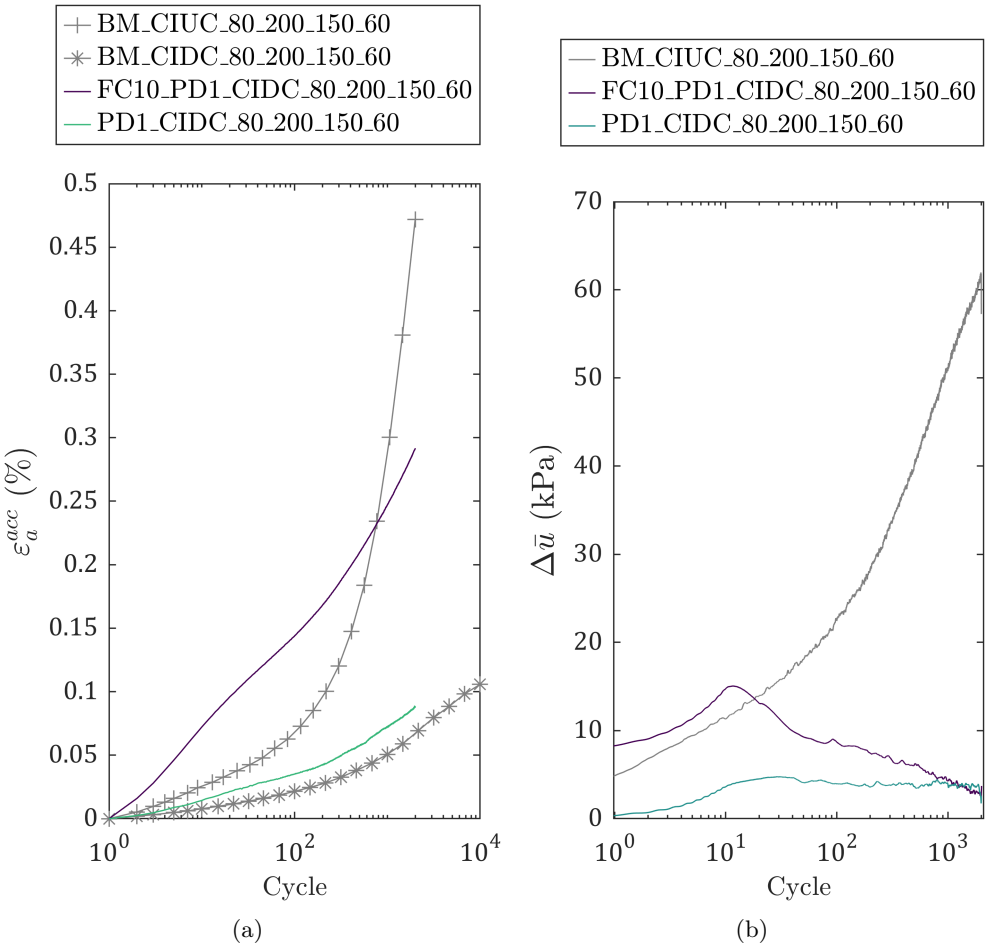

Figure 5.16: Partially drained test results for $p_0' = 200$ kPa, $e^* = 0.58$, $\eta = 0.75$, $\zeta_b = 0.3$, showing, (a) axial strain accumulation ε_a^{acc}, and (b) moving mean excess pore pressure $\Delta\bar{u}$.

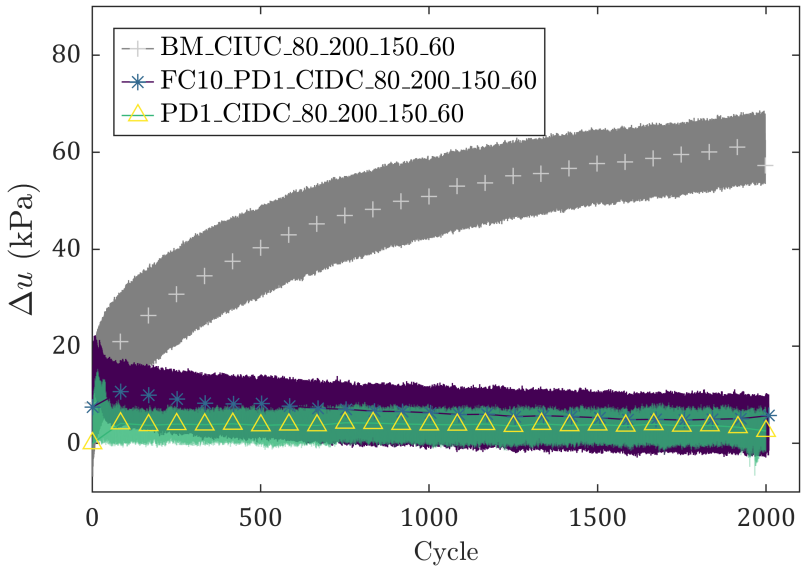

Figure 5.17: Full pore pressure response of partially drained silty sample FC10_PD1_80_200_150_60 and clean partially drained and undrained comparisons

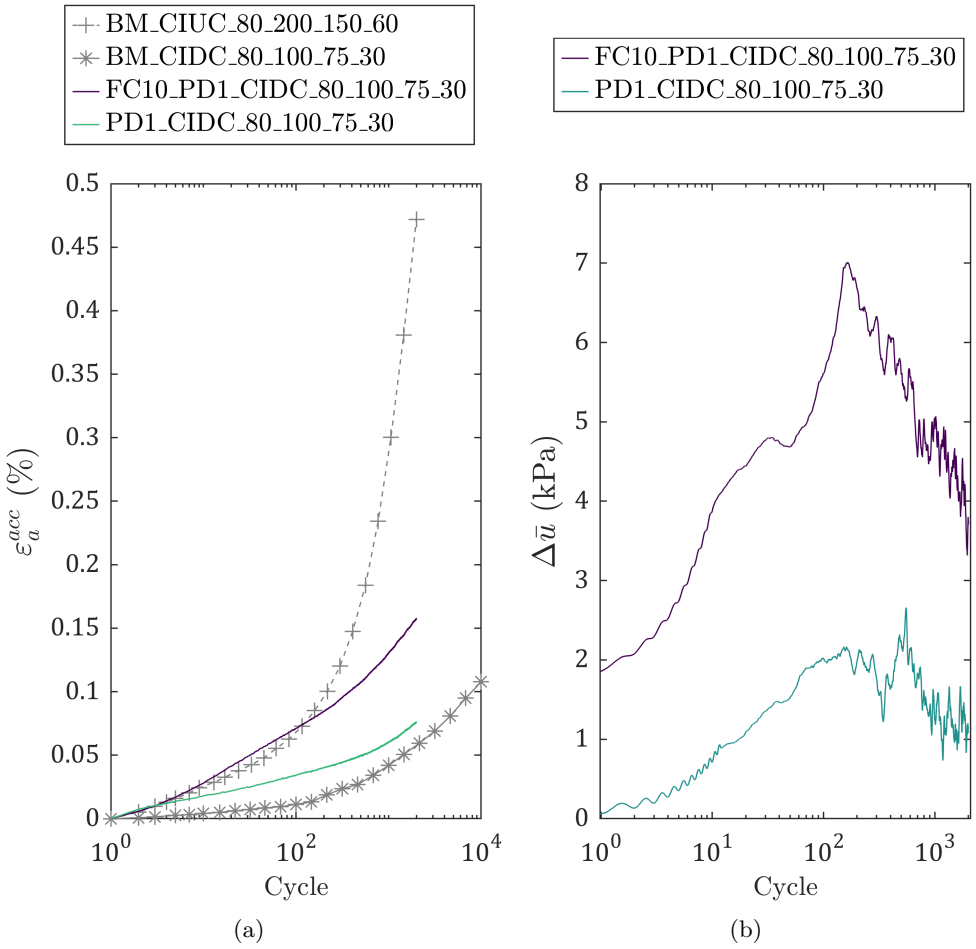

Figure 5.18: Partially drained test results for $p'_0 = 100$ kPa, $e^* = 0.58$, $\eta = 0.75$, $\zeta_b = 0.3$, showing, (a) axial strain accumulation ε_a^{acc}, and (b) moving mean excess pore pressure $\Delta\bar{u}$.

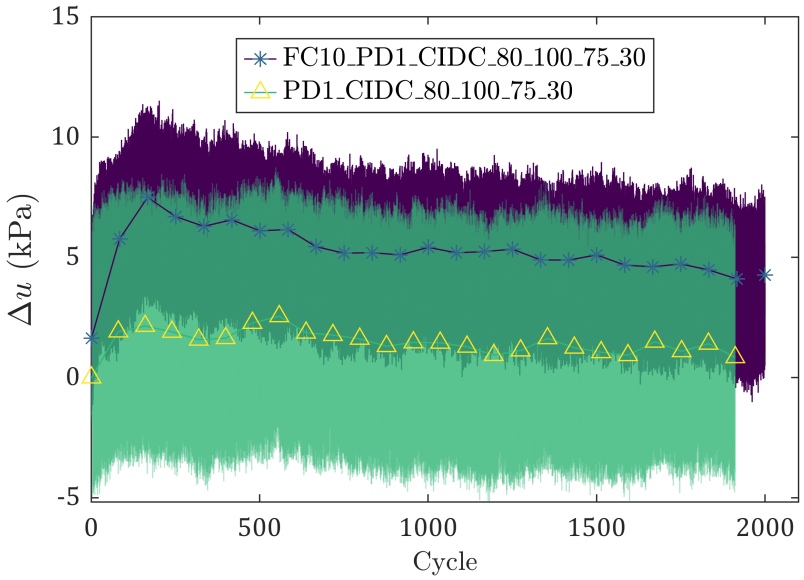

Figure 5.19: Full pore pressure response of partially drained silty sample FC10_PD1_80_100_75_30, with clean partially drained comparison.

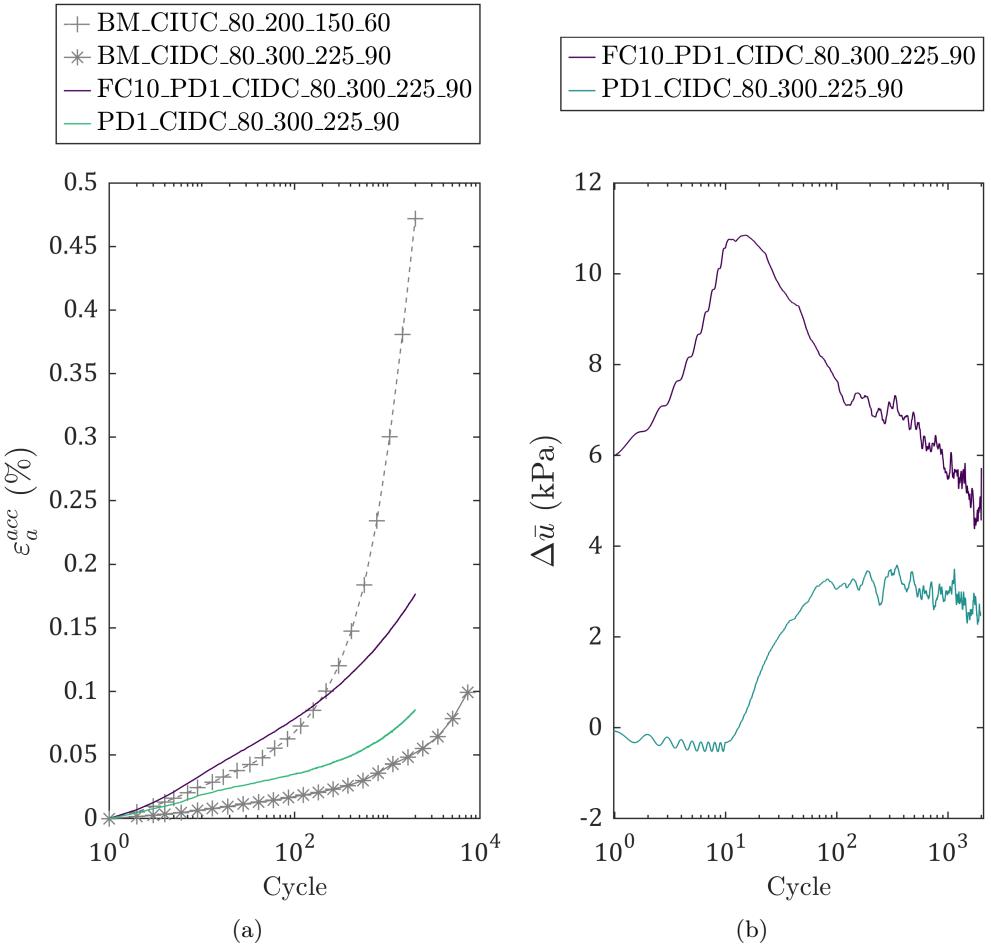

Figure 5.20: Partially drained test results for $p_0' = 300$ kPa, $e^* = 0.58$, $\eta = 0.75$, $\zeta_b = 0.3$, showing, (a) axial strain accumulation ε_a^{acc}, and (b) moving mean excess pore pressure $\Delta\bar{u}$.

dissipation. The results from the $p_0' = 300$ kPa test, Figure 5.20 and Figure 5.21, again exhibit similar conclusions. The outcomes of these tests are consistent in terms of axial strain accumulation, with $\varepsilon_a^{acc} \approx 0.16\%$ observed after 2000 cycles.

It is evident that the partially drained response is more onerous for silty sand samples. Although the clean and silty sand samples exhibit similar volumetric strain in the drained cyclic tests, the amount of pore pressure accumulation is significantly higher. This induced pore pressure response results in a reduction in stiffness, leading to a more contractive response than that observed in clean sand samples. This phenomenon is attributed to the lower number of sand particles per unit volume of the sample. During partially drained loading, the silty sand samples demonstrate a greater tendency to contract due to the collapsible fabric. This results in higher levels of pore pressure accumulation owing to the increased contractive strain. These findings align with results in the literature indicating a greater potential for liquefaction of silty sand samples (Porcino et al., 2017). However, the implication is that the drainage regime in potentially partially drained cases becomes more important when fines are present.

The pore pressure response of the partially drained silty sand tests reveals a highly

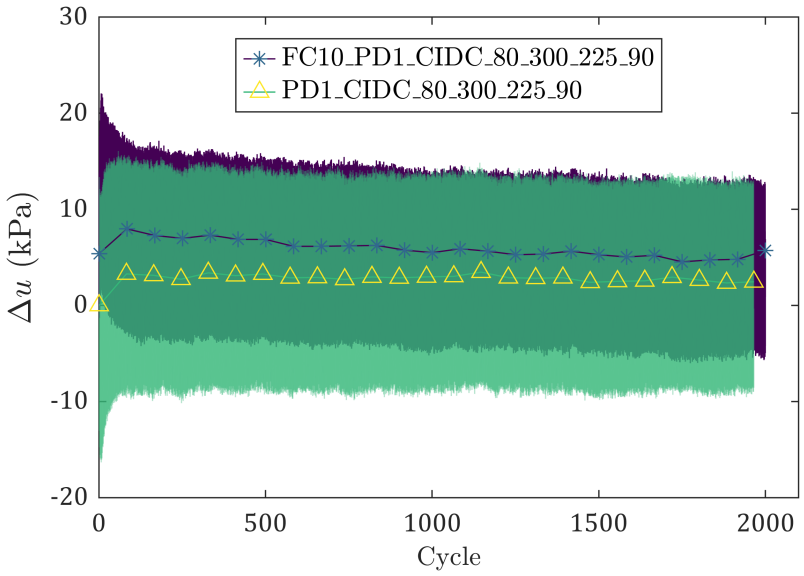

Figure 5.21: Full pore pressure response of partially drained silty sample FC10_PD1_80_100_75_30, with clean partially drained comparison.

collapsible fabric. The samples were prepared to the same equivalent void ratio e^* as the fully drained silty tests, which did not exhibit the same collapsible behaviour. The onset of excess pore pressure development within the sample likely disturbed the fines, permitting a greater degree of contraction. In the early phases of the test, this induced higher levels of pore pressure, resulting in increased contraction and pore pressure response. As the sample densified into a new structure, the degree of pore pressure accumulation decreased, leading to a greater degree of dissipation than accumulation.

The method of applying a partially drained condition, utilising a granular filter to restrict flow, has a varied impact on the sample. When the contractive strain is low, the degree of drainage required to maintain drained conditions is also low. Conversely, if the contractive volumetric strain is higher, the required degree of drainage increases, resulting in a higher pore pressure response and consequently greater contraction in the 'more undrained' sample. Thus, minor changes in the strain rate can have a multiplicative effect, with increased strain and increased excess pore pressure occurring simultaneously in a coupled response. This leads to significant differences in strain accumulation and pore pressure development, as evidenced in Figure 5.16.

Comparing the results of the partially drained and drained silty sand samples, the equivalent void ratio framework was unable to accurately unify the response for these cases. Results in the literature examining the use of the equivalent void ratio concept for undrained conditions have produced varied conclusions. Increases in fines content at the same global void ratio can enhance or diminish the resistance to liquefaction (Xu et al., 2021). However, results from multiple studies demonstrate that the use of the equivalent void ratio e^* generates a unified cyclic resistance curve (Hsiao et al., 2016; Huang et al., 2011; Porcino et al., 2017; Qadimi et al., 2014; Rahman et al., 2008; Xu et al., 2021). Xu et al. (2021) examined the impact of average particle size on the resistance to

liquefaction at varied fines content. The results showed a lower CRR_{15} (cyclic stress ratio for liquefaction after 15 cycles) value at higher fines content. However, when analysing the results normalised with e^*, the cyclic resistance curves are unified. The chosen value of the parameter b was calibrated specifically for the sand in use, rather than the empirical method implemented in this thesis. This suggests that soil-specific calibration of the b value would facilitate better prediction of the response regarding the results of this thesis. However, the value of b is clearly sensitive, posing challenges for effective calibration.

The results of the drained tests on silty sands exhibited good consistency with the results of the drained clean sand tests. Furthermore, within the partially drained tests, the strain accumulation response is highly sensitive to the pore pressure response; therefore, minor changes in the effective void ratio e^* would significantly impact the predicted strain. The results of the partially drained silty sand tests suggest a response positioned between the drained clean sand results for $e = 0.58$ and $e = 0.62$. Given the marginal increase in axial strain response caused by partially drained conditions, the equivalent void ratio would likely be closer to that of the denser sand. Therefore, the minimal change in equivalent void ratio that is predicted to induce a similar response indicates that small alterations to the b value can induce significant changes in axial strain response. In the present tests the absolute magnitude of strain accumulation is small after 2000 cycles ($\varepsilon_a \approx 0.15\%$). Therefore, the effects of varied strain accumulation could be considered less critical than achieving a reasonable overall prediction using the default method for selecting b.

5.5 Summary

This chapter presented tests examining the impact of partial drainage on clean and silty sand samples. The initial drained cyclic tests on silty sand samples indicated that the rates of volumetric and axial strain accumulation are comparable in samples prepared to the same equivalent void ratio e^*. The selected b value for use in the equivalent void ratio equation (Equation (3.2)) provided a better correlation at lower fines content. The value of b was derived from an empirical relationship found in the literature. However, this value can be calibrated for a specific soil using monotonic tests on samples with varying fines content. If this procedure were implemented, it could have yielded improved results. Considering the additional testing required for this, the relatively consistent results achieved were sufficiently satisfactory in the drained cyclic case.

The results of the benchmark fully undrained test on clean sand exhibited increased axial strain accumulation compared to the equivalent fully drained test. However, the excess pore pressure ratio reached $r_u \approx 0.3$ after 2000 cycles, thus the sample did not reach failure. The findings indicated that the strain accumulation significantly exceeded that of the fully drained case; however, the rate of strain accumulation remained moderate. The imposed stress path played a critical role in the resistance to liquefaction.

Tests examining the impact of partially drained conditions demonstrated an increase in strain accumulation as the drainage regime became more restricted, i.e. approaching

the undrained state. Results indicated a higher degree of axial strain accumulation for all tests conducted with the less permeable filter (PD1). The axial strain response was intermediate between the fully drained and fully undrained responses. Volumetric strains for all tested samples in the benchmark and partially drained conditions were generally low ($\varepsilon_v \approx 0.08\%$). Consequently, despite the restricted drainage flow, the excess pore pressure build-up remained low, not differing greatly from the response observed in the fully drained scenario. However, as anticipated, the extent of excess pore pressure accumulation correlated directly with the permeability of the filter.

The case of the high cyclic amplitude loading with filter PD1 observed in Figure 5.11 exhibited significantly different axial and volumetric strain accumulation compared to the relevant fully drained case. The drained case showed dilative volumetric strain in the later cycles, which was not observed in the partially drained case despite crossing further over the PTL. Both axial and volumetric strains were purely compressive, leading to a solely positive pore pressure response. It is possible that the lower mean effective stress permitted the sample to continue exhibiting contractive behaviour. Moreover, the test concluded after 2000 cycles, prior to the drained test demonstrating shearing-induced dilation; thus, this behaviour may have been observed had the test been allowed to continue.

In all cases, the accumulated excess pore pressure response was positive, despite negative cycles of pore pressure during unloading and tests crossing the PTL. This behaviour aligns with observations reported in the literature, where partially drained cyclic element tests demonstrate only stiffness reduction and positive pore pressure accumulation (Frick et al., 2025; Jostad et al., 2021).

Results examining the effect of partial drainage on the cyclic secant shear modulus, G_{sec}, demonstrated a moderate influence of excess pore pressure on stiffness. During the initial phases of cycling, where volumetric strain and pore pressure accumulation remained low, the stiffness response remained unchanged. However, as the excess pore pressure increased, there was a significant decline in secant stiffness, which continued to decrease throughout the test. This effect was moderate, corresponding with a moderate increase in accumulated axial strain ($\varepsilon_a \approx 0.15\%$ for the partially drained test compared to $\varepsilon_a \approx 0.1\%$ in the relevant fully drained test).

The partially drained tests on silty sand samples exhibited significantly different results compared to the clean sand samples. Despite similar response in the fully drained tests on samples prepared to the same equivalent void ratio, the tests with partial drainage showed greater strain accumulation in the silty sands. The results showed high pore pressure accumulation at first, with a response that matched or exceeded the undrained clean sand benchmark, which then dissipated quickly due to the high pressure differential across the filter. The disparity in pore pressure response can be attributed to a more collapsible and unstable fabric in the silty sand samples. The highly contractive fabric of the silty sand samples caused a rapid initial pore pressure response, leading to higher strain accumulation. Following the contractive phase the pore pressure dissipated, and the sample densified. The samples then exhibited a stiffer response, although still reduced compared to the clean

sand samples. The lack of recovery in stiffness can be attributed to the maintained excess pore pressure, and continuous accumulation of volumetric strain. The results indicate that the chosen value of b for determining the equivalent void ratio did not yield accurate results in the partially drained case. This is in spite of the fact the drained silty sand tests showed close agreement with the drained clean sand results. This highlights the increased difficult in calibrating the to equivalent void ratio parameters for use in partially drained conditions.

Chapter 6
Centrifuge Testing of Monopiles in Congleton Sand: Methodology

The following chapter presents the methodology used for the completion of the campaign of centrifuge tests. This chapter outlines the test design procedure, including the constraints and requirements of the campaign. Details are provided regarding the equipment and preparation procedures employed, encompassing the centrifuge, sand, instruments, model pile, and saturation. Finally, the test programme is described, detailing the loads applied, control systems, testing schedule, and data management.

6.1 Centrifuge test design

The following section outlines the design process for the centrifuge experimental campaign. The design process involved developing the aims of the experiments and identifying the requirements and constraints of the tests.

6.1.1 Objectives of the experimental campaign

The primary aim was to investigate the response of new-generation monopiles to cyclic loading. The prototype monopile diameters of interest were D_{p}= 10, 12, and 14 m. As discussed in Section 1.1.1, these diameters are representative of several OWT monopiles currently being installed or planned in the near future. Within this aim certain specific research objectives were targeted. Firstly, the experimental campaign sought to investigate a non-dimensional drainage scaling factor that quantified the relationship between loading period, soil properties, and monopile geometry for predicting soil drainage response. Secondly, the current project examined the effects of drainage on the cyclic response of monopiles during operational loading, particularly concerning the values of D and L/D relevant to new-generation monopiles. Finally, the experimental campaign assessed the response of large-diameter monopiles to storm loading.

As previously discussed, the increasing size of OWT foundations is likely to cause a shift in the drainage regime of the soil surrounding the monopile. The impact of changes in diameter is not fully understood, particularly regarding cyclic loading; therefore, this experimental campaign aimed to investigate this phenomenon.

The scaling factor $MkT/\gamma_w D^2$ (Klinkvort et al., 2018) can provide a useful means of estimating the drainage regime for a given loading case. However, this has not been verified experimentally; therefore, a key aim of this campaign was to perform a parametric investigation of the scaling factor. The soil conditions remained consistent throughout

all tests, but the soil permeability, k (via the pore fluid viscosity), loading period, T, and diameter, D were varied. Further to the drainage factor investigation, the results of each cyclic test provide standalone insight into the response of the soil, particularly the drainage response. Load history is also an important factor in the response of a foundation system to cyclic loads. This campaign included repeat tests and tests of increasing amplitude to examine the impact of load history on foundation response.

The diameter of the prototype examined could be varied by altering the model monopile diameter, D_{m}. This campaign used two model piles of $D_{\mathrm{m}} = 83$ mm and 100 mm. By applying the same normalised load to the pile, it was possible to directly investigate the effect of pile diameter on soil response.

The loading period, T, was examined. To scale the loading period in centrifuge tests to match reality, T is scaled 1:1/η, where η (g) represents the scaling factor resulting from the centrifugal acceleration (Table 2.1). Additionally, to examine the drainage factor, T could be further varied while maintaining all other parameters for direct investigation.

Finally, permeability, k, affects the drainage regime around a foundation. To modify permeability, the viscosity of the pore fluid can be controlled. Seepage in centrifuge tests scales at 1:η. Therefore, to achieve consistent scaling with dynamic time (Table 2.1), the pore fluid must have a viscosity of $\eta\mu_w$, (μ). Moreover, it is possible to further adapt the apparent permeability by modifying the viscosity of the pore fluid beyond the requirements for scaling. This approach allows for a direct examination of permeability within the drainage scaling factor.

The sand used in these tests was Congleton HST-95 sand, tested at the element level in Chapters 4 and 5. The primary density of interest within the triaxial campaign was $D_r = 80\%$, which reflects the most commonly found conditions in the North Sea (Section 3.2). The centrifuge tests also targeted a density of $D_r = 80\%$. Congleton sand is a naturally occurring deposit in the north-west of England, with a morphology that closely resembles that found in many deposits in the North Sea (Figure 3.5).

The campaign was designed to allow investigation of monotonic and cyclic loading on new-generation monopiles. To investigate the monotonic response, a displacement controlled pushover test was employed. The cyclic tests examined both the response to idealised loading and realistic storm loading. For the idealised soil response, uniform sinusoidal displacement was imposed. For storm loading, a simulated load time history of a storm event was imposed.

6.1.2 Centrifuge test requirements

The following section outlines the requirements and consequent design considerations for the experimental campaign.

In order to investigate large diameter monopiles, the prototype diameter had to be maximised. Firstly, this was achieved through the selection of the largest model that did not introduce too significant boundary effects. Secondly, the scaling factor η was maximised to achieve the largest possible prototype diameter. The beam centrifuge was capable of

providing acceleration of up to 250g, but the dynamic actuator was rated up to 100g which limited the possible value of η.

The total pile length was required to reach $8D$, with an embedded depth, L, of $3D$ and an eccentricity, e, of $4D$, plus an additional length D above the loading point for the allowance of settlement and the attachment of a mass. This pile geometry corresponds to many of the monopiles currently being installed (Gaertner et al., 2020), as well as the field test piles of the PICASO project (Byrne et al., 2020*a*). Furthermore, to facilitate loading via the actuator, the pile was required to extend above the top surface of the strongbox.

To record the conditions of the pile and the surrounding soil, the pile needed to be fitted with sensors. The pile mounted sensors included PPTs, accelerometers, and strain gauges. These sensors could be mounted internally or externally, each offering specific advantages. The pile geometry was designed to accommodate the installation of these sensors.

6.1.3 Centrifuge test constraints

The first constraint to consider is the maximum value of the scaling factor, η, that can be applied. The maximum allowable acceleration was 100g; however, this is not the only limitation on η. When increasing η, the pore fluid viscosity and loading period must be scaled accordingly. Pore fluid viscosity scales at 1:η, and loading period scales at 1:1/η. There are two considerations for pore fluid: the maximum viscosity that can feasibly be attained and the time required to saturate the model. The chosen viscous fluid, an aqueous methyl-cellulose solution, allows for a high viscosity. However, the difficulty of preparing a consistent and smooth solution increases with viscosity. Saturation time correlates directly with viscosity. The predicted saturation time, considering the maximum allowable applied head and soil permeability, was around six days with a 100cSt solution. Our allocated time in the centrifuge lab was limited; therefore, this would be impractical and a lower scaling factor had to be considered. The scaling of T in line with η required the use of a dynamic actuator. Using $\eta = 100$ would have necessitated the application of loads at up to 80Hz. This frequency exceeded the tested range of the actuator available. The inertial effects were considered in the data analysis (Section 7.4.1). Furthermore, at such high frequencies, inertial effects could become dominant. Considering the above, it was decided to carry out tests at $\eta = 50$, which led to a predicted maximum saturation time of three days, and a maximum loading frequency of 45 Hz.

Having set η at 50g, this informed the design process for the pile geometry. As discussed, the prototype dimensions depend on the model dimensions and η. To test prototypes of up to $D_\mathrm{p} = 14$ m, as outlined in the experimental aims, a model monopile with a diameter of 280 mm was required. However, model monopiles of this diameter would introduce significant boundary effects. The available strongboxes for our experiments were cylinders of 750 mm × 750 mm (diameter×height). From literature, the minimum allowable distances from the pile to the edge of the model were $3.5D$ horizontally from the front edge of the pile (Takahashi et al., 2022), and $1.25D$ vertically from the base of the



Figure 6.1: Beam centrifuge of the ETH Zurich Geotechnical Centrifuge Centre (ETHZ, n.d.)

pile (Choo et al., 2016). Given a model pile diameter of 280 mm, the required strongbox diameter would be $3.5D + 3.5D + D = 2240$ mm, exceeding the available dimensions, therefore the pile dimensions were restricted.

Considering that the prototype pile geometry could not match the desired diameter, the chosen pile needed to have the maximum possible diameter within the boundary constraints. Further to reviewing the literature, numerical analyses were completed by Dimitrios Konstantinidis to inform the maximum allowable pile diameter. This analysis established minimum allowable distances of $3.25D$ horizontally from the front edge of the pile to the box, and $1D$ vertically from the base of the pile to the base of the sand. Applying these limits, the largest pile diameter was set at 100mm (the maximum allowable model monopile diameter), with the second smaller pile set at 83mm.

The final constraint was pile installation. As discussed, the pile was instrumented with pile mounted PPTs and strain gauges, and extended beyond the top surface of the strongbox. Pile-mounted instrumentation requires internal wiring along the length of the pile and a mount for the sensor. Given the sensitivity of these instruments, the installation method needed to be wished-in-place. Alternative installation methods include 1g jacking and jacking in-flight (Klinkvort et al., 2013), which better matches installation methods used in reality. However, the plug formed inside the pile during jacking would interfere with the instruments. Additionally, despite a closer representation of reality, it is difficult to quantify the effects jacking has on sand density and the fabric surrounding the monopile, which can complicate future modelling of the test results.

6.2 Centrifuge

All tests were conducted using the geotechnical beam centrifuge at the ETH Zurich Geotechnical Centrifuge Centre (Figure 6.1). The centrifuge has a diameter of 8.2 m,

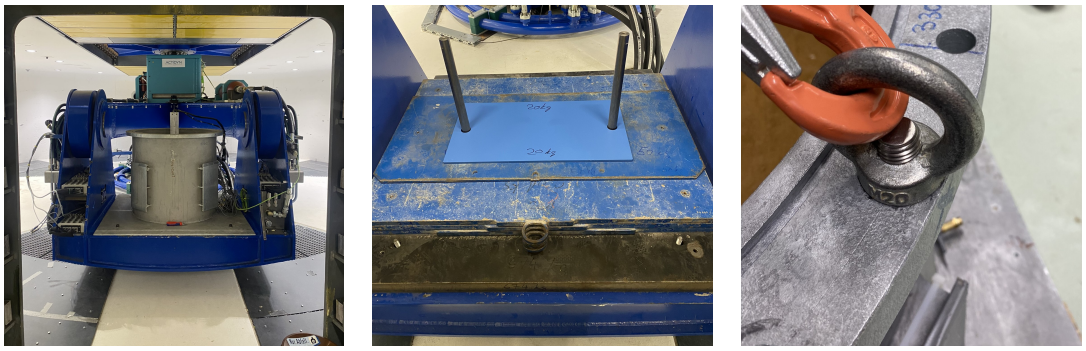

(a) (b) (c)

Figure 6.2: Strongbox details, showing: (a) Strongbox in place on the basket, (b) counterweights for the centrifuge beam, (c) mounting points for lifting and attachment.

with a maximum capacity of 500 Gton and a maximum g-field of 250 g. The large radius enhances the uniformity of the g-field across the model.

The models were prepared in cylindrical strongboxes measuring 750 mm in diameter and height (Figure 6.2(a)). The boxes were constructed from steel with 30 mm thick walls, ensuring minimal compliance under load. They incorporated mounting points for supporting the pile installation frame, lifting the box into position, attaching to the basket, and securing the actuator frame to the strongbox. Taps were installed at the base of the boxes to facilitate saturation prior to testing and drainage afterward.

On the opposite side of the centrifuge arm, a separate cradle supported counterweights. The final weight of the prepared model, along with the actuator and frame, were considered for the selection of the counterweights. The precise selection of counterweights minimised vibration and stress on the centrifuge arms and axis.

All tests were completed at 50g, targeted at $1/3^{\text{rd}}$ of the embedment depth of the pile. To maintain the load eccentricity for the different pile lengths, the sand model was poured at varying heights within the boxes. Consequently, the radius of the rotation of interest was adjusted to align with the change in the target depth within the box . The applied centripetal acceleration a_c is given in Equation (6.1), where ω is the rotational velocity, and r_c is the radius. The radii of rotation at $1/3^{\text{rd}}$ embedment depth were 3.646 m and 3.737 m for the 83 mm pile and the 100 mm pile, respectively. Thus, the required rotational frequency was 110.76 rpm for the 83 mm pile and 109.4 rpm for the 100 mm pile.

$$a_c = r\omega^2 \tag{6.1}$$

6.3 Equipment

6.3.1 Instrumentation

Table 6.1 details the sensors used in the campaign. The pile was instrumented with accelerometers, strain gauges, and PPTs (Figure 6.4). Additionally, the experiment used laser displacement sensors, LVDTs, PPTs in the soil, a load cell at the actuator mounting point, and an accelerometer mounted to the base of the box. The layout of the sensors used is presented in Figure 6.3. The accelerometers were mounted using bespoke 3D printed housings, located inside the pile. Wheatstone bridge strain gauge pairs measured internal bending moments and were also mounted internally to prevent damage. PPTs were fixed to the pile via 3D printed housings, with access to the outer soil through a 4 mm hole in the pile wall. Additionally, PPTs were distributed in the soil in a grid over the plane of loading. The faces of the soil PPTs were oriented perpendicular to the plane of loading to prevent interference from p-waves generated during loading. Higher range PPTs were positioned lower in the model where the total pressures were expected to be greater. A single LVDT was situated $0.8D$ in front of the pile on the soil surface to measure soil settlement and heave during the test. Five laser displacement sensors monitored the pile position. Three horizontal lasers were directed at the pile surface, and two vertical lasers were directed at a top cap. The lasers were mounted in fixed positions on the actuator mounting frame, therefore at different relative positions for the two different pile sizes. An accelerometer was mounted to the base of the box. This allowed an accurate recording of the applied g level at the base of the box. A load cell was placed between the actuator and the pile. The layout of the sensors is detailed in Figure 6.3.

Table 6.1: Sensors Used

Sensor	Product Name	Range	Accuracy	Number
Accelerometer	Miniature DeltaTron (c) Mems 4518	±500g	0.02%	5
Wheatstone Bridge Strain Gauge	HBM K-CLY4	5%	0.005%	8
Pore Pressure Transducer	Keller 2MI-X micro PPTs	3, 6 & 10 Bar	±0.5% FS	18
Linear Variable Displacement Transducer	Measurement Specialties 500 MHR	±12.7 mm	0.25% FS	1
Laser Displacement Transducer	Micro Epsilon ILD1420-50	50 mm	2 μm	5
Load cell	ME Messsystems KR55	5 kN	0.05% FS	1

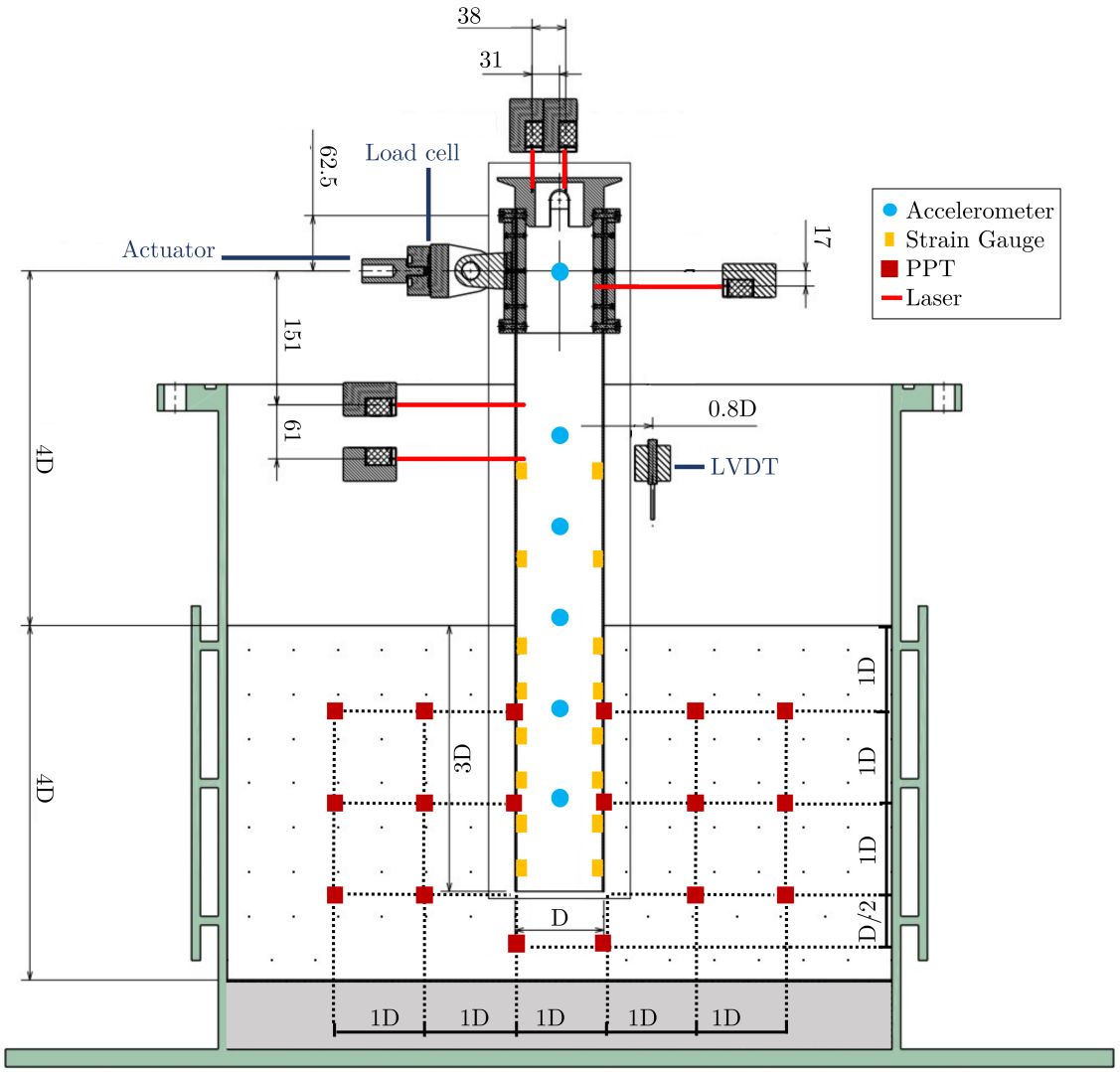

Figure 6.3: Experimental layout, including sensor locations. Model scale, dimensions in mm

6.3.2 Actuator

The required cyclic loads were high frequency at model scale, up to 45 Hz. This necessitated the use of a hydraulic dynamic actuator. The actuator was a 60 mm bore double-acting hydraulic cylinder, capable of a static load up to 50 kN. It had a maximum dynamic capability of 150 Hz with a stroke of 210 mm, although the full stroke diminishes as the frequency increases. The actuator was controlled by a dynamic feedback control system. Load was applied through pressure within the hydraulic system, controlled by the opening of valves. The relatively low loads required for the drainage investigation, ~200 N, amounted to 0.4% of the actuator capacity. At this low level, the presence of parasitic loads from system friction, prevented smooth control during a sinusoidal load package. Therefore, displacement controlled cycles of set displacement amplitude were applied, as the control system provided more consistent time histories with this input.

The actuator was housed in a steel frame mounted to the top surface of the strongbox

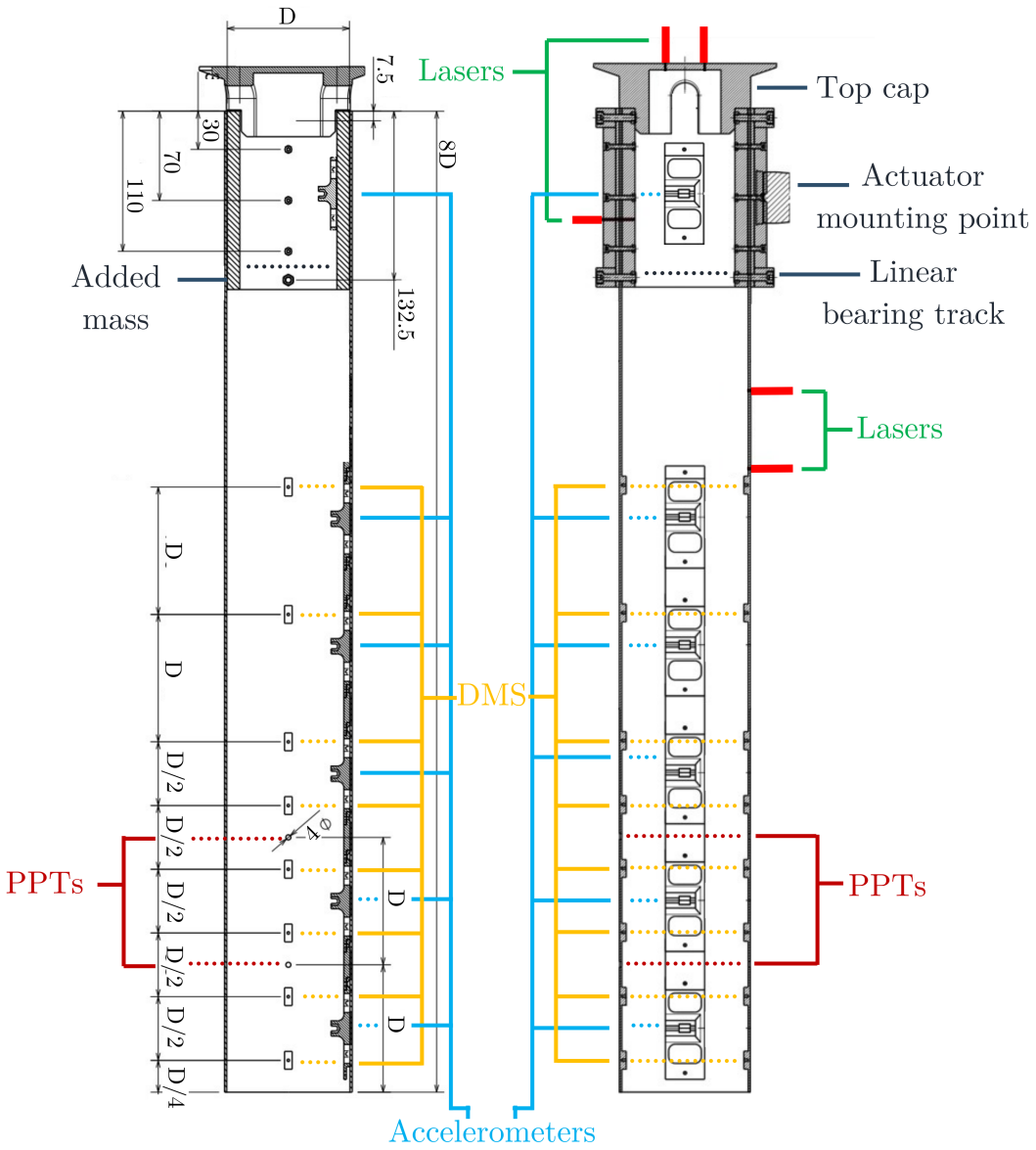

Figure 6.4: Instrumented pile, PPT housing not shown here only hole for access point, accelerometers positioned onto surface of pile with 3D printed housing to ensure correct locations.

(Figure 6.6(d)). The frame construction was designed to flex 1 mm at 120g under a 20 kN applied load. This stiffness was significantly higher than that of the foundation system, and allowed for accurate measurement of the actual foundation displacement. The load cell exhibited greater levels of compliance, 1% axial strain at 100% load. However, the use of displacement sensors independent of the load system mitigated this issue.

The actuator was mounted to the pile using a sliding hinge bearing system to minimise parasitic loads. The actuator ram was attached to the load cell, then to a rotational bearing (Figure 6.6(b)). The rotational bearing was fixed to an attachment point on the pile with a bush (Figure 6.6(c)). This attachment point was mounted onto a linear bearing, allowing for free rotational and vertical movement while maintaining full contact with the pile. Consequently, only a horizontal force could be applied from the actuator to the pile.

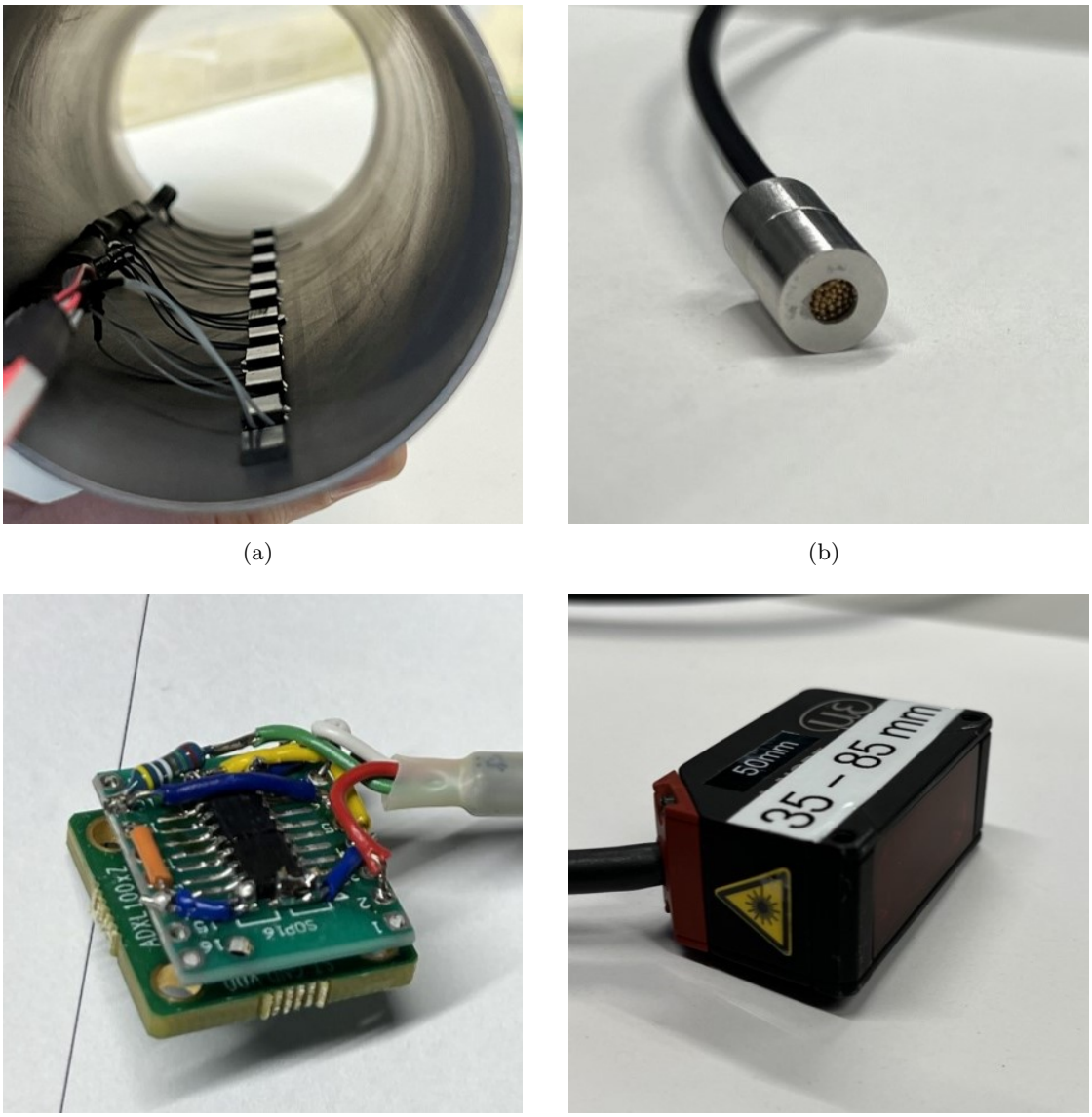

(a) (b)

(c) (d)

Figure 6.5: Instruments, showing: (a) strain gauges inside the monopile, (b) ppt for the pile and in the soil, (c) mems accelerometer and, (d) displacement laser.

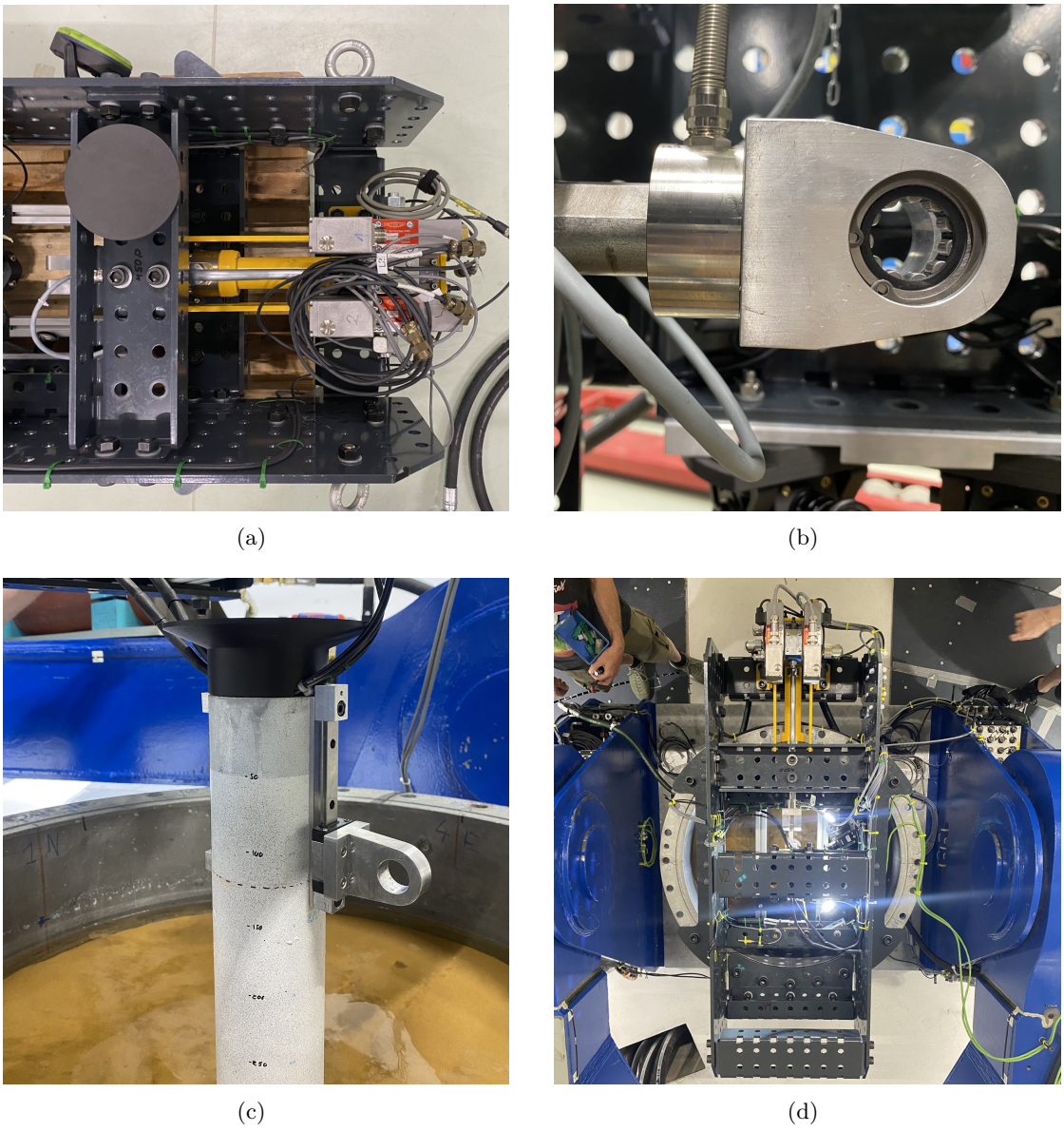

(a) (b)

(c) (d)

Figure 6.6: Actuator details, showing: (a) actuator in the mounting frame, (b) rotational bearing, (c) actuator attachment point and linear bearing, (d) actuator frame in place on the strongbox.

6.4 Pile

The use of two piles of differing diameter allowed the investigation of the non-dimensional scaling factor $MkT/\gamma_w D^2$. As discussed, the diameters of the model monopiles, D_m, were set at 83 and 100 mm. The true diameter of the prototype was limited by the dimensions of the strong box and the value of η. Tested at 50g, the models corresponded to prototypes of $D = 4.15$ and 5 m. This was below the range of interest for this campaign ($D \geqslant 10$ m). Therefore, an additional scaling of the loading period T was applied, maintaining the dimensionless drainage factor $MkT/\gamma' D^3$, corresponding to a reference monopile diameter D_ref. For drainage factor calculations, the constrained stiffness, M, at nominal depth $1D$

was taken as a function of the root of the mean effective stress, therefore D. The prototype loading period was calculated to maintain the dimensionless factor relative to the reference monopile:

$$\frac{M_{\text{ref}} k T_{\text{ref}}}{\gamma_w D_{\text{ref}}^2} = \frac{M_{\text{ref}} \sqrt{\frac{D_p}{D_{\text{ref}}}} k T_p}{\gamma_w D_{\text{p}}^2} \tag{6.2}$$

$$T_p = T_{\text{ref}} \left(\frac{D_{\text{p}}}{D_{\text{ref}}} \right)^{3/2} \tag{6.3}$$

By maintaining the dimensionless factor, it was hypothesised that the drainage regime of the smaller diameter prototype would correspond to that of the larger diameter reference pile of interest.

Klinkvort et al. (2018) also propose a dimensionless factor for the scaling of monopile flexural response, $E_p I_p / E_s D^4$. Where $E_p I_p$ is the flexural rigidity of the monopile and E_s is the soil stiffness. A reference steel ($E = 210$ GPa) monopile of diameter $D = 10$ m was taken. The model monopile was designed with aluminium ($E = 69$ GPa) to increase thickness and improve workability. The design of the model monopile maintained the dimensionless flexural factor. The resulting monopile dimensions, with the reference monopile used for design, are detailed in Table 6.2. The monopile was sandblasted to provide a rough interface with the sand. The monopiles were fitted with added masses to represent the nacelle mass. The scaled masses were selected to match a $D = 6$ m reference OWT (Escalera Mendoza et al., 2021). The mass was scaled to match the 5 m diameter of the larger prototype using $M_p / M_{ref} = D_p^2 / D_{ref}^2$.

Table 6.2: Monopile properties with example reference monopile $D_{\text{ref}} = 10$ m. Each monopile has matched scaling factors $MkT/\gamma_w D^2$ and $E_p I_p / E_s / D^4$.

Parameter	**M1**	**P1**	**M2**	**P2**	**Ref**
Acceleration (g)	50	1	50	1	1
Diameter (m)	0.083	4.15	0.1	5	10
Embedded length (m)	0.249	12.45	0.3	15	30
Eccentricity (m)	0.332	16.6	0.4	20	40
Thickness (m)	0.0016	0.08	0.0021	0.1	0.098
E (GPa)	69	69	69	69	210
EI_y (NM^2)	2.33×10^4	1.46×10^{11}	5.1×10^4	3.19×10^{11}	7.85×10^{12}
Period T (s)	0.036	1.8	0.048	2.4	6.8
Tower & Nacelle Mass (kg)	2.09	2.6×10^5	3.26	4.1×10^5	1.9×10^6

6.5 Material

6.5.1 Gravel and Hostun sand

A layer of gravel was added beneath the sand model before pouring. This served as a permeable base for saturation and drainage during testing. Additionally, it allowed the

height of the base of the sand to be raised inside the box, maintaining e and L across the two different pile sizes, considering that the location of the actuator was fixed. The gravel was medium grain sized D_{50} = 7 mm, well-rounded, with a particle density of G_s = 2.69. The gravel was added in 20 kg increments, then compacted and levelled. It was added until the required height was achieved. Height measurements were taken with a laser measure from a flat plate resting on the gravel surface, which negated the differences in height within the particle arrangement.

Above the surface of the gravel, a fine steel mesh was placed. The mesh served as a barrier between the gravel and the sand. It had openings of 0.15 mm and was cut to fit the diameter of the box, with an additional 6 cm added for fixing and sealing to the wall of the box. Any leaks of sand in the mesh became apparent during the pluviation process, leading to the formation of pits in the sand surface. If any leaks were identified, model preparation was restarted.

The mesh opening of 0.15 mm was too large for pluviating the Congleton sand directly onto it. To prevent the Congleton sand from falling into the gravel layer, a shallow layer of Hostun sand was pluviated onto the mesh first. The material properties of the Hostun sand are presented in Table 6.3. The Hostun sand was hand pluviated through a sieve with a 2 mm opening to the required height, then levelled using a plate.

The material used for testing in this campaign was Congleton HST-95 sand (Table 6.3), matching the triaxial testing campaign (Chapters 4 and 5).

Table 6.3: Material properties of Congleton HST-95, and Hostun HN31 sand (Hostun properties from Adamidis et al. (2022))

Parameter	**Congleton HST-95**	**Hostun HN31**
Specific Gravity, Gs	2.63	2.65
Minimum void ratio, $e_{\min}$	0.538	0.671
Maximum void ratio, $e_{\max}$	0.782	1.049
Target void ratio, e	0.58	-
Average grain size, D_{50} (mm)	0.150	0.341
Coefficient of uniformity, d_{60}/d_{10}	2.15	1.48

6.5.2 Calibration

The target void ratio for testing was e = 0.58 (80% D_r), similar to North Sea conditions (Section 3.2). The model was prepared using an automated sand raining system. The pluviator opening and drop height were adjusted to achieve the target void ratio. A series of calibration pours were performed. Void ratio was measured using density boxes after the method of Rosquoet et al. (2007). The boxes were arranged in an array, starting at the base and moving further up the model as pluviation progressed. Boxes were placed next to the pile to measure the effect of shadowing (Figure 6.7(a)). A sieve with a 2 mm opening was placed around the pile (Figure 6.7(b)) to disperse the sand during pluviation and mitigate the effect of shadowing. The calibration of the raining system gave an opening of



(a) (b) (c)

Figure 6.7: Pluviation details showing: (a) density pots next to pile to quantify shadowing, (b) sieve around pile and, (c) pluviation in progress.

32 mm with a drop height of 830 mm above the current height of the model. Measurement of shadowing effects found an increase in the void ratio of up to 0.03, or reduction of D_r by 10 % around the pile. The shadowing effects were limited to within less than $1D$ away from the pile.

6.5.3 Pluviation

After calibration, all models were completed using the same methodology. The pluviator was raised to the correct drop height, and sand was poured in two horizontal passes over the box with the sieve attached. The height of the sand level was measured across the model, and the average value informed the new pluviator height. The box was arranged so that the loading plane was perpendicular to the pluviation direction to minimise the effects of shadowing in front of the monopile. Pile cables, which could not be removed, were placed directly above the pile supports and positioned along the diagonal of the box so that the affected area beneath was away from the plane of loading. A 3D printed bespoke funnel, the exact diameter of the pile, was placed on top of the pile to direct all sand pluviated over the pile area into the pile.

The cyclic tests contained an array of PPTs within the soil. The PPTs were arranged in a grid across the loading plane, in front of, behind, and below the pile. The configuration of the PPTs is illustrated in Figure 6.3. Both horizontal and vertical locations were defined in terms of D, ensuring consistent relative positioning within the soil for both piles. The horizontal location was fixed at a predefined value. The vertical location corresponded to the current height of the sand surface during the pluviation process, maintained as close as possible to the desired height. Horizontal location measurements were taken relative to the top surface of the box (Figure 6.8(a)), subsequently referenced with a laser directed straight down from that position. The PPT was then placed at that location, and fixed to the wall of the box with tape (Figure 6.8(c)). The vertical depth in the box was recorded with a laser measure. The PPTs rested on the soil surface without support to minimise local stiffening.

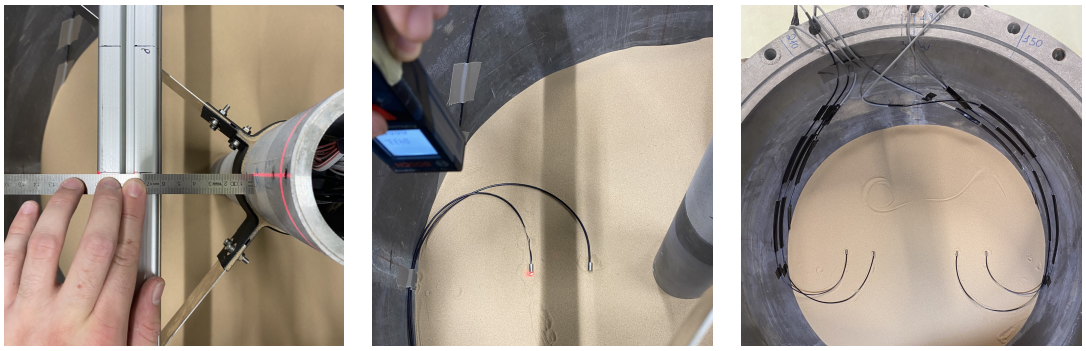

(a) (b) (c)

Figure 6.8: PPT placement: (a) horizontal location relative to the top surface of the box, (b) positioned on sand surface with laser pointer and, (c) fixed to wall of box with tape and directed upwards.

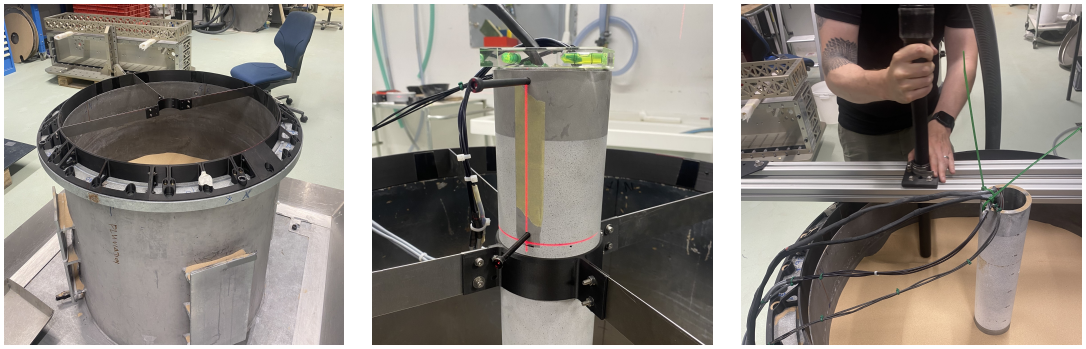

(a) (b) (c)

Figure 6.9: Pile placement and final height showing: (a) pile support with slender arms, (b) pile positioned relative to laser guide and spirit level and, (c) vacuum used to level sand to final height.

During pluviation, once the sand reached $1D$ above the Hostun layer, the pile was installed. The pile was supported by a frame attached to the top of the strongbox. The frame arms were metal strips, of minimal thickness to minimise the effect on pluviation. The pile was held by a 3D printed support in two halves (Figure 6.9(a)). The design allowed removal of the support after pluviation without disturbing the pile and the surrounding sand. The pile was positioned centrally via the support and aligned using a laser guide. The horizontal plane of the laser guide was set at a known height above the top of the box, and the corresponding height was marked on the pile. The vertical plane was aligned with the box mounting points, and the pile rotation was located with the linear bearing track bolt holes (Figure 6.9(b)). Careful placement was required to align the rotation of the pile with the actuator mounting point, which had a tolerance of only 3 mm. A spirit level was used to set the pile vertically.

Pluviation was continued beyond the required height, after which the pile support was removed. The final height was achieved by vacuuming off sand with a nozzle attached to a frame which maintained the required height (Figure 6.9(c)). Finally, the whole box was weighed to calculate the weight of sand added.

6.6 Saturation

6.6.1 Viscous fluid

The model was required to be fully saturated for the analysis of the drainage regime. Cyclic tests were saturated with viscous fluid, while the drained monotonic tests, where seepage scaling was not necessary, were saturated with water. Saturation was the most time-consuming phase of the model preparation. Therefore, as previously mentioned, the chosen viscosity was limited to reduce saturation time. Three out of four of the cyclic models were prepared with a 50 cSt solution, and one model was prepared with a 66.5 cSt solution to parametrically investigate the effect of permeability.

The viscous fluid used was an aqueous methyl-cellulose solution. The alternative solution of silicone oils was discounted due to issues with disposal, increased risk to health, and inability to wash the sand post-testing.

Preparation of the methyl-cellulose solution was completed using the methodology of Adamidis et al. (2015). The method first required dissolving the powdered form in water heated to 90 °C. The powder was dispersed in a concentrated solution, with 30% of the final volume, to give a more manageable volume for heating and mixing. The concentrated solution was mixed using a power drill mounted to a stand. The solution was then cooled in an ice-water bath to 25°C. At 25°C a hydration reaction occurs and the viscosity is attained. Whilst cooling, the solution was continually mixed to stop precipitation. The concentrated solution was then diluted further to the required volume and thus viscosity. The diluted solution was mixed in a large steel mixing tank, with vacuum attachments. Once prepared to the correct volume and viscosity, the fluid was mixed and vacuumed until fully de-aired. The fluid was left to de-air for at least 12 hrs, then a final viscosity measurement was taken at 24 °C.

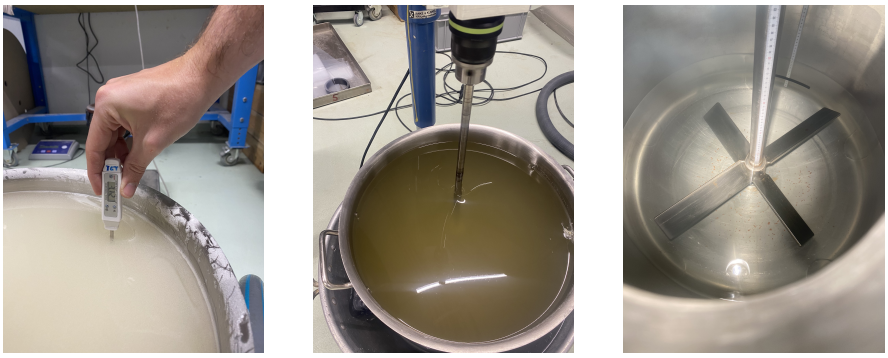

(a) (b) (c)

Figure 6.10: Viscous fluid preparation, showing: (a) concentrated solution, (b) mixing drill for concentrated solution, and (c) stirrer inside mixing tank.

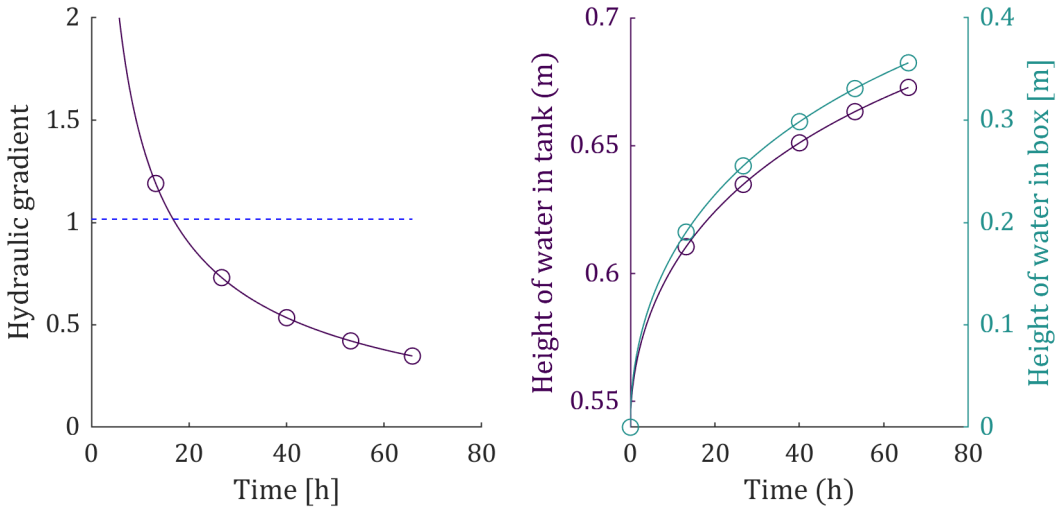

(a) (b)

Figure 6.11: Plots of estimated saturation time, showing: (a) hydraulic gradient plot, initial asymptotic curve due to low depth of saturated soil, calculations show head did not exceed effective stress limits and, (b) applied head calculated with estimated height of fluid in box.

6.6.2 Saturation

After the viscous fluid was prepared, the model was saturated. The chosen method was an applied hydraulic head saturation under vacuum. The box was sealed with a top cap; an extension in the top cap allowed sealing over the pile. Subsequently, the model was vacuumed and flushed with CO_2 three times before a final vacuum was applied. The CO_2 was introduced from the top of the model to reduce the risk of fluidizing the sand and destroying the pluviated fabric.

After flushing, the fluid height was measured from an external standpipe relative to the base of the box. The tank was raised to the required height for the targeted head. The value of the head was calculated so that the upwards flow did not reduce the effective stress below 66 % of the final post-saturation effective stress at 1g. Consequently, the critical hydraulic gradient was never reached. The additional restraint of 66 % effective stress prevented any local fluidization along preferential paths. The plot shown in Figure 6.11(a) gives the estimated hydraulic gradient with time. The initial curve is asymptotic and the hydraulic gradient exceeds 1. This is due to the low depth of saturated soil early on in the process. Hydraulic gradient is $i = h_2 - h_1/l$, where h_2 is the head at the base equal to the applied head, the head at the surface $h_1 = 0$, and l is the distance between those two points. Consequently, at the start of saturation when $l \approx 0$, i tends to infinity. However, the pore pressure was calculated and did not exceed the effective stress limit in these early stages. The head applied was increased with time as the saturated height also increased, which reduced the saturation time without violating the maximum effective stress threshold (Figure 6.11(b)).

Saturation was terminated after the fluid reached 5 cm above the surface of the sand. This additional fluid was added to prevent the uppermost sand in the centre of the box

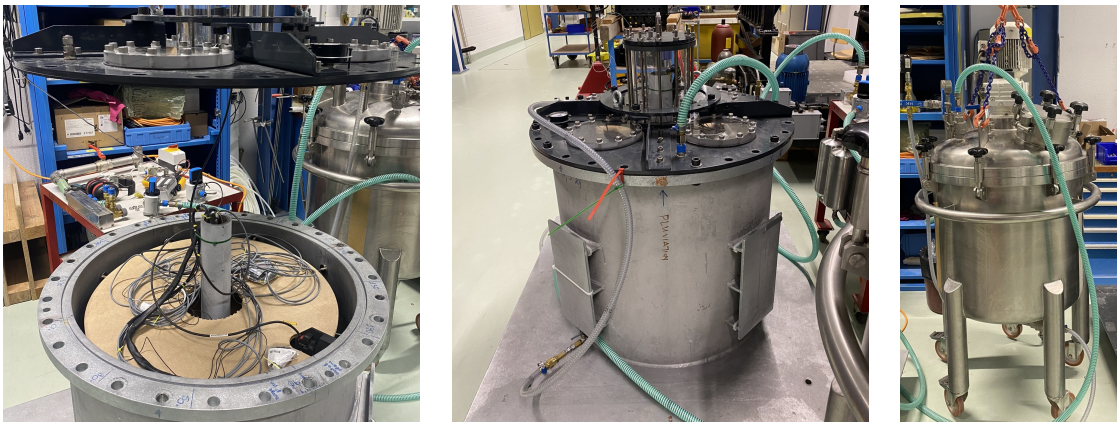

(a) (b) (c)

Figure 6.12: Saturation apparatus, showing: (a) Sensor cables placed inside the box, (b) vacuum seal top cap in place, (c) mixing tank lifted to maintain constant head.

from drying out due to the parabolic shape of the fluid surface induced by the acceleration field. After saturation, a value for the degree of saturation was calculated. The estimation was performed using the method of Okamura et al. (2012). The model was de-pressurised to -0.3 Bar and then re-pressurised back to atmospheric pressure. Assuming the fluid, sand, pile, and instrumentation to be incompressible, any change in volume resulted from air in the fluid. The volume of air can be calculated from equation 6.4, where V_a is the volume of air, $\Delta(h_1 - h_2)$ is the change in height of the fluid surface less the change in height of the box base, p_1 is the initial pressure, p_2 is the final pressure, and A is the plan area of the model. The fluid surface level was measured using a laser displacement sensor directed at a float. Another laser displacement sensor measured the change in height at the centre of the base of the box. A PPT measured the internal air pressure. The saturation ratio is $S = V_a/V_w$. All models achieved saturation ratios > 0.98.

$$V_a = \frac{\Delta(h_1 - h_2)}{(p_1/p_2) - 1} A \tag{6.4}$$

6.7 Pre-test procedure and test management

Once the model preparation was completed, the box was installed into the centrifuge. The total weight of the box, saturated model, pile, and instrumentation was recorded using a crane weighing scale, after which appropriate counterweights were installed. The box was then lowered into position from the lab floor onto the centrifuge swing and bolted into place. Subsequently, the actuator frame was installed, followed by the attachment of the actuator. The instruments were connected to the data acquisition (DAQ) system, with their connection points and calibration files updated accordingly. The DAQ software used was Catman, which provided control over the logging rate and generated real-time plots of the results.

The centrifuge was then spun up to the target rpm. The spin-up process was conducted

gradually, to minimise overshooting and resulting overconsolidation. A spin-up file was recorded for each test at a sampling rate of 100 Hz. Monotonic tests were recorded at 100 Hz, while cyclic tests were recorded at 2500 Hz.

Cyclic tests comprised multiple phases, with each phase recorded in a separate file, and recording ceased shortly after the load packet was applied. Displacement-controlled cyclic tests were conducted at a specified frequency and displacement amplitude for a predetermined number of cycles. The trace was sinusoidal, with a build up phase at the start. The actuator increased to the required cyclic amplitude over several cycles. Cycle counting commenced once the displacement amplitude was reached.

Load controlled cyclic tests required the input of a load time history. The simulated load time history applied is detailed in Section 6.8.3 The time period the time history was scaled as necessary for the targeted dimensionless drainage factor. The actuator tended to overshoot the input load amplitude due to the sensitive calibration of the system stiffness. Given that the calibration was unique to each model, it was not possible to perform a calibration without destroying the model. A cautious approach was taken to initially scale the storm amplitude down to find the peak load amplitude output relative to the input amplitude. From this result, the required amplitude scale factor could be calculated.

6.8 Loads

6.8.1 Monotonic loading

The monotonic loading was applied with displacement control up to a predetermined structural limit. The displacement was applied at 0.05 mm/s, which was sufficiently slow for drained response even in the higher viscosity cyclic tests. The ultimate load was calculated as follows:

$$M_{\mathrm{yMAX}} = \frac{\sigma_y I_y}{r} \tag{6.5}$$

$$F_{\mathrm{MAX}} = \frac{M_y}{e} \tag{6.6}$$

Where the yield stress $\sigma_y = 160$ MPa, I_p is the second moment of area, r_p is the monopile radius, and e is the load eccentricity (Table 6.2). The resulting ultimate load, with a safety factor of 1.5, was 2.6 kN for pile (P)1 ($D = 83$ mm) and 3.9 kN for P2 ($D = 100$ mm) at model scale.

The subsequent cyclic loads were scaled in amplitude relative to the nominal ultimate failure load, H_{ULT}, taken at mudline displacement, $y_0 = 0.1D_{\mathrm{p}}$.

6.8.2 Displacement controlled cyclic loading

The actuator control system was better able to apply low amplitude sinusoidal displacement controlled cycles, than the equivalent load controlled cycles. As such, the direct investigation into the dimensionless drainage factor was completed using displacement controlled cycles.

Table 6.4: Load simulation inputs

Parameter	Values
Rated power (MW)	15
Rated wind speed (m/s)	10.59
Cut-in, cut-out speed (m/s)	3-25
Controller	Variable-speed pitch control
Rotor speed (rpm)	5–7.55
Rotor diameter (m)	240
Hub height above sea level (m)	150
Embedded pile length (m)	30
Monopile diameter (m)	10
1st tower modal frequency (Hz)	0.16
Water depth (m)	30
Significant wave height (m)	9.9
Spectral peak period (s)	13.8
Mean hub wind speed (m/s)	47.3
Turbulence intensity (%)	11

The control system required the input of cyclic amplitude, average displacement, frequency, tolerance and number of cycles. The tolerance was set at 10% of the double cyclic amplitude. The frequency was determined by the targeted dimensionless drainage factor (Table 6.2). The number of cycles varied. The displacement amplitude was set with respect to actuator level displacement y_a, to give one way cyclic loading. The actuator ramped up slowly to the average displacement in a monotonic push. Cyclic loading commenced with low amplitude cycles initially, before ramping up to the target amplitude. Cycle counting began after the cyclic amplitude reached the target level within the tolerance. Upon completing the cycles, the actuator ramped back down, returning to the average displacement. Pore pressures were allowed to dissipate between each event. For tests where the amplitude varied, the actuator was slowly moved to the required displacement average, with some cases necessitating unloading.

6.8.3 Load controlled storm loading

The load controlled storm events were based on a simulated time history. The following section, detailing the simulation method, was written by Gerard Ryan, who completed the simulation. To simulate storm loads, an aero-hydro-servo-elastic code (Ryan et al., 2024*a*) was used for the IEA 15-MW reference turbine (Gaertner et al., 2020) supported by a monopile. Table 6.4 lists the simulation parameters. To match the test piles, L was adjusted to 30 m, and the sand void ratio to 0.58. The monotonic soil reaction was modelled following Burd et al. (2020). Stochastic wind fields were modelled using the Kaimal spectrum (IEC-61400-3-1, 2019) and generated using TurbSim (Kelley et al., 2005). Rayleigh damping was modelled with a structural critical damping ratio of 0.6 % (Ryan et

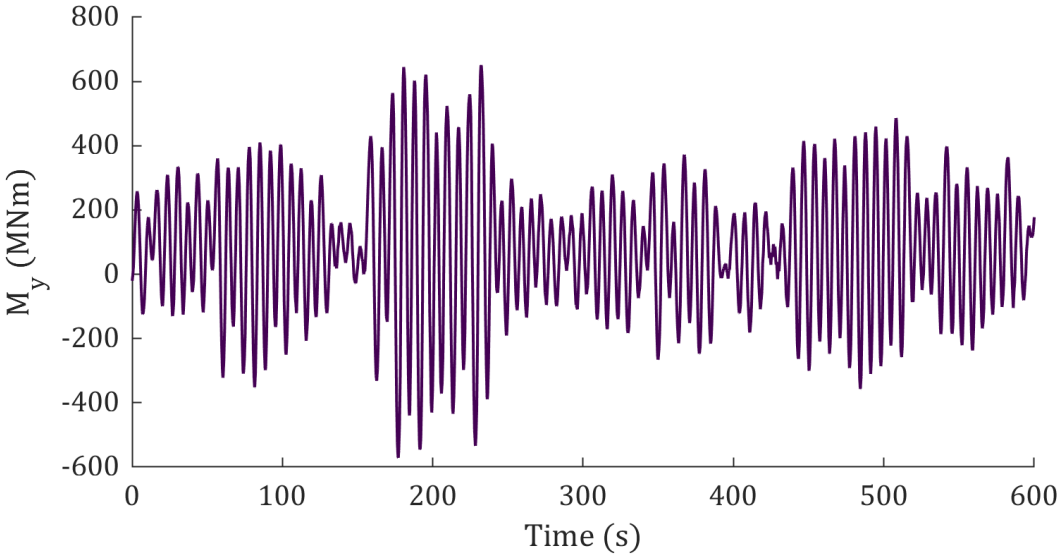

Figure 6.13: Simulated mudline moment plot against time, units are in scale of the simulated monopile

al., 2024*a*). Soil-structure interaction was modelled with multi-surface plasticity, capturing the hysteretic response. Morison et al. (1950) equation was used for hydrodynamic loads. Keulegan-Carpenter numbers were less than 5, therefore Cm = 2 and Cd = 0.7. Linear random wave theory was used to generate surface elevations and fluid particle kinematics (Ryan et al., 2024*b*). Wave fields were generated using JONSWAP spectra and assumed to be unidirectional (IEC-61400-3-1, 2019). The output in the scale of the simulated monopile is presented in Figure 6.13.

The simulation produced 10 minutes of load time history, representing the peak load of a 35 hr storm. The final applied time history consisted of a ramping up and a ramping down phase, with three repeats of the the 10 min peak load. The time history was a multi-frequency excitation, representing the complex loads applied to OWTs. The peak load period in the frequency domain was scaled to match the required frequency of the reference pile of interest Table 6.2. The peak load amplitude was scaled to reach $0.5H_{\mathrm{ULT}}$ for the majority of tests, and $0.75H_{\mathrm{ULT}}$ for certain tests termed Extreme Storms.

6.9 Test programme

The tests completed are outlined in Section 6.9. A total of six models were prepared, three for each model monopile. For each monopile, one model was prepared for a reference monotonic test, and two models were prepared for cyclic tests. In the cyclic tests, displacement controlled cycles were applied first, followed by the storm loads, and concluded with an end of test pushover. Additionally, one model for each monopile was subjected to a sine sweep between the storm phase and the pushover. Each cyclic model was tested at the

Table 6.5: Achieved void ratio and pore fluid viscosity

Test	**Void ratio**	**Viscosity (cSt)**	**Fluid temp. meas (°C)**
T1	0.57	1	-
T2	0.62	1	-
T3	0.60	48.9	23.6
T4	0.61	50.2	22.9
T5	0.60	66.4	23.5
T6	0.61	48	24.7

loading period of the D_{ref}= 10, 12, and 14m reference monopiles, for both displacement and load controlled cycles. The drained monotonic tests test (T)1 and T2 were saturated with water, 1 cSt. The cyclic tests T3, T4, and T6 were saturated with a viscous fluid of 50 cSt. Test T5 was saturated with a 66.5 cSt viscous fluid. The final achieved void ratios and measured pore fluid viscosity are presented in Table 6.5. An actuator overshoot issue was encountered during T4. The applied load output exceeded the desired load input, resulting in soil liquefaction and a loss of stiffness. Since the load control system depended on an internal estimate of stiffness, the system lost control and produced a significantly greater amplitude load sequence than intended. Consequently, the results of this test have been excluded. An example of naming is provided below and detailed in Table 6.6.

$$\underbrace{\text{T4}}_{a}_\underbrace{4}_{b}_\underbrace{\text{D10}}_{c}_\underbrace{03\text{A}}_{d}_\underbrace{\text{D}}_{e}_\underbrace{\text{r}}_{f}$$

Table 6.6: Test nomenclature

Key	**Description**	**Nomenclature**
a	Test model number	T 1-6
b	Load packet number	b
c	Reference pile diameter (m)	D 10, 12, 14
d	Amplitude	Displacement control: dA ($d = y_a/D$)
		Load control: dA ($d = H/H_{\text{ult}}$)
e	Control	D: Displacement control
		S: Storm (load control)
		SE: Extreme Storm (load control)
f	Repeat event	r

Table 6.7: Test programme of all tests completed. *T4 reached liquefaction after actuator overshoot, T4_5 cyclic test has been truncated in the results, T4_6 pushover is affected by the overloading. †When the displacement cyclic amplitude is reduced, the actuator is pulled back to the midpoint of the new packet before loading.

Name	Load	Control	Freq. (Hz)	Ampl. (y_a/D) (H_{ult})	Cycles (n)	D_{ref} (m)
T1_M	Mono.	Disp.	-	-	-	-
T2_M	Mono.	Disp.	-	-	-	-
T3_1_D10_03A_D	Cyc.	Disp.	27.4	0.03	400	10
T3_2_D12_03A_D	Cyc.	Disp.	36	0.03	400	12
T3_3_D14_03A_D	Cyc.	Disp.	45.3	0.03	400	14
T3_4_D10_03A_D_r	Cyc.	Disp.	27.4	0.03	400	10
T3_5_D12_25A_S	Strm.	Load	36	0.25	-	12
T3_6_D12_50A_S	Strm.	Load	36	0.5	-	12
T3_7_D12_75A_SE	Strm.	Load	36	0.75	-	12
T3_8_D10_50A_S	Strm.	Load	27.4	0.5	-	10
T3_9_D12_50A_S_r	Strm.	Load	36	0.5	-	12
T3_10_D14_50A_S	Strm.	Load	45.3	0.5	-	14
T3_11_M	Mono.	Disp.	-	-	-	-
T4_1_D10_03A_D	Cyc.	Disp.	20.5	0.03	200	10
T4_2_D12_03A_D	Cyc.	Disp.	27	0.03	200	12
T4_3_D14_03A_D	Cyc.	Disp.	34	0.03	200	14
T4_4_D10_03A_D_r	Cyc.	Disp.	20.5	0.03	200	10
T4_5_D12_50A_S*	Strm.	Load	27	0.5	-	12
T4_6_M*	Mono.	Disp.	-	-	-	-
T5_1_D10_03A_D	Cyc.	Disp.	20.5	0.03	1000	10
T5_2_D12_03A_D	Cyc.	Disp.	27	0.03	1000	12
T5_3_D14_03A_D	Cyc.	Disp.	34	0.03	1000	14
T5_4_D10_008A_D†	Cyc.	Disp.	20.5	0.008	1000	10
T5_5_D10_015A_D	Cyc.	Disp.	20.5	0.015	1000	10
T5_6_D10_022A_D	Cyc.	Disp.	20.5	0.022	1000	10
T5_7_D10_03A_D_r	Cyc.	Disp.	20.5	0.03	1000	10
T5_8_D12_60A_S	Strm.	Load	27	0.6	-	12
T5_9_D12_25A_S	Strm.	Load	27	0.25	-	12
T5_10_D12_50A_S	Strm.	Load	27	0.5	-	12
T5_11_D12_75A_SE	Strm.	Load	27	0.75	-	12
T5_12_D10_50A_S	Strm.	Load	20.5	0.5	-	10
T5_13_D12_50A_S_r	Strm.	Load	27	0.5	-	12
T5_14_D14_50A_S	Strm.	Load	34	0.5	-	14
T5_15_SINESWEEP	-	Disp.	-	-	-	-
T5_16_M	Mono.	Disp.	-	-	-	-
T6_1_D10_008A_D	Cyc.	Disp.	20.5	0.008	1000	10
T6_2_D10_015A_D	Cyc.	Disp.	20.5	0.015	1000	10
T6_3_D10_022A_D	Cyc.	Disp.	20.5	0.022	1000	10

Name	Load	Control	Freq. (Hz)	Ampl. (y_a/D) (H_{ult})	Cycles (n)	D_{ref} (m)
T6_4_D10_03A_D	Cyc.	Disp.	20.5	0.03	1000	10
T6_5_D12_008A_D†	Cyc.	Disp.	27	0.008	1000	12
T6_6_D12_015A_D	Cyc.	Disp.	27	0.015	1000	12
T6_7_D12_022A_D	Cyc.	Disp.	27	0.022	1000	12
T6_8_D12_03A_D	Cyc.	Disp.	27	0.03	1000	12
T6_9_D14_008A_D†	Cyc.	Disp.	34	0.008	1000	14
T6_10_D14_015A_D	Cyc.	Disp.	34	0.015	1000	14
T6_11_D14_022A_D	Cyc.	Disp.	34	0.022	1000	14
T6_12_D14_03A_D	Cyc.	Disp.	34	0.03	1000	14
T6_13_D10_008A_D_r†	Cyc.	Disp.	20.5	0.008	1000	10
T6_14_D10_015A_D_r	Cyc.	Disp.	20.5	0.015	1000	10
T6_15_D10_022A_D_r	Cyc.	Disp.	20.5	0.022	1000	10
T6_16_D10_03A_D_r	Cyc.	Disp.	20.5	0.03	1000	10
T6_17_D12_50A_S	Strm.	Load	27	0.5	-	12
T6_18_D10_50A_S	Strm.	Load	20.5	0.5	-	10
T6_19_D14_50A_S	Strm.	Load	34	0.5	-	14
T6_20_D12_75A_SE	Strm.	Load	27	0.75	-	12
T6_21_D12_50A_S	Strm.	Load	27	0.5	-	12
T6_22_SINESWEEP	-	Disp.	-	-	-	-
T6_23_M	Mono.	Disp.	-	-	-	-

6.10 Data management and analysis

Test recording began before the load started and concluded shortly after the packets were applied. This ensured that no data was lost during the early or late stages of the history. The presented data has been truncated to remove these tails. Each sensor was recorded separately (the strain gauges were recorded as a pair at the same height on opposite sides of the monopile). The sensors were recorded at the same sampling frequency for each stage: 100 Hz for the monotonic tests and 2500 Hz for the cyclic tests. The output data was saved in a separate file for each stage.

Data recording was completed using Catman, the centrifuge data aquisition system. The data was exported as .mat files, which included a field for the time history and a field containing the name, unit, and length of each time history. A maximum of 43 sensors were used, the details of which are discussed in Section 6.3.1. The measurements are detailed in Table 6.8. The data is saved on the server at ETH Zurich, a backup hard drive, and the Oxford OneDrive server.

An initial processing was completed, presenting time histories of the data grouped by sensor type. Subsequently, visual examinations of the data quality and relationships were conducted to guide further analysis.

Table 6.8: Measurements taken during testing

Measurement	Sensor	Recorded unit
Load	Load cell	kN
Pile displacement	Displacement laser	mm
Soil displacement	LVDT	mm
Pile acceleration	Accelerometers	g
Centrifuge acceleration	Accelerometers	g
Pore pressure	PPTs	Bar
Bending moment	Strain gauges	Nm

Table 6.9: Normalised factors

Factor	Input data	Normalised
Lateral load, H	Load	$H/\gamma' D^3$
Mudline moment, M	Load, e	$M/\gamma' D^4$
Internal pile moment, M	Moment	$M/\gamma' D^4$
Displacement, y	Displacement	y/D
Rotation, θ	Displacement	θ
Excess pore pressure, p_e	u, z	r_u

All data is presented normalised relative to the geometry of the test. Normalisation has been completed with the standard factors used in research on monopiles. Normalisation factors are presented in Table 6.9. H is the applied lateral load (kN), measured by the load cell at the actuator. γ' is the buoyant unit weight of the soil, 10.05 kN/m^3. M is the bending moment, either mudline or internal. Mudline bending moment is taken as $H \cdot e$, where e $e = 4D$. The internal bending moment is derived from the pile-mounted strain gauges. Displacement y is presented at either the actuator (y_a) or mudline (y_0) level. Displacement is calculated from the laser measurements at known heights on the pile. θ, is also computed from the laser displacement sensors. Results of pore pressures are presented as r_u, calculated from Equation (6.7), where u is the absolute value of pore pressure (measured), $\sigma'_{v,0}$ is the initial vertical effective stress, Z is the depth, and γ' is the buoyant unit weight (10.01 kN/m^3).

$$r_u = u/\sigma'_{v,0}$$
$$\sigma'_{v,0} = z\gamma' \tag{6.7}$$

6.11 Summary

This chapter described the test design and methodology employed for the centrifuge testing campaign. The test design was guided by the literature review, an assessment of the limitations of the available equipment, and the prioritisation of factors most relevant to the research objectives. A summary of the equipment and model preparation procedures was

presented, including specifications of the beam centrifuge system, pile design, instrumentation, and the sand pluviation and saturation processes. Following this, the test procedures, test schedule, and the approach to data management and processing were detailed.

Chapter 7
Centrifuge Testing of Monopiles in Congleton Sand: Results

The following chapter presents the results and discussion of the centrifuge testing campaign. First, the results of the reference monotonic tests, T1 and T2 are presented (Section 6.9), followed by the cyclic loading results. Given the numerous individual packets of the cyclic tests, some of which are repetitions or conducted under similar conditions, a condensed version is provided here. The first displacement controlled cyclic event, T3_1_D10_-03A_D, is presented in full. The subsequent tests are primarily compared to this event, highlighting key points of interest.

The monotonic results were designed to provide the backbone loading curve and the reference ultimate monotonic load, H_{ULT}, defined at mudline displacement $y_0 = 0.1D$.

The cyclic tests were designed to provide information on the effects of the dimensionless drainage scaling factor ($MkT/\gamma_w D^2$) parameters (k, T, and D) and the load history on the drainage regime. Consequently, the results presented concentrate on these key areas. The test design allowed each variable parameter within the dimensionless drainage factor to be examined independently. T3 served as a benchmark, T4 varied the diameter, T5 altered the viscosity, thereby affecting permeability, and T6 examined the effects of the load history. All cyclic tests targeted the same three values of the dimensionless drainage factor, corresponding to reference monopile diameters of $D_{ref} = 10, 12, 14$ m. The chapter is divided into analysis of the dimensionless drainage factor, then load history effects.

7.1 Monotonic results

The following section presents the monotonic results of tests T1 and T2. The monotonic tests were saturated with water and performed under drained conditions; therefore, there were no PPTs in the soil, and analysis of the drainage regime is not presented.

Presented in Figure 7.1 are the load displacement curves, both loads and displacements have been normalised. The nominal ultimate load H_{ULT} is overlaid. The resulting values for $H_{\mathrm{ULT}}/\gamma' D^3$ are 6.56 for T1 and 6.13 for T2.

The displacement controlled push was terminated before the pile reached yield as detailed in Section 6.8.1. After reaching this limit, the pile was pulled back to zero load. The stiff response is characteristic of a typical unloading.

The results for H_{ULT} were applied to subsequent cyclic tests as a reference for the cyclic load amplitude.

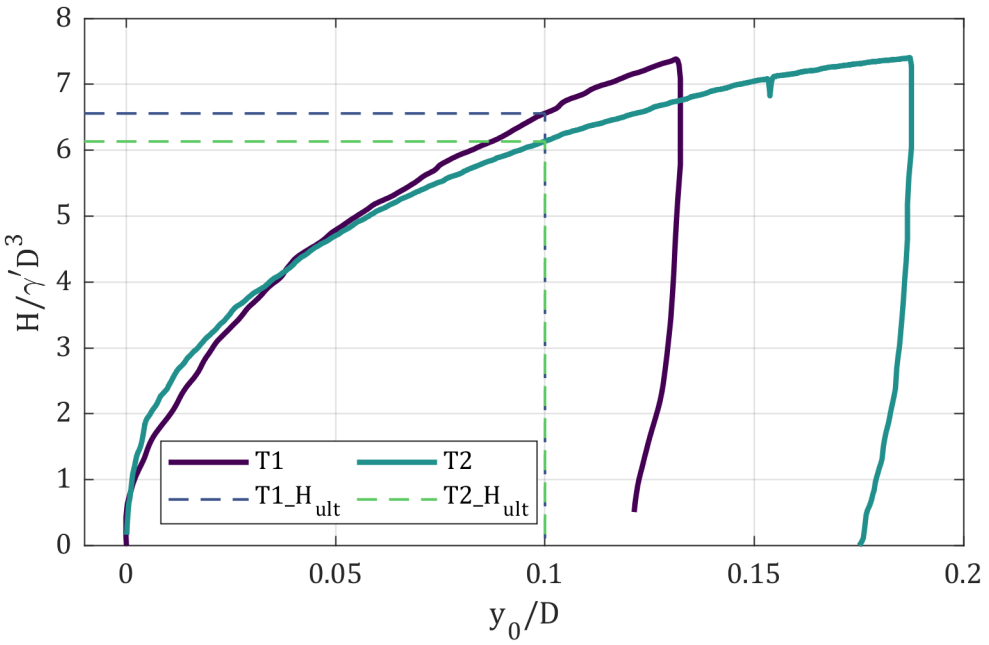

Figure 7.1: Load-displacement curves for pushover tests T1_M and T2_M. Overlaid is the nominal ultimate load H_{ULT}.

7.2 Reference displacement controlled cyclic tests

The following section presents an in-depth analysis of results from two reference displacement controlled cyclic tests. The initial results demonstrate the system response during T3_1_D10_03A_D (displacement controlled at the actuator level, one-way regular sinusoidal cycling, amplitude $y_a/D = 0.03$, dimensionless drainage factor equivalent to $D_{ref} = 10$ m). These findings indicate the typical relationship between load, displacement, and pore pressure response during cyclic loading events. The results also illustrate the methods employed for data analysis. Furthermore, the results reveal the response of virgin soil, which differs significantly from that of pre-loaded soil. It should be noted that 'shadowing' led to a reduction in sand density around the monopile by up to $D_r = 10\%$.

Following this, analysis is presented for a repeat event, T3_4_D10_03A_D_r. The load and displacement relationships for this event illustrate the system behaviour in a preloaded soil. This provides insight into the behaviour of the majority of events within the testing schedule, highlighting their disparity from the initial loading events of each model.

7.2.1 Reference first event: T3_1

The first cyclic test, T3 (Section 6.9), was completed using the D_{m}= 83 mm pile (D_{p}=4.15 m) with applied actuator displacement y_a=0.03, with loading period equivalent to a D_{ref} = 10 m pile (T_m = 0.036 s).

The plots in Figure 7.2 present the load and displacement results of the first event, T3_1_D10_03A_D. Figure 7.2 (a) shows the applied actuator displacement alongside the

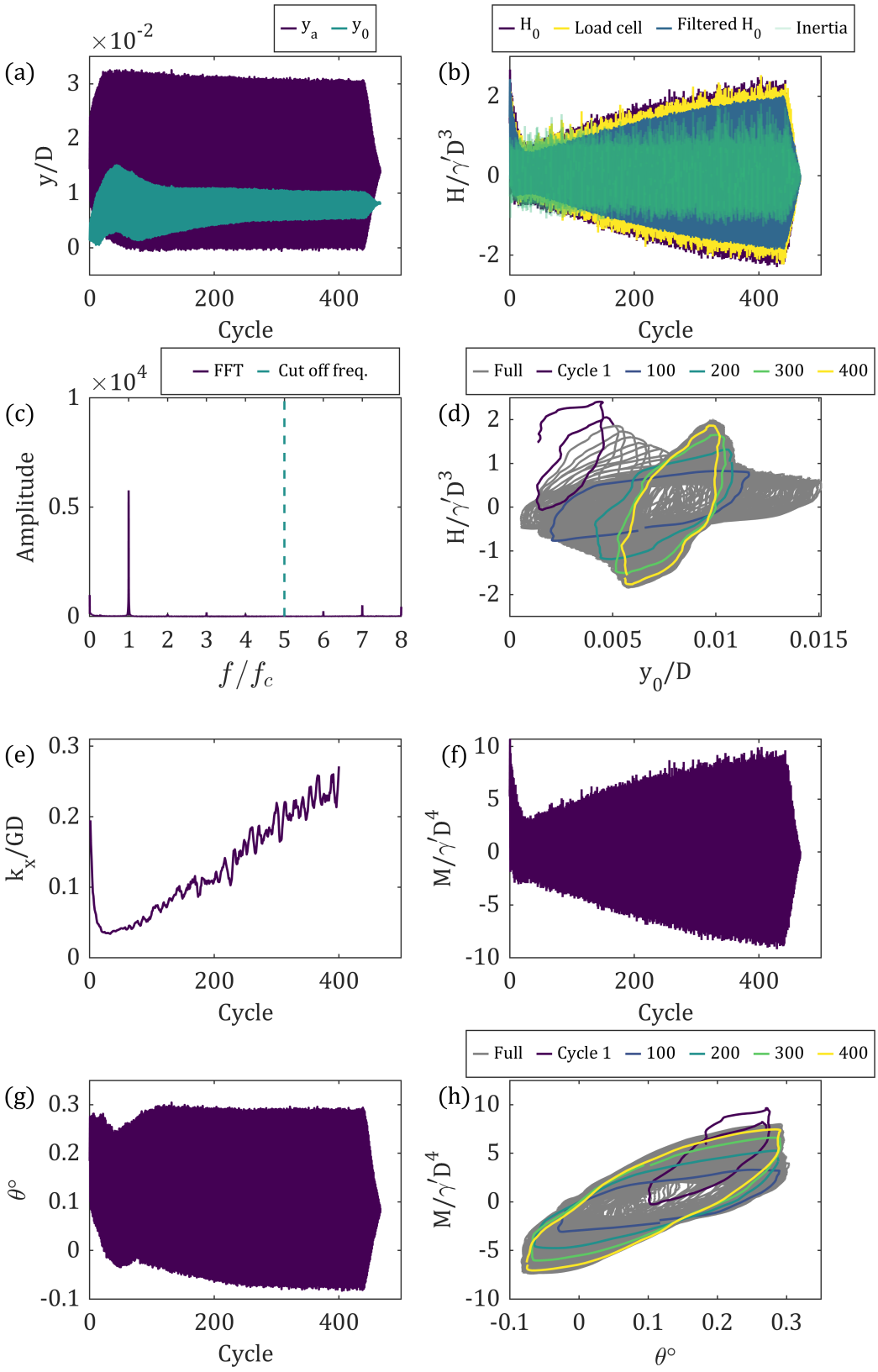

Figure 7.2: Reference displacement controlled test, T3_1_D10_03A_D, showing plots of: (a) applied actuator displacement, y_a, and resultant mudline displacement, y_0. (b) Loads with traces of: the measured load, the calculated inertial load, the mudline load excluding inertial effects, H_0, and the filtered load with a low-pass filter at 137 Hz. (c) Frequency domain plot of H_0, displaying the frequency normalised by the characteristic load frequency $f_c = 27.4$ Hz applied by the actuator. The cut-off frequency for the filtered load of (b) is overlaid. (d) Load vs Displacement. Load displayed is filtered H_0 with example cycles overlaid. (e) System stiffness, k_x, where subscript x signifies the horizontal direction. Stiffness calculated following Richards (2019). (f) Mudline moment, defined as $H_0 \cdot e$ (g) Mudline rotation (h) Moment vs Rotation with example cycles.

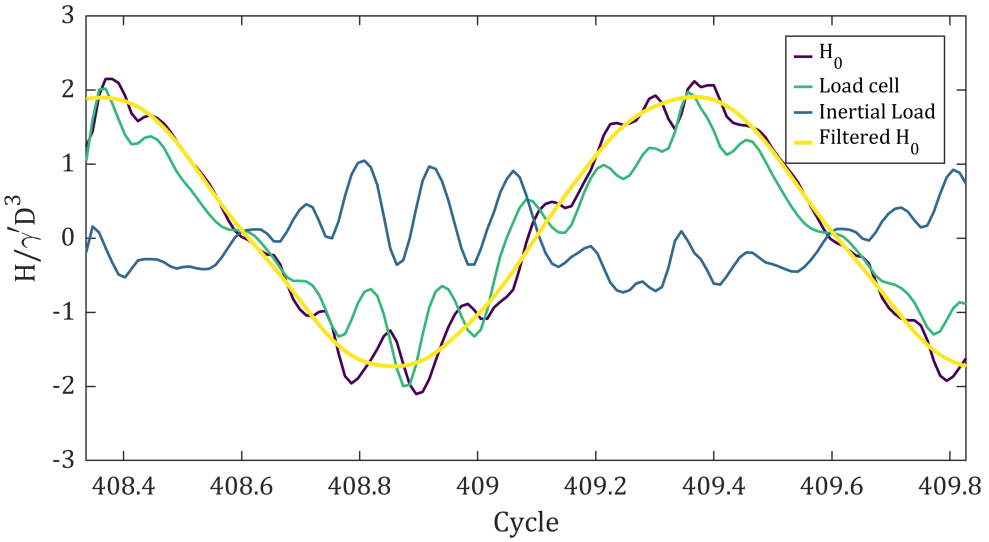

Figure 7.3: Extract of the load trace of Figure 7.2 (b). The measured load is anti-phase with the inertial force. H_0, the load applied to the mudline, is the sum of the the measured load and the inertial force. The filtered load is produced via a low-pass filter, set with a cut-off at 5 times the characteristic loading frequency, f_c.

resultant mudline displacement. The actuator was set to apply 400 cycles of y_a=0.03 D. The initial cycles displayed increasing actuator displacement amplitude while the control system gradually adjusted to the targeted amplitude. Cycle counting began after this point, hence the loading continues after the prescribed number of cycles. After 400 cycles were completed, the actuator ramped back down to a stop. The cyclic average was defined in relation to the actuator, with a midpoint of half the cyclic amplitude, y_a=0.015 D, to give one way cyclic loading at actuator level. The prescribed actuator cycles were uniform sinusoidal displacements. The mudline displacement, y_0, initially rose rapidly from zero, accompanied by larger displacement cycles, which subsequently stabilised towards a steady state by the end of the loading event.

Figure 7.2 (b) shows the load time history. The traces presented include the load cell readings, the calculated inertial load, the resultant mudline load H_0, and filtered H_0. The high frequency of loading resulted in a significant inertial load. The accelerometers distributed along the pile enabled the calculation of this inertial load for the pile. Figure 7.3 shows an extract of Figure 7.2 (b), which illustrates the calculation of H_0. The plots indicate that the inertial load, ma, is out of phase with the applied load. This is to be expected as load is in phase with displacement, whereas displacement should be out of phase with acceleration.

$$H_0 = H - ma \tag{7.1}$$

Equation (7.1) gives H_0, the load applied at the mudline, which is used to estimate the stiffness of the system. The inertial load is subtracted from the reading of the load cell to give H_0. Accelerometers below the mudline were discounted based on their readings because their influence on the load felt at the mudline was minimal. The three accelerometers above the mudline were used in the calculation of the inertial load. Each was assigned

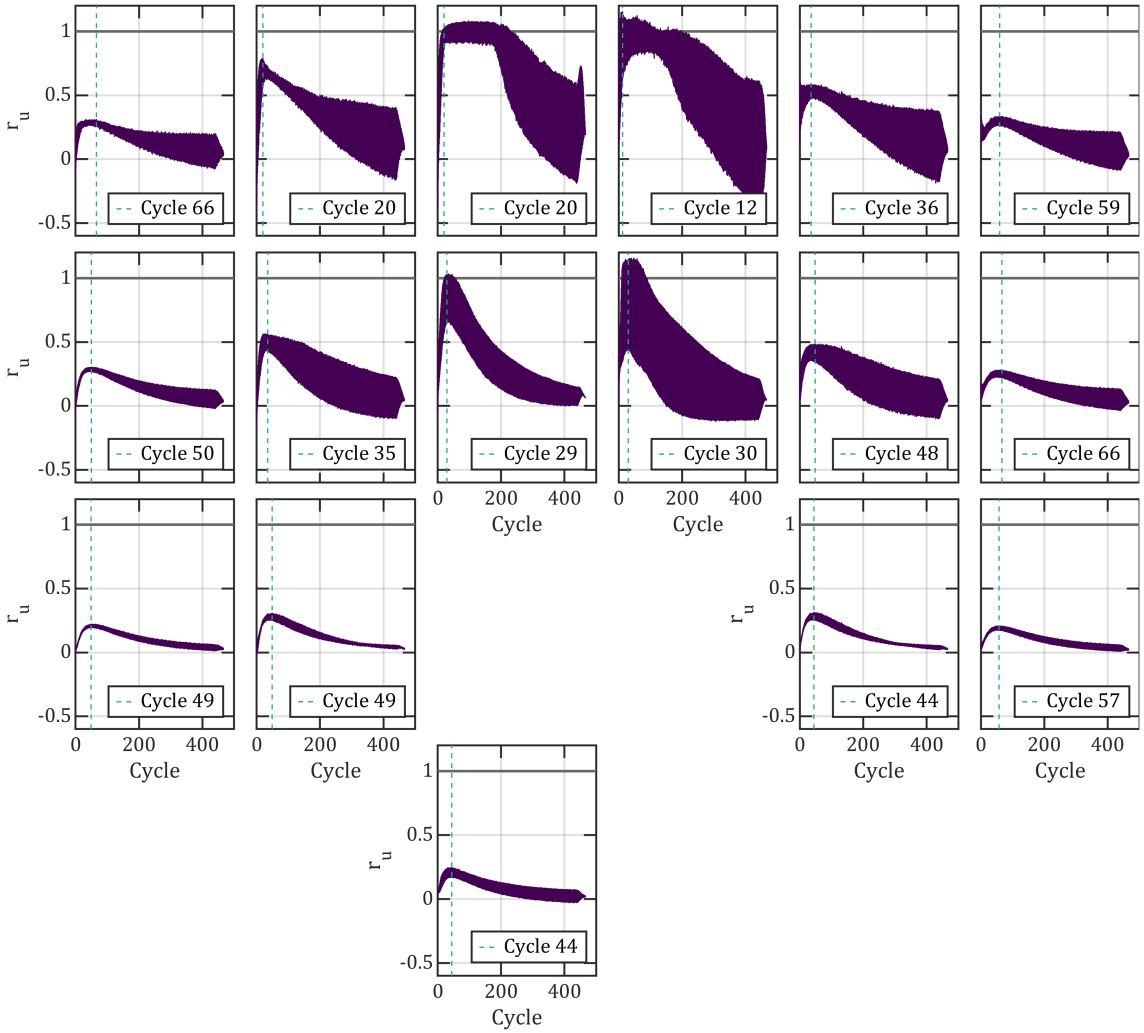

Figure 7.4: Pore pressure response measured at each PPT. All plots presented are on equal axes. Subplot locations correspond to the PPT locations within the soil (Figure 7.5). Overlaid are the points at which maximum r_u response was recorded. Increased r_u is seen towards the surface of the soil and closer to the pile. As horizontal distance increases from the pile, the number of cycles taken to reach maximum r_u increases.

a relevant mass, with the accelerometer at the top of the pile accounting for the added top mass (Table 6.2) as well as the distributed mass per unit length, while the two lower accelerometers only accounted for the distributed mass. The contribution of the inertial load from the top mass was significantly greater than that from the distributed mass.

The resulting mudline load used in subsequent analysis, H_0, was filtered to remove high-frequency components. The cutoff frequency for the low-pass filter was set at $5\times$ the loading frequency, f. The applied load included significant high-frequency parasitic components from the actuator system (Figure 7.2 (c)). The filtered load was used for presentation of load-displacement plots, and the calculation of secant stiffness (Figure 7.2 (e)). The results of lateral load are normalised by $\gamma' D^3$, and bending moment by $\gamma' D^4$. Alternative normalisation could have included the embedded length, L, and load eccentricity, e, i.e. $H/\gamma' DLe$ for lateral load, and $M/\gamma' DLe^2$ for bending moment. However, the ratios of

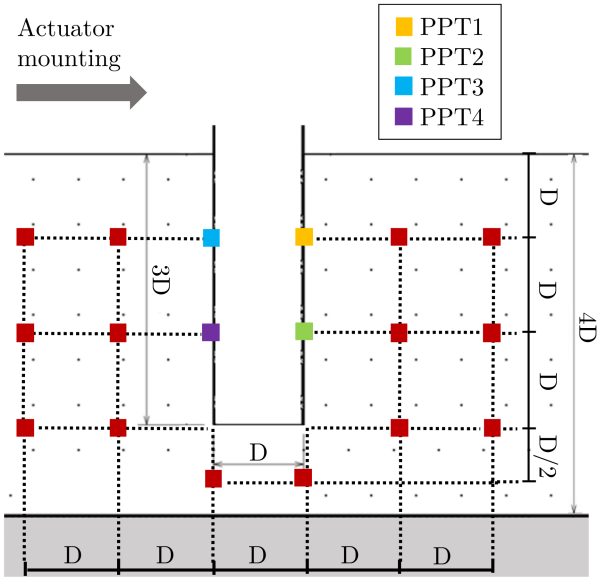

Figure 7.5: Diagram of the location of PPTs in the soil. The forward loading direction is defined as that in front of the actuator, and the direction of the first loading half-cycle. Therefore, PPT1 and PPT2 are on the front of the pile and PPT 3 and PPT4 are on the back of the pile.

L/D and e/L were maintained consistent throughout each test, therefore the comparative normalisation would have yielded the same results. The chosen normalisation factors were selected for brevity.

The load time history (Figure 7.2 (b)) exhibits an initial high load, followed by a significant decrease and then a gradual rise in the cyclic load amplitude. The early high load and subsequent drop was caused by the onset of liquefaction, as can be seen in Figure 7.4. As the loading event progressed, the pore pressures dissipated, and the soil surrounding the pile re-solidified. The gradual restoration of soil stiffness led to a steady increase in load.

The drainage regime of the cyclic tests was recorded using a grid of PPTs installed in the soil. The location of the PPTs was determined relative to the diameter, D, and consequent embedded length, L. This allowed for a comparison of the drainage of the soil system across tests with differing D. The placement of the PPTs is illustrated in Figure 7.5. Results of pore pressures are presented as the excess pore pressure ratio r_u, calculated using Equation (6.7).

Figure 7.4 shows excess pore pressure ratio, r_u, against cycle number for each PPT. The arrangement of the subplots within the grid corresponds to the position of PPTs within the soil, with loading from left to right, as shown in Figure 7.5. The PPT below the pile in front is not shown here as it was defective for T3. The overall trend for all sensors was an initial increase in excess pore water pressure (u), followed by dissipation towards a steady state. The increase in u is the cause of the drop in system stiffness (Figure 7.2 (e)) due to the corresponding reduction in effective stress. The results indicate increased u close to, and towards the top of the pile. The sensors at the top of the pile exhibit a plateaued response at $r_u = 1$, indicating sustained liquefaction. Sensors at the base of the

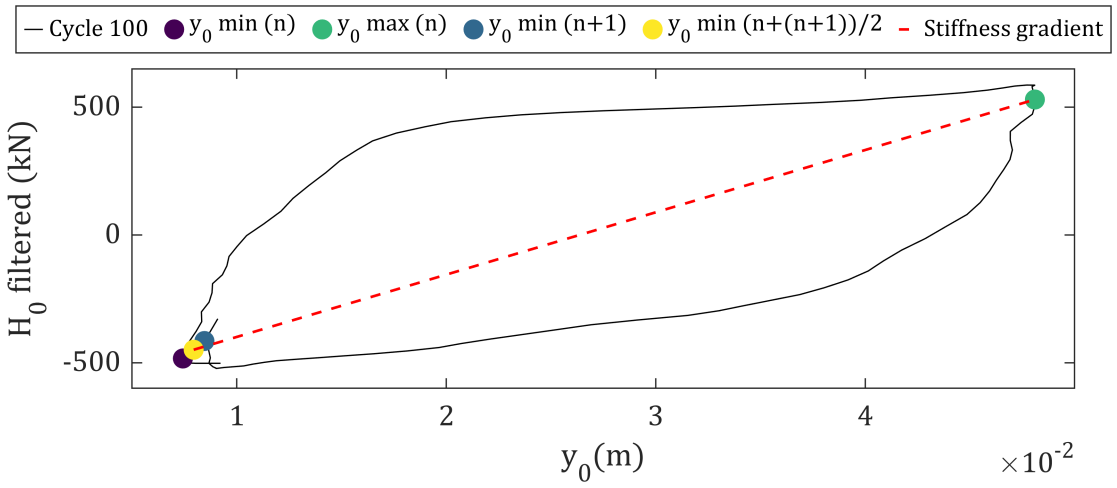

Figure 7.6: Example cycle of filtered H_0 vs y_0. Stiffness is calculated using the points overlaid, following Richards (2019). The gradient of the line between the average (y_0 min (n+(n+1))/2) of the point of minimum displacement of the current cycle (y_0 min (n)) and the next cycle (y_0 min (n+1)), and the point of maximum displacement of the current cycle (y_0 max (n)).

pile also show liquefaction (r_u= 1), although this occurs over a small number of cycles with dissipation starting earlier. The max r_u value diminishes with increased depth within the soil, which is expected as the pile movement is greater towards the surface. The reduction in r_u with increased horizontal distance from the pile is due to reduced strain within the soil. The plots of Figure 7.4 are overlaid with the cycle in which the greatest pore pressure response, $r_{\text{u MAX}}$, was achieved for that sensor. The plots of the top pile sensors, where the soil is liquefied for a sustained period, show that there are many cycles where $r_u \approx 1$. Therefore, the highlighted cycle is taken at the first instance of $r_u = 1$. The cycle of $r_{\text{u MAX}}$ increases with horizontal distance from the pile. This demonstrates the expanded region of soil mobilisation as the test progresses. The soil surrounding the pile was softened, leading to mobilisation of soil further from the pile to take the load.

The evolution of stiffness through the test is shown in Figure 7.2 (e). The stiffness is calculated using the method of Richards (2019), as demonstrated in Figure 7.6. To eliminate the effect of ratcheting on the stiffness calculation, the stiffness is determined between the point of maximum displacement and the average of the points of minimum displacement from the current and subsequent cycle, indicated as the green and yellow dots in the plot.

Figure 7.2 (d) shows the load displacement plot for the event (the load displayed is the filtered load at the mudline, H_0). This illustrates the early increase in mudline displacement, y_0, from zero towards the midpoint, as the cycle number increases. The plot also indicates the increase in stiffness throughout the test following the initial liquefaction. Cycle 100 exhibits reduced load and increased displacement consistent with the reduced stiffness of Figure 7.2 (e) as expected due to the reduction of effective stress around the pile at that instant. As the load event progresses excess pore pressures dissipate (Figure 7.4), and effective stress and system stiffness are restored; the cycles reach an increased load

for lower displacement. The initial overshoot in mudline displacement amplitude, shown in Figure 7.2 (a), is caused by the control system stabilising with updates in the system stiffness. Around cycle 100, while the stiffness remains low, the mudline cyclic amplitude stays relatively high. The low soil stiffness allows large pile movements within the soil under the prescribed actuator displacement. As the loading event advances, the system stiffness increases (Figure 7.2 (e)), leading to increased pile flexure and a reduction in y_0 cyclic amplitude.

Figure 7.2 (f) shows the time history of mudline moment throughout the test. The mudline moment is calculated as $H_0 \times e$, where e is the load eccentricity. The time history follows the same pattern as H_0 (Figure 7.2 (b)), influenced by soil liquefaction and subsequent excess pore pressure dissipation. Figure 7.2 (g) provides the pile rotation history. The pattern is similar to the actuator displacement, exhibiting a steady oscillation in rotation, θ, between 0 and 0.3°. However, a kink is observed early in the trace, corresponding to the mudline displacement trace and is also attributed to the stabilization of the actuator system. Expectedly, the mudline displacement magnitude was more significantly affected by the initial liquefaction compared to the mudline rotation given the way displacement was controlled at the actuator level. Figure 7.2 (h) presents the moment-rotation plot for the test. The increase in stiffness throughout the test following initial liquefaction, as in the load-displacement plot of Figure 7.2 (d), is evident here.

7.2.2 Reference repeat event: T3_4

Following the first displacement controlled event of T3, three additional displacement controlled events were applied. The next two were for different D_{ref}, and therefore, loading period, so not directly comparable. The fourth event, T3_4_D10_03A_D_r, was conducted under identical load conditions, serving as a repeat. This allows for an analysis of load history effects, discussed later, and provides an indication of the steady state of the system under continued cycling. Figure 7.7 gives the load and displacement time histories for this event. The presentation and analysis were performed in the same way as for Figure 7.2. After an initial ramp in displacement magnitude, a steady state was maintained throughout the duration of the cycles in all measured data. This steady state was similar to the conditions reached at the end of T3_1_D10_03A_D (Figure 7.2).

7.2.3 Reference first and repeat event comparison: T3_1, T3_4

Figure 7.8 shows H_0 and y_0 against cycle number for the first event, T3_1_D10_03A_D, and the repeat event, T3_4_D10_03A_D_r. It can be seen that the response in T3_1 was close to but not yet fully at steady state conditions for either load or mudline displacement. The events between T3_1 and T3_4 are likely to have caused some densification and pile movement, hence the trace of T3_4 not following exactly at the levels of load and mudline displacement reached at the end of T3_1. Figure 7.9 shows the pore pressure response against cycle number for both events. PPT1 is the top front sensor, and PPT2 is the base

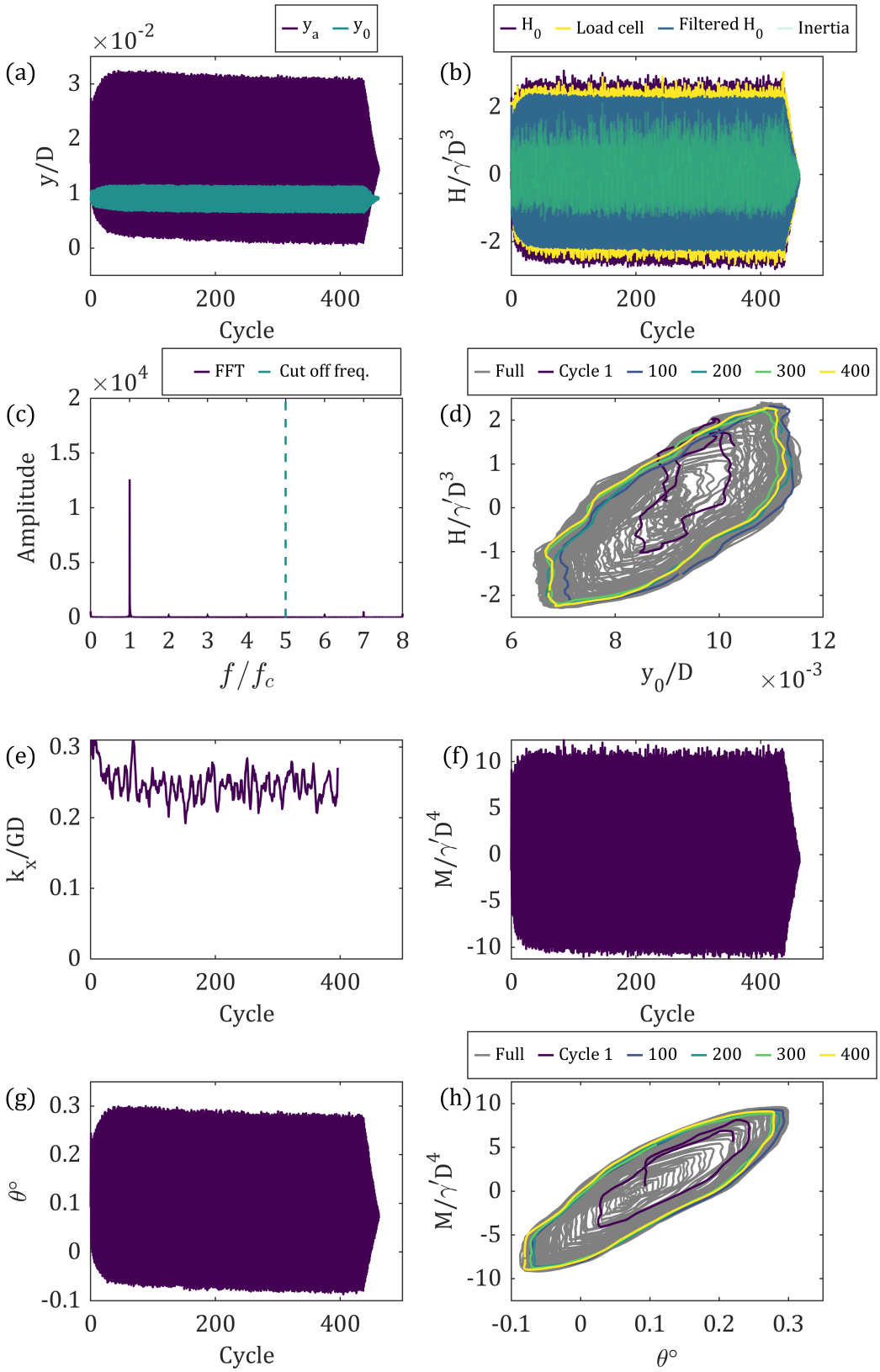

Figure 7.7: Plots of load and displacement response during T3_4_D10_03A_D_r:(a)y_a and y_0. (b)Measured, inertial, mudline (H_0) and filtered load. (c)Frequency domain plot of H_0. (d) Filtered H_0 vs y_0. (e) System stiffness, k_x. (f) Mudline moment, M. (g) Pile rotation. (h) Filtered M vs θ.

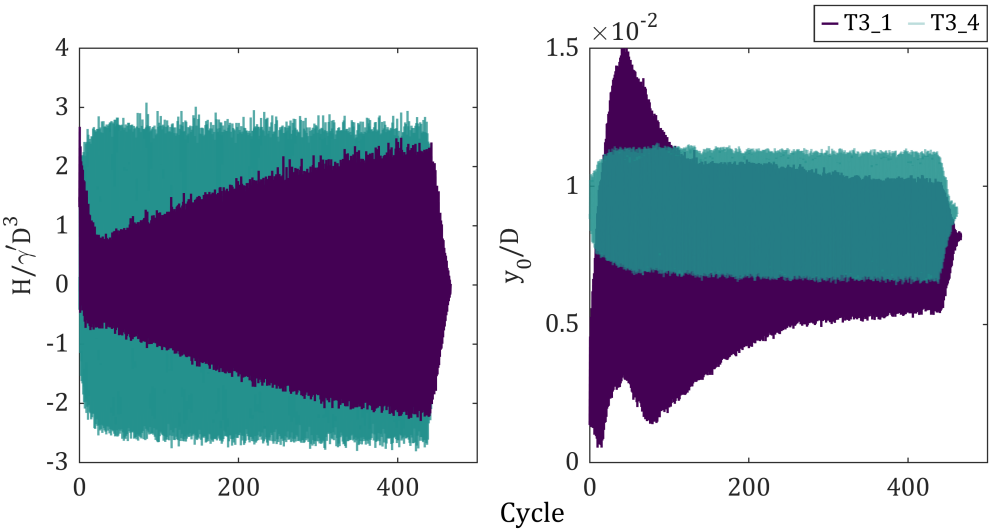

Figure 7.8: Reference first and repeat events, T3_1_D10_03A_D and T3_4_D10_03A_D_r, showing H_0 and y_0 against cycle number for each event.

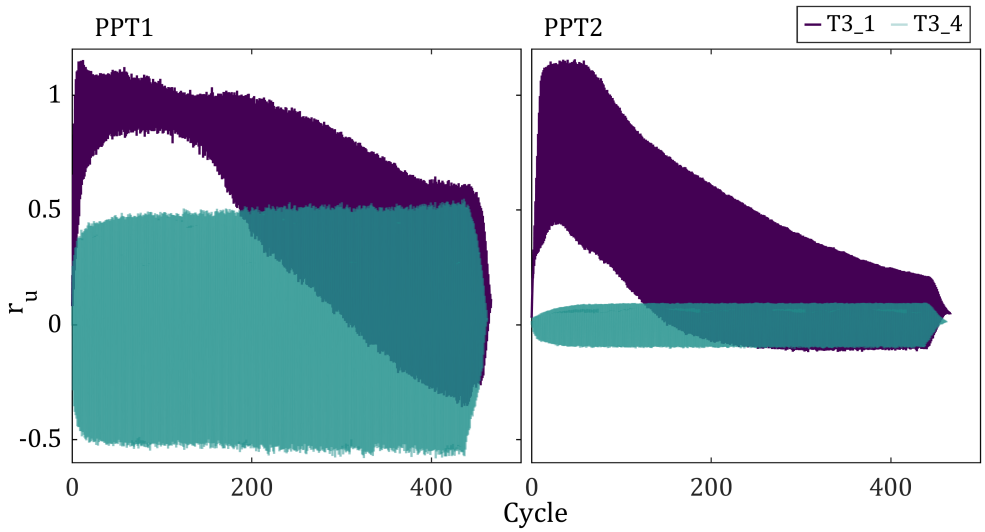

Figure 7.9: T3_1_D10_03A_D and T3_4_D10_03A_D_r, showing u response normalised as r_u, at PPT1 and PPT2, against cycle number for each event.

front sensor (Figure 7.5). These plots show a similar trend of steady state in response for T3_4, indicating that the response of T3_1 is heading towards this state but has not yet reached it. The pore pressure response of T3_4 for both sensors shows minimal accumulation of u. The oscillation in u for PPT1 is greater than that of T3_1, with cycles between -0.5 and 0.5 r_u. The densified soil, with higher D_r, had lower permeability allowing for a greater degree of negative u before it is dissipated. The magnitude was lower in PPT2 during T3_4 due to reduced pile movement with increased depth, as the surrounding soil stiffens. Additionally, there is no liquefaction for PPT1 during T3_4, and therefore there would have been minimal vertical drainage and consequent increases in u down the pile.

Figure 7.10 shows the pore pressure response of PPT1 against cycle number. Overlaid

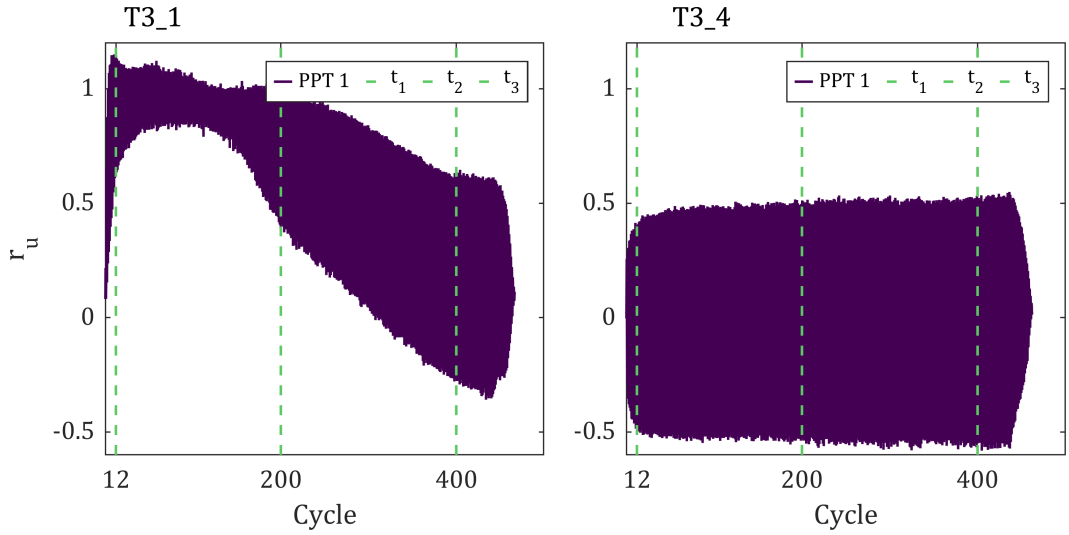

Figure 7.10: T3_1_D10_03A_D and T3_4_D10_03A_D_r, showing r_u at PPT1 against cycle number for each event. Overlaid are key cycles selected for further analysis in the contour plots shown in Figure 7.11.

is the cycle number of key cycles presented in Figure 7.11. The cycle indicated as t_1 is taken at the point of $r_{\text{u MAX}}$ of PPT1 for T3_1. The following cycles, t_2 and t_3, are taken at the instant of $r_{\text{u MAX}}$ for cycles 200 and 400. Figure 7.11 shows the contour plots of pore pressure distribution in the soil for T3_1 and T3_4 at t_1, t_2 and t_3. The loading direction is from left to right in all plots. The plots depict only the area of soil within the bounds of the PPT locations. At the soil surface, r_u is assumed to be 0. The values of r_u are calculated based on initial vertical effective stress. The plots for T3_1 show increased u in front of the pile, corresponding to the loading direction, and reduced response with increased horizontal distance from the pile and depth below the surface (as shown by Figure 7.4). At t_1, there is liquefaction at the pile surface in front, with significant r_u over a large area within the soil. By t_2, the affected area has significantly reduced, and high r_u is localised at the top pile sensors. For both t_1 and t_2, the response is approximately symmetric, with an even distribution in front of and behind the pile. At t_3, the response is greatly reduced with peak $r_u \approx 0.5$. Additionally, the response is concentrated at the front of the pile, as all accumulated u has now dissipated, and the pore pressure response is cycling in phase with loading. The plots of T3_4 show a similar distribution at all time instances. The distribution is approximately antisymmetric. At the top of the pile, there is positive u in front and corresponding negative u behind the pile, of equal magnitude ($|r_u| \approx 0.5$). The negative response behind the pile is greatest at $1D$, likely due to the increased length of the drainage pathway from the area of high pressure in front of the pile. Further down the pile, the response is inverted, with positive u behind the pile and negative response in front. This indicates that the point of pile rotation has changed from below the pile at the start of T3_1 to within the pile length during T3_4.

Figure 7.12 shows extracts of the mudline and actuator displacement at t_1, t_2 and t_3, from T3_1_D10_03A_D. The plots indicate that mudline displacement is approximately

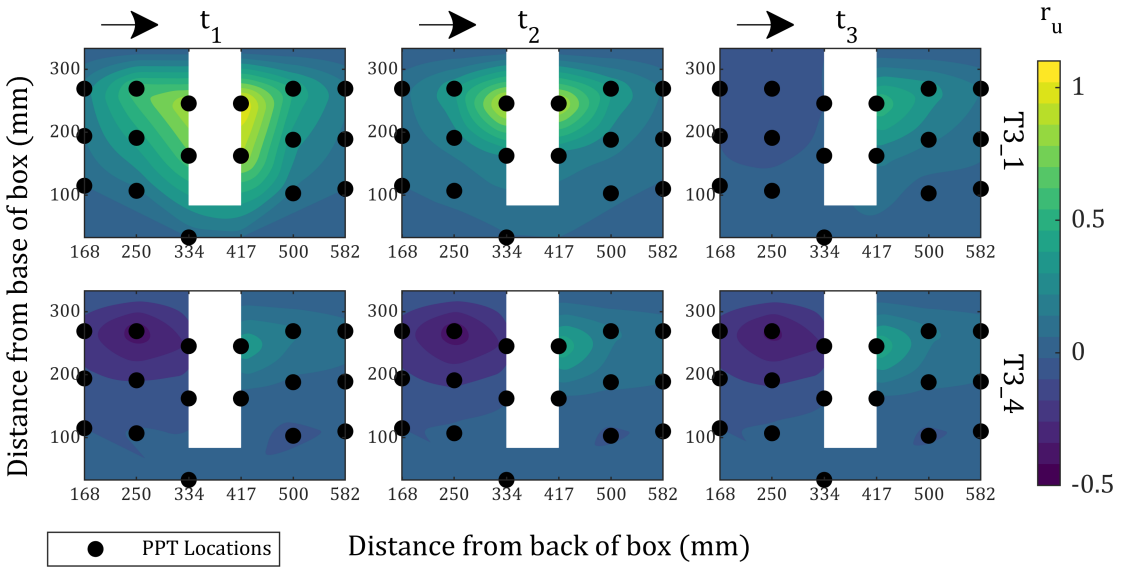

Figure 7.11: Contour plot of the u distribution within the soil during events T3_1_D10_03A_D and T3_4_D10_03A_D_r. Each time instance corresponds to the cycles labelled in Figure 7.10. Response is illustrated with r_u calculated based on initial vertical effective stress. Loading is from left to right.

in phase with actuator displacement, exhibiting a small phase difference and a slight delay relative to the actuator. This phase shift is consistent across all instances, even as mudline displacement decreases throughout the test. Figure 7.13 presents extracts of y_0 and H_0. Once again, the load and displacement are approximately in phase; however, the lag is more pronounced. The lag between displacement and load seen here is caused by damping in the system, as evidenced by the area enclosed within the loops of Figure 7.2 (d). The inverse proportionality of y_0 and H_0 cyclic amplitude is further demonstrated here. As the soil stiffens, the load response for the applied actuator displacement increases with corresponding decreased mudline displacement.

Figure 7.14 shows the evolution of the relationship between load and u. At all instances the load is approximately in phase with the front PPTs, PPT1 and PPT2 (Figure 7.5). In contrast the PPTs at the back of the pile, PPT3 and PPT4, are out of phase with the load when maximum values are considered. The traces indicate that the pore pressures developed are caused by normal forces, with compression induced positive pore pressure, and suction induced negative pore pressure. The r_u response reduces upon unloading and there is no indication of a double frequency, this indicates that the pore pressures are a product of pre-phase transformation contraction which switches to post-phase transformation dilation. The pore pressure response on PPT1 at t_3 shows a truncated peak above $r_u = 0.5$. This is likely due to shearing induced dilation in the front of the pile limiting pore pressure accumulation. PPT3 (behind the pile) is not truncated during increasing r_u half-cycles, indicating the absence of sufficient shear strain due to the forward one way cyclic loading in terms of displacement, instead it shows a gradual change in increase in pressure, followed by a fast reversal in accumulation of u coinciding with load reversal. The traces show that

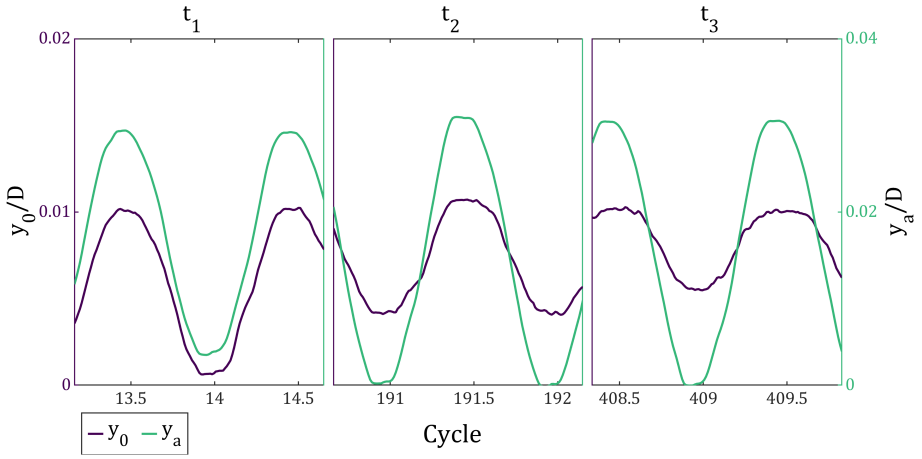

Figure 7.12: Extract of the traces of mudline displacement response, y_0, and the applied actuator displacement, y_a, from T3_1_D10_03A_D. Traces are extracted at the time instances labelled in Figure 7.10. y_0 traces correspond to the left y axes, and y_a to right y axes.

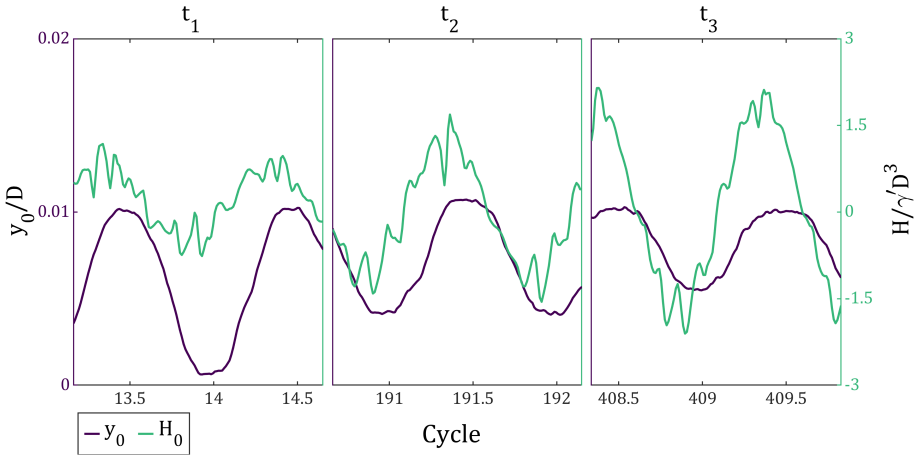

Figure 7.13: Extract of the traces of mudline displacement response, y_0, and mudline load, H_0, from T3_1_D10_03A_D. Traces are extracted at the time instances labelled in Figure 7.10. y_0 traces correspond to the left y axes, and H_0 to right y axes. H_0 shown is unfiltered.

when liquefaction is reached it is transient, with r_u decreasing when the pile displacement reverses. As a result, when load is applied the monopile is never surrounded by fully liquefied soil.

The results of the reference displacement tests show a clear relationship between load, displacement, and pore pressure response. The applied actuator displacement resulted in changing load and mudline displacement, corresponding to the changing stiffness of the pile system. During the early phases of the first test on unloaded soil rapid pore pressure accumulation led to a reduction in system stiffness and allowed high mudline displacement. The initially collapsible soil structure settled into a denser configuration as the excess pore pressures dissipated. This coincided with an increase in mudline level load, and a decrease in mudline displacement for the applied actuator displacement. The soil stiffened as excess pore pressures dissipated following initial liquefaction. Suction behind the pile was still present while excess pore pressures had accumulated to high values.

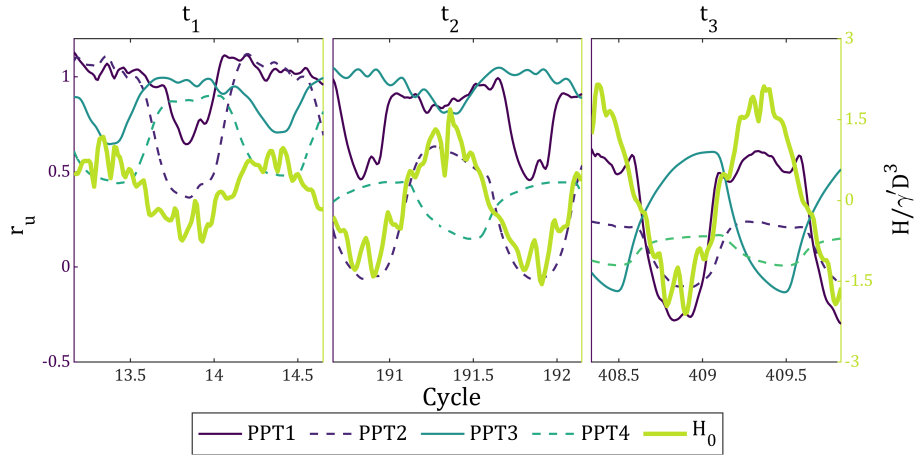

Figure 7.14: Extract of the traces of mudline load, H_0, and r_u at each pile mounted PPT, from T3_1_D10_03A_D. Traces are extracted at the time instances labelled in Figure 7.10. r_u traces correspond to the left y axes, and H_0 to right y axes. H_0 shown is unfiltered. PPT numbers refer to the PPT locations shown in Figure 7.5.

During the repeat test, on a preloaded soil, the system response commenced at a steady state. The soil fabric was no longer collapsible, negating large r_u accumulation upon load application. Higher soil stiffness induced by previous densification around the pile led to higher loads, with lower mudline displacement. The pore pressure response of the soil was limited to oscillation with minimal accumulation. Significant oscillation occurred, with high degrees of negative and positive excess pore pressure centred around $r_u = 0$. Pore pressure accumulation appears to have only occurred on unloaded soil, with a collapsible fabric following pluviation. While the response of the first event was illuminating in terms of pore water pressure effects, it is unlikely that such a collapsible fabric would exist following the installation of a pile in-situ, making the response of the repeat event more realistic.

7.3 Reference load controlled storm test

The following section outlines the results of a reference load-controlled storm event. The test programme included multiple storm events for each model, which were performed after the completion of the displacement controlled tests. The load amplitude for the majority of tests was set at $H = 0.5H_{\mathrm{ULT}}$; additionally, an extreme storm was applied at $H = 0.75H_{\mathrm{ULT}}$ with D_{ref}= 12 m. Prior to the main programme of tests, a conservative low amplitude storm test was applied to each model to allow calibration of the actuator. Results from a reference storm event, T3_6_D12_50A_S, are provided in detail to illustrate the typical system response.

The full load and displacement response of the reference test T3_6_D12_50A_S is shown in Figure 7.15. In the load and displacement plots (Figure 7.15 (a) and (b)), it is evident that during this test, the peak load and actuator displacement exceed the levels observed in the displacement controlled tests. However, this occurs only briefly during

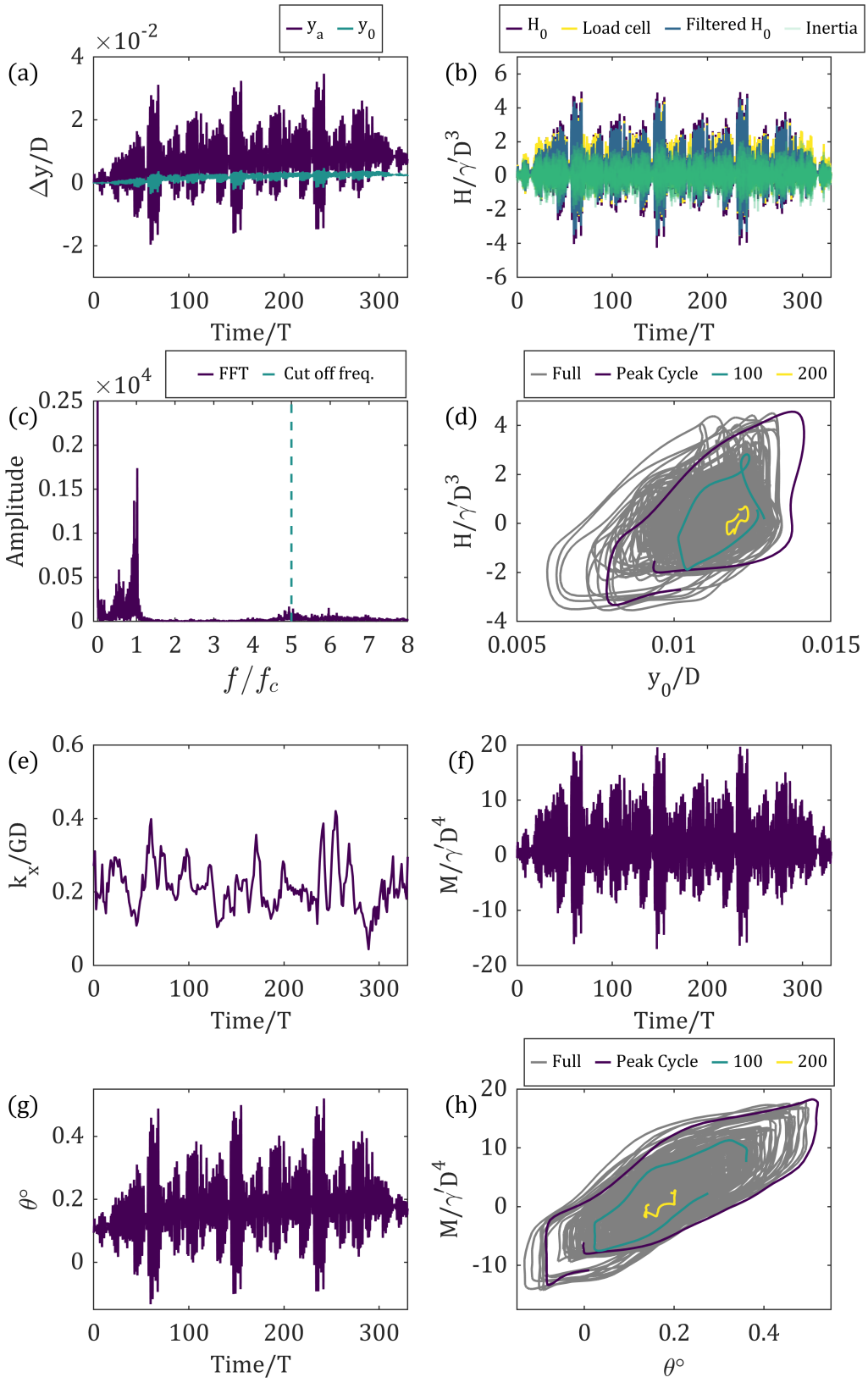

Figure 7.15: Plots of load and displacement response during T3_6_D12_50A_S. Time histories are plotted against normalised time, $Time/T$, where T is the loading period $T_m = 0.028$ s of the $D_{ref} = 12$ m monopile (Table 6.2). The plots are equivalent to Figure 7.2, where a more detailed caption is given. Subplots show: (a)y_a and y_0. (b)Measured, inertial, mudline (H_0) and filtered loads. (c)Frequency domain plot of H_0 normalised by $f_c = 36$ Hz. (d) Filtered H_0 vs y_0. (e) Stiffness, k_x. (f) Mudline moment, M. (g) Pile rotation, θ (h) Filtered M vs θ.

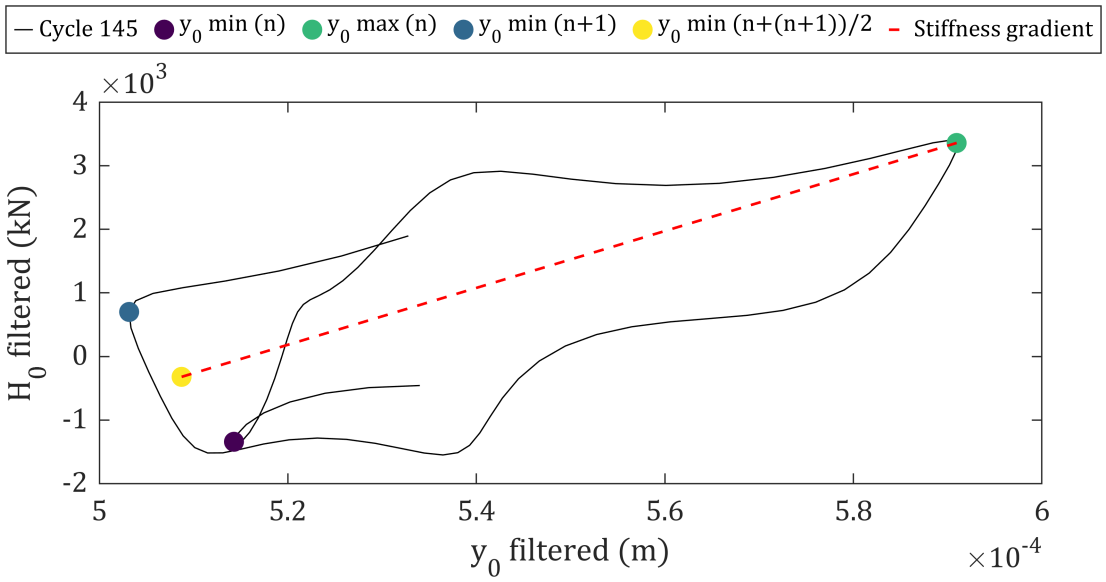

Figure 7.16: Example cycle of filtered H_0 vs y_0 during T3_6_D12_50A_S. Stiffness is calculated using the points overlaid, following the method of Richards (2019), further detail is provided in Figure 7.6. The multi-frequency load history complicates the stiffness relationship, leading to significantly varied cycle-by-cycle stiffness evolution.

the peak applied load. For most cycles, the load and displacement remain approximately equivalent to those of the displacement controlled tests (Figure 7.2). The actuator and mudline displacement plots are presented here and in all subsequent plots of storm displacement response in terms of Δy. This is taken as the change in displacement across the event, i.e. displacement is zeroed at the start of each event. This approach facilitates the comparison of events where the varied load history results in different starting points for each event.

The frequency domain plot shown in (c) indicates that the majority of the load is applied at $f = 36$ Hz (model scale), corresponding to $f = 0.145$ Hz for the D_{ref}= 12 m monopile to maintain the same drainage factor. However, there is a significant proportion of lower frequency load, reflecting the multi-frequency excitation of the load simulation (Section 6.8.3). Additionally, there is a portion of high frequency parasitic excitation above $4f_c$ from the actuator system. In plots (d) and (h) the load and moment are filtered to eliminate the higher frequency components, following the same methodology applied to the displacement controlled tests. The filter applied was a low-pass Butterworth filter at the cut off frequency highlighted in (c). The cut off is 5× the characteristic frequency f_c. The stiffness shown in (e) is calculated using the filtered load.

Both the load displacement, (d), and moment rotation, (h), plots exhibit less consistent cycles than the displacement controlled tests, owing to the variability in the applied loads. However, in the largest cycles shown in Figure 7.15 (d), some displacement accumulation is evident, indicated by the translation of cycles towards the right for equal loads. The highlighted “Peak Cycle”, is the last cycle of the higher amplitude instances seen in the load history in (b).

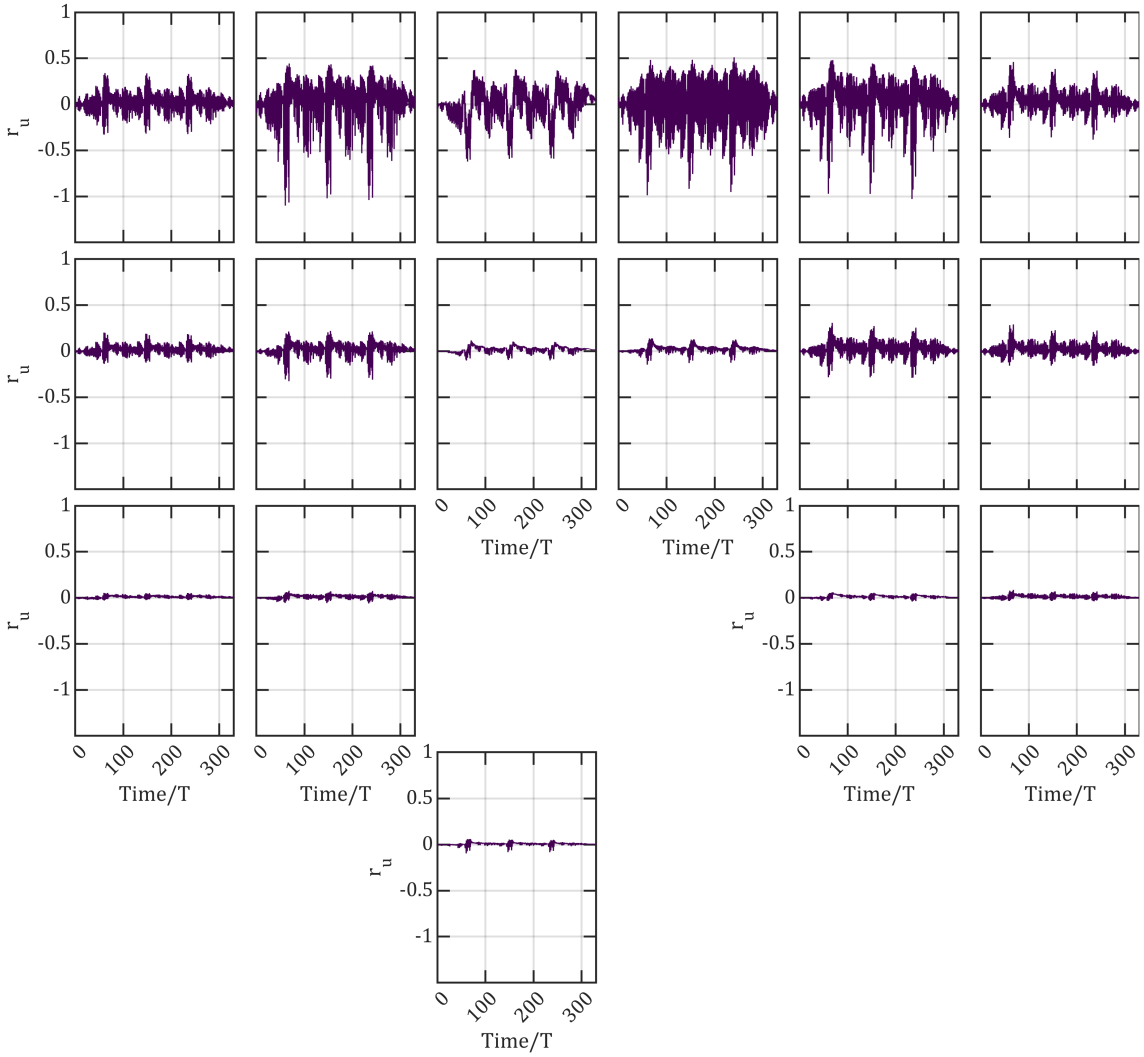

Figure 7.17: Pore pressure response measured at each PPT. Response is plotted as excess pore pressure ratio, r_u, against normalised time, $Time/T$. Axes labels given on the lowest subplot for concise presentation, all plots presented on equal axes. Subplot locations correspond to the PPT locations within the soil (Figure 7.5). Increased response is seen towards the surface of the soil, and closer to the pile.

The trace shown in Figure 7.16 gives an example cycle during T3_6. This illustrates the definition of stiffness determined during the storm events. The same methodology employed for the displacement controlled tests is followed (Figure 7.6). The method removes the effect of ratcheting from the stiffness calculation. However, as can be seen here, the complex load history applied led to more significant variation in the calculated secant stiffness time history in Figure 7.15 (e). The point of highest stiffness is concurrent with the peak loads. During these loads the highest suction is generated behind the pile. This is coupled with a limited accumulation of pore pressure in front of the pile caused by shearing induced dilation. Following the peak of stiffness, there is a sharp drop in stiffness, coinciding with a drop in the applied load and an increase in the average r_u. The relationship between stiffness and load is linked to the pore pressure response.

The plots shown in Figure 7.17 illustrate the u response during T3_6. As seen in

the results for the displacement controlled tests (Figure 7.4), the measured response is greatest at the top layer of sensors, decreasing with depth below the surface. Additionally, a comparable trend of reduced response with increasing horizontal distance from the pile is observed. As discussed in reference to Figure 7.11, there is a greater response observed $1D$ behind the pile at the top surface. The spikes of negative r_u are of greater magnitude than the positive spikes, this is the case both in front of and behind the pile. The points of increased negative response coincide with the peak loads. Following this there is a period of accumulated pore pressure, caused by unloading after the shearing of the peak loads. The pore pressure accumulation is limited during peak loads, caused by shearing induced dilation. However, following this the pore pressure accumulates, leading to a drop in stiffness as discussed.

7.4 Dimensionless factor analysis

The following section presents results for analysis of the dimensionless drainage factor $MkT/\gamma D^2$. Results are divided into two sections relating the regular displacement controlled tests, and multi-frequency load controlled storm events. The events displayed have been chosen with the closest possible conditions, particularly with regards to load history. Furthermore, the chosen events depict the effect of loading with matched and with different drainage factors.

7.4.1 Dimensionless factor analysis: displacement controlled tests

The following section outlines the results of the displacement controlled tests examining the dimensionless drainage factor, $MkT/\gamma' D^2$. The results presented assess the validity of the drainage factor both for events where the factor is maintained and varied.

For this analysis, events have been selected to review the validity of the drainage factor under various conditions. The first loading event of tests T3, T4, and T5 (T3_1_D10_-03A_D, T4_1_D10_03A_D, T5_1_D10_03A_D), which were completed with equivalent loading conditions and drainage factor, are presented for comparison. In cases where the selected event was applied to a preloaded model, an effort was made to select the closest matching load history. Events where D_{ref} is equivalent are nominally of the same drainage factor; thus, where D_{ref} is varied, the drainage factor is varied. Taking this into account, the events chosen for further analysis of the maintained drainage factor include T3_4_-D10_03A_D, T4_4_D10_03A_D, T5_7_D10_03A_D, and T6_16_D10_03A_D. All of these events were performed on a preloaded model with the same loading conditions, providing further insight into the drainage factor. For examination of a varied drainage factor, events T6_8_D12_03A_D, T6_12_D14_03A_D, and T6_16_D10_03A_D are presented. These events, completed on the same model, were performed after significant preloading. Therefore, the initial soil conditions, whilst not identical, were closely matched. This allowed for an effective analysis of the varied loading period as part of the drainage factor.

First events with matched drainage factor and loading: T3_1, T4_1, T5_1

The first events of T3, T4 and T5 were loaded under the same conditions relative to D_{ref}, and therefore drainage factor, for a varying number of cycles. However, the setup for each test was different. The pile in T3 had a prototype diameter D_{p}= 4.15 m and was saturated with 50 cSt pore fluid. T4 had a pile of D_{p}= 5 m, and also saturated with 50 cSt pore fluid. In contrast, T5 had a pile of D_{p}= 4.15 m but was saturated with 66.5 cSt pore fluid. The increase in viscosity for T5 resulted in a drainage factor matching that of T4 for any given loading period. The loading period for each event was set in relation to the given reference monopile, D_{ref}, as discussed in Section 6.4. Consequently, for test T3, the loading period was shorter compared to T4 and T5 for an equivalent event (Table 6.2).

Figure 7.18 shows the time histories of H_0 and y_0 against cycle number for the first events of T3, T4, and T5. The plot of the load against the cycle number demonstrates a consistent response in load evolution across all events. T3_1 and T4_1 had a reduced number of cycles; consequently, they did not reach the steady state condition observed in T5_1. The absolute load for T4, with a larger D_{p}, was correspondingly larger. However, the normalised load follows the same trend and amplitude as the other piles.

The results for y_0 are less consistent. All of the tests exhibit a similar trend of increased displacement at the onset of the event, followed by a reduction in displacement as the test progressed. The displacement averages of T3 and T4 appear to be converging towards similar midpoints (as shown in Figure 7.25), however the average of T5 remains lower $y_{0\ \text{av}} \approx 0.004D$. This is in spite of the same applied actuator displacement (Figure 7.19(a)). The magnitude of y_0 oscillation is varied between the tests, with the lowest oscillation during T3_1.

The moving mean pore pressure response of each test is very similar, as seen in Figure 7.19(b). This plot showed the average pore pressure response across each test, measured at PPT1. The moving mean was calculated across a moving window of size equivalent to two cycles. The degree of pore pressure accumulation, and rate of dissipation is consistent across each test. This is in spite of the fact that the pile diameter, loading period, and pore fluid viscosity was not maintained and provides strong evidence for the validity of the drainage factor.

Figure 7.43 shows the full pore pressure response of the tests at PPT1 and PPT2. Once again, the time history of u is very similar across all tests. There is initial liquefaction for all tests in both sensors, followed by dissipation towards $r_{\text{u av}}$= 0. T5_1 reaches steady state as sufficient cycles were applied, whereas T3_1 and T4_1 do not achieve this level. The three tests with variations in diameter and permeability demonstrate matched drainage responses.

Figure 7.21 presents the time histories of u for T3_1 and T4_1. Overlaid on the plot are the key cycles at which contour plots are presented in Figure 7.22. The drainage response for each cycle is illustrated at the instant of maximum u of PPT1. The contour

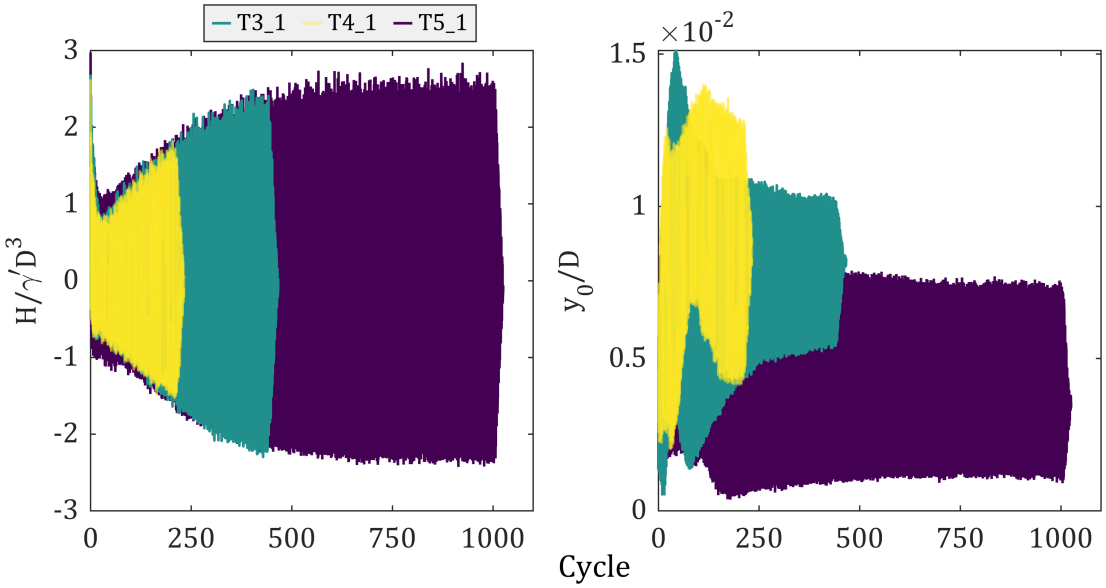

Figure 7.18: Mudline load, H_0, and mudline displacement y_0, from T3_1_D10_03A_D, T4_1_D10_03A_D and T5_1_D10_03A_D. Loading period, pore fluid viscosity and model diameter were varied, but drainage factor was maintained.

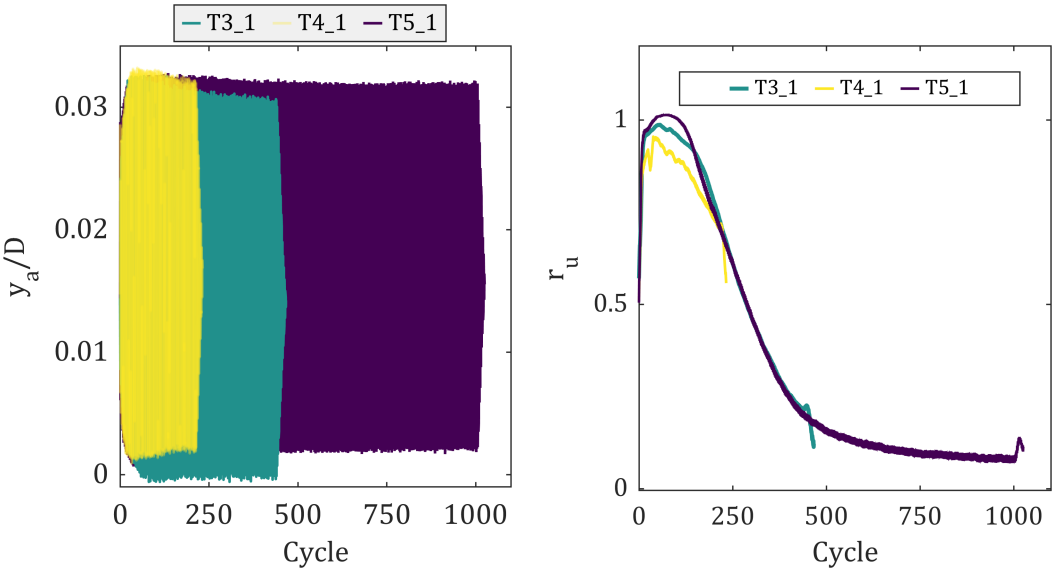

Figure 7.19: First events of displacement controlled tests T3_1_D10_03A_D, T4_1_D10_03A_D and T5_1_D10_03A_D subplots, showing: (a) applied actuator displacement is maintained across all tests, (b) moving mean r_u showing accumulation of u in each test. Pore pressure is measured at PPT1.

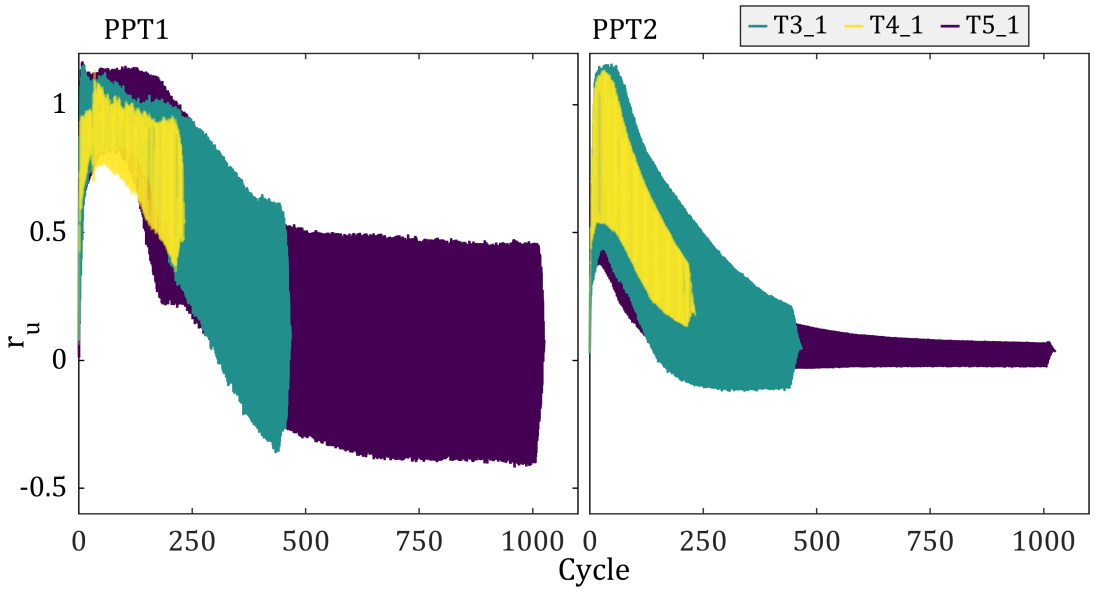

Figure 7.20: Excess pore pressure ratio, r_u, at PPT1 and PPT2, from T3_1_D10_03A_D, T4_1_D10_03A_D and T5_1_D10_03A_D. Response shows good agreement, providing strong evidence for the drainage factor maintained across different events.

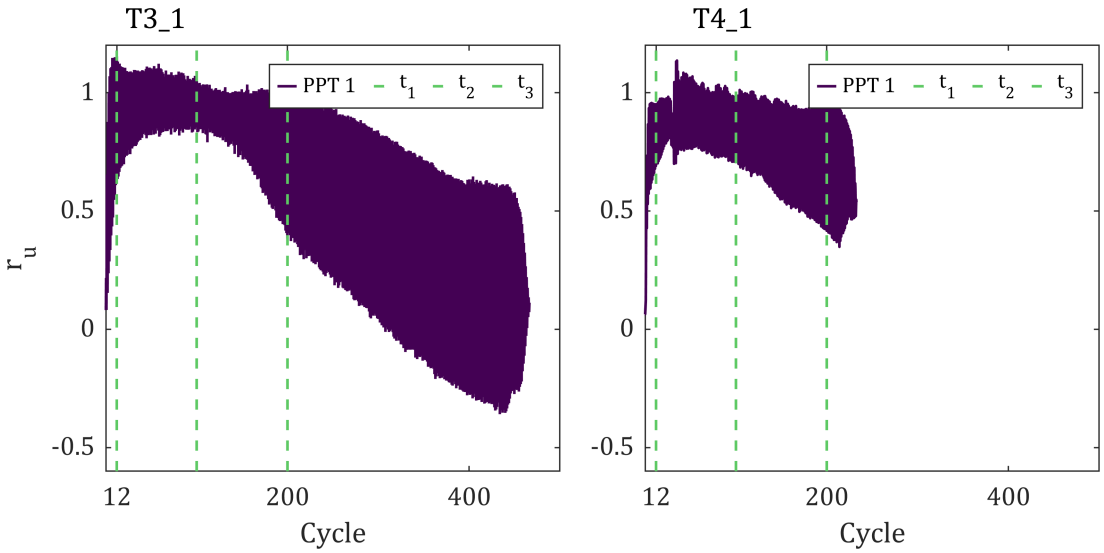

Figure 7.21: Excess pore pressure ratio, r_u, at PPT1 against cycle number from T3_1_D10_03A_D and T4_1_D10_03A_D. Overlaid are key cycles selected for further analysis in the contour plots shown in Figure 7.22. The selected cycles are: cycle 12 - maximum u at PPT1 during T3_1, cycle 100 - midpoint of T4_1, cycle 200 - end of T4_1.

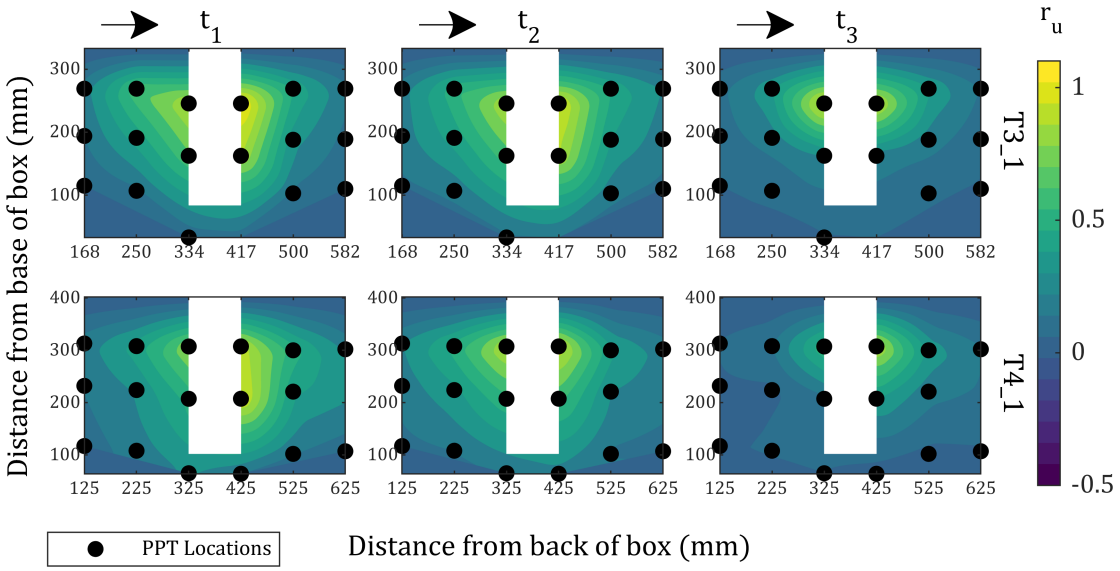

Figure 7.22: Excess pore pressure ratio, r_u, distribution from T3_1_D10_03A_D and T4_1_D10_03A_D. Time instances shown are the points of maximum u response, at PPT1, during the cycles labelled in Figure 7.21.

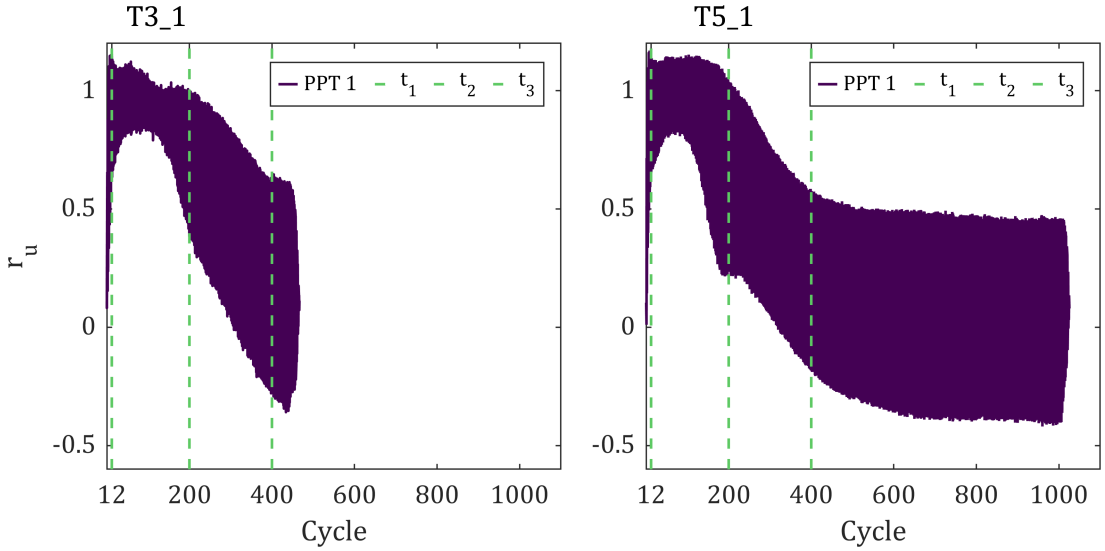

Figure 7.23: Excess pore pressure ratio, r_u, at PPT1 against cycle number from T3_1_D10_03A_D and T5_1_D10_03A_D. Overlaid are key cycles selected for further analysis in the contour plots shown in Figure 7.24. The selected cycles are: cycle 12 - maximum u at PPT1 during T3_1, cycle 200 - midpoint of T3_1, cycle 400 - end of T3_1.

plots exhibit a consistent drainage response within the soil at each time instant for the two different tests. The initial drainage response indicates liquefaction at the pile surface, with higher r_u at the front of the pile, in the loading direction. As time progresses, dissipation occurs; however, full dissipation has not been achieved at t_3, after 200 cycles.

Figure 7.23 presents the time instances for comparison of T3_1 and T5_1. These tests continued for a greater number of cycles than T4_1, therefore the last time instance, t_3, is taken at cycle 400. Figure 7.24 shows the contour plots of u distribution for T3_1 and T5_1. At t_1, the response is similar, showing liquefaction in front of the pile at the

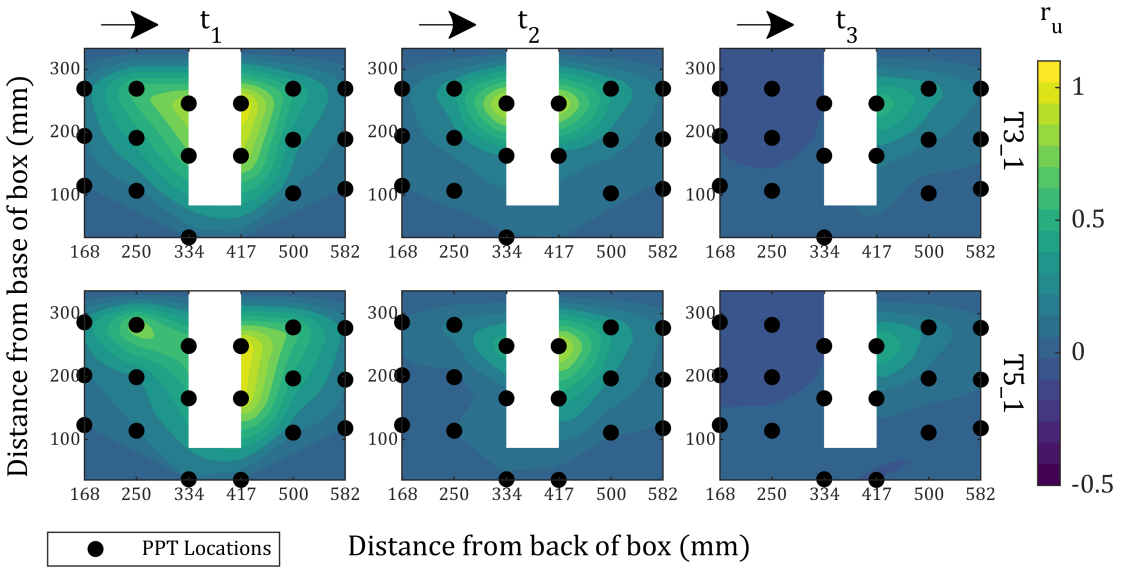

Figure 7.24: Excess pore pressure ratio, r_u, distribution from T3_1_D10_03A_D and T5_1_D10_03A_D. Time instances shown are the points of maximum u response, at PPT1, during the cycles labelled in Figure 7.23.

pile surface, as also observed for T4_1. As the loading events progressed, dissipation continued, along with early indications of an anti-symmetric u distribution as seen in T3_4 (Figure 7.11). The distribution of u within the soil is comparable for both tests at all time instances. Furthermore, the distribution at t_2 is also similar to T4_1 at the same cycle (Figure 7.22: T4_1, t_3).

Overall the response of tests T3, T4, and T5 is very similar in all respects. The normalised values of load and pore pressure response showed a consistent evolution with cycle number. Evolution of pore pressure response within the soil was shown to be consistent for all tests. The results presented here confirm the validity of the hypothesised dimensionless drainage factor. Therefore, results should also be expected to be quantitatively representative for all reference diameters examined ($D_{ref} > 10$ m).

Repeat events with matched drainage factor and loading: T3_4, T4_4, T5_7, T6_16

Figure 7.25 shows the load and mudline displacement response of T3_4_r, T4_4_r, T5_7_r and T6_16_r. These tests are conducted with matched drainage factors ($D_{ref} = 10$ m), consistent with T3_1, T4_1, and T5_1 (Figure 7.18). However, in this case, the system has been pre-loaded, creating a densified soil structure around the pile. As seen in Figure 7.7 the mudline displacement, load, and pore pressure oscillation is steady across the length of the test. The load history of each model is equivalent in terms of load and displacement amplitude experienced, but the number of cycles and events prior is varied. The similarity of load and displacement amplitude experienced implies that the current soil state is consistent for each event.

The plot of H_0 (Figure 7.25 (a)) shows similar load response for each test. It is likely

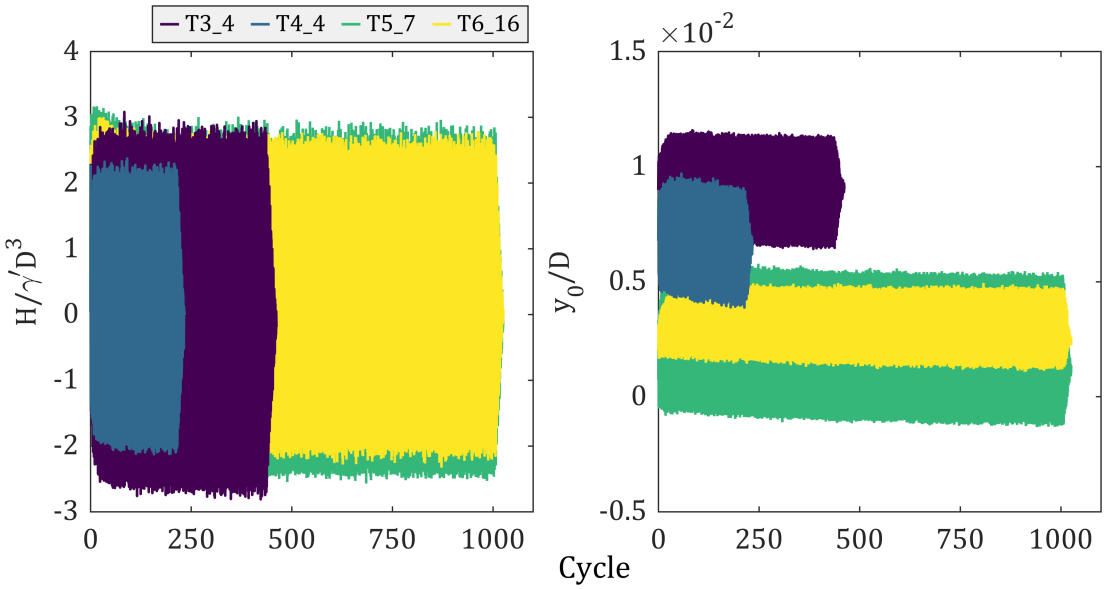

Figure 7.25: Mudline load, H_0, and mudline displacement y_0, from T3_4_D10_03A_D_r, T4_4_D10_03A_D_r, T5_7_D10_03A_D_r and T6_16_D10_03A_D_r. Loading period, pore fluid viscosity and model diameter varied, but drainage factor maintained (D_{ref} = 10 m). Prior loading variations account for differences in response.

the load response of test T4_4 is lower because it had experienced significantly fewer preceding cycles of the same amplitude (T3_4 = 1200, T4_4 = 600, T5_7 = 3000, T6_16 = 3000) indicating that potentially less densification had occurred.

The y_0 cyclic amplitude of each test was variable, although the magnitude of oscillation was not too different for tests T3_4, T4_4, and T5_7. T5_7 had the greatest cyclic amplitude, and had values of $y_{0\ av}$ comparable to T6_16. The reduced cyclic amplitude of T6_16 compared to the other tests was likely due to the increased number of total cycles previously experienced for T6_16 (T3_4=1200, T4_4=600, T5_7 = 6000, T6_16 = 15000). The variation in $y_{0\ av}$ across the tests was due to differences in the testing schedule for each model. The testing schedule of T5 and T6 required a reset of the actuator before events tested at lower cyclic amplitude (Section 6.9: T5_5, T6_5, T6_9, T6_13). Consequently, the pile was pulled back to a lower $y_{0\ av}$, then retested in a stiffer soil that experienced no liquefaction; therefore, the $y_{0\ av}$ never recovered back to the previous levels. In addition, the testing schedules applied varied numbers of cycles in the first event for each model. Therefore, pile displacement accumulation varied during the first event when the system stiffness was significantly lower. Once u dissipation had occurred and the system stiffness recovered, the pile was set in its current position, and subsequent cycling resulted primarily in oscillation with reduced displacement accumulation. Test T4_1 was terminated after 200 cycles, after which the pore pressures were allowed to dissipate before commencing the next event. Therefore, the time for rearrangement of pile position during low system stiffness was reduced.

The pore pressure response of each event is shown in Figure 7.26. The oscillation of u at PPT1 of tests T3_4 and T4_4, r_u= ±0.5, is approximately double that of T5_7 and

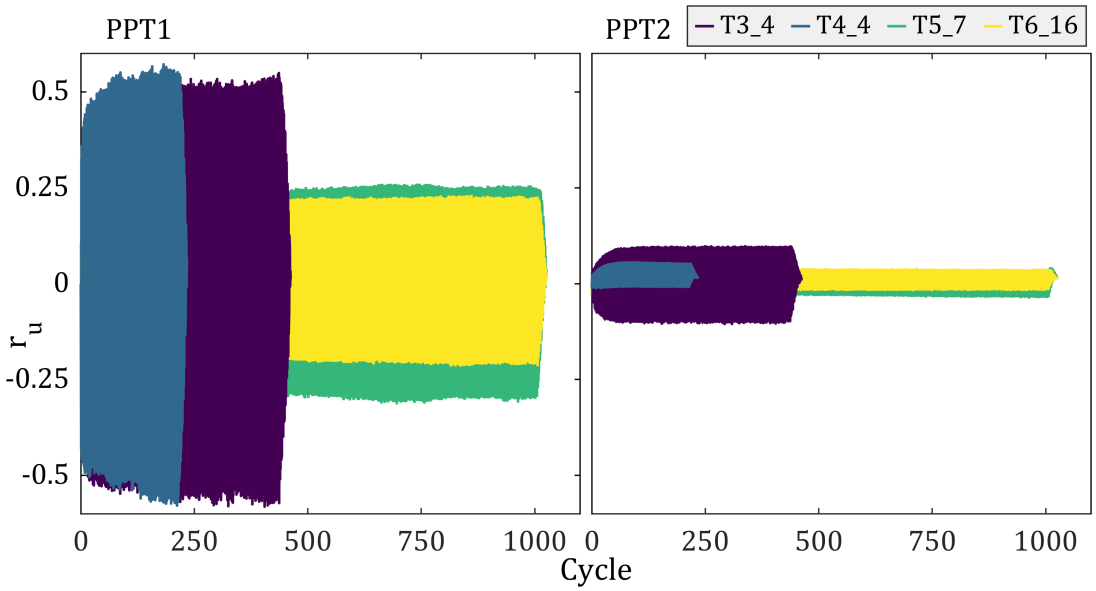

Figure 7.26: Excess pore pressure ratio, r_u, at PPT1 and PPT2, from T3_4_D10_03A_D_r, T4_4_D10_03A_D_r, T5_7_D10_03A_D_r and T6_16_D10_03A_D_r. There is significant variation in response, accounted for by differences in prior load history. Loading on more significantly preloaded soil causes no mean u accumulation.

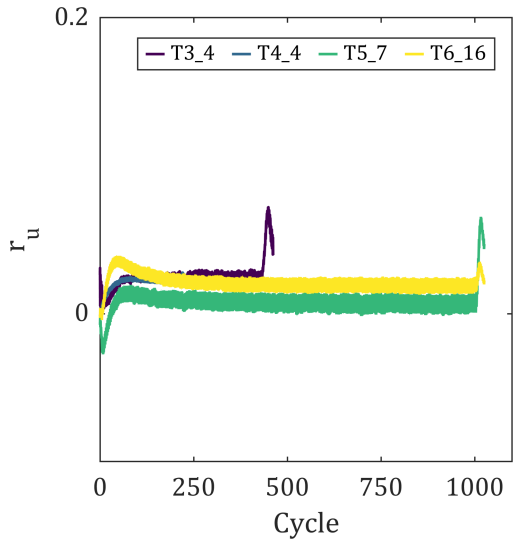

Figure 7.27: Moving mean excess pore pressure ratio, r_u, at PPT1, from T3_4_D10_03A_D_r, T4_4_D10_03A_D_r, T5_7_D10_03A_D_r and T6_16_D10_03A_D_r. There is little accumulation experienced in these preloaded events.

T6_16, $r_u = \pm 0.25$. Consistently with the previous discussion, this is due to load history effects. The oscillation at PPT2, towards the base of the pile, is significantly reduced, as previously discussed (Figure 7.9). However, the substantial amplitude of oscillation at PPT1, particularly during tests T3_4 and T4_4, indicates that the foundation system cannot be considered fully drained. The traces of $r_{\text{u mean}}$ shown in Figure 7.27 for PPT1 further demonstrate the steady state of u and show no significant accumulation across the cycles.

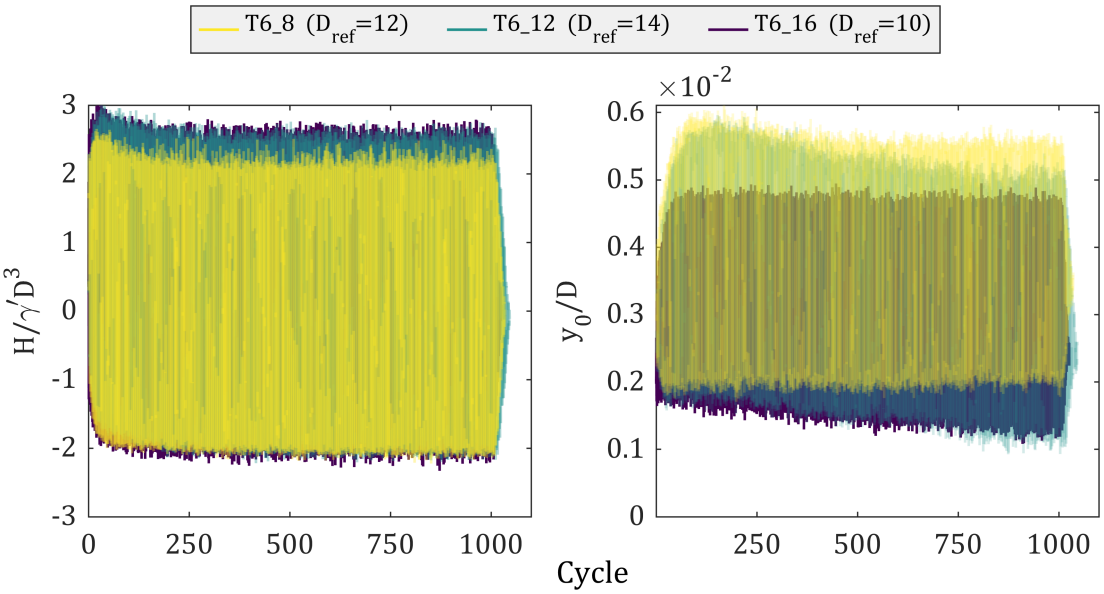

Figure 7.28: Mudline load, H_0, and mudline displacement y_0, from T6_8_D12_03A_D, T6_12_D14_03A_D and T6_16_D10_03A_D_r. These events were applied to the same model, at varying f, corresponding to the D_{ref} examined. The displacement amplitude applied for each event was maintained, and did not exceed the levels previously experienced.

Varied drainage factor during T6: T6_8, T6_12, T6_16

The testing schedule of T6 allowed for the most effective examination of the drainage factor concerning load events of varied D_{ref}. The events T6_8_D12_03A_D, T6_12_-D14_03A_D, and T6_16_D10_03A_D_r were subjected to the same number of cycles and displacement cyclic amplitude, having previously experienced identical displacement amplitude. Although the number of cycles varied among the tests, the previous loading established a steady-state response for the foundation system. Moreover, each event was conducted on the same model; thus, the parameters of D and, to a certain extent, k and M were consistent. Consequently, the variation in the loading period, T, with respect to the varied D_{ref} enabled the assessment of the drainage factor at different values.

Figure 7.28 shows the H_0 and y_0 response of T6_8, T6_12 and T6_16. The load response is comparable for each, with a slightly lower response in T6_8 (D_{ref}= 12 m). This may be attributed to the fewer cycles previously experienced. The y_0 response for each event is also consistent. A slight reverse ratcheting is observed during T6_12 and T6_16.

Figure 7.29 shows the pore pressure response of each event. There are larger oscillations of u at PPT1 during T6_16, while the responses of T6_8 and T6_12 are identical. The response at PPT2 remains consistently low across all events. The increased amplitude of oscillation at PPT1 during T6_16 contradicts the prediction of the drainage factor, that drainage should reduce with increases in D. Furthermore, the order of events means that T6_16 has previously experienced the highest number of cycles, and therefore the y_0 and u response should be reduced. The trace of accumulated u shown in Figure 7.30 also indicates a matched response for events T6_8 and T6_12, with slightly higher accumulation

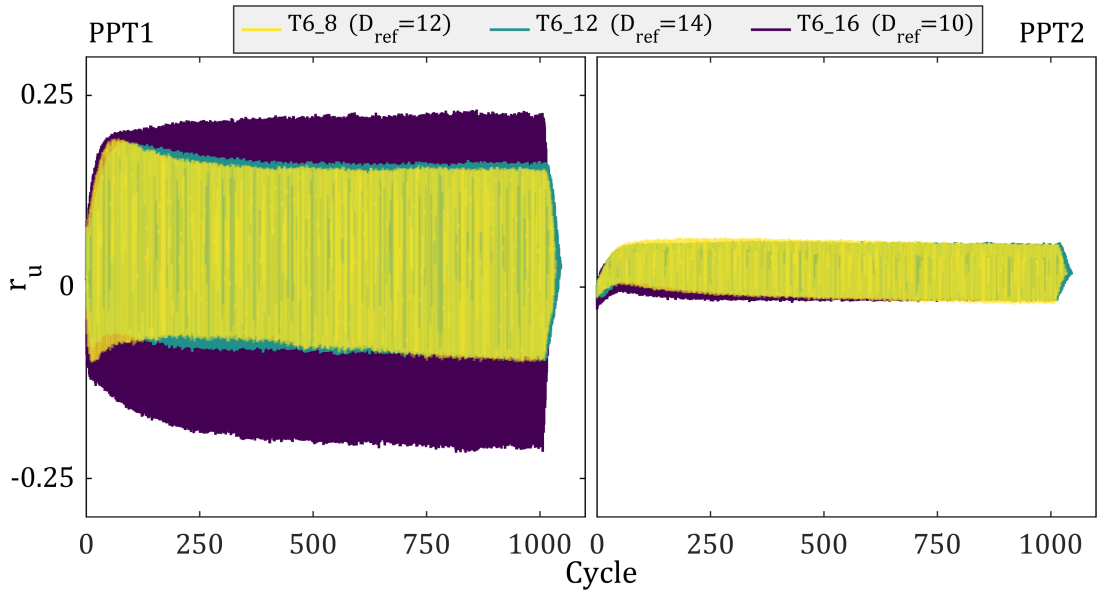

Figure 7.29: Excess pore pressure ratio, r_u, at PPT1 and PPT2, from T6_8_D12_03A_D, T6_12_D14_03A_D and T6_16_D10_03A_D_r. These events were applied to the same model, at varying f, corresponding to the D_{ref} examined. The displacement amplitude applied for each event was maintained, and did not exceed the levels previously experienced. The response is similar across all events, particularly at PPT2. However, a small increase in response is seen during T6_16. This is contrary to expectations of both greater response with increased D_{ref}, and reduced response with increased preloading and could indicate dynamic effects.

than T6_16. However, the magnitude of accumulation is low and therefore may not be significant. In contrast to the oscillatory response, the accumulation response aligns with the expected outcome regarding load history and D_{ref}.

Figure 7.31 and Figure 7.32 present the comparison of u distribution within the soil for T6_12 (D_{ref}= 14 m) and T6_16 (D_{ref}= 10 m). The value of drainage factor is most varied between these two events. The cycles presented are t_1 = cycle 100, t_2 = cycle 400, and t_3 = cycle 800. The distribution is consistent across all instances for each event, with greater variation observed in front of and behind the pile at the top layer of sensors. This trend aligns with observations in Figure 7.29. The distribution remains approximately anti-symmetric, as seen in all events with pre-loading, indicating a point of rotation within the length of the pile. However, the variation in u at lower levels is reduced compared to previous plots (Figure 7.11), reflecting a lower level of displacement at greater depths with increased densification around the pile.

The results of these tests are contrary to the expectations of reduced drainage with increased D_{ref}. The requirement for increased loading frequency to model the drainage factor of a larger monopile may lead to dynamic effects that influence the pore pressure response. The results shown in Figure 7.33(b) examine the impact of dynamic effects during a sinesweep performed at the end of T6 after storm loading. The sinesweep applied displacement controlled sinusoidal excitation ranging from 10 to 50 Hz, covering the full range of loading frequencies applied during testing. The amplification factor was calculated using Section 7.4.1, the resulting value was normalised by the amplification factor at 50 Hz.

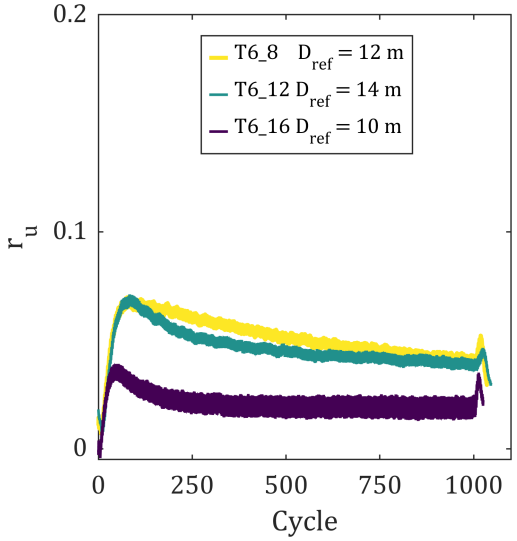

Figure 7.30: Moving mean excess pore pressure ratio, r_u, at PPT1, from T6_8_D12_03A_D, T6_12_D14_03A_D and T6_16_D10_03A_D_r. The levels of accumulation are small for all events, but with slight increases for the events of increased D_{ref} and reduced preloading.

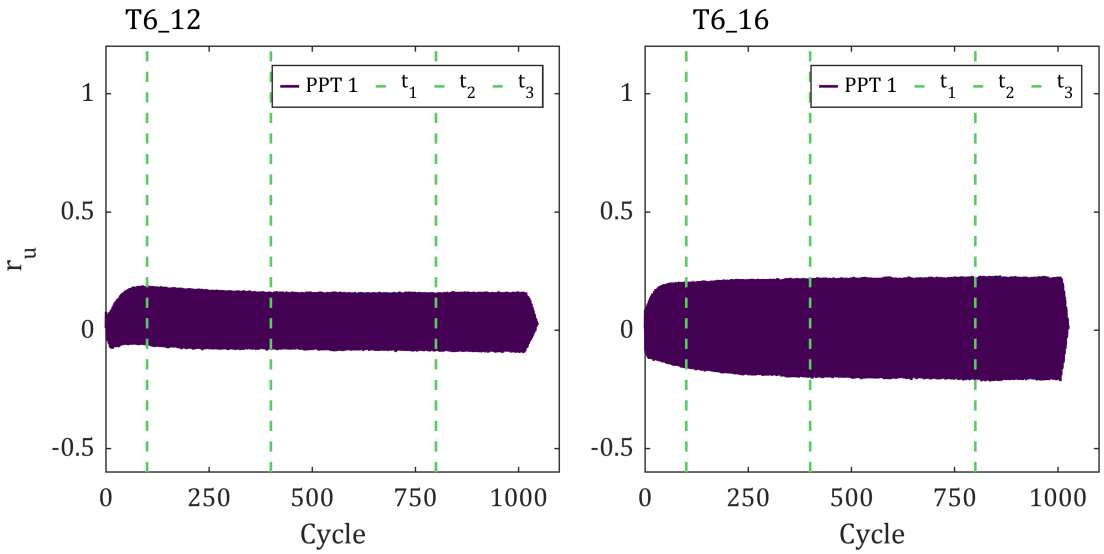

Figure 7.31: Excess pore pressure ratio, r_u, at PPT1 against cycle number from T6_12_D14_03A_D and T6_16_D10_03A_D_r. Overlaid are key cycles selected for further analysis in the contour plots shown in Figure 7.32. The selected cycles are: 100, 400 and 800.

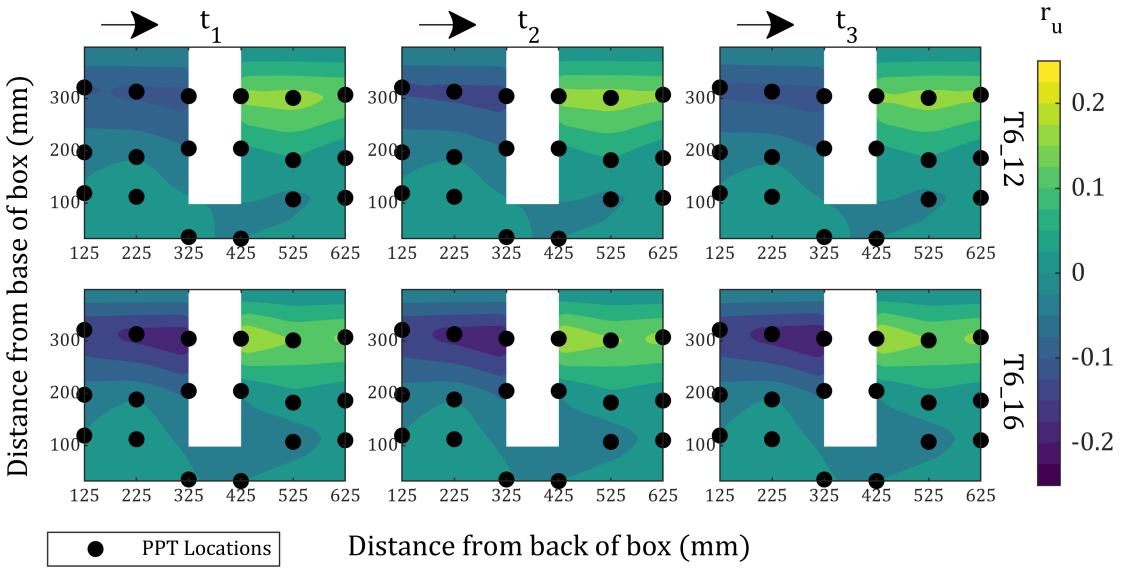

Figure 7.32: Excess pore pressure ratio, r_u, distribution from T6_12_D14_03A_D and T6_16_D10_03A_D_r. Time instances shown are the points of maximum u response, at PPT1, during the cycles labelled in Figure 7.31. N.B. the contour scale is reduced compared to earlier plots to improve contrast.

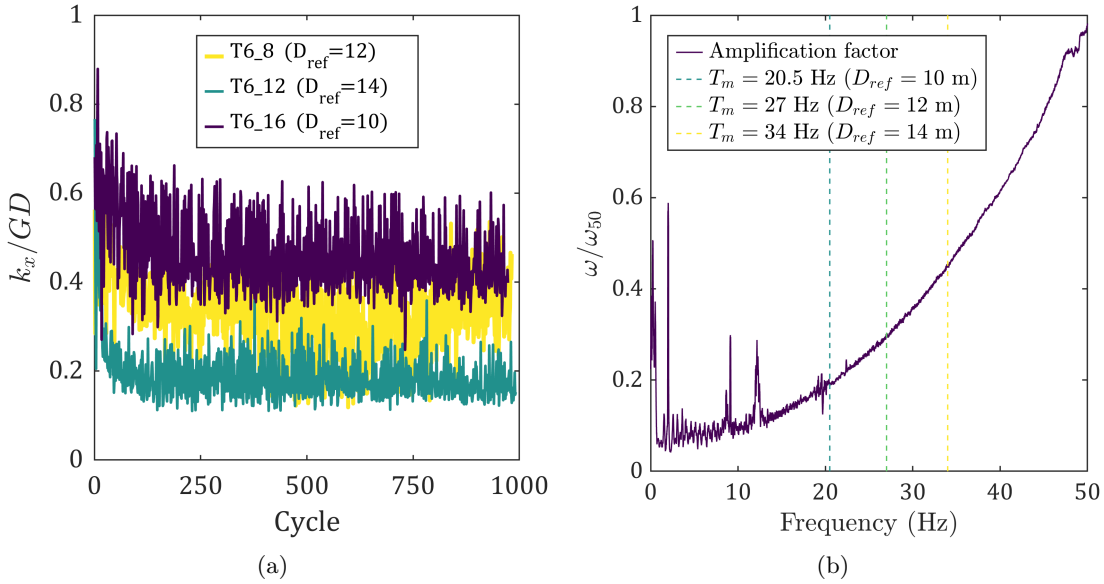

Figure 7.33: Analysis of displacement controlled tests T6_8, T6_12, and T6_16 for dynamic effects of increased loading frequency. These events were applied to the same model, at varying f, corresponding to the D_{ref} examined. (a) System stiffness decreasing with increased loading frequency. (b) Normalised amplification factor during a sinesweep performed after the storm events of T6. The results shown are calculated based on the excitation at accelerometer 3 (below the mudline) divided by the applied excitation at the actuator. Normalisation is calculated with ω_{50} at 50 Hz excitation.

The results indicate that a resonant peak was not reached within the range of sampled frequencies; however, a clear trend of increased excitation with increased frequency is evident. This demonstrates that the higher frequency tests, corresponding to increased D_{ref}, exhibit a more resonant response. The results of Figure 7.33(a) indicate a reduction in stiffness with increased reference monopile diameter, D_{ref}. These loads were applied with displacement control; therefore, lower stiffness indicates a lower load, leading to reduced oscillation of excess pore pressure. The results underscore a potential issue with the methodology for investigating dimensionless drainage scaling factor, whereby dynamic effects alter the attained results.

$$\omega = \frac{\text{FFT(Accelerometer 3)}}{\text{FFT(Actuator)}} \tag{7.2}$$

Varied drainage factor with the same loading period during T3_4_r and T5_2

The design of tests T3 and T5 facilitated the investigation of model monopiles with varied reference diameters while maintaining similar loading frequencies at the model scale. This enabled the assessment of the dimensionless drainage factor, negating any dynamic effects, as discussed in the previous section. Tests T3_4_D10_03A_D_r and T5_2_D12_03A_-D were conducted on monopiles of the same size, $D_p = 4.15$ m, at comparable loading frequencies of 27.4 and 27 Hz, previously loaded with the same amplitude of displacement controlled cycles. T5 was saturated with 66.5 cSt pore fluid, in contrast to the 50 cSt used for T3; therefore, the effective permeability of the system was reduced. Consequently, although the tests were conducted at similar loading frequencies, the reference monopile diameters differed (T3_4: $D_{ref} = 10$ m, T5_2: $D_{ref} = 12$ m).

Figure 7.34 shows the load and mudline displacement response to the applied actuator displacement, $y_a = 0.03D$, during T3_4 and T5_2. The load response is slightly reduced during T5_2, indicating a less stiff response. This correlates with the increased mudline displacement oscillation. The load history for both events was comparable (T3 = 1200 cycles, T5 = 1000 cycles). The pore pressure oscillation at PPT1 and PPT2 is illustrated in Figure 7.35. The diminished stiffness of T5_2, and consequently reduced load for the applied actuator displacement, resulted in a decrease in amplitude of pore pressure oscillation. However, the amplitude of oscillation is closer in magnitude than during the different events of Figure 7.29. The moving mean excess pore pressure response of both events is presented in Figure 7.36. There is a clear trend indicating increased pore pressure accumulation for T5_2, associated with a larger reference monopile. As both tests were conducted at similar loading frequencies, the likelihood of dynamic effects influencing the pore pressure response is minimised. The expected trend of increased positive excess pore pressure accumulation is more distinctly observed here.

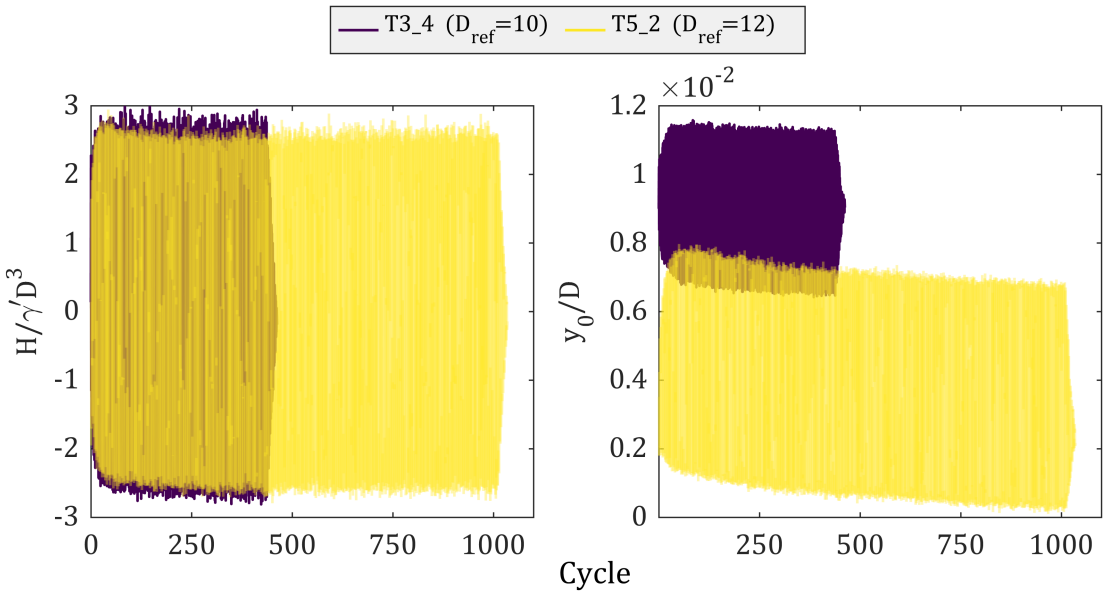

Figure 7.34: Mudline load, H_0, and mudline displacement y_0, from T3_4_D10_03A_D_r and T5_2_D12_03A_D. These events were applied at a similar loading frequency, at different effective k, corresponding to the D_{ref} examined. The displacement amplitude applied for each event was maintained, and did not exceed the levels previously experienced.

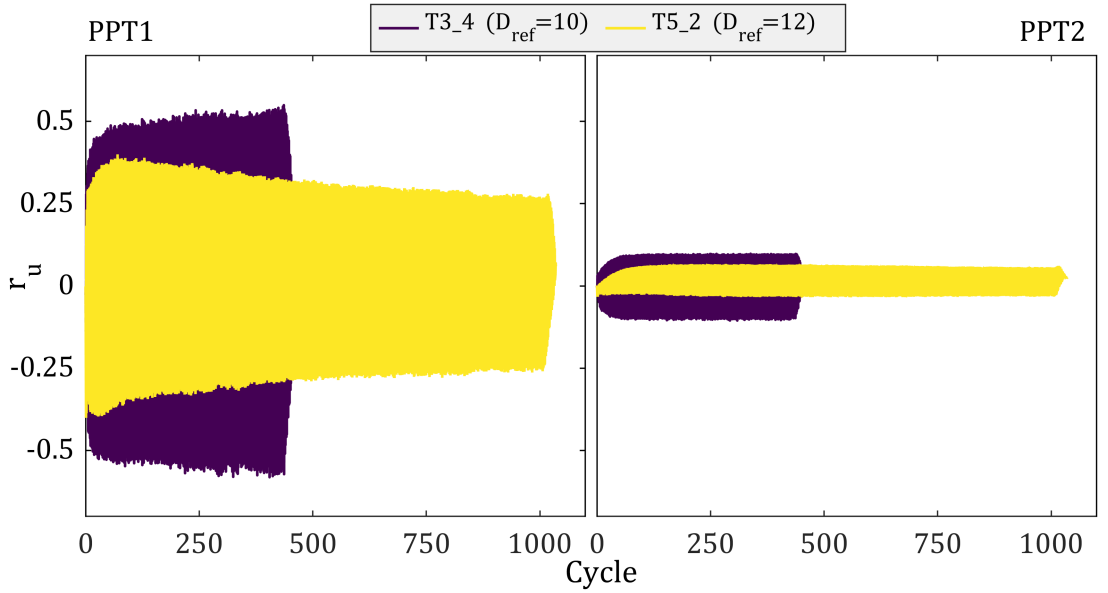

Figure 7.35: Excess pore pressure ratio, r_u, at PPT1 and PPT2, from T3_4_D10_03A_D_r and T5_2_D12_03A_D. These events were applied at a similar loading frequency, at different effective k, corresponding to the D_{ref} examined. The pore pressure oscillation is similar for both events, albeit more oscillation occurs during T3_4 with a lower diameter reference monopile.

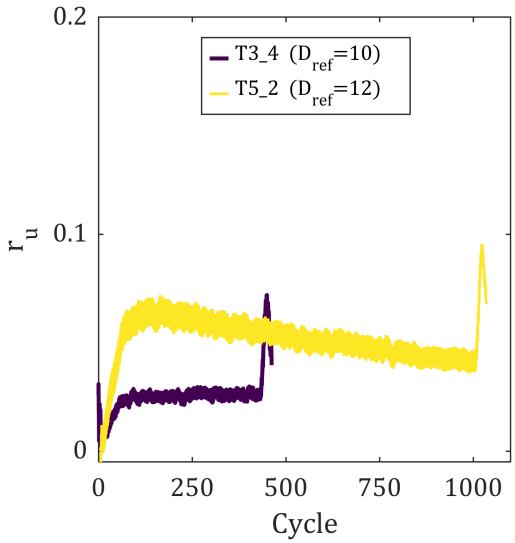

Figure 7.36: Moving mean excess pore pressure ratio, r_u, at PPT1, from T3_4_D10_03A_D_r and T5_2_D12_03A_D. The degree of excess pore pressure accumulation is increased during T5_2 with a larger diameter reference monopile.

The results presented in this section provide robust evidence for the validity of the dimensionless drainage factor. When the factor is consistent between tests, the responses in pore pressure, load, and mudline displacement are similar, despite variations in the parameters within the factor. The clearest indication of this is shown in Figure 7.18, the first loading events, where loading history is identical. When differences in response are noticeable, they are attributable to discrepancies in prior load history, which lead to variations in soil stiffness, one of the parameters of the drainage factor. In these cases, the drainage factor is not preserved, even with equivalent loading periods and amplitudes. Therefore, the dimensionless factor is valid, though the significance of loading history must be acknowledged. Furthermore, the presence of dynamic effects had an impact on results. Where the reference monopile diameter was different, controlled by variations in the loading period, the degree of excitation varied. As the actuator applied displacement controlled cycles, when the degree of excitation was increased (Figure 7.33(b)), the level of load applied was reduced. Consequently, the degree of pore pressure oscillation was also reduced.

7.4.2 Load controlled storm tests: dimensionless factor analysis

The following section presents results for analysis of the non-dimensional scaling factor during storm events. The test schedule for the storm loading events was varied similarly to the displacement controlled tests, incorporating variations in amplitude, loading period, and load sequence.

The extreme storm events T3_7_D12_75A_SE, T5_11_D12_75A_SE, and T6_-20_D12_75A_SE are compared. These events were executed with varied D,k, and T, while the D_{ref}, and consequently the drainage factor, was maintained. The loads applied during these events were equivalent, and the preloading amplitude was consistent, differing

only in the number of load cycles previously experienced. Following this, the results of T5_12_D10_50A_S, T5_13_D12_50A_S_r, and T5_14_D14_50A_S are discussed in relation to events of varied D_{ref}, and thus drainage factor. These events were conducted consecutively on the same model; therefore, the variation of T corresponding to D_{ref} can be analysed in isolation. The presence of different load history effects between these events is unavoidable. However, the amplitude of preloading exceeded the applied load in each case. Therefore, the most important factor of load history is maintained.

Extreme storm events with equal drainage factor: T3_7, T5_11, T6_20

Tests T3_7_D12_75A_SE, T5_11_D12_75A_SE, and T6_20_D12_75A_SE were the extreme storm events of each model. These tests were matched in drainage factor corresponding to D_{ref}= 12 m. However, the monopile of T6 had a prototype diameter of D_{p}= 5 m, and the viscosity of T5 was 66.5 cSt, therefore, the loading period was increased to maintain the drainage factor compared to T3 (Table 6.2). To account for the varied loading period, the plots have been presented with normalised time, $Time/T$, where T is the nominal loading period. Considering the tests had varied conditions while maintaining the drainage factor, they provide a useful means of comparison for load-controlled tests.

Figure 7.37 shows the H_0 and y_0 response of the events. The load response is consistent throughout the duration of the test, with marginally increased loads reached during T3_7. The small discrepancies in load may be attributed to varying soil conditions. However, the loads applied by the actuator had a greater tolerance compared to the displacement controlled tests. The mudline displacement response indicates displacement cycles with an underlying accumulation response for all events. The level of accumulation is greatest for T3_7, while T6_20 exhibits the least movement. The prior load history effect can partially explain this trend, as T3_7 experienced the least loading prior to the event. However, T5_11 had the greatest level of prior storm loading, with an event of H=0.6H_{ULT}, (T5_8_D12_60A), previously applied. The final displacement controlled test for T5 and T6 (Figure 7.25), shows a greater level of mudline displacement, during T5_11 compared to T6_16. Therefore, the increased number of cycles applied to T6, albeit of lower amplitude, may have increased the stiffness of the system, accounting for the reduced mudline accumulation seen here. Separately, the difference in D_{p} between the tests may account for the variation, with tests T3_7 and T5_11 performed on the monopile of D_{p}= 4.15 m, and T6_20 performed on the larger monopile, D_{p}= 5 m. Therefore, with loading a different loading periods to maintain the same value of the dimensionless scaling factor, the effects of resonance may account for the variation seen.

Figure 7.38 shows the pore pressure response for these events. There are substantial in-cycle oscillations in r_u at PPT1, with the greatest observed in T3_7. Once more, the larger magnitude is the negative suction for all events. The amplitude of oscillation at PPT2, at the base of the pile, is diminished, aligning with the trend observed in the displacement controlled tests. The trend of oscillation, accumulation, and dissipation is consistent over time across all events, albeit with varying magnitudes.

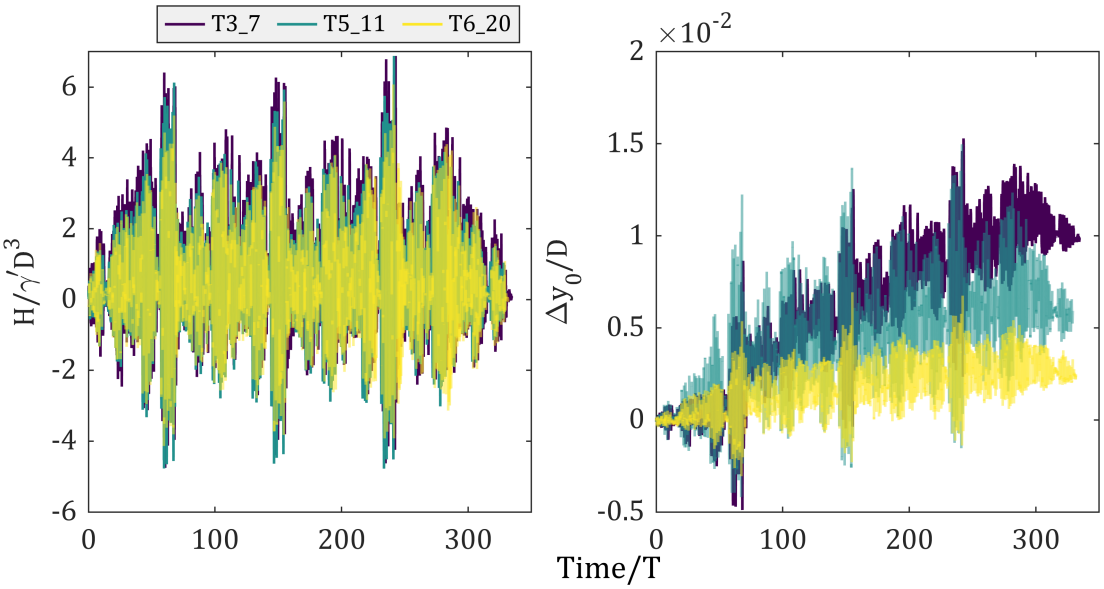

Figure 7.37: Mudline load, H_0, and mudline displacement y_0, from extreme storm events T3_7_D12_75A_SE, T5_11_D12_75A_SE and T6_20_D12_75A_SE. Loading period, pore fluid viscosity and model diameter varied, but drainage factor maintained. The targeted applied load is maintained across all events. Response is plotted against normalised time, $Time/T$, to account for the differences in loading period. The accumulated mudline displacement is greatest in T3_7, followed by T5_11 and T6_20 showing the least. Differences are attributed to prior load history effects.

Figure 7.39 shows the mean pore pressure response of each event. The trend of u accumulation and dissipation is maintained across all events. A greater level of accumulation is also observed during T3_7. Furthermore, the degree of suction is higher in T5_11. Minor differences in response, attributed to load history effects notwithstanding, the results of these tests provide strong evidence of the validity of the examined drainage scaling factor.

Storms with equal amplitude and varied drainage factor: T5_12, T5_13, T5_14

The drainage factor can be further examined with the observation of T5_12_D10_50A_S, T5_13_D12_50A_S_r, and T5_14_D14_50A_S. These events succeed the extreme storm event of T5_11 and are all loaded with the same load amplitude. However, the D_{ref} of each event is varied, consequently the loading period is varied for each event. This sequence of loading occurred at the end of the testing schedule for T5, thus, the load history of each event is similar. Furthermore, the load levels applied in each event falls below the levels previously achieved, having previously been loaded with both the calibrating test, T5_8_D12_60A_S, and the extreme event, T5_11_D12_75A_SE. Therefore, the prior load history effects observed here should be similar for all events.

Figure 7.40 shows the load and displacement response of these events. Both plots exhibit a similar response across events, without any accumulation of displacement. Fig-

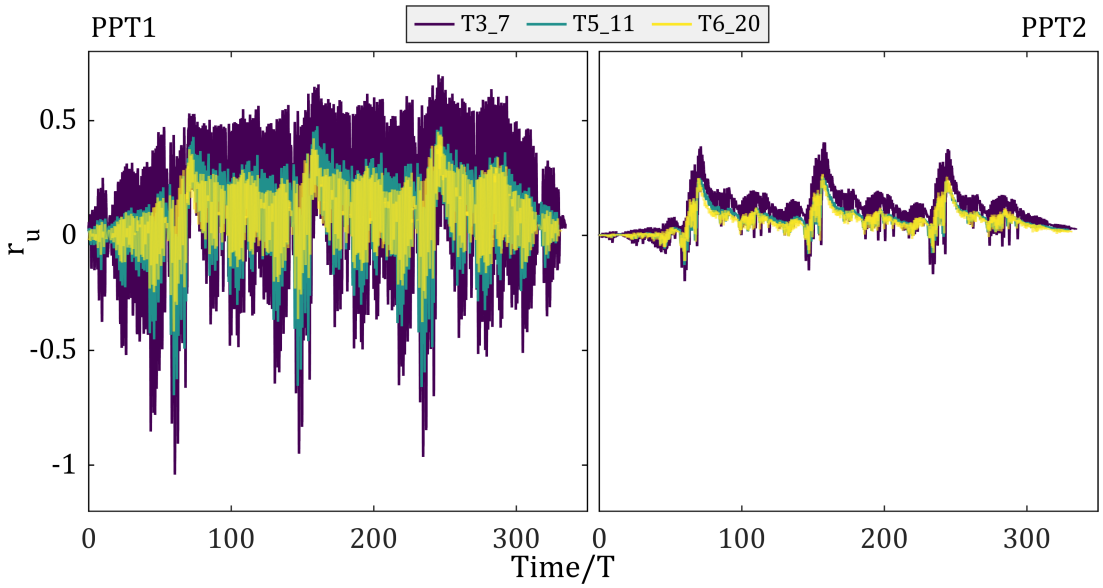

Figure 7.38: Excess pore pressure ratio, r_u, at PPT1 and PPT2, from extreme storm events T3_7_D12_75A_SE, T5_11_D12_75A_SE and T6_20_D12_75A_SE. The pore pressure response at PPT1 is greatest in T3_7, followed by T5_11 and T6_20. Differences are attributable to prior load history effects.

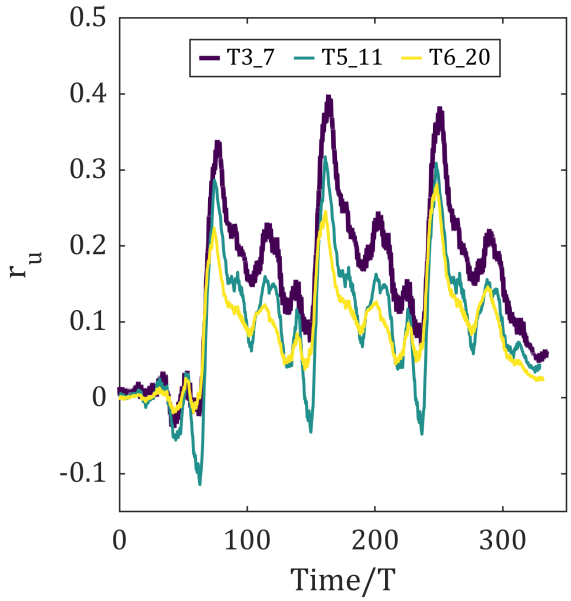

Figure 7.39: Moving mean excess pore pressure ratio, r_u, at PPT1, from extreme storm events T3_7_D12_75A_SE, T5_11_D12_75A_SE and T6_20_D12_75A_SE. The response is plotted against normalised time, $Time/T$, to account for the differences in loading period. Considering this, the trend for u accumulation and dissipation is matched, providing good evidence for the relationship between, T, D, and k. The response is greatest during T3_7, owing to the reduced preloading.

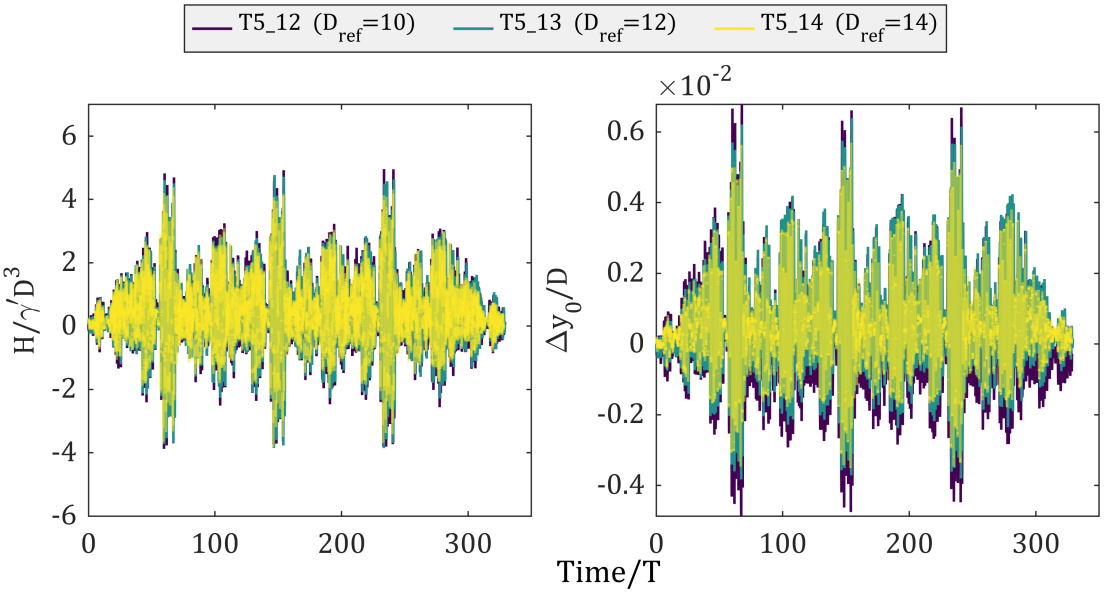

Figure 7.40: Mudline load, H_0, and mudline displacement y_0, from storm events T5_12_D10_50A_S, T5_13_D12_50A_S_r and T5_14_D14_50A_S. These events were applied on the same model, therefore D and k are maintained. The loading events were applied at varied loading frequency, to examine different D_{ref} values. Response is plotted against normalised time, $Time/T$, to account for the differences in loading period.

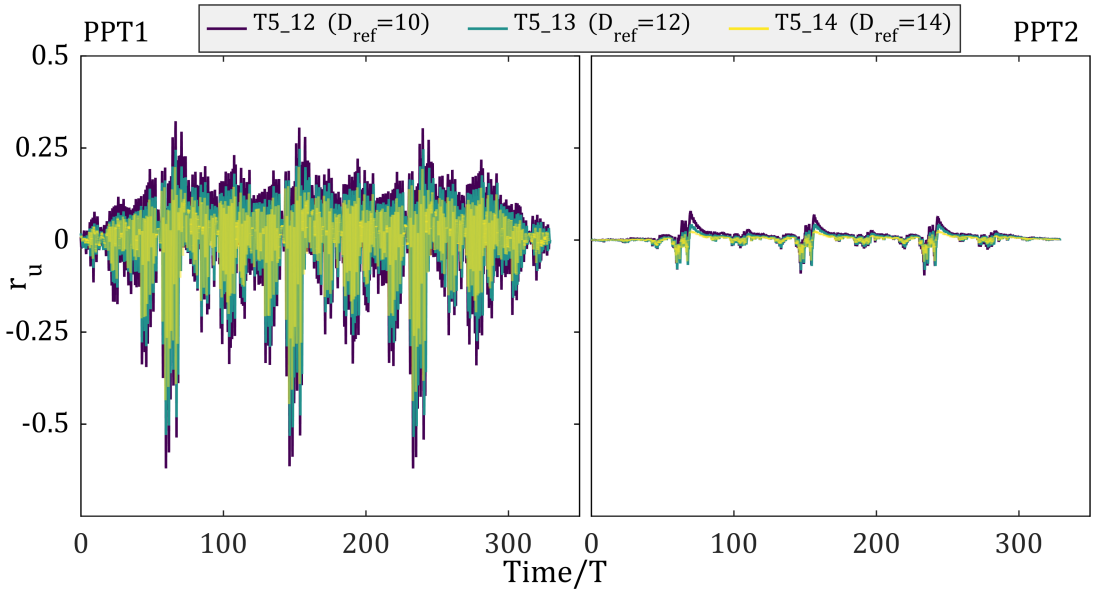

Figure 7.41: Excess pore pressure ratio, r_u, at PPT1 and PPT2, from storm events T5_12_D10_50A_S, T5_13_D12_50A_S_r and T5_14_D14_50A_S. A similar response is observed across all events, with minor reduction in response with each subsequent event. This indicates a decreased sensitivity of response for the range of D_{ref} examined.

ure 7.41 presents the pore pressure response, which is consistent across all events, with a slight reduction in events later within the testing schedule. The similarity in response indicates a reduced sensitivity to changes in D_{ref} for the range examined; there is no indication of increased r_u accumulation as D_{ref} increases. The reduction in magnitude of r_u with each successive event aligns with the observed effects of load history.

7.5 Load history analysis

The following section examines the effect of load history on pile response.

Test T6 was specifically designed to examine this effect and is therefore analysed thoroughly in this section. The first comparative analysis examines the impact of preloading. T6_4 was the first event during T6 of equivalent amplitude to events T3_1, T4_1 and T5_-1. The test schedule for T6 implemented three cyclic events with increasing displacement amplitude prior to T6_4. Therefore, during T6_4 the soil had been preloaded, providing key evidence for assessing load history effects. Following this, the results from T6_1_-D10_008A_D, T6_2_D10_015A_D, T6_3_D10_022A_D, and T6_4_D10_03A_D are presented. These events were selected to illustrate the impact of higher amplitude preloading on system response. Additionally, events T6_13, T6_14, T6_15, and T6_16 are included. These events are a repeat of the first four events of T6, with identical loads, applied at the end of the testing schedule. The comparison between these events provides further evidence for the analysis of load history effects. Finally, the events T4_4_-D10_03A_D_r and T6_16_D10_03A_D_r are compared. These events were conducted on different models prepared under the same conditions, differing only in the level of preloading. In contrast to the comparison of T6_4 and T6_16, the level of preloading applied to T4_4 was of the same amplitude as T6_16, differing only in the number of cycles.

Following the presentation of displacement controlled tests, results of storm events are shown for the analysis of load history effects. The first comparison is between the first three storm events of T3: T3_5_D12_25A_S, T3_6_D12_50A_S, and T3_7_D12_75A_SE. These events were conducted sequentially on the same model, with the load amplitude increasing between each event. They were performed without any prior storm events, only displacement controlled tests. Therefore, as the amplitude increased for each subsequent event, the current amplitude exceeded storm loading levels previously applied. The second comparison is between T3_6_D12_50A_S and T3_9_D12_50A_S_r, which consists of the reference storm event and a repeat following the extreme storm loading. The conditions of these tests were identical, apart from the load history. This allows for a robust comparison between events where the current loading does and does not exceed the load history.

Preloading before first event of: T3_1, T4_1, T5_1, T6_4

In Section 7.4.1 the greatest level of u response was observed during the first events. The soil close to the pile was likely of lower density owing to shadowing effects from pluviation and had not been subjected to prior loading. Therefore, the soil exhibited low stiffness, and displacement and u accumulation during cyclic loading was high. The test schedule of T6 applied three events of lower amplitude prior to an event of the same amplitude as the first event in other tests (T6_4_D10_03A_D). The plots shown in Figure 7.42 illustrate the H_0 and y_0 response of T6_4 in comparison to the first events T3_1, T4_1 and T5_1. There is a small reduction of load at the outset, accompanied by a low level of y_0 accumulation. However, for the majority of the event, the response remains steady, without the initial liquefaction followed by increase in stiffness that relates to the increasing load and reducing mudline displacement seen in the other tests. The u response shown in Figure 7.43 indicates a significantly reduced accumulation of u in T6_4 at both PPT1 and PPT2. There is a low peak reached after a greater number of cycles. The accumulated u then dissipates, reaching a low amplitude steady-state oscillation earlier than in the other tests. The reduction in max r_u clearly demonstrates the importance of load history when examining the drainage response. The prior load history of T6_4 resulted in a stiffer soil from the outset, with a much reduced excess pore pressure accumulation, in spite of the previous loading being of lower amplitude. The implication for real world situations is that the installation process, along with the low levels of cyclic operational loading will provide a pre-loading effect that will prevent severe u accumulation and liquefaction during high amplitude cycles.

First events of T6, with increasing displacement amplitude: T6_1-4

Figure 7.44 shows the H_0 and y_0 response of T6_1-4, indicating the load history prior to T6_4. The displacement amplitude is increased in each event (Figure 7.45(a) T6_1: y_a=0.008D, T6_2: y_a=0.015D, T6_3: y_a=0.022D, T6_4: y_a=0.03D). The H_0 and y_0 amplitudes increase with the applied actuator displacement. There are small variations in H_0 and y_0 at the outset of each event; however, the response reaches a steady state at a low number of cycles. Figure 7.46 shows the pore pressure response. At PPT1, the accumulation of u increases from T6_1 to T6_2. However, the degree of accumulation does not increase with the subsequent events, T6_3 and T6_4. The response for events T6_2, T6_3, and T6_4 is similar, though marked by a later peak and greater cyclic amplitude with each subsequent event. The response at PPT2 increases in both amplitude and oscillation with each event of greater amplitude. This increase at PPT2 is due to a larger mobilised displacement further down the pile as amplitude increases. The degree of accumulation further up the pile does not increase with each event; therefore, the vertical drainage pathway would have a similar effect in each case. The load history of T6_4, in comparison to T3_1, T4_1, and T5_1, explains the differing responses, as previously discussed. Moreover, considering the test setup, the shadowing effects of

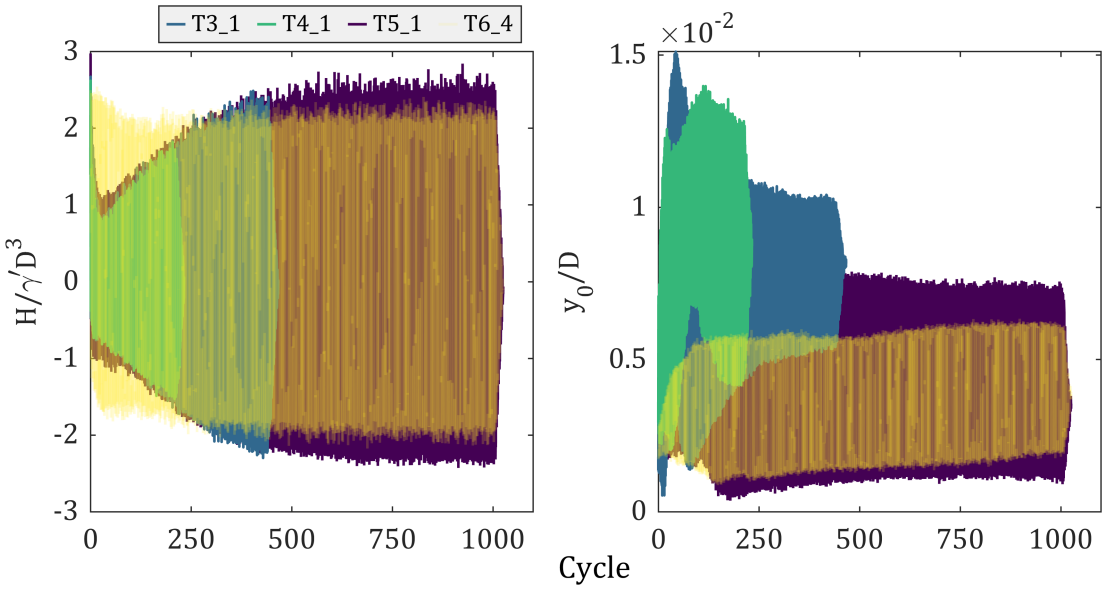

Figure 7.42: Mudline load, H_0, and mudline displacement y_0, from T3_1_D10_03A_D, T4_1_D10_03A_D, T5_1_D10_03A_D, and T6_4_D10_03A_D. Loading period, pore fluid viscosity and model diameter varied, but drainage factor and displacement amplitude were the same. For events T3_1, T4_1 and T5_1, where the load was applied to previously unloaded soil, the response is matched and evolves with subsequent cycles. During T6_4, where the soil is preloaded, the response differs and quickly reaches a steady-state.

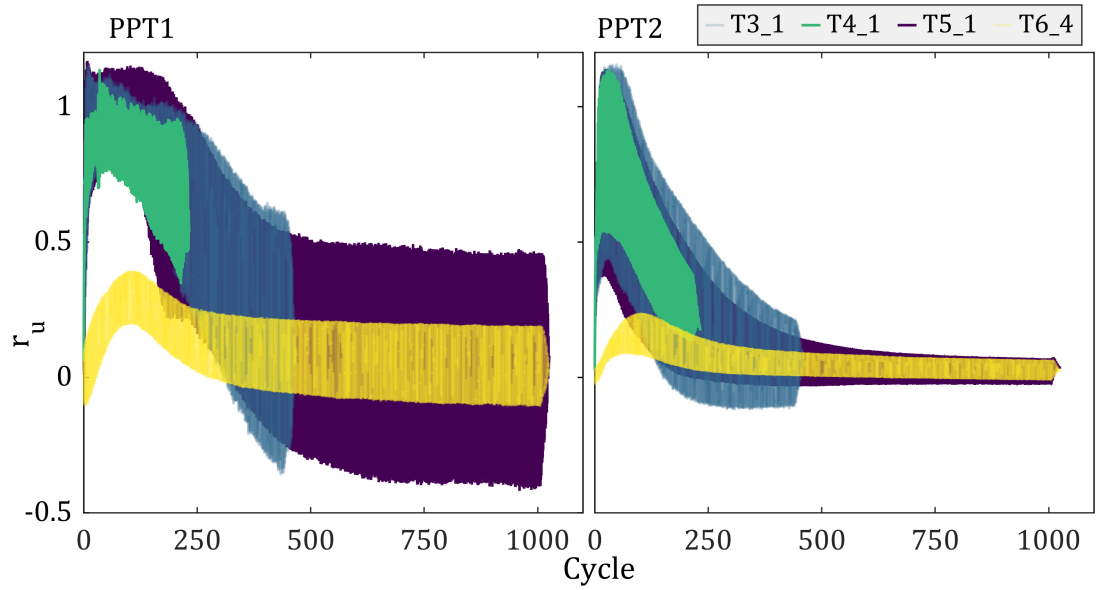

Figure 7.43: Excess pore pressure ratio, r_u, at PPT1 and PPT2, from T3_1_D10_03A_D, T4_1_D10_03A_D, T5_1_D10_03A_D, and T6_4_D10_03A_D. Drainage factor and displacement amplitude maintained, with preloading on T6_4. Events T3_1, T4_1 and T5_1, show significant r_u magnitude at PPT1 and PPT2, which is matched for each event. During T6_4, where the soil is preloaded, the u cyclic amplitude and accumulation are significantly reduced.

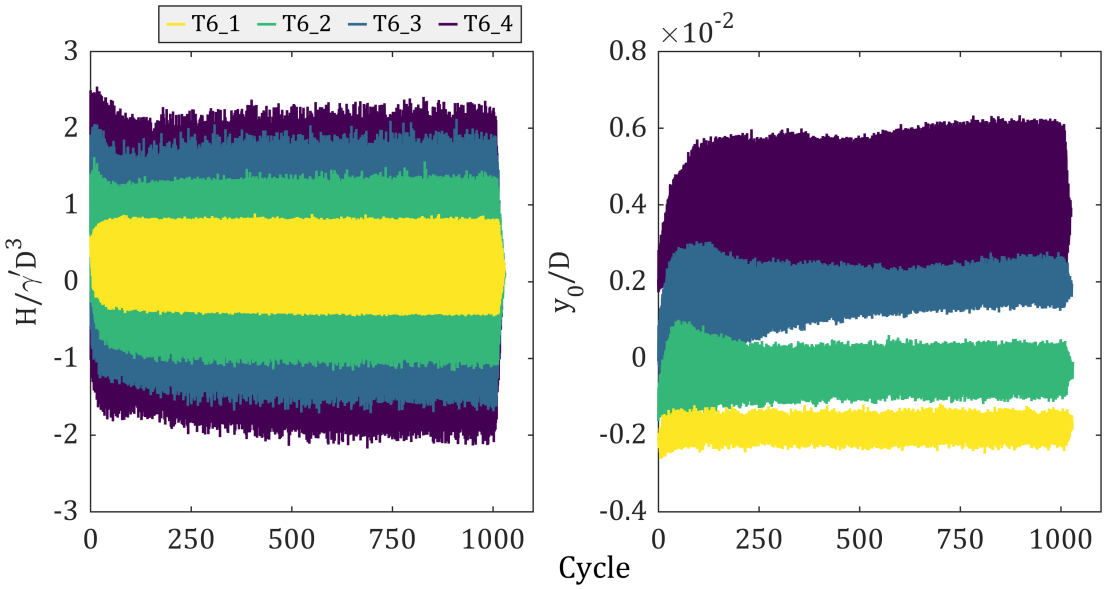

Figure 7.44: Mudline load, H_0, and mudline displacement y_0, from T6_1_D10_008A_D, T6_2_D10_015A_D, T6_3_D10_022A_D, and T6_4_D10_03A_D. Performed consecutively on the same model, for the same drainage scaling factor ($D_{ref} = 10$ m), with increasing y_a with each event. Steady increase in H_0 and y_0 response with increased applied y_a.

pluviation heightened with proximity to the pile. Consequently, the lowest density and stiffness soil would have been situated immediately surrounding the pile. During lower amplitude events T6_1 and T6_2, this soil would have been mobilised, somewhat in isolation from the soil further out from the pile. Thus, this soil would have densified, and the accumulation of u from the initial cycles occurred in progressively larger areas, rather than simultaneously. This also accounts for the limit on the maximum u achieved during T6_2, T6_3, and T6_4. Despite the displacement amplitude increasing in each test, the newly affected soil was less affected by shadowing therefore the magnitude of r_u was reduced.

Repeat events of T6, with increasing displacement amplitude: T6_13-16

Within the test schedule, a series of repeat tests were conducted at the end of the displacement controlled tests of T6 (T6_13_D10_008A_D_r, T6_14_D10_015A_D_r, T6_15_D10_022A_D_r and T6_16_D10_03A_D_r). These repeat tests were subjected to the same conditions as T6_1-4, but with preloading exceeding or equal in amplitude to the load currently applied. Figure 7.47 shows a somewhat similar response in load and mudline displacement to the events of T6_1-4. The small amount of accumulated u during T6_1-4 did not elicit significant reduction in stiffness. However, this minor reduction in stiffness accounts for the differences in load and mudline displacement response. The pore pressure response shown in Figure 7.48 does not exhibit any accumulation of u. The level of oscillation within each cycle is greater than observed in the equivalent response of events T6_1-4. The magnitude of oscillation increases with each increment of applied displacement as expected. This evidences the importance of load history in the drainage

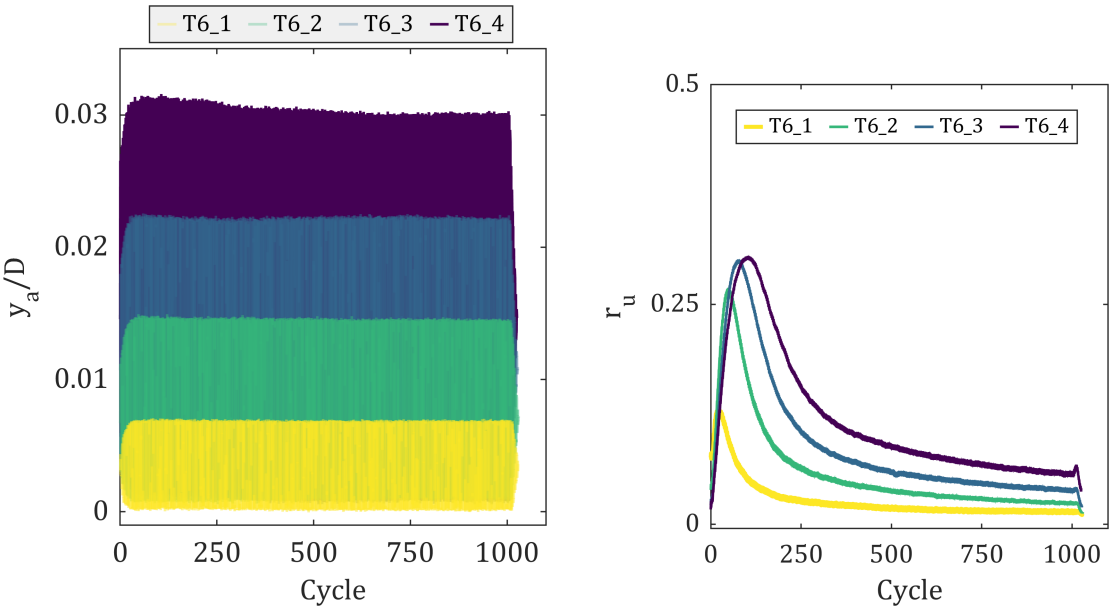

Figure 7.45: Applied actuator displacement, y_a, and mean excess pore pressure ratio, r_u, from T6_1_D10_008A_D, T6_2_D10_015A_D, T6_3_D10_022A_D, and T6_4_D10_03A_D. Performed consecutively on the same model, for the same drainage scaling factor ($D_{ref} = 10$ m), with increasing y_a with each event: (a) y_a is increased steadily with each event, (b) Moving mean r_u showing accumulation of u at PPT1 in each test. Level of accumulation caps at $r_u \approx 0.25$, despite increased y_a.

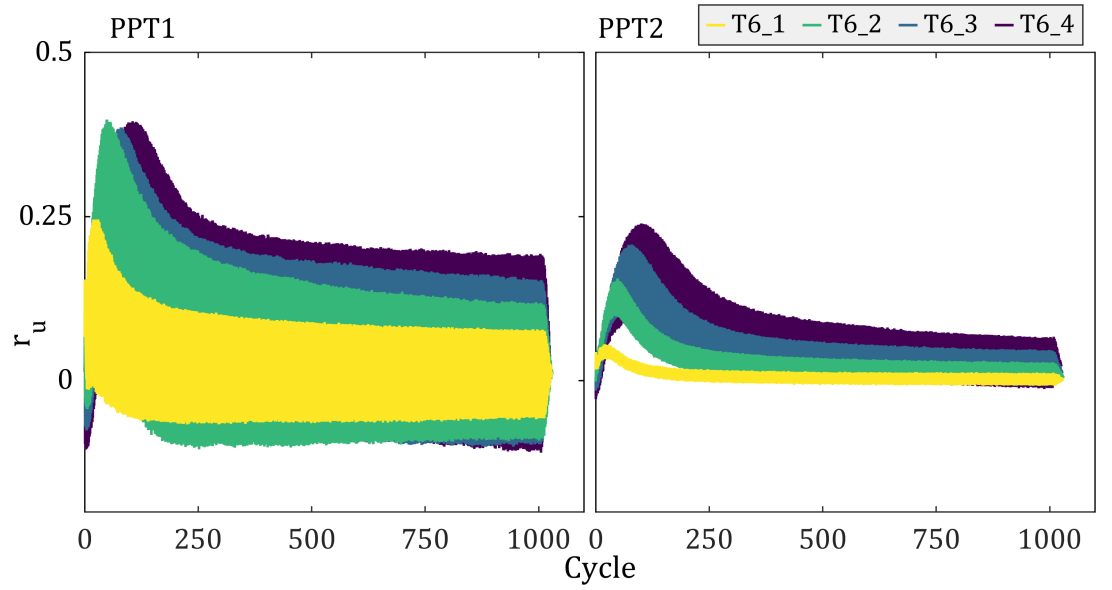

Figure 7.46: Excess pore pressure ratio, r_u, at PPT1 and PPT2, from T6_1_D10_008A_D, T6_2_D10_015A_D, T6_3_D10_022A_D, and T6_4_D10_03A_D. Performed consecutively on the same model, for the same drainage scaling factor ($D_{ref} = 10$ m), with increasing y_a with each event. Response at PPT1 is similar for events T6_2-4, but steadily increases with each event at PPT2. The preloading before each event reduces the level of u response at PPT1. However, increased displacement mobilised down the pile with each event, increases the level of response at PPT2.

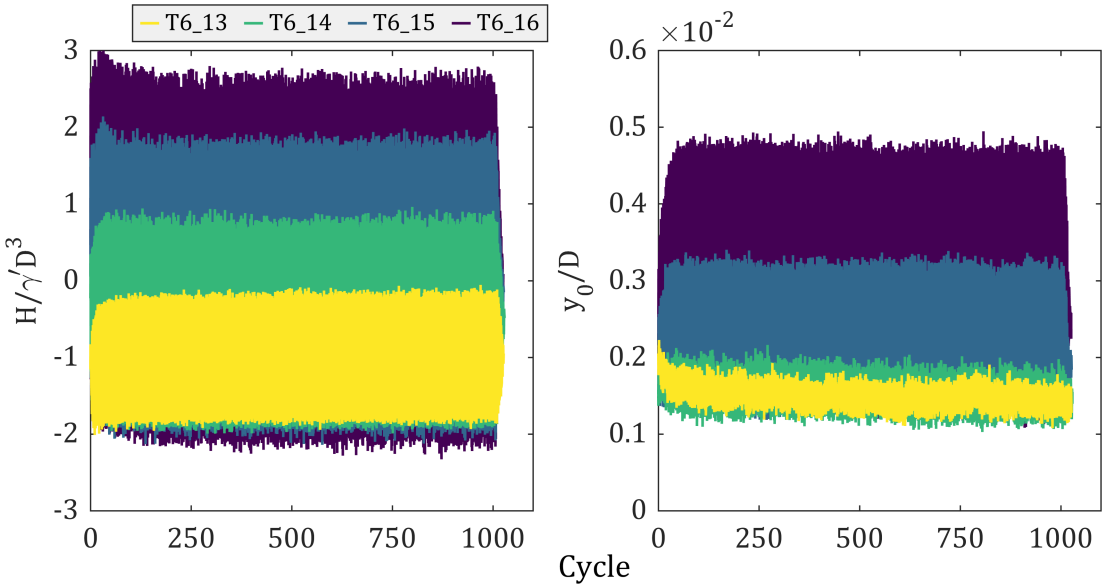

Figure 7.47: Mudline load, H_0, and mudline displacement y_0, from T6_13_D10_008A_D_r, T6_14_D10_015A_D_r, T6_15_D10_022A_D_r, and T6_16_D10_03A_D_r. Performed consecutively on the same model, maintained $D_{ref} = 10$ m, varied y_a. The level of preloading for each event was similar in this instance.

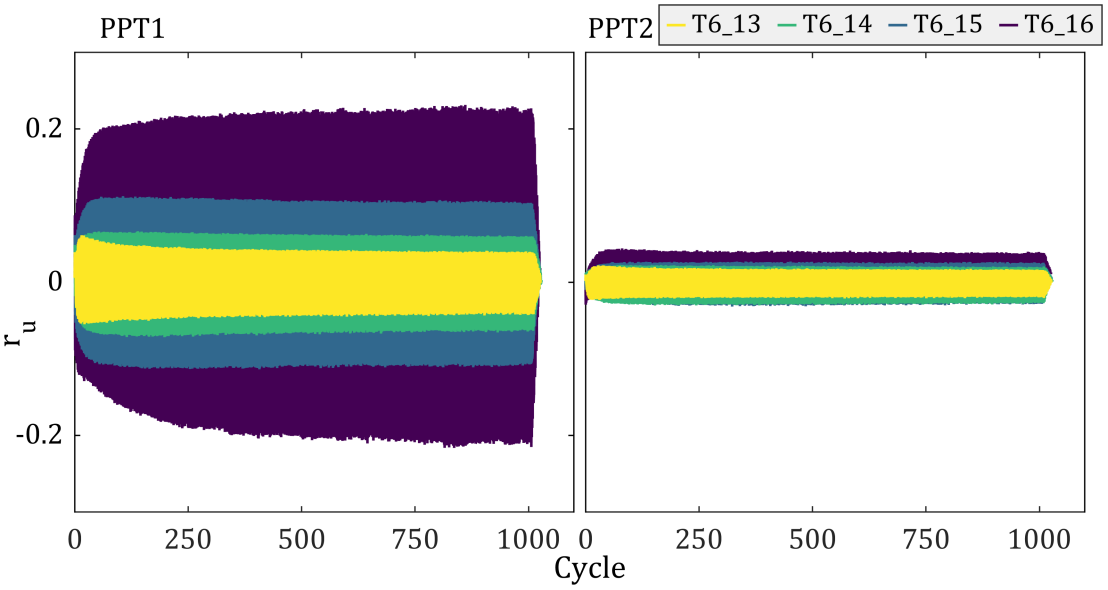

Figure 7.48: Excess pore pressure ratio, r_u, at PPT1 and PPT2, from T6_13_D10_008A_D_r, T6_14_D10_015A_D_r, T6_15_D10_022A_D_r, and T6_16_D10_03A_D_r. No accumulation is seen here, only u oscillation. Cyclic amplitude at PPT1 increases steadily with increased y_a. Response at PPT2 is minimal and maintained, across all events.

response of the soil. When the soil was loaded beyond previously experienced levels, as in each event of T6_1-4, there was an accumulation of u. In cases of loading limited to levels previously experienced, there was no accumulation, only oscillation, for the displacement magnitudes examined.

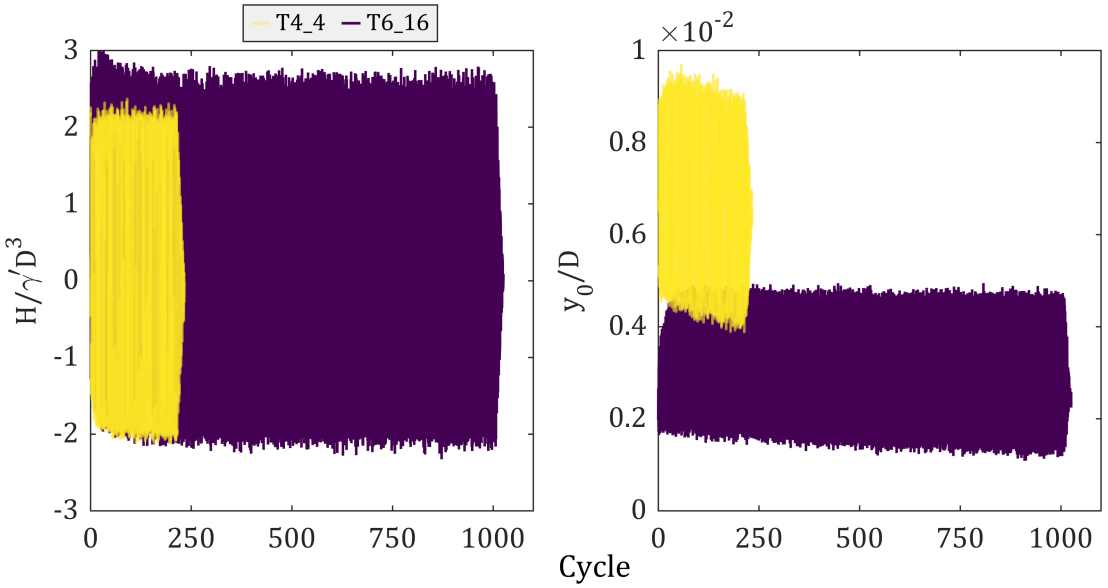

Figure 7.49: Mudline load, H_0, and mudline displacement y_0, from T4_4_D10_03A_D_r and T6_16_D10_03A_D_r. Performed on models prepared to the same conditions, and applied displacements were the same, therefore D, D_{ref}, y_a, k were maintained. The two events differed only in load history. A slightly reduced load response is observed in T4_4. The midpoint of y_0 is varied, owing to variations in the testing schedule.

Repeat events of T6, with varied preloading: T6_13, T6_14, T6_15, T6_16

The events T4_4_D10_03A_D_r and T6_16_D10_03A_D_r are cases where all conditions were the same (D, D_{ref}, y_a, k), differing only in the load history prior to each event. The plots shown in Figure 7.49 demonstrate a similar load response, with a slightly reduced peak load in T4_4. This reduction is attributed to the differing load history, as discussed previously; with increased cycles, the densifying effect is enhanced, leading to greater stiffness. The y_0 response shows corresponding inversion in response, compared with load. T6_16, with a stiffer soil, exhibits lower displacement amplitude. The differing midpoint of cycling has been previously discussed.

The pore pressure response in Figure 7.50 exhibits greater oscillation amplitude in T4_4 at PPT1. This aligns with the observations from H_0 and y_0 responses. The increased amplitude of displacement resulted in heightened levels of pore pressure response. The oscillation level at PPT2 is low and consistent across both events. The degree of movement at greater depths within the pile diminished as the soil stiffens.

Figure 7.51 presents the time instances at which the u distribution within the soil is shown in Figure 7.52. The magnitude of response is greater in T4_4 at all instances. However, the distribution for both events is similar. The distribution is maintained at all instances for both events.

This section presented results examining the impact of load history. It is evident that when the amplitude of previously experienced load exceeds the levels currently applied, pore pressure accumulation is diminished. Furthermore, as the number of load cycles

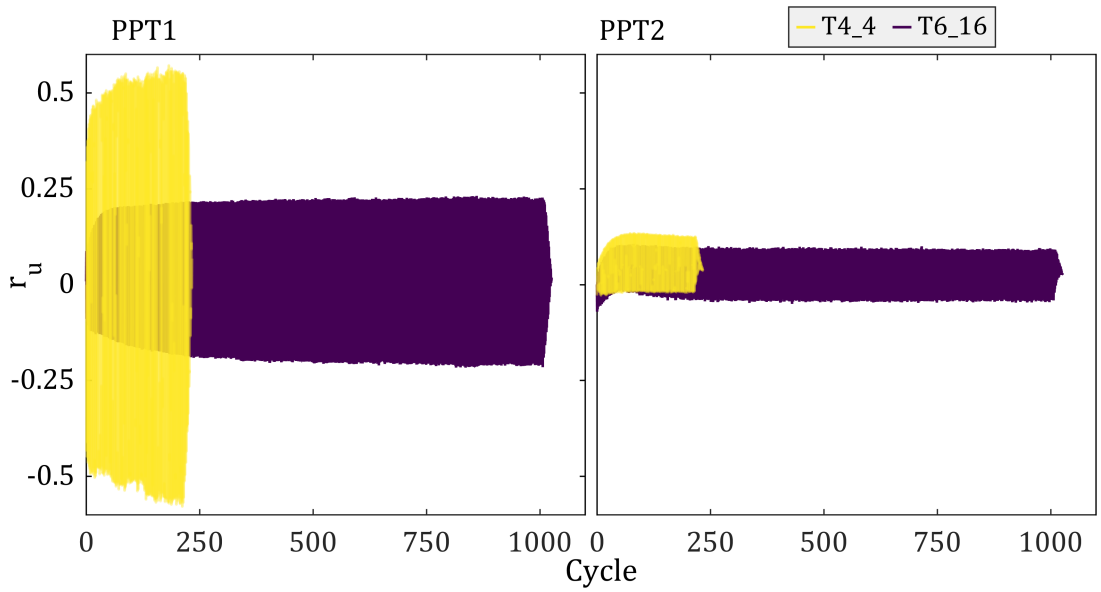

Figure 7.50: Excess pore pressure ratio, r_u, at PPT1 and PPT2, from T4_4_D10_03A_D_r and T6_16_D10_03A_D_r. Significantly increased response at PPT1 during T4_4, owing to the reduced levels of preloading.

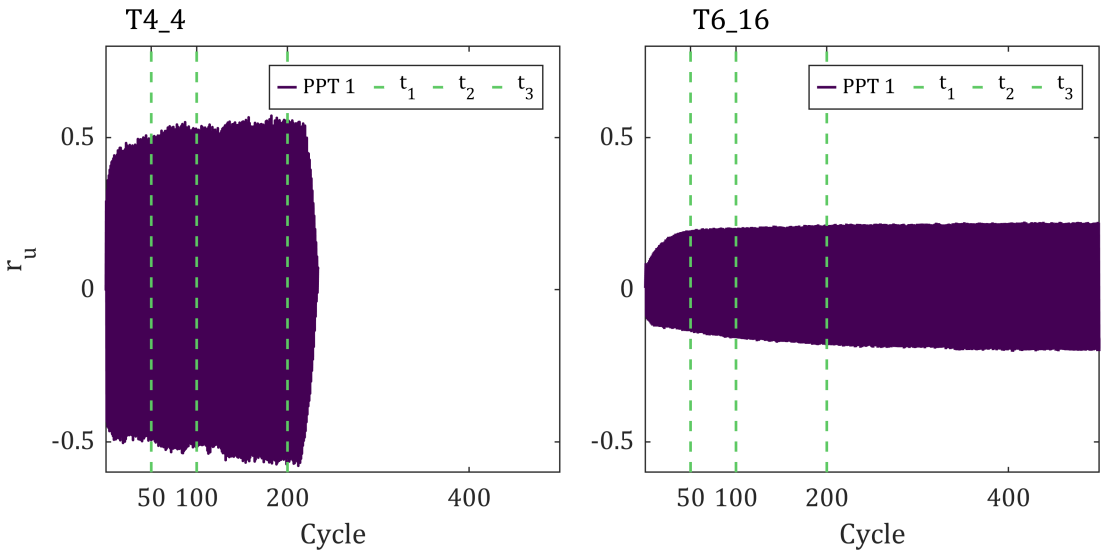

Figure 7.51: Excess pore pressure ratio, r_u, at PPT1 against cycle number from T4_4_D10_03A_D_r and T6_16_D10_03A_D_r. Overlaid are key cycles selected for further analysis in the contour plots shown in Figure 7.52. The selected cycles are: 50, 100 and 200.

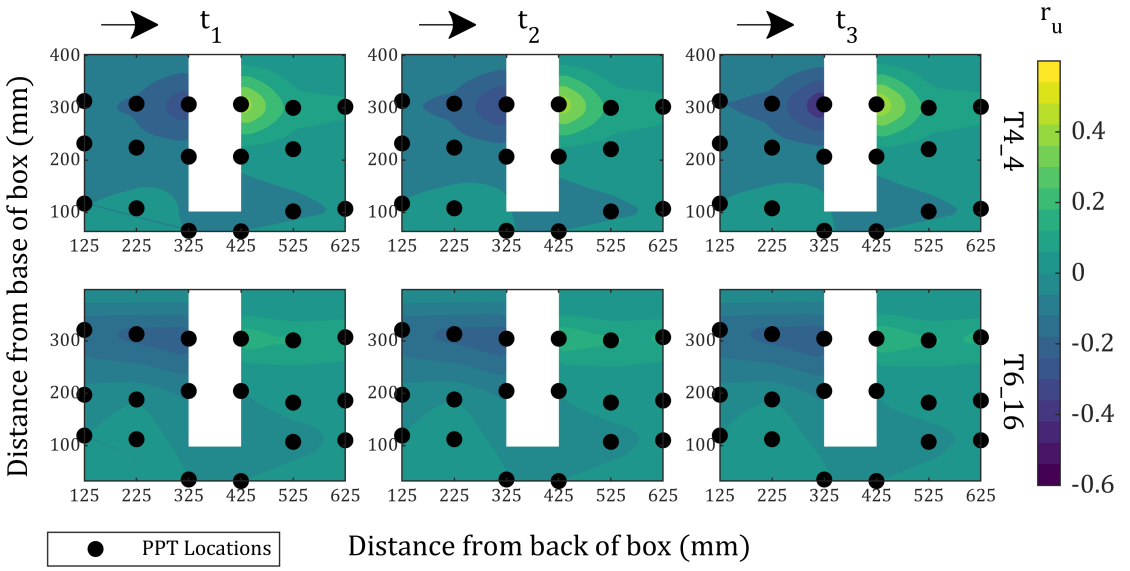

Figure 7.52: Excess pore pressure ratio, r_u, distribution from T4_4_D10_03A_D_r and T6_16_D10_03A_D_r. Time instances shown are the points of maximum u response, at PPT1, during the cycles labelled in Figure 7.51. N.B. the contour scaled to the limits of these tests to improve contrast. Increased pore pressure response is observed towards the top of T4_4. The distribution at greater soil depth is similar for both events. The response is consistent across all time instances for both events.

increases, the degree of densification increases, resulting in increased stiffness, a reduction in mudline displacement, and consequently reduced pore pressure oscillation. In instances where the loading exceeds the amplitude of any preloading, there is a greater level of excess pore pressure accumulation. The magnitude of accumulation is dependent on the ratio of new load amplitude to preloading amplitude. The results of Figure 7.45 indicate that with progressive levels of load amplitude, as may be expected in reality, pore pressure accumulation is minimised.

7.5.1 Load controlled storm tests: load history analysis

The following section outlines results focused on the effect of load history on foundation response during storm loading events.

Storms with varied amplitude and load history: T3_5, T3_6, T3_7

Events T3_5_D12_25A_S, T3_6_D12_50A_S, and T3_7_D12_75A_SE were performed in succession on model T3, following the displacement controlled tests. The events were identical in duration but differed in the load amplitude applied and the load amplitude history. Figure 7.53 shows the load and mudline response of these events. The load plot shows the load amplitude increasing with each subsequent event. The mudline displacement is also greater for each subsequent event, both in terms of cyclic amplitude and accumulated displacement. As discussed in Section 7.3, the load applied during T3_6 only momentarily exceeds the loads applied during the displacement controlled events, with the majority at a

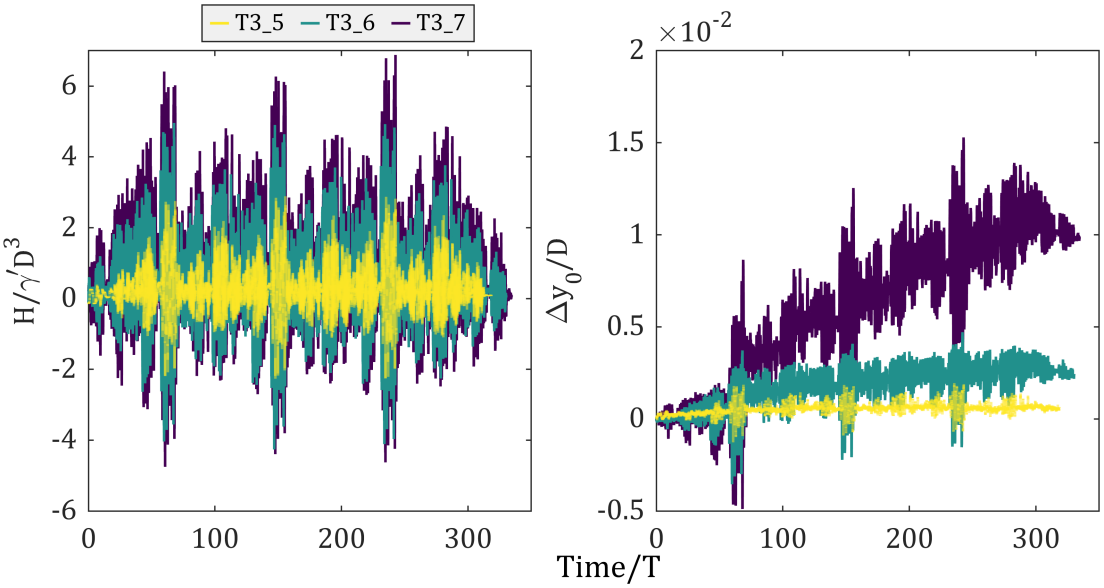

Figure 7.53: Mudline load, H_0, and mudline displacement y_0, from storm events T3_5_D12_25A_S, T3_6_D12_50A_S and T3_7_D12_75A_SE. Performed consecutively on the same model, therefore D and k are maintained. D_{ref} is maintained, with varied H_0 and load history. The mudline response is minimal during T3_5, where the load applied is less than previously experienced. A minor increase in y_0 is observed during T3_6. During T3_7, where the load consistently exceeds levels previously experienced, the y_0 response is markedly increased.

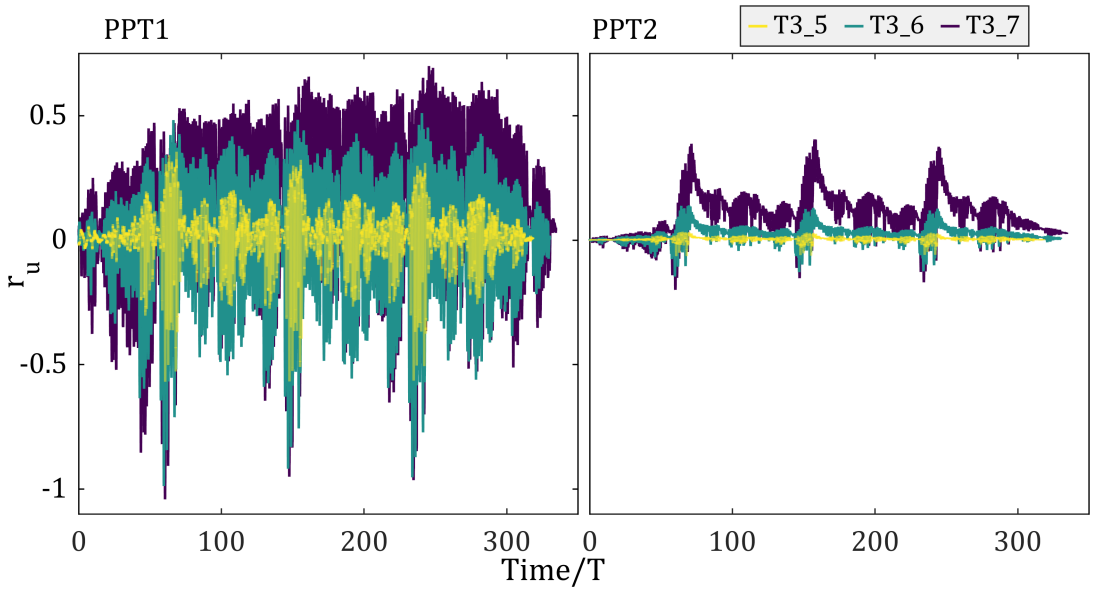

Figure 7.54: Excess pore pressure ratio, r_u, at PPT1 and PPT2, from storm events T3_5_D12_25A_S, T3_6_D12_50A_S and T3_7_D12_75A_SE. The pore pressure response is greatest at PPT1 and PPT2 during T3_7, owing to consistently greater H_0 than previously applied.

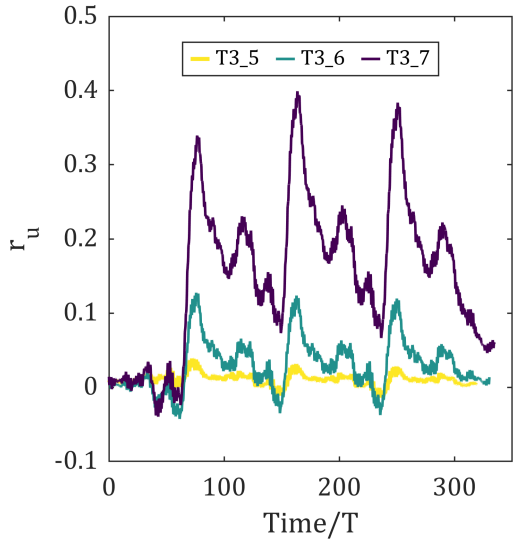

Figure 7.55: Moving mean excess pore pressure ratio, r_u, at PPT1, from storm events T3_5_D12_25A_S, T3_6_D12_50A_S and T3_7_D12_75A_SE. Accumulated u is greatest during T3_7, where H_0 exceeds the load previously applied. The accumulated u does not fully dissipate before the next spike in accumulation. This explains the accumulation of y_0 during T3_7 observed in Figure 7.53.

similar level or below. In contrast, the loads applied during T3_7 (SE) consistently exceed the previously applied loads. Consequently, the degree of displacement accumulation is significantly greater during T3_7. The level of accumulation increases suddenly at the first instance of peak load. Prior to this, the displacement oscillation is marginally greater than T3_6, but the level of accumulation is matched. Once the first peak load has been applied, the degree of accumulation remains high for the duration of the event, despite the following reduction of load.

Figure 7.54 shows the pore pressure response for each event. The oscillation levels observed at PPT1 and PPT2 correspond with the increase in applied load for each event. Figure 7.55 illustrates the accumulated u for each event. The accumulation rises with each subsequent event. The onset of accumulation aligns with the trends in load history previously discussed. However, the degree of accumulation seen in T3_7 is such that, during the dissipation phases between the peak loads, u never recovers back to $r_u = 0$. Consequently, the stiffness of the foundation is reduced for the duration of the event, accounting for the trend in Δy_0 seen in Figure 7.53.

The results of Figure 7.56 present an extract of the load time history at peak load and immediately thereafter. The plots of load and r_u shown in Figure 7.56 (b) and (c) reveal significant behaviour of the excess pore pressure response during the peak loads. The trace in (b) illustrates how the excess pore pressure response begins to accumulate after the peak loads have subsided. The moving mean excess pore pressure is maintained at $r_u \approx 0$ during peak loading, as the positive excess pore pressures are minimised by shearing-induced dilation. After the peak loads, excess positive pore pressure accumulates. Figure 7.56 (c) demonstrates the relationship between r_u and load. In the negative section

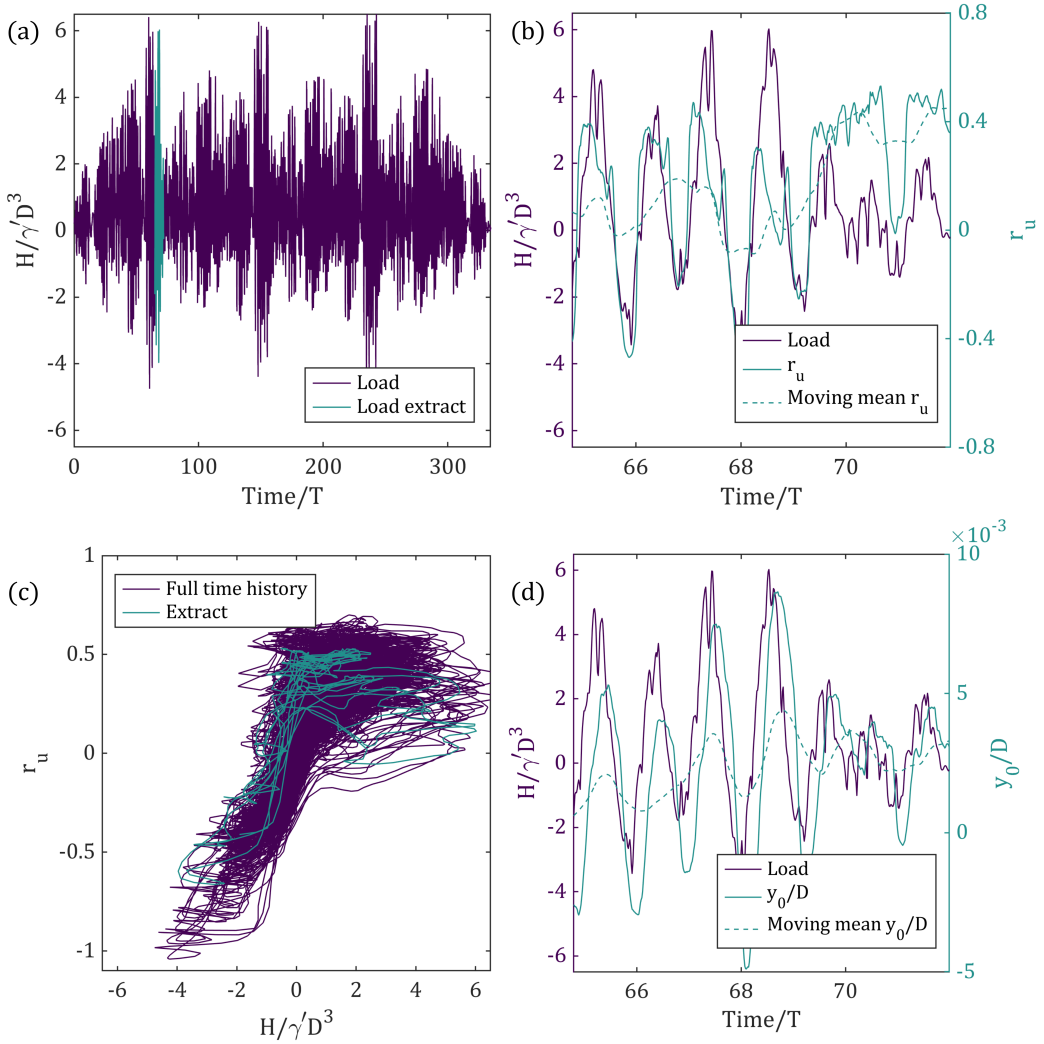

Figure 7.56: Storm event T3_7_D12_75A_SE showing: (a) Load time history with extract at point of peak load. (b) Peak load extract with r_u at PPT1, accumulation of excess pore pressure occurs after the peak loads have subsided. (c) r_u at PPT1 against load, showing a proportional response in the negative half of loading cycle, and a limit on the pore pressure response in the extreme positive loads. (d) Peak load extract with mudline displacement y_o. Significant mudline displacement accumulation occurs after the peaks loads have subsided.

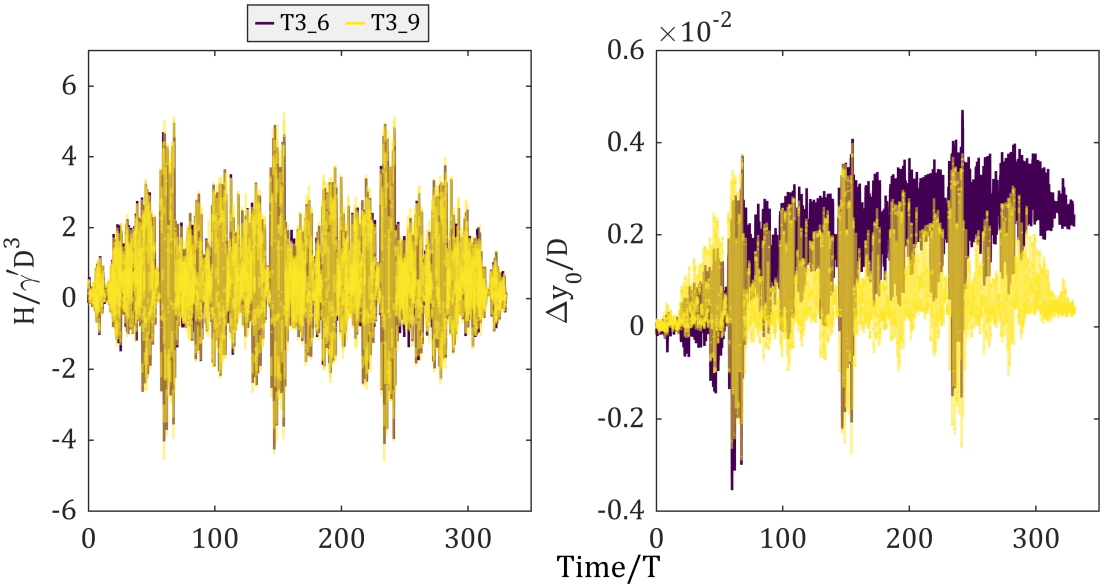

Figure 7.57: Mudline load, H_0, and mudline displacement y_0, from storm events T3_6_D12_50A_S and T3_9_D12_50A_S_r. These events occurred before and after the extreme storm event T3_7. Therefore, the load history of T3_9 significantly differs from T3_6. The H_0 applied is consistent across each event. The y_0 response is significantly reduced during T3_9, owing to the load history effect.

of the trace, during the reverse load half-cycle, the negative excess pore pressure response is approximately linear, with a continual increase in negative excess pore pressure as the load decreases. During the positive forward load half-cycle, the pore pressure response plateaus as the load increases. This response is caused by dilation induced by shearing at the extreme of the load half-cycle. The presence of dilation is highlighted by the double peak of r_u in Figure 7.56 (b). Initially, the pore pressure rises with load; however, as load increases, the pore pressure response is truncated. As the load reduces, the positive excess pore pressure rises again. Figure 7.56 shows the mudline displacement response extract alongside the applied load. The accumulation of mudline displacement is minimised during the peak loads due to the presence of negative excess pore pressure. As pore pressure begins to accumulate after the peak loads have subsided, the degree of mudline displacement accumulation starts to rise. This highlights the beneficial effects of negative excess pore pressure for system stiffness.

First storm and repeat: T3_6, T3_9

Following the extreme storm event, T3_7, a repeat event was applied, T3_9_D12_50A_-S_r, performed under the same conditions as T3_6. Figure 7.57 shows the load and mudline response for these events. The load plot shows identical applied load. The mudline displacement plot demonstrates a greater degree of accumulation in T3_6, with similar levels of oscillation. The effect of prior loading history is evident here, as the applied storm is essentially identical. The degree of excess pore pressure accumulation is marginally greater in T3_6, in line with the increased displacement accumulation (Figure 7.58).

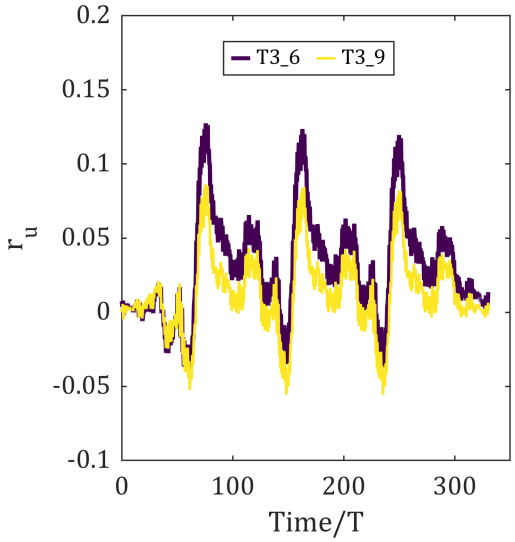

Figure 7.58: Mean excess pore pressure ratio, r_u, at PPT1, from storm events T3_6_D12_50A_S and T3_9_D12_50A_S_r. The accumulated u is reduced during T3_9, owing to load history. The difference in u_{acc} is consistent with the y_0 response seen in Figure 7.57

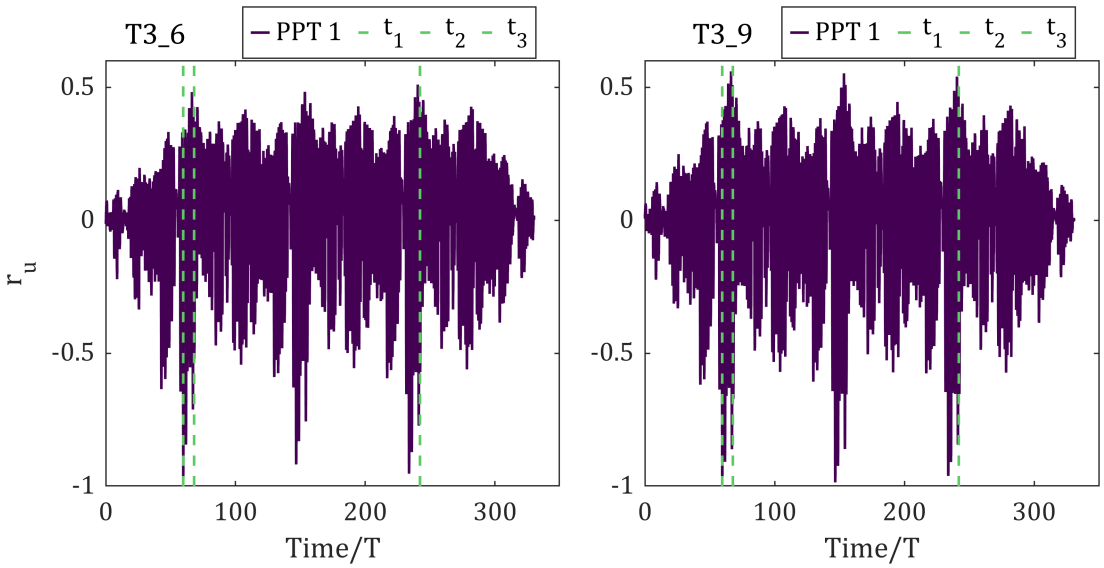

Figure 7.59: Excess pore pressure ratio, r_u, at PPT1 against cycle number from storm events T3_6_D12_50A_S and T3_9_D12_50A_S_r. Overlaid are key instances selected for further analysis in the contour plots shown in Figure 7.60. The selected instances are: the point of minimum r_u response at PPT1, the following maximum r_u response at PPT1, and the maximum r_u response at PPT1 during the final peak load.

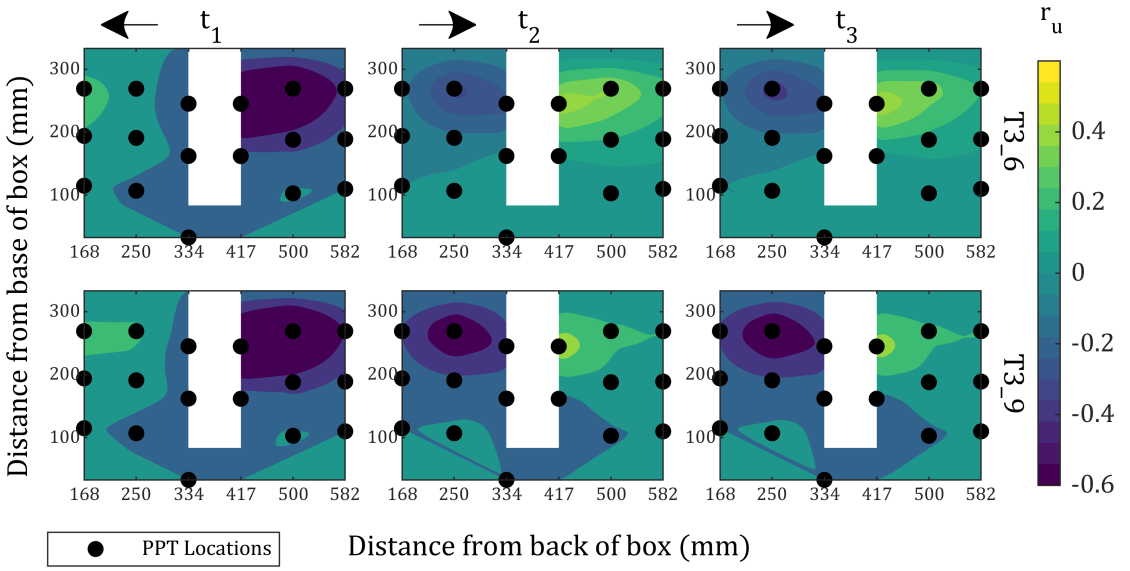

Figure 7.60: Excess pore pressure ratio, r_u, distribution from storm events T3_6_D12_50A_S and T3_9_D12_50A_S_r. Time instances shown are labelled in Figure 7.59. Loading is reversed at t_1, and in the forward direction for t_2 and t_3. N.B. the contour scaled to the limits of these tests to improve contrast. The distribution at t_1, is consistent across both events. The positive u response in front of the pile is increased during T3_6.

Presented in Figure 7.59 is the pore pressure response at PPT1 for both events, with the key cycles presented in the contour plots overlaid. The contour plots, Figure 7.60, shown here display the instances of minimum and maximum r_u at PPT1. Time t_1 illustrates the distribution during the first significant negative spike in r_u at PPT1. Here, the u distribution is consistent for both events. Significant suction (negative r_u) is observed on the top layer of PPTs in front of the pile, accompanied by an increase in u behind the pile. The anti-symmetric distribution is also evident. However, at instances t_2 and t_3, there are differences in the contour plots between the two events. During T3_6, the level of suction behind the pile is lower, with positive u observed in front of the pile. However, areas of higher magnitude suction are present behind the pile during T3_9. This suction increased the system stiffness, which aligns with explanation for reduced displacement accumulation seen during T3_9.

7.6 End of test pushover results

Figure 7.61 presents the end of test pushover results from all tests. These tests were conducted at the conclusion of the testing schedule, following the application of all cyclic loading events. Loading was applied under drained conditions. A pull back was performed on T5_16_M and T6_23_M, after the structural limit was reached. The backbone curves of T3-6, tested post-cyclic loading events, exhibit good agreement. There is an initial steep response, followed by softening. During the initial phase, the curves quickly exceed the reference backbone curves of T1 and T2, where loading was applied on an undisturbed soil. This suggests that the cyclic loading events caused significant densification of the soil,

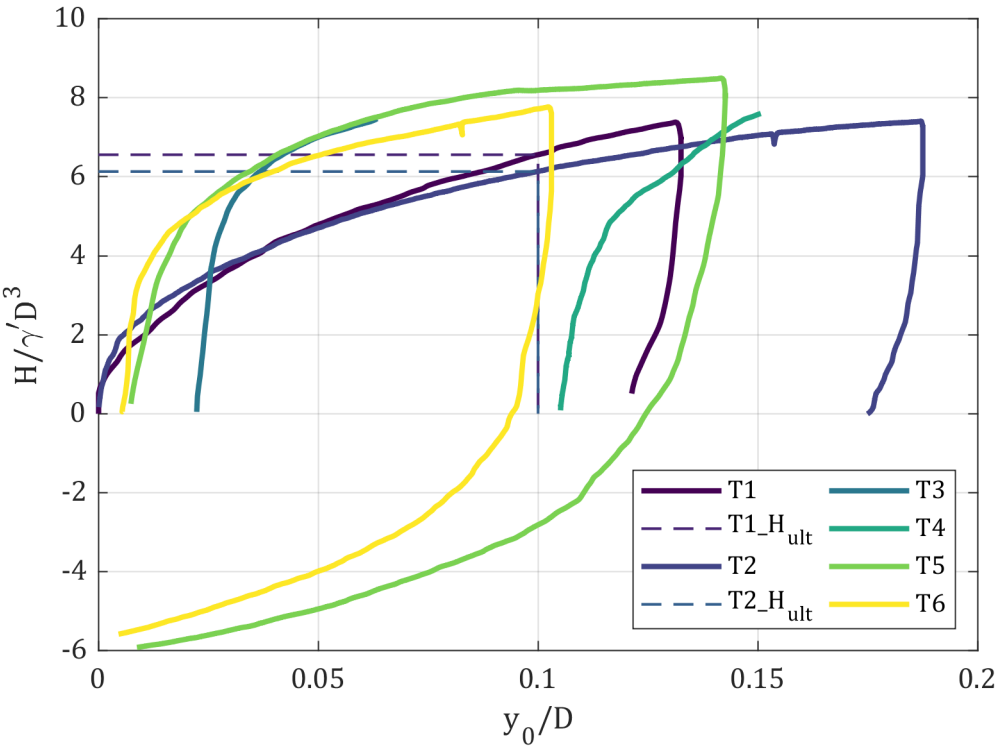

Figure 7.61: End of test pushover plots of H vs y_0 for all tests: T1_M, T2_M, T3_11_M, T4_6_M, T5_16_M and T6_23_M. Starting points of each trace for T3-6 are representative of the start of each push, and the pile position at the end of cyclic loading. Overlaid are the points of H_{ULT}, derived from T1_M and T2_M, at $y_0 = 0.1D$. Forward loading was terminated at the pre-defined structural limit.

resulting in a stiffer response. This observation is consistent with the findings from the cyclic loading results.

The loading history of the cyclic events during T3-6 account for the differences in the starting point of y_0. Therefore, the initial y_0 in T3 is slightly higher than T5 and T6. T4 begins loading beyond the ultimate limit, $y_0 = 0.1D$. As previously discussed, the storm event applied, caused complete liquefaction due to the actuator malfunctioning, resulting in a significant degree of y_0 accumulation.

The events T3, T5, and T6 show good agreement in response. The curves converge onto a single backbone curve following the initial stiff response, despite differing starting points. The traces of T3 and T5 are most closely matched, with T6 slightly lower. This discrepancy is likely attributable to variations in monopile diameter and its impact on normalisation. As evidenced by the reference tests T1 and T2, the curves align closely; however, T2, performed on the $D_{\mathrm{p}} = 5$ m pile, settles slightly beneath T1, which is consistent with the variations observed between T6, and T3 and T5.

T4 follows a shape comparable to T3, T5, and T6, although it originates from a different initial point. While the initial stiffness remains consistent, the degree of softening is reduced, and the load reaches the structural limit before the backbone curve can be fully captured.

7.7 Discussion of partial drainage effects

The assumption of drained conditions in sand for foundation design has long been the norm. However, extensive literature exists based on element-level testing and numerical modelling that highlights the issue of partial drainage. The results of the centrifuge experimental campaign demonstrate the partially drained conditions around large diameter monopiles in sand. There are notable differences in the results of this campaign compared to the conclusions found in literature.

The results of the experimental campaign confirmed the hypothesised dimensionless drainage factor in both displacement controlled and load-controlled events. Furthermore, the results demonstrated the significance and sensitivity of prior loading history. This effect is associated with the drainage factor through the parameters M and k, which relate to the soil conditions. Thus, the drainage factor is validated for soils with comparable initial conditions. Additionally, the results of the storm events revealed critical behaviour of system response under partially drained conditions.

The degree of pore pressure accumulation was linked to load history, particularly the amplitude of previous loads. However, within a loading event, pore pressure accumulation occurred directly after the peak loads, rather than during. The peak loads induced significant negative suction, alongside dilation-induced limits on pore pressure accumulation. Consequently, during these peak loads, the average pore pressure did not accumulate substantially. After the peak load had diminished, the disturbed soil exhibited a tendency to contract, resulting in accumulated mudline displacement in the forward load direction and positive excess pore pressure accumulation. This implies a positive stiffening effect during the peak load, as mudline displacement is restricted by negative excess pore pressure resulting from strong suction effects behind the pile and dilation in front. Furthermore, this highlights the significant importance of loading sequence, as the point of accumulated pore pressure and mudline displacement is indirectly linked to the applied load. A lag is observed in accumulation of mudline displacement post peak load. A potential scenario with a high peak load followed by low load, and sufficient time for excess pore pressure dissipation, may lead to minimal displacement accumulation.

Numerical simulations based on undrained shearing from element tests, such as the PDCAM method (Jostad et al., 2015) rely on relationships between load, displacement, and pore pressure for the construction of contour diagrams. The contour diagrams employ packages of regular loads of varied amplitude, often through the rain counting method, to predict the degree of displacement and pore pressure accumulation. A complex relationship between load amplitude and displacement accumulation was demonstrated in the results presented here. Minimal displacement accumulation occurred if the load levels previously applied exceeded the current levels. Additionally, displacement accumulation occurred after the peak loads were applied. This may preclude the application of rain-counting methods for predicting the load-displacement relationship. Furthermore, the predicted behaviour at different load levels is based on numerical modelling and element level testing (Jostad

et al., 2021). As demonstrated in the results of Chapter 5, and shown in the literature (Jostad et al., 2021), the pore pressure accumulation from element level tests is consistently positive. By basing the predictions of pile response on element tests focused on shearing, the effects of normal loads, such as those leading to suction, could not be appropriately accounted for. Furthermore, the results demonstrated the complex relationship between pore pressure accumulation and load applied. Pore pressure accumulation occurred after the peak loads and was significantly affected by load history. Additionally, the load history with a multi-frequency excitation complicated the pore pressure response, with temporal variations between large loads leading to discrepancies in the dissipation response and the accumulation of mudline displacement. The simplistic method of rain-counting loads and contour diagrams used for calculating equivalent peak load cycle numbers cannot account for these complexities. Indeed, the conclusions of numerical simulations of monopile behaviour using the PDCAM method do not capture the response demonstrated in this experimental campaign. Jostad et al. (2022) predicts the pore pressure response explicitly via calibration with undrained simple shear tests, which are applied to a series of idealised loads taken from a peak storm load period using the rain counting method. The results show a consistent reduction in stiffness resulting from the accumulated positive excess pore pressure. However, the authors also state that the actual response is complicated by the onset of dilation, leading to increases in shear stiffness, and the monopile response may be positively or negatively affected by partially drained conditions.

Numerical simulations employing fully coupled analysis with implicit modelling of cyclic loading have also been documented in the literature. Tasiopoulou et al. (2021) conducted numerical simulations of bucket foundation response during cyclic loading, utilising the Ta-Ger model. The results of these simulations indicate a pore pressure response between fully drained and undrained. The results indicate a rotation response which is close to fully drained, before pore pressure accumulation leads to the sudden reduction in foundation stiffness leading to rapid failure. This analysis is not representative of the results presented here, which show limited displacement accumulation after large loads, followed by pore pressure dissipation leading to a recovery of the foundation stiffness.

Frick et al. (2025) performed numerical simulations of the partially drained response of monopiles with results aligned with the aforementioned literature, indicating a reduction in stiffness due to excess pore pressure accumulation. The simulation procedure,like the methods of Jostad et al. (2022), relied on undrained simple shear tests to predict the pore pressure response. The outcomes of these element tests indicated positive excess pore pressure accumulation, which was associated with a dissipation rate. The outcome was a consistently reduced effective stress and angle of friction, resulting in accumulated displacement.

The results of the literature consistently predict additional accumulated displacement due to excess pore pressure accumulation. The findings of the present study indicate that the relationship between pore pressure response, load, and displacement is complex, influenced by loading history and order, leading to varied outcomes. Element level tests (Chapter 5)

consistently demonstrated increased strain accumulation under partially drained conditions. Consequently, literature that bases its expectations on similar element tests tends to yield overly conservative results. The variation in response between the model and element level tests may be attributed to differing stress paths. The dominant stress paths in the monopile tests likely differ significantly, exhibiting much greater degrees of normal stresses and lower shear stresses. The variation in stress paths between the element tests and the model tests may explain much of the difference in behaviour. The key PPTs presented in the centrifuge results were directly in front and behind the pile. Numerical investigations in the literature (X. Cheng et al., 2021) indicate a considerably greater proportion of normal compressive load σ_x and a diminished presence of shear loads at these locations. This is contrasted with standard triaxial tests, or simple shear tests, with a more significant shear load. The results of element level tests with varied stress paths (e.g. Wichtmann et al. (2015)) indicate significantly altered pore pressure responses. Therefore, the application of standard element level testing for numerical investigations of monopile response may be inappropriate. In particular, the positive effects of pore pressure reduction behind the pile have not received enough attention in literature.

7.8 Summary

This chapter presented the results of a series of centrifuge tests on monopiles in sand. The tests aimed to examine the response of large diameter monopiles subjected to cyclic loading, with a particular focus on the drainage regime in the soil. To achieve this objective, a parametric investigation was completed on the dimensionless drainage scaling factor, $MkT/\gamma' D^3$, as well as an examination of the impact of load history. The campaign included two reference monotonic tests, which provided H_{ULT} set at $y_0 = 0.1D$ for the selection of loads applied during the cyclic events. Each model was subjected to a series of displacement controlled cyclic events, followed by load controlled storm events, culminating in a final pushover. The cyclic testing schedule for both the displacement controlled and storm events was designed to facilitate the investigation of the stated aims.

For the investigation of the drainage factor, parameters k, T, and D were systematically varied for validation. Results where the drainage factor was maintained, that is where D_{ref} was maintained, show good agreement in response. Notably, the results of the equivalent first events show identical responses, as well as very similar responses during the extreme storms. These tests were performed with equivalent D_{ref}, albeit performed with different k, T, and D. The similarity in response provides strong evidence for the validity of the drainage factors. However, tests performed with the same loads on the same model, with variations in loading period and hence different D_{ref} show no clear variation in response. In some cases, the results directly contradict the predicted outcome of a reduced drainage response with increases in loading frequency, thus D_{ref}. It is possible that the change in response was minimal for the range of D_{ref} examined. However, the range of $D = 10-14$ m is realisitic for new generation monopiles. Results indicate that no significant change should

be expected if diameters were to increase up to 14 m, a potential upper limit for currently considered monopile diameters. It should be noted that the methodology for examining changes in effective diameter, variations in T, may impact the results. Whilst the earlier results indicate the validity of the drainage factor and the consequent relationship between T and D, the increases in load frequency applied to alter D_{ref} inevitably lead to changes in dynamic system behaviour.

The testing schedule enabled an investigation into the impact of load history on system response. Equivalent tests were conducted on the same model and across different models after varying degrees of preloading. Additionally, tests of steadily increasing amplitude revealed the influence of preloading amplitude on response. The level of preloading was altered in duration and amplitude throughout the schedule, facilitating a comprehensive analysis of the effect. The significance of load history was shown to be critical when assessing response, in both displacement controlled and storm events. During equivalent events, differing only in load history, the y_0 and u responses were significantly increased when the level of load history was reduced. This was most pronounced in cases where the amplitude of load history was lower than the levels currently being applied. Comparisons of events and their subsequent repeats showed consistently reduced response for the repeat event, where the load history matched or exceeded the levels currently applied. In sequences of events where the amplitude consistently increased with each subsequent event, the response varied significantly when the new amplitude exceeded the previous levels, beyond the increase in the loads applied. Furthermore, the application of a series of lower amplitude events, before significant loading, as seen in T6_1-4, reduced the accumulated and cyclic response of both u and y_0. This demonstrated a beneficial effect for the foundation response.

When considered in unison, the load history effect should be analysed in relation to the drainage factor. The previously applied loads induce a densifying effect that influences the values of M and k, assumed to be consistent across the events. Evaluating the evolution of these values during the tests conducted on the same model is complex, particularly concerning the permeability k. However, the assumption of uniform values across all events is likely invalid. Thus, this must be considered when assessing the validity of the drainage factor.

The results provide insight into the behaviour of monopiles in reality. While the test conditions did not fully replicate real-world scenarios, particularly due to the shadowing effects caused by the pluviation installation method that affected the initial events, the observed behaviours during the remaining sequence are relevant. An important consideration is the assessment of the impact of increasing diameter, resulting in a less drained system, on the foundation response. In realistic conditions of pile installation and operational pre-loading, although the level of oscillation of u can be significant during a storm, the accumulation of excess pore pressures could be more limited than currently assumed, and its effects on pile response might be negated by suction and dilation.

Comparing the results of the centrifuge tests with the partially drained cyclic triaxial

series of Chapter 5 reveals several significant observations. In all cases of the partially drained element tests, increases in partial drainage through restricted drainage led to positive accumulated excess pore pressure and increases in accumulated strain. This effect was most evident in the silty sand partial drainage series. The fabric of the silty sand samples was more collapsible. In these instances, the degree of pore pressure and axial strain accumulation was significantly greater. This effect is also seen in the centrifuge tests during the first event. The soil fabric surrounding the pile was influenced by shadowing effects, which resulted in a more collapsible fabric. As the pore pressures dissipated, either post-cycling or during the event, the densified soil exhibited considerably less pore pressure accumulation. However, the partially drained element tests, never exhibited any suction induced negative excess pore pressure since the focus was on shearing.

The results of the storm load events revealed significant results regarding the impact of soil stiffness. The applied load was partially one-way, with an average load in the forward direction. However, the pore pressure response showed far greater response in the negative direction. The onset of shearing induced dilation in the forward direction limited the accumulated negative excess pore pressure, during the peak loads. This effect, combined with the high negative pore pressure at the back of the pile induced a stiffening effect. This behaviour is not appropriately accounted for in current practice. Numerical predictions based on contour diagrams predict an accumulation of excess pore pressure, inducing increased strain accumulation. Considering the qualitative difference in behaviour observed between the centrifuge tests, and the element tests, simplified numerical methodologies appear to be over-conservative. Future research should aim to calibrate constitutive models against stress paths that are more representative of the critical conditions highlighted in the results of this study, and to implement these models in numerical simulations validated for their capacity to reproduce the beneficial effects of suction and dilation observed in the experiments.

Chapter 8
Conclusions

8.1 Introduction

This thesis presented the findings of an experimental campaign investigating the effects of partial drainage on sand subjected to cyclic loading with a focus on the response around offshore monopiles. The campaign included a series of element level tests, as well as centrifuge tests of monopiles on the same sand. Through a carefully designed element testing programme, the campaign provided insight into the behaviour of sand subjected to cyclic loading under a range of initial conditions, drainage regimes and fines content. The first phase of testing provided benchmark results under a range of conditions on Congleton sand. These results served as a basis for comparison for advanced tests and facilitated calibration of the SANISAND-MS soil constitutive model. The second phase of research examined the influence of partial drainage and fines content on the cyclic response of Congleton sand, offering insight into the relationship between these factors during cyclic loading. These tests generated novel data regarding long-term cyclic loading of sands. Lastly, a series of centrifuge tests were conducted to evaluate the validity of a proposed non-dimensional drainage scaling factor and to assess the response of large diameter monopiles to extreme storm loading. Together, these complementary experimental campaigns contribute to a deeper understanding of partially drained cyclic behaviour in sands and provide valuable data for further research.

All experiments were conducted on Congleton sand at a consistent density, enabling direct comparisons between element-scale and model-scale responses, thus establishing a unified dataset for future research and modelling efforts. The key findings of this research are summarised in the following sections, followed by practical recommendations and suggestions for future work.

8.2 Key contributions

8.2.1 Benchmark testing

Novel testing apparatus

A key contribution of this research lies in the development and implementation of an advanced cyclic triaxial testing methodology, specifically tailored to investigate the response of sand under partially drained conditions. This methodology was formulated through a careful integration of existing approaches, adapted to meet the unique objectives of the study. A significant aspect of this development was the adoption of a slurry deposition sample preparation technique, selected following a sample preparation investigation. To

support this technique, bespoke apparatus was designed and manufactured based on the work of Carraro et al. (2008). This enabled the consistent preparation of homogeneous samples, including those with varying fines content, a key requirement for investigating the influence of fines on cyclic behaviour.

In addition, a novel partial drainage filter was developed at the University of Oxford, based on the methodology proposed by Suzuki et al. (2020). This filter system enabled controlled drainage conditions to be replicated reliably during cyclic triaxial testing, bridging the gap between idealised fully drained and undrained scenarios. The combination of these experimental innovations facilitated a series of complex cyclic triaxial tests investigating the relationship between drainage conditions and fines content during cyclic loading.

Benchmark test results

An important contribution of this thesis is the development of a comprehensive experimental database, as required for the calibration of advanced constitutive models, through a series of monotonic and cyclic triaxial tests on Congleton sand under both drained and undrained conditions. These tests were designed to serve as a benchmark dataset for evaluating sand behaviour under various loading scenarios and drainage conditions. The results aligned with established findings in the literature, further emphasising the critical role of initial conditions, particularly sand density and cyclic stress ratio, in governing the strain response under cyclic loading. Using this dataset, the SANISAND-MS constitutive model was calibrated for simulation of the test data. The model was subsequently validated against both monotonic and cyclic drained test results.

8.2.2 Advanced cyclic triaxial tests

Fines content

An additional contribution of this study is the investigation into the influence of non-plastic fines content on the cyclic behaviour of Congleton sand under drained loading conditions. The experimental programme included tests on specimens with 10% and 15% fines by mass, enabling an assessment of how increasing fines content affects the deformation response during cyclic loading.

The results were employed to assess the applicability of the equivalent intergranular void ratio framework in predicting cyclic behaviour. For both fines contents, the response was broadly consistent with benchmark tests on clean sand when the equivalent void ratio was held constant, suggesting that this framework remains a useful predictive tool. However, as the fines content increased, slight deviations in the cyclic response were observed, indicating potential limitations of the approach when applied to sands with higher fines content.

Partial drainage

This research also contributes to the understanding of sand behaviour under partially drained conditions through a dedicated series of triaxial element tests. These tests were designed to create partially drained conditions, bridging the gap between idealised fully drained and undrained conditions. The partially drained conditions were imposed using a "filter" which created delayed drainage conditions. By maintaining controlled partial drainage during cyclic loading, the tests provided data on the evolution of pore pressure and strain response in sands subjected to long term cyclic loading.

The results clearly demonstrated that positive excess pore pressure is generated during cyclic loading when drainage is restricted. This pore pressure accumulation, in turn, was shown to contribute to increased strain accumulation over time. These findings highlight the critical influence of drainage conditions on the cyclic response of sand and indicate that careful consideration is required for the design of offshore foundations.

Partial drainage with fines content

This thesis presents a novel element-level investigation into the combined effects of partial drainage and increased fines content on the cyclic response of sand. By designing a series of triaxial tests that simultaneously incorporated both factors, the study explored complex soil behaviour not typically captured in conventional testing approaches.

The results revealed that the concept of equivalent void ratio, while effective under fully drained conditions, lost its predictive validity under partially drained cyclic loading. The presence of fines, coupled with restricted drainage, led to a collapsible soil fabric that exhibited highly contractive behaviour. This contractive response generated significant positive excess pore pressure during cyclic loading, which in turn promoted accelerated strain accumulation. The soil-specific calibration of the b parameter from the equivalent void ratio concept may have yielded improved results. However, the results of this thesis highlighted the sensitivity of this parameter when predicting the accumulated strain response of soils.

8.2.3 Centrifuge model testing

Drainage scaling factor

A further major contribution of this research is the centrifuge modelling investigation into the validity of a proposed non-dimensional drainage scaling factor for partially drained cyclic loading. A series of centrifuge tests was conducted on large-diameter monopiles in sand, designed to systematically vary key parameters influencing drainage, while maintaining similarity in the scaling factor.

The parametric study demonstrated that the drainage factor provided a useful means of achieving consistency in partially drained behaviour when both the scaling factor and the loading history were preserved. Under these conditions, the monopile response was highly

consistent across tests, offering strong validation of the theoretical proposition. However, when the prior loading history was altered, or when the drainage factor was applied to monopiles with larger diameters, the results became less clear. These findings suggest that while the drainage scaling factor is valid, its application is sensitive to load history. The results of tests of varied reference monopile diameter were likely affected by the presence of dynamic effects, generated by high loading frequencies. Additionally, the low range of reference monopile diameters tested may have limited the impact of the varied loading frequencies applied. Further testing with a greater range of tested monopile diameters, facilitated with increased model monopile diameters may have yielded improved results.

Importantly, the study highlighted the critical role of load history in shaping the soil-structure interaction response under cyclic loading. The observed sensitivity to load sequence challenges the assumptions underpinning cumulative damage models such as Miner's rule, indicating that such simplified approaches may be inadequate for predicting the performance of monopile foundations, especially under partially drained conditions.

Storm loading of large diameter monopiles

The final major contribution of this thesis is the investigation of large-diameter monopile behaviour under storm loading conditions, conducted through a series of centrifuge model tests. These tests examined the response of monopiles subjected to extreme storm events time histories including variations in both loading period and magnitude. The aim was to better understand how extreme storm loading events influence pore pressure generation and stiffness degradation in partially drained soils.

The results revealed a significantly partially drained response, with pronounced pore pressure oscillations during each cycle of loading. When the applied load exceeded the stress levels from previous loading cycles, accumulation of positive excess pore pressure was observed, often once the large cycles were complete. This pore pressure build-up led to a reduction in average system stiffness.

However, the tests also identified the development of negative excess pore pressures during the reverse loading phase which contributed to a transient stiffening of the soil. Shearing induced dilation during large load cycles limited the onset of positive excess pore pressures, coupled with the suction effects of reverse loading, leading to increased effective stress. This behaviour was not observed in the corresponding element-level tests, suggesting that model-scale effects, such as more complex drainage pathways or stress paths, play a significant role in the overall response. The divergence between element and model-scale behaviour raises important questions about the applicability of current design methods for partially drained conditions, which are often based on simplified or idealised assumptions derived from element testing. Element level tests focused on cyclic shearing in triaxial conditions, this led to increased positive excess pore pressure. Conversely, the centrifuge model experiments imposed a range of load paths on the soil structure. These load paths induced negative excess pore pressures during reverse loading, and limited positive excess pore pressures by dilation induced shearing in the forward load. These

findings underscore the need for more nuanced approaches in the design of offshore monopile foundations subjected to storm loading. The data provided in this thesis provides an opportunity to develop and validate novel constitutive models, capable of replicating the system response demonstrated. In particular, future research should focus on calibrating constitutive models against stress paths that more closely represent the critical conditions identified in this study. These models should then be implemented in numerical simulations and validated for their ability to reproduce the beneficial effects of suction and dilation observed experimentally.

8.3 Key implications

The results of the experimental campaign combined to provide key insight into the effect of partial drainage on the cyclic loading response of sand around large monopile foundations. The triaxial testing campaign showed that partially drained soil elements exhibit increased pore pressure response compared to fully drained. This pore pressure response always induced a positive excess pore pressure accumulation, causing a reduction in stiffness, and consequent increase in strain. The rate of drainage out of the sample was a key factor for predicting the rate of pore pressure accumulation, combined with loading induced changes in volumetric strain. The behaviour can not be entirely predicted by the drainage response of the fully drained sample. Furthermore, the partially drained response of silty sand samples was markedly different from the clean sand case. Axial strain accumulation in the partially drained clean sand tests was slightly greater than the fully drained tests. When testing on samples at the same equivalent intergranular void ratio, e^*, increased fines content created a collapsible fabric susceptible to significantly greater contractive strain.

The partially drained response of sand around model monopiles in the centrifuge differed from the element level testing. During the initial phases of loading, where shadowing effects around the monopile created a lower density, collapsible fabric, significant positive excess pore pressures accumulated rapidly in line with element level results. However, the soil conditions of the first events are unlikely to be representative of those found in reality. Installation effects and the lack of shadowing will create a dense soil fabric with a higher resistance to liquefaction. Once the pore pressures had dissipated, during or after the first loading event, the new, denser fabric did not exhibit significant pore pressure accumulation; rather oscillation was observed. In fact, the pore pressure reached significantly negative values during the reverse loading half-cycle. This, combined with dilation-induced limits to the positive pore pressure response during the positive loading half-cycle, created a stiffening effect on the monopile response. This effect was visible during both displacement controlled uniform cyclic loading and load controlled storm loading. The implication of this finding is that the use of element level testing using conventional load paths, does not accurately represent the response of soil around a monopile foundation under cyclic loading. Element level tests examine stress paths dominated by shearing and have been shown to only predict positive excess pore pressure accumulation with increasing loading cycles,

leading to a reduction in stiffness. In contrast, suction and dilation around a monopile can lead to stiffening, particularly during large loading cycles. Simplified modelling methods seeking to predict the monopile response based on conventional element testing, such as those based on contour diagrams, may be overly conservative in their predictions.

8.4 Future work

8.4.1 Partially drained element testing

The work presented in this thesis provides valuable data on the behaviour of cyclic loading of sands under partially drained conditions. However, the testing schedule was limited by time factors. Within this schedule, there are notable gaps that could be addressed in future research. The tests conducted were targeted 80% D_r, the typical density of North Sea sand deposits. However, a further set of tests performed across a range of densities would offer a clearer understanding of the fundamental soil response. Additionally, further tests conducted over a more comprehensive range of stress ratios are warranted. Tests involving stress paths that intersect the PTL would enhance the confidence in the results presented. Furthermore, element tests which replicate representative stress paths around the monopile extracted through numerical modelling should be conducted. Simplifications will be needed for a triaxial device, otherwise a hollow cylinder or true-triaxial may be necessary.

The results of the partially drained silty sand tests yielded significant findings, raising questions around the equivalent void ratio concept for tests performed under partially drained conditions. This effect was evident; however, the full range of response based on fines content and sample density influenced this outcome was not investigated. A testing schedule that encompasses these variables would generate a valuable dataset. The ultimate objective could be to develop an updated framework for predicting the influence of fines content on the cyclic loading response. Furthermore, silty sand tests using soil-specific calibration of the b parameter from the equivalent void ratio concept would provide greater confidence in the results.

8.4.2 Centrifuge testing

The schedule of the centrifuge testing campaign was constrained by time. Consequently, the number of tests completed was restricted. The methodology, including sample preparation, benchmark tests on the same material, piles, and instrumentation, has already been developed and yielded positive results. Thus, there is a clear opportunity for further work.

One area for further investigation could be to provide fully drained cyclic tests. Basd on the findings presented, investigating drained cyclic loading of large diameter monopiles may yield results with a more onerous displacement response than the partially drained case, as the suction-induced stiffening effect observed in the partially drained case will not occur in the drained condition. This result would be contrary to the prevalent hypothesis

and methods in current design and could be an opportunity for cost savings, however, it requires validation. The completion of these tests could be achieved by water saturation of the model.

Furthermore, the testing schedule could be modified to provide data on varied drainage factor conditions with improved isolation of load history effects. All tests were loaded with a D_{10} equivalent loading frequency as the initial loading event. It is evident that the first test had no prior loading history effects and provided the best validation of the drainage factor. Consequently, maintaining the same loading sequence across models would yield a reliable source of validation for the drainage factor. Furthermore, mitigating the impact of dynamic effects on the monopile response would provide clearer validation of the dimensionless drainage scaling factor. This could be achieved through larger prototype monopile diameters with either increased gravitational scaling or larger model monopiles. The test schedule of T6 provided the most realistic loading scenario, characterised by low amplitude initial loading. Thus, the rate of pore pressure response was significantly reduced. It would be preferable to load any further tests in this manner.

Finally, the element testing results revealed the significance of fines content on the partially drained response. Centrifuge model testing of sands containing fines would yield important results. However, the model preparation would be significantly more complicated, given the challenges associated with pluviation for sands containing fines. The element tests also emphasised the importance of density on the cyclic response. Building on this, centrifuge tests on models of different density would be of interest.

8.4.3 Numerical modelling

Given the substantial quantity of experimental data presented in this thesis across various conditions and testing types on the same sand, there is a clear opportunity for a numerical modelling investigation of partial drainage effects around large diameter monopiles. The data provided could be employed to calibrate soil constitutive models for finite element modelling that should be validated against the centrifuge investigation results.

8.5 Summary

With the increasing size of OWT monopile diameters required to support larger turbines, the question of the induced drainage regime during cyclic loading arises. This thesis sought to examine the impact of a partially drained regime during cyclic loading through a range of tests at different scales.

A series of triaxial element tests on clean sand under drained and undrained conditions provided benchmark results for comparison with silty and partially drained cyclic test results. The results of these benchmark tests were used to calibrate the SANISAND-MS soil constitutive model, producing good replication of the test data, albeit across a limited range of initial conditions. Further advanced testing on partially drained silty sand samples was provided to examine the stated aims of examining the impact of partial drainage and

fines content on sample response to cyclic loading. The results showed good agreement with literature on the effects of partial drainage. The accumulation of positive excess pore pressures reduced the stiffness and increased the strain response. Furthermore, silty sand samples loaded under fully drained conditions showed similar results to the benchmark results at the same equivalent void ratio, validating the equivalent void ratio framework employed. However further work is needed to normalise the expected response under partially drained conditions. Where pore pressures were allowed to develop, the collapsible fabric of the silty samples induced a significantly higher pore pressure response, leading to increased strain accumulation when compared to the clean sand results.

The centrifuge testing campaign built on the results of the partially drained element level tests, examining the drainage regime around large diameter monopiles. The results were used to validate a hypothesised non-dimensional drainage factor, and examine the foundation response during extreme storm events. Initial loading induced fast pore pressure accumulation with stiffness reduction. However, further loading events showed an increase in stiffness caused by suction in the reverse loading half-cycle. This phenomena was not observed in the element level testing, highlighting the limits of standard stress path element tests to predict realistic partially drained soil response around monopiles.

This thesis provided data which demonstrated novel behaviours, not seen in literature. The current field of offshore geotechnical research has a strong focus on this area, given the issues previously discussed. Therefore, this thesis provides useful insight and data provided that is readily usable for further numerical modelling efforts, given the range of conditions tested and the already calibrated advanced constitutive model.

Bibliography

Adamidis, O., and Anastasopoulos, I. (2022), "Cyclic liquefaction resistance of sand under a constant inflow rate", *Géotechnique*, 74/10: 1019–32. doi: 10.1680/jgeot.21.00082.

Adamidis, O., and Madabhushi, G. (2015), "Use of viscous pore fluids in dynamic centrifuge modelling", *International Journal of Physical Modelling in Geotechnics*, 15/3: 141–9. doi: 10.1680/ijpmg.14.00022.

Adamidis, O., Vasic, N., and Kassas, K. (2017), *Small strain shear modulus of Hostun sand*, tech. rep. November.

Albiker, J., Achmus, M., Frick, D., and Flindt, F. (2017), "1 g Model Tests on the Displacement Accumulation of Large-Diameter Piles Under Cyclic Lateral Loading", *Geotechnical Testing Journal*, 40/2: 173–84. doi: 10.1520/GTJ20160102.

Andersen, K. H. (2015), "Cyclic soil parameters for offshore foundation design", *Frontiers in offshore geotechnics III* 5.

Arulnathan, R., Boulanger, R. W., and Riemer, M. F. (1998), "Analysis of Bender Element Tests", *Geotechnical Testing Journal*, 21/2: 120–31. doi: 10.1520/gtj10750j.

ASTM D7181-20 (2020), "Standard test method for consolidated drained triaxial compression test for soils", *ASTM International*: 1–12. doi: 10.1520/D7181-20.of.

Azeiteiro, R. J. N., Coelho, P. A. L. F., Taborda, D. M., and Grazina, J. C. D. (2017), "Critical State–Based Interpretation of the Monotonic Behavior of Hostun Sand", *Journal of Geotechnical and Geoenvironmental Engineering*, 143/5: 04017004. doi: 10.1061/(ASCE)GT.1943-5606.0001659.

Bachynski, E. E., Page, A., and Katsikogiannis, G. (2019), "Dynamic response of a large-diameter monopile considering 35-hour storm conditions", *Proceedings of the International Conference on Offshore Mechanics and Arctic Engineering - OMAE* 10: 1–9. doi: 10.1115/OMAE2019-95170.

Balaam, T. D. (2020), "Development and Calibration of Cyclic Loading Models for Monopile Foundations in Clay", PhD thesis (University of Oxford). doi: 10.13039/501100000266.

Baldi, G., Hight, D. W., and Thomas, G. (1988), "State-of-the-Art Paper: A Reevaluation of Conventional Triaxial Test Methods", in *Advanced Triaxial Testing of Soil and Rock* (100 Barr Harbor Drive, PO Box C700, West Conshohocken, PA 19428-2959: ASTM International), 219–9. doi: 10.1520/STP29080S, http://www.astm.org/doiLink.cgi?STP29080S.

Baldi, G., and Nova, R. (1984), "Membrane Penetration Effects in Triaxial Testing", *Journal of Geotechnical Engineering*, 110/3: 403–20. doi: 10.1061/(ASCE)0733-9410(1984)110:3(403).

Been, K., and Jefferies, M. G. (1985), "A state parameter for sands", *Géotechnique*, 35/2: 99–112. doi: 10.1680/geot.1985.35.2.99.

Been, K., and Jefferies, M. G. (2004), "Stress-dilatancy in very loose sand", *Canadian Geotechnical Journal*, 41/5: 972–89. doi: 10.1139/T04-038;WEBSITE:WEBSITE:NRC-SITE;ISSUE:ISSUE:10.1139/CGJ4105;WGROUP:STRING:CSP.

Blaker, Ø., and Andersen, K. H. (2019), "Cyclic properties of dense to very dense silica sand", *Soils and Foundations*, 59/4: 982–1000. doi: 10.1016/J.SANDF.2019.04.002.

Bolton, M. D. (1986), "The strength and dilatancy of sands", *Géotechnique*, 36/1: 65–78. doi: 10.1680/geot.1986.36.1.65.

Bonal, J., Donohue, S., and McNally, C. (2012), "Wavelet analysis of bender element signals", *Geotechnique*, 62/3: 243–52. doi: 10.1680/geot.9.P.052.

British Standards Institution (1990), *Methods of test for soils for civil engineering purposes — Part 3* (1; BS 1377:19, London), 40.

Brown, S. F., Austin, G., and Overy, R. F. (1980), "Instrumented Triaxial Cell for Cyclic Loading of Clays.", *Geotechnical Testing Journal*, 3/4: 145–52. doi: 10.1520/gtj10911j.

Brown, S. F., and Snaith, M. S. (1974), "The measurement of recoverable and irrecoverable deformations in the repeated load triaxial test", *Géotechnique*, 24/2: 255–9. doi: 10.1680/geot.1974.24.2.255.

Burd, H. J., Taborda, D. M., Zdravkovic, L., Abadie, C. N., Byrne, B., Houlsby, G. T., Gavin, K., Igoe, D., Jardine, R. J., Martin, C. M., McAdam, R. A., Pedro, A. M. G., and Potts, D. M. (2020), "PISA design model for monopiles for offshore wind turbines: application to a marine sand", *Géotechnique*, 70/11: 1048–66. doi: 10.1680/jgeot.18.P.277.

Byrne, B., Aghakouchak, A., Buckley, R., Burd, H. J., Gengenbach, J., Houlsby, G. T., McAdam, R. A., Martin, C. M., Schranz, F., Sheil, B., and Suryasentana, S. (2020*a*), "PICASO: Cyclic lateral loading of offshore wind turbine monopiles", *Frontiers in Offshore Geotechnics IV- Proceedings of the 4th International Symposium on Frontiers in Offshore Geotechnics, ISFOG 2021*.

Byrne, B., Houlsby, G. T., Burd, H. J., Gavin, K., Igoe, D., Jardine, R. J., Martin, C. M., McAdam, R. A., Potts, D. M., Taborda, D. M., and Zdravkovic, L. (2020*b*), "PISA design model for monopiles for offshore wind turbines: Application to a stiff glacial clay till", *Geotechnique*, 70/11: 1030–47. doi: 10.1680/JGEOT.18.P.255.

Byrne, B., McAdam, R. A., Burd, H. J., Beuckelaers, W. J. A. P., Gavin, K., Houlsby, G. T., Igoe, D., Jardine, R. J., Martin, C. M., Muir Wood, A., Potts, D. M., Gretlund, J. S., Taborda, D. M., and Zdravkovic, L. (2020*c*), "Monotonic laterally loaded pile testing in a dense marine sand at Dunkirk", *Geotechnique*, 70/11: 986–98. doi: 10.1680/JGEOT.18.PISA.004.

Byrne, B., McAdam, R. A., Burd, H. J., Beuckelaers, W. J. A. P., Gavin, K., Houlsby, G. T., Igoe, D., Jardine, R. J., Martin, C. M., Muir Wood, A., Potts, D. M., Gretlund, J. S., Taborda, D. M., and Zdravkovic, L. (2020*d*), "Monotonic laterally loaded pile testing in a stiff glacial clay till at Cowden", *Geotechnique*, 70/11: 970–85. doi: 10.1680/JGEOT.18.PISA.003.

Byrne, B., McAdam, R. A., Burd, H. J., Houlsby, G. T., Martin, C. M., Beuckelaers, W. J. A. P., Zdravkovic, L., Taborda, D. M., Potts, D. M., Jardine, R. J., Ushev, E., Liu, T., Abadias, D., Gavin, K., Igoe, D., Doherty, P., Gretlund, J. S., Andrade, M. P., Muir Wood, A., Schroeder, F., Turner, S., and Plummer, M. (2017), "PISA: New Design Methods for Offshore Wind Turbine Monopiles", *Offshore Site Investigation Geotechnics 8th International Conference Proceedings*: 142–61. doi: 10.3723/osig17.142.

Carraro, J. A. H., and Prezzi, M. (2008), "A new slurry-based method of preparation of specimens of sand containing fines", *Geotechnical Testing Journal*, 31/1: 1–11. doi: 10.1520/gtj100207.

Carraro, J. A. H., Prezzi, M., and Salgado, R. (2009), "Shear Strength and Stiffness of Sands Containing Plastic or Nonplastic Fines", *Journal of Geotechnical and Geoenvironmental Engineering*, 135/9: 1167–78. doi: 10.1061/(asce)1090-0241(2009)135:9(1167).

Chaloulos, Y., Tasiopoulou, P., Giannakou, A., Chacko, J., Aghakouchak, A., and Stergiou, T. (2024), "Fully-Coupled cyclic time-history analyses of monopile foundations in sand", *Ocean Engineering*, 298: 116691. doi: 10.1016/J.OCEANENG.2024.116691.

Chen, W. B., Liu, K., Feng, W. Q., and Yin, J. H. (2020), "Partially drained cyclic behaviour of granular fill material in triaxial condition", *Soil Dynamics and Earthquake Engineering*, 139. doi: 10.1016/j.soildyn.2020.106355.

Cheng, K., Heron, C. M., Prendergast, L. J., and Marshall, A. M. (2020), "Centrifuge tests of monopile foundations under one-way cyclic lateral loading", *4th European Conference on Physical Modelling in Geotechnics - ECPMG 2020*, 2010: 235–42.

Cheng, X., Diambra, A., Ibraim, E., Liu, H., and Pisanò, F. (2021), "3d fe-informed laboratory soil testing for the design of offshore wind turbine monopiles", *Journal of Marine Science and Engineering*, 9/1: 1–15. doi: 10.3390/jmse9010101.

Choo, Y.-w., and Kim, D. (2016), "Experimental Development of the p-y Relationship for Large-Diameter Offshore Monopiles in Sands: Centrifuge Tests", *Journal of Geotechnical and Geoenvironmental Engineering*, 142/1: 04015058. doi: 10.1061/(ASCE)GT.1943-5606.0001373.

Clayton, C. R. I. (2011), "Stiffness at small strain: research and practice", *Géotechnique*, 61/1: 5–37. doi: 10.1680/geot.2011.61.1.5.

Clayton, C. R. I., and Khatrush, S. A. (1986), "A new device for measuring local axial strains on triaxial specimens", *Géotechnique*, 36/4: 593–7. doi: 10.1680/geot.1986.36.4.593.

Costanzo, G., Brindley, G., and Tardieu, P. (2025), *Wind energy in Europe: 2024 Statistics and the outlook for 2025-2030*, tech. rep. (WindEurope), https://windeurope.org/intelligence-platform/product/wind-energy-in-europe-2024-statistics-and-the-outlook-for-2025-2030/.

Cubrinovski, M., and Ishihara, K. (2002), "Maximum and minimum void ratio characteristics of sands", *Soils and Foundations*, 42/6: 65–78. doi: 10.3208/SANDF.42.6{_}65.

Cuéllar, P., Georgi, S., Baeßler, M., and Rücker, W. (2012), "On the quasi-static granular convective flow and sand densification around pile foundations under cyclic lateral loading", *Granular Matter*, 14/1: 11–25. doi: 10.1007/S10035-011-0305-0/METRICS.

Da Fonseca, A. V., Ferreira, C., and Fahey, M. (2009), "A Framework Interpreting Bender Element Tests, Combining Time-Domain and Frequency-Domain Methods", *Geotechnical Testing Journal*, 32/2: 91–107. doi: 10.1520/GTJ100974.

Dafalias, Y. F., and Manzari, M. T. (2004), "Simple Plasticity Sand Model Accounting for Fabric Change Effects", *Journal of Engineering Mechanics*, 130/6: 622–34. doi: 10.1061/(ASCE)0733-9399(2004)130:6(622).

Dafalias, Y. F., and Taiebat, M. (2016), "Sanisand-Z: Zero elastic range sand plasticity model", *Geotechnique*, 66/12: 999–1013. doi: 10.1680/jgeot.15.P.271.

DGI (1996), *Minimum Index Void Ratio, e_min (Danish Method)/Maximum Index Void Ratio, e_max (Danish Method). DGI Product Sheet #000 96-07-02.* Tech. rep. (Lyngby: Danish Geotechnical Institute).

Dilip, A., Wang, Y., and Adamidis, O. (2025), "Identification of the critical state line of sands using coupled shear-volumetric strain paths", *Acta Geotechnica*.

DNV AS (2021), *DNV-ST-0126 Support structures for wind turbines* (Høvik, Norway: DNV).

Dominguez-Quintans, C., Carraro, J. A. H., and Zdravkovic, L. (2023), "A Critical Assessment of the Effect of Initial Fabric on Key Small-Strain Design Parameters of Slurry-Deposited Silts and Sands", *Journal of Geotechnical and Geoenvironmental Engineering*, 149/7: 1–16. doi: 10.1061/JGGEFK.GTENG-11305.

Dominguez-Quintans, C., Quinteros, V. S., Carraro, J. A. H., Zdravkovic, L., and Jardine, R. J. (2019), "Quality assessment of a new in-mould slurry deposition method for triaxial specimen reconstitution of clean and silty sands", *E3S Web of Conferences*, 92: 1–6. doi: 10.1051/e3sconf/20199202010.

Drnevich, P., Clayton, C. R. I., Khatrush, S. A., Bica, A., and Siddique, A. (1989), "The Use of Hall Effect Semiconductors in Geotechnical Instrumentation", *Geotechnical Testing Journal*, 12/1: 69. doi: 10.1520/GTJ10676J.

Dyvik, R., and Madshus, C. (1987), "Lab measurements of Gmax using bender elements", *International Journal of Rock Mechanics and Mining Sciences & Geomechanics Abstracts*, 24/2: 56. doi: 10.1016/0148-9062(87)92023-7.

Emery, J. J., Finn, W. D. L., and Lee, K. W. (1973), "Uniformity of saturated sand samples", *ASTM STP* 523: 182–94.

Erten, D., and Maher, M. H. (1995), "Cyclic undrained behavior of silty sand", *Soil Dynamics and Earthquake Engineering*, 14/2: 115–23. doi: 10.1016/0267-7261(94)00035-F.

Escalera Mendoza, A. S., Todd Griffith, D., Qin, C., -, a., Wen, K. Z., Dehtyriov, D., Byrne, B., Zheng, H., Zhang, H., Li, G., McWilliam, M. K., Natarajan, A., Pollini, N., Dykes, K., and Barter, G. (2021), "Conceptual monopile and tower sizing for the IEA Wind Task 37 Borssele reference wind farm", *Journal of Physics: Conference Series*, 2018/1: 012025. doi: 10.1088/1742-6596/2018/1/012025.

Escribano, D. E., Nash, D. F. T., and Diambra, A. (2019), "Local and Global Volumetric Strain Comparison in Sand Specimens Subjected to Drained Cyclic and Monotonic Triaxial Compression Loading", *Geotechnical Testing Journal*, 42/4: 20170054. doi: 10.1520/GTJ20170054.

ETHZ (n.d.), *KRUPP Centrifuge| ETH Zurich*, https://geotechnics.ethz.ch/geotechnical-centrifuge-center/krupp-centrifuge.html.

Frick, D., Abdel-Rahman, K., Goldau, N., and Achmus, M. (2025), "Numerical investigation on the capacity decrease of monopiles in sand due to cyclic loading", in *Proceedings of ISFOG 2025: 5th International Symposium on Frontiers in Offshore Geotechnics* (International Society for Soil Mechanics and Geotechnical Engineering). doi: 10.53243/ISFOG2025-66.

Fugro (2020), "EUAF-FGBM-SOIL-TM-751: Preparation of sand and silt specimens using Ladd's under-compaction method", *Fugro Test Methods*.

Gaertner, E., Rinker, J., Sethuraman, L., Anderson, B., Zahle, F., and Barter, G. (2020), "Definition of the IEA 15 MW Offshore Reference Wind Turbine", *Technical Report NREL/TP-5000-75698 March 2020*: 1–44.

García-Rojo, R., and Herrmann, H. J. (2005), "Shakedown of unbound granular material", *Granular Matter*, 7/2-3: 109–18. doi: 10.1007/s10035-004-0186-6.

Garga, V. K., and Zhang, H. (1997), "Volume changes in undrained triaxial tests on sands", *Canadian Geotechnical Journal*, 34/5: 762–72. doi: 10.1139/t97-038.

Garnier, J., Gaudin, C., Springman, S., Culligan, P., Goodings, D., Konig, D., Kutter, B., Phillips, R., Randolph, M., and Thorel, L. (2007), "Catalogue of scaling laws and similitude questions in geotechnical centrifuge modelling", *International Journal of Physical Modelling in Geotechnics*, 7/3: 1–23. doi: 10.1680/ijpmg.2007.070301.

Georgiannou, V. N., Burland, J. B., and Hight, D. W. (1990), "The undrained behaviour of clayey sands in triaxial compression and extension", *Géotechnique*, 40/3: 431–49. doi: 10.1680/geot.1990.40.3.431.

Ghionna, V. N., and Porcino, D. (2006), "Liquefaction Resistance of Undisturbed and Reconstituted Samples of a Natural Coarse Sand from Undrained Cyclic Triaxial Tests", *Journal of Geotechnical and Geoenvironmental Engineering*, 132/2: 194–202. doi: 10.1061/(ASCE)1090-0241(2006)132:2(194).

Greening, P. D., and Nash, D. F. T. (2004), "Frequency domain determination of G0 using bender elements", *Geotechnical Testing Journal*, 27/3: 288–94. doi: 10.1520/gtj11192.

Hardin, B. O., and Black, W. L. (1968), "Vibration Modulus of Normally Consolidated Clay", *Journal of the Soil Mechanics and Foundations Division*, 94/2: 353–69. doi: 10.1061/JSFEAQ.0001100.

Hardin, B. O., and Richart, F. E. (1963), "Elastic Wave Velocities in Granular Soils", *Journal of the Soil Mechanics and Foundations Division*, 89/1: 33–65. doi: 10.1061/jsfeaq.0000493.

Hsiao, D. H., and Phan, V. T. A. (2016), "Evaluation of static and dynamic properties of sand–fines mixtures through the state and equivalent state parameters", *Soil Dynamics and Earthquake Engineering*, 84: 134–44. doi: 10.1016/J.SOILDYN.2016.02.006.

Huang, A. B., and Chuang, S. Y. (2011), "Correlating Cyclic Strength with Fines Contents Through State Parameters", *Soils and Foundations*, 51/6: 991–1001. doi: 10.3208/SANDF.51.991.

IEC-61400-3-1 (2019), *Design Requirements for Fixed Offshore Wind Turbines* (Geneva, Switzerland), 1–148.

Ishihara, K. (1993), "Liquefaction and flow failure during earthquakes", *Geotechnique*, 43/3: 351–451. doi: 10.1680/geot.1993.43.3.351.

Ishihara, K., and Okada, S. (1982), "Effects of Large Preshearing on Cyclic Behaviour of Sand", *Soils and Foundations*, 22/3: 109–25. doi: 10.3208/SANDF1972.22.3{_}109.

Ishihara, K., Troncoso, J., Kawase, Y., and Takahashi, Y. (1980), "Cyclic Strength Characteristics of Tailings Materials", *Soils and Foundations*, 20/4: 127–42. doi: 10.3208/sandf1972.20.4{_}127.

ISO (2022), *ISO 17892-4:2016 Geotechnical investigation and testing Laboratory testing of soil Part 4: Determination of particle size distribution*, https://www.iso.org/standard/55246.html.

Jamiolkowski, M., Lo Presti, D. C. F., and Manassero, M. (2003), "Evaluation of Relative Density and Shear Strength of Sands from CPT and DMT", *Soil Behavior and Soft Ground Construction*, 40659/January: 201–38. doi: 10.1061/40659(2003)7.

Jardine, R. J., Symes, M. J., and Burland, J. B. (1984), "The Measurement of soil stiffness in the triaxial apparatus", *Géotechnique*, 34/3: 323–40. doi: 10.1680/geot.1984.34.3.323.

Jones, L., White, J., and Truong, L. (2020), "On the Triaxial Testing of Sand for Offshore Wind Turbine Foundation Design", *Proceedings of the 4th International Symposium on Frontiers in Offshore Geotechnics*, January: 1137–48.

Jostad, H. P., Carotenuto, P., Yusuke, S., and Sivasithamparam, N. (2021), "Measuring and Modelling Cyclic Response of Dense Sand Under Partially Drained Conditions", in *Lecture Notes in Civil Engineering*, cxxv (Springer International Publishing), 447–55. doi: 10.1007/978-3-030-64514-4{_}43, http://link.springer.com/10.1007/978-3-030-64514-4_43.

Jostad, H. P., Dahl, B. M., Page, A., Sivasithamparam, N., and Sturm, H. (2019), "Evaluation of soil models for improved design of offshore wind turbine foundations in dense sand", *Geotechnique*, 70/8: 682–99. doi: 10.1680/JGEOT.19.TI.034.

Jostad, H. P., Grimstad, G., Andersen, K. H., and Sivasithamparam, N. (2015), "A fe procedure for calculation of cyclic behaviour of offshore foundations under partly drained conditions", *Frontiers in Offshore Geotechnics III - Proceedings of the 3rd International Symposium on Frontiers in Offshore Geotechnics, ISFOG 2015*: 153–70.

Jostad, H. P., Liu, H., Sivasithamparam, N., and Ragni, R. (2022), "Cyclic Capacity of Monopiles in Sand under Partially Drained Conditions: A Numerical Approach", *Journal of Geotechnical and Geoenvironmental Engineering*, 149/2: 04022129. doi: 10.1061/JGGEFK.GTENG-10435.

Kelley, N., and Jonkman, B. (2005), *Overview of the TurbSim Stochastic Inflow Turbulence Simulator*, tech. rep. (National Renewable Energy Laboratory), 1–13, papers2://publication/uuid/84B33CE0-C9E4-4106-8CFC-7678530808B4.

Kementzetzidis, E., Corciulo, S., Versteijlen, W. G., and Pisanò, F. (2019), "Geotechnical aspects of offshore wind turbine dynamics from 3D non-linear soil-structure simulations", *Soil Dynamics and Earthquake Engineering*, 120: 181–99. doi: 10.1016/J.SOILDYN.2019.01.037.

Klinkvort, R. T., Black, J. A., Bayton, S. M., Haigh, S. K., Madabhushi, G., Blanc, M., Thorel, L., Zania, V., Bienen, B., and Gaudin, C. (2018), "A review of modelling effects in centrifuge monopile testing in sand", *Physical Modelling in Geotechnics*, 1/July: 719–24. doi: 10.1201/9780429438660-108.

Klinkvort, R. T., Hededal, O., and Springman, S. (2013), "Scaling issues in centrifuge modelling of monopiles", *International Journal of Physical Modelling in Geotechnics*, 13/2: 38–49. doi: 10.1680/ijpmg.12.00010.

Klotz, E. U., and Coop, M. R. (2002), "On the identification of critical state lines for sands", *Geotechnical Testing Journal*, 25/3: 289–302. doi: 10.1520/gtj11090j.

Knudsen, S., Powell, J. M., Lunne, T., Thomsen, N. V., Krogh, L., and Barwise, A. (2021), "Development of New Robust Procedures for the Determination of Maximum and Minimum Dry Densities of Sand", in *4th International Symposium on Frontiers in Offshore Geotechnics, Austin, Texas.*

Kuerbis, R., Negussey, D., and Vaid, Y. P. (1988*a*), "Effect of gradation and fines content on the undrained response of sand", *International Journal of Rock Mechanics and Mining Sciences & Geomechanics Abstracts*, 27/1: 6. doi: 10.1016/0148-9062(90)90054-6.

Kuerbis, R., and Vaid, Y. P. (1988*b*), "Sand sample preparation - the slurry deposition method", *Soils and Foundations*, 28/4: 107–18. doi: 10.3208/sandf1972.28.4{_}107.

Kuwano, R., and Jardine, R. J. (2002), "On the applicability of cross-anisotropic elasticity to granular materials at very small strains", *Géotechnique*, 52/10: 727–49. doi: 10.1680/geot.2002.52.10.727.

Ladd, R. S. (1978), "Preparing Test Specimens Using Undercompaction", *Geotechnical Testing Journal*, 1/1: 16–23.

Lade, P. V. (2016), *Triaxial Testing of Soils* (Wiley). doi: 10.1002/9781119106616, https://onlinelibrary.wiley.com/doi/book/10.1002/9781119106616.

Lade, P. V., and Yamamuro, J. A. (1997), "Effects of nonplastic fines on static liquefaction of sands", *Canadian Geotechnical Journal*, 34/6: 918–28. doi: 10.1139/t97-052.

Lafayette, W., and Fellow, P. (2000), "Shear Strength and Stiffness of Silty Sand", *Journal of Geotechnical and Geoenvironmental Engineering*, 126/May: 451–62.

Leblanc, C., Byrne, B., and Houlsby, G. T. (2010), "Response of stiff piles to random two-way lateral loading", *Geotechnique*, 60/9: 715–21. doi: 10.1680/GEOT.09.T.011/ASSET/IMAGES/SMALL/GEOT60-715-F11.GIF.

LeBlanc, C., Houlsby, G. T., and Byrne, B. (2010), "Response of stiff piles in sand to long-term cyclic lateral loading", *Geotechnique*, 60/2: 79–90. doi: 10.1680/geot.7.00196.

Li, S., Zhang, Y., and Jostad, H. P. (2019), "Drainage conditions around monopiles in sand", *Applied Ocean Research*, 86/September 2018: 111–6. doi: 10.1016/j.apor.2019.01.024.

Li, Y., Yang, Y., Yu, H. S., and Roberts, G. (2018), "Effect of sample reconstitution methods on the behaviors of granular materials under shearing", *Journal of Testing and Evaluation*, 46/6: 2718–25. doi: 10.1520/JTE20170126.

Liao, C., Chen, J., and Zhang, Y. (2019), "Accumulation of pore water pressure in a homogeneous sandy seabed around a rocking mono-pile subjected to wave loads", *Ocean Engineering*, 173/June 2018: 810–22. doi: 10.1016/j.oceaneng.2018.12.072.

Liu, H., Abell, J. A., Diambra, A., and Pisanò, F. (2019), "Modelling the cyclic ratcheting of sands through memory-enhanced bounding surface plasticity", *Geotechnique*, 69/9: 783–800. doi: 10.1680/JGEOT.17.P.307/ASSET/IMAGES/SMALL/JGEOT.17.P.307-F18.GIF.

Liu, H., Pisanò, F., Jostad, H. P., and Sivasithamparam, N. (2022), "Impact of cyclic strain accumulation on the tilting behaviour of monopiles in sand: An assessment of the Miner's rule based on SANISAND-MS 3D FE modelling", *Ocean Engineering*, 250/November 2021: 110579. doi: 10.1016/j.oceaneng.2022.110579.

Lo, S. R., Chu, J., and Lee, I. K. (1989), "A Technique for Reducing Membrane Penetration and Bedding Errors", *Geotechnical Testing Journal*, 12/4: 311–6. doi: 10.1520/GTJ10991J.

Madabhushi, G. (2017), *Centrifuge Modelling for Civil Engineers* (CRC Press). doi: 10.1201/9781315272863, https://www.taylorfrancis.com/books/9781351989305.

Mandolini, A., Diambra, A., and Ibraim, E. (2021), "Stiffness of granular soils under long-term multiaxial cyclic loading", *Géotechnique*, 71/9: 795–811. doi: 10.1680/jgeot.19.TI.018.

Manzari, M. T., and Dafalias, Y. F. (1997), "A critical state two-surface plasticity model for sands", *Geotechnique*, 47/2: 255–72. doi: 10.1680/geot.1997.47.2.255.

Matešić, L., and Vucetic, M. (2003), "Strain-Rate Effect on Soil Secant Shear Modulus at Small Cyclic Strains", *Journal of Geotechnical and Geoenvironmental Engineering*, 129/6: 536–49. doi: 10.1061/(asce)1090-0241(2003)129:6(536).

McCoy, A., Musial, W., Hammond, R., Mulas Hernando, D., Duffy, P., Beiter, P., Pérez, P., Baranowski, R., Reber, G., and Spitsen, P. (2024), *Offshore Wind Market Report: 2024 Edition*, tech. rep. (Golden, CO (United States): National Renewable Energy Laboratory), https://www.nrel.gov/docs/fy24osti/90525.pdf.

Miner, M. A. (1945), "Cumulative Damage in Fatigue", *Journal of Applied Mechanics*, 12/3: A159–A164. doi: 10.1115/1.4009458.

Mitchell, J. K., and Soga, K. (2005), *Fundamentals of soil behavior* (3rd edn., Wiley), 437.

Mog, K., and Anbazhagan, P. (2022), "Evaluation of the damping ratio of soils in a resonant column using different methods", *Soils and Foundations*, 62/1: 101091. doi: 10.1016/J.SANDF.2021.101091.

Molenkamp, F., and Tatsuoka, F. (1983), "Discussion of " Compression of Free-ends During Triaxial Testing " by Robert W. Sarsby, Nikolas Kalteziotis, and Essam H. Haddad (January, 1982)", *Journal of Geotechnical Engineering*, 109/5: 766–71. doi: 10.1061/(ASCE)0733-9410(1983)109:5(766).

Möller, J. K., Taborda, D. M., Kontoe, S., and Potts, D. M. (2024), "A shear history model for capturing the liquefaction resistance of sands at various cyclic stress ratios", *Computers and Geotechnics*, 166: 105940. doi: 10.1016/J.COMPGEO.2023.105940.

Morison, J., Johnson, J., and Schaaf, S. (1950), "The Force Exerted by Surface Waves on Piles", *Journal of Petroleum Technology*, 2/05: 149–54. doi: 10.2118/950149-g.

Niemunis, A., Wichtmann, T., and Triantafyllidis, T. (2005), "A high-cycle accumulation model for sand", *Computers and Geotechnics*, 32/4: 245–63. doi: 10.1016/j.compgeo.2005.03.002.

Nikitas, G., Vimalan, N. J., and Bhattacharya, S. (2016), "An innovative cyclic loading device to study long term performance of offshore wind turbines", *Soil Dynamics and Earthquake Engineering*, 82: 154–60. doi: 10.1016/J.SOILDYN.2015.12.008.

O'Sullivan, R. (2020), *Offshore Wind in Europe Key trends and statistics 2020*, vol. 3, tech. rep. 2, 14–7.

O'Sullivan, R., and Guillet, G. (2022), *Financing and investment trends: The European Wind Industry in 2021*, tech. rep. (WindEurope), 1–40, https://windeurope.org/intelligence-platform/product/financing-and-investment-trends-2021/.

Okamura, M., and Inoue, T. (2012), "Preparation of fully saturated models for liquefaction study", *International Journal of Physical Modelling in Geotechnics*, 12/1: 39–46. doi: 10.1680/ijpmg.2012.12.1.39.

Page, A., Klinkvort, R. T., Bayton, S. M., Zhang, Y., and Jostad, H. P. (2021), "A procedure for predicting the permanent rotation of monopiles in sand supporting offshore wind turbines", *Marine Structures*, 75: 102813. doi: 10.1016/J.MARSTRUC.2020.102813.

Page, A., Næss, V., De Vaal, J. B., Eiksund, G. R., and Nygaard, T. A. (2019), "Impact of foundation modelling in offshore wind turbines: Comparison between simulations and field data", *Marine Structures*, 64: 379–400. doi: 10.1016/J.MARSTRUC.2018.11.010.

Porcino, D., and Diano, V. (2017), "The influence of non-plastic fines on pore water pressure generation and undrained shear strength of sand-silt mixtures", *Soil Dynamics and Earthquake Engineering*, 101: 311–21. doi: 10.1016/J.SOILDYN.2017.07.015.

Qadimi, A., and Mohammadi, A. (2014), "Evaluation of state indices in predicting the cyclic and monotonic strength of sands with different fines contents", *Soil Dynamics and Earthquake Engineering*, 66: 443–58. doi: 10.1016/J.SOILDYN.2014.08.002.

Qi, S., and Knappett, J. A. (2022), "Effect of soil permeability on soil–structure and structure–soil–structure interaction of low-rise structures", *Géotechnique*, 72/9: 784–99. doi: 10.1680/jgeot.20.P.109.

Rahman, M. M., Lo, S. R., and Baki, M. A. L. (2011), "Equivalent granular state parameter and undrained behaviour of sand–fines mixtures", *Acta Geotechnica*, 6/4: 183–94. doi: 10.1007/s11440-011-0145-4.

Rahman, M. M., Lo, S. R., and Dafalias, Y. F. (2014), "Modelling the static liquefaction of sand with low-plasticity fines", *Geotechnique*, 64/11: 881–94. doi: 10.1680/geot.14.P.079.

Rahman, M. M., Lo, S. R., and Gnanendran, C. T. (2008), "On equivalent granular void ratio and steady state behaviour of loose sand with fines", *Canadian Geotechnical Journal*, 45/10: 1439–56. doi: 10.1139/T08-064.

RenewableUK (2025), *Global Offshore Wind pipeline June 2025*, https://www.renewableuk.com/energypulse/reports/global-offshore-wind-pipeline-june-2025/.

Retsch GmbH (2018), *Manual: Evaluation Software CAMSIZER P4*, tech. rep.

Richards, I. (2019), "Monopile foundations under complex cyclic lateral loading", PhD thesis (University of Oxford), 239pp.

Robertson, P. K. (2009), "Interpretation of cone penetration tests - A unified approach", *Canadian Geotechnical Journal*, 46/11: 1337–55. doi: 10.1139/T09-065.

Roscoe, K. H., Schofield, A. N., and Wroth, C. P. (1958), "On The Yielding of Soils", *Géotechnique*, 8/1: 22–53. doi: 10.1680/geot.1958.8.1.22.

Rosquoet, F., Thorel, L., Garnier, J., and Canepa, Y. (2007), "Lateral cyclic loading of sand-installed piles", *Soils and Foundations*, 47/5: 821–32. doi: 10.3208/sandf.47.821.

Rowe, P. W., and Barden, L. (1964), "Importance of Free Ends in Triaxial Testing", *Journal of the Soil Mechanics and Foundations Division*, 90/1: 1–27. doi: 10.1061/JSFEAQ.0000586.

Ryan, G., Adcock, T. A., and McAdam, R. A. (2024*a*), "Influence of soil plasticity models on offshore wind turbine response", *Wind Energy*, 27/2: 131–51. doi: 10.1002/we.2876.

Ryan, G., McAdam, R. A., and Adcock, T. A. (2024*b*), "Influence of Non-linear Wave Load Models on Monopile Supported Offshore Wind Turbines for Extreme Conditions", *Ocean Engineering*.

Rychlik, I. (1987), "A new definition of the rainflow cycle counting method", *International Journal of Fatigue*, 9/2: 119–21. doi: 10.1016/0142-1123(87)90054-5.

Salgado, R., Bandini, P., Member, S., and Karim, A. (2000), "Shear Strength and Stiffness of Silty Sand", *Journal of Geotechnical and Geoenvironmental Engineering*, 126/5: 451–62. doi: 10.1061/(ASCE)1090-0241(2000)126:5(451).

Sarsby, R. W., Kalteziotis, N., and Haddad, E. H. (1980), "Bedding error in triaxial tests on granular media", *Géotechnique*, 30/3: 302–9. doi: 10.1680/geot.1980.30.3.302.

Shahabi, A. A., Das, B. M., and Tarquin, A. J. (1985), "Empirical relation for coefficient of permeability of sand", *International Journal of Rock Mechanics and Mining Sciences & Geomechanics Abstracts*, 22/4: 116. doi: 10.1016/0148-9062(85)93025-6.

Shirley, D. J., and Hampton, L. D. (1978), "Shear-wave measurements in laboratory sediments", *The Journal of the Acoustical Society of America*, 63/2: 607–13. doi: 10.1121/1.381760.

Stewart, H. E. (1986), "Permanent strains from cyclic variable-amplitude loadings", *Journal of Geotechnical Engineering*, 112/6: 646–60. doi: 10.1061/(ASCE)0733-9410(1986)112:6(646).

Suzuki, Y., Carotenuto, P., Dyvik, R., and Jostad, H. P. (2020), "Experimental study of modeling partially drained dense sand behavior in monotonic triaxial compression loading tests", *Geotechnical Testing Journal*, 43/5. doi: 10.1520/GTJ20190097.

Sze, H. Y., and Yang, J. (2014), "Failure Modes of Sand in Undrained Cyclic Loading: Impact of Sample Preparation", *Journal of Geotechnical and Geoenvironmental Engineering*, 140/1: 152–69. doi: 10.1061/(asce)gt.1943-5606.0000971.

Tafili, M., Knittel, L., Gauger, V., Wichtmann, T., and Stutz, H. H. (2024), "Experimental study on monotonic to high-cyclic behaviour of sand-silt mixtures", *Acta Geotechnica*, 19/7: 4227–40. doi: 10.1007/S11440-023-02126-6/TABLES/5.

Taiebat, M., and Dafalias, Y. F. (2008), "SANISAND: Simple anisotropic sand plasticity model", *International Journal for Numerical and Analytical Methods in Geomechanics*, 32/8: 915–48. doi: 10.1002/nag.651.

Takahashi, A., Omura, N., Kobayashi, T., Kamata, Y., and Inagaki, S. (2022), "Centrifuge model tests on large-diameter monopiles in dense sand subjected to two-way lateral cyclic loading in short-term", *Soils and Foundations*, 62/3: 101148. doi: 10.1016/j.sandf.2022.101148.

Tamang, B., Kim, U., Jin, J., Lee, S., and Kim, Y. (2022), "Undrained monotonic shear behavior of sand mixed with a small amount of fines content", *Acta Geotechnica*, 2. doi: 10.1007/s11440-022-01776-2.

Tasiopoulou, P., Chaloulos, Y., Gerolymos, N., Giannakou, A., and Chacko, J. (2021), "Cyclic lateral response of OWT bucket foundations in sand: 3D coupled effective stress analysis with Ta-Ger model", *Soils and Foundations*, 61/2: 371–85. doi: 10.1016/j.sandf.2020.12.002.

Tatsuoka, F., Teachavorasinskun, S., Dong, J., Kohata, Y., and Sato, T. (1994), "Importance of Measuring Local Strains in Cyclic Triaxial Tests on Granular Materials", in *Dynamic Geotechnical Testing II* (100 Barr Harbor Drive, PO Box C700, West Conshohocken, PA 19428-2959: ASTM International), 288–8. doi: 10.1520/STP13220S, http://www.astm.org/doiLink.cgi?STP13220S.

Thevanayagam, S. (2007), "Intergrain contact density indices for granular mixes - I: Framework", *Earthquake Engineering andd Engineering Vibration*, 6/2: 123–34.

Thevanayagam, S., Fiorillo, M., and Liang, J. (2000), "Effect of Non-Plastic Fines on Undrained Cyclic Strength of Silty Sands", in *Soil Dynamics and Liquefaction 2000* (Reston, VA: American Society of Civil Engineers), 77–91. doi: 10.1061/40520(295)6, http://ascelibrary.org/doi/10.1061/40520%28295%296.

Thevanayagam, S., Shenthan, T., Mohan, S., and Liang, J. (2002), "Undrained Fragility of Clean Sands, Silty Sands, and Sandy Silts", *Journal of Geotechnical and Geoenvironmental Engineering*, 128/10: 849–59. doi: 10.1061/(ASCE)1090-0241(2002)128:10(849).

Theyse, H. L., Legge, F. T., Pretorius, P. C., and Wolff, H. (2007), "A Yield Strength Model for Partially Saturated Unbound Granular Material", *Road Materials and Pavement Design*, 8/3: 423–48. doi: 10.1080/14680629.2007.9690082.

Vaid, Y. P., and Negussey, D. (1984), "Relative Density of Pluviated Sand Samples", *Soils and Foundations*, 24/2: 101–5. doi: 10.3208/SANDF1972.24.2{_}101.

Vaid, Y. P., and Negussey, D. (1988), "Preparation of Reconstituted Sand Specimens", *Advanced Triaxial Testing of Soil and Rock*: 405–5. doi: 10.1520/stp29090s.

Vaid, Y. P., Sivathayalan, S., and Stedman, D. (1999), "Influence of Specimen-Reconstituting Method on the Undrained Response of Sand", *Geotechnical Testing Journal*, 22/3: 187–95. doi: 10.1520/gtj11110j.

Villalobos Jara, F. (2006), "Model testing of foundations for offshore wind turbines", PhD thesis (University of Oxford). doi: 10.5287/ORA-M8GAAMEYK.

Wallace, S. (2021), *Fugro Test method: Particle Density: EUAF-FGBM-SOIL-TM-401*, tech. rep. (Wallingford: Fugro Marine GB Ltd.).

Watanabe, K., and Kusakabe, O. (2013), "Reappraisal of loading rate effects on sand behavior in view of seismic design for pile foundation", *Soils and Foundations*, 53/2: 215–31. doi: 10.1016/j.sandf.2013.02.003.

Wichtmann, T., Niemunis, A., and Triantafyllidis, T. (2005), "Strain accumulation in sand due to cyclic loading: Drained triaxial tests", *Soil Dynamics and Earthquake Engineering*, 25/12: 967–79. doi: 10.1016/j.soildyn.2005.02.022.

Wichtmann, T., Niemunis, A., and Triantafyllidis, T. (2007), "Strain accumulation in sand due to cyclic loading: Drained cyclic tests with triaxial extension", *Soil Dynamics and Earthquake Engineering*, 27/1: 42–8. doi: 10.1016/j.soildyn.2006.04.001.

Wichtmann, T., Niemunis, A., and Triantafyllidis, T. (2010*a*), "On the determination of a set of material constants for a high-cycle accumulation model for non-cohesive soils", *International Journal for Numerical and Analytical Methods in Geomechanics*, 34/4: 409–40. doi: 10.1002/nag.821.

Wichtmann, T., Niemunis, A., and Triantafyllidis, T. (2010*b*), "Strain accumulation in sand due to drained cyclic loading: On the effect of monotonic and cyclic preloading (Miner's rule)", *Soil Dynamics and Earthquake Engineering*, 30/8: 736–45. doi: 10.1016/j.soildyn.2010.03.004.

Wichtmann, T., Steller, K., and Triantafyllidis, T. (2020), "On the influence of the sample preparation method on strain accumulation in sand under high-cyclic loading", *Soil Dynamics and Earthquake Engineering*, 131/April 2018: 106028. doi: 10.1016/j.soildyn.2019.106028.

Wichtmann, T., and Triantafyllidis, T. (2004), "Influence of a cyclic and dynamic loading history on dynamic properties of dry sand, part II: Cyclic axial preloading", *Soil Dynamics and Earthquake Engineering*, 24/11: 789–803. doi: 10.1016/j.soildyn.2004.05.002.

Wichtmann, T., and Triantafyllidis, T. (2015), "An experimental database for the development, calibration and verification of constitutive models for sand with focus to cyclic loading: part I—tests with monotonic loading and stress cycles", *Acta Geotechnica*, 11/4: 739–61. doi: 10.1007/s11440-015-0402-z.

Wichtmann, T., and Triantafyllidis, T. (2017), "Strain accumulation due to packages of cycles with varying amplitude and/or average stress – On the bundling of cycles and the loss of the cyclic preloading memory", *Soil Dynamics and Earthquake Engineering*, 101: 250–63. doi: 10.1016/J.SOILDYN.2017.07.012.

Wolf, J., Woolf, D., and Bricheno, L. (2020), "Impacts of climate change on storms and waves relevant to the coastal and marine environment around the UK", *MCCIP Science Review 2020*: 132–57. doi: 10.14465/2020.arc07.saw.

Wood, F. M., Yamamuro, J. A., and Lade, P. V. (2008), "Effect of depositional method on the undrained response of silty sand", *Canadian Geotechnical Journal*, 45/11: 1525–37. doi: 10.1139/T08-079.

Wroth, C. P., and Bassett, R. H. (1965), "A Stress–Strain Relationship for the Shearing Behaviour of a Sand", *Géotechnique*, 15/1: 32–56. doi: 10.1680/geot.1965.15.1.32.

Xu, L. Y., Cai, F., Chen, W. Y., Zhang, J. Z., Pan, D. D., Wu, Q., and Chen, G. X. (2021), "Undrained cyclic response of a dense saturated sand with various grain sizes and contents of nonplastic fines: Experimental analysis and constitutive modeling", *Soil Dynamics and Earthquake Engineering*, 145: 106727. doi: 10.1016/j.soildyn.2021.106727.

Yamamuro, J. A., and Lade, P. V. (1997), "Static liquefaction of very loose sands", *Canadian Geotechnical Journal*, 34/6: 905–17. doi: 10.1139/T97-057/ASSET/T97-057.FP.PNG{_}V03.

Yang, J., Liu, X., Rahman, M. M., Lo, S. R., Goudarzy, M., and Schanz, T. (2018), "Shear wave velocity and stiffness of sand: The role of non-plastic fines", *Geotechnique*, 68/10: 931–4. doi: 10.1680/jgeot.16.D.006.

Yang, J., Wei, L. M., and Dai, B. B. (2015), "State variables for silty sands: Global void ratio or skeleton void ratio?", *Soils and Foundations*, 55/1: 99–111. doi: 10.1016/j.sandf.2014.12.008.

Yang, Z. X., Lit, X. S., and Yang, J. (2008), "Quantifying and modelling fabric anisotropy of granular soils", *Geotechnique*, 58/4: 237–48. doi: 10.1680/GEOT.2008.58.4.237.

Yao, T., and Li, W. (2023), "Effect of initial fabric from sample preparation on the mechanical behaviour of a carbonate sand from the South China Sea", *Engineering Geology*, 326/November 2022: 107311. doi: 10.1016/j.enggeo.2023.107311.

Yoshimine, M., and Ishihara, K. (1998), "Flow potential of sand during liquefaction", *Soils and Foundations*, 38/3: 189–98. doi: 10.3208/SANDF.38.3{_}189.

Zeghal, M., and Tsigginos, C. (2015), "A micromechanical analysis of the effect of fabric on low-strain stiffness of granular soils", *Soil Dynamics and Earthquake Engineering*, 70: 153–65. doi: 10.1016/j.soildyn.2014.12.018.

Zhao, C., Koseki, J., and Sasaki, T. (2018), "Image based local deformation measurement of saturated sand specimen in undrained cyclic triaxial tests", *Soils and Foundations*, 58/6: 1313–25. doi: 10.1016/J.SANDF.2018.07.008.

Zhu, B., Ren, J., Wu, L. y., Kong, D., Ye, G. l., Yang, Q., and Lai, Y. (2020), "Effect of Loading Rate on Lateral Pile-Soil Interaction in Sand Considering Partially Drained Condition", *China Ocean Engineering*, 34/6: 772–83. doi: 10.1007/s13344-020-0070-0.

Zhu, B., Ren, J., Yuan, S., Zhu, J., Yang, Q., Gao, Y., and Kong, D. (2021), "Centrifuge Modeling of Monotonic and Cyclic Lateral Behavior of Monopiles in Sand", *Journal of Geotechnical and Geoenvironmental Engineering*, 147/8: 04021058. doi: 10.1061/(asce)gt.1943-5606.0002566.

Zlatovic, S., and Ishihara, K. (1997), "Normalized behaviour of Very Loose Non-Plastic Soils: Effects of Fabric", *Japanese Geotechnical Society*, 37/4: 47–56.